Author:
Nave, Sandrine

Title:
Phase behaviour and interfacial properties of double-chain anionic surfactants.

PHASE BEHAVIOUR AND INTERFACIAL PROPERTIES OF DOUBLE-CHAIN ANIONIC SURFACTANTS

by

SANDRINE NAVE

A thesis submitted to the University of Bristol in accordance with the requirements of the degree of Doctor of Philosophy in the School of Chemistry, Faculty of Science.

June 2001

Word count - fifty six thousands eight hundred and sixty one

ABSTRACT

The adsorption and aggregation properties of eighteen anionic di-chain sodium sulfosuccinates have been studied in aqueous and microemulsion systems. The compounds were (*i*) linear ("di-C*n*SS"), (*ii*) isomeric branched ("AOTs"), or (*iii*) phenyl-tipped ("di-PhC*n*SS") analogues of the branched double-chain sodium 2-ethylhexylsulfosuccinate (Aerosol-OT or AOT). In addition, two sodium sulfoglutaconates with selected chain (linear and branched structure) were studied. These were also AOT-analogues but with a modified head group (one extra -CH_2- spacer group). All surfactants were synthesised and highly purified to investigate on the interactions between molecular structure and surfactant performances.

Tensiometry and neutron reflection were used to quantify adsorption and molecular packing at the air-water interface, whereas phase stability studies and Small-Angle Neutron Scattering (SANS) were used to characterise microemulsion formation and structure of the aggregates in oil-water systems. Branching the hydrophobic moiety and/or substitution of one terminal methyl for a phenyl group had significant effects on the physico-chemical properties of both interfaces.

Tensiometric measurements on surfactant aqueous systems showed that surface tensions, efficiency and effectiveness are mainly affected by variations in tail structure (in particular chain length) rather than in head groups. In addition molecular packing, and even minor structural changes such as those observed in the AOTs series, could be related to surfactant molecular geometry. For the branched surfactants, a "branching ratio" was derived, expressed in terms of extent and position of each alkyl branch in the tail, that accounted well for the trends observed in aggregation and interfacial packing.

In oil-water systems, phase behaviour studies showed that only compounds with a minimum "disorder" in their hydrophobic group (e.g., by branching and/or substitution for phenyl terminal group) formed simple ternary water-in-oil microemulsions. None of the di-C*n*SS series, for instance, stabilised such systems unless a co-surfactant was added. SANS measurements showed that all systems contained spherical water droplets stabilised by a surfactant monolayer, and just like at the air-water interface, for constant head group structure, molecular packing was correlated to surfactant tail structures. Within the AOTs series, changes in molecular architecture had very little effect on surfactant performance as microemulsifiers, whereas temperature appeared to be the most significant factor for microemulsion formation. This effect was related to the different aqueous solubility of each surfactant as a function of temperature. Studies of Winsor microemulsion phase progression by interfacial tension measurements in salt/water-surfactant-oil systems confirmed the major role of surfactant aqueous solubility in dictating the microemulsion phase behaviour.

ACKNOWLEDGEMENTS

I would firstly like to thank Dr. Julian Eastoe for all his advice and invaluable support throughout the project. His keenness and natural enthusiasm has given me an even greater enjoyment of the subject.

I would also like to acknowledge Dr. Richard Heenan at the Rutherford lab for all his help in running neutron scattering experiments and use of his data analysis program, Alan Pitt (Kodak, Ltd.) for supplying some of the materials and sharing his extensive knowledge about surfactants with us, Prof. Hirofumi Okabayashi and his research group at the Nagoya Institute of Technology for all their help and hospitality during my visit to their laboratory, and all the technical staff in the Bristol chemistry department.

Of course, special thanks go to past and present occupants of W302 for moral support and for keeping the lab so bubbly during weekends. In particular, thanks go to Alex, the so excellent 'computer man', Alison and Ali for their valuable FISHing advice, and last but not least, thank you, Ray, for timing our tea breaks.

AUTHOR'S DECLARATION

The work described in this thesis was undertaken in the Department of Physical and Theoretical Chemistry within the School of Chemistry at the University of Bristol, under the supervision of Dr Julian Eastoe between November 1997 and June 2001. This thesis is the original work of the author unless otherwise stated. No part of this work has previously been submitted for a degree at this or any other university. The views expressed in this thesis are those of the author and not of the University of Bristol.

Bristol, June 28th 2001

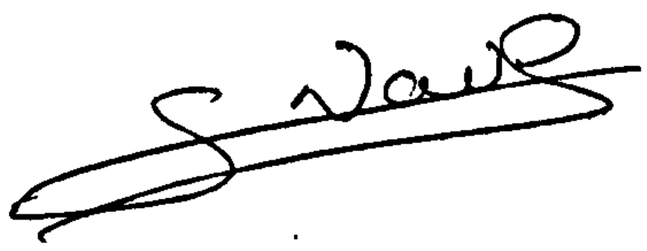

Sandrine Nave

PUBLISHED PAPERS

ARISING FROM THIS THESIS

Micellization of hydrocarbon surfactants in supercritical carbon dioxide
Eastoe, J.; Paul, A.; Nave, S.; Steytler, D. C.; Robinson, B. H.; Rumsey, E.; Thorpe, M; Heenan, R. K.
Journal of the American Chemical Society **2001**, *123*, 988-989.

What is so special about aerosol-OT? 1. Aqueous systems
Nave, S.; Eastoe, J.; Penfold, J.
Langmuir **2000**, *16*, 8733-8740.

What is so special about aerosol-OT? 2. Microemulsion systems
Nave, S.; Eastoe, J.; Heenan, R. K.; Steytler, D.; Grillo, I.
Langmuir **2000**, *16*, 8741-8748.

Adsorption of ionic surfactants at the air-solution interface
Eastoe, J.; Nave, S.; Downer, A.; Paul, A.; Rankin, A.; Tribe, K.; Penfold, J.
Langmuir **2000**, *16*, 4511-4518.

Infrared absorption spectra of Aerosol-OT homologous sodium dialkylsulfosuccinates and the effect of crystal polymorphism on the environment of the succinate segment
Nagasoe, Y.; Ichiyanagi, N.; Okabayashi, H.; Nave, S.; Eastoe, J.; O'Connor, C. J.
Colloid and Polymer Science **1999**, *277*, 1051-1057.

Raman scattering spectra of Aerosol-OT homologous sodium dialkylsulfosuccinates and the environment of their hydrophobic chains
Nagasoe, Y.; Ichiyanagi, N.; Okabayashi, H.; Nave, S.; Eastoe, J.; O'Connor, C. J.
Colloid and Polymer Science **1999**, *277*, 947-956.

Raman and IR spectroscopic studies of the interaction between counterion and polar group in self-assembled systems of AOT-homologous "sodium dialkyl sulfosuccinates"
Nagasoe, Y.; Ichiyanagi, N.; Okabayashi, H.; Nave, S.; Eastoe, J.; O'Connor, C. J.
Physical Chemistry Chemical Physics **1999**, *1*, 4395-4407.

What is so special about aerosol-OT? 3. Modification of the head group
Nave, S.; Eastoe, J.; Steytler, D.; Grillo, I.
(to be published).

TABLE OF CONTENTS

LIST OF TABLES

LIST OF FIGURES

PROJECT OVERVIEW

The aim of this research project is to shed light on the properties of surfactant interfacial film structure, with particular reference to Aerosol-OT based-systems, and to identify molecular requirements for surfactants to give enhanced microemulsion stability. The structure of this thesis is set out in the chapter descriptions given below.

- **Chapter 1** is a brief introduction to surfactants in general – i.e., chemistry, uses and development – followed by a short description of the aims of this research work.

- **Chapters 2** and **3** cover some of the basic theory behind surfactant adsorption and aggregation properties in aqueous and microemulsion systems respectively.

- **Chapter 4** details the preparative and analytical methods used for synthesis, purification and analytical characterisation of the surfactants.

- **Chapter 5** describes important findings on aqueous properties of double-chained surfactants. Experimental details and results of methods used to characterise adsorption and aggregation properties of sulfosuccinate surfactants in water are then presented.

- **Chapter 6** deals with the formation and stability of microemulsions formed by such compounds. A summary of recent research on microemulsions stabilised by double-chained surfactants is first introduced.

- **Chapter 7** presents the adsorption and aggregation behaviour of two sodium sulfoglutaconate surfactants at both interfaces. These systems have modified head groups with respect to succinates like normal AOT. Results are discussed with particular reference to sulfosuccinate analogues.

CHAPTER 1

INTRODUCTION

1.1 SURFACTANTS IN COLLOIDAL SYSTEMS

The term *colloid* (which means "glue" in Greek) was first introduced in 1861 by Thomas Graham to describe the "pseudosolutions" in aqueous systems of silver chloride, sulfur, and Prussian blue which were prepared by Francesco Selmi in the mid-nineteenth century [1]. Such systems were characterised by a lack of sedimentation under the influence of gravity, as well as low diffusion rates. Graham thus deduced that the colloidal size range is approximately 1 μm down to 1 nm (i.e., 10^{-6} – 10^{-9} m). This characteristic still holds today and colloids are generally described as systems consisting of one substance finely dispersed in another. These substances are referred to as the dispersed phase and dispersion medium (or continuous phase) respectively, and can be a solid, a liquid, or a gas. Such combinations together with large surface areas associated with the characteristic size of colloidal particles give rise to a large variety of systems, practical applications and interfacial phenomena.

Amongst these systems, the most common and ancient class is probably the *lyophobic* ("liquid-hating") colloids, composed of insoluble or immiscible components. They can be traced back to the 1850's when Michael Faraday prepared colloidal gold sols, which involve solid particles in water [2]. More commonly encountered examples of lyophobic colloids are milk (liquid fat dispersed as fine drops in an aqueous phase), smoke (solid particles dispersed in air), fog (small liquid droplets dispersed in air), paints (small solid particles dispersed in liquid), jelly (large protein molecules dispersed in water), and bone (small particles of calcium phosphate dispersed in a solid matrix of collagen). A second and more recent class includes the *lyophilic* ("liquid-loving")

colloids, which are solutions that form spontaneously and are thermodynamically stable. These systems consist of solute molecules that are polymers (i.e., of much larger size than the solvent molecules), and as such form a large and distinct area of research (polymer science).

Another major group of colloidal systems, also classified as lyophilic, is that of the so-called *association colloids*. These are aggregates of *amphiphilic* (both "oil and water-loving") molecules that associate in a dynamic and thermodynamically driven process that may be simultaneously a molecular solution and a true colloidal system. Such molecules are commonly termed "surfactants", a contraction of the term *surface-active agents*. As will be introduced below and described in more detail in Chapter 2, surfactants are an important and versatile class of chemicals. Due to their dual nature, they are associated with many useful interfacial phenomena, e.g., wetting, and as such are found in many diverse industrial products and processes.

1.2 CHARACTERISTIC FEATURES OF SURFACTANTS

Surface-active agents are organic molecules that, when dissolved in a solvent at low concentration, have the ability to adsorb (or locate) at interfaces, thereby altering significantly the physical properties of those interfaces. The term "interface" is commonly employed here to describe the boundary in liquid/liquid, solid/liquid and gas/liquid systems, although in the latter case the term "surface" can also be used. This adsorption behaviour can be attributed to the solvent nature and to a chemical structure for surfactants that combine both a polar and a non-polar (amphiphilic) group into a single molecule. To accommodate for their dual nature, amphiphiles therefore "sit" at interfaces so that their lyophobic moiety keeps away from strong solvent interactions while the lyophilic part remains in solution. Since water is the most common solvent, and is the liquid of most academic and industrial interest, amphiphiles will be described with regard to their "hydrophilic" and "hydrophobic" moieties, or "head" and "tail" respectively.

Adsorption is associated with significant energetic changes since the free energy of a surfactant molecule located at the interface is lower than that of a molecule solubilised in either bulk phase. Accumulation of amphiphiles at the interface (liquid/liquid or gas/liquid) is therefore a spontaneous process and results in a decrease of the interfacial (surface) tension. However, such a definition applies to many substances: medium- or long-chain alcohols are surface active (e.g., *n*-hexanol, dodecanol) but these are not considered as surfactants. True surfactants are distinguished by an ability to form oriented monolayers at the interface (here air/water or oil/water) and, most importantly, self-assembly structures (micelles, vesicles) in bulk phases. They also stand out from the more general class of surface-active agents owing to emulsification, dispersion, wetting, foaming or detergency properties.

Both adsorption and aggregation phenomena result from the hydrophobic effect [3]; i.e., the expulsion of surfactant tails from water. Basically this originates from water–water intermolecular interactions being stronger than those between water–tail. Finally another characteristic of surfactants, when their aqueous concentration exceeds approximately 40%, is an ability to form liquid crystalline phases (or lyotropic mesophases). These systems consist of extended aggregation of surfactant molecules into large organised structures.

Owing to such a versatile phase behaviour and diversity in colloidal structures, surfactants find application in many industrial processes, essentially where high surface areas, modification of the interfacial activity or stability of colloidal systems are required. The variety of surfactants and the synergism offered by mixed-surfactant systems [4] also explains the ever-growing interest in fundamental studies and practical applications. Listing the various physical properties and associated uses of surfactants is beyond the scope of this thesis. However, a few relevant examples are presented in the following section, giving an idea of their widespread industrial use.

1.3 CLASSIFICATION AND APPLICATIONS OF SURFACTANTS

1.3.1. Types of surfactants

Numerous variations are possible within the structure of both the head and tail group of surfactants. The head group can be charged or neutral, small and compact in size, or a polymeric chain. The tail group is usually a single or double, straight or branched hydrocarbon chain, but may also be a fluorocarbon, or a siloxane, or contain aromatic group(s). Commonly encountered hydrophilic and hydrophobic groups are listed in Tables 1.1 and 1.2 respectively.

Since the hydrophilic part normally achieves its solubility either by ionic interactions or by hydrogen bonding, the simplest classification is based on surfactant head group type, with further subgroups according to the nature of the lyophobic moiety. Four basic classes therefore emerge as:

- the anionics and cationics, which dissociate in water into two oppositely charged species (the surfactant ion and its counterion),
- the non-ionics, which include a highly polar (non charged) moiety, such as polyoxyethylene ($-OCH_2CH_2O-$) or polyol groups,
- the zwitterionics (or amphoterics), which combine both a positive and a negative group.

With the continuous search for improving surfactant properties, new structures have recently emerged that exhibit interesting synergistic interactions or enhanced surface and aggregation properties. These novel surfactants have attracted much interest in the last twenty years and include the catanionics, bolaforms, gemini (or dimeric) surfactants, polymeric and polymerisable surfactants [5,6]. Characteristics and typical examples are shown in Table 1.3. Another important driving force for this research is the need for enhanced surfactant biodegradability. In particular for personal care products and household detergents, regulations [7] require high biodegradability and non-toxicity of each component present in the formulation.

Table 1.1 Common hydrophilic groups found in commercially available surfactants

Class	General structure
Sulfonate	$R–SO_3^- M^+$
Sulfate	$R–OSO_3^- M^+$
Carboxylate	$R–COO^- M^+$
Phosphate	$R–OPO_3^- M^+$
Ammonium	$R_xH_yN^+X^-$ (x = 1-3, y = 4-x)
Quaternary ammonium	$R_4N^+X^-$
Betaines	$RN^+(CH_3)_2CH_2COO^-$
Sulfobetaines	$RN^+(CH_3)_2CH_2CH_2SO_3^-$
Polyoxyethylene (POE)	$R–OCH_2CH_2(OCH_2CH_2)_nOH$
Polyols	Sucrose, sorbitan, glycerol, ethylene glycol, etc
Polypeptide	R–NH–CHR–CO–NH–CHR'–CO–...–CO_2H
Polyglycidyl	$R–(OCH_2CH[CH_2OH]CH_2)_n$ –...–$OCH_2CH[CH_2OH]CH_2OH$

Table 1.2 Common hydrophobic groups used in commercially available surfactants

Group	General structure	
Natural fatty acids	$CH_3(CH_2)_n$	n = 12-18
Petroleum paraffins	$CH_3(CH_2)_nCH_3$	n = 8-20
Olefins	$CH_3(CH_2)_nCH = CH_2$	n = 7-17
Alkylbenzenes	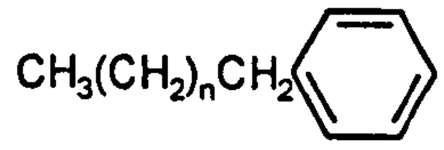	n = 6-10, linear or branched
Alkylaromatics	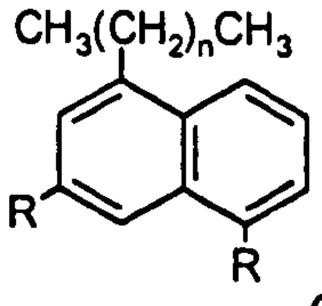	n = 1-2 for water soluble, n = 8 or 9 for oil soluble surfactants
Alkylphenols	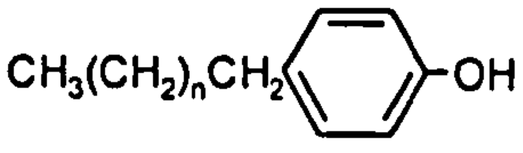	n = 6-10, linear or branched
Polyoxypropylene	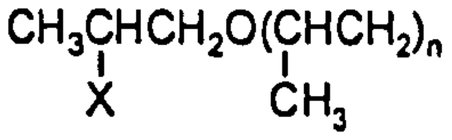	n = degree of oligomerisation, X = oligomerisation initiator
Fluorocarbons	$CF_3(CF_2)_nCOOH$	n = 4-8, linear or branched, or H-terminated
Silicones	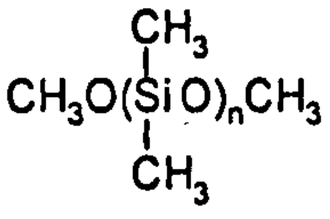	

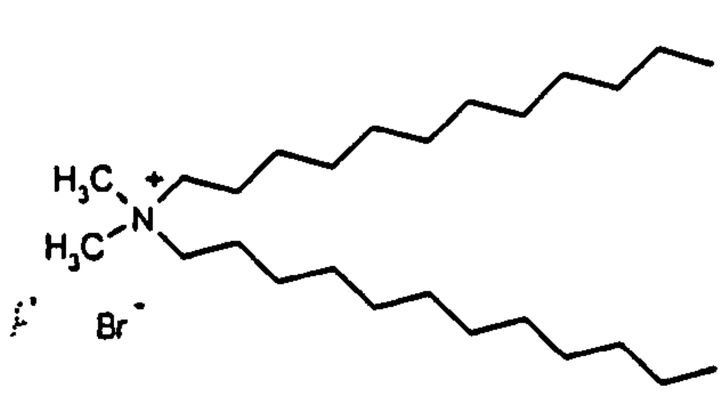

Cationic: *n*-didodecyldimethylammonium bromide (DDAB)

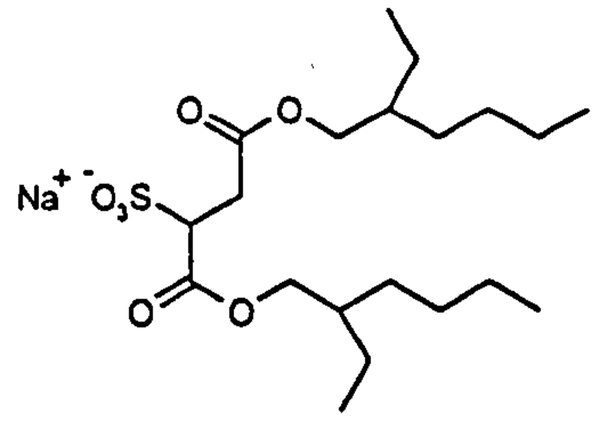

Anionic: Sodium bis(2-ethylhexyl) sulfosuccinate (Aerosol-OT or AOT)

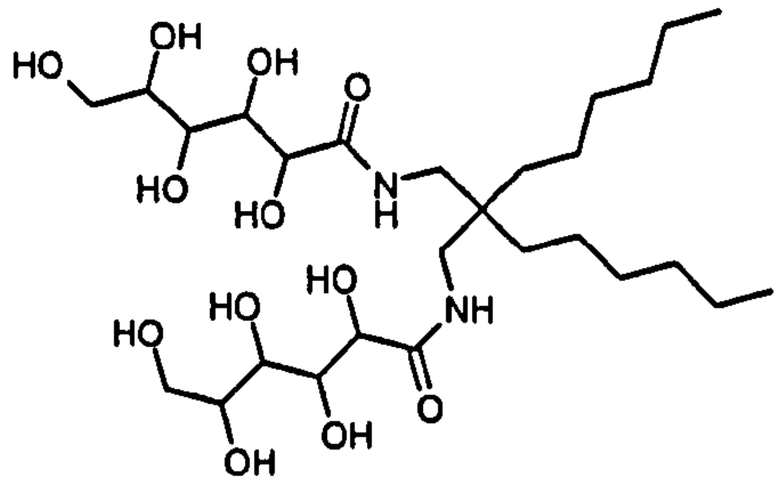

Non-ionic: di(hexyl)glucamide (di-(C6-Glu))

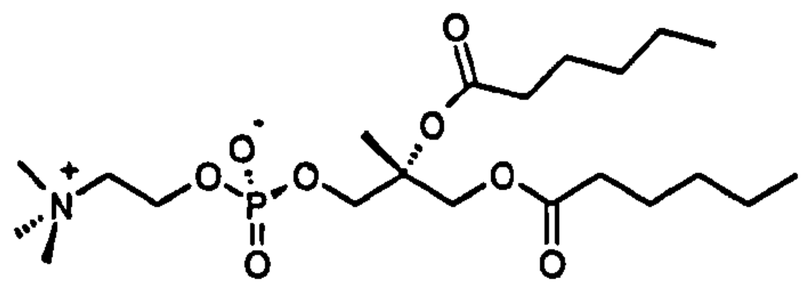

Zwitterionic: di-hexylphosphatidylcholine ((diC6)PC)

Figure 1.1 Chemical structure of typical double-chain surfactants.

Table 1.3 Structural features and examples of new surfactant classes

Classes	Structural characteristics	Example
Catanionic	Equimolar mixture of cationic and anionic surfactants (no inorganic counterion)	*n*-dodecyltrimethylammonium *n*-dodecyl sulfate (DTADS) $C_{12}H_{25}(CH_3)_3N^+ \ ^-O_4SC_{12}H_{25}$
Bolaform	Two charged headgroups connected by a long linear polymethylene chain	Hexadecanediyl-1,16-bis(trimethyl ammonium bromide) $Br^-(CH_3)_3N^+-(CH_2)_{16}-N^+(CH_3)_3Br^-$
Gemini (or dimeric)	Two identical surfactants connected by a spacer close to or at the level of the headgroup	Propane-1,3-bis(dodecyldimethyl ammonium bromide) C_3H_6 -1,3-bis[$(CH_3)_2N^+C_{12}H_{25}Br$]
Polymeric	Polymer with surface active properties	Copolymer of isobutylene and succinic anhydride 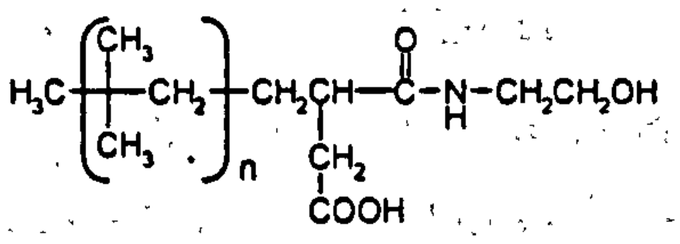
Polymerisable	Surfactant that can undergo homo-polymerisation or copolymerisation with other components of the system	11-(acryloyloxy)undecyltrimethyl ammonium bromide 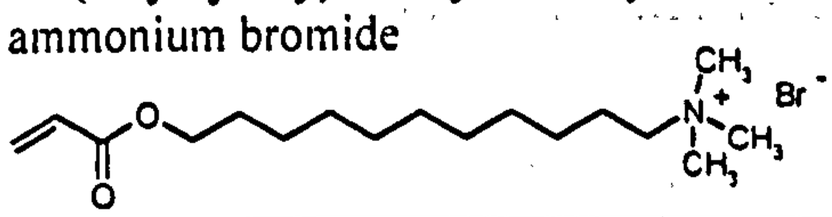

This thesis concentrates on four series of double-chain anionics. which are essentially alkyl sulfonate surfactants. A typical example of such series. widely used in surface chemistry research, is sodium bis(2-ethylhexyl)sulfosuccinate. often referred to by its American Cyanamid trade name Aerosol-OT, or AOT. Its chemical structure is illustrated in Figure 1.1, along with other typical double-chain compounds within the four basic surfactant classes.

1.3.2 Surfactant uses and development

Surfactants may be from natural or synthetic sources. The first category includes naturally occurring amphiphiles such as the lipids, which are surfactants based on glycerol and are vital components of the cell membrane. Also in this group are the so-called "soaps", the first recognised surfactants [8]. These can be traced back to Egyptian times; by combining animal and vegetable oils with alkaline salts a soap-like material was formed, and this was used for treating skin diseases, as well as for washing. Soaps remained the only source of natural detergents from the seventh century till the early twentieth century, with gradually more varieties becoming available for shaving and shampooing, as well as bathing and laundering. In 1916, in response to a World War I-related shortage of fats for making soap, the first synthetic detergent was developed in Germany. Known today simply as detergents, synthetic detergents are washing and cleaning products obtained from a variety of raw materials.

Nowadays, synthetic surfactants are essential components in many industrial processes and formulations [9-11]. Depending on the precise chemical nature of the product, the properties of, for example emulsification, detergency and foaming may be exhibited in varying degree. The number and arrangement of the hydrocarbon groups together with the nature and position of the hydrophilic groups combine to determine the surface-active properties of the molecule. For example C12 to C20 is generally regarded as the range covering optimum detergency, whilst wetting and foaming are best achieved with shorter chain lengths. Structure-performance relationships and chemical compatibility are therefore key elements in surfactant-based formulations, so that much research is devoted to this area.

Amongst the different classes of surfactants, anionics are used in greater volume than any other types, mainly because of the ease and low cost of manufacture. They contain negatively charged head group, e.g., carboxylates ($-CO_2^-$), used in soaps, sulfate ($-OSO_3^-$), and sulfonates ($-SO_3^-$) groups. Their main applications are in detergency, personal care products, emulsifiers and soaps.

Cationics have positively charged head groups – e.g., trimethylammonium ion ($-N(CH_3)_3^+$) – and are mainly involved in applications related to their absorption at surfaces. These are generally negatively charged (e.g., metal, plastics, minerals, fibres, hairs and cell membranes) so that they can be modified upon treatment with cationic surfactants. They are therefore used as anticorrosion and antistatic agents, flotation collectors, fabric softeners, hair conditioners and bactericides.

Non-ionics contain groups with a strong affinity for water due to strong dipole-dipole interactions arising from hydrogen bonding, e.g., ethoxylates ($-(OCH_2CH_2)_m OH$). One advantage over ionics is that the length of both the hydrophilic and hydrophobic groups can be varied to obtain maximum efficiency in use. They find applications in low temperature detergents and emulsifiers.

Zwitterionics constitute the smallest surfactant class due to their high cost of manufacture. They are characterised by excellent dermatological properties and skin compatibility. Because of their low eye and skin irritation, common uses are in shampoos and cosmetics.

1.4 PROJECT AIMS

Considering the variety in the chemistry and applications of surfactant, a key element is to establish the links between molecular structure and physico-chemical action. Then picking or synthesising the compound that will do the job best becomes less like a lottery, and more predictable.

This thesis focuses on the effect of surfactant molecular structure on adsorption and aggregation behaviour in aqueous and microemulsion systems. In particular, surfactant film properties at both interfaces are investigated using conventional physical methods such as tensiometry and conductivity, as well as more advanced techniques such as neutron reflectivity (NR) and small-angle neutron scattering (SANS).

One particular objective of this project is to investigate the effect of chain branching. In particular, the study focuses on the well-known Aerosol-OT, and the reason for its exceptional efficiency as a microemulsifier. By synthesising and characterising a range of branched sodium sulfosuccinates (all AOT-analogues) it should be possible to delineate structure-performance relationships and by comparing these structural variants, to pinpoint the effects of chain branching in AOT itself. From a more general viewpoint, the study should shed light on the physico-chemical origins of microemulsion formation.

A second central objective is to evaluate film rigidities as a function of alkyl chain length in water-in-oil (w/o) microemulsions. To this aim, a family of di-alkyl sulfosuccinates was custom-synthesised and the w/o phase behaviour determined as a function of alkyl chain length. By combining small-angle neutron scattering and tensiometric methods, the microemulsion droplet structure and film rigidities can be obtained. The results should complement those recently obtained for non-ionic [12], cationic [13] and zwitterionic [14] amphiphiles, and allow the separate contributions from surfactant chains and ionic head groups to be identified. At first sight, the film rigidity approach appears rather esoteric since it relies on advanced mathematical principles and physical concepts. However, in a distilled form, the findings from this research could eventually be applied to understanding and improving industrial formulations.

1.5 REFERENCES

1. Evans, D. F.; Wennerström, H. *'The Colloidal Domain'* Wiley-VCH, 1999, New York.
2. Faraday, M., Phil. Trans. Royal. Soc., **1857**, *147*, 145.
3. Tanford, C. *'The Hydrophobic Effect: formation of micelles and biological membranes'* John Wiley & Sons, 1978, USA.
4. Ogino, K.; Abe, M., Eds. *'Mixed Surfactants Systems'* Marcel Dekker, 1993, New York.
5. Robb, I. D. *'Specialist Surfactants'* Blackie Academic & Professional, 1997, London.
6. Holmberg, K. Ed. *'Novel Surfactants'* Marcel Dekker, 1998, New York.
7. Hollis, G. Ed. *'Surfactants UK'* Tergo-Data, 1976.
8. The Soap and Detergent Association home page, http://www.sdahq.org/.
9. Karsa, D. R.; Goode, J. M.; Donnelly, P. J. Eds. *'Surfactants Applications Directory'* Blackie & Son, 1991, London.
10. Dickinson, E. in *'An Introduction to Food Colloids'* Oxford University Press, 1992, Oxford.
11. Solans, C.; Kunieda, H. Eds. *'Industrial Applications of Microemulsions'* Marcel Dekker, 1997, New York.
12. Gradzielski, M.; Langevin, D.; Farago, B. *Phys. Rev. E.* **1996**, *53*, 3900.
13. Eastoe, J.; Sharpe, D.; Heenan, R. K.; Egelhaaf, S. *J. Phys. Chem.* **1997**, *101*, 944.
14. Eastoe, J.; Sharpe, D. *Langmuir* **1997**, *13*, 3289.

CHAPTER 2

AQUEOUS BEHAVIOUR OF SURFACTANTS

Surfactants, literally, are active at a surface and that includes any of the liquid/liquid, liquid/gas or liquid/solid systems, so that the subject is quite broad. This chapter summarises notions relevant to the present research project, with particular emphasis on adsorption and aggregation phenomena at the air-water interface. For a more thorough account of the theoretical background of surfactancy, the reader is referred to specific textbooks and monographs keyed throughout this chapter.

2.1 ADSORPTION OF SURFACTANTS AT INTERFACES

2.1.1 Surface tension and surface activity

Due to the different environment of molecules located at an interface compared to those from either bulk phase, an interface is associated with a surface free energy. At the air-water surface for example, water molecules are subjected to unequal short-range attraction forces and, thus, undergo a net inward pull to the bulk phase. Minimisation of the contact area with the gas phase is therefore a spontaneous process, explaining why drops and bubbles are round. The surface free energy per unit area, defined as the *surface tension* (γ_o), is then the minimum amount of work (W_{min}) required to create new unit area of that interface (ΔA), so $W_{min} = \gamma_o \times \Delta A$. Another, but less accurate, definition of surface tension is given as the force acting normal to the liquid-gas interface per unit length of the resulting thin film on the surface.

A surface-active agent is therefore a substance that at low concentrations adsorbs thereby changing the amount of work required to expand that interface. In particular surfactants can significantly reduce interfacial tension due to their dual chemical nature as introduced in Chapter 1. Considering the air-water boundary, the force driving adsorption is unfavourable hydrophobic interactions within the bulk phase. There, water molecules strongly interact with one another through van der Waals forces and hydrogen bonding, so the presence of amphiphilic molecules dissolved in the bulk phase, through their hydrocarbon group, causes distortion of this solvent structure increasing the free energy of the system. This is known as the hydrophobic effect [1]. Less work is required to bring a surfactant molecule to the surface than a water molecule, so that migration of the surfactant to the surface is a spontaneous and favourable process. At the gas-liquid interface, the result is the creation of new unit area of surface and the formation of an *oriented surfactant monolayer* with the hydrophobic tails pointing out of, and the head group inside, the water phase. The balance against the tendency of the surface to contract under normal surface tension forces causes an increase in the surface (or expanding) pressure π, and therefore a decrease in surface tension of the solution γ. The surface pressure is defined as $\pi = \gamma_o - \gamma$, where γ_o is the surface tension of a clean air-water surface.

Depending on the surfactant molecular structure, adsorption takes place over various concentration ranges and rates, but typically, above a well-defined concentration – the critical micelle concentration (CMC) – micellisation or aggregation takes place. At the CMC, the interface is at (near) maximum coverage and to minimise further free energy, molecules begin to aggregate in the bulk phase. Above the CMC, the system then consists of an adsorbed monomolecular layer, free monomers and micellised surfactant in the bulk, with all these three states in equilibrium. The structure and formation of micelles will be briefly described in Section 2.3. Below the CMC, adsorption is a dynamic equilibrium with surfactant molecules arriving at, and leaving, the surface at equal rate. Nevertheless, a time-averaged value for the surface concentration can be defined and quantified either directly or indirectly using thermodynamic equations (see Section 2.1.2).

Dynamic surface tension – as opposed to the equilibrium quantity – is an important property of surfactant systems as it governs many important industrial and biological applications [2-5]. Examples are printing and coating processes where an equilibrium surface tension is never attained, and a new area of interface is continuously formed. In any surfactant solution, the equilibrium surface tension is not achieved instantaneously and surfactant molecules must first diffuse from the bulk to the surface, then adsorb, whilst also achieving the correct orientation. Therefore, a freshly formed interface of a surfactant solution has a surface tension very close to that of the solvent, and this dynamic surface tension will then decay over a certain period of time to the equilibrium value. This relaxation can range from milliseconds to days depending on the surfactant type and concentration. In order to control this dynamic behaviour, it is necessary to understand the main processes governing transport of surfactant molecules from the bulk to the interface. This area of research therefore attracts much attention and recent developments can be found in references [6-8]. In the present research work, however, the equilibrium surface tension will always be considered.

2.1.2 Surface excess and thermodynamics of adsorption

Following on the formation of an oriented surfactant monolayer, a fundamental associated physical quantity is the *surface excess*. This is defined as the concentration of surfactant molecules in a surface plane, relative to that at a similar plane in the bulk. A common thermodynamic treatment of the variation of surface tension with composition has been derived by Gibbs [9].

An important approximation associated with this Gibbs adsorption equation is the "exact" location of the interface. Consider a surfactant aqueous phase α in equilibrium with vapour β. The interface is a region of indeterminate thickness τ across which the properties of the system vary from values specific to phase α to those characteristic of β. Since properties within this real interface cannot be well defined, a convenient assumption is to consider a mathematical plane, with zero thickness, so that the properties of α and β apply right up to that dividing plane positioned at some specific value X. Figure 2.1 illustrates this ideal system.

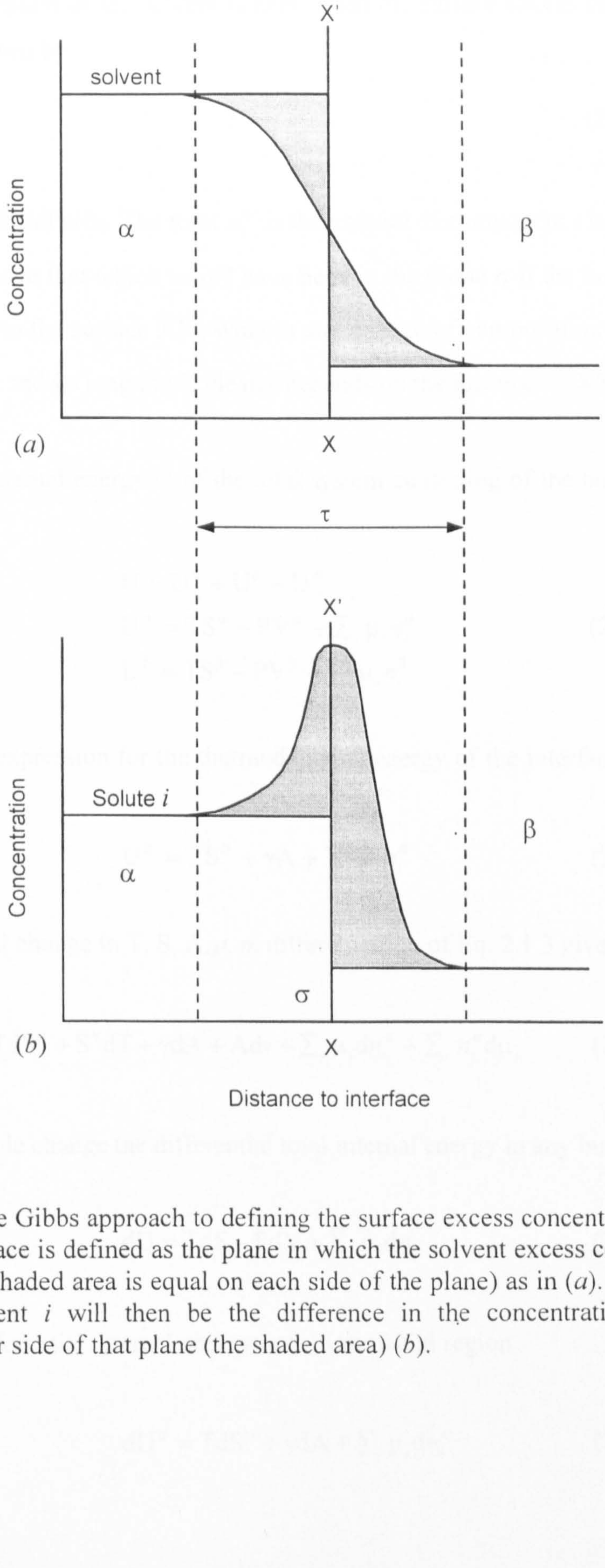

Figure 2.1 In the Gibbs approach to defining the surface excess concentration Γ, the Gibbs dividing surface is defined as the plane in which the solvent excess concentration becomes zero (the shaded area is equal on each side of the plane) as in (*a*). The surface excess of component *i* will then be the difference in the concentrations of that component on either side of that plane (the shaded area) (*b*).

In the definition of the Gibbs dividing surface X is arbitrarily chosen so that the surface excess adsorption of the solvent is zero. Then the surface excess concentration of component *i* is given by

$$\Gamma_i^{\sigma} = \frac{n_i^{\sigma}}{A} \qquad (2.1.1)$$

where A is the interfacial area. The term n_i^{σ} is the amount of component *i* in the surface phase σ over and above that which would have been in the phase σ if the bulk phases α and β had extended to the surface XX', without any change of composition. Γ_i^{σ} may be positive or negative, and its magnitude clearly depends on the location of XX'.

Now consider the internal energy U of the total system consisting of the bulk phases α and β

$$\begin{aligned} U &= U^{\alpha} + U^{\beta} + U^{\sigma} \\ U^{\alpha} &= TS^{\alpha} - PV^{\alpha} + \sum_i \mu_i n_i^{\alpha} \\ U^{\beta} &= TS^{\beta} - PV^{\beta} + \sum_i \mu_i n_i^{\beta} \end{aligned} \qquad (2.1.2)$$

The corresponding expression for the thermodynamic energy of the interfacial region σ is

$$U^{\sigma} = TS^{\sigma} + \gamma A + \sum_i \mu_i n_i^{\sigma} \qquad (2.1.3)$$

For any infinitesimal change in T, S, A, μ, *n*, differentiation of Eq. 2.1.3 gives

$$dU^{\sigma} = TdS^{\sigma} + S^{\sigma}dT + \gamma dA + Ad\gamma + \sum_i \mu_i dn_i^{\sigma} + \sum_i n_i^{\sigma} d\mu_i \qquad (2.1.4)$$

For a small, reversible change the differential total internal energy in any bulk phase is

$$dU = TdS - PdV + \sum_i \mu_i dn_i \qquad (2.1.5)$$

similarly for the differential internal energy in the interfacial region

$$dU^{\sigma} = TdS^{\sigma} + \gamma dA + \sum_i \mu_i dn_i^{\sigma} \qquad (2.1.6)$$

subtracting Eq. 2.1.6 from 2.1.4 leads to

$$S^{\sigma}dT + Ad\gamma + \sum_i n_i^{\sigma} d\mu_i = 0 \qquad (2.1.7)$$

Then at constant temperature, with the surface excess of component *i*, Γ_i^{σ}, as defined in Eq. 2.1.1, the general form of the Gibbs equation is

$$d\gamma = -\sum_i \Gamma_i^{\sigma} d\mu_i \qquad (2.1.8)$$

For a simple system consisting of a solvent and a solute, denoted by the subscripts 1 and 2 respectively, then Eq. 2.1.8 reduces to

$$d\gamma = -\Gamma_1^{\sigma} d\mu_1 - \Gamma_2^{\sigma} d\mu_2 \qquad (2.1.9)$$

Considering the choice of the Gibbs dividing surface position; i.e., so that $\Gamma_1^{\sigma} = 0$, then Eq. 2.1.9 simplifies to

$$d\gamma = -\Gamma_2^{\sigma} d\mu_2 \qquad (2.1.10)$$

where Γ_2^{σ} is the solute surface excess concentration.

The chemical potential is given by

$$\mu_i = \mu_i^{o} + RT \ln a_i \quad \text{so} \quad d\mu_i = \text{cste} + RT d\ln a_i \qquad (2.1.11)$$

where μ_i^{o} is the standard chemical potential of component *i* at 1 Atm and 298 K.

Therefore applying to Eq. 2.1.10 gives the common form of the Gibbs equation for non-dissociating materials (e.g., non-ionic surfactants)

$$d\gamma = -\Gamma_2^{\sigma} RT d\ln a_2 \qquad (2.1.12)$$

or

$$\Gamma_2^{\sigma} = -\frac{1}{RT}\frac{d\gamma}{d\ln a_2} \qquad (2.1.13)$$

For dissociating solutes, such as ionic surfactants of the form R^-M^+ and assuming ideal behaviour below the CMC, Eq. 2.1.12 becomes

$$d\gamma = -\Gamma_R^\sigma d\mu_R - \Gamma_M^\sigma d\mu_M \qquad (2.1.14)$$

If no electrolyte is added, electroneutrality of the interface requires that $\Gamma_R^\sigma = \Gamma_M^\sigma$. Using the mean ionic activities so that $a_2 = (a_R a_M)^{1/2}$ and substituting in Eq. 2.1.14 gives the Gibbs equation for 1:1 dissociating compounds

$$\Gamma_2^\sigma = -\frac{1}{2RT}\frac{d\gamma}{d\ln a_2} \qquad (2.1.15)$$

If swamping electrolyte is introduced (i.e., sufficient salt to make electrostatic effects unimportant) and the same gegenion M^+ as the surfactant is present, then the activity of M^+ is constant and the pre-factor becomes unity, so that Equation 2.1.13 is valid.

For materials that are strongly adsorbed at an interface such as surfactants, a dramatic reduction in interfacial (surface) tension is observed with small changes in bulk phase concentration. The practical applicability of this relationship is that the relative adsorption of a material at an interface, its surface activity, can be determined from measurement of the interfacial tension as a function of solute concentration. Note that in Eq. 2.1.13 and 2.1.15, for dilute surfactant systems, the concentration can be substituted for activity without serious loss of accuracy.

Figure 2.2 shows a typical decay of surface tension of water on increase in surfactant concentration, and how the Gibbs equation (Eq. 2.1.13 or 2.1.15) is used to quantify adsorption at the surface. At low concentrations a gradual decay in surface tension is observed (from the surface tension of pure water i.e., 72.5 mN m^{-1} at 25 °C) corresponding to an increase in the surface excess of component 2 (region A to B). Then at concentrations close to the CMC, the surface tends to a constant value so the surface tension curve is essentially linear (region B to C).

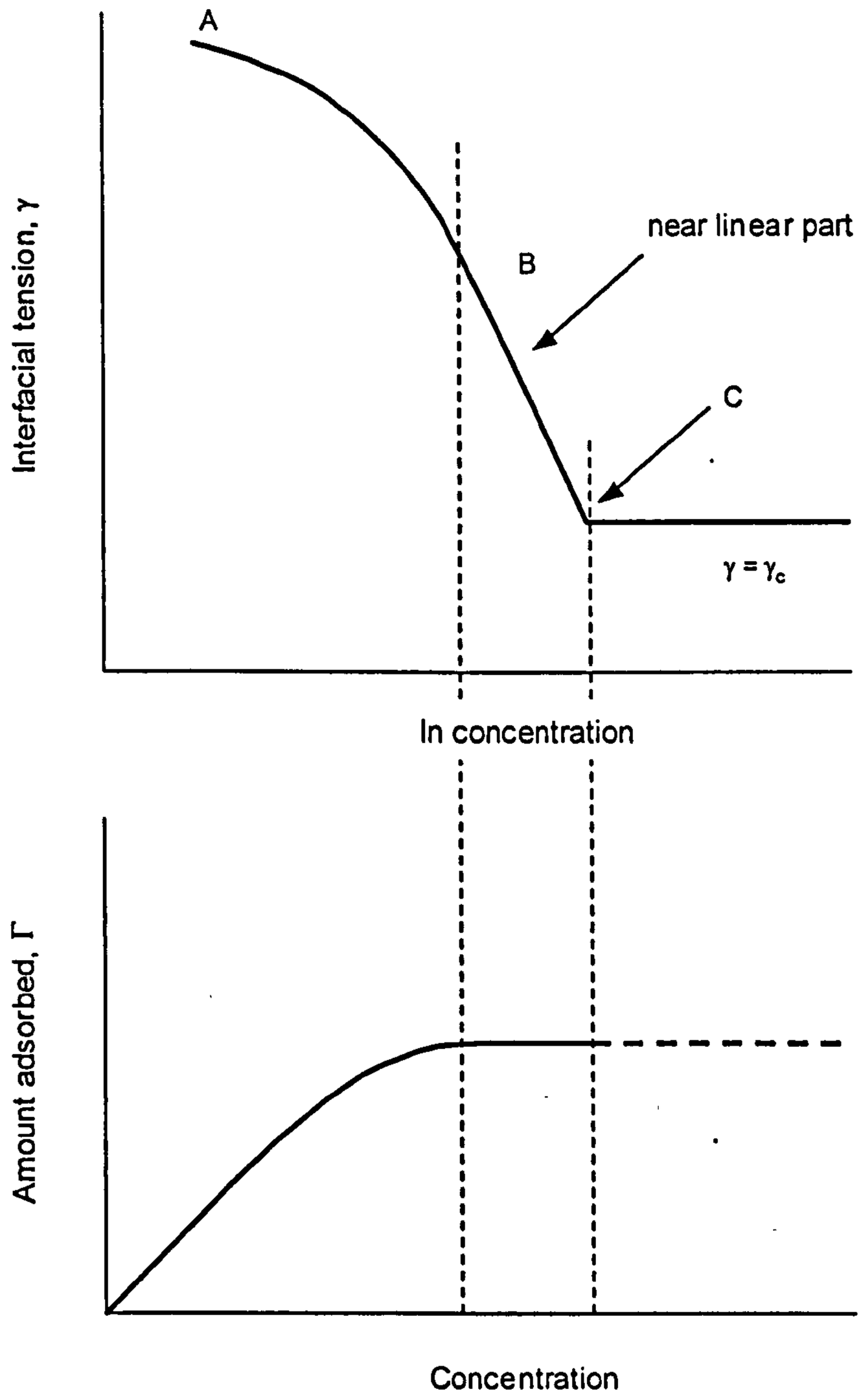

Figure 2.2 Determination of the interfacial adsorption isotherm from surface tension measurement and the Gibbs adsorption equation.

The value for the Gibbs pre-factor in the case of ionic surfactants has recently been a matter of discussion (e.g., refs. 10-13). Of particular concern is the question whether, in the case of ionics, complete dissociation occurs giving rise to a pre-factor of 2, or a depletion layer in the sub-surface could be present so that a somewhat lower pre-factor could be expected. Recent detailed experiments combining tensiometry and neutron reflectivity, which enables direct measurement of the surface excess, have confirmed the use of a pre-factor of 2 in the case of ionics [14], and this will be discussed in more detail in Chapter 5.

Although the Gibbs equation is the most commonly used mathematical relation for adsorption at liquid-liquid and liquid-gas interfaces, other adsorption isotherms have been proposed such as the Langmuir [15], the Szyszkowski [16] and the Frumkin [17] equations. The Gibbs equation itself has been simplified by Guggenheim and Adam with the choice of a different dividing plane and where the interfacial region is considered as a separate bulk phase (of finite volume) [18].

2.1.3 Efficiency and effectiveness of surfactant adsorption

The performance of a surfactant in lowering the surface tension of a solution can be discussed in terms of (1) the concentration required to produce a given surface tension reduction and (2) the maximum reduction in surface tension that can be obtained regardless of the concentration. These are referred to as the surfactant *efficiency* and *effectiveness* respectively.

A good measure of the *surfactant adsorption efficiency* is the concentration of surfactant required to produce a 20 mN m^{-1} reduction in surface tension. At this somewhat pre-determined value, the surfactant concentration is close to the minimum concentration needed to produce maximum adsorption at the interface. This is confirmed by the Frumkin adsorption equation (2.1.16), which relates the reduction in surface tension (or surface pressure π) and surface excess concentration.

$$\gamma_0 - \gamma = \pi = -2.303RT\,\Gamma_m \log\left(1 - \frac{\Gamma_1}{\Gamma_m}\right) \qquad (2.1.16)$$

The maximum surface excess generally lies in the range $1 - 4.4\times10^{-10}$ mol cm^{-2} [19]: solving Eq. 2.1.16 indicates that when the surface tension has been reduced by 20 mN m^{-1}, at 25°C, the surface is 84 – 99.9% saturated. The negative logarithm of such concentration, pC_{20}, is then a useful quantity since it can be related to the free energy change $\Delta G°$ involved in the transfer of a surfactant molecule from the interior of the bulk liquid phase to the interface. The surfactant adsorption efficiency thus relates to the structural groups in the molecule via the standard free energy change of the individual groups (i.e., free energies of transfer of methylene, terminal methyl, and head groups). In particular, for a given homologous series of straight-chain surfactants in water, $CH_3(CH_2)_n$–M, where M is the hydrophilic head group and n is the number of methylene units in the chain, and when the systems are at π = 20 mN m^{-1}, the standard free energy of adsorption is

$$\Delta G° = n\,\Delta G°(\text{-}CH_2\text{-}) + \Delta G°(M) + \Delta G°(CH_3\text{-}) \qquad (2.1.17)$$

Then the adsorption efficiency is directly related to the length of the hydrophobic chain (the hydrophilic group remains the same), viz.

$$-\log(C)_{20} = pC_{20} = n\left[\frac{-\Delta G°(\text{-}CH_2\text{-})}{2.303RT}\right] + \text{constant} \qquad (2.1.18)$$

$\Delta G°(M)$ is considered as a constant and it is assumed that Γ_m does not differ significantly with increasing chain length, and that activity coefficients are unity. The efficiency factor pC_{20} therefore increases linearly with the number of carbon atoms in the hydrophobic chain. This is also described by Traube's rule [20] (Eq. 2.1.19).

$$\text{Log } C_s = B - n \text{ Log } K_T \qquad (2.1.19)$$

C_s is the surfactant concentration, B is a constant, n is the chain length within a homologous series and K_T is Traube's constant. For hydrocarbon straight chain surfactants K_T is usually around 3 [21] or by analogy to Eq. 2.1.18 is given by

$$\frac{C_n}{C_{n+1}} = K_T = \exp\left[\frac{-\Delta G°(-CH_2-)}{2RT}\right] \qquad (2.1.20)$$

For compounds having a phenyl group in the hydrophobic chain it is equivalent to about three and one-half normal $-CH_2-$ groups.

The larger pC_{20} the more efficiently the surfactant is adsorbed at the interface and the more efficiently it reduces surface tension. The other main factors that contribute to an increase in surfactant efficiency are summarised below:

- A straight alkyl chain as the hydrophobic group, rather than a branched alkyl chain containing the same number of carbon atoms.
- A single hydrophilic group situated at the end of the hydrophobic group, rather than one (or more) at a central position.
- A non-ionic or zwitterionic hydrophilic group, rather than an ionic one.
- For ionic surfactants, a reduction in the effective charge by (a) use of a more tightly bound (less hydrated) counterion and (b) increase in ionic strength of the aqueous phase.

The choice of 20 mN m^{-1} as a standard value of surface tension lowering for the definition of adsorption efficiency is convenient but somewhat arbitrary, and is not valid for systems where surfactants differ significantly in maximum surface excess or when the surface pressure is less than 20 mN m^{-1}. Pitt *et al.* [22] circumvented this problem by defining $\Delta\gamma$ as half the surface pressure at the CMC.

The performance of a surfactant can also be discussed in terms of *effectiveness of adsorption*. This is usually defined as the maximum lowering of surface tension γ_{min} regardless of concentration, or as the surface excess concentration at surface saturation Γ_m since it represents the maximum adsorption. γ_{min}, and Γ_m, are controlled mainly by the critical micelle concentration, and for certain ionics by the solubility limit or Krafft temperature T_k, which will be described briefly in Section 2.2.1. The effectiveness of adsorption is an important factor in determining such properties as foaming, wetting, and emulsification, since Γ_m through the Gibbs adsorption equation gives a measure of the interfacial packing.

The efficiency and effectiveness of surfactants do not necessarily run parallel, and it is commonly observed – as shown by Rosen's extensive data listing [19] – that materials producing significant lowering of the surface tension at low concentrations (i.e., they are more efficient) have smaller Γ_m (i.e., they are less effective). In determining surfactant efficiency the role of the molecular structure is primarily thermodynamic, while its role in effectiveness is directly related to the relative size of the hydrophilic and hydrophobic portions of the adsorbing molecule. The area occupied by each molecule is determined either by the hydrophobic chain cross-sectional area, or the area required for closest packing of head groups, whichever is greater. Therefore, surfactant films can be tightly or loosely packed resulting in very different interfacial properties. For instance, straight chains and large head groups (relative to the cross tail section) favour close, effective packing, while branched, bulky, or multiple hydrophobic chains hinder effective close packing at the interface. On the other hand, within a series of single straight chain surfactants, increasing the hydrocarbon chain length from C8 to C20 will have little effect on adsorption effectiveness. [19]

2.2 SURFACTANT SOLUBILITY

In aqueous solution, when all available interfaces are saturated, the overall energy reduction may continue through other mechanisms. Depending on the system composition, a surfactant molecule can play different roles in terms of aggregation (formation of micelles, liquid crystal phases, bilayers or vesicles, etc). The physical manifestation of one such mechanism is crystallisation or precipitation of surfactant from solution – that is, bulk-phase separation. While most common surfactants have a substantial solubility in water, this can change significantly with variations in hydrophobic tail length, head group nature, counterion valence, solution environment, and most importantly, temperature.

2.2.1 The Krafft temperature

As for most solutes in water, increasing temperature produces an increase in solubility. However, for ionic surfactants, which are initially insoluble, there is often a temperature at which the solubility suddenly increases very dramatically. This is known as the Krafft point or Krafft temperature, T_K, and is defined as the intersection of the solubility and the CMC curves, i.e., it is the temperature at which the solubility of the monomeric surfactant is equivalent to its CMC at the same temperature. This is illustrated in Figure 2.3. Below T_K, surfactant monomers only exist in equilibrium with the hydrated crystalline phase, and above T_K, micelles are formed providing much greater surfactant solubility.

The Krafft point of ionic surfactants is found to vary with counterion [23], alkyl chain length and chain structure. Knowledge of the Krafft temperature is crucial in many applications since below T_K the surfactant will clearly not perform efficiently; hence typical characteristics such as maximum surface tension lowering and micelle formation cannot be achieved. The development of surfactants with a lower Krafft point but still being very efficient at lowering surface tension (i.e., long chain compounds) is usually achieved by introducing chain branching, multiple bonds in the alkyl chain or bulkier hydrophilic groups thereby reducing intermolecular interactions that promote crystallisation.

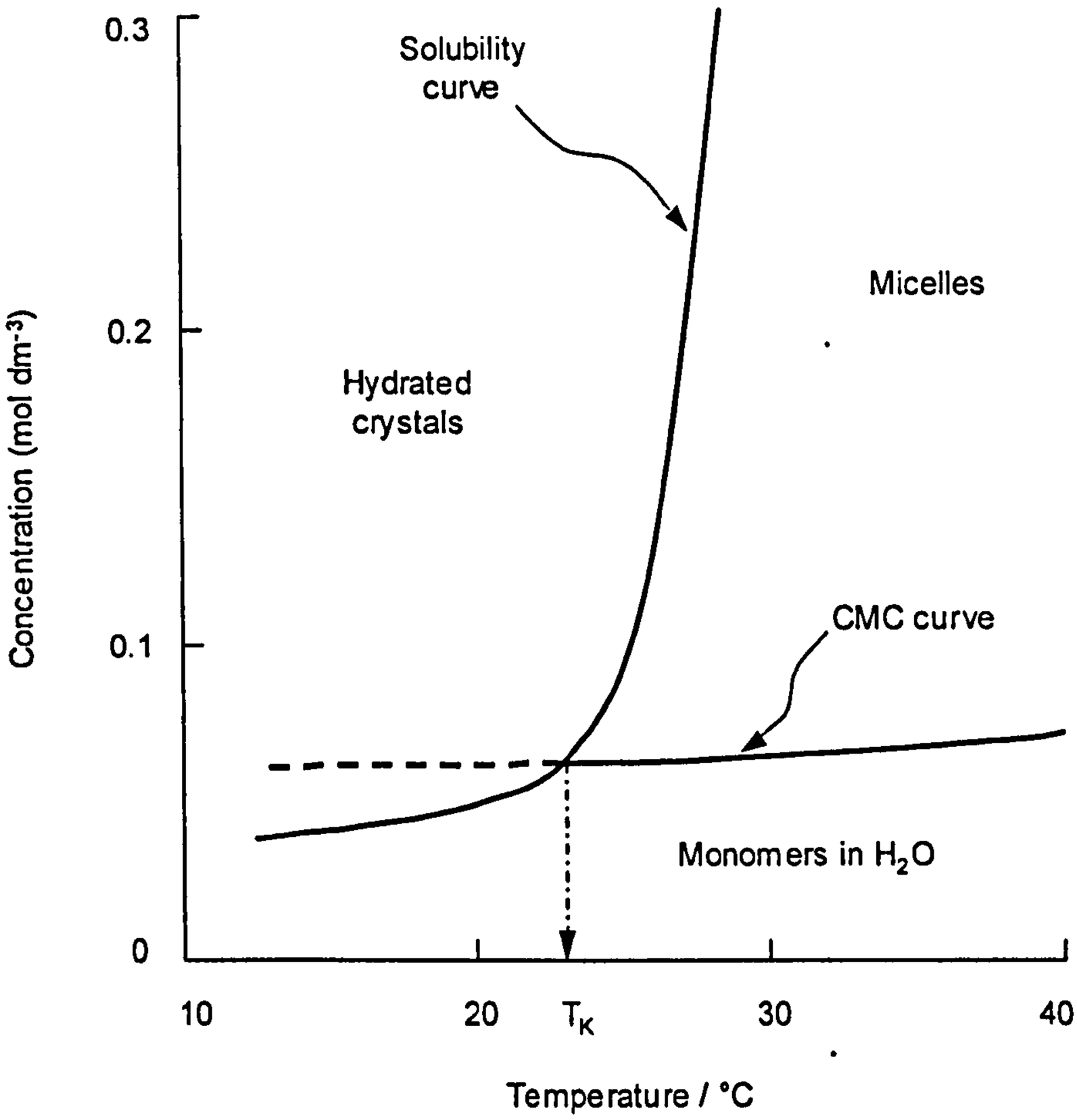

Figure 2.3 The Krafft temperature T_K is the point at which surfactant solubility equals the critical micelle concentration. Above T_K, surfactant molecules form a dispersed phase; below T_K, hydrated crystals are formed.

2.2.2 The Cloud point

For non-ionic surfactants, a common observation is that micellar solutions tend to become visibly turbid at a well-defined temperature. This is often referred to as the cloud point, above which the surfactant solution phase separates. Above the cloud point, the system consists of an almost micelle-free dilute solution at a concentration equal to its CMC at that temperature, and a surfactant-rich micellar phase. This separation is caused by a sharp increase in aggregation number and a decrease in intermicellar repulsions [24,25] that produces a difference in density of the micelle-rich and micelle-poor phases. Since much larger particles are formed, the solution becomes visibly turbid with large micelles efficiently scattering light. As with Krafft temperatures, the cloud point depends on chemical structure. For polyoxyethylene (POE) non-ionics, the cloud point increases with increasing OE content for a given hydrophobic group, and at constant OE content it may be lowered by decreasing the hydrophobe size, broadening the POE chain-length distribution, and branching in the hydrophobic group [26].

2.3 MICELLISATION

In addition to forming oriented interfacial monolayers, surfactants can aggregate to form *micelles*, provided their concentration is sufficiently high. They are typically clusters of at most 50–100 surfactant molecules, whose size and shape are governed by geometric and energy factors. Micelle formation occurs over a fairly sharply defined region called the *critical micelle concentration* (CMC). Above the CMC, additional surfactant forms the aggregates, whereas the concentration of the unassociated monomers remains almost constant. As a result, a rather abrupt change in concentration dependence at much the same point can be observed in common equilibrium or transport properties (Figure 2.4).

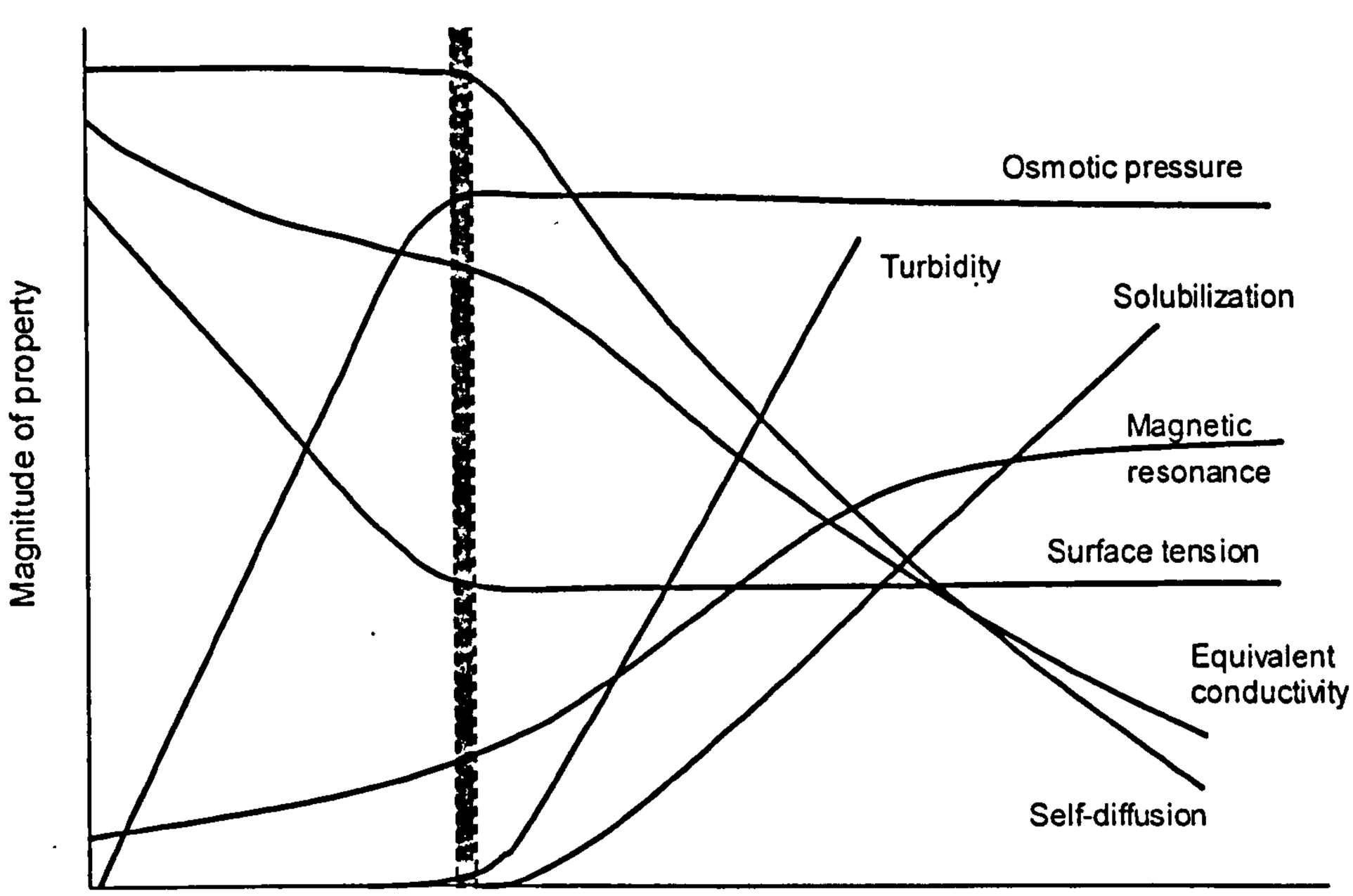

Figure 2.4 Schematic representation of the concentration dependence of some physical properties for solutions of a micelle-forming surfactant. (After Lindman and Wennerström, *Topics in Current Chemistry*, Vol. 87, Springer-Verlag, Berlin, 1980)

2.3.1 Thermodynamics of micellisation

Micelles are dynamic species, in that there is a constant, rapid interchange – typically on a microsecond timescale – of molecules between aggregate and solution phase. This constant formation-dissociation process relies on a subtle balance of interactions. These come from contacts between (1) hydrocarbon chain – water, (2) hydrocarbon – hydrocarbon chains, (3) head group – head group, and (4) from solvation of the head group. Therefore, the net free energy change upon micellisation, ΔG_m, can be written as

$$\Delta G_m = \Delta G(HC) + \Delta G(contact) + \Delta G(packing) + \Delta G(HG) \qquad (2.3.1)$$

where

- $\Delta G(HC)$ is the free energy associated with transferring hydrocarbon chains out of water and into the oil-like interior of the micelle.
- $\Delta G(contact)$ is a surface free energy attributed to solvent-hydrocarbon contacts in the micelle.
- $\Delta G(packing)$ is a positive contribution associated with confining the hydrocarbon chain to the micelle core.
- $\Delta G(HG)$ is a positive contribution associated with head group interactions, including electrostatic as well as head group conformation effects.

Aggregation of surfactant molecules partly results from the tendency of the hydrophobic groups to minimise contacts with water by forming oily microdomains within the solvent. There, alkyl – alkyl interactions are maximised, while hydrophilic head groups remain surrounded by water.

The traditional picture of micelle formation thermodynamics is based on the Gibbs-Helmholtz equation ($\Delta G_m = \Delta H_m - T\Delta S_m$). At room temperature the process is characterised by a small, positive enthalpy, ΔH_m, and a large, positive entropy of micellisation, ΔS_m. The latter is considered as the main contribution to the negative ΔG_m value, and so has led to the controversial idea that micellisation is an entropy-driven process. High positive values of ΔS_m are indeed surprising since aggregation, in terms of configurational entropy, should result in a negative contribution (i.e., formation of ordered aggregates from free surfactant monomers). In addition, large values of ΔH_m would have been expected since hydrocarbon groups have very little solubility in water, and consequently a high enthalpy of solution.

A generally accepted mechanism that accounts for such conflicts is that when alkyl groups are surrounded by water, the H_2O molecules form clathrate cavities (i.e., stoichiometric crystalline solids in which water forms cages around solutes), thereby increasing either the strength or number of effective hydrogen bonds [27]. Therefore, the predominant effect of the hydrocarbon molecule is to increase the degree of structure in the immediately surrounding water. This is one of the main features of the *hydrophobic effect*, a subject that was explored in detail by Tanford [1] to account for the very slight solubility of hydrocarbons in water. During the formation of micelles, the reverse process occurs: as lyophobic residues aggregate, the highly structured water around each chain collapses back to ordinary bulk water thereby accounting for the apparent large overall gain in entropy, ΔS_m. This water-structure effect was also invoked by other researchers [28,29].

Such an interpretation, however, has been strongly challenged by more recent studies of aqueous systems at high temperatures (up to 166°C) and micellisation in hydrazine solutions [30]. In these systems water loses most of its peculiar structural properties and the formation of structured water around lyophobic species is no longer possible.

The mechanism of micelle formation from surfactant monomers, S, can be described by a series of equilibria:

$$S + S \xleftrightarrow{K_2} S_2 + S \xleftrightarrow{K_3} S_3 \ldots \xleftrightarrow{K_n} S_n + S \longleftrightarrow \ldots \quad (2.3.2)$$

with equilibrium constants K_n for $n = 2 - \infty$, and where the various thermodynamic parameters ($\Delta G°$, $\Delta H°$, $\Delta S°$) for the aggregation process can be expressed in terms of K_n. However, each K_n cannot be measured individually, so different approaches have been proposed to model the energetics of the process of self-association. Although not totally accurate, two simple models are generally encountered: the closed-association and the phase separation models. In the closed-association model, with the size range of spherical micelles around the CMC being very limited, it is assumed that only one of K_n value is dominant, and micelles and monomeric species are considered to be in chemical equilibrium.

$$nS \longleftrightarrow S_n \quad (2.3.3)$$

n is the number of molecules of surfactant, S, associating to form the micelle (i.e., the aggregation number). In the phase separation model, the micelles are considered to form a new phase within the system at and above the critical micelle concentration, and

$$nS \longleftrightarrow mS + S_n \quad (2.3.4)$$

where *m* is the number of free surfactant molecules in the solution and S_n the new phase. In both cases, equilibrium between monomeric surfactant and micelles is assumed with a corresponding equilibrium constant, K_m, given by

$$K_m = \frac{[\text{micelles}]}{[\text{monomers}]^n} = \frac{[S_n]}{[S]^n} \quad (2.3.5)$$

where brackets indicate molar concentrations and *n* is the number of monomers in the micelle, the aggregation number. Although micellisation is itself a source of non-ideality [31,32], it is assumed in Eq. 2.3.5 that activities may be replaced by concentrations.

From Eq. 2.3.5, the standard free energy of micellisation per mole of micelles is given by

$$\Delta G_m^\circ = -RT \ln K_m = -RT \ln S_n + nRT \ln S \qquad (2.3.6)$$

while the standard free energy change per mole of surfactant is

$$\frac{\Delta G_m^\circ}{n} = -\frac{RT}{n} \ln S_n + RT \ln S \qquad (2.3.7)$$

At (or near) the CMC, $S \approx S_n$, so that the first term on the right side of Eq. 2.3.7 can be neglected, and an approximate expression for the free energy of micellisation per mole of a neutral surfactant is

$$\Delta G_{M,m}^\circ \approx RT \ln(CMC) \qquad (2.3.8)$$

In the case of ionic surfactants, the presence of the counterion and its degree of association with the monomer and micelle must be considered. The mass-action equation becomes

$$nS^x + (n-p)C^y \leftrightarrow S_n^a \qquad (2.3.9)$$

where C is the concentration of free counterions. The degree of dissociation of the surfactant molecules in the micelle, α, the micellar charge, is given by $\alpha = p/n$.
The ionic equivalent to Eq. 2.3.5 is then

$$K_m = \frac{[S_n]}{[S^x]^n \times [C^y]^{(n-p)}} \qquad (2.3.10)$$

where p is the concentration of free counterions associated with, but not bound to the micelle. The standard free energy of micelle formation becomes

$$\Delta G_m^\circ = -RT\{\ln[S_n] - n\ln[S^x] - (n-p)\ln[C^y] \qquad (2.3.11)$$

At the CMC $[S^{-(+)}] = [C^{+(-)}]$ = CMC for a fully ionised surfactant, and the standard free energy change per mole of surfactant can be obtained from the approximation:

$$\Delta G^{\circ}_{M,m} \approx RT\left(2-\frac{p}{n}\right)\ln(CMC) \quad . \qquad (2.3.12)$$

When the ionic micelle is in a solution of high electrolyte content, the situation described by Eq. 2.3.12 reverts to the simple non-ionic case given by Eq. 2.3.8.

From the Gibbs function and second law of thermodynamics, $\Delta S°$ for non-ionic surfactants is given as

$$\Delta S° = -\frac{d(\Delta G°)}{dT} = -RT\frac{d\ln(CMC)}{dT} - R\ln(CMC) \qquad (2.3.13)$$

From the Gibbs function and Eq. 2.3.8 and 2.3.13, the enthalpy of micellisation for non-ionic surfactants, ΔH^{e}, is given by

$$\Delta H° = \Delta G° + T\Delta S° = -RT^2\frac{d\ln(CMC)}{dT} \qquad (2.3.14)$$

and similarly for ionics,

$$\Delta H° = -RT^2\left(2-\frac{p}{n}\right)\frac{d\ln(CMC)}{dT} \qquad (2.3.15)$$

Both the phase separation and closed association models have disadvantages. One difficulty is activity coefficients: assuming ideality can be erroneous considering the large effective micelle size and charge in comparison to dilute solutions of surfactant monomers. However, the model described above is useful enough to be applied to the systems presented in this study. Another disadvantage is the assumption of micellar monodispersity. To counteract this problem, the multiple equilibrium model was proposed, which is an extension of the closed association model. It allows a distribution function of aggregation numbers in micelles to be calculated. A full account of this model and its derivation can be found in references [33-35].

2.3.2 Factors affecting the CMC

Many factors are known to affect strongly the CMC. Of major effect is the structure of the surfactant, as will be described below. Also important, but to a lesser extent, are parameters such as counterion nature, presence of additives, change in temperature, which should be considered when discussing the critical micelle concentration.

The hydrophobic group: the 'tail'

The length of the hydrocarbon chain is a major factor determining the CMC. For a homologous series of linear single-chain surfactants the CMC decreases logarithmically with carbon number. The relationship usually fits the Klevens equation [36]

$$\log_{10}(\text{CMC}) = A - B\text{n}_\text{c} \qquad (2.3.16)$$

where A and B are constants for a particular homologous series and temperature, and n_c is the number of carbon atoms in the chain, C_nH_{2n+1}. The constant A varies with the nature and number of hydrophilic groups, while B is constant and approximately equal to $\log_{10} 2$ ($B \approx 0.29 - 0.30$) for all paraffin chain salts having a single ionic head group (i.e., reducing the CMC to approximately one-half per each additional $-CH_2-$ group).

Interestingly, for straight-chain dialkyl sulfosuccinates Eq. 2.3.16 is still valid [37] and $B \approx 0.62$, which essentially doubles the value for the single chain compounds. Alkyl chain branching and double bonds, aromatic groups or some other polar character in the hydrophobic part produce noticeable changes in CMC. In hydrocarbon surfactants, chain branching gives a higher CMC than a comparable straight chain surfactant [19], and introduction of a benzene ring in the chain is equivalent to about 3.5 carbon atoms.

The hydrophilic group

For surfactants with the same hydrocarbon chain, varying the hydrophile nature (i.e., from ionic to non-ionic) has an important effect on the CMC values. For instance, for a C12 hydrocarbon the CMC with an ionic head group lies in the range of 1×10^{-3} mol dm^{-3}, while a C12 non-ionic material exhibits a CMC in the range of 1×10^{-4} mol dm^{-3}. The exact nature of the ionic group, however, has no dramatic effect, since a major driving force for micelle formation is the entropy factor discussed above.

Counterion effects

In ionic surfactants micelle formation is related to the interactions of solvent with the ionic head group. Since electrostatic repulsions between ionic groups are greatest for complete ionisation, an increase in the degree of ion binding will decrease the CMC. For a given hydrophobic tail and anionic head group, the CMC decreases as $Li^+ > Na^+ > K^+ > Cs^+ > N(CH_3)_4^+ > N(CH_2CH_3)_4^+ > Ca^{2+} \approx Mg^{2+}$. For cationic series such as the dodecyltrimethylammonium halides, the CMC decreases in the order $F^- > Cl^- > Br^- > I^-$. In addition, varying counterion valency produces a significant effect. Changing from monovalent to di- or trivalent counterions produces a sharp decrease in the CMC.

Effect of added salt

The presence of an indifferent electrolyte causes a decrease in the CMC of most surfactants. The greatest effect is found for ionic materials. The principal effect of the salt is to partially screen the electrostatic repulsion between the head groups and so lower the CMC. For ionics, the effect of adding electrolyte can be empirically quantified viz.

$$\log_{10}(\mathrm{CMC}) = -a \log_{10} C_i + b \qquad (2.3.17)$$

Non-ionic and zwitterionic surfactants exhibit a much smaller effect and Eq. 2.3.17 does not apply.

Effect of temperature

The influence of the temperature on micellisation is usually weak, reflecting subtle changes in bonding, heat capacity and volume that accompany the transition. The effects of temperature on the CMC is, however, quite complex. It was shown, for example, that the CMC of most ionic surfactants passes through a minimum as the temperature is varied from 0 to 70°C [38]. As already mentioned (Section 2.2), the major effects of temperature are the Krafft and cloud points.

2.3.3 Structure of micelles and molecular packing

Early studies [39,40] showed that, with ionic single alkyl chain compounds spherical micelles form. In particular, in 1936 Hartley [41] described such micelles as spherical aggregates whose alkyl groups form a hydrocarbon liquid-like core, and whose polar groups form a charged surface. Later, with the development of zwitterionic and non-ionic surfactants, micelles of very different shapes were encountered. The different geometries were found to depend mainly on the structure of the surfactant, as well as environmental conditions (e.g., concentration, temperature, pH, electrolyte content).

In the micellisation process, molecular geometry plays an important role and it is essential to understand how surfactants can pack. The main structures encountered are spherical micelles, vesicles, bilayers, or inverted micelles. As described previously, two opposing forces control the self-association process: hydrocarbon – water interactions that favour aggregation (i.e., pulling surfactant molecules out of the aqueous environment), and head group interactions that work in the opposite sense. These two actions can be considered as an attractive interfacial tension term due to hydrocarbon tails and a repulsion term depending on the nature of the hydrophilic group. More recently, this basic idea was reviewed and quantified by Mitchell and Ninham [42] and Israelachvili [43], resulting in the concept that aggregation of surfactants is controlled by a balanced molecular geometry. In brief, the geometric treatment relates the overall free energy of association to three critical geometric characteristics (Figure 2.5):

- the minimum interfacial area occupied by the head group, a_o;
- the volume of the hydrophobic tail(s), v;
- the maximum extended chain length of the tail in the micelle core, l_c.

Formation of a spherical micelle requires l_c to be equal to or less than the micelle core radius, R_{mic}. Then for such a shape, an aggregation number, N, can be expressed either as the ratio of micellar core volume, V_{mic}, and that for the tail, v:

$$N = V_{mic} / v = \left[(4/3)\pi R_{mic}^3\right] / v \qquad (2.3.18)$$

or as the ratio between the micellar area, A_{mic}, and the cross-sectional area, a_o:

$$N = A_{mic} / a_o = \left[4\pi R_{mic}^2\right] / a_o \qquad (2.3.19)$$

Equating Eq. 2.3.18 and 2.3.19

$$v/(a_o R_{mic}) = 1/3 \qquad (2.3.20)$$

Since l_c cannot exceed R_{mic} for a spherical micelle

$$v/(a_o l_c) \leq 1/3 \qquad (2.3.21)$$

More generally, this defines a critical packing parameter, P_c, as the ratio of volume to surface area:

$$P_c = v/(a_o l_c) \qquad (2.3.22)$$

The parameter v varies with the number of hydrophobic groups, chain unsaturation, chain branching and chain penetration by other compatible hydrophobic groups, while a_o is mainly governed by electrostatic interactions and head group hydration. P_c is a useful quantity since it allows the prediction of aggregate shape and size. The predicted aggregation characteristics of surfactants covering the whole range of geometric possibilities are summarised in Table 2.1 and Figure 2.6.

Table 2.1 Expected aggregate characteristics in relation to surfactant critical packing parameter, $P_c = v/a_o l_c$

P_c	General Surfactant type	Expected Aggregate Structure
< 0.33	Single-chain surfactants with large head groups	Spherical or ellipsoidal micelles
0.33 - 0.5	Single-chain surfactants with small head groups, or ionics in the presence of large amounts of electrolyte	Large cylindrical or rod-shaped micelles
0.5 - 1.0	Double-chain surfactants with large head groups and flexible chains	Vesicles and flexible bilayers structures
1.0	Double-chain surfactants with small head groups or rigid, immobile chains	Planar extended bilayers
>1.0	Double-chain surfactants with small head groups, very large and bulky hydrophobic groups	Reversed or inverted micelles

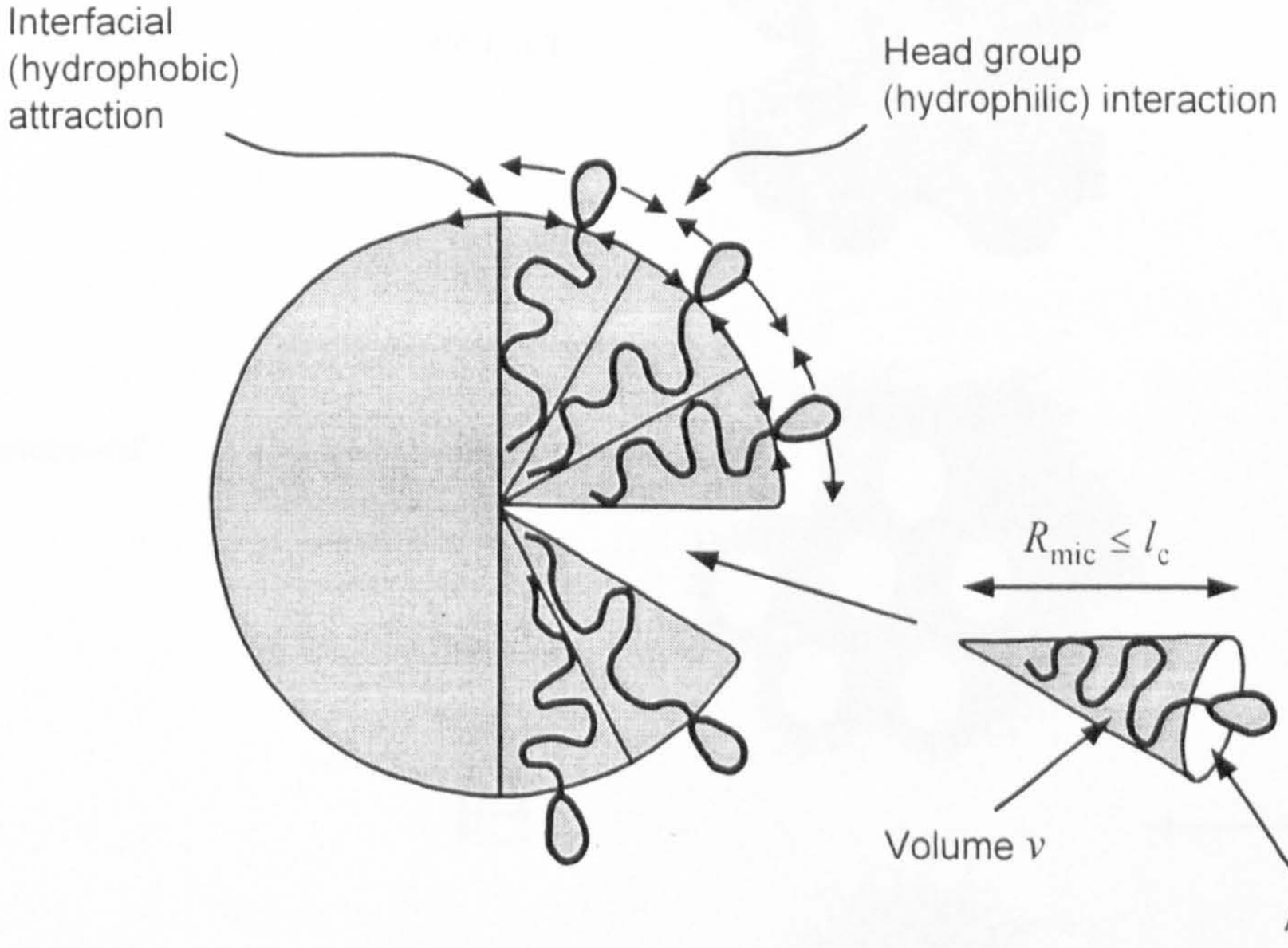

Figure 2.5 The critical packing parameter P_c (or surfactant number) relates the head group area, the extended length and the volume of the hydrophobic part of a surfactant molecule into a dimensionless number $P_c = v/a_o l_c$. (After Israelachvili [43] p. 247)

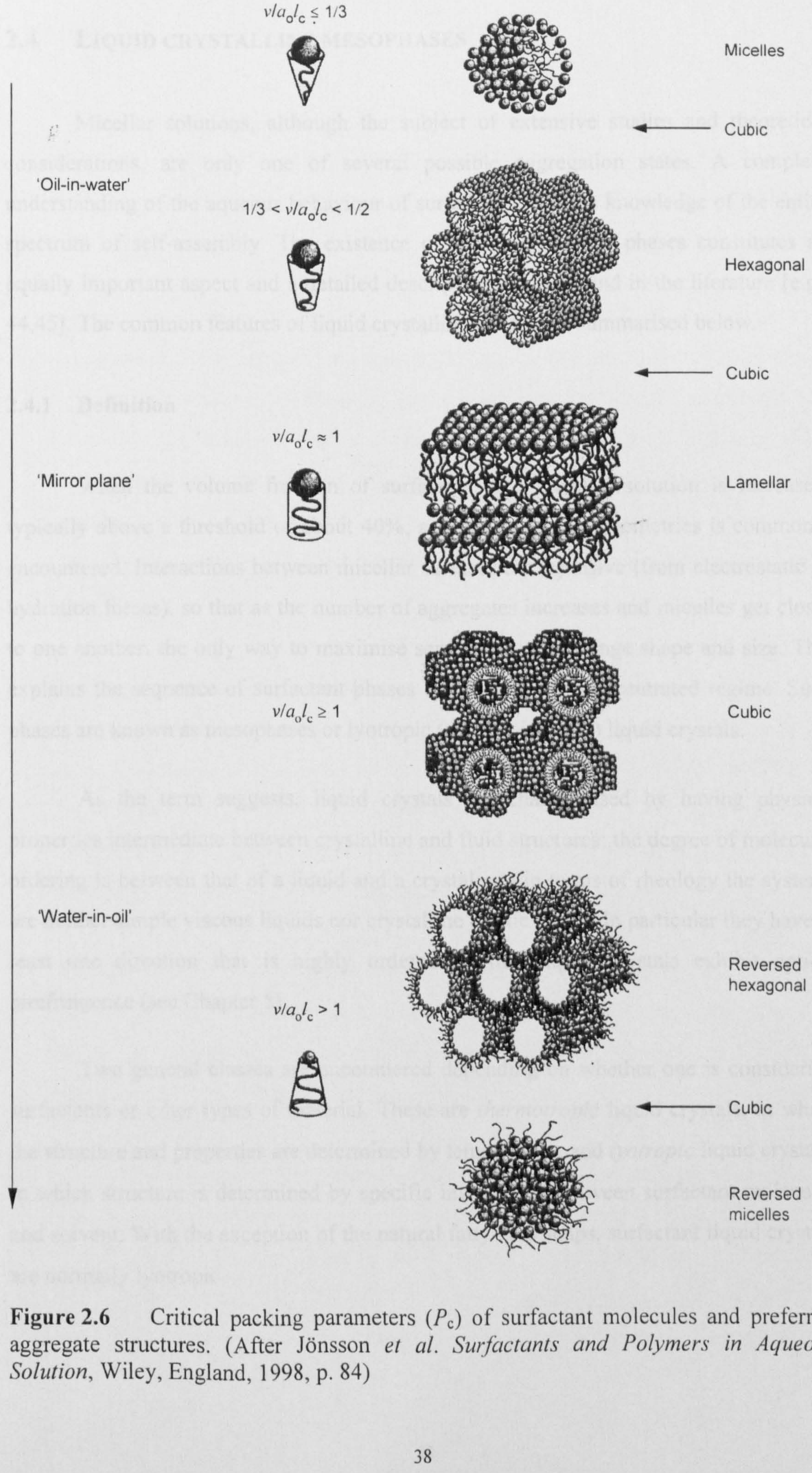

Figure 2.6 Critical packing parameters (P_c) of surfactant molecules and preferred aggregate structures. (After Jönsson *et al. Surfactants and Polymers in Aqueous Solution*, Wiley, England, 1998, p. 84)

2.4 LIQUID CRYSTALLINE MESOPHASES

Micellar solutions, although the subject of extensive studies and theoretical considerations, are only one of several possible aggregation states. A complete understanding of the aqueous behaviour of surfactants requires knowledge of the entire spectrum of self-assembly. The existence of liquid crystalline phases constitutes an equally important aspect and a detailed description can be found in the literature [e.g., 44,45]. The common features of liquid crystalline phases are summarised below.

2.4.1 Definition

When the volume fraction of surfactant in a micellar solution is increased, typically above a threshold of about 40%, a series of regular geometries is commonly encountered. Interactions between micellar surfaces are repulsive (from electrostatic or hydration forces), so that as the number of aggregates increases and micelles get closer to one another, the only way to maximise separation is to change shape and size. This explains the sequence of surfactant phases observed in the concentrated regime. Such phases are known as mesophases or lyotropic (solvent-induced) liquid crystals.

As the term suggests, liquid crystals are characterised by having physical properties intermediate between crystalline and fluid structures: the degree of molecular ordering is between that of a liquid and a crystal and in terms of rheology the systems are neither simple viscous liquids nor crystalline elastic solids. In particular they have at least one direction that is highly ordered so that liquid crystals exhibit optical birefringence (see Chapter 5).

Two general classes are encountered depending on whether one is considering surfactants or other types of material. These are *thermotropic* liquid crystals, in which the structure and properties are determined by temperature, and *lyotropic* liquid crystals, in which structure is determined by specific interactions between surfactant molecules and solvent. With the exception of the natural fatty acid soaps, surfactant liquid crystals are normally lyotropic.

2.4.2 Structures

The main structures associated with two-component surfactant–water systems are: hexagonal (normal or inverted), lamellar, and several (not so well defined) cubic phases. Table 2.2 summarises the notations commonly associated with these phases and their structures are shown in Figure 2.6.

- The *hexagonal phase* is composed of a close-packed array of (infinitely) long cylindrical micelles, arranged in a hexagonal pattern. The micelles may be "normal" (in water, H_1) in that the hydrophilic head groups are located on the outer surface of the cylinder, or "inverted" (H_2), with the hydrophilic group located internally. Since all the space between adjacent cylinders is filled with hydrophobic groups, the cylindrical micelles are more closely packed than those found in the H_1 phase. As a result, H_2 phases occupy a much smaller region of the phase diagram and are much less common.

- The *lamellar phase* (L_α) is built up of alternating water-surfactant bilayers. The hydrophobic chains possess a significant degree of randomness and mobility, and the surfactant bilayer can range from being stiff and planar to being very flexible and undulating. The level of disorder may vary smoothly or change abruptly, depending on the specific system, so that it is possible for a surfactant to pass through several distinct lamellar phases.

- The *cubic phase* may have a wide variety of structural variations and occurs in many different parts of the phase diagram. They are optically isotropic systems and so cannot be well characterised from simple polarised light microscopy. So far two main groups of cubic phases have been identified:

  i. The micellar cubic phases (I_1 and I_2) – built up of regular packing of small micelles (or reversed micelles in the case of I_2). As shown on the schematic Figure 2.7, the micelles are short prolates arranged in a body-centred cubic close-packed array [46,47].

ii. The bicontinuous cubic phases (V_1 and V_2) – are thought to be rather extended, porous, connected structures in three dimensions. They are considered to be formed by either connected rod-like micelles, similar to branched micelles, or bilayer structures. Denoted V_1 and V_2, they can be normal or reverse structures and are positioned between H_1 and L_α and between L_α and H_2 respectively.

In addition to having different structures these common forms also show different viscosities, in the order

Cubic > Hexagonal > Lamellar .

Cubic phases are generally the more viscous since they have no obvious shear plane and so layers of surfactant aggregates cannot slide easily relative to each other. Hexagonal phases typically contain 30-60% water by weight but are very viscous since cylindrical aggregates can move freely only along their length. Lamellar phases are generally less viscous than the hexagonal phases due to the ease with which each parallel layers can slide over each other during shear.

Table 2.2 Most common lyotropic liquid crystalline and other phases found in binary surfactant–water systems

Phase structure	Symbol	Other names
Lamellar	L_α	Neat
Hexagonal	H_1	Middle
Reversed hexagonal	H_2	
Cubic (normal micellar)	I_1	Viscous isotropic
Cubic (reversed micellar)	I_2	
Cubic (normal bicontinuous)	V_1	Viscous isotropic
Cubic (reversed bicontinuous)	V_2	
Micellar	L_1	
Reversed micellar	L_2	

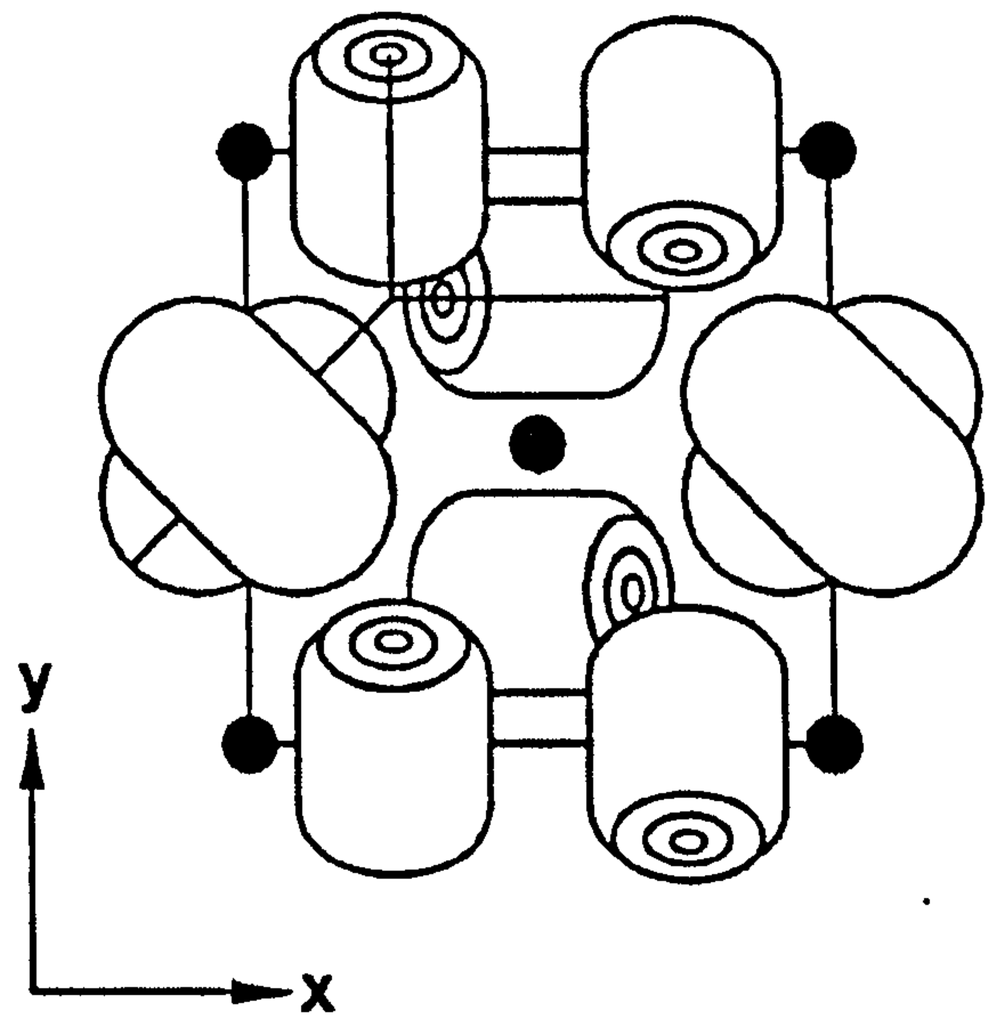

Figure 2.7 Structure of a cubic phase built up of discrete micelles, as proposed by Fontell *et al.* [46].

2.4.3 Phase diagrams

The sequence of mesophases can be identified simply by using a polarising microscope and the isothermal technique known as a phase cut. Briefly, starting from a small amount of surfactant, a concentration gradient is set up spanning the entire phase diagram, from pure water to pure surfactant. Since crystal hydrates and some of the liquid crystalline phases are birefringent, viewing in the microscope between crossed polars shows up the complete sequence of mesophases. This qualitative technique is described for a series of double chain sulfosuccinates in Chapter 5.

Transformations between different mesophases are controlled by a balance between molecular packing geometry and inter-aggregate forces. As a result, the system characteristics are highly dependent on the nature and amount of solvent present. Generally, the main types of mesophases tend to occur in the same order and in roughly the same position in the phase diagram. Figures 2.8 and 2.9 show binary phase diagrams of non-ionic $C_{16}EO_8$–water and anionic sodium bis(2-ethylhexyl)sulfosuccinate–water systems respectively.

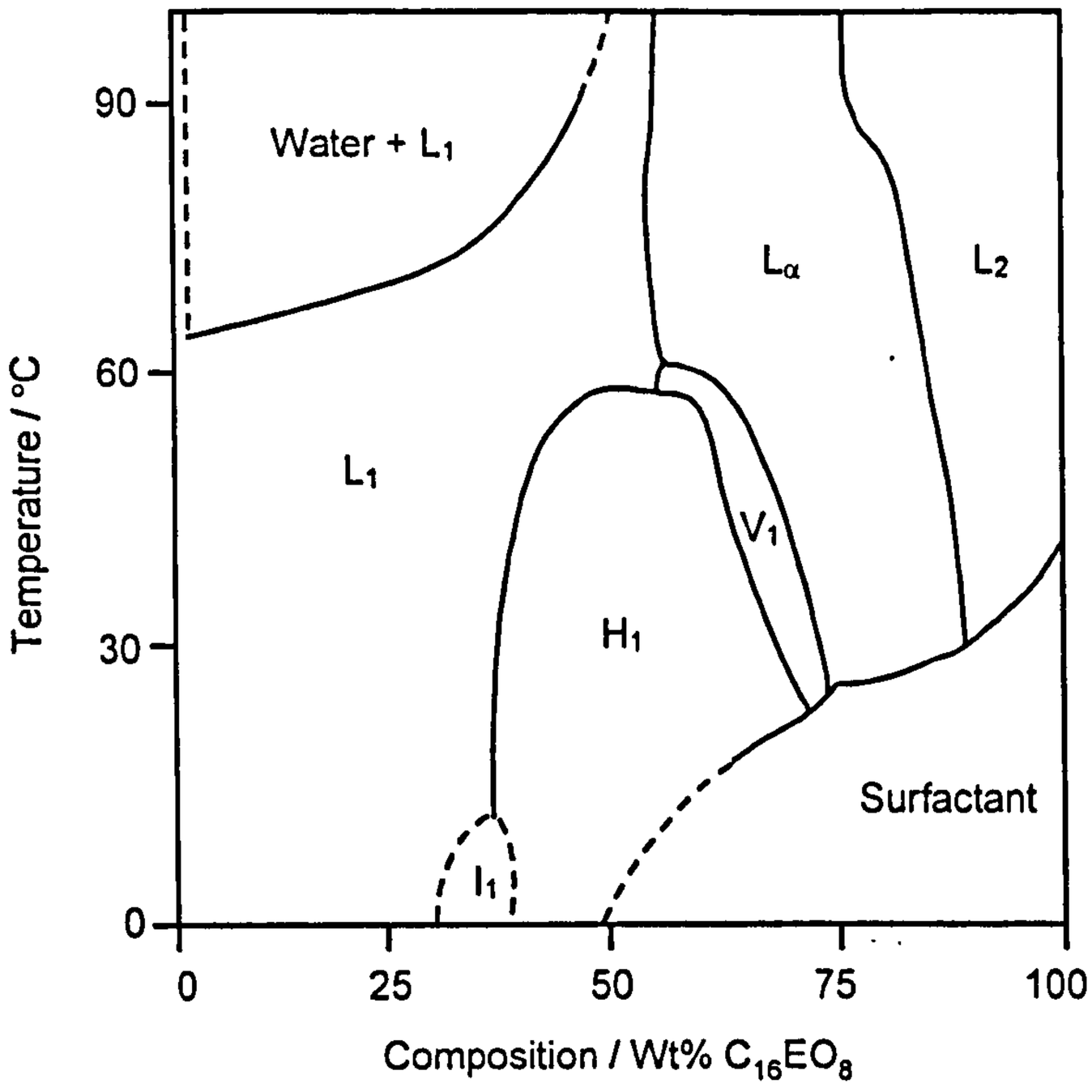

Figure 2.8 Phase diagram for the non-ionic $C_{16}EO_8$ illustrating the various liquid crystalline phases. L_1 and L_2 are isotropic solutions. See Table 2.2 for details of the other phases. (After Mitchell *et al. J. Chem. Soc. Faraday Trans. I* **1983**, *79*, 975)

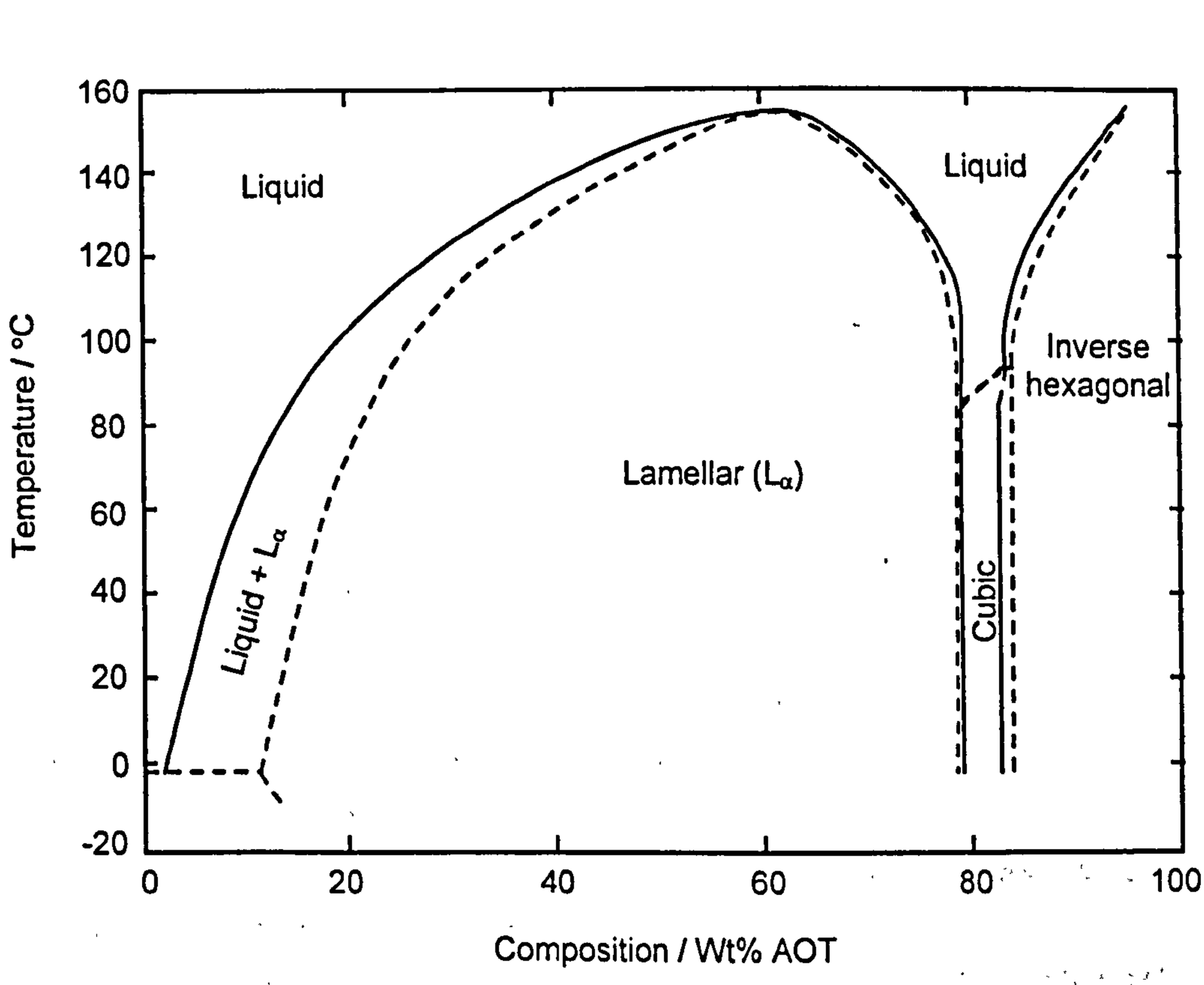

Figure 2.9 Binary phase diagram of sodium bis(2-ethylhexyl)sulfosuccinate (AOT)–water system. (After Laughlin [44])

2.5 REFERENCES

1. Tanford, C. *'The Hydrophobic Effect: formation of micelles and biological membranes'* John Wiley & Sons, 1978, USA.
2. Dukhin, S. S.; Kretzschmar, G.; Miller, R. *'Dynamics of Adsorption at Liquid Interfaces'* Elsevier. Amsterdam, 1995.
3. Rusanov, A. I.; Prokhorov, V. A. *Interfacial Tensiometry*, Elsevier, Amsterdam, 1996.
4. Chang, C.-H.; Franses, E. I. *Colloid Surf.* **1995**, *100*, 1.
5. Miller, R.; Joos, P.; Fainermann, V. *Adv. Colloid Interface Sci.* **1994**, *49*, 249.
6. Lin, S. -Y.; McKeigue, K.; Maldarelli, C. *Langmuir* **1991**, *7*, 1055.
7. Hsu, C. -H.; Chang, C. -H.; Lin, S. -Y. *Langmuir* **1999**, *15*, 1952.
8. Eastoe, J.; Dalton, J. S. *Adv. Colloid Interface Sci.* **2000**, *85*, 103.
9. Gibbs, J. W. *The Collected Works of J. W. Gibbs*, Longmans, Green, New York, 1931, Vol. I, p. 219.
10. Elworthy, P. H.; Mysels, K. J. *J Colloid Interface Sci.* **1966**, *21*, 331
11. Lu, J. R.; Li, Z. X.; Su, T. J.; Thomas, R. K.; Penfold, J. *Langmuir* **1993**, *9*, 2408.
12. Bae, S.; Haage, K.; Wantke, K.; Motschmann, H. *J. Phys. Chem. B* **1999**, *103*, 1045.
13. Downer, A.; Eastoe, J.; Pitt, A. R.; Penfold, J.; Heenan, R. K. *Colloids Surf. A* **1999**, *156*, 33.
14. Eastoe, J.; Nave, S.; Downer, A.; Paul, A.; Rankin, A.; Tribe, K.; Penfold, J. *Langmuir* **2000**, *16*, 4511.
15. Langmuir, I. *J. Am. Chem. Soc.* **1848**, *39*, 1917.
16. Szyszkowski, B. *Z. Phys. Chem.* **1908**, *64*, 385.
17. Frumkin, A. *Z. Phys. Chem.* **1925**, *116*, 466.
18. Guggenheim, E. A.; Adam, N. K. *Proc. Roy. Soc. (London)*, **1933**, *A139*, 218.
19. Rosen, M. J. *'Surfactants And Interfacial Phenomena'*, John Wiley & Sons, 1989, USA.
20. Traube, I. *Justus Liebigs Ann. Chem.* **1891**, *265*, 27.
21. Tamaki, K.; Yanagushi, T.; Hori, R. *Bull. Chem. Soc. Jpn.* **1961**, *34*, 237.
22. Pitt, A. R.; Morley, S. D; Burbidge, N. J.; Quickenden, E. L. *Coll. Surf. A* **1996**, *114*, 321.
23. Hato, M.; Tahara, M.; Suda, Y. *J. Coll. Interface Sci.* **1979**, *72*, 458.
24. Staples, E. J.; Tiddy, G. J. T. *J. Chem. Soc., Faraday Trans. I* **1978**, *74*, 2530
25. Tiddy, G. J. T. *Phys. Rep.* **1980**, *57*, 1.
26. Schott, H. *J. Pharm. Sci.* **1969**, *58*, 1443.
27. Frank, H. S.; Evans, M.W. *J. Chem. Phys.* **1945**, *13*, 507.
28. Evans, D. F.; Wightman, P. J. *J. Colloid Interface Sci.* **1982**, *86*, 515.
29. Patterson, D.; Barbe, M. *J. Phys. Chem.* **1976**, *80*, 2435.
30. Evans, D. F. *Langmuir* **1988**, *4*, 3.
31. Hunter, R. J. *'Foundations of Colloid Science Volume I'*, Oxford University Press, 1987, New York.
32. Evans, D. F.; Ninham, B. W. *J. Phys. Chem.* **1986**, *90*, 226.
33. Corkhill, J. M.; Goodman, J. F.; Walker, T.; Wyer, J. *Proc. Roy. Soc. (London),A* **1969**, *312*, 243.
34. Mukerjee, P. *J. Phys. Chem.* **1972**, *76*, 565.
35. Aniansson, E. A. G.; Wall, S. N. *J. Phys. Chem.* **1974**, *78*, 1024.

36. Klevens, H. *J. Am. Oil Chem. Soc.* **1953**, *30*, 7, 4.
37. Williams, E. F.; Woodberry, N. T.; Dixon, J. K. *J. Colloid Interface Sci.* **1957**, *12*, 452.
38. Kresheck, G. C. In *Water-a comprehensive treatise*, pp. 95-167. Ed. F. Franks, Plenum Press, 1975, New York.
39. McBain, J. W. *Trans. Faraday Soc.* **1913**, *9*, 99.
40. Reychler, *Kolloid-Z.*, **1913**, *12*, 283.
41. Hartley, G. S. *'Aqueous solutions of paraffin chain salts'*, Hermann & Cie, Paris, 1936.
42. Mitchell, D. J.; Ninham, B. W. *J. Chem. Soc. Faraday Trans. 2* **1981**, *77*, 601.
43. Israelachvili, J. N. *Intermolecular and Surface Forces*, Academic Press, London, 1985, p. 251.
44. Laughlin, R. G. '*The Aqueous Phase Behaviour of Surfactants*', Academic Press, London, 1994.
45. Chandrasekhar, S. *'Liquid Crystals'* Cambridge University Press, 1992, New York.
46. Fontell, K.; Kox, K. K.; Hansson, E. *Mol. Cryst. Liquid Cryst. Letters* **1985**, *1*, 9.
47. Fontell, K. Coll. Polymer Sci. **1990**, *268*, 264.

CHAPTER 3

SURFACTANTS IN MICROEMULSION SYSTEMS

This chapter is devoted to another important property of surfactants, that of stabilization of water-oil films and formation of microemulsions. These are a special kind of colloidal dispersion that attract a great deal of attention because of their ability to solubilise otherwise insoluble materials (e.g., apolar compounds in aqueous phase). Industrial applications of microemulsions have escalated in the last 40 years following an increased understanding of formation, stability and the role of surfactant molecular architecture. This chapter reviews main theoretical features relevant to the present work and some common techniques used to characterize microemulsion phases.

3.1 MICROEMULSIONS: DEFINITION AND HISTORY

One of the best definitions of microemulsions is from Danielsson and Lindman [1] *"a microemulsion is a system of water, oil and an amphiphile which is a single optically isotropic and thermodynamically stable liquid solution"*. In some respects, microemulsions can be considered as small-scale versions of emulsions, i.e., droplet type dispersions either of oil-in-water (o/w) or of water-in-oil (w/o), with a size range in the order of 5–50 nm in drop radius. Such a description, however, lacks precision since there are significant differences between microemulsions and ordinary emulsions (or macroemulsions). In particular, in emulsions the average drop size grows continuously with time so that phase separation ultimately occurs under gravitational force, i.e., they

are thermodynamically unstable and their formation requires input of work. The drops of the dispersed phase are generally large (> 0.1 μm) so that they often take on a milky rather than translucent appearance. For microemulsions, once the conditions are right, spontaneous formation occurs. As for simple aqueous systems, microemulsion formation is dependent on surfactant type and structure. If the surfactant is ionic and contains a single hydrocarbon chain (e.g., sodium dodecylsulphate, SDS) microemulsions are only formed if a co-surfactant (e.g., a medium size aliphatic alcohol) and/or electrolyte (e.g., 0.2 M NaCl) are also present. With double chain ionics (e.g., Aerosol-OT) and some non-ionic surfactants a co-surfactant is not necessary. This results from one of the most fundamental properties of microemulsions, that is, an ultra-low interfacial tension between the oil and water phases, $\gamma_{o/w}$: the main role of the surfactant is to reduce $\gamma_{o/w}$ sufficiently – i.e., lowering the energy required to increase the surface area – so that spontaneous dispersion of water or oil droplets occurs and the system is thermodynamically stable. As described in Section 3.2.1, the occurrence of ultra-low tensions is crucial for the formation of microemulsions and is dependent on the system composition.

Microemulsions were not really recognized until the work of Hoar and Schulman in 1943, who reported a spontaneous emulsion of water and oil on addition of a strong surface-active agent [2]. The term "microemulsion" was first used even later by Schulman *et al.* [3] in 1959 to describe a multiphase system consisting of water, oil, surfactant and alcohol, which forms a transparent solution. There has been much debate about the word "microemulsion" to describe such systems [4]. Although not systematically used today, some prefer the names "micellar emulsion" [5] or "swollen micelles" [6]. Microemulsions were probably discovered well before the studies of Schulmann: australian housewives have used since the beginning of last century water/eucalyptus oil/soap flake/white spirit mixtures to wash wool, and the first commercial microemulsions were probably the liquid waxes discovered by Rodawald in 1928. Interest in microemulsions really stepped up in the late 1970's and early 1980's when it was recognized that such systems could improve oil recovery and when oil prices reached levels where tertiary recovery methods became profit earning [7]. Nowadays this is no longer the case, but other microemulsion applications were discovered, e.g., catalysis, preparation of submicron particles, solar energy conversion,

liquid–liquid extraction (mineral, proteins, etc.). Together with classical applications in detergency and lubrication, the field remains sufficiently important to continue to attract a number of scientists. From the fundamental research point of view, a great deal of progress has been made in the last 20 years in understanding microemulsion properties. In particular, interfacial film stability and microemulsion structures can now be characterized in detail owing to the development of new and powerful techniques such as small-angle neutron scattering (SANS). The following sections deal with fundamental microemulsion properties, i.e., formation and stability, surfactant films, classification and phase behaviour.

3.2 THEORY OF FORMATION AND STABILITY

3.2.1 Interfacial tension in microemulsions

A simple picture for describing microemulsion formation is to consider a subdivision of the dispersed phase into very small droplets. Then the configurational entropy change, ΔS_{conf}, can be approximately expressed as [8]:

$$\Delta S_{conf} = -nk_B[\ln\phi + \{(1-\phi)/\phi\}\ln(1-\phi)] \qquad (3.2.1)$$

where n is the number of droplets of dispersed phase, k_B is the Boltzmann constant and ϕ is the dispersed phase volume fraction. The associated free energy change can be expressed as a sum of the free energy for creating new area of interface, $\Delta A\gamma_{12}$, and configurational entropy in the form [9]:

$$\Delta G_{form} = \Delta A\gamma_{12} - T\Delta S_{conf} \qquad (3.2.2)$$

where ΔA is the change in interfacial area A (equal to $4\pi r^2$ per droplet of radius r) and γ_{12} is the interfacial tension between phases 1 and 2 (e.g., oil and water) at temperature T (Kelvin). Substituting Eq. 3.2.1 into 3.2.2 gives an expression for obtaining the maximum interfacial tension between phases 1 and 2. On dispersion, the droplet number

increases and ΔS_{conf} is positive. If the surfactant can reduce the interfacial tension to a sufficiently low value, the energy term in Eq. 3.2.2 ($\Delta A\gamma_{12}$) will be relatively small and positive, thus allowing a negative (and hence favourable) free energy change, that is, spontaneous microemulsification.

In surfactant-free oil–water systems, $\gamma_{o/w}$ is of the order of 50 mN m^{-1}, and during microemulsion formation the increase in interfacial area, ΔA, is very large, typically a factor of 10^4 to 10^5. Therefore in the absence of surfactant, the second term in Eq. 3.2.2 is of the order of 1000 k_BT, and in order to fulfill the condition $\Delta A\gamma_{12} \leq T\Delta S_{conf}$, the interfacial tension should be very low (approximately 0.01 mN m^{-1}). Some surfactants (double chain ionics [10,11] and some non-ionics [12]) can produce extremely low interfacial tensions – typically 10^{-2} to 10^{-4} mN m^{-1} – but in most cases, such low values cannot be achieved by a single surfactant since the CMC is reached before a low value of $\gamma_{o/w}$ is attained. An effective way to further decrease $\gamma_{o/w}$ is to include a second surface-active species (either a surfactant or medium-chain alcohol), that is a co-surfactant. This can be understood in terms of the Gibbs equation extended to multicomponent systems [13]. It relates the interfacial tension to the surfactant film composition and the chemical potential, μ, of each component in the system, i.e.,

$$d\gamma_{o/w} = -\sum_i (\Gamma_i d\mu_i) \approx -\sum_i (\Gamma_i RT d\ln C_i) \qquad (3.2.3)$$

where C_i is the molar concentration of component *i* in the mixture, and Γ_i the surface excess (mol m^{-2}). Assuming that surfactants and co-surfactants, with concentration C_s and C_{co} respectively, are the only adsorbed components (i.e., $\Gamma_{water} = \Gamma_{oil} = 0$), Eq. 3.2.3 becomes:

$$d\gamma_{o/w} = -\Gamma_s RT d\ln C_s - \Gamma_{co} RT d\ln C_{co} \qquad (3.2.4)$$

Integration of Eq. 3.2.4 gives:

$$\gamma_{o/w} = \gamma^{\circ}_{o/w} - \int_0^{C_s} \Gamma_s RT d\ln C_s - \int_0^{C_{co}} \Gamma_{co} RT d\ln C_{co} \qquad (3.2.5)$$

Eq. 3.2.5 shows that $\gamma^{\circ}_{o/w}$ is lowered by two terms, both from the surfactant and co-surfactant (of surface excesses Γ_s and Γ_{co} respectively) so their effects are additive. It should be mentioned, however, that the two molecules should be adsorbed simultaneously and should not interact with each other (otherwise they lower their respective activities), i.e., are of completely different chemical nature, so that mixed micellisation does not occur. With certain surfactant–co-surfactant systems the interfacial tension can become so low that further increase in concentration is not possible without making $\gamma_{o/w}$ negative. Overbeek [14] studied variation of $\gamma_{o/w}$ with concentration for the system brine–cyclohexane–*n*-pentanol–SDS (Figure 3.1): a transient negative $\gamma_{o/w}$ value is reached implying spontaneous expansion of the interface by taking up the excess of surfactant and co-surfactant. This is illustrated in Figure 3.1 with the plot for 20% pentanol. Then $\gamma_{o/w}$ increases back to a small positive equilibrium value, generating a microemulsion spontaneously. Such thermodynamic treatment was originated by Ruckenstein and Chi [15] and Overbeek [8]. Equations 3.2.1 and 3.2.2 are very approximate; in particular, additional terms should be included to account for any specific interactions between droplets [15].

3.2.2 kinetic stability

Internal contents of the microemulsion droplets are known to exchange, typically on the millisecond time scale [16,17]. They diffuse and undergo collisions. If collisions are sufficiently violent, then the surfactant film may rupture thereby facilitating droplets exchange, that is the droplets are kinetically unstable. However, if one disperses the system in sufficiently small droplets (< 500 Å), the tendency to coalesce will be counteracted by an energy barrier. Then the system will remain dispersed and transparent for a long period of time (months) [18]. Such a microemulsion is said to be kinetically stable [19]. The mechanism of droplet coalescence has been reported for AOT w/o microemulsions [16]; the droplet exchange process was characterized by a second order rate constant k_{ex}, which is believed to be activation controlled (hence the activation energy, E_a, barrier to fusion) and not purely diffusion controlled. Other studies [20] have shown that the dynamic aspects of microemulsions are affected by the

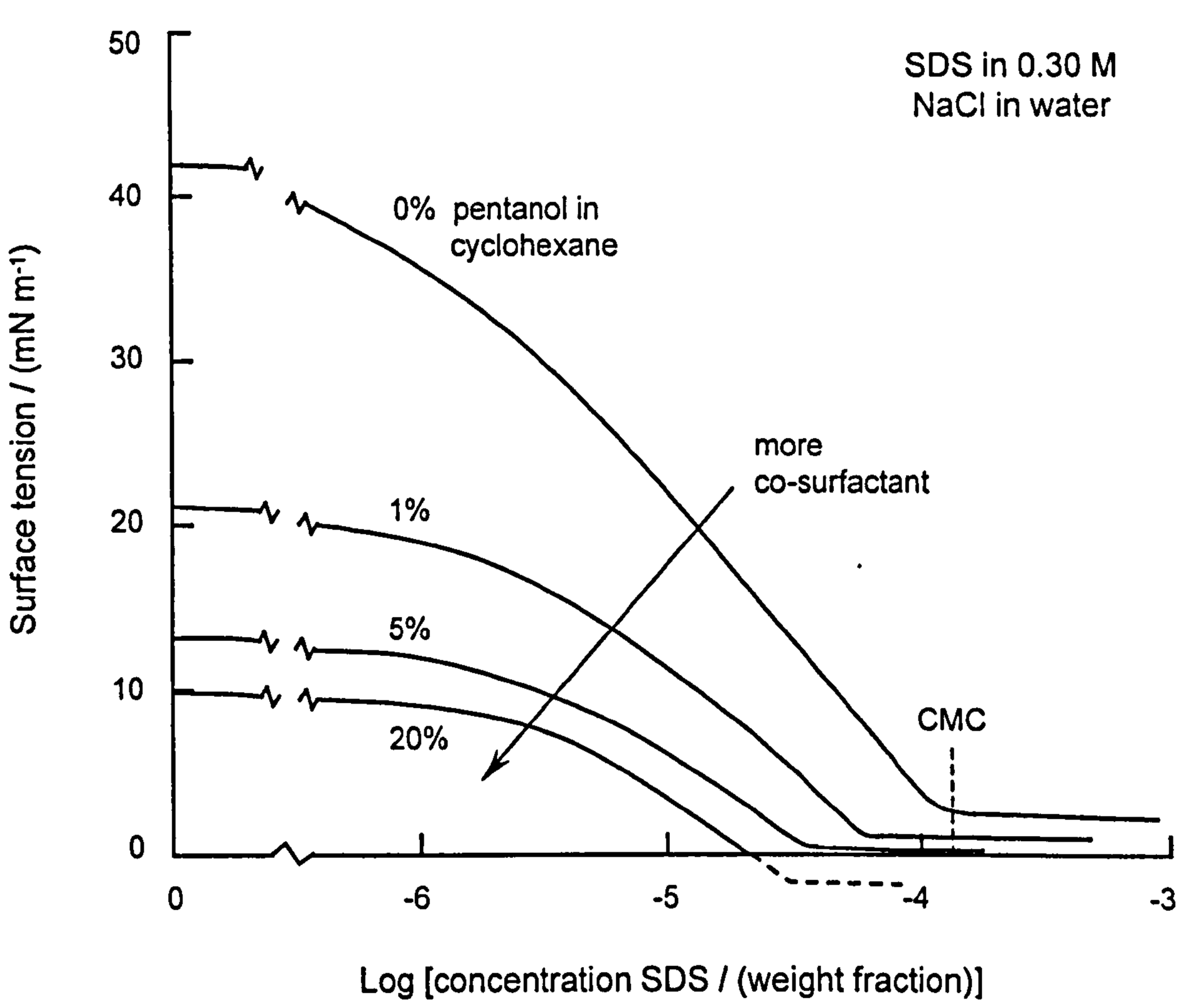

Figure 3.1 Interfacial tension between solutions of sodium dodecylsulphate (SDS) in aqueous 0.30 M NaCl and solutions of *n*-pentanol in cyclohexane. In brine solution SDS can bring the interfacial to nearly zero and with 20% pentanol *zero interfacial tension is reached before micelles of SDS in water are formed.* (after Lekkerkerker *et al.* [14]).

flexibility of the interfacial film, that is film rigidity (see Section 3.3.3), through a significant contribution to the energy barrier. Under the same experimental conditions, different microemulsion systems can have different k_{ex} values [16]: for AOT w/o system at room temperature, k_{ex} is in the range 10^6–10^9 dm^3 mol^{-1} s^{-1}, and for non-ionics C_iE_j, 10^8–10^9 dm^3 mol^{-1} s^{-1} [16,17,20]. In any case, an equilibrium droplet shape and size is always maintained and this can be studied by different techniques [20].

3.3 PHYSICOCHEMICAL PROPERTIES

This section gives an overview of the main parameters required to characterize microemulsions. They will be used and discussed further with reference to w/o microemulsions with anionic surfactants (Chapters 6 and 7). References will be made to related behaviour for planar interfaces presented in Chapter 2.

3.3.1 Predicting microemulsion type

A well-known classification of microemulsions is that of Winsor [21] who identified four general types of phase equilibria:

- Type I: the surfactant is preferentially soluble in water and oil-in-water (o/w) microemulsions form (Winsor I). The surfactant-rich water phase coexists with the oil phase where surfactant is only present as monomers at small concentration.
- Type II: the surfactant is mainly in the oil phase and water-in-oil (w/o) microemulsions form. The surfactant-rich oil phase coexists with the surfactant-poor aqueous phase (Winsor II).
- Type III: a three-phase system where a surfactant-rich middle-phase coexists with both excess water and oil surfactant-poor phases (Winsor III or middle-phase microemulsion).
- Type IV: a single-phase (isotropic) micellar solution, that forms upon addition of a sufficient quantity of amphiphile (surfactant plus alcohol).

Depending on surfactant type and sample environment, types I, II, III or IV form preferentially, the dominant type being related to the molecular arrangement at the interface (see below). As illustrated in Figure 3.2, phase transitions are brought about by increasing either electrolyte concentration (in the case of ionic surfactants) or temperature (for non-ionics). Table 3.1 summarizes the qualitative changes in phase behaviour of anionic surfactants when formulation variables are modified [22].

Various investigators have focused on interactions in an adsorbed interfacial film to explain the direction and extent of interfacial curvature. The first concept was that of Bancroft [23] and Clowes [24] who considered the adsorbed film in emulsion systems to be duplex in nature, with an inner and an outer interfacial tension acting independently [25]. The interface would then curve such that the inner surface was one of higher tension. Bancroft's rule was stated as *"that phase will be external in which the emulsifier is most soluble"*; i.e., oil-soluble emulsifiers will form w/o emulsions and water-soluble emulsifiers o/w emulsions. This qualitative concept was largely extended and several parameters have been proposed to quantify the nature of the surfactant film. They are briefly presented in this section. Further details concerning the three microemulsion types and their location in the phase diagram will be given in Section 3.3.3.

The R-ratio

The R-ratio was first proposed by Winsor [21] to account for the influence of amphiphiles and solvents on interfacial curvature. The primary concept is to relate the energies of interaction between the amphiphile layer and the oil and water regions. Therefore, this R-ratio compares the tendency for an amphiphile to disperse into oil, to its tendency to dissolve in water. If one phase is favoured, the interfacial region tends to take on a definite curvature. A brief description of the concept is given below, and a full account can be found elsewhere [26].

In micellar or microemulsion solutions, three distinct (single or multicomponent) regions can be recognized: an aqueous region, W, an oil or organic region, O, and an amphiphilic region, C. As shown in Figure 3.3, it is useful to consider the interfacial zone as having a definite composition, separating essentially bulk-phase water from bulk-phase oil. In this simple picture, the interfacial zone has a finite thickness, and will contain, in addition to surfactant molecules, some oil and water.

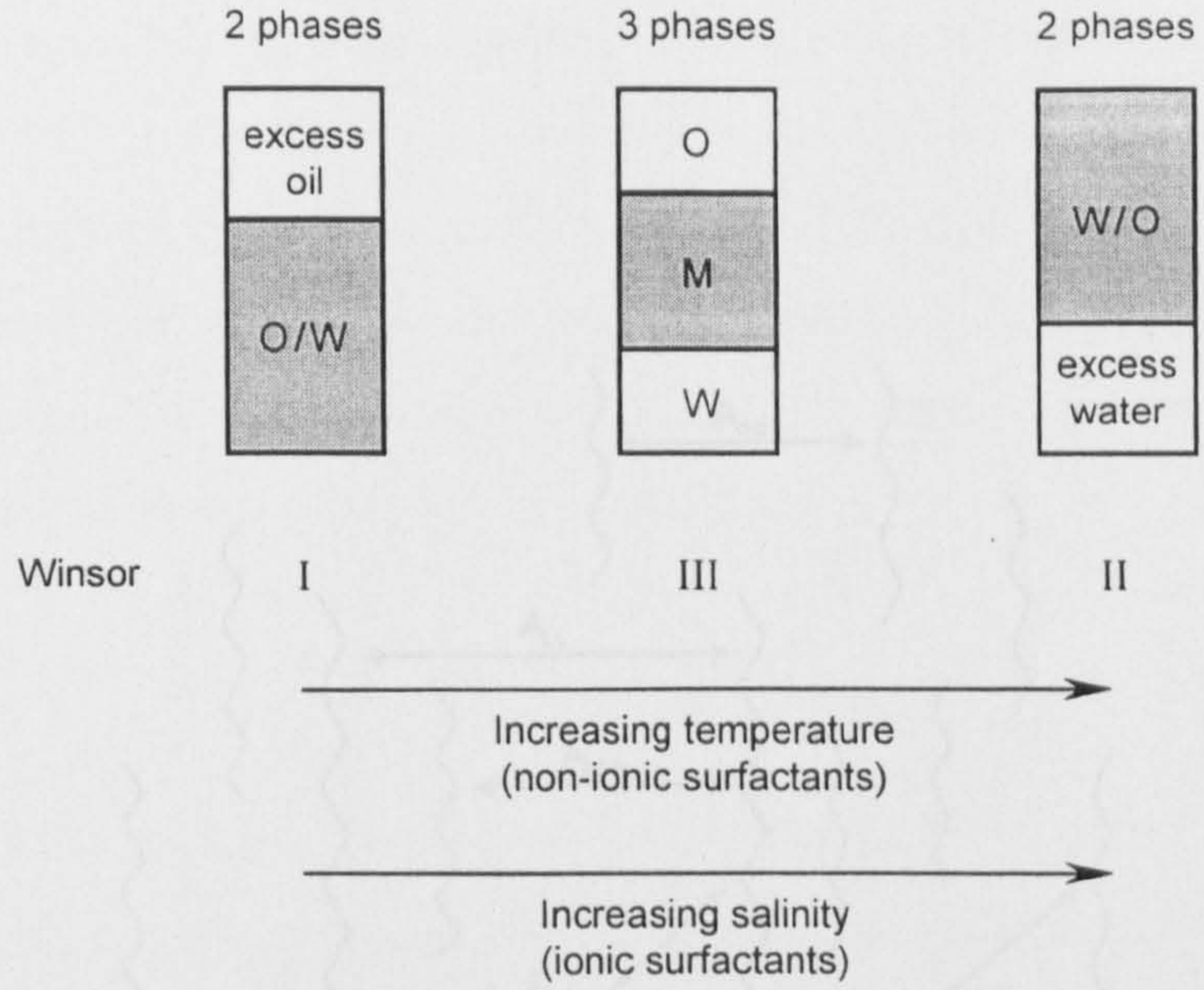

Figure 3.2 Winsor classification and phase sequence of microemulsions encountered as temperature or salinity is scanned for non-ionic and ionic surfactant respectively. Most of the surfactant resides in the shaded area. In the three-phase system the middle-phase microemulsion (M) is in equilibrium with both excess oil (O) and water (W).

Table 3.1 Qualitative effect of several variables on the observed phase behaviour of anionic surfactants. After Bellocq *et al.* [22]

Scanned variables (increase)	Ternary diagram transition
Salinity	I → III → II
Oil: Alkane carbon number	II → III → I
Alcohol: low M.W.[a]	I → III → II
high M.W.[b]	I → III → II
Surfactant: lipophilic chain length	I → III → II
Temperature	II → III → I

[a]Concentration effect of low molecular weight alcohols (M.W.) (methanol, ethanol, propanol)
[b]Concentration effect of higher molecular weight alcohols (butanol and higher M.W.)

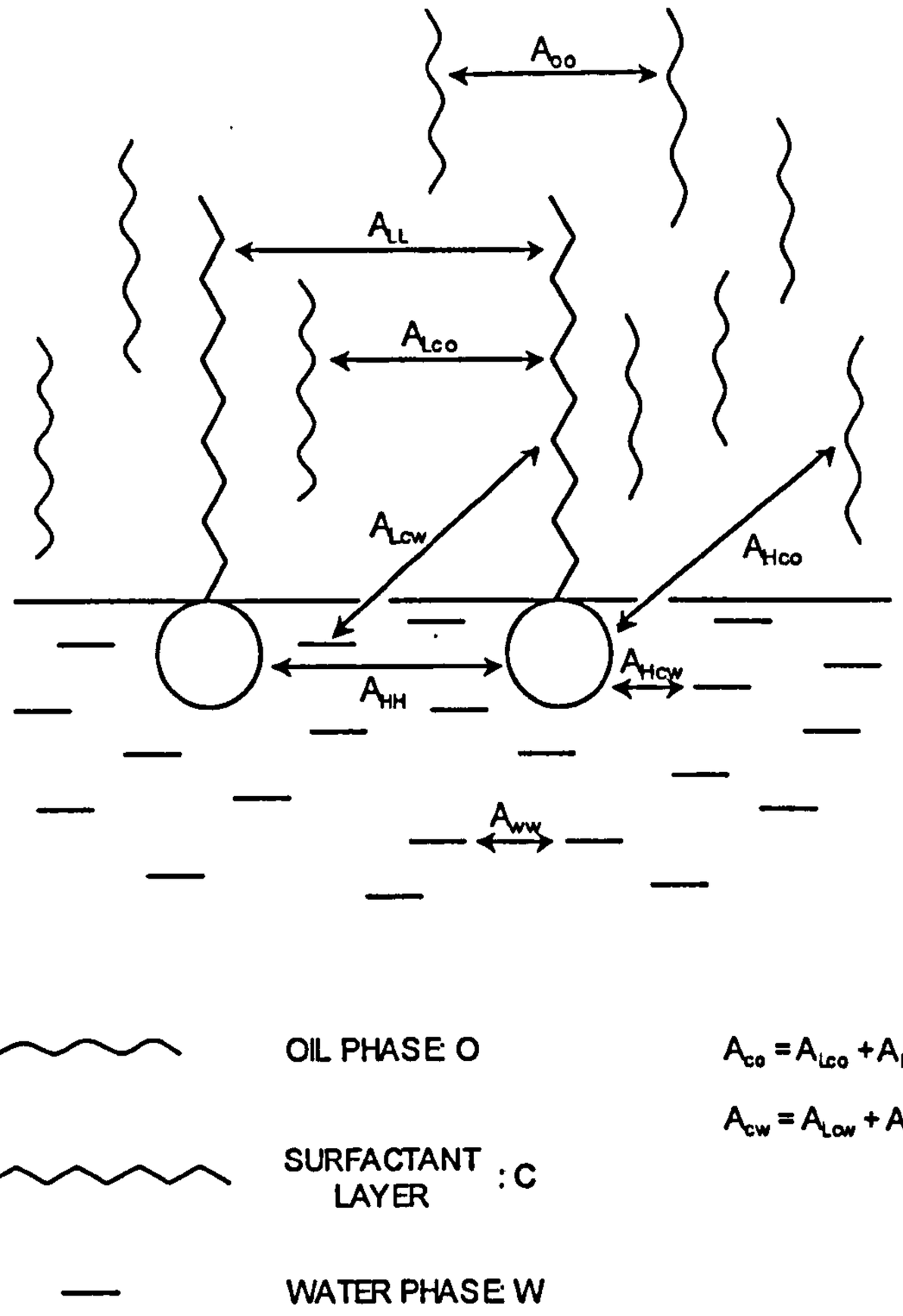

Figure 3.3 Interaction energies in the interfacial region of an oil-surfactant-water system.

Cohesive interaction energies therefore exist within the C layer, and these determine interfacial film stability. They are depicted schematically in Figure 3.3: the cohesive energy between molecules x and y is defined as A_{xy}, and is positive whenever interaction between molecules is attractive. A_{xy} is depicted as the cohesive energy per unit area between surfactant, oil and water molecules residing in the anisotropic interfacial C layer. For surfactant–oil and surfactant–water interactions A_{xy} can be considered to be composed of two additive contributions:

$$A_{xy} = A_{Lxy} + A_{Hxy} \qquad (3.3.1)$$

where A_{Lxy} quantifies interaction between nonpolar portions of the two molecules (typically London dispersion forces) and A_{Hxy} represents polar interactions, especially hydrogen bonding or Colombic interactions. Thus, for surfactant–oil and surfactant–water interactions, cohesive energies to be considered are:

- $A_{co} = A_{Lco} + A_{Hco}$ (3.3.2)
- $A_{cw} = A_{Lcw} + A_{Hcw}$ (3.3.3)

A_{Hco} and A_{Lcw} are generally very small values and can be ignored.

Other cohesive energies are those arising from the following interactions:

- water–water, A_{ww}
- oil–oil, A_{oo}
- hydrophobic–hydrophobic parts (L) of surfactant molecules, A_{LL}
- hydrophilic–hydrophilic parts (H) of surfactant molecules, A_{HH}

The cohesive energy A_{co} evidently promotes miscibility of the surfactant molecules with the oil region, and A_{cw} with water. On the other hand, A_{oo} and A_{LL} oppose miscibility with oil, while A_{ww} and A_{HH} oppose miscibility with water. Therefore, interfacial stability is ensured if the difference in solvent interactions in C with oil and water bulk phases is sufficiently small. Too large a difference, i.e., too strong affinity of C for one phase or the other, would drive to a phase separation.

Winsor expressed qualitatively this variation in dispersing tendency by:

$$R = \frac{A_{co}}{A_{cw}} \qquad (3.3.4)$$

To account for the structure of the oil, and the interactions between surfactant molecules, an extended version of the original R-ratio was proposed [26]:

$$R = \frac{(A_{co} - A_{oo} - A_{ll})}{(A_{cw} - A_{ww} - A_{llll})} \qquad (3.3.5)$$

As mentioned before, in many cases, A_{Hco} and A_{Lcw} are negligible, so A_{co} and A_{cw} can be approximated respectively to A_{Lco} and A_{Hcw}.

In brief, Winsor's primary concept is that this R-ratio of cohesive energies, stemming from interaction of the interfacial layer with oil, divided by energies resulting from interactions with water, determines the preferred interfacial curvature. Thus, if R > 1, the interface tends to increase its area of contact with oil while decreasing its area of contact with water. Thus oil tends to become the continuous phase and the corresponding characteristic system is type II (Winsor II). Similarly, a balanced interfacial layer is represented by R = 1.

Packing parameter and microemulsion structures

Changes in film curvature and microemulsion type can be addressed quantitatively in terms of geometric requirements. This concept was introduced by Israelachivili *et al.* [27] and is widely used to relate surfactant molecular structure to interfacial topology. As described in Section 2.3.3, the preferred curvature is governed by relative areas of the head group, a_o, and the tail group, v/l_c (see Figure 2.6 for the possible aggregate structures). In terms of microemulsion type;

- if $a_o > v/l_c$, then an oil-in-water microemulsion forms,
- if $a_o < v/l_c$, then an water-in-oil microemulsion forms,
- if $a_o = v/l_c$, then a middle-phase microemulsion is the preferred structure.

Hydrophilic–Lipophilic Balance (HLB)

Another concept relating molecular structure to interfacial packing and film curvature is HLB, the hydrophilic–lipophilic balance. It is generally expressed as an empirical equation based on the relative proportions of hydrophobic and hydrophilic groups within the molecule. The concept was first introduced by Griffin [28] who characterized a number of surfactants, and derived an empirical equation for non-ionic alkyl polyglycol ethers (C_iE_j) based on the surfactant chemical composition [29]:

$$\mathrm{HLB} = \left(\mathrm{E_j\ wt\% + OH\ wt\%}\right)/5 \qquad (3.3.6)$$

where E_j wt% and OH wt% are the weight percent of ethylene oxide and hydroxide groups respectively.

Davies *et al.* [30] proposed a more general empirical equation that associates a constant to the different hydrophilic and hydrophobic groups:

$$\mathrm{HLB} = \left[\left(n_H \times \mathrm{H}\right) - \left(n_L \times \mathrm{L}\right)\right] + 7 \qquad (3.3.7)$$

where H and L are constants assigned to hydrophilic and hydrophobic groups respectively, and n_H and n_L the number of these groups per surfactant molecule.

For bicontinuous structures, i.e., zero curvature, it was shown that HLB ≈ 10 [31]. Then w/o microemulsions form when HLB < 10, and o/w microemulsion when HLB > 10. HLB and packing parameter describe the same basic concept, though the latter is more suitable for microemulsions. The influence of surfactant geometry and system conditions on HLB numbers and packing parameter is illustrated in Figure 3.4.

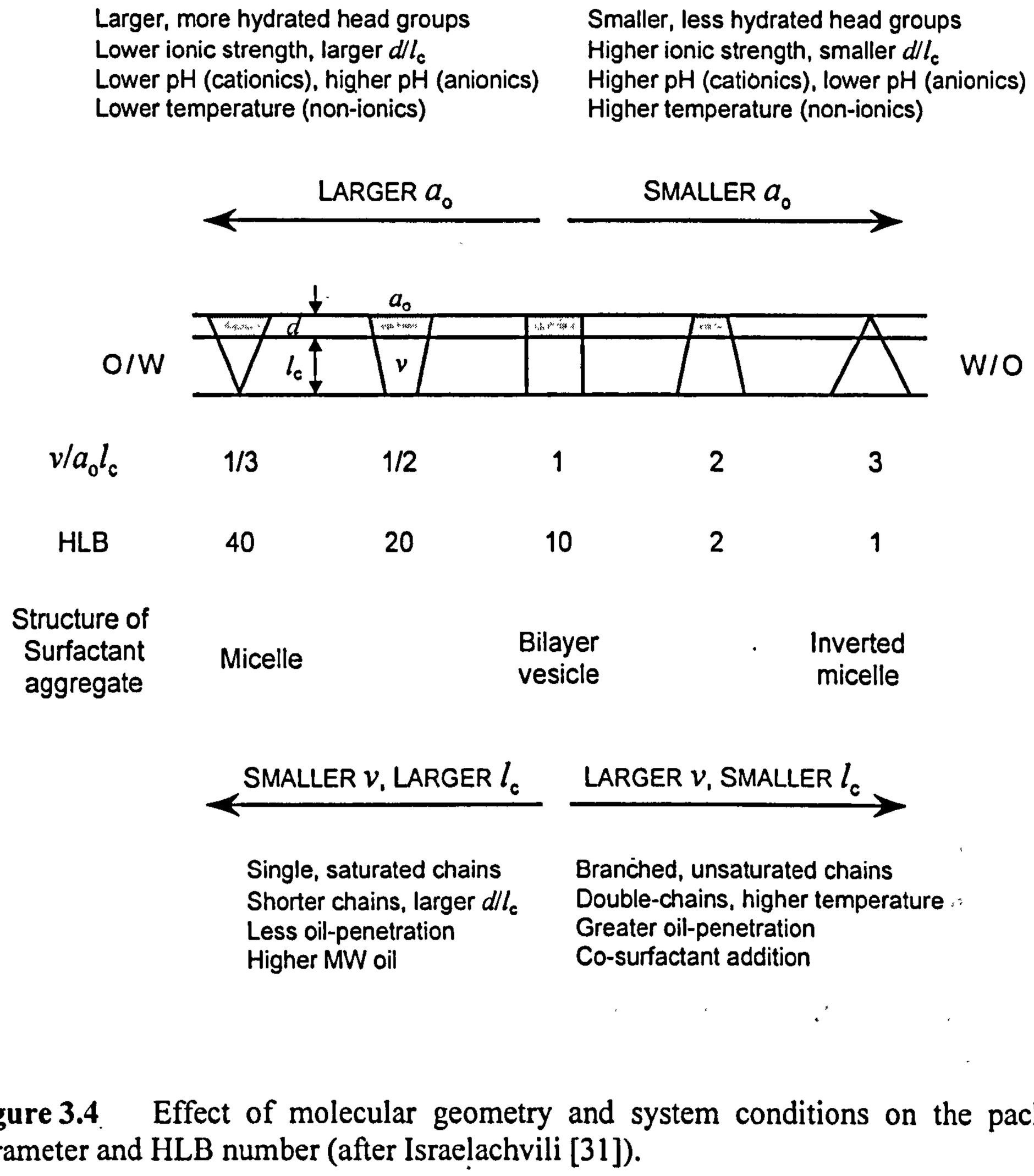

Figure 3.4 Effect of molecular geometry and system conditions on the packing parameter and HLB number (after Israelachvili [31]).

Phase Inversion Temperature (PIT)

Non-ionic surfactants form water–oil microemulsions (and emulsions) with a high temperature sensitivity. In particular, there is a specific phase inversion temperature (PIT) and the film curvature changes from positive to negative. This critical point was defined by Shinoda *et al.* [32]:

- if T < PIT, an oil-in-water microemulsion forms (Winsor I),
- if T > PIT, a water-in-oil microemulsion forms (Winsor II),
- at T = PIT, a middle-phase microemulsion exists (Winsor III) with a spontaneous curvature equal to zero, and a HLB number (Eq. 3.3.6) approximately equal to 10.

The HLB number and PIT are therefore connected; hence the term HLB temperature is sometimes employed [33].

3.3.2 Surfactant film properties

The mechanical properties of a surfactant film at an oil–water interface can be characterized by three phenomenological constants: tension, bending rigidity, and spontaneous curvature. Their relative importance depends on the constraints felt by the film. It is important to understand how these parameters relate to interfacial stability since surfactant films determine the static and dynamic properties of microemulsions (and emulsions). These include phase behaviour and stability, structure, and solubilisation capacity.

Ultra-low interfacial tension

Interfacial (or surface) tensions, γ, were defined in Chapter 2 for planar surfaces, and the same principle applies for curved liquid–liquid interfaces, i.e., it corresponds to the work required to increase interfacial area by unit amount. As mentioned in Section 3.2.1, microemulsion formation is accompanied by ultra-low interfacial oil–water tensions, $\gamma_{o/w}$, typically 10^{-2} to 10^{-4} mN m^{-1}. They are affected by the presence of a co-surfactant, as well as electrolyte and/or temperature, pressure, and oil chain length.

Several studies have been reported on the effect of such variables on $\gamma_{o/w}$. In particular, Aveyard and coworkers performed several systematic interfacial tension measurements on both ionics [34,35] and non-ionics [36], varying oil chain length, temperature, and electrolyte content. For example, in the system water–AOT–*n*-heptane, at constant surfactant concentration (above its CMC), a plot of $\gamma_{o/w}$ as a function of electrolyte (NaCl) concentration shows a deep minimum that corresponds to the Winsor phase inversion; i.e., upon addition of NaCl, $\gamma_{o/w}$ decreases to a minimum critical value (Winsor III structure), then increases to a limiting value close to 0.2–0.3 mN m^{-1} (Winsor II region). At constant electrolyte concentration, varying temperature [34], oil chain length and co-surfactant content [35] have a similar effect. With non-ionics, a similar tension curve and phase inversion are observed, but on increasing temperature [36]. In addition, when increasing surfactant chain length, the interfacial tension curves shift to higher temperatures and the minimum in $\gamma_{o/w}$ decreases [37]. Ultra-low interfacial tensions cannot be measured with standard techniques such as Du Nouy Ring, Wilhelmy plate, or drop volume (DVT). Appropriate techniques for this low tension range are spinning drop tensiometry (SDT) and surface light scattering [38]; SDT will be described in Chapter 5.

Spontaneous curvature

Spontaneous (or natural or preferred) curvature C_o is defined as the curvature formed by a surfactant film when a system consists of equal amounts of water and oil. Then, there is no constraint on the film, which is free to adopt the lowest free energy state. Whenever one phase is predominant, there is a deviation from C_o. In principle, every point on a surface possesses two principal radii of curvature, R_1 and R_2 and their associated principal curvatures are $C_1 = 1/R_1$ and $C_2 = 1/R_2$. Mean and Gaussian curvatures are used to define the bending of surfaces. They are defined as follows [39]:

Mean curvature: $C = \frac{1}{2}(1/R_1 + 1/R_2)$

Gaussian curvature: $\kappa = 1/R_1 \times 1/R_2$

C_1 and C_2 are determined as follows: every point on the surface of the surfactant film has two principal radii of curvature, R_1 and R_2 as shown in Figure 3.5. If a circle is placed tangentially to a point p on the surface and if the circle radius is chosen so that its second derivative at the contact point equals that of the surface in the direction of the tangent (of normal vector, n), then the radius of the circle is a radius of curvature of the surface. The curvature of the surface is described by two such circles chosen in orthogonal (principal) directions as shown in Figure 3.5(*a*).

For a sphere, R_1 and R_2 are equal and positive (Figure 3.5(*b*)). For a cylinder R_2 is indefinite (Figure 3.5(*c*)) and for a plane, both R_1 and R_2 are indefinite. In the special case of a saddle, $R_1 = -R_2$, i.e., at every point the surface is both concave and convex with the same radii (Figure 3.5(*d*)). Both a plane and saddle have the property of zero mean curvature.

The curvature C_o depends both on the composition of the phases it separates and on surfactant type. One argument applied to the apolar side of the interface is that oil can penetrate to some extent between the surfactant hydrocarbon tails (Figure 3.6). The more extensive the penetration, the more curvature is imposed toward the polar side. This results in a decrease of C_o since, by convention, positive curvature is toward oil (and negative toward water). The longer the oil chains, the less they penetrate the surfactant film and the smaller the effect on C_o. Recently, Eastoe *et al*. have studied the extent of solvent penetration in microemulsions stabilized by di-chained surfactants, using SANS and selective deuteration. Results suggested that oil penetration is a subtle effect, which depends on the chemical structures of both surfactant and oil. In particular, unequal surfactant chain length [40-43] or presence of C = C bonds [44] result in a more disordered surfactant/oil interface, thereby providing a region of enhanced oil mixing. For symmetric di-chained surfactants (e.g., DDAB and AOT), however, no evidence for oil mixing was found [42]. The effect of alkane structure, and molecular volume on the oil penetration was also investigated with n-heptane, and cyclohexane. The results indicate that heptane is essentially absent from the layers, but the more compact cyclohexane has a greater penetrating effect [43].

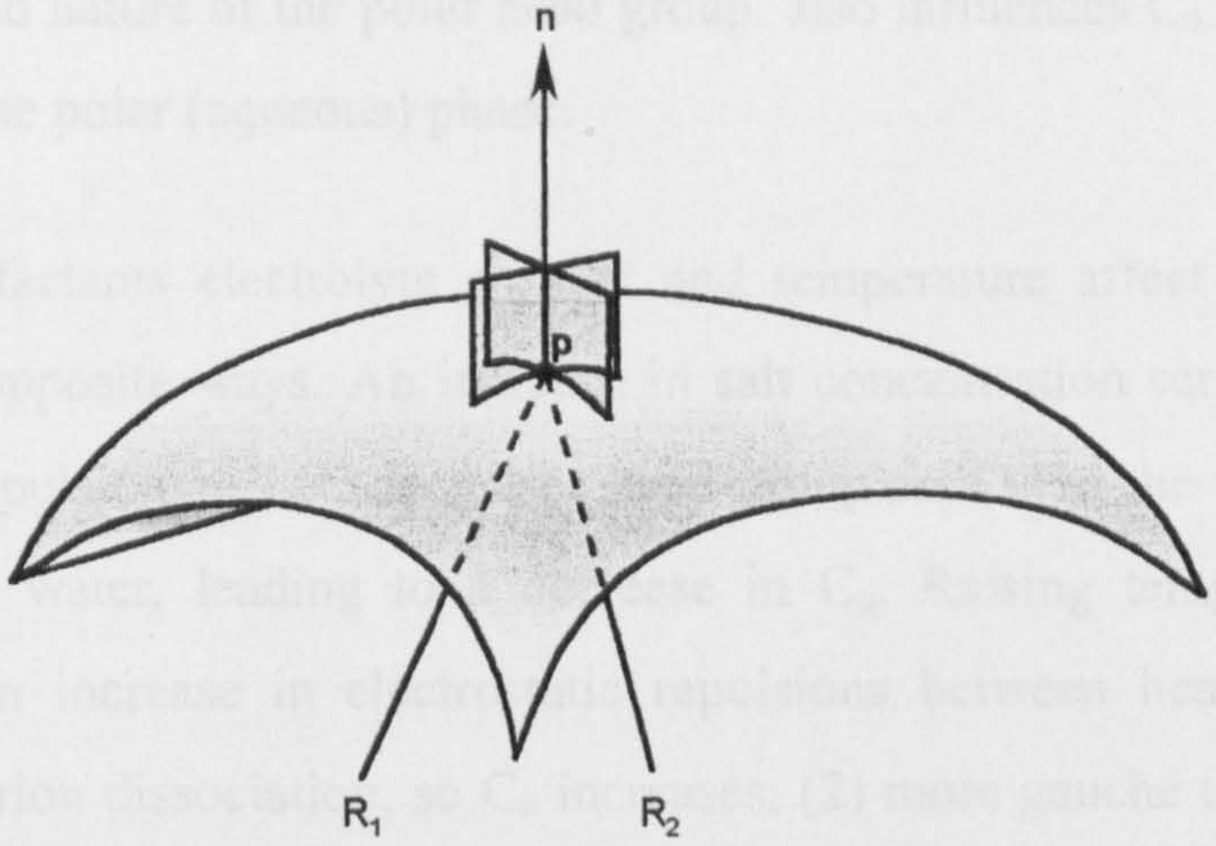

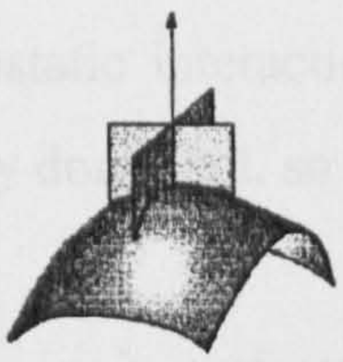

(b) $R_1 > 0$, $R_2 > 0$

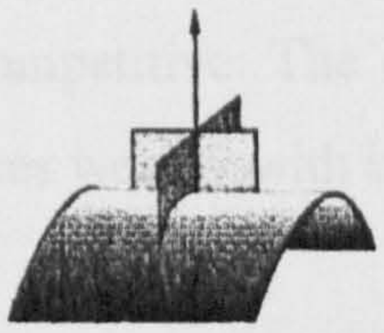

(c) $R_1 = \infty$, $R_2 > 0$

(d) $R_1 < 0$, $R_2 > 0$

Figure 3.5 Principal curvatures of different surfaces. (a) Intersection of the surfactant film surface with planes containing the normal vector (n) to the surface at the point p. (*b*) convex curvature, (*c*) cylindrical curvature, (*d*) saddle-shaped curvature. After Hyde *et al*. [39].

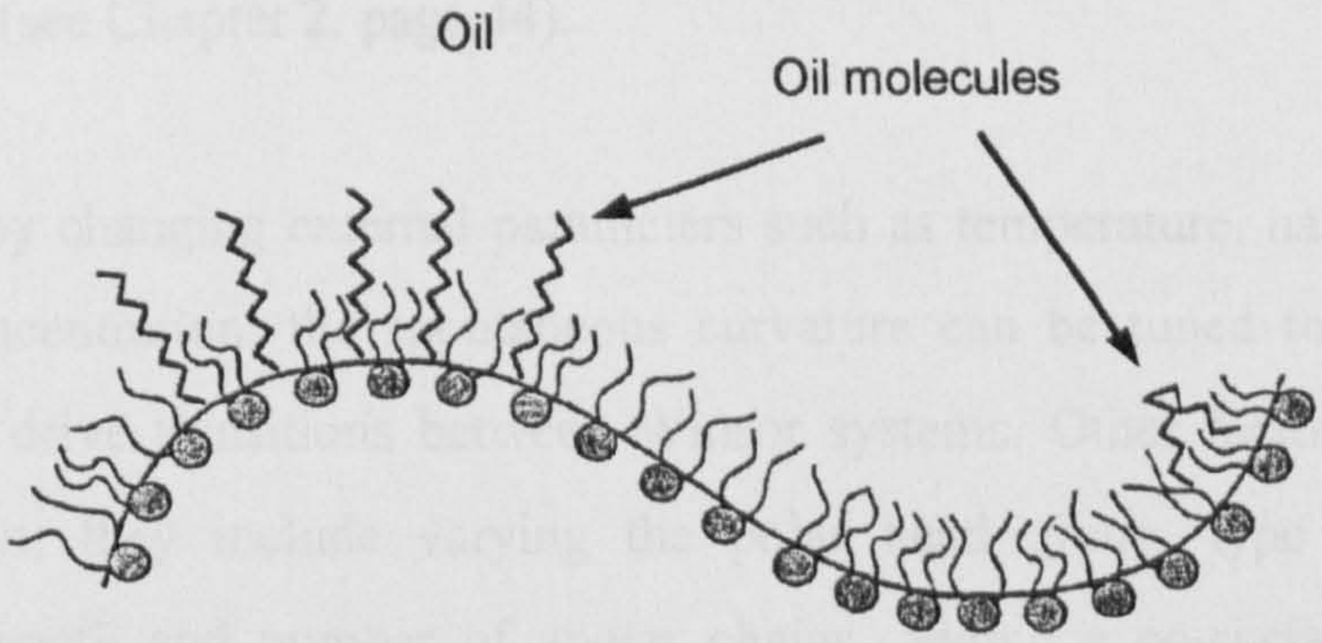

Figure 3.6 Penetration of oil molecules between the apolar chains in the surfactant film. Note the greater extent of penetration when the film curves toward water.

Surfactant type, and nature of the polar head group, also influences C_o through different interactions with the polar (aqueous) phase:

- For ionic surfactants electrolyte content and temperature affect the spontaneous curvature in opposite ways. An increase in salt concentration screens electrostatic head group repulsions – i.e., decreases head group area – so the film curves more easily toward water, leading to a decrease in C_o. Raising temperature has two effects: (1) an increase in electrostatic repulsions between head groups due to higher counterion dissociation, so C_o increases; (2) more gauche conformations are induced in the surfactant chains, which become more coiled, resulting in a decrease in C_o. Therefore the combined effects of temperature on the apolar chains and on electrostatic interactions are competitive. The electrostatic term is believed to be slightly dominant, so C_o increases weakly with increasing temperature.

- For non-ionic surfactants, unsurprisingly, electrolytes have very little effect on C_o, whereas temperature is a critical parameter due to the strong dependence of their solubility (in water or oil) on temperature. For surfactants of the C_iE_j type as temperature increases water becomes a less good solvent for the hydrophilic units and penetrates less into the surfactant layer. In addition, on the other side of the film, oil can penetrate further into the hydrocarbon chains, so that increasing temperature for this type of surfactant causes a strong decrease in C_o. This phenomenon explains the strong temperature effects on the phase equilibria of such surfactants as shown in Figure 2.8 (see Chapter 2, page 44).

Thus, by changing external parameters such as temperature, nature of the oil or electrolyte concentration, the spontaneous curvature can be tuned to the appropriate value, and so drive transitions between Winsor systems. Other factors affect C_o in a similar fashion; they include varying the polar head group, type and valency of counterions, length and number of apolar chains, adding a co-surfactant, or mixing surfactants.

Film bending rigidity

Film rigidity is an important parameter associated with interfacial curvature. The concept of film bending energy was first introduced by Helfrich [45] and is now considered as an essential model for understanding microemulsion properties. It can be described by two elastic moduli [46] that measure the energy required to deform the interfacial film from a preferred mean curvature:

- the mean bending elasticity (or rigidity), K, associated with the mean curvature, that represents the energy required to bend unit area of surface by unit amount. K is positive, i.e., spontaneous curvature is favoured;
- the elasticity $\overline{K}$, associated with the Gaussian curvature, that accounts for the film topology. $\overline{K}$ is also in Joules and is negative for spherical structures or positive for bicontinuous cubic phases.

Theoretically, it is expected that bending moduli should depend on surfactant chain length [47], area per surfactant molecule in the film [48] and electrostatic head group interactions [49].

The film rigidity theory is based on the interfacial free energy associated with film curvature. The free energy, F, of a surfactant layer at a liquid interface may be given by the sum of an interfacial energy term, F_i, a bending energy term, F_b, and an entropic term, F_{ent}. For a droplet type structure this is written as [50]:

$$F = F_i + F_b + F_{ent} = \gamma A + \int\left[\frac{K}{2}(C_1 + C_2 - 2C_o)^2 + \overline{K}C_1C_2\right]dA + nk_BTf(\phi) \qquad (3.3.8)$$

where γ is the interfacial tension, A is the total surface area of the film, K is the mean elastic bending modulus, $\overline{K}$ is the Gaussian bending modulus, C_1 and C_2 are the two principal curvatures, C_o the spontaneous curvature, n is the number of droplets, k_B is the Boltzmann constant, and $f(\phi)$ is a function accounting for the entropy of mixing of the microemulsion droplets, where ϕ is the droplet core volume fraction. For $\phi < 0.1$, it was shown that $f(\phi) = [\ln(\phi) - 1]$ [50]. Microemulsion formation is associated with ultra-low interfacial tension, γ, so the γA term is small compared to F_b and F_{ent} and can be ignored as an approximation.

As mentioned previously, the curvatures C_1, C_2 and C_o can be expressed in terms of radii as $1/R_1$, $1/R_2$, and $1/R_o$ respectively. For spherical droplets, $R_1 = R_2 = R$, and the interfacial area is $A = n4\pi R^2$. Note that R and R_o are core radii rather than droplet radii [50]. Solving Eq. 3.3.8 and dividing by area A, the total free energy, F, for spherical droplets (of radius R) is expressed as:

$$\frac{F}{A} = 2K\left(\frac{1}{R} - \frac{1}{R_o}\right)^2 + \frac{\overline{K}}{R^2} + \left[\frac{k_B T}{4\pi R^2} f(\phi)\right] \qquad (3.3.9)$$

For systems where the solubilisation boundary is reached (WI or WII region), a microemulsion is in equilibrium with an excess phase of the solubilisate and the droplets have achieved their maximum size, i.e., the maximum core radius, R_{max}^{av}. Under this condition the minimization of the total free energy leads to a relation between the spontaneous radius, R_o, and the elastic constants K and $\overline{K}$ [51]:

$$\frac{R_{max}^{av}}{R_o} = \frac{2K + \overline{K}}{2K} + \frac{k_B T}{8\pi K} f(\phi) \qquad (3.3.10)$$

A number of techniques have been used to determine K and $\overline{K}$ separately, in particular, ellipsometry, X-ray reflectivity, and small-angle X-ray scattering (SAXS) techniques [52-54]. De Gennes and Taupin [55] have developed a model for bicontinuous microemulsions. For $C_o = 0$ the layer is supposed to be flat in the absence of thermal fluctuations. They introduced the term ξ_K, the persistence length of the surfactant layer that relates to K via:

$$\xi_K = a\exp(2\pi K / k_B T) \qquad (3.3.11)$$

where a is a molecular length and ξ_K is the correlation length for the normals to the layer, i.e., the distance over which this layer remains flat in the presence of thermal fluctuations. ξ_K is extremely sensitive to the magnitude of K. When $K >> k_B T$, ξ_K is macroscopic, i.e., the surfactant layer is flat over large distances and ordered structures such as lamellar phases may form. If K is reduced to $\sim k_B T$ then ξ_K is microscopic,

ordered structures are unstable and disordered phases such as microemulsions may form. Experiments reveal that K is typically between 100 k_BT for condensed insoluble monolayers [56] and about 10 k_BT for lipid bilayers [57-59] but can decrease below k_BT in microemulsion systems [60]. The role of $\overline{K}$ is also important, however, there are few measurements of this quantity in the literature [e.g., 53,61]. Its importance in determining the structure of surfactant–oil–water mixtures is still far from clear.

An alternative, more accessible, method to quantify film rigidities is to calculate the composite parameter $(2K+\overline{K})$ using tensiometry and SANS techniques. This parameter can be derived for droplet microemulsion at the solubilisation boundary, WI or WII system, by combining the radius of the droplet with interfacial tensions or droplet polydispersity. Two expressions can be derived from Eq. 3.3.9 and 3.3.10.

1. *Using the interfacial tension $\gamma_{o/w}$ (measured by SLS or SDT) and the maximum mean core radius R_{max}^{av} (measured by SANS):*

$\gamma_{o/w}$ at the interface between microemulsion and excess phases at the solubilisation boundary can be expressed in terms of these elastic moduli and R_{max}^{av} [52]. Any new area created must be covered by a monolayer of surfactant, and so this energy may be calculated in the case of WI or WII systems since the surfactant monolayer is taken from around the curved microemulsion droplets [56]. To do this it is necessary to unbend the surfactant film, introducing a contribution from K, of $2K/(R_{max}^{av})^2$. The resulting change in the number of microemulsion droplets introduces an entropic contribution and a contribution due to the change in topology involving $\overline{K}$, of $\overline{K}/(R_{max}^{av})^2$. So the interfacial tension between the microemulsion and excess phase is given by:

$$\gamma_{o/w} = \frac{2K+\overline{K}}{(R_{max}^{av})^2} + \frac{k_BT}{4\pi(R_{max}^{av})^2} f(\phi) \qquad (3.3.11)$$

which gives for the bending moduli:

$$2K+\overline{K} = \gamma_{o/w}(R_{max}^{av})^2 - \frac{k_BT}{4\pi} f(\phi) \qquad (3.3.12)$$

2. *Using the Schultz polydispersity width* $p = \sigma/R^{av}_{max}$ *obtained from SANS analysis:*

Droplet polydispersity relates to the bending moduli through thermal fluctuations of the microemulsion droplets. Safran [62] and Milner [63] described the thermal fluctuations by an expansion of the droplet deformation in terms of spherical harmonics. The principal contribution to these fluctuations was found to arise from the deformation mode $l = 0$ only [50]; and $l = 0$ deformations are fluctuations in droplet size, i.e., changes of the mean droplet radius and hence the droplet polydispersity. In the case of the two phase equilibria at maximum solubilisation (WI or WII), this polydispersity, p, may be expressed as a function of K and $\overline{K}$:

$$p^2 = \frac{u_o^2}{4\pi} = \frac{k_B T}{8\pi(2K + \overline{K}) + 2k_B T f(\phi)} \qquad (3.3.13)$$

where u_o is the fluctuation amplitude for the $l = 0$ mode. This polydispersity is given by the SANS Schultz polydispersity parameter σ/R^{av}_{max} [64], and Eq. 3.3.13 can be written:

$$2K + \overline{K} = \frac{k_B T}{8\pi(\sigma/R^{av}_{max})^2} - \frac{k_B T}{4\pi} f(\phi) \qquad (3.3.14)$$

Therefore Eq. 3.3.12 and 3.3.14 give two accessible expressions for the sum $(2K + \overline{K})$ using data from SANS and tensiometry. This approach has been shown to work well with non-ionic films in WI systems [50,65], and also cationic [64] and zwitterionic [66] layers in WII microemulsions. Figure 3.7 shows results obtained by Eastoe *et al.* for these latter two as a function of alkyl carbon number *n*-C. The good agreement between equation 3.3.12 and 3.3.14 suggests they can be used with confidence. These values are in line with current statistical mechanical theories [48], which suggest that K should vary as *n*-$C^{2.5}$ to *n*-C^3, whereas there is only a small effect on $\overline{K}$.

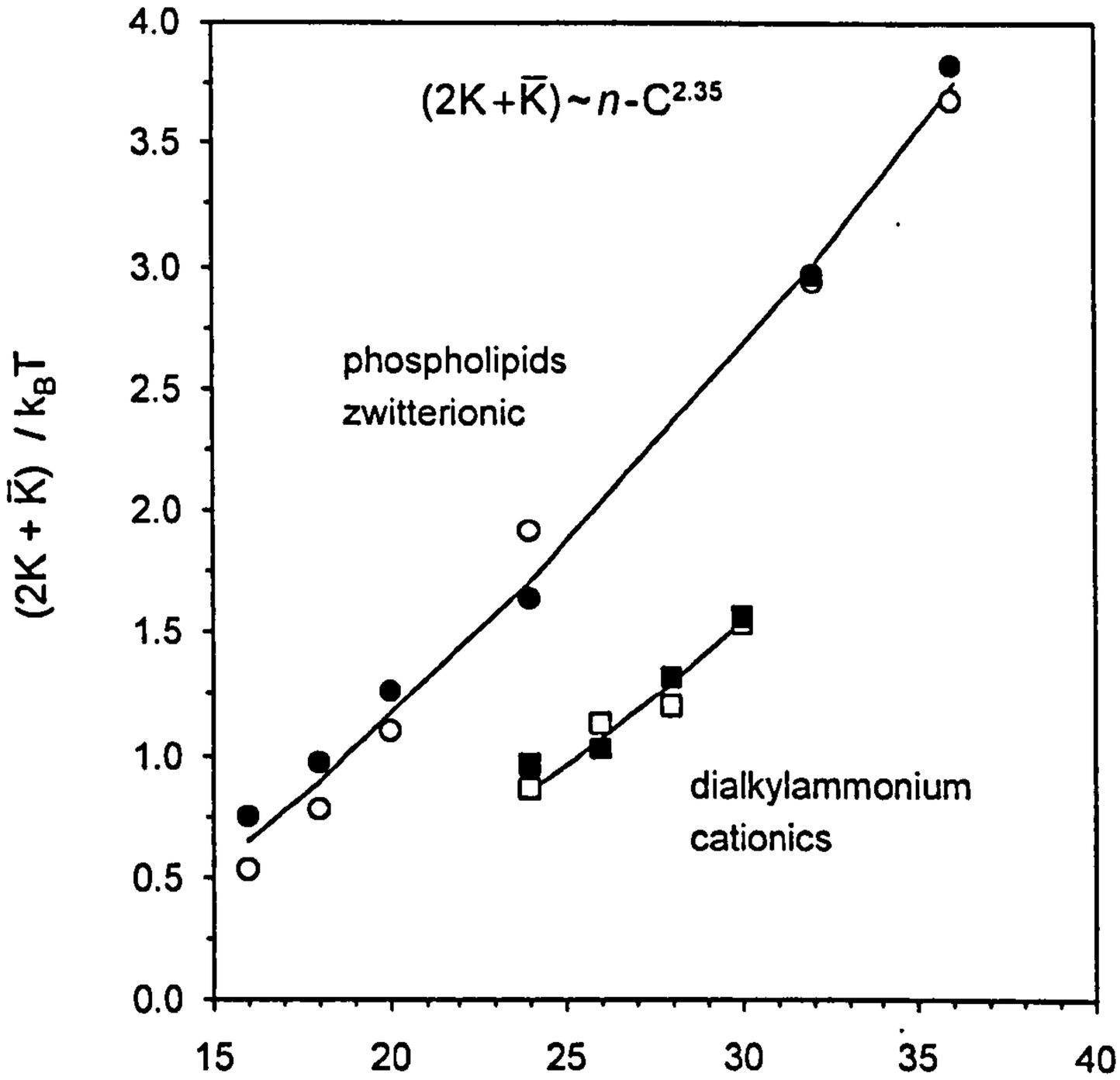

SANS	$(2K+\bar{K}) = \frac{k_B T}{8\pi(\sigma/R_{max}^{av})^2} - \frac{k_B T}{4\pi} f(\phi)$	● ■
SANS & tensiometry	$(2K+\bar{K}) = \gamma_{o/w}(R_{max}^{av})^2 - \frac{k_B T}{4\pi} f(\phi)$	○ □

Figure 3.7 Film rigidities $(2K + \bar{K})$ as a function of total alkyl carbon number *n*-C from Winsor II microemulsions. The lines are guides to the eye. After Eastoe *et al.* [64,66].

3.3.3 Phase behaviour

Solubilisation and interfacial properties of microemulsions depend upon pressure, temperature and also on the nature and concentration of the components. The determination of phase stability diagrams (or phase maps), and location of the different structures formed within these water(salt)–oil–surfactant–alcohol systems in terms of variables are, therefore, very important. Several types of phase diagram can be identified depending on the number of variables involved. In using an adequate mode of representation, it is possible to describe not only the limits of existence of the single and multiphase regions, but also to characterize equilibria between phases (tie-lines, tie-triangles, critical points, etc.). Below is a brief description of ternary and binary phase maps, as well as the phase rule that dictates their construction.

Phase rule

The phase rule enables the identification of the number of variables (or degrees of freedom) depending on the system composition and conditions. It is generally written as [67]:

$$F = 2 + N - P \qquad (3.3.15)$$

where F is the number of possible independent changes of state or degrees of freedom, N the number of independent chemical constituents, and P the number of phases present in the system. A system is called invariant, monovariant, bivariant, and so on, according to whether F is zero, 1, 2, and so on. For example, in the simplest case of a system composed of three components and two phases, F is univariant at a fixed temperature and pressure. This means that the mole or weight fraction of one component in one of the phases can be specified but all other compositions in both phases are fixed. In general, microemulsions contain at least three components: oil (O), water (W) and amphiphile (S), and as mentioned previously a co-surfactant (alcohol) and/or an electrolyte are usually added to tune the system stability. In this thesis, all systems can be considered as simple O–W–S systems: whenever a co-surfactant is used, the ratio oil:alcohol is kept constant and it is assumed that the alcohol does not interact with any other component so that the mixture can be treated (to a first approximation) as a three-component system. At constant pressure, the composition–temperature phase behaviour

can be presented in terms of a phase prism, as illustrated in Figure 3.8. However, the construction of such a phase map is rather complex and time consuming so it is often convenient to simplify the system by studying specific phase-cuts. The number of variables can be reduced either by keeping one term constant and/or by combining two or more variables. Then, ternary and binary phase diagrams are produced.

Ternary phase diagrams

At constant temperature and pressure, the ternary phase diagram of a simple three-component microemulsion is divided into two or four regions as shown in Figure 3.9. In each case, every composition point within the single-phase region above the demixing line corresponds to a microemulsion. Composition points below this line correspond to multiphase regions comprising in general microemulsions in equilibrium with either an aqueous or an organic phase or both, i.e., Winsor type systems (see Section 3.3.1).

Any system whose overall composition lies within the two-phase region (e.g., point *o* in Figures 3.9(*a*) and 3.9(*c*)) will exist as two phases whose compositions are represented by the ends of the "tie-line", i.e., a segment formed by phases *m* and *n*. Therefore, every point on a particular tie-line has identical coexisting phases (*m* and *n*) but of different relative volumes. When the two conjugate phases have the same composition ($m = n$), this corresponds to the plait (or critical) point, *p*.

If three phases coexist (Figure 3.9(*b*)), i.e., corresponding to WIII, the system at constant temperature and pressure is, according to the phase rule, invariant. Then, there is a region of the ternary diagram that consists of three-phase systems having invariant compositions and whose boundaries are tie-lines in the adjacent two-phase regions that surround it. This region of three-phase invariant compositions is therefore triangular in form and called "tie-triangle" [26]. Any overall composition, such as point *q* (Figure 3.9(*b*)) lying within the tie-triangle will divide into three phases having compositions corresponding to the vertices A, B, and C of the triangle. The compositions A, B, and C are invariant in the sense that varying the position *q*, the overall composition, throughout the triangle will result in variations in the amounts of the phases A, B, and C but not in their composition.

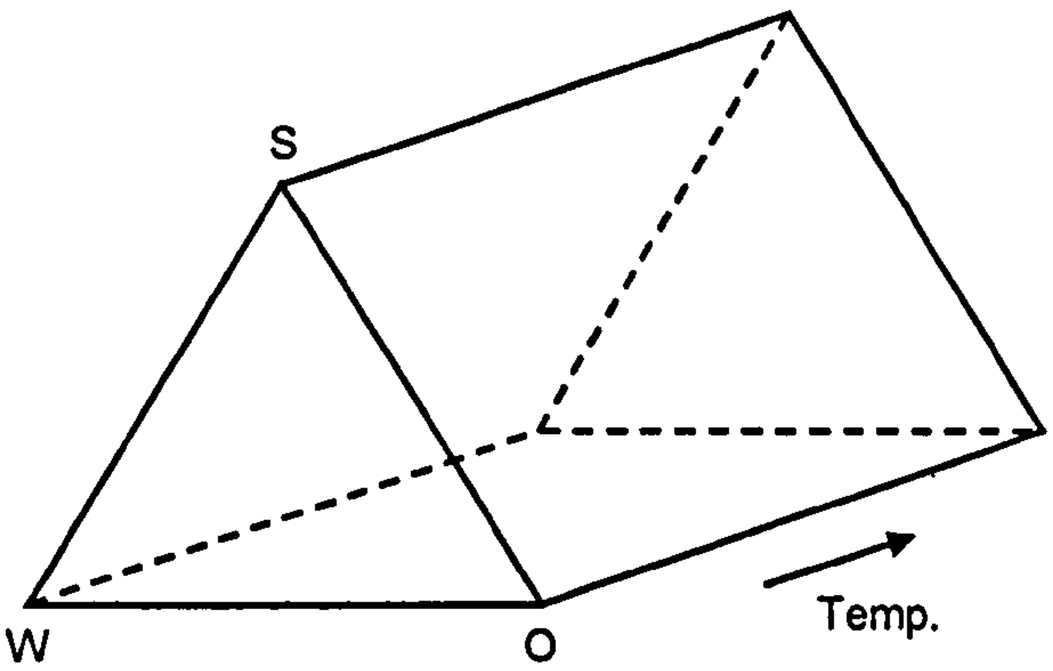

Figure 3.8 The phase prism, describing the phase behaviour of a ternary system at constant pressure.

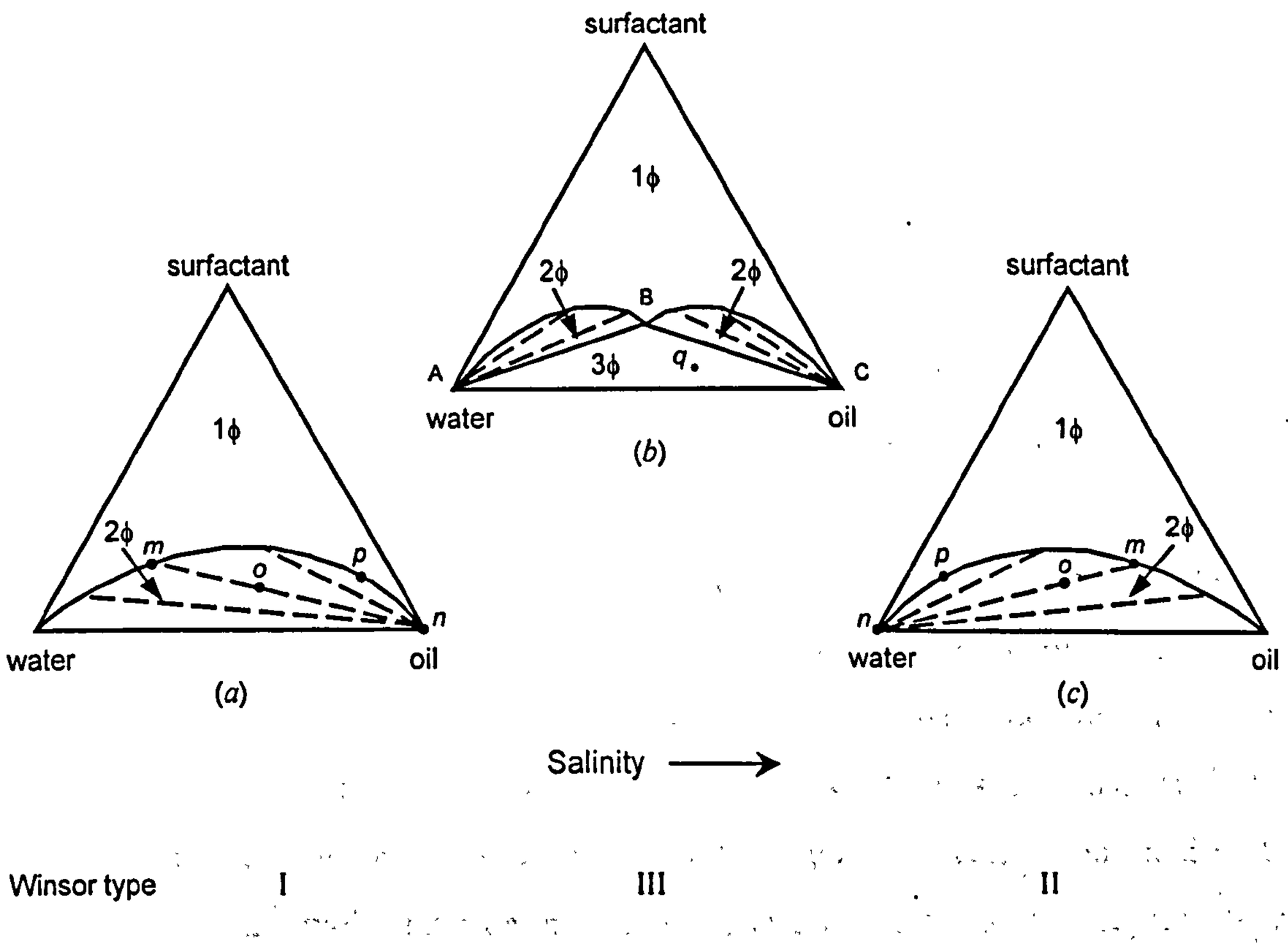

Figure 3.9 Ternary diagram representations of two- and three-phase regions formed by simple water–oil–surfactant systems at constant temperature and pressure. (*a*) Winsor I type, (*b*) Winsor III type, (*c*) Winsor II type systems.

Binary phase diagrams

As mentioned previously, ternary diagrams can be further simplified by fixing some parameters and/or combining two variables together (e.g., water and electrolyte into brine, or water and oil into water–to–oil ratio), i.e., reducing the degrees of freedom. Then, determining the phase diagram of such systems reduces to a study of a planar section through the phase prism. Examples of such pseudo-binary diagrams are given in Figures 3.10 to 3.12 for non-ionic and anionic surfactants.

Figure 3.10 shows the schematic phase diagram for a non-ionic surfactant–water–oil ternary system. Since temperature is a crucial variable in the case of non-ionics, the pseudo-binary diagram is represented by the planar section defined by $\phi_w = \phi_o$, where ϕ_w and ϕ_o are the volume fractions of water and oil respectively. Then, at constant pressure, defining the system in a single-phase region requires the identification of two independent variables (F = 2), i.e., temperature and surfactant concentration. The section shown in Figure 3.10(*b*) can be used to determine T_L and T_U, the lower and upper temperatures, respectively, of the phase equilibrium W+M+O (with M, the microemulsion phase), and the minimum amount of surfactant necessary to solubilise equal amounts of water and oil, denoted C_s^* [68]. The lower C_s^* the more efficient the surfactant. Figure 3.11 illustrates the determination of a second possible section for a non-ionic surfactant–water–oil ternary system: pressure and surfactant concentration are kept constant, leaving the two variables, temperature and water–to–oil ratio ($\phi_{w\text{-}o}$). This diagram shows the various surfactant phases obtained as a function of temperature and water–to–oil ratio [68]. The third example (Figure 3.12) concerns an anionic surfactant, Aerosol-OT, and is of interest here since this particular pseudo-binary phase diagram will be used throughout this thesis. In order to obtain F = 2 when defining the ternary W–O–S system in a single-phase region at constant pressure, the surfactant concentration parameter is fixed. Then, the two variables are temperature and *w*, the water–to–surfactant molar ratio defined as *w* = [water] / [surfactant]. *w* represents the number of water molecules solubilised per surfactant molecule, so that this phase diagram characterizes the surfactant efficiency, as a microemulsifier. Further details on the phase behaviour of AOT can be found elsewhere [69,70], and this particular type of binary phase diagram will be illustrated in Chapters 6 and 7 for a series of AOT-like surfactants.

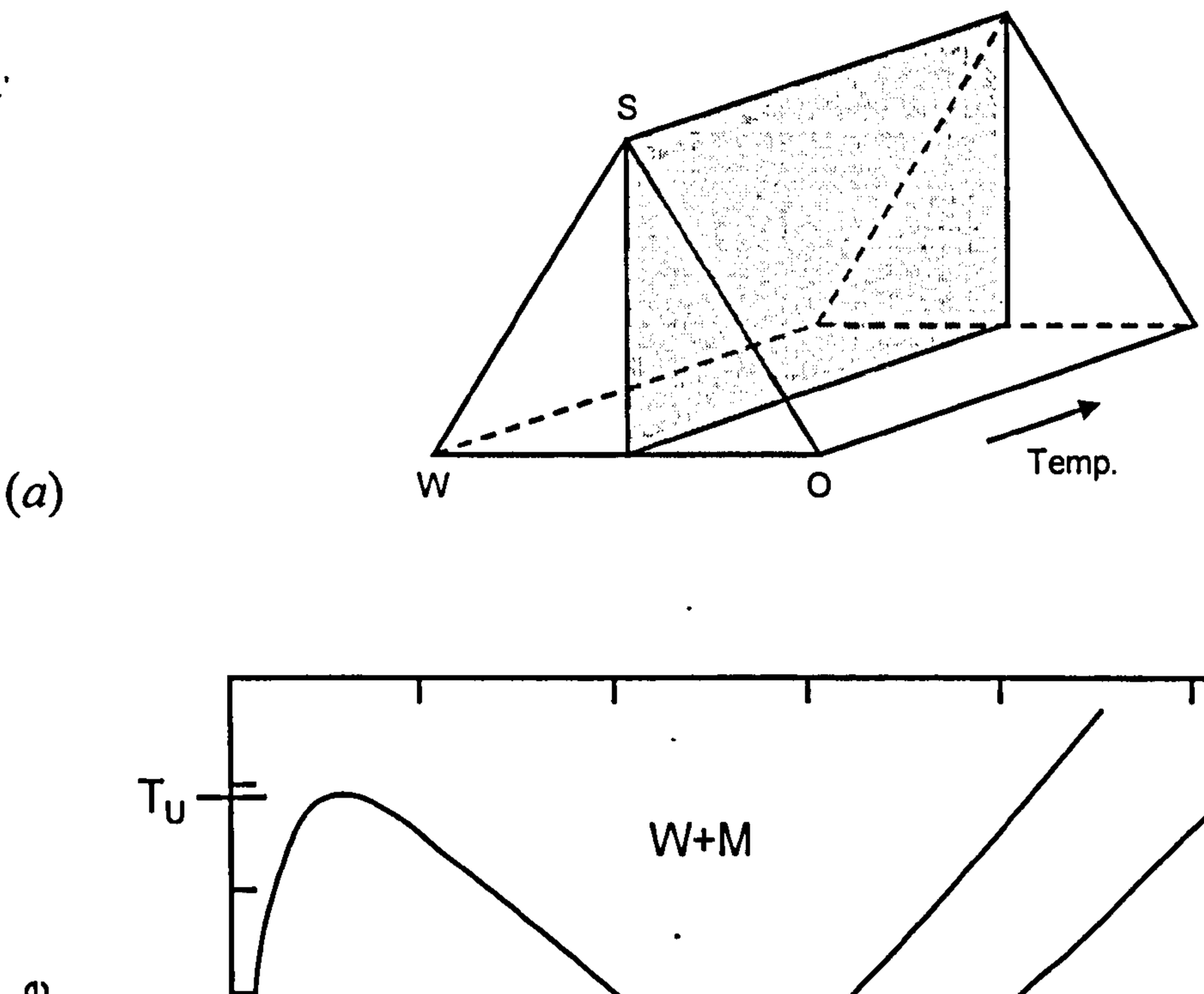

Figure 3.10 Binary phase behaviour in ternary microemulsion systems formed with non-ionic surfactants. (*a*) Illustration of the section through the phase prism at equal water and oil content. (*b*) Schematic phase diagram plotted as temperature versus surfactant concentration C_s. T_L and T_U are the lower and upper temperatures, respectively, of the phase equilibrium W+M+O. T^* is the temperature at which the three-phase triangle is an isosceles, i.e., when the middle-phase microemulsion contains equal amounts of water and oil. This condition is also termed 'balanced'. C_s^* is the surfactant concentration in the middle-phase microemulsion at balanced conditions. 'Lam' denotes a lamellar liquid crystalline phase. After Olsson and Wennerström [68].

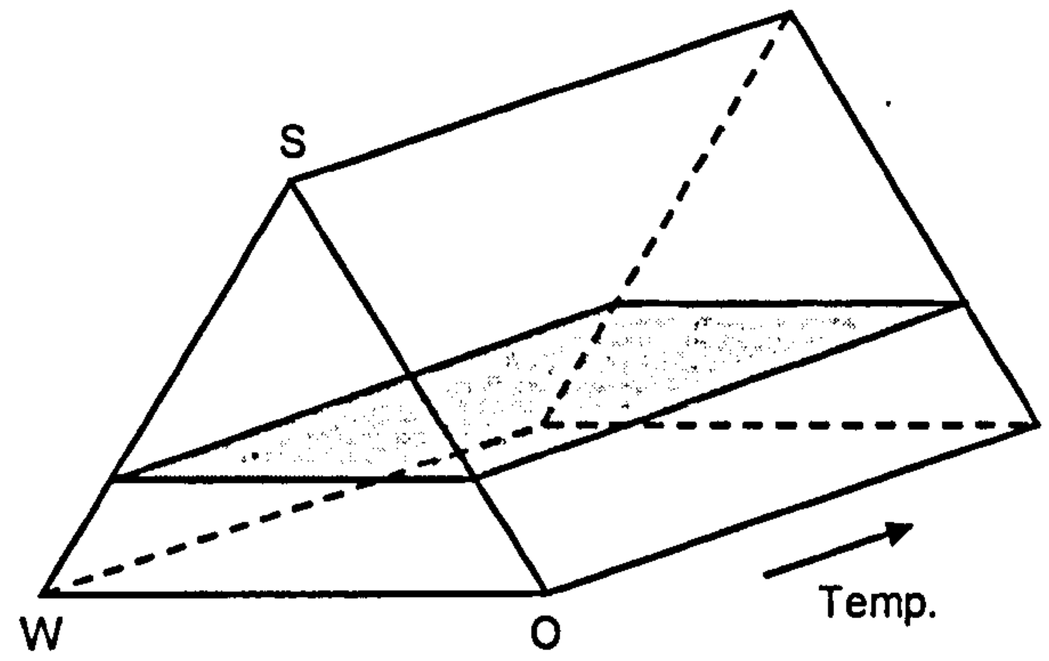

(a)

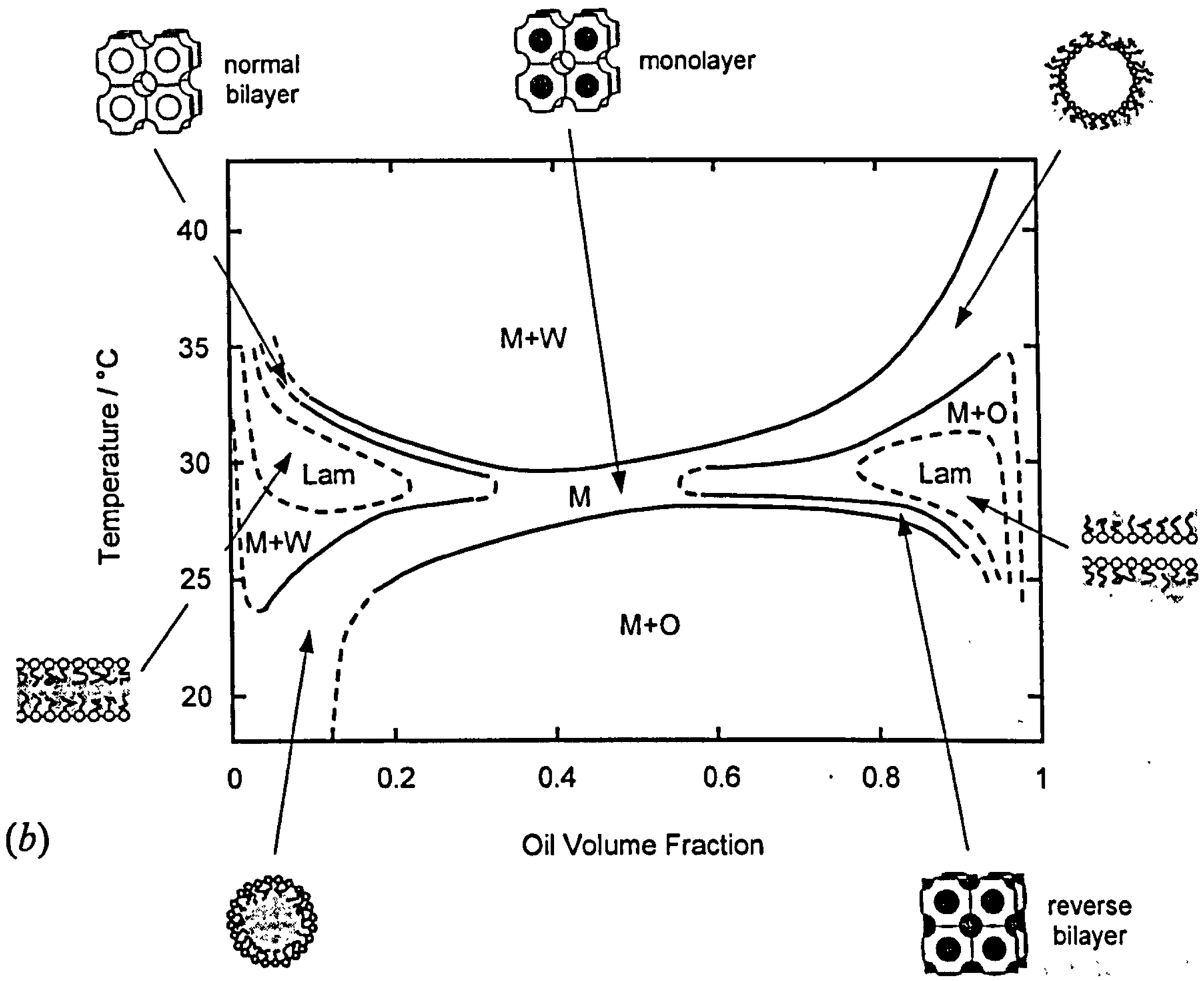

(b)

Figure 3.11 Binary phase behaviour in ternary microemulsion systems formed with non-ionic surfactants. (*a*) Illustration of a section at constant surfactant concentration through the phase prism. (*b*) Schematic phase diagram, plotted as temperature versus volume fraction of oil, ϕ_o, at constant surfactant concentration. Also shown are various microstructures found in different regions of the microemulsion phase, M. At higher temperatures the liquid phase is in equilibrium with excess water (M+W), and at lower temperatures with excess oil (M+O). At intermediate temperatures a lamellar phase is stable at higher water contents and higher oil contents, respectively. After Olsson and Wennerström [68].

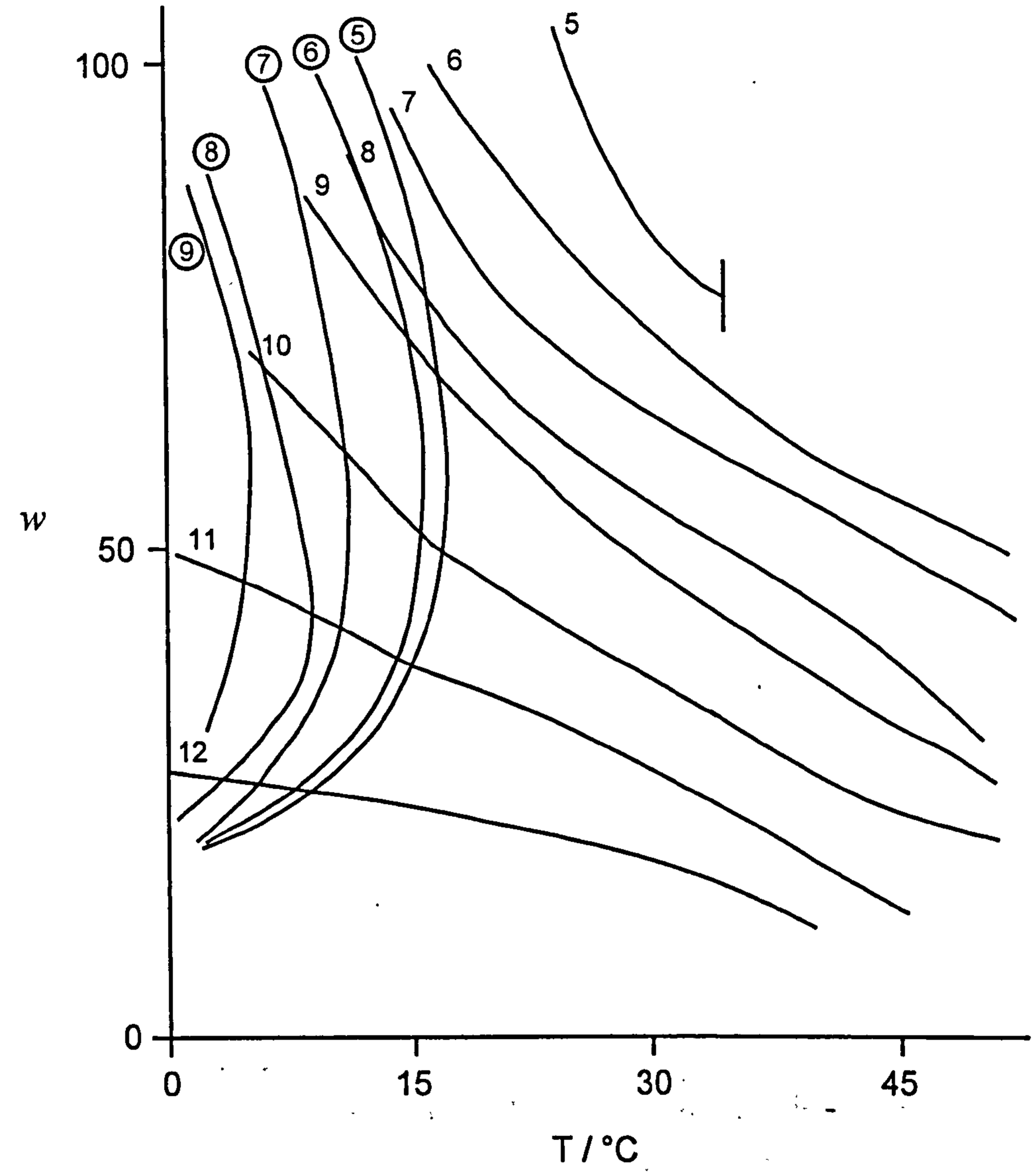

Figure 3.12 Pseudo-binary phase diagram in ternary microemulsion systems formed with the anionic surfactant Aerosol-OT (AOT) in various straight-chain alkane solvents. The water–to–surfactant molar ratio, *w*, is plotted versus temperature at constant surfactant concentration and pressure. Alkane carbon numbers are indicated; ringed numbers correspond to the lower temperature (solubilisation) boundary, T_L, and un-ringed numbers to the upper temperature (haze) boundary, T_U. The single phase microemulsion region is located between T_L and T_U. Below T_L the system consists of a microemulsion phase in equilibrium with excess water (WII type), and above T_U the single microemulsion phase separates into a surfactant-rich phase and an oil phase. After Fletcher *et al.* [16].

3.4 SMALL-ANGLE NEUTRON SCATTERING

The determination of molecular organisation within colloidal systems is an important aspect when studying relationships between physical properties and molecular structure. Scattering techniques provide the most obvious methods for obtaining quantitative information on size, shape and structure of colloidal particles, since they are based on interactions between incident radiations (e.g., light, X-ray or neutrons) and particles. The size range of micelles, microemulsions, or other colloidal dispersions is approximately $10 - 10^4$ Å, so valuable information can be obtained if the incident wavelength, λ, falls within this range. Therefore, microemulsion droplets or micelles, in the order of 10^2 Å in size, are well characterized by X-ray ($\lambda = 0.5 - 2.3$ Å) and neutrons ($\lambda = 0.1 - 30$ Å), while for larger colloidal particles, light scattering ($\lambda = 4000 - 8000$ Å), is best. In addition, considering the Bragg equation that defines the angle of diffraction θ of radiation of wavelength λ for a separation of lattice planes d:

$$\lambda = 2d\sin\theta \qquad (3.4.1)$$

it can be seen that small particles such as microemulsion droplets will scatter at small angles, so that small-angle neutron scattering (SANS) can be used to study such systems [71].

Although the first neutron reactors were built in the late 1940's and 1950's, literature for application of neutron scattering to condensed matter appeared only in the late 1970's. In the last twenty years, with the development of more powerful neutron production sites, and progress in the technology of large area detectors and high resolution spectrometers, SANS has become a more accessible technique and, in particular, has been used successfully to study micellisation, microemulsion and liquid crystal structures. SANS is thus a relatively recent technique but is now one of the most powerful tools to characterize molecular aggregates.

In the following sections a summary of neutron scattering theory and methods for SANS data analysis is given. Emphasis is given essentially to the applicability of SANS to microemulsion systems, in accordance to the structural studies described in Chapters 6 and 7.

3.4.1 Neutron basics

A neutron is an uncharged (electrically neutral) subatomic particle with mass m = 1.675×10^{-27} kg (1,839 times that of the electron), spin ½, and magnetic moment -1.913 nuclear magnetons. Neutrons are stable when bound in an atomic nucleus, whilst having a mean lifetime of approximately 1000 seconds as a free particle. The neutron and the proton form nearly the entire mass of atomic nuclei, so they are both called nucleons. Neutrons are classified according to their wavelength and energy as "epithermal" for short wavelengths ($\lambda \sim 0.1$ Å), "thermal", and "cold" for long wavelengths ($\lambda \sim 10$ Å). The desired range of λ is obtained by moderation of the neutrons during their production, either in reactors or spallation sources.

Neutrons interact with matter through strong, weak, electromagnetic and gravitational interactions. However, it is their interactions via two of these forces – the short-range strong nuclear force and their magnitude moments – that make neutron scattering such a unique probe for condensed-matter research. The most important advantages of neutrons over other forms of radiation in the study of structure and dynamics on a microscopic level are summarised below:

- Neutrons are uncharged, which allows them to penetrate the bulk of materials. They interact via the strong nuclear force with the nuclei of the material under investigation.
- The neutron has a magnetic moment that couples to spatial variations of magnetization on the atomic scale. They are therefore ideally suited to the study of magnetic structures, and the fluctuations and excitations of spin systems.
- The energy and wavelength of neutrons may be matched, often simultaneously, to the energy and length scales appropriate for the structure and excitations in condensed matter. The wavelength, λ, is dependent on the neutron velocity following the de Broglie relation:

$$\lambda = \frac{h}{mv} \qquad (3.4.2)$$

where h is Planck's constant (6.63×10^{-34} J s) and v the particle velocity.

The associated kinetic energy is:

$$E = \tfrac{1}{2}mv^2 \text{ or } E = \frac{h^2}{2(m\lambda)^2} \qquad (3.4.3)$$

Because their energy and wavelength depend on their velocity it is possible to select a specific neutron wavelength by the time-of-flight technique.

- The neutron does not significantly perturb the system under investigation, so the results of neutron scattering experiments can be clearly interpreted.
- Neutrons are non-destructive, even to delicate biological materials.
- The high-penetrating power of neutrons allows probing the bulk of materials and facilitates the use of complex sample-environment equipment (e.g., for creating extremes of pressure, temperature and magnetic field).
- Neutrons scatter from materials by interacting with the nucleus of an atom rather than the electron cloud. This means that the scattering power (cross-section) of an atom is not strongly related to its atomic number (the number of positive protons in the atom, and therefore number of electrons, since the atom must remain neutral), unlike X-rays and electrons where the scattering power increases in proportion to the atomic number. Therefore, with neutrons light atoms such as hydrogen can be distinguished in the presence of heavier ones. Similarly, neighbouring elements in the periodic table generally have substantially different scattering cross sections and so can be distinguished. The nuclear dependence of scattering also allows isotopes of the same element to have substantially different scattering lengths for neutrons. Hence isotopic substitution can be used to label different parts of the molecules making up a material.

3.4.2 Neutron sources

Neutron beams may be produced in two ways: by nuclear fission in reactor-based neutron sources, or by spallation in accelerator-based neutron sources. A brief description of these processes is given below, with particular reference to the two world's most intense neutron sources, i.e., the Institut Laue-Langevin (ILL) in Grenoble,

France [72], and the ISIS Facility at the Rutherford Appleton Laboratory in Didcot, U.K. [73].

- *Reactor-based neutron source*: neutrons have traditionally been produced by fission in nuclear reactors optimised for high neutron brightness. In this process, thermal neutrons are absorbed by uranium-235 nuclei, which split into fission fragments and evaporate a very high-energy (MeV) constant neutron flux (hence the term "steady-state" or "continuous" source). After the high-energy (MeV) neutrons have been thermalised to meV energies in the surrounding moderator, beams are emitted with a broad band of wavelengths. The energy distribution of the neutrons can be shifted to higher energy (shorter wavelength) by allowing them to comė into thermal equilibrium with a "hot source" (at the ILL this is a self-heating graphite block at 2400 K), or to lower energies with a "cold source" such as liquid deuterium at 25 K [74]. The resulting Maxwell distributions of energies have the characteristic temperatures of the moderators (Figure 3.13(*a*)). Wavelength selection is generally achieved by Bragg scattering from a crystal monochromator or by velocity selection through a mechanical chopper. In this way high-quality, high-flux neutron beams with a narrow wavelength distribution are made available for scattering experiments. The most powerful of the reactor neutron sources in the world today is the 58 MW HFR (High-Flux Reactor) at the ILL.

- *Accelerator-based pulsed neutron source*: in these sources neutrons are released by bombarding a heavy-metal target (e.g., U, Ta, W), with high-energy particles (e.g., H^+) from a high-power accelerator – a process known as spallation. The methods of particles acceleration tend to produce short intense bursts of high-energy protons, and hence pulses of neutrons. Spallation releases much less heat per useful neutron than fission (typically 30 MeV per neutron, compared with 190 MeV in fission). The low heat dissipation means that pulsed sources can deliver high neutron brightness – exceeding that of the most advanced steady-state sources – with significantly less heat generation in the target. The most powerful spallation neutron source in the world is the ISIS facility. It is based around a 200 μA, 800 MeV, proton synchrotron operating at 50 Hz, and a tantalum (Ta) target which releases approximately 12 neutrons for every incident proton.

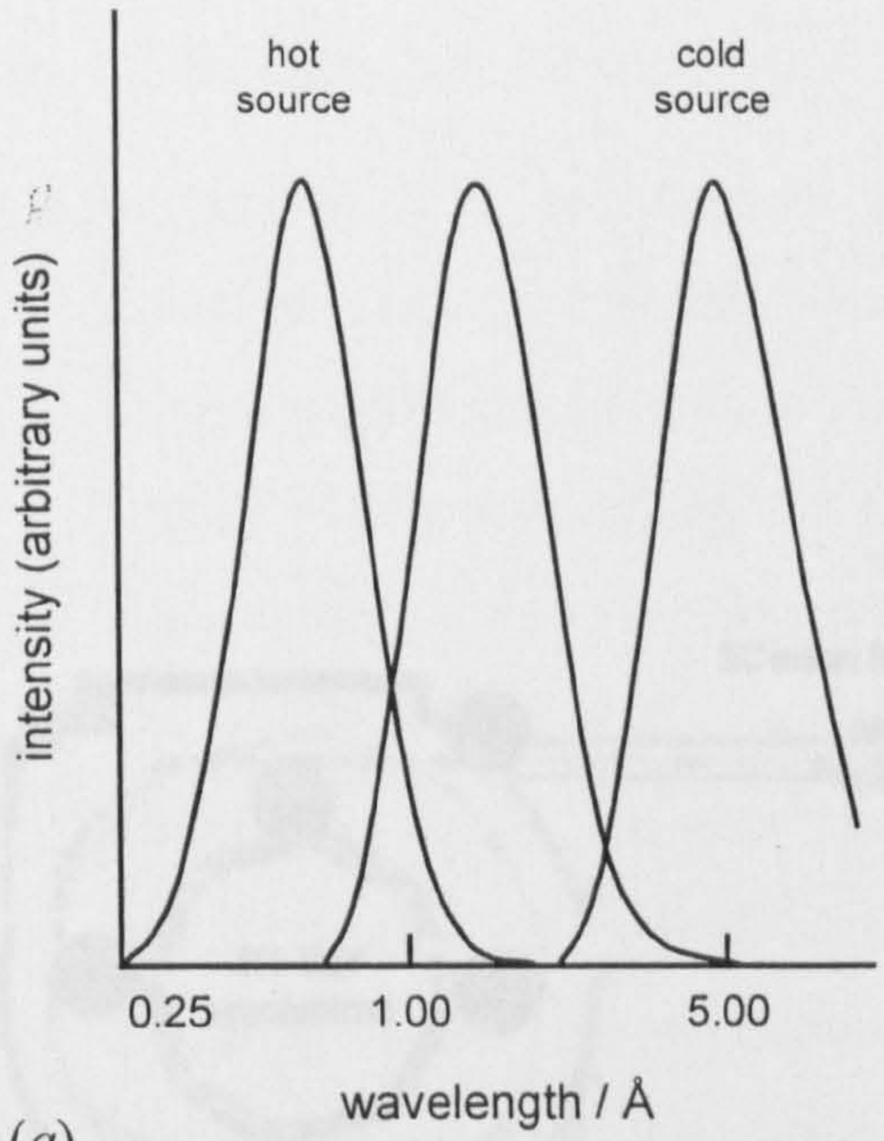

(*a*)

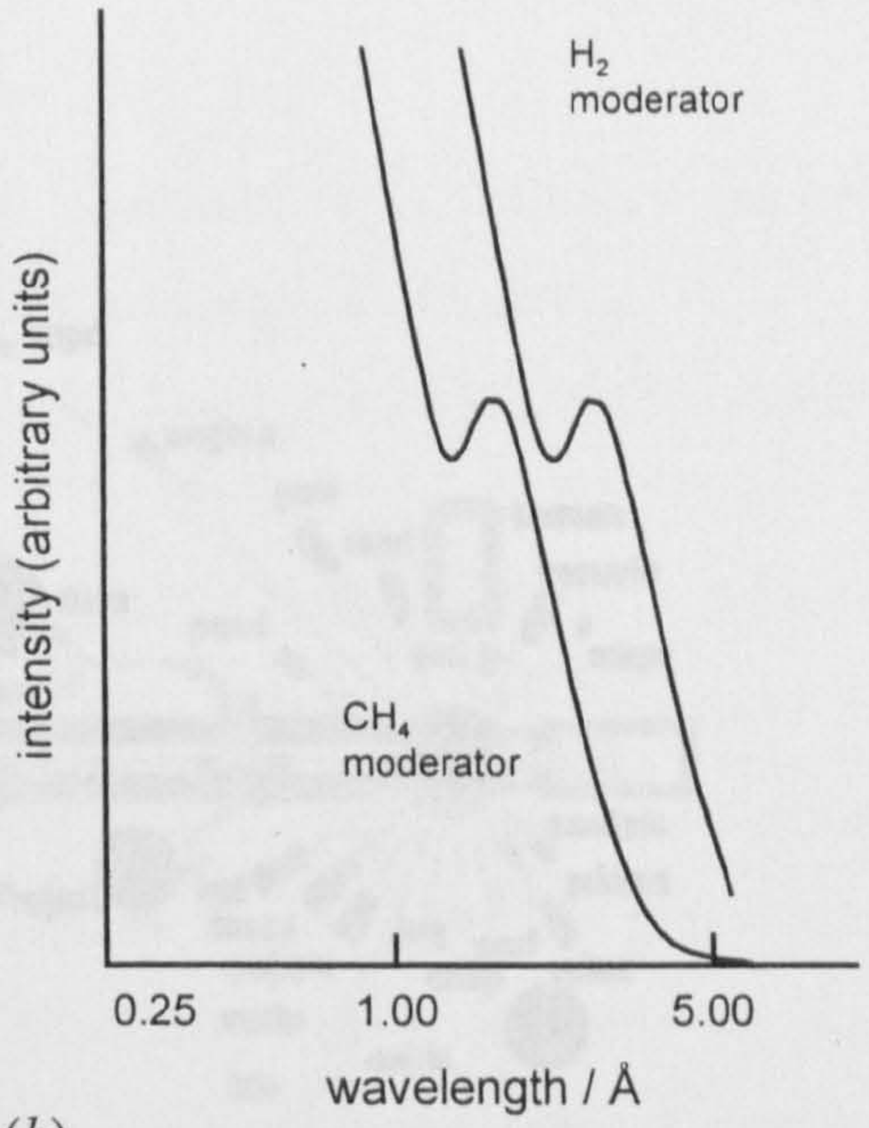

(*b*)

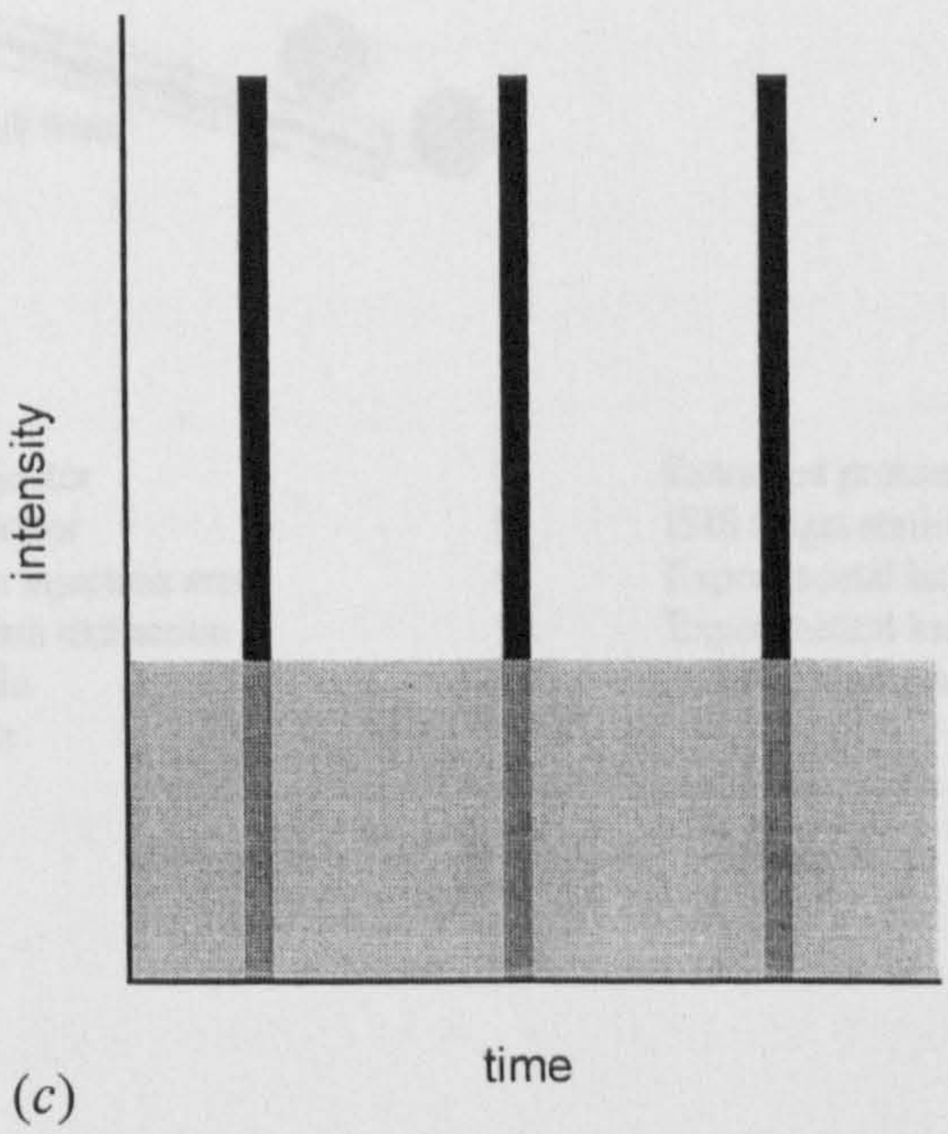

(*c*)

Figure 3.13 (*a*) Typical wavelength distributions for neutrons from a reactor, showing the spectra from a hot source (2400 K), a thermal source and a cold source (25 K). The spectra are normalised so that the peaks of the Maxwell distributions are unity.
(*b*) Typical wavelength spectra from a pulsed spallation source. The H_2 and CH_4 moderators are at 20 K and 100 K respectively. The spectra have a high-energy "slowing" component and a thermalised component with a Maxwell distribution. Again the spectra are normalised at unity.
(*c*) Neutron flux as a function of time at a steady-state source (grey) and a pulsed source (black). Steady-state sources, such as ILL, have high time-averaged fluxes, whereas pulsed sources, such as ISIS, are optimised for high brightness (not drawn to scale). After [73].

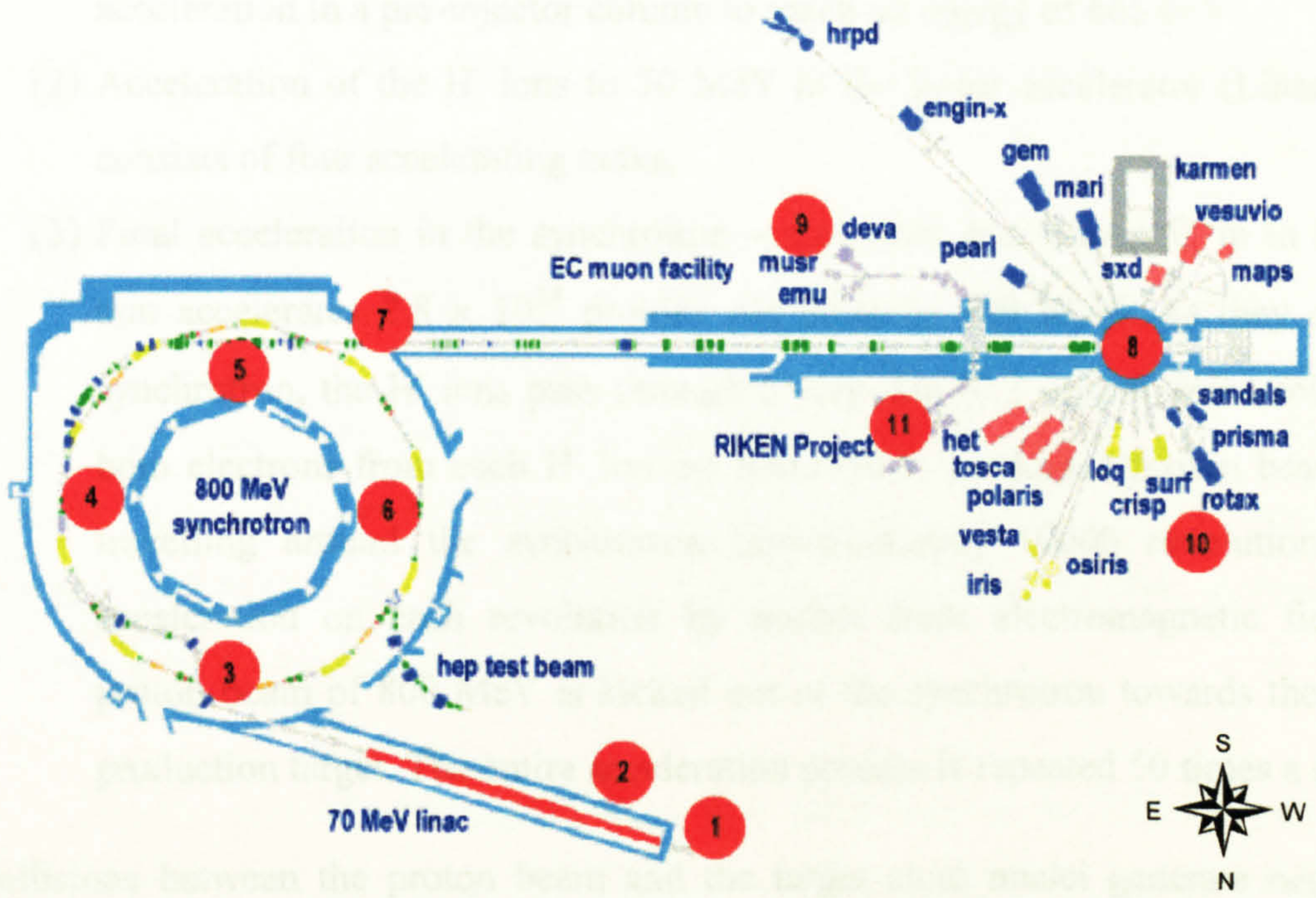

1. Ion source and pre-injector
2. 70 MeV linear accelerator
3. 800 MeV synchrotron injection area
4. Fast kicker proton beam extraction
5. Synchrotron south side
6. Synchrotron west side
7. Extracted proton beam tunnel
8. ISIS target station
9. Experimental hall, south side
10. Experimental hall, north side
11. RIKEN superconducting pion decay line

Figure 3.14 Schematic layout of the spallation pulsed neutron source at the Rutherford Appleton Laboratory, ISIS, Didcot, U.K. Beam tubes radiate out from the ISIS target and deliver pulses of "white" neutrons – i.e., neutrons having a wide range of energies – to 18 instruments [73].

At ISIS, the production of particles energetic enough to produce efficient spallation involves three stages (see Figure 3.14):

(1) Production of H^- ions (proton with two electrons) from hydrogen gas and acceleration in a pre-injector column to reach an energy of 665 keV.

(2) Acceleration of the H^- ions to 70 MeV in the linear accelerator (Linac) which consists of four accelerating tanks.

(3) Final acceleration in the synchrotron – a circular accelerator 52 m in diameter that accelerates 2.8×10^{13} protons per pulse to 800 MeV. As they enter the synchrotron, the H^- ions pass through a very thin (0.3 μm) alumina foil so that both electrons from each H^- ion are removed to produce a proton beam. After travelling around the synchrotron (approximately 10000 revolutions), with acceleration on each revolution by pushes from electromagnetic fields, the proton beam of 800 MeV is kicked out of the synchrotron towards the neutron production target. The entire acceleration process is repeated 50 times a second.

Collisions between the proton beam and the target atom nuclei generate neutrons in large quantities and of very high energies. As in fission, they must be slowed by passage through moderating materials so that they have the right energy (wavelength) to be useful for scientific investigations. This is achieved by hydrogenous moderators around the target. These exploit the large inelastic-scattering cross-section of hydrogen to slow down the neutrons passing through, by repeated collisions with the hydrogen nuclei. The moderator temperature determines the spectral distributions of neutrons produced, and this can be tailored for different type of experiments (Figure 3.13(*b*)). The moderators at ISIS are ambient temperature water (316 K, H_2O), liquid methane (100 K, CH_4) and liquid hydrogen (20 K, H_2).

The characteristics of the neutrons produced by a pulsed source are therefore significantly different from those produced at a reactor (Figure 3.13(*c*)). The time-averaged flux (in neutrons per second per unit area) of even the most powerful pulsed source is low in comparison with reactor sources. However, judicious use of time-of-flight (TOF) techniques that exploit the high brightness in the pulse can compensate for this. Using TOF techniques on the white neutron beam gives a direct determination of the energy and wavelength of each neutron.

3.4.3 SANS instruments

In neutron scattering experiments, instruments count the number of scattered neutrons as a function of wave vector Q, which depends on the scattering angle θ and wavelength λ (see Section 3.4.4). For elastic scattering – i.e., when scattered neutrons have essentially identical energy to the incident neutrons – this corresponds to measuring with *diffractometers* the momentum change. Information about the spatial distribution of nuclei can then be obtained in systems ranging in size and complexity from small unit-cell crystals, through disordered systems such as glasses and liquids, to "large-scale" structures such as surfactant aggregates and polymers. *Spectrometers*, on the other hand, additionally measure the energy lost (or gained) by the neutron as it interacts with the sample, i.e., inelastic scattering. These data can then be related to the dynamic behaviour of the sample.

In this work, SANS experiments were performed on the LOQ spectrometer at ISIS and D22 diffractometer at ILL. As described in Section 3.4.2, and to take advantage of the different characteristics of reactor and pulsed sources, neutron scattering experiments performed on these two instruments differ in detail. In particular, on D22 a single-wavelength beam is normally used and monochromatic beams can be produced by wavelength selection by velocity selection through a mechanical chopper. In contrast, "white" beams that contain neutrons with a wide range of wavelengths are used on LOQ. Energy analysis of the scattered beam is achieved by measuring the total time-of-flight, i.e., the time the neutron takes to travel from the source to the sample. As a result of the different wavelength spreads, the detectors on LOQ and D22 differ significantly. For constant λ, the scattering intensity must be measured at different angles to cover the required Q-range. This is achieved on D22 by varying the sample-to-detector distance, using a moveable detector. On LOQ, the neutron pulse wavelength varies, and is determined by TOF method, so the position of the detector is fixed. Figures 3.15 and 3.16 show schematic layout of the two instruments. More technical details can be found elsewhere [72,73,75].

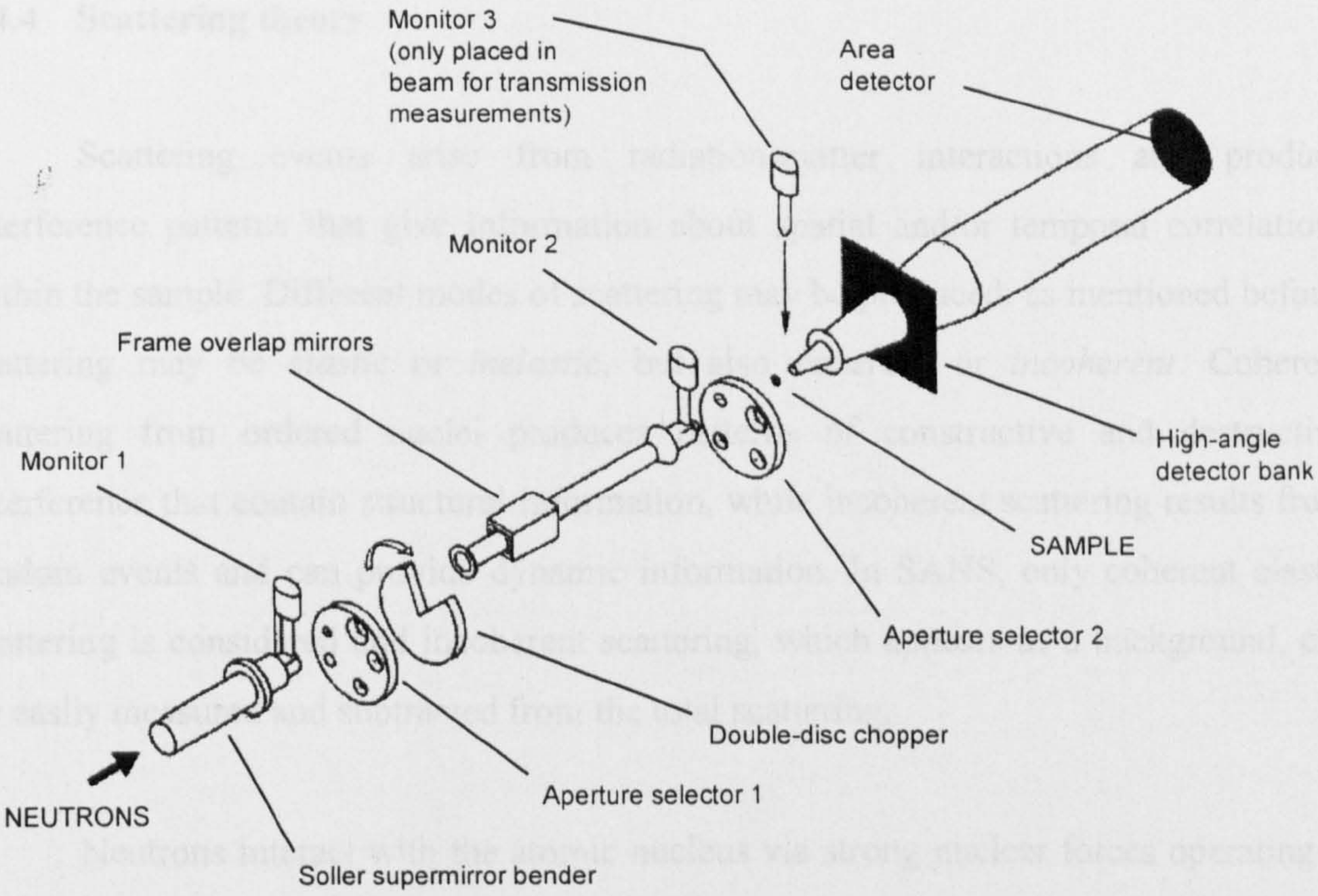

Figure 3.15 Schematic layout of the LOQ instrument, ISIS, Didcot, U.K [72]. After interaction with the sample (typical neutron flux at sample = 2×10^5 cm^{-2} s^{-1}), the beam passes into a vacuum tube containing a ^{3}H gas filled detector (active area 64×64 cm^2 with pixel size 6×6 mm^2) placed 4.5 m from the sample. Incident wavelengths range ~ 2.2 – 10 Å, and the scattering angle < 7° gives a useful Q-range of 0.009 – 0.249 Å^{-1}.

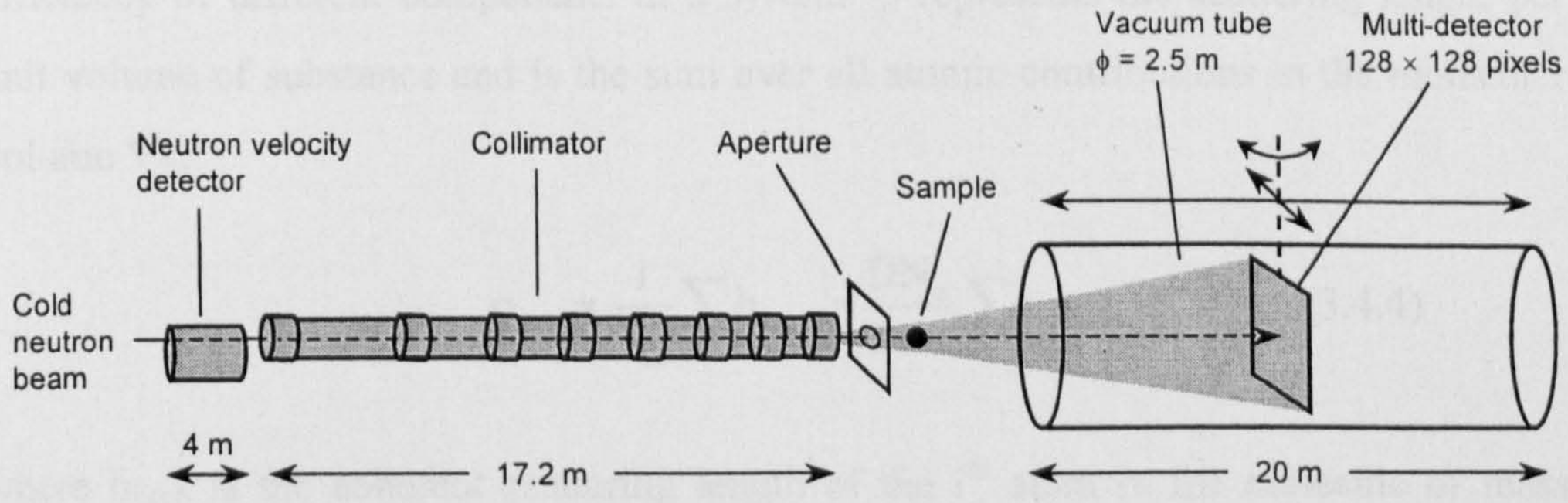

Figure 3.16 Schematic layout of the D22 instrument, ILL, Grenoble, France [71]. The maximum neutron flux at sample is 1.2×10^8 cm^{-2} s^{-1}. D22 possesses the largest area multi-detector (^{3}He) of all small-angle scattering instruments (active area 96×96 cm^2 with pixel size 7.5×7.5 mm^2). It moves inside a 2.5 m wide and 20 m long vacuum tube providing sample-to-detector distances of 1.35 m to 18 m; it can be translated laterally by 50 cm, and rotated around its vertical axis to reduce parallax. D22 thus covers a total Q-range of up to 1.5 Å^{-1} for $\lambda = 2.6$ Å (0.85 Å^{-1} for $\lambda = 4.6$ Å, $\Delta\lambda/\lambda$ = 5-10 %).

3.4.4 Scattering theory

Scattering events arise from radiation-matter interactions and produce interference patterns that give information about spatial and/or temporal correlations within the sample. Different modes of scattering may be produced: as mentioned before, scattering may be *elastic* or *inelastic*, but also *coherent* or *incoherent*. Coherent scattering from ordered nuclei produces patterns of constructive and destructive interference that contain structural information, while incoherent scattering results from random events and can provide dynamic information. In SANS, only coherent elastic scattering is considered and incoherent scattering, which appears as a background, can be easily measured and subtracted from the total scattering.

Neutrons interact with the atomic nucleus via strong nuclear forces operating at very short range (~ 10^{-15} m), i.e., much smaller than the incident neutron wavelength (~ 10^{-10} m). Therefore, each nucleus acts as a point scatterer to the incident neutron beam, which may be considered as a plane wave. The strength of interaction of free neutrons with the bound nucleus can be quantified by the *scattering length*, b, of the atom, which is isotope dependent. In practice, the mean coherent neutron *scattering length density*, ρ_{coh}, abbreviated as ρ, is a more appropriate parameter to quantify the scattering efficiency of different components in a system. ρ represents the scattering length per unit volume of substance and is the sum over all atomic contributions in the molecular volume V_m:

$$\rho_{coh} = \frac{1}{V_m}\sum_i b_{i,coh} = \frac{DN_a}{Mw}\sum_i b_{i,coh} \qquad (3.4.4)$$

where $b_{i,coh}$ is the coherent scattering length of the i^{th} atom in the molecule of mass density D, and molecular weight Mw. N_a is Avogadro's constant. Some useful scattering lengths are given in Table 3.2, and scattering length density for selected molecules in Table 3.3 [76]. The difference in b values for hydrogen and deuterium is significant, and this is exploited in the contrast-variation technique to allow different regions of molecular assemblies to be examined; i.e., one can "see" proton-containing hydrocarbon-type material dissolved in heavy water D_2O (see Section 3.4.5).

Table 3.2 Selected values of coherent scattering length, b [76]

Nucleus	b / (10^{-12} cm)
^{1}H	-0.3741
^{2}H (D)	0.6671
^{12}C	0.6646
^{16}O	0.5803
^{19}F	0.5650
^{23}Na	0.3580
^{31}P	0.5131
^{32}S	0.2847
Cl	0.9577

Table 3.3 Coherent scattering length density of selected molecules, ρ, at 25°C [76]. [a]Value calculated for the deuterated form of the surfactant ion only (i.e., without sodium counterions), and where the tails only are deuterated

Molecule		ρ / (10^{10} cm^{-2})
Water	H_2O	-0.560
	D_2O	6.356
Heptane	C_7H_{16}	-0.548
	C_7D_{16}	6.301
AOT	$(C_8H_{17}COO)CH_2CHSO_3^-$ (Na^+)	0.542
	$(C_8D_{17}COO)CH_2CHSO_3^-$ (Na^+)	5.180[a]

In neutron scattering experiments, the intensity of the scattered wave, I, is measured as a function of a scattering angle, θ, which in the case of SANS is usually much less than 10°. Figure 3.17 illustrates schematically a SANS experiment where an incident neutron beam is scattered by a sample. The incident wave is a plane wave, whose amplitude can be written as [77]:

$$A_{in} = A_o \cos(\underline{k}_o \cdot \underline{R} - \Omega_o t) \qquad (3.4.5)$$

A_o is the original amplitude, $\underline{k}_o$ is the wave vector of magnitude $\frac{2\pi}{\lambda}$, $\underline{R}$ is a position vector, Ω_o is the frequency, and t the time. In static experiments, where relative motions of molecules are ignored, there is no time dependence, and if complex amplitudes are considered, Eq. 3.4.5 reduces to:

$$A_{in} = A_o \exp(i\underline{k}_o \cdot \underline{R}) \qquad (3.4.6)$$

When this wave hits an atom, a fraction of it is scattered, radiating spherically around the scattering centre:

$$A_{sc} = \frac{A_o b}{r} \exp(i\underline{k}_o \cdot \underline{R}) \qquad (3.4.7)$$

where b is the scattering length and r the distance between two point scattering nuclei (Figure 3.18*a*). If the atom is not at the origin but at a position vector $\underline{R}$, the wave scattered in the direction of $\underline{k}_s$ will be phase shifted by $\underline{Q} \cdot \underline{R}$ with respect to the incident wave (Figure 3.18*b*). $\underline{Q}$ is the scattering vector and relates to the scattering angle θ via

$$\underline{Q} = \underline{k}_s - \underline{k}_o \qquad (3.4.8)$$

and the magnitude of $\underline{Q}$ is given by the cosine rule:

$$Q^2 = k_o^2 + k_s^2 - 2k_o k_s \cos\theta \qquad (3.4.9)$$

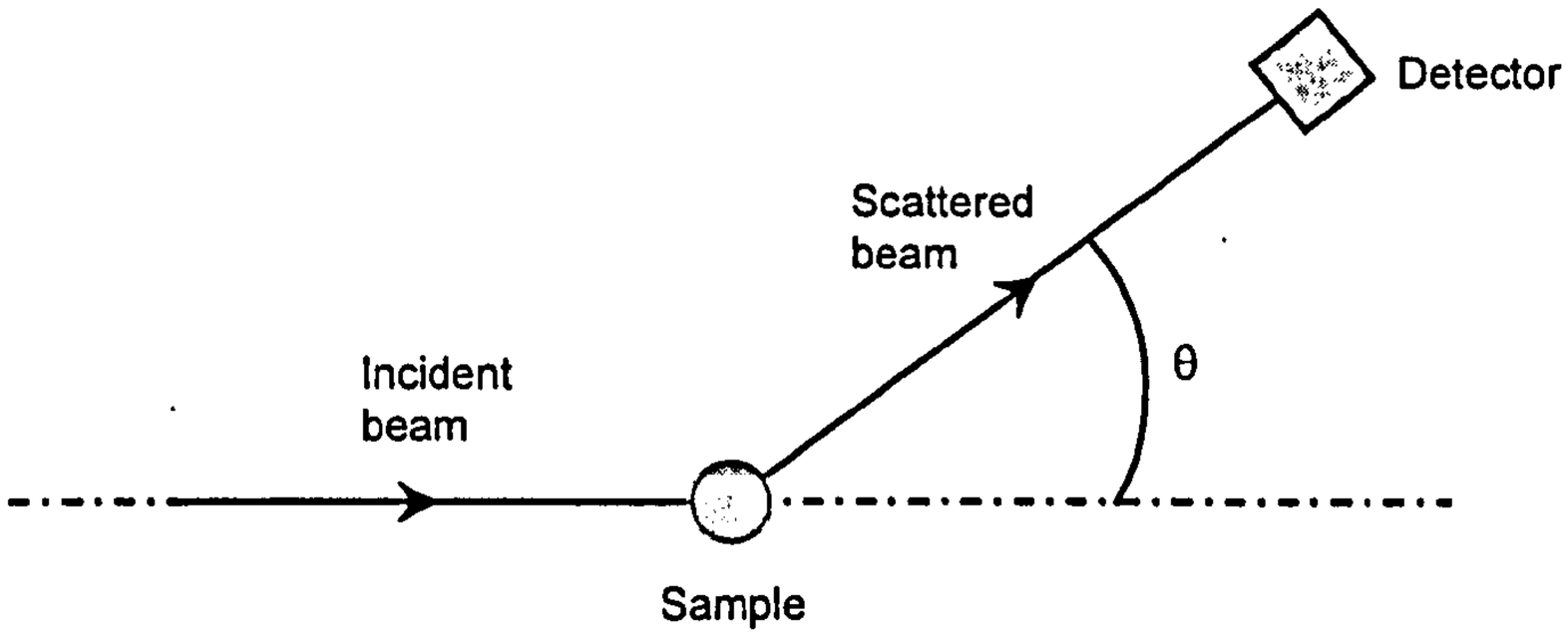

Figure 3.17 Schematic instrumental setup of a small-angle scattering experiment. Sample-to-detector distance is usually 1 – 20 m; scattering angle $\theta < 10°$.

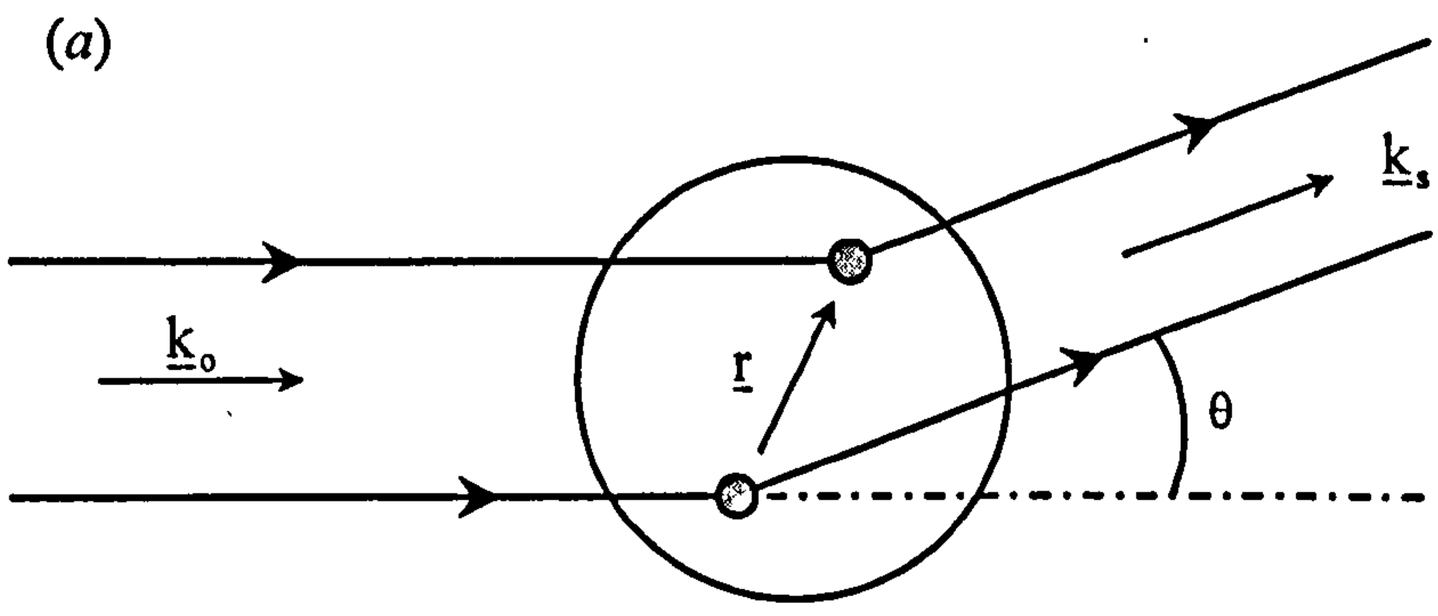

Figure 3.18 Geometrical relationships in scattering experiments. (*a*) Phase difference between two point scatterers spatially related by the position vector r. The incident and scattered radiation have wave vector k_o and k_s, respectively. For elastic scattering $|k_o| = |k_s| = 2\pi n/\lambda$. (*b*) Determination of the scattering vector $Q = k_s - k_o$, of amplitude $Q = (4\pi/\lambda)\sin(\theta/2)$.

For coherent elastic scattering, $|k_o| = |k_s| = \frac{2\pi n}{\lambda}$, where n is the refractive index of the medium, which for neutron is ~ 1, so $|\underline{Q}|$ can be obtained by simple geometry as:

$$|\underline{Q}| = Q = 2|k_o| \sin\frac{\theta}{2} = \frac{4\pi}{\lambda}\sin\frac{\theta}{2} \qquad (3.4.10)$$

The magnitude Q has dimensions of reciprocal length and units are commonly $Å^{-1}$. It relates to the spatial sample properties, with large structures scattering at low Q (and angle) and small structures at higher Q values.

Accordingly, the amplitude of the scattered wave at angle θ for an atom at position $\underline{R}$ from the origin is:

$$A_{sc} = \frac{A_o b}{r}\exp[i(\underline{k}_o r - \underline{Q}\cdot\underline{R})] \qquad (3.4.11)$$

Equation 3.4.11 is only valid for the simple case where two point scatterers are considered. In the more realistic case of a very large number of atoms present, the total scattered amplitude is then written as:

$$A_{sc} = \frac{A_o}{r}\exp(i\underline{k}_o r)\sum_i b_i \exp(-i\underline{Q}\cdot\underline{R}_i)] \qquad (3.4.12)$$

In the specific case of SANS and Q-range involved (distances ~ 10 to 1000 Å, scattering vectors Q ~ 0.006 to 0.6 $Å^{-1}$), samples can be treated as discrete particles dispersed in a continuous medium, and the scattering is controlled by the scattering length density, ρ:

$$\rho(\underline{R}) = \frac{1}{v}\sum_j b_j \delta(\underline{R} - \underline{R}_j) \qquad (3.4.13)$$

where the sum extends over a volume v which is large compared with interatomic distances but small compared to the resolution of the experiment.

Then the scattered amplitude is the Fourier transform of this density in the irradiated volume V:

$$A_{sc}(\underline{Q}) = \int_{V} \rho(\underline{R}) \exp(-i\underline{Q} \cdot \underline{R}) d\underline{R} \qquad (3.4.14)$$

Radiation detectors do not measure amplitudes as they are not sensitive to phase shift, but instead the intensity I_{sc} of the scattering (or power flux), which is the squared modulus of the amplitude:

$$I_{sc}(\underline{Q}) = \left\langle \left| A(\underline{Q}) \right|^2 \right\rangle = \left\langle A(\underline{Q}) \cdot A^*(\underline{Q}) \right\rangle \qquad (3.4.15)$$

For an ensemble of n_p identical particles, Eq. 3.4.15 becomes [78]:

$$I_{sc}(Q) = n_p \left\langle \left\langle \left| A_{sc}(Q)^2 \right| \right\rangle_o \right\rangle_s \qquad (3.4.16)$$

where the ensemble averages are over all orientations, o, and shapes, s.

Therefore, there is a convenient relationship (Eq. 3.4.10) between the two instrumental variables, θ and λ, and the reciprocal distance, Q, which is related (via Eq. 3.4.14) to the positional correlations r between point scattering nuclei in the sample under investigation. These parameters are related to the scattering intensity $I(Q)$ (Eq. 3.4.16) which is the measured parameter in a SANS experiment, and contains information on intra-particle and inter-particle structure.

3.4.5 Neutron scattering by micellar aggregates

For monodisperse homogeneous spherical particles of radius R, volume V_p, number density n_p (cm^{-3}) and coherent scattering length density ρ_p, dispersed in a medium of density ρ_m, the normalised SANS intensity $I(Q)$ (cm^{-1}) may be written as [79]:

$$I(Q) = n_p \Delta\rho^2 V_p^2 P(Q,R) S(Q) \qquad (3.4.17)$$

where $\Delta\rho = \rho_p - \rho_m$ (cm^{-2}). The first three terms in Eq. 3.4.17 are independent of Q and account for the absolute intensity of scattering. A so-called *scale factor*, S_F, can then be defined where:

$$S_F = n_p(\rho_p - \rho_m)^2 V_p^2 = \phi_p \cdot \Delta\rho^2 \cdot V_p \qquad (3.4.18)$$

ϕ_p is the volume fraction of particles. The scale factor is a measure of the validity and consistency of a model used when analysing SANS data; i.e., the S_F value obtained from model fitting can be compared to the calculated value (from Eq. 3.4.18). The last two terms in Eq. 3.4.17 are Q-dependent functions. P(Q,R) is the single particle form factor arising from intra-particle scattering. It describes the angular distribution of the scattering due to the particle shape and size. S(Q) is the structure factor arising from inter-particle interactions. To better understand the influence of each term, two scattering profiles are illustrated on Figure 3.19 for the cases of repulsive and attractive forces between interacting homogeneous spheres [78]. It shows how P(Q) and S(Q) can combine to give the overall intensity I(Q). These scattering functions are briefly discussed below.

Single particle form factor P(Q)

P(Q) is the function from which information on the size and shape of particles can be obtained. An approximate representation of the form factor P(Q,R) for spheres is shown in Figure 3.19. In general, it appears as a decay although under high resolution maxima and minima are expected at high Q values. The function P(Q) is usually defined as 1.0 at Q = 0. General expressions of P(Q) are known for a wide range of different shapes such as homogeneous spheres, spherical shells, cylinders, concentric cylinders and discs [77]. For a sphere of radius R:

$$P(Q,R) = \left[\frac{3(\sin QR - QR\cos QR)}{(QR)^3}\right]^2 \qquad (3.4.19)$$

For certain systems such as microemulsions, a polydispersity function may be introduced to account for the particle-size distribution. For spherical droplets, this contribution may be represented by a Schultz distribution function $X(R_i)$ [80,81]

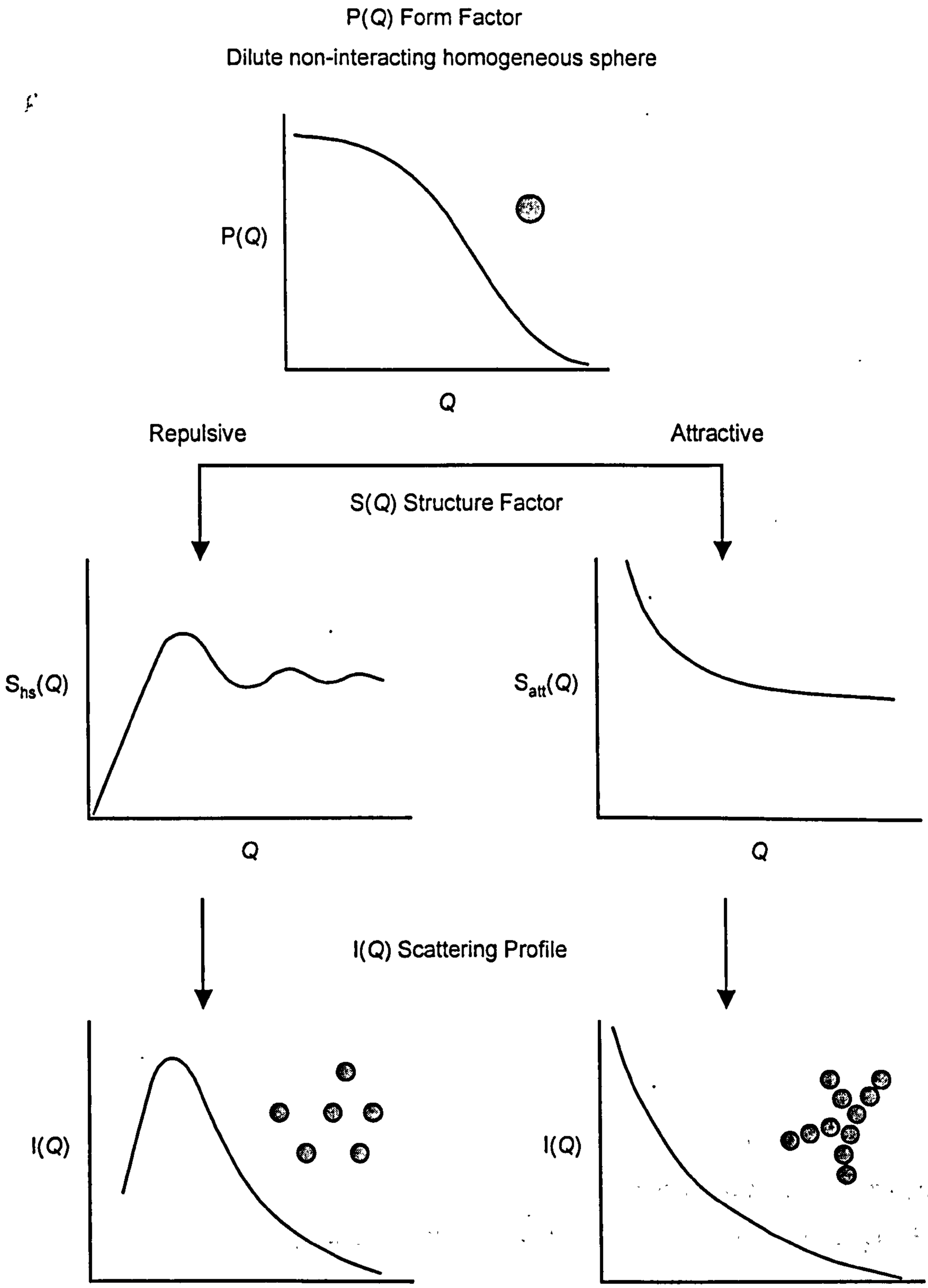

Figure 3.19 Schematic representation of the particle form P(Q,R) and structure S(Q) factors for attractive and repulsive homogeneous spheres, and their contribution to the scattered intensity I(Q). After [78].

defined by an average radius R^{av} and a root mean square deviation $\sigma = \frac{R^{av}}{(Z+1)^{1/2}}$ with Z a width parameter. P(Q,R) may then be expressed as:

$$P(Q,R) = \left[\sum_i P(Q,R_i)X(R_i)\right] \qquad (3.4.20)$$

Structure factor S(Q)

The inter-particle structure factor S(Q) depends on the type of interactions in the system, i.e., attractive, repulsive or excluded volume. For spherical particles with low attractive interactions, a reasonable first approximation is a hard-sphere potential, $S_{hs}(Q)$, given by [82]:

$$S_{hs}(Q) = \frac{1}{1 - n_p \cdot f(R_{hs}\phi_{hs})} \qquad (3.4.21)$$

where $R_{hs} = R^{av}_{core} + t$ is the hard-sphere radius (with t the hydrocarbon layer thickness) and $\phi_{hs} = \frac{4}{3}\pi R^3_{hs} n_p$ is the hard-sphere volume fraction. The intensity of scattering (Eq. 3.4.17) can then be rewritten as:

$$I(Q) = \phi_p \Delta\rho^2 V_p \left[\sum_i P(Q,R_i)X(R_i)\right] S(Q,R_{hs},\phi_{hs}) \qquad (3.4.22)$$

As shown in Figure 3.19, $S_{hs}(Q)$ is important at low Q values where it reduces the scattering intensity and produces a peak in I(Q) profile at $Q_{max} = 2\pi/D$, with D the mean nearest neighbour distance in the sample. For dilute, non-interacting, systems $\phi_{hs} \rightarrow 0$, so the structure factor disappears, i.e., S(Q) → 1. For interacting systems, an effective way of reducing S(Q) is by diluting the system [83], or for charged particles by adding salt [84].

For systems where attractive interactions have to be considered, particularly in the vicinity of phase separation regions or cloud point in binary phase diagrams, a structure factor known as the Ornstein-Zernike (OZ) expression may be used [78]:

$$S_{OZ}(Q) = 1 + \frac{S(0)}{1 + (Q\xi)^2} \quad . \qquad (3.4.23)$$

where $S(0) = n_p k_B T \chi$, with k_B Boltzmann's constant, T the temperature, and χ the isothermal compressibility. ξ is a correlation length. Far from phase boundaries, $S(0) \rightarrow 0$, and so $S_{OZ}(Q)$ disappears, i.e., $S(Q) \rightarrow 1$.

Neutron contrast variation

As mentioned previously, the very different neutron scattering lengths of hydrogen and deuterium are exploited in SANS experiments to reveal details of structure and composition at interfaces. This is routinely applied in microemulsion droplets where different regions can be highlighted by selectively varying the scattering length density of the surfactant, oil or aqueous phase. Three contrasts are commonly studied – core, shell and drop – which can be fitted individually or simultaneously [85]. Figure 3.20 illustrates the scattering length density profiles for a water–AOT–*n*-heptane microemulsion for the three contrasts. The initial situation, where all components are hydrogenated, is shown in Figure 3.20(*a*). As reported in Table 3.3, the scattering length densities of H_2O, *n*-heptane and AOT are very similar, so that deuteration of the water and/or oil phases allows contrast match of specific regions within the system. The distance from the droplet centre is Z, and so ρ depends on Z owing to the presence of the different materials. Apart from a few subtle effects, such as hydrogen bonding, this isotopic exchange does not usually affect the chemical or physical properties of the system significantly.

3.4.4 SANS approximations

A first estimation of the size and shape of particles can be obtained from simple relations between I(Q) and the particle radius (or thickness) based on a few assumptions and/or approximations.

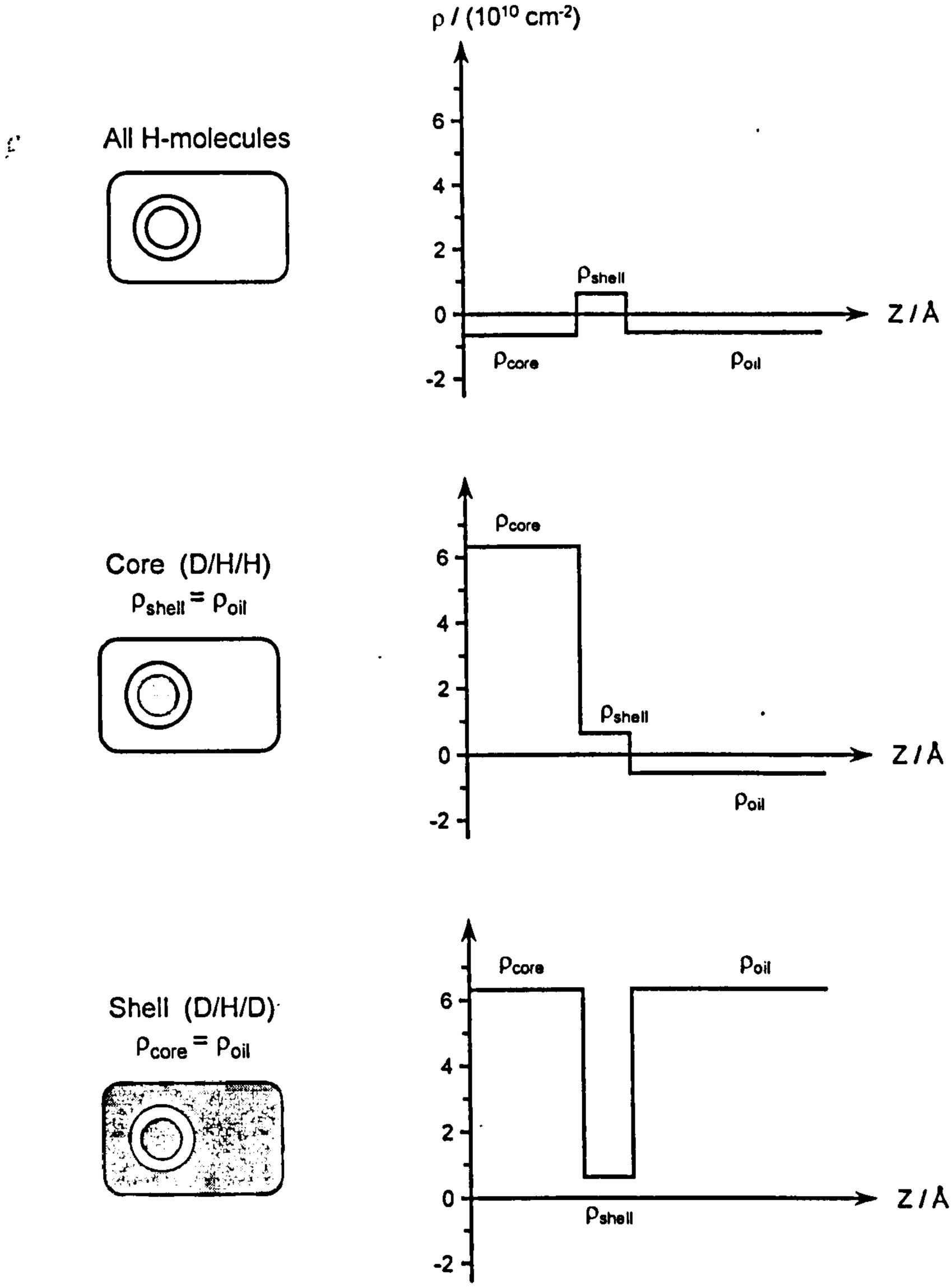

Figure 3.20 Elucidation of the structure of water–AOT–*n*-heptane microemulsion droplets by contrast variation. The scattering length density, ρ, depends on Z, the distance from the centre of a droplet.

Guinier approximation

The SANS profile I(Q) is very sensitive to different particle shapes. In particular, the Guinier approximation relates the low Q part of the scattering plot to a radius of gyration R_g of the particle. At low Q (Guinier regime), the single particle form factor P(Q,R) for dilute systems simplifies to [86]:

$$P(Q,R) = 1 - \frac{Q^2 R_g^2}{3} \qquad (3.4.24)$$

where R_g is the root mean square value of the radius averaged over the volume of particle, and relates to the shape of the particle:

- For spheres or cylinders $\quad R_g = \left(\frac{3}{5}\right)^{1/2} R \qquad (3.4.25)$
- For thin discs $\quad R_g = \frac{R}{4^{1/2}} \qquad (3.4.26)$
- For long rods $\quad R_g = \frac{L}{12^{1/2}} \qquad (3.4.27)$

R is the radius of the spheres or cylinders, or disc thickness, and L is the rod length.

Assuming $S(Q) = 1$ and $1 - X^2 \approx \exp(-X^2)$, Eq. 3.4.17 becomes:

$$I(Q) \approx \phi_p \Delta\rho^2 V_p \exp\left(-\frac{Q^2 R_g^2}{3}\right) \qquad (3.4.28)$$

The Guinier plot – i.e., ln I(Q) versus Q^2 – yields a curve that includes a straight part up to the limit $QR_g < 1$. The associated slope is $-\frac{R_g^2}{3}$, and so R_g can be determined for any isometric particles. Another useful expression for the Guinier approximation is [77,87]:

$$I(Q) \propto Q^{-D} \exp\left(-\frac{Q^2 R^2}{K}\right) \qquad (3.4.29)$$

Equations 3.4.28 and 3.4.29 are equivalent. They are valid for non-interacting particles (i.e., $S(Q) \rightarrow 1$) only, and over a restricted Q-range. The proportionality constant

depends on the concentration and isotopic composition. The exponent D is 1 for cylinders, 2 for discs, and 0 for spheres. R is the characteristic dimension of the particle, i.e., the cross sectional radius for cylinders, the thickness for discs, and the radius for spheres. K is an integer of value 4 for cylinders, 12 for discs, and 5 for spheres. Depending on the geometry, the dimension R can be obtained by plotting different quantities against Q^2:

- $\ln[I(Q)\cdot Q]$ vs. Q^2: $\text{cylinder radius} = \sqrt{\text{slope}\times 4}$ (3.4.30)
- $\ln[I(Q)\cdot Q^2]$ vs. Q^2: $\text{disk thickness} = \sqrt{\text{slope}\times 2}$ (3.4.31)
- $\ln[I(Q)]$ vs. Q^2 ($QR < 1$): $\text{sphere radius} = \sqrt{\text{slope}\times 5}$ (3.4.32)

Therefore the most probable particle shape can be predicted by comparison of the three different $I(Q)$. Q^D vs. Q^2 plots (i.e., the one giving a linear decay).

Porod approximation

At high Q values, the intensity from SANS is sensitive to the scattering from local interface rather than the overall inter-particle structure. Then $I(Q)$ is related to the total interfacial area S, and the asymptotic intensity (see Figure 3.21) may be analysed using the Porod equation [88,89]:

$$I(Q) = 2\pi\Delta\rho^2\left(\frac{S}{V}\right)Q^{-4} \qquad (3.4.33)$$

where S/V is the total interfacial area per unit volume of solution (cm^{-1}). The Porod equation is only valid for smooth interfaces and a Q-range >> 1/R (Porod regime). Assuming all the surfactant molecules are located at the interface, the average area per surfactant head group, a_s, can be estimated from:

$$a_s = \left(\frac{S/V}{N_s}\right) \qquad (3.4.34)$$

where N_s is the number density of surfactant molecules (i.e., surfactant concentration × Avogadro's number). The Porod approximation can also be used to estimate the particle

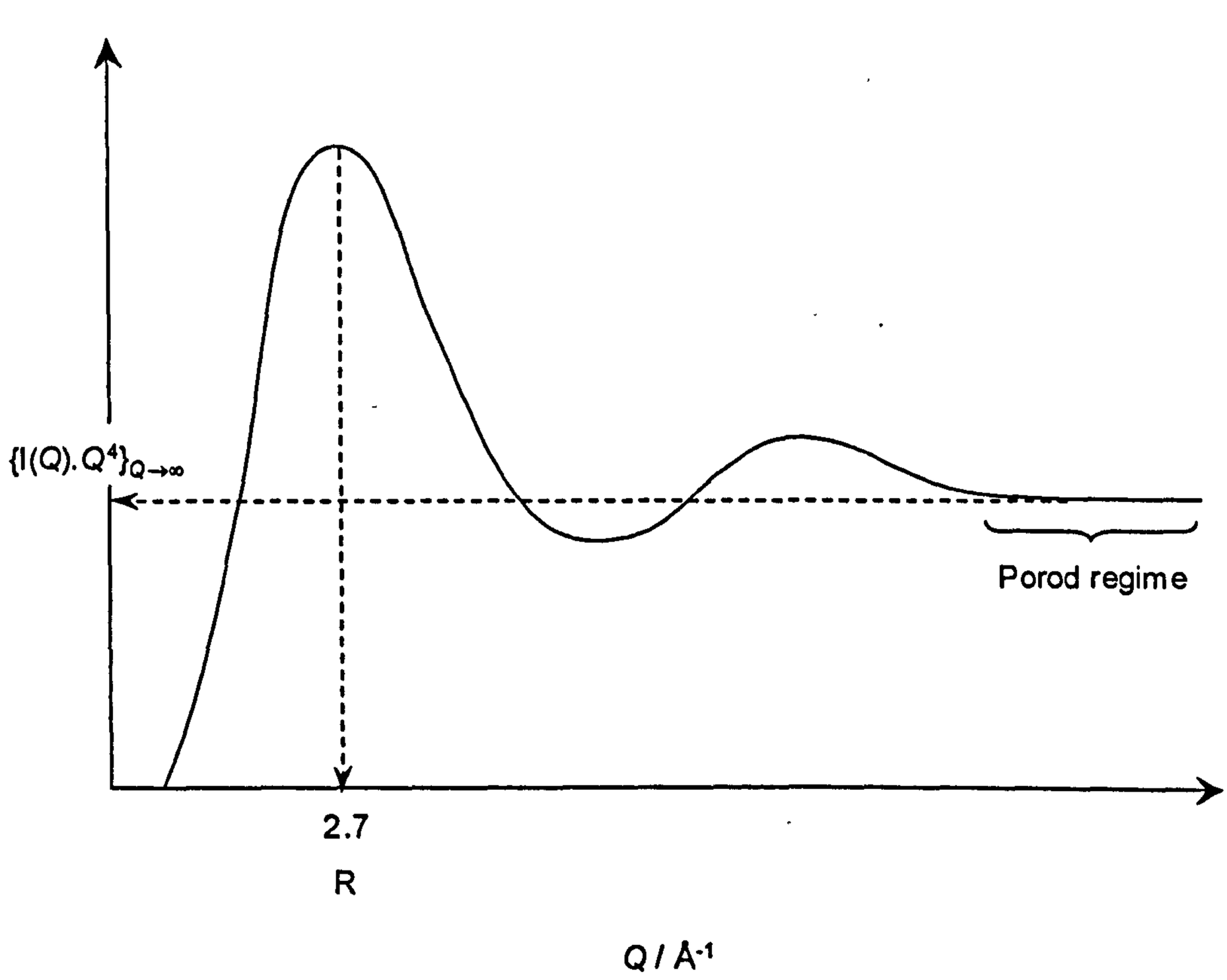

Figure 3.21 Schematic diagram of a Porod plot for near-monodisperse spheres (see text for details).

radius [78]. For monodisperse spheres of radius R, a plot of $\left[I(Q)\cdot Q^4\right]$ vs. Q gives a first maximum at $Q \approx 2.7/R$ and a minimum at $Q \approx 4.5/R$ (see Figure 3.21).

The Guinier and Porod approximations thus offer simple relations that allow a first estimation of the size and shape of colloidal particles. However, they are limited to dilute, non-interacting systems. As mentioned in the previous section, dilution or addition of salt allow the screening of interactions, so that the assumption $S(Q) = 1$ in the low Q-range becomes valid and the Guinier approximation can be applied. For microemulsions, these conditions do not always hold since their stability might break down upon dilution and addition of salt may introduce structural changes. In such cases, information about the size and shape of aggregates are obtained by fitting SANS experimental data to more complex mathematical models, such as those derived for polydisperse spherical droplets and introduced in this Section. More details about these models can be found elsewhere [79,90].

3.5 REFERENCES

1. Danielsson, I.; Lindman, B. *Colloids Surf. A* **1981**, *3*, 391.
2. Sjöblom, J.; Lindberg, R.; Friberg, S. E. *Adv. Colloid Interface Sci.* **1996**, 125.
3. Schulman, J. H.; Stoeckenius, W.; Prince, M. *J. Phys. Chem.* **1959**, *63*, 1677.
4. Shinoda, K.; Friberg, S. *Adv. Colloid Interface Sci.* **1975**, *4*, 281.
5. Adamson, A. W. *J. Colloid Interface Sci.* **1969**, *29*, 261.3.
6. Friberg, S. E.; Mandell, L.; Larsson, M. *J. Colloid Interface Sci.* **1969**, *29*, 155.
7. Shah, D. O., Ed. '*Surface Phenomena in Enhanced Recovery*' Plenum Press, 1981, New York.
8. Overbeek, J. Th. G. *Faraday Discuss. Chem. Soc.* **1978**, *65*, 7.
9. Tadros, Th. F.; Vincent, B. in '*Encyclopaedia of Emulsion Technology*' Becher, P. Ed., Vol. 1, Marcel Dekker, 1980, New York.
10. Kunieda, H.; Shinoda, K. *J. Colloid Interface Sci.* **1980**, *75*, 601.
11. Chen, S. J.; Evans, F. D.; Ninham, B. W. *J. Phys. Chem.* **1984**, *88*, 1631.
12. Kahlweit, M.; Strey, R.; Busse, G. *J. Phys. Chem.* **1990**, *94*, 3881.
13. Hunter, R. J. '*Introduction to Modern Colloid Science*' Oxford University Press, 1994, Oxford.
14. Lekkerkerker, H. N. W.; Kegel, W. K.; Overbeek, J. Th. G. *Ber. Bunsenges Phys. Chem.* **1996**, *100*, 206.
15. Ruckenstein, E.; Chi, J. C. *J. Chem. Soc. Faraday Trans.* **1975**, *71*, 1690.
16. Fletcher, P. D. I.; Howe, A. M.; Robinson, B. H. *J. Chem. Soc. Faraday Trans. 1* **1987**, *83*, 985.
17. Fletcher, P. D. I.; Clarke, S.; Ye, X. *Langmuir* **1990**, *6*, 1301.
18. Biais, J.; Bothorel, P.; Clin, B.; Lalanne, P. *J. Colloid Interface Sci.* **1981**, *80*, 136.
19. Friberg, S.; Mandell, L.; Larson, M. *J. Colloid Interface Sci.* **1969**, *29*, 155.
20. Fletcher, P. D. I.; Horsup, D. I. *J. Chem. Soc. Faraday Trans. 1* **1992**, *88*, 855.
21. Winsor, P. A. *Trans. Faraday Soc.* **1948**, *44*, 376.
22. Bellocq, A. M.; Biais, J.; Bothorel, P.; Clin, B.; Fourche, G.; Lalanne, P.; Lemaire, B.; Lemanceau, B.; Roux, D. *Adv. Colloid Interface Sci.* **1984**, *20*, 167.
23. Bancroft, W. D. *J. Phys. Chem.* **1913**, *17*, 501.
24. Clowes, G. H. A. *J. Phys. Chem.* **1916**, *20*, 407.
25. Adamson, A. W. '*Physical Chemistry of Surfaces*' Interscience, 1960, p 393.
26. Bourrel, M.; Schechter, R. S. '*Microemulsions and Related Systems*' Marcel Dekker, 1988, New York.
27. Israelachvili, J. N.; Mitchell, D. J.; Ninham, B. W. *J. Chem. Soc. Faraday Trans. 2* **1976**, *72*, 1525.
28. Griffin, W. C. *J. Cosmetics Chemists* **1949**, *1*, 311.
29. Griffin, W. C. *J. Cosmetics Chemists* **1954**, *5*, 249.
30. Davies, J. T. *Proc. 2nd Int. Congr. Surface Act.* Vol. I Butterworths, 1959, London.
31. Israelachvili, J. N. *Colloids Surf. A* **1994**, *91*, 1.
32. Shinoda, K.; Saito, H. *J. Colloid Interface Sci.* **1969**, *34*, 238.

33. Shinoda, K.; Kunieda, H. in '*Encyclopaedia of Emulsion Technology*' Becher, P. Ed., Vol. 1, Marcel Dekker, 1983, New York.
34. Aveyard, R.; Binks, B. P.; Clarke, S.; Mead, J. *J. Chem. Soc. Faraday Trans. 1* **1986**, *82*, 125.
35. Aveyard, R.; Binks, B. P.; Mead, J. *J. Chem. Soc. Faraday Trans. 1* **1986**, *82*, 1755.
36. Aveyard, R.; Binks, B. P.; Fletcher, P. D. I. *Langmuir* **1989**, *5*, 1210.
37. Sottmann, T.; Strey, R. *Ber. Bunsenges Phys. Chem.* **1996**, *100*, 237.
38. Langevin, D., Ed. '*Light Scattering by Liquid Surfaces and Complementary Techniques*' Marcel Dekker, 1992, New York.
39. Hyde, S.; Andersson, K.; Larsson, K.; Blum, Z.; Landh, S.; Ninham, B. W. '*The Language of Shape*' Elsevier, 1997, Amsterdam.
40. Eastoe, J.; Dong, J.; Hetherington, K. J.; Steytler, D. C.; Heenan, R. K. *J. Chem. Soc. Faraday Trans.* **1996**, *92*, 65.
41. Eastoe, J.; Hetherington, K. J.; Sharpe, D.; Dong, J.; Heenan, R. K.; Steytler, D. C. *Langmuir* **1996**, *12*, 3876.
42. Eastoe, J.; Hetherington, K. J.; Sharpe, D.; Dong, J.; Heenan, R. K.; Steytler, D. C. *Colloids Surf. A* **1997**, *128*, 209.
43. Eastoe, J.; Hetherington, K. J.; Sharpe, D.; Steytler, D. C.; Egelhaaf, S.; Heenan, R. K. *Langmuir* **1997**, *13*, 2490.
44. Bumajdad, A.; Eastoe, J.; Heenan, R. K.; Lu, J. R.; Steytler, D. C.; Egelhaaf, S. *J. Chem. Soc. Faraday Trans.* **1998**, *94*, 2143.
45. Helfrich, W. Z. *Naturforsch.* **1973**, *28c*, 693.
46. Kellay, H.; Binks, B. P.; Hendrikx, Y.; Lee, L. T.; Meunier, J. *Adv. Colloid Interface Sci.* **1994**, *9*, 85.
47. Safran, S. A.; Tlusty, T. *Ber. Bunsenges. Phys. Chem.* **1996**, *100*, 252.
48. Szleifer, I.; Kramer, D.; Ben-Shaul, A.; Gelbart, W. M.; Safran, S. *J. Chem. Phys.* **1990**, *92*, 6800.
49. Winterhalter, M.; Helfrich, W. *J. Phys. Chem.* **1992**, *96*, 327.
50. Gradzielski, M.; Langevin, D.; Farago, B. *Phys. Rev. E* **1996**, *53*, 3900.
51. Safran, S. A. in '*Structure and Dynamics of Strongly Interacting Colloids and Supramolecular Aggregates in Solution*' Vol. 369 of *NATO Advanced Study Institute, Series C: Mathematical and Physical Sciences*, Chen, S. H.; Huang, J. S.; Tartaglia, P. Ed.; Kluwer, Dortrecht, 1992.
52. Meunier, J.; Lee, L. T. *Langmuir* **1991**, *46*, 1855.
53. Kegel, W. K.; Bodnar, I.; Lekkerkerker, H. N. W. *J. Phys. Chem.* **1995**, *99*, 3272.
54. Sicoli, F.; Langevin, D.; Lee, L. T. *J. Chem. Phys.* **1993**, *99*, 4759.
55. De Gennes, P. G.; Taupin, C. *J. Phys. Chem.* **1982**, *86*, 2294.
56. Daillant, J.; Bosio, L.; Benattar, J. J.; Meunier, J. *Europhys. Lett.* **1989**, *8*, 453.
57. Shneider, M. B.; Jenkins, J. T.; Webb, W. W. *Biophys. J.* **1984**, *45*, 891.
58. Engelhardt, H; Duwe, H. P.; Sackmann, E. *J. Phys. Lett.* **1985**, *46*, 395.
59. Bivas, I.; Hanusse, P.; Botherel, P.; Lalanne, J.; Aguerre-Chariol, O. *J. Physique* **1987**, *48*, 855.
60. Di Meglio, J. M.; Dvolaitzky, M. Taupin, C. *J. Phys. Chem.* **1985**, *89*, 871.

61. Farago, B.; Huang, J. S.; Richter, D.; Safran, S. A.; Milner, S. T. *Progr. Colloid Polym. Sci.* **1990**, *81*, 60.
62. Safran, S. A. *J. Chem. Phys.* **1983**, *78*, 2073.
63. Milner, S. T.; Safran, S. A. *Phys. Rev. A* **1987**, *36*, 4371.
64. Eastoe, J.; Sharpe, D.; Heenan, R. K.; Egelhaaf, S. *J. Phys. Chem. B* **1997**, *101*, 944.
65. Gradzielski, M.; Langevin, D. *J. Mol. Struct.* **1996**, *383*, 145.
66. Eastoe, J.; Sharpe, D. *Langmuir* **1997**, *13*, 3289.
67. Rock, P. A. '*Chemical Thermodynamics*' MacMillan, 1969, London.
68. Olsson, U.; Wennerström, H. *Adv. Colloid Interface Sci.* **1994**, *49*, 113.
69. Robinson, B. H.; Toprakcioglu, C.; Dore, J.-C.; Chieux, P. *J. Chem. Soc. Faraday Trans. 1* **1984**, *80*, 13.
70. Eastoe, J.; Robinson, B. H.; Steytler, D. C.; Thorn-Leeson, D. *Adv. Coll. Int. Sci.* **1991**, *36*, 1.
71. Bacon, G. E. '*Neutron Scattering in Chemistry*' Butterworths, 1977, London.
72. ILL World Wide Web page: http://www.ill.fr
73. ISIS World Wide Web page: http://www.isis.rl.ac.uk
74. Finney, J.; Steigenberger, S. *Physics World* **1997**, *10*, issue 12 (report published on PhysicsWorld Web page: http://www.physicsweb.org/article/world/10/12/7).
75. Heenan, R. K; Penfold, J.; King, S. M. *J. Appl. Cryst.* **1997**, *30*, 1140.
76. King, S. M. '*Small-Angle Neutron Scattering*' a report published on ISIS Web page, 1997.
77. Cabane, B. in '*Surfactant Solutions: New Methods of Investigation*', (Ed. Zana, R.), Surfactant Science Series vol 22, p57-139, Marcel Dekker Inc., 1987, New York.
78. Eastoe, J. in '*New Physico-Chemical Techniques for the Characterisation of Complex Food Systems*', (Ed. Dickinson, E.), p268-294, Blackie, 1995, Glasgow.
79. Ottewill, R. H. in '*Colloidal Dispersions*', (Ed. Goodwin, J. W.), R.S.C, 1982, London.
80. Chen, S-H. *Ann. Rev. Phys. Chem.* **1986**, *37*, 351.
81. Kotlarchyk, M.; Chen, S-H.; Huang, J. S.; Kim, M. W. *J. Phys. Chem.* **1984**, *29*, 2054.
82. Ashcroft, N. W.; Lekner, J. *Phys. Rev.* **1966**, *145*, 83.
83. Cebula, D. J.; Myers, D. Y.; Ottewill, R. H. *Colloid Polym. Sci.* **1982**, *260*, 96.
84. Goodwin, J. W.; Ottewill, R. H.; Owens, S. M.; Richardson, R. A.; Hayter, J. B. *Macromol. Chem. Suppl.* **1985**, *10/11*, 499.
85. Heenan, R. K.; Eastoe, J. *J. Appl. Cryst.* **2000**, *33*, 749.
86. Guinier, A. *Annales de Physique* **1939**, *12*, 161.
87. Porte, G. in '*Micelles, Membranes, Microemulsions, and Monolayers*' (Eds. Gelbart, W. M.; Ben-Shaul, A.; Roux, D.), Springer-Verlag, 1994, New York, p105-145.
88. Porod, G. *Koll. Z.* **1951**, *124*, 82.
89. Auvray, L.; Auroy, P. in '*Neutron, X-Ray and Light-Scattering*' (Eds. Lindner, P.; Zemb, Th.), Elsevier Science Publishers, 1991, Holland.
90. Markovic, I.; Ottewill, R. H.; Cebula, D. J.; Field, I.; Marsh, J. *Colloid Polym. Sci.* **1984**, *262*, 648.

CHAPTER 4

SURFACTANT SYNTHESIS

This chapter details the synthesis of the three groups of anionic surfactants examined in the thesis. They are sodium salts of di-chain sulfosuccinates and sulfoglutaconates. Table 4.1 outlines the surfactant molecular structures and nomenclature used in this work.

4.1 EXPERIMENTAL

4.1.1 Materials

All solvents used during the reaction and purification procedures were dried and distilled beforehand as detailed elsewhere [1]. Water was obtained from either a Millipore Milli-Q Plus or a R0100HP Purite system, of resistivity 18.2 MΩ cm. Other materials used in the syntheses are listed below.

- Butan-1-ol 99 %, Aldrich.
- Pentan-1-ol 99 %, Aldrich.
- Hexan-1-ol 99 %, Aldrich.
- n-hexyl-d_{13} alcohol 98.5 % D, CDN Isotope.
- Heptanol-1-ol 99 %, Aldrich.
- Octan-1-ol 99 %, Aldrich.
- 2-Ethyl-1-hexanol 98 %, Aldrich.
- 2-Propyl-1-pentanol 99 %, Aldrich.
- 2,4,4-Trimethyl-1-pentanol 98 %, Aldrich.

Table 4.1 Surfactant molecular structure and nomenclature

Starting alcohol	Tail Structure	Nomenclature
butan-1-ol	$CH_3(CH_2)_3O$-	di-C4SS
pentan-1-ol	$CH_3(CH_2)_4O$-	di-C5SS
hexan-1-ol	$CH_3(CH_2)_5O$-	H-di-C6SS
n-hexyl-d_{13} alcohol	$CD_3(CD_2)_5O$-	D-di-C6SS
heptan-1-ol	$CH_3(CH_2)_6O$-	di-C7SS
octan-1-ol	$CH_3(CH_2)_7O$-	di-C8SS
2-ethyl-1-hexanol	$CH_3(CH_2)_3CH(C_2H_5)CH_2O$-	AOT①
2-propyl-1-pentanol	$CH_3(CH_2)_2CH(C_3H_7)CH_2O$-	AOT②
2,4,4-trimethyl-1-pentanol	$(CH_3)_3CCH_2CH(CH_3)CH_2O$-	AOT③
3,5,5-trimethyl-1-hexanol	$(CH_3)_3CCH_2CH(CH_3)(CH_2)_2O$-	AOT④
4-methyl-3-heptanol	$CH_3(CH_2)_2CH(CH_3)CH(C_2H_5)O$-	AOT⑤
6-methyl-2-heptanol	$CH_3CH(CH_3)(CH_2)_3CH(CH_3)O$-	AOT⑥
2-phenyl-ethan-1-ol	$(C_6H_5)(CH_2)_2O$-	di-PhC2SS
3-phenyl-propan-1-ol	$(C_6H_5)(CH_2)_3O$-	di-PhC3SS
4-phenyl-butan-1-ol	$(C_6H_5)(CH_2)_4O$-	di-PhC4SS
5-phenyl-pentan-1-ol	$(C_6H_5)(CH_2)_5O$-	di-PhC5SS
2-phenyl-propan-1-ol	$(C_6H_5)CH(CH_3)CH_2O$-	Br-di-PhC3SS
3-phenyl-2,2-dimethylpropan-1-ol	$(C_6H_5)CH_2C(CH_3)_2CH_2O$-	Br-di-PhC5SS
hexan-1-ol	$CH_3(CH_2)_5O$-	di-C6GLU
2-ethyl-1-hexanol	$CH_3(CH_2)_3CH(C_2H_5)CH_2O$-	AOTGLU

- 3,5,5-Trimethyl-1-hexanol 90 %, Aldrich.
- 4-Methyl-3-heptanol 99+ %, Aldrich.
- 6-Methyl-2-heptanol 99 %, Aldrich.
- Fumaryl chloride 95 %, Avocado.
- Maleic anhydride 99 %, Avocado.
- Glutaconic acid - Puriss > 97 %, Fluka.
- N,N-dimethylaniline 99 %, Aldrich.
- Sodium metabisulfite 97 %, Avocado.
- Sodium sulfite 98+ %, Avocado.
- Toluene-4-sulfonic acid monohydrate - 98.5 %, Aldrich.
- Tetrahydrofuran (THF) - anhydrous, 99.9 %, Aldrich.
- Toluene - Analar, BDH
- Hydrochloric acid GPR grade, BDH.
- Sodium hydrogen carbonate GPR grade, BDH.
- Anhydrous magnesium sulphate GPR grade > 99 %, BDH.
- Ethyl acetate GPR grade, min. assay 99 %, BDH.
- Diethyl ether GPR grade, min. assay 98 %, BDH.
- Absolute ethanol, assay 99.4-100 %, Hayman.
- Silica TLC plates, Merck.
- Petroleum ether 60/80 Analar, BDH
- Cellulose extraction thimbles - 30 × 100 mm, single thickness, Whatman.
- Nitrogen gas - 'white spot', oxygen free, BOC Gases.
- Phosphorus pentoxide, Aldrich.

4.1.2 Synthesis and purification

The synthetic route followed was the same for all the sulfosuccinates and sulfoglutaconates and involved three stages: (*i*) esterification of the appropriate alcohol to yield the diester (two possible routes, see later); (*ii*) sulfonation of the double bond; (*iii*) purification by Soxhlet extraction, washing, recrystallisation, and foam fractionation. Note that the phenyl-tipped surfactants were supplied by Kodak, Harrow, and therefore, were only subjected to step (*iii*).

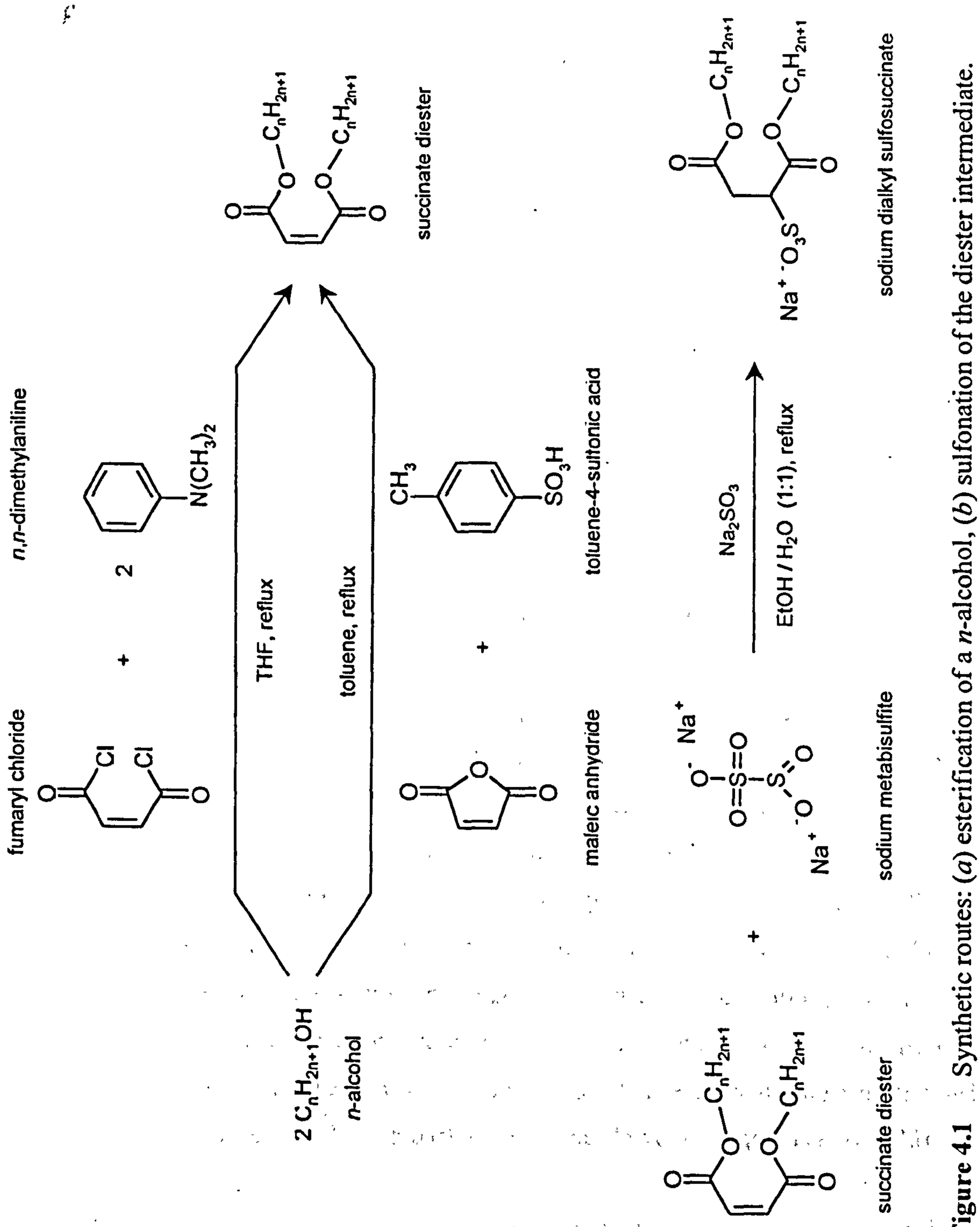

Figure 4.1 Synthetic routes: (*a*) esterification of a *n*-alcohol, (*b*) sulfonation of the diester intermediate.

Reaction schemes for the esterification and sulfonation steps are outlined in Figure 4.1, and are based on standard procedures [2,3]. In step (*a*) the diester intermediate may be formed by reaction of fumaryl chloride or maleic anhydride with the appropriate alcohol. In this work, both reactions were followed, and as described later, the choice of the most appropriate esterification route depended on the structure of the starting alcohol. Preparation of the proteated and deuterated isotopes of di-C6SS (H- and D-di-C6SS, respectively) are given below by way of example. The diester intermediate of H-di-C6SS was prepared via the fumaryl chloride route, while the maleic anhydride route was applied to the deuterated compound. Variations in the esterification procedure for other surfactants are noted in the text.

(i) Esterification of H- and D-n-hexyl alcohol

Fumaryl chloride route. *n*-Hexanol (40.5 g, 2.2 eq.) and dimethylaniline (43.6 g, 2.0 eq.) were dissolved in dry tetrahydrofuran (THF, 150 ml) in a three-neck round-bottomed flask, fitted with a condenser, pressure-equalised dropping funnel and thermometer. The reaction vessel was flushed with N_2, and fumaryl chloride (27.5 g, 1.0 eq.) was added dropwise over twenty minutes with stirring. A brown/purple solution was formed and internal temperature rised to approximately 65 °C. The reaction mixture was then refluxed (70 °C) and TLC plates developed periodically (4:1 hexane:ethyl acetate eluent, viewed under UV and/or with potassium permanganate solution) to check for residual fumaryl chloride. After 4 hours the reaction was complete, THF was removed by rotary evaporation, and the remaining purple oil was dissolved in diethyl ether. The ethereal solution was washed sequentially with 10 % hydrochloric acid (300 cm^3) and saturated aqueous sodium hydrogen carbonate solution (300 cm^3) until the aqueous phase was clear. The ethereal extracts were dried over anhydrous magnesium sulfate, filtered and rotary evaporated to yield a dark oil. The crude diester was distilled under reduced pressure (185 °C, 5 mbar) to yield a bright yellow liquid (78 % yield).

Maleic anhydride route. *n*-hexyl-d_{13} alcohol (5.01 g, 2.0 eq.), maleic acid (2.13 g, 1.0 eq.) and toluene-4-sulfonic acid (0.83 g, 0.2 eq.) were mixed with toluene (60 ml) in a round bottom flask fitted with a Dean and Stark trap apparatus to remove water. The mixture was refluxed (110 °C) with stirring for approximately 10 hours, and water from the esterification distilled over within 30 minutes. The theoretical volume of water to be collected was calculated from the number of moles of maleic anhydride and

toluene-4-sulfonic acid present. The reaction was considered complete when no further water was evolved, and a TLC plate of the reaction mixture showed no trace of residual maleic acid. The reaction mixture was cooled to 70 °C and washed against hot water (4 × 75 cm^3). Toluene was removed by rotary evaporation, and the residual material was distilled under reduced pressure (201°C, 17 mbar) to yield the pure diester as a colourless liquid (82 % yield).

Both esterification routes gave similar high yields and worked equally well for linear sodium sulfosuccinates of chain length C6 and above. However, the maleic anhydride route was found to be preferable due, mainly, to its simpler and cleaner work-up (in particular washing of the by-products). This route was also used for the syntheses of the glutaconate analogues of di-C6SS and AOT (di-C6GLU and AOTGLU, see Table 4.1) where appropriate alcohols were reacted with glutaconic (instead of maleic) acid. For some alcohols, however, due to the use of a Dean and Stark trap, the maleic anhydride route was unsuitable. This was the case for short chain alcohols, such as butanol and pentanol, that have boiling points below that of the toluene/water azeotrope being removed (110.7 °C). Therefore, the diester intermediates of di-C4SS and di-C5SS were prepared via the fumaryl chloride route. Another limitation of the maleic anhydride route was the lower reactivity of the anhydride with the alcohol compared to fumaryl chloride. This was considered in the synthesis of the diester of AOT⑤ and -⑥: the presence of bulky side groups next to the hydroxide function was found to hinder diester formation. Esterification failed when the maleic anhydride route was used, whereas reactions with fumaryl chloride were successful, with high diester yields.

All diester intermediates were subjected to ^{1}H NMR analyses. Typical spectra of selected compounds are presented in Section 4.2. The sulfonation step (Figure 4.1(*b*)) was then applied to all succinate and glutaconate diesters, and a general procedure is detailed below for H-di-C6SS only.

(ii) Sulfonation

Bis(1-hexyl) fumarate (40.1 g, 1.0 eq.) was dissolved in a 1:1 mixture of ethanol:water (250 ml) in a round-bottomed flask equipped with a reflux condenser. Sodium metabisulfite (29.5 g, 1.1 eq.) was added and the mixture was refluxed with stirring for 4 hours. Sodium sulfite (16.0 g, 0.90 eq.) was added portion-wise during the first hour. The reaction was monitored by TLC (eluting with ethyl acetate) looking for the disappearance of the high running diester to give baseline material. If some residual diester remained after 2 hours, additional disulfite (1.0 g) and sulfite (0.5 g) were added until the reaction was complete. After cooling, the reaction mixture was decanted off (leaving unreacted sodium sulfite in the reaction vessel). The solvent was removed carefully on a rotary evaporator to give the crude surfactant as a white solid. The product was dried in a vacuum oven for 15 hours (60 °C, 12 mbar). For all diesters, the sulfonation step gave high conversion to the corresponding sodium surfactants. However, due to the presence of excess salt, the exact percentage could not be assessed at this stage.

Inherent in the sulfonation step was introduction of inorganic contaminants (i.e., excess sodium salts) that had to be thoroughly removed before the surfactant could be investigated in aqueous and microemulsion systems. To obtain "surface chemically pure" surfactants, four separate stages were necessary. General procedures are described below, and any variation with surfactant type is mentioned.

(iii) Purification

Soxhlet extraction. Soxhlet extraction removed inorganic materials left over from the sulfonation step. Dry bis(1-hexyl) sulfosuccinate was packed into a cellulose fibre thimble and placed in a Soxhlet extraction apparatus. The extraction solvent, ethyl acetate, was dried over anhydrous magnesium sulphate and distilled prior to use. Ethyl acetate (250ml) and anti-bump granules were added to a round-bottomed flask and the apparatus protected from atmospheric moisture with a drying tube. The solvent was refluxed through the thimble for 24 hours. The solvent was removed from the extract by rotary evaporation.

In some cases, prior to the soxhlet extraction, the crude surfactant was dissolved in ethyl acetate (250 cm^3) and excess salt extracted with water (30 cm^3). Organic extracts were collected and solvent removed by rotary evaporation. This intermediate

step could only be applied to long chain surfactants (C7 and above), since their solubility in water is low, allowing effective separation from inorganic contaminants. In order to minimise loss of surfactant in the aqueous phase and to improve the efficiency of the extraction process, it was found essential to use small volumes of water (20–40 cm^3) relative to the organic phase.

Washing. Washing removed residual inorganic material. The product from the above stage was dissolved in the minimum quantity of dried, distilled methanol and centrifuged at 25 °C, 8000 rpm for 45 minutes. The supernatant was decanted and any residual solids were discarded. The solvent was removed by rotary evaporation. This centrifugation step was found essential for the complete removal of any residual electrolyte, due to the extremely low solubility of salt in methanol. The purification cycle was repeated until no further solid was obtained after centrifugation. Once a clear solution of surfactant in methanol was obtained (cloudy solutions were indicative of incompletely purified materials), the solvent was evaporated and the surfactant dried in a vacuum oven. Note that dried, distilled acetone was used in some cases instead of methanol, and this worked equally well.

Recrystallisation. This purification step ensured there was no contamination of the surfactant by organic impurities (starting alcohol and/or unreacted diester). All linear dialkyl surfactants were recrystallised twice from methanol, following the method of William *et al.* [3]. The product from centrifugation was dissolved in the minimum quantity of hot absolute methanol, cooled to ambient temperature and then cooled further by immersion in an ice-water slurry. Crystals were separated by filtration and washed with aliquots of chilled solvent. The linear phenyl-tipped sulfosuccinates (di-PhC2SS and di-PhC4SS) were recrystallised twice from toluene, following the same technique. Final materials were dried under vacuum (60 °C, 12 mbar) for at least 24 hours, and stored in sealed vials in a desiccating cabinet over refreshed phosphorus pentoxide. All branched surfactants (AOT series, Br-di-PhC3SS, Br-di-PhC5SS, AOTGLU), and odd members of the di-PhC*n*SS series could not be recrystallised due to the absence of an accessible Krafft temperature. All the above materials were waxy in nature, whereas others were crystalline compounds.

Foam fractionation. This was the final purification step to remove surface-active impurities. Aqueous solutions of the surfactants were made up at just below the CMC [4]. Nitrogen gas was passed through a calcium sulfate drying set-up and a carbon filter, and then bubbled through aqueous solutions of HCl and NaOH, followed by several flasks of pure water before finally reaching the surfactant solution. It was necessary to control the gas flow and vacuum suction rates to allow sufficient drainage time before the foam was removed. The pure surfactants were recovered by rotary evaporation of water from these solutions and dried as before. Foam fractionation was found to be very effective at removing trace quantities of surface-active impurities, and was applied successfully on the H- and D-di-C6SS surfactants. A detailed discussion of this study is given in Chapter 5 (Section 5.2.2). However, foam fractionation is a time-consuming technique, and cannot be carried out on large amounts of materials (especially for surfactants with low CMC). Considering the minor effect of trace quantities of impurities on the physico-chemical properties studied in this work (see Chapter 5), other surfactants were not foam fractionated.

4.2 SURFACTANT ANALYSIS

Nuclear magnetic resonance and elemental analysis were used to characterise purity of the surfactants with regard to organic (unreacted alcohol and/or diester) and inorganic (excess salt) contaminants.

4.2.1 Nuclear Magnetic Resonance (NMR) spectroscopy

Proton NMR spectra were recorded on a JEOL Lambda 300 MHz machine (NMR service, School of Chemistry, University of Bristol). Processed spectra were further analysed using JEOL SpecNMR software to obtain integration values for each group of identical protons. Samples of approximately 0.7 ml were prepared at 50–100 mg ml^{-1} concentration by dissolving materials under investigation in $CDCl_3$ or d_6-acetone, depending on solubility. Tetramethylsiloxane (TMS) was used as internal reference (chemical shift set at 0 ppm), and only a trace amount is necessary (i.e., vapour from TMS bottle bubbled into sample).

^{1}H NMR spectra were obtained for all diester intermediates and final products. Some examples of the spectra of each surfactant series are discussed below. Due to incomplete deuteration of the solvents (d-chloroform or d-acetone), residual proton signals are present, giving a singlet at 7.25 ppm and a quintet at 2.05 ppm for $CHCl_3$ and $(CH_3)_2CO$ respectively.

As expected, spectra for diester and surfactant molecules show similar signals for methyl, methylene, and methyne protons of the chains (i.e., protons *a*, *b*, *c*, *d*, and *g*). For ^{1}H spectra of diesters, notable points are disappearance of the peak corresponding to the proton of the alcohol function (i.e., a singlet in the range 0.5 – 4.0 ppm, depending on chemical environment), and appearance of additional signals for methylene protons next to the ester functions (i.e., protons *d* at approximately 4.1 ppm). Other characteristic signals for diesters are protons of the double bond obtained at high chemical shifts (i.e., protons *e* for the succinates, and *f* and *g* for the glutaconates, at approximately 6.5 and 7.0 ppm). As seen in Figures 4.2 and 4.4, depending on the esterification route, splitting patterns for those protons differ slightly. Fumarate diesters are of trans configuration only so one singlet is obtained at ~ 7.0 ppm, whereas maleate diesters have the cis and trans configurations so two singlets are observed at ~ 6.5 ppm and ~ 7.0 ppm respectively. For ^{1}H spectra of surfactants, notable points are the absence of any diester peaks at around 6.5 - 7 ppm, and the appearance of two extra peaks at ~ 3.15 and ~ 4.3 ppm, corresponding to protons *e* and *f*, respectively, in the head group. Note that, as the double bond is lost after sulfonation, the choice of fumarate or maleate diester has no effect on the final surfactant. Generally, splitting patterns for protons within the head group of the glutaconate diesters (i.e., protons *e*, *f*, and *g*) are more complex. Signals are mainly split by coupling into patterns of doublets, triplets, quintets, septets, or even more, and this is caused by head group asymmetry and the slight difference in environment at the two chain-ends. For di-PhC4SS (Figure 4.6), as for all phenyl sulfosuccinates, characteristic signals are those due to protons of the aromatic group, at around 7.2 ppm.

Details of proton assignments and integration for the selected NMR spectra are given in Tables 4.2 and 4.3, for the succinates and glutaconates respectively. Integrals were in good agreement with theoretical values. All other diester and surfactant molecules were analysed in the same way, and characteristic peaks were identified. For brevity, corresponding spectra are omitted.

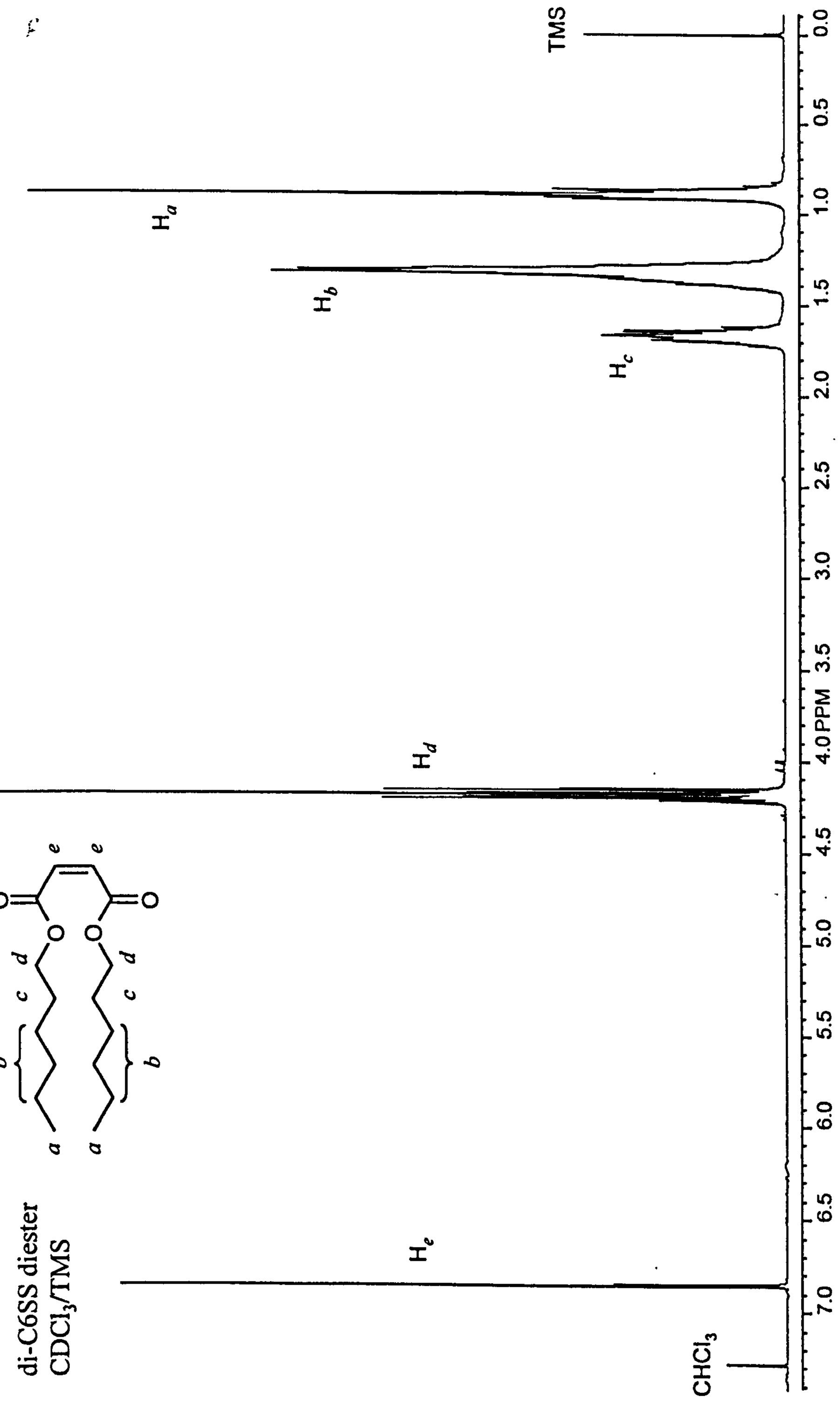

Figure 4.2 ^{1}H NMR spectrum of di-C6SS diester, obtained from fumaryl chloride route.

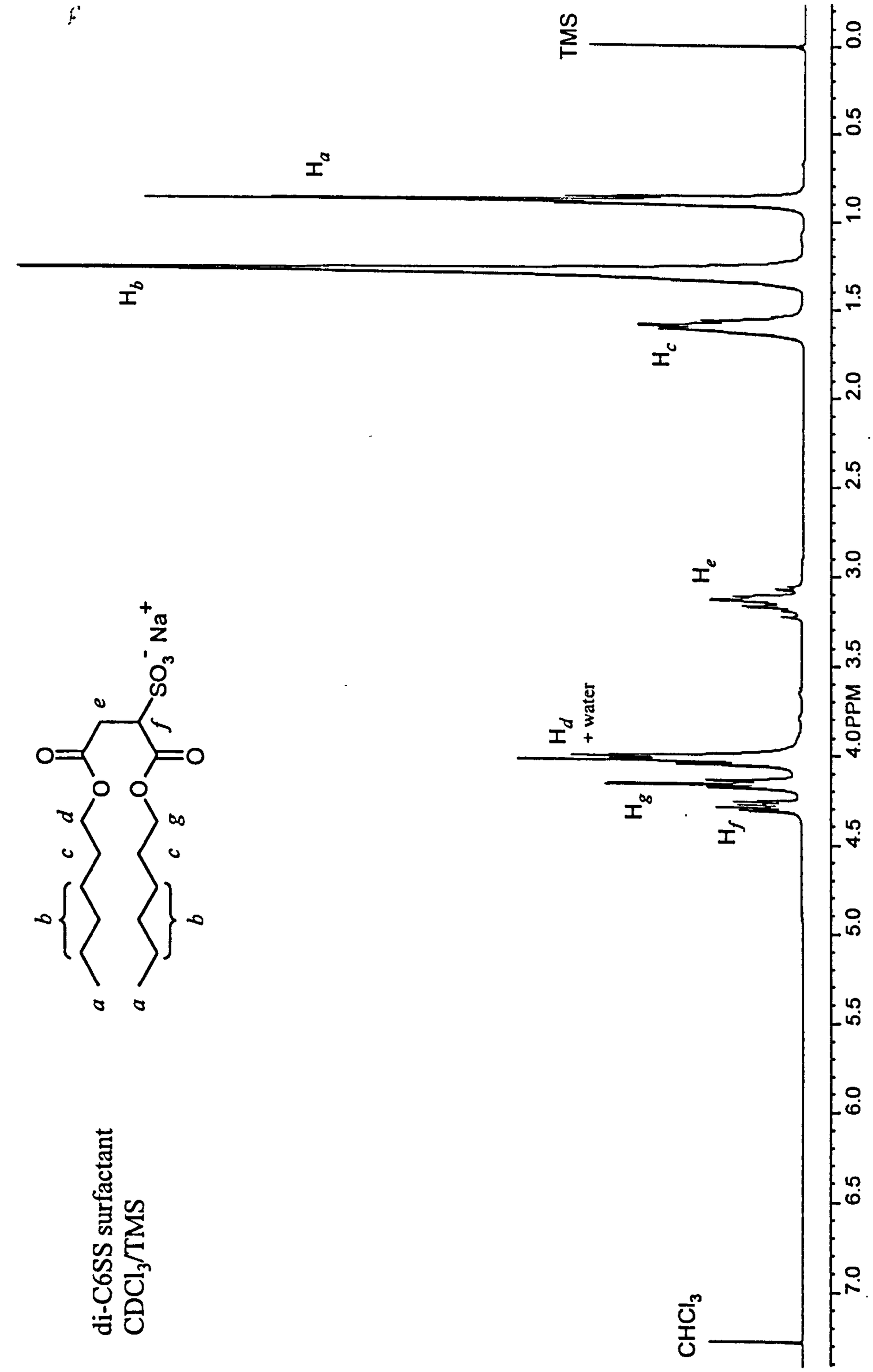

Figure 4.3 ^{1}H NMR spectrum of di-C6SS surfactant.
di-C6SS surfactant
$CDCl_3$/TMS

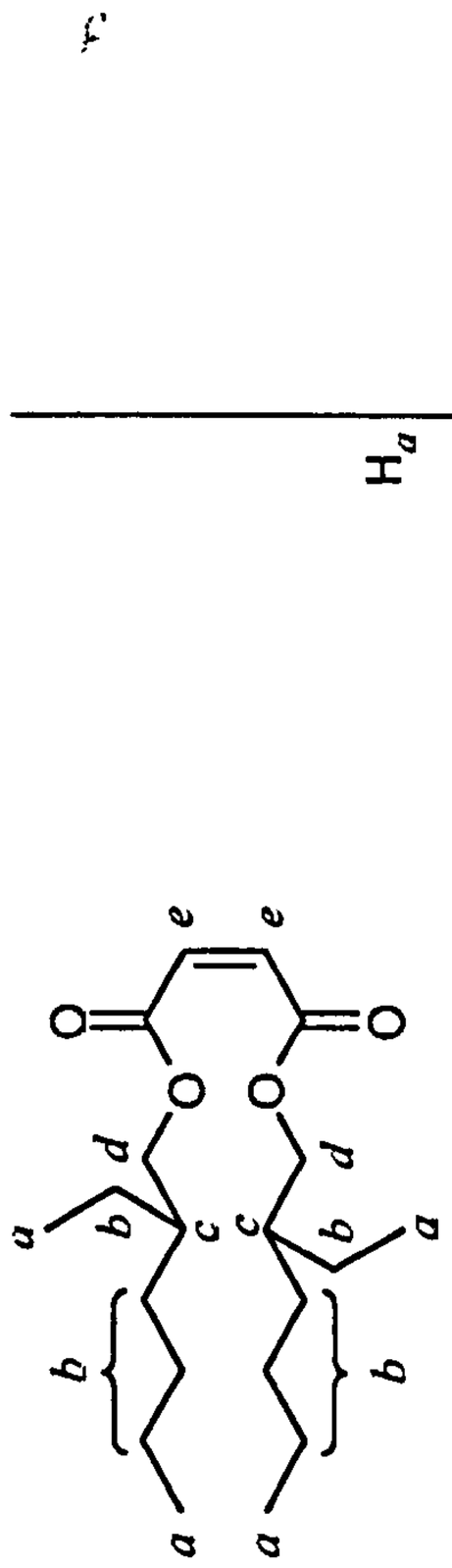

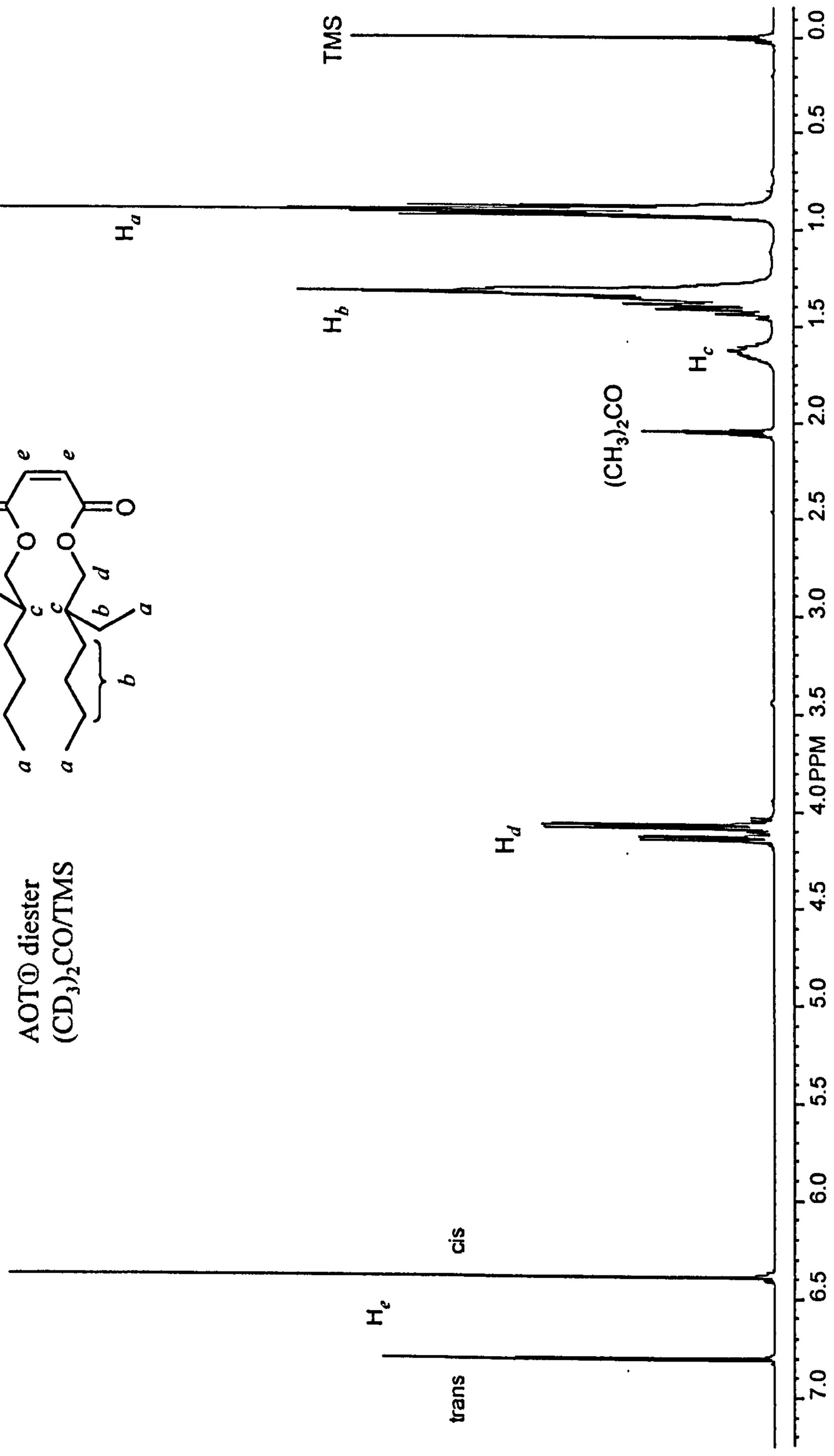

Figure 4.4 ^1H NMR spectrum of AOT① diester, obtained from maleic anhydride route.

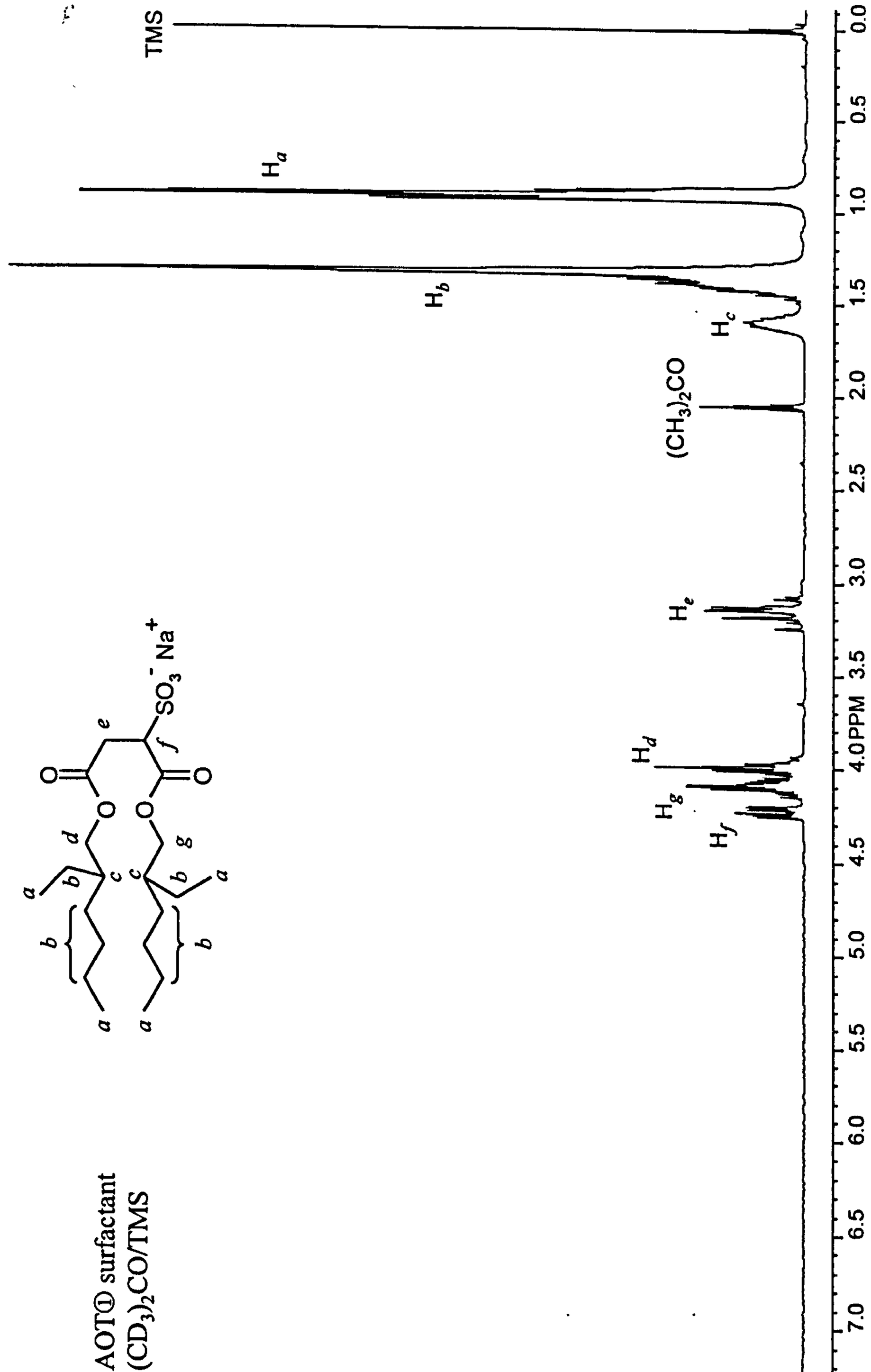

AOT® surfactant
$(CD_3)_2CO$/TMS

Figure 4.5 ^1H NMR spectrum of AOT® surfactant.

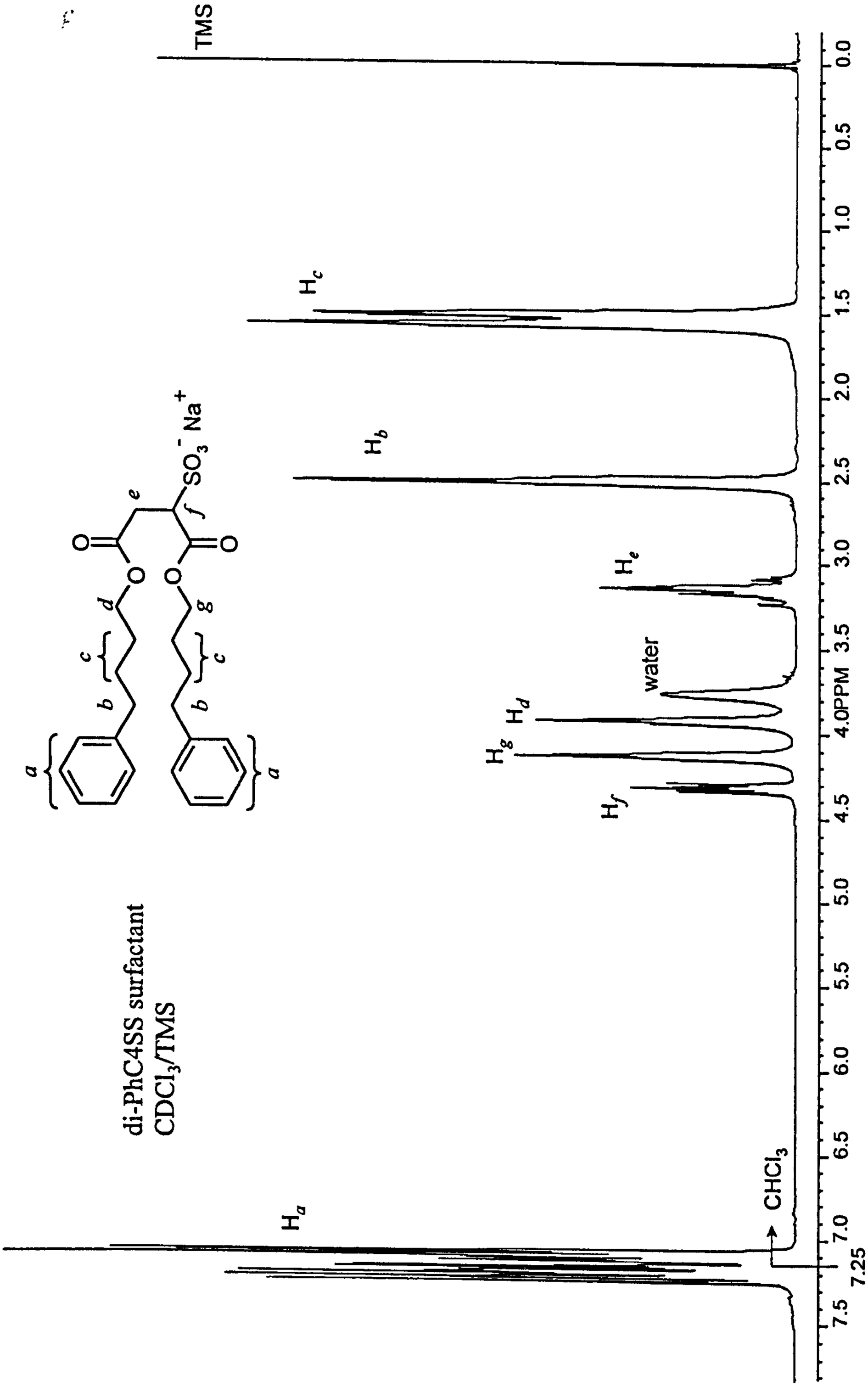

Figure 4.6 ^{1}H NMR spectrum of di-PhC4SS surfactant.

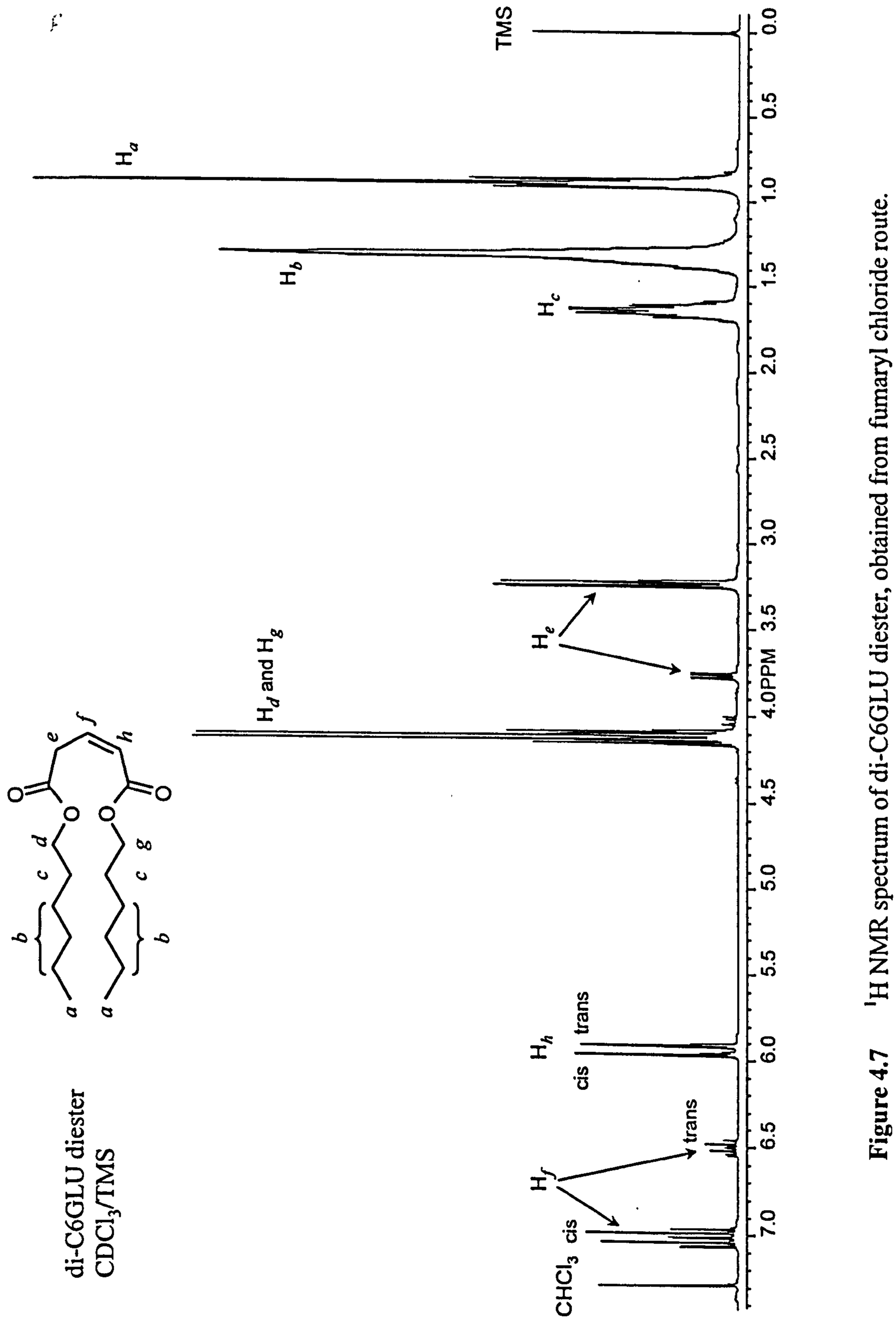

di-C6GLU diester
$CDCl_3$/TMS

Figure 4.7 ^{1}H NMR spectrum of di-C6GLU diester, obtained from fumaryl chloride route.

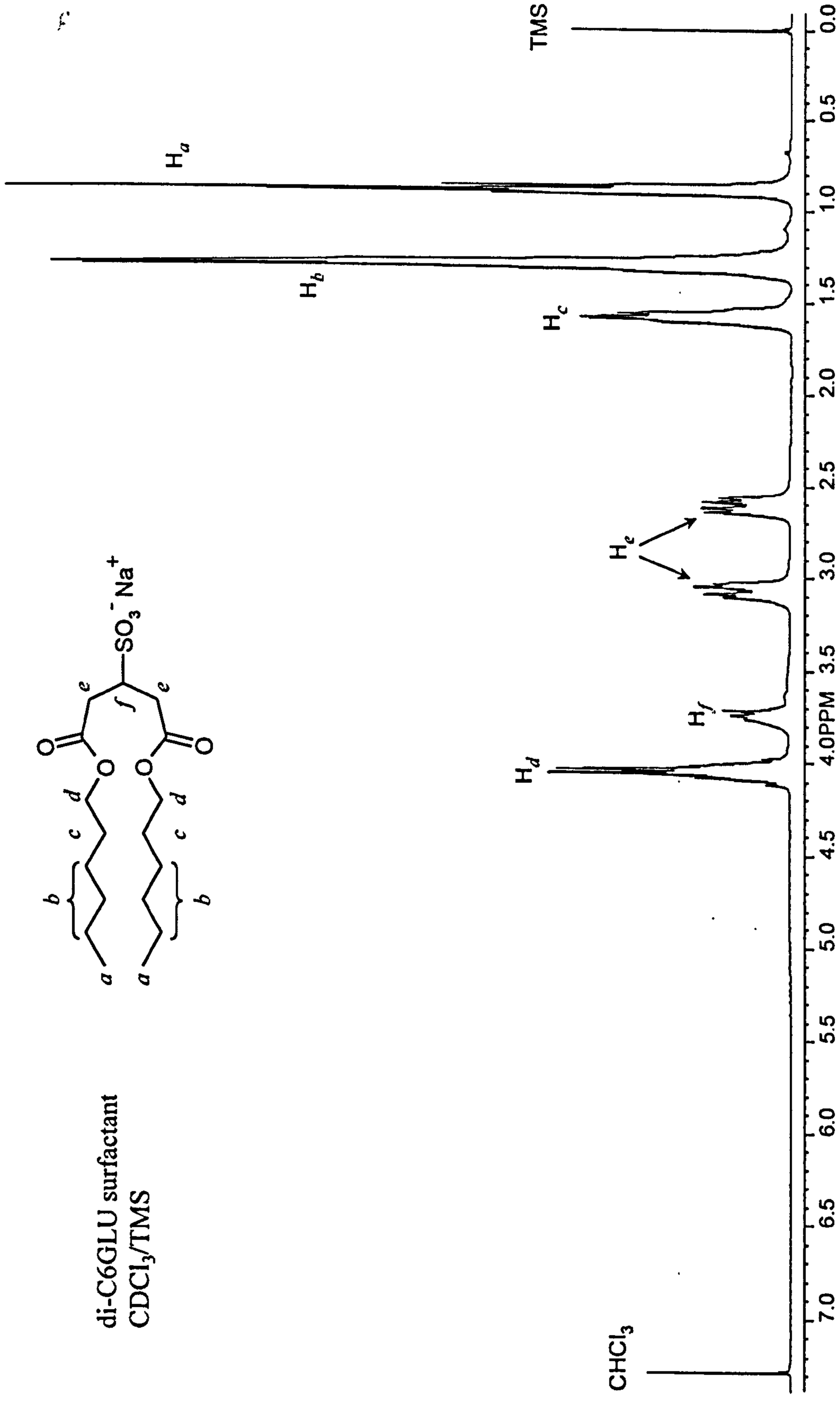

Figure 4.8 ^{1}H NMR spectrum of di-C6GLU surfactant.
di-C6GLU surfactant
$CDCl_3$/TMS

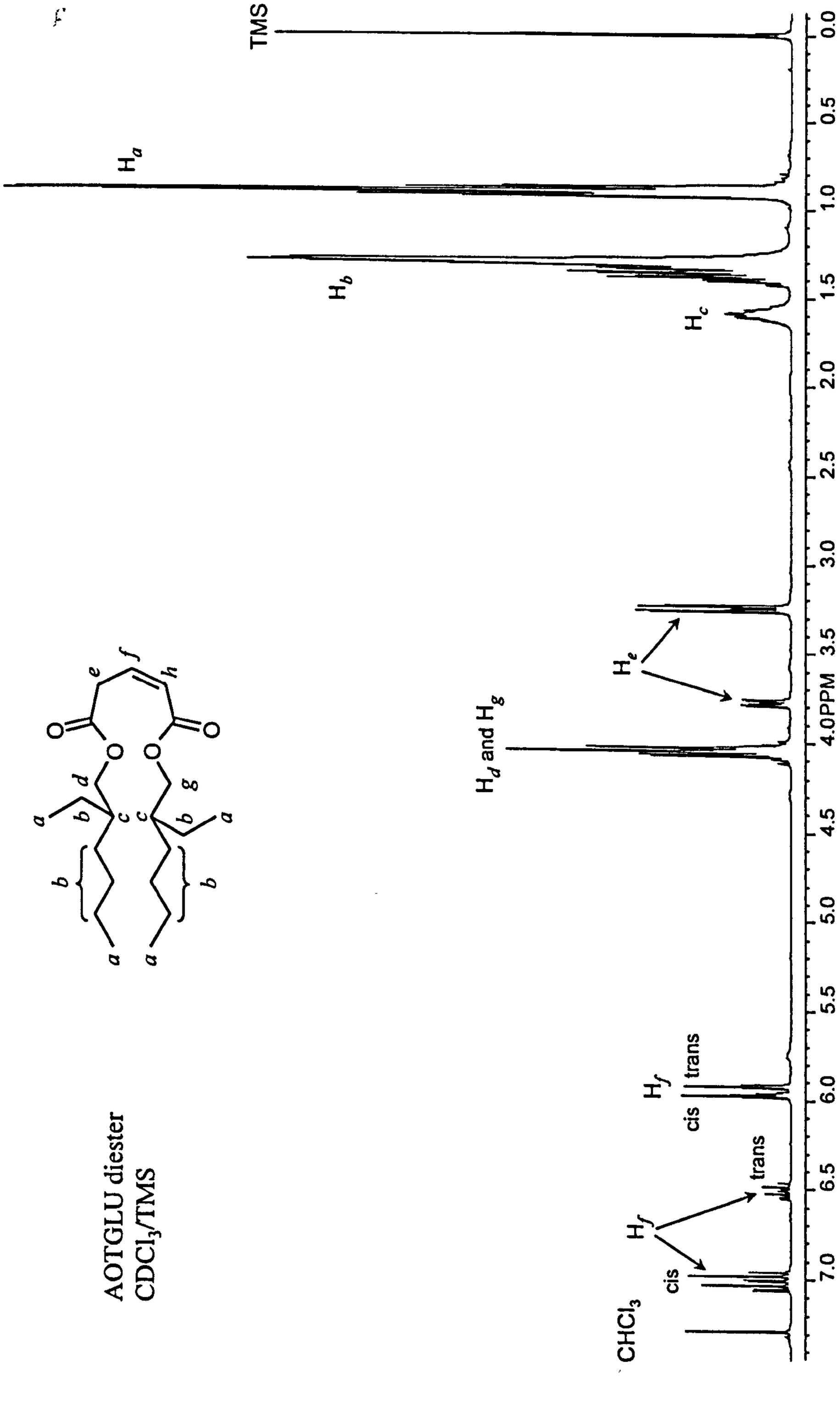

AOTGLU diester
$CDCl_3$/TMS

Figure 4.9 ^{1}H NMR spectrum of AOTGLU diester, obtained from fumaryl chloride route.

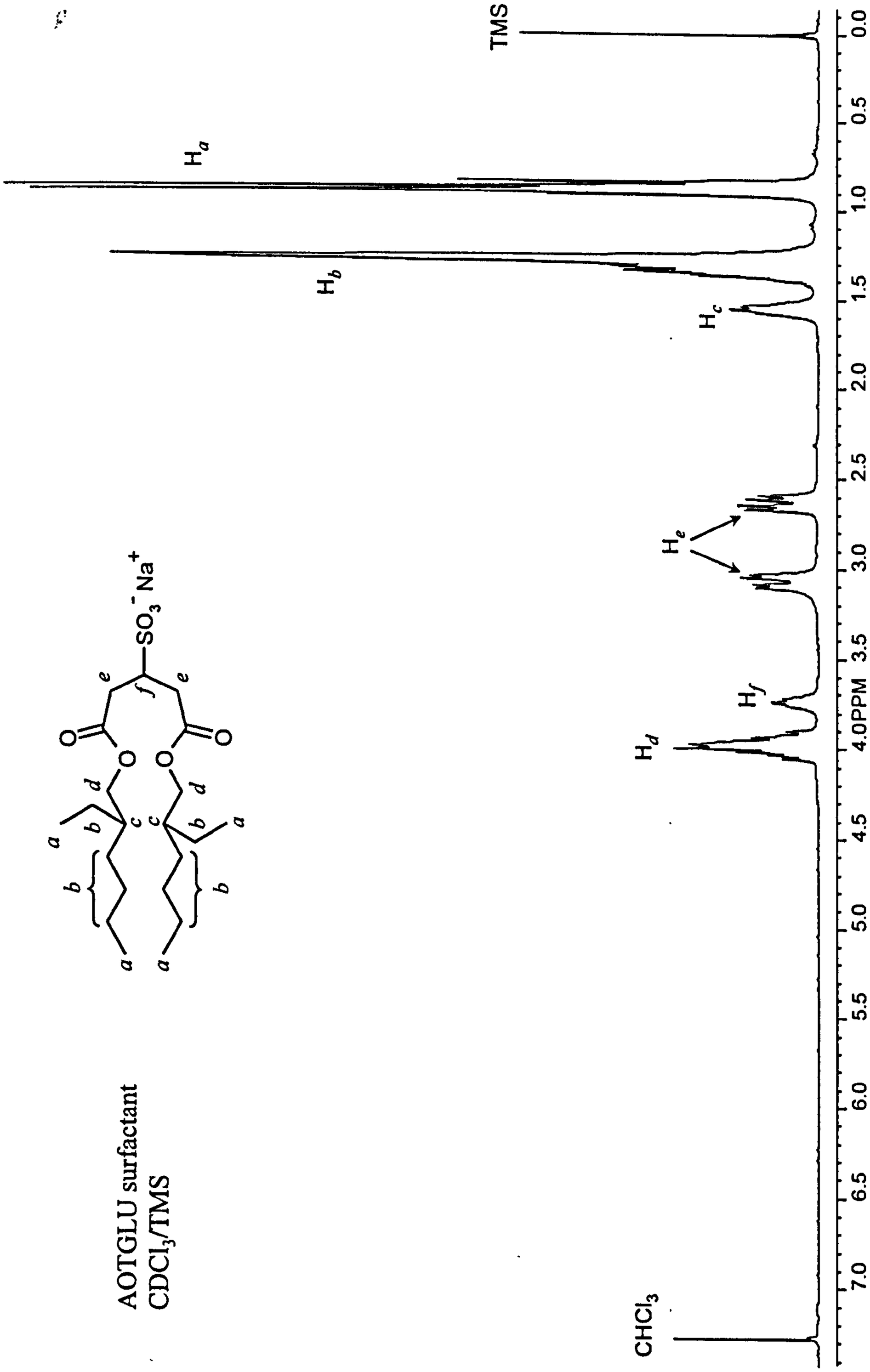

Figure 4.10 ^{1}H NMR spectrum of AOTGLU surfactant.

AOTGLU surfactant
$CDCl_3$/TMS

Table 4.2 Data from ^{1}H NMR spectra analysis of selected succinates (Figures 4.2 to 4.6)

Chemical shift	Molecular fragment	Relative value	Integration	Identified proton
di-C6SS diester				
0.80 - 1.00	CH_3-C-	0.20735	*6*	H*a*
1.16 - 1.46	-C-CH_2-C-	0.42041	12.2	H*b*
1.57 - 1.78	-C-CH_2-C-O-	0.14113	4.08	H*c*
4.11 - 4.27	-C-CH_2-O-CO-R	0.13456	3.89	H*d*
6.82 - 6.88	-CH=C-CO-	0.06451	1.87	H*e* trans
AOT① diester				
0.78 - 1.02	CH_3-C-	0.30168	*12*	H*a*
1.20 - 1.51	-C-CH_2-C-	0.40799	16.2	H*b*
1.55 - 1.74	-C-CH_2-C-O-	0.05176	2.06	H*c*
4.00 - 4.23	-C-CH_2-O-CO-R	0.10003	3.98	H*d*
6.33 - 6.44	-CH=C-CO-	0.03368	1.34	H*e* cis
6.75 - 6.84	-CH=C-CO-	0.01443	0.57	H*e* trans

Chemical shift	Molecular fragment	Relative value	Integration	Identified proton
di-C6SS surfactant				
0.77 - 1.01	CH_3-C-	0.18280	*6*	H*a*
1.15 - 1.43	-C-CH_2-C-	0.36635	12.0	H*b*
1.47 - 1.72	-C-CH_2-C-O-	0.12093	3.97	H*c*
2.99 - 3.31	-C-CH_2-COOR	0.06448	2.12	H*e*
3.89 - 4.11	-C-CH_2-O-CO-R	0.13921	4.57	H*d*
4.10 - 4.24	-C-CH_2-O-CO-R	0.06492	2.13	H*g*
4.23 - 4.40	-C-CH-COOR	0.03489	1.15	H*f*
AOT① surfactant				
0.78 - 1.03	CH_3-C-	0.28940	*12*	H*a*
1.22 - 1.50	-C-CH_2-C-	0.38673	16.0	H*b*
1.51 - 1.72	-C-CH_2-C-O-	0.05197	2.15	H*c*
3.05 - 3.28	-C-CH_2-COOR	0.04742	1.97	H*e*
3.91 - 4.04	-C-CH_2-O-CO-R	0.04809	1.99	H*d*
4.04 - 4.18	-C-CH_2-O-CO-R	0.04768	1.98	H*g*
4.19 - 4.28	-C-CH-COOR	0.02269	0.94	H*f*
di-PhC4SS diester				
1.41 - 1.74	Ph-C-CH_2-C-	0.25108	7.86	H*c*
2.40 - 2.65	-C-CH_2-C-O-	0.12423	3.89	H*b*
3.03 - 3.29	-C-CH_2-COOR	0.05930	1.86	H*e*
3.68 - 3.85	H_2O	0.05406	1.69	water
3.86 - 4.03	-C-CH_2-O-CO-R	0.06352	1.99	H*d*
4.05 - 4.23	-C-CH_2-O-CO-R	0.06222	1.95	H*g*
4.26 - 4.42	-C-CH-COOR	0.03179	1.00	H*f*
7.01 - 7.32	Ph-H	0.31930	*10*	H*a*

Table 4.3 Data from ^{1}H NMR spectra analysis of the glutaconates (Figures 4.7 to 4.10)

Chemical shift	Molecular fragment	Relative value	Integration	Identified proton	Chemical shift	Molecular fragment	Relative value	Integration	Identified proton
di-C6GLU diester					**di-C6GLU surfactant**				
0.76 - 1.00	CH_3-C-	0.19268	*6*	H*a*	0.75 - 1.00	CH_3-C-	0.17440	*6*	H*a*
1.15 - 1.46	-C-CH_2-C-	0.38756	12.1	H*b*	1.15 - 1.42	-C-CH_2-C-	0.34843	12.0	H*b*
1.48 - 1.77	-C-CH_2-C-O-	0.13094	4.08	H*c*	1.45 - 1.72	-C-CH_2-C-O-	0.11531	3.97	H*c*
3.15 - 3.32	ROOC-CH_2-C=C-	0.05151	1.60	H*e*	2.48 - 2.76	ROOC-CH_2-C-C-	0.06748	2.32	H*e*
3.70 - 3.82	ROOC-CH_2-C=C-	0.01053	0.33	H_e	2.94 - 3.20	ROOC-CH_2-C-C-	0.06643	2.28	H_e
3.97 - 4.21	-C-CH_2-O-CO-R	0.12893	4.01	H*d* and H*g*	3.68 - 3.86	-C-CH-C-COOR	0.03562	1.22	H*f*
5.87 - 5.94	-C=CH-COOR	0.01423	0.44	H*h* trans	3.92 - 4.18	-C-CH_2-O-CO-R	0.11554	3.98	H*d*
5.94 - 6.02	-C=CH-COOR	0.01523	0.47	H*h* cis					
6.41 - 6.58	-CH=C-CO-	0.00511	0.16	H*f* trans					
6.92 - 7.10	-CH=C-CO-	0.02407	0.75	H*f* cis					
AOTGLU diester					**AOTGLU surfactant**				
0.78 - 1.01	CH_3-C-	0.29191	*12*	H*a*	0.72 - 1.00	CH_3-C-	0.29393	*12*	H*a*
1.18 - 1.47	-C-CH_2-C-	0.38894	16.0	H*b*	1.13 - 1.46	-C-CH_2-C-	0.39178	16.2	H*b*
1.50 - 1.70	-C-CH_2-C-O-	0.05042	2.07	H*c*	1.45 - 1.70	-C-CH_2-C-O-	0.05084	2.02	H*c*
3.19 - 3.32	ROOC-CH_2-C=C-	0.03630	1.49	H*e*	2.49 - 2.76	ROOC-CH_2-C-C-	0.04845	1.93	H*e*
3.72 - 3.83	ROOC-CH_2-C=C-	0.01240	0.51	H_e	2.90 - 3.31	ROOC-CH_2-C-C-	0.05764	2.29	H_e
3.96 - 4.14	-C-CH_2-O-CO-R	0.09465	3.89	H*d* and H*g*	3.64 - 3.84	-C-CH-C-COOR	0.02420	0.96	H*f*
5.89 - 5.94	-C=CH-COOR	0.01079	0.44	H*h* trans	3.84 - 4.17	-C-CH_2-O-CO-R	0.09728	3.87	H*d*
5.94 - 6.01	-C=CH-COOR	0.01255	0.52	H*h* cis					
6.44 - 6.57	-CH=C-CO-	0.00524	0.21	H*f* trans					
6.92 - 7.09	-CH=C-CO-	0.01729	0.71	H*f* cis					

Within each series, surfactants exhibit similar ^1H spectra, and the only difference arises from the alkyl chain length. Therefore, each molecule can be characterised by a proton ratio defined as the number of end group protons (from $-CH_3$ and/or -Ph groups) over methylene and methyne protons within hydrophobic moieties. Table 4.4 shows the good agreement obtained between theoretical and experimental values, indicating that all surfactants have the expected molecular structure.

Table 4.4 Proton ratios (end group vs. methylene and methyne protons within hydrophobic moieties) derived from analysis of ^1H NMR spectra of sulfosuccinates and sulfoglutaconates surfactants

Surfactant	$H_{(CH_3+Ph)}$:$H_{(CH_2+CH)}$ ratio in hydrophobic group	
	theoretical	experimental
di-C4SS	0.500	0.498
di-C5SS	0.375	0.371
H-di-C6SS	0.300	0.294
D-di-C6SS	0.300	0.301
di-C7SS	0.250	0.247
di-C8SS	0.214	0.213
AOT①	0.545	0.541
AOT②	0.545	0.547
AOT③	4.800	4.276
AOT④	3.429	3.760
AOT⑤	1.125	1.119
AOT⑥	1.125	1.133
di-PhC2SS	1.250	1.248
di-PhC3SS	0.833	0.845
di-PhC4SS	0.625	0.637
di-PhC5SS	0.500	0.494
Br-di-PhC3SS	2.667	2.803
Br-di-PhC5SS	2.750	2.743
di-C6GLU	0.300	0.295
AOTGLU	0.545	0.543

4.2.2 Elemental analysis

Samples were submitted for elemental analysis of C, H and S (micro-analytical laboratory, School of Chemistry, University of Bristol) where applicable. From repeat measurements, the typical standard deviation for the percentage mass determined by elemental analysis was found to be approximately 0.3 to 0.8 %. As shown in Table 4.6, the agreement between theoretical and experimentally determined values is generally good and in most cases within the error. In particular, the good agreement between experimental and theoretical amounts of sulfur indicates that the extraction, washing and recrystallisation procedures effectively removed residual inorganic material.

Table 4.6 Elemental analysis results for sulfosuccinate and sulfoglutaconate surfactants.

Surfactant	Percentage by mass					
	Theoretical			Experimental		
	C	H	S	C	H	S
di-C4SS	43.37	6.37	9.65	42.95	6.41	9.44
di-C5SS	46.66	6.99	8.90	46.07	7.25	8.75
H-di-C6SS	49.49	7.52	8.25	48.80	7.77	8.02
D-di-C6SS	46.35	7.05	7.73	45.87	7.18	7.64
di-C7SS	51.91	7.99	7.70	51.51	8.19	7.59
di-C8SS	54.04	8.39	7.21	53.94	9.59	7.09
AOT①	54.04	8.39	7.21	53.74	8.29	6.98
AOT②	54.04	8.39	7.21	54.10	8.50	7.35
AOT③	54.04	8.39	7.21	53.63	8.56	7.31
AOT④	55.91	8.74	6.78	55.97	8.68	6.71
AOT⑤	54.04	8.39	7.21	54.15	8.26	7.28
AOT⑥	54.04	8.39	7.21	54.13	8.26	7.17
di-PhC2SS	56.07	4.94	7.48	55.98	4.65	7.33
di-PhC3SS	57.89	5.52	7.02	57.83	5.42	6.81
di-PhC4SS	59.49	6.03	6.62	59.32	6.03	6.48
di-PhC5SS	60.92	6.49	6.25	60.59	6.99	6.17
Br-di-PhC3SS	57.89	5.52	7.02	57.69	5.14	7.08
Br-di-PhC5SS	60.92	6.49	6.25	60.31	6.51	6.16
di-C6GLU	50.73	7.76	7.97	50.02	7.70	7.52
AOTGLU	55.00	8.57	6.99	54.70	9.10	6.70

4.3 CONCLUSIONS

Eighteen sulfosuccinates and two sulfoglutaconates have been successfully synthesised. NMR analysis and elemental analysis show that all surfactants are of high chemical purity, and there is no significant residual inorganic material present. All surfactants are thus amenable to characterisation in aqueous and microemulsion systems, and this is described in Chapters 5 to 7.

4.4 REFERENCES

1. Harwood, L. M.; Moody, C. J. '*Experimental Organic Chemistry*' Blackwell Scientific: Oxford, 1989.
2. Corkill, J. M.; Goodman, J. F.; Walker, T. *Trans. Faraday Soc.* **1965**, *61*, 589.
3. William, E. F.; Woodberry, N. T.; Dixon, J. K. *J. Colloid Sci.* **1957**, *12*, 452.
4. Mysels, K. J. *Langmuir* **1986**, *2*, 423.

CHAPTER 5

AQUEOUS PHASE BEHAVIOUR OF DI-CHAIN SODIUM SULFOSUCCINATES

This chapter describes adsorption and aggregation behaviour in aqueous solution of three series of anionic surfactants – linear, branched and phenyl-tipped di-chain sodium sulfosuccinates. The aim is to identify how small variations in the molecular structure of the hydrophobic moiety affect the physico-chemical properties of these surfactants. For aqueous solutions, tensiometry and neutron reflection are two reliable methods to assess the amount of surfactant adsorbed at the air–water interface. They allow a quantitative characterisation of the amphiphile performance and provide structural information in terms of surfactant and solvent distributions at the interface. This chapter falls into three parts. In the first section, after a brief background description to the techniques, procedures for obtaining a sufficiently high surface chemical purity and the application of the Gibbs equation to achieve agreement between tensiometry and neutron reflection are discussed. Partial structure factor experiments with the linear di-C6SS are analysed to give quantitative information on the interfacial structure and the results are compared with those obtained recently for its branched analogue AOT (*Prog. Colloid Polym. Sci.* **1995**, *98*, 243 and *J. Phys. Chem. B* **1997**, *101*, 1615). In the second section, the discussion focuses mainly on results from tensiometric measurements, i.e., variation of CMC, efficiency and effectiveness at reducing surface tensions, as well as molecular packing at the air–solution interface. Finally, the concentrated region of the binary surfactant–water diagram is explored through observation of the different liquid crystalline mesophases formed.

5.1 EXPERIMENTAL TECHNIQUES

Neutron reflection (NR) and drop volume tensiometry (DVT) are the two main techniques used in this work to assess the adsorbed amounts. NR is a very useful and reliable method since it provides a direct measure of the surface excess, and also permits structural features of the interface to be elucidated. Just like SANS (see Section 3.4), the only disadvantage is the necessity to carry out expensive experiments at neutron facilities, and in some cases the need for deuterated solvents and/or surfactants. Tensiometry, on the other hand, is a very accessible method but only provides indirect determination of the surface excess via surface tension measurements and application of the Gibbs equation (see Section 2.1.2).

The main features of neutron reflection and tensiometry (drop volume and du Noüy Ring) techniques are described below. Certain material and basic definitions relevant to NR have already been covered in Chapter 3 in relation to small-angle scattering, and where necessary reference is made.

5.1.1 Neutron reflection

Background theory

The properties of neutrons and their interaction with matter have been presented in Section 3.4 with particular interest in scattering from small particles. Here, reflection of neutrons from a flat surface is considered. The reflectivity profile R(Q) gives information on the structure normal to the interface, and, as with reflection of light, the refractive index, n, normal to the surface is important. For any material n for neutrons is wavelength dependent [1], i.e.,

$$n = 1 - \lambda^2 A + i\lambda C \qquad (5.1.1)$$

where $A = \frac{Nb}{2\pi}$ and $C = \frac{N\sigma_{abs}}{4\pi}$ are constants, with N an atomic number density, b a bound scattering length and σ_{abs} the absorption cross-section (which may often be ignored). Figure 5.1 shows the reflection of a fraction of the incident neutron beam by a smooth surface; the rest being either transmitted or adsorbed.

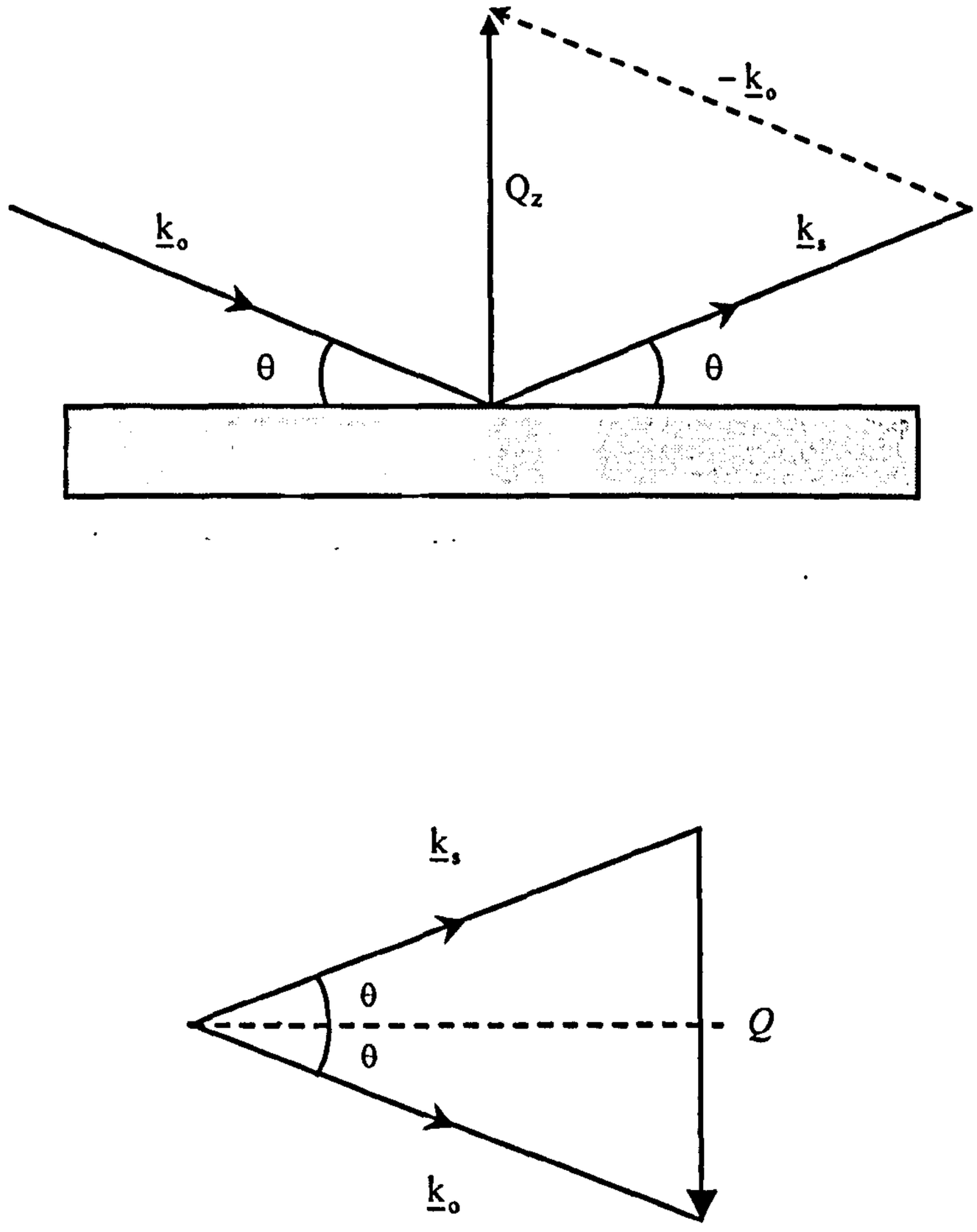

Figure 5.1 Geometry of a neutron reflection experiment and direction of the scattering vector Q, where k_o and k_s are the incident and scattered wave vectors, and θ is the scattering angle.

As for SANS, elastic scattering only is considered, i.e., specular reflection, when the moduli of the incident and reflected wave vectors, k_o and k respectively, are equivalent ($|k_o| = |k|$). A scattering vector Q_z defined in one dimension only, i.e., the z direction perpendicular to the sample surface, is then given as:

$$Q_z = \frac{4\pi n}{\lambda}\sin\theta \qquad (5.1.2)$$

where n is the refractive index. The reflected intensity $R(Q_z)$ is thus measured as a function of Q_z either by varying the wavelength of the neutron beam, λ, and keeping the angle of incidence, θ, constant (method at pulsed neutron sources), or by selecting a constant λ value and varying θ (at reactor sources).

For a plane wave incident upon a surface, if the first medium is air $n_0 \approx 1$, total external reflection occurs below a critical incidence angle $\theta_0 = \theta_c$, and a critical value Q_c, defined by the wavelength λ_c or angle θ_c, is reached. For a clean D_2O surface (Figure 5.2(*a*)) if $\theta < \theta_c$ (i.e., below Q_c) then there is total reflection and $R(Q) \equiv 1$, whilst above Q_c the reflectivity falls off sharply as Q^{-4}. The region where $R(Q) = 1$ is used to determine the scale factor. In the case of a surfactant monolayer on a water subphase (Figure 5.2(*b*)), Q_c is usually reached when measurements are made at $\theta < 1.5°$ [2]. On passing through an adsorbed layer the incident neutron beam is partially transmitted and reflected. Waves are reflected from both top and bottom surfaces of the thin interfacial film. There is then an interference between these two reflected beams, resulting in the appearance of a "fringe" in the $R(Q)$ profile. The position of a minimum Q_{min} is related to the layer thickness τ by $Q_{min} \approx 2\pi/\tau$ (Figure 5.2(*b*)).

The analysis of specular reflectivity in single- or multiple-layer systems can be done either by comparison with a reflectivity profile calculated using an exact optical matrix method, or by using the kinematic (or Born) approximation method which originates from classical scattering theory.

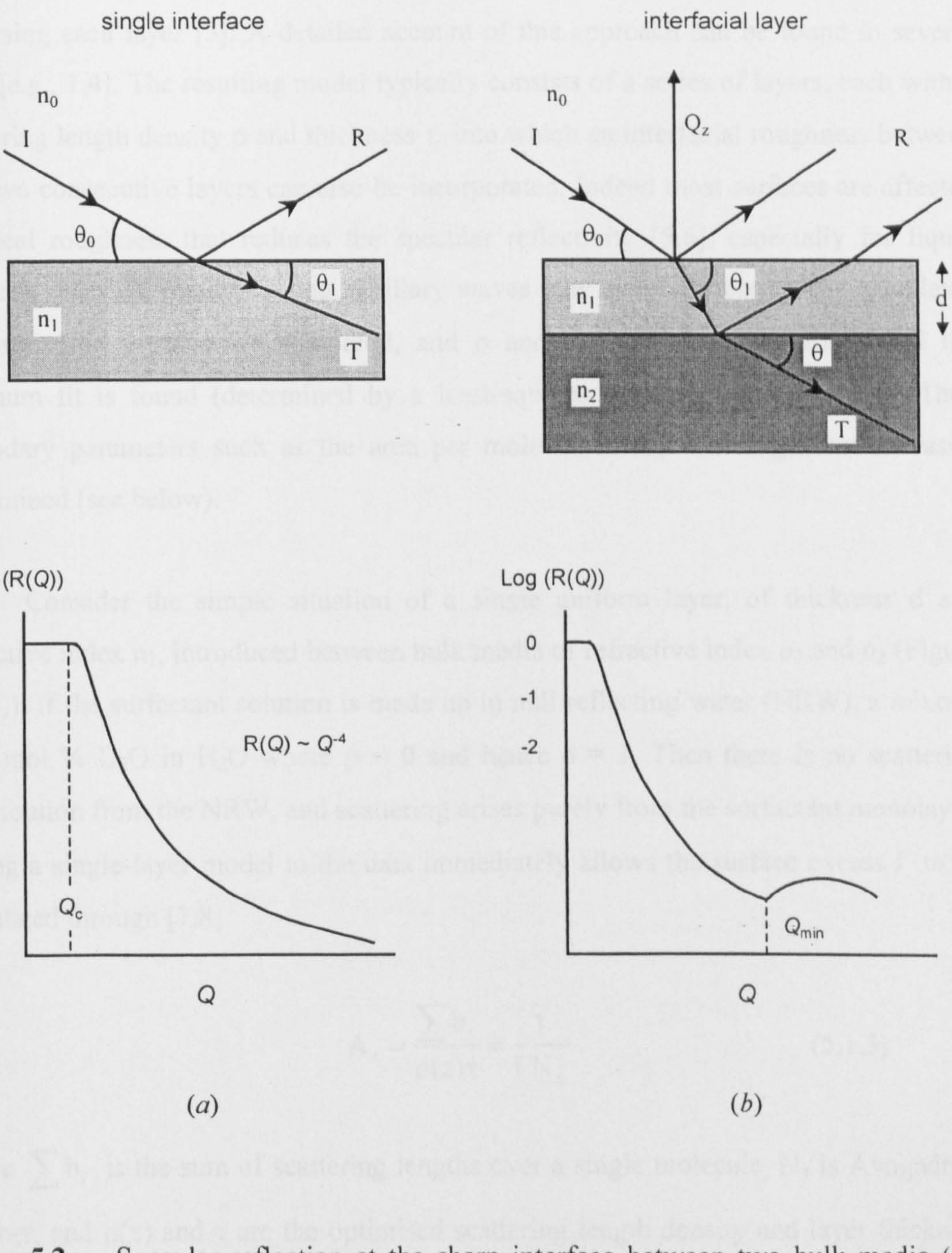

Figure 5.2 Specular reflection at the sharp interface between two bulk media (*a*), and for a thin interfacial layer (*b*) of thickness d sandwiched between two media. I, R and T are the incident, reflected and transmitted beams respectively. Other symbols as defined in the text. Also illustrated are schematic R(*Q*) profiles for the two situations. (Redrawn from [2].)

In the first approach, a characteristic matrix per layer is defined that relates electric vectors in successive layers in terms of Fresnel reflection coefficients – combining refractive index and reflected angle – and phase factors introduced on traversing each layer [3]. A detailed account of this approach can be found in several texts [e.g., 1,4]. The resulting model typically consists of a series of layers, each with a scattering length density ρ and thickness τ, into which an interfacial roughness between any two consecutive layers can also be incorporated. Indeed most surfaces are affected by local roughness that reduces the specular reflectivity [5,6], especially for liquid surfaces where thermally excited capillary waves may also be present. The calculated and measured profiles are compared, and ρ and τ for each layer varied until the optimum fit is found (determined by a least-squares iterative fitting process). Then secondary parameters such as the area per molecule or the coverage can be easily determined (see below).

Consider the simple situation of a single uniform layer, of thickness d and refractive index n_1, introduced between bulk media of refractive index n_0 and n_2 (Figure 5.2(*b*)). If the surfactant solution is made up in null reflecting water (NRW), a mixture of 8 mol % D_2O in H_2O where $\rho = 0$ and hence $n = 1$. Then there is no scattering contribution from the NRW, and scattering arises purely from the surfactant monolayer. Fitting a single-layer model to the data immediately allows the surface excess Γ to be calculated through [7,8]

$$A_s = \frac{\sum b_i}{\rho(z)\tau} = \frac{1}{\Gamma N_a} \qquad (5.1.3)$$

where $\sum b_i$ is the sum of scattering lengths over a single molecule, N_a is Avogadro's number, and $\rho(z)$ and τ are the optimised scattering length density and layer thickness determined by fitting. The absolute value of τ is model dependent and will vary with the choice of the distribution function employed to describe the scattering length density profile normal to the surface. However, as described by Simister *et al.* [9], the sets of $\rho(z)$ values required to give a good fit exactly compensate for the change in τ so that A_s is independent of the uncertainty in τ.

A second analysis method is the kinematic (or Born) approximation [10]. In this approach, the reflectivity $R(Q_z)$ is related to the scattering length density profile normal to the interface, $\rho(z)$, by

$$R(Q_z) = \frac{16\pi^2}{Q_z^2}\left|\hat{\rho}(Q_z)\right|^2 \qquad (5.1.4)$$

where $\hat{\rho}(Q_z)$ is the one-dimensional Fourier transform of $\rho(z)$,

$$\hat{\rho}(Q_z) = \int_{-\infty}^{+\infty} \exp(-iQ_z z)\rho(z)dz \qquad (5.1.5)$$

Details of the development of the kinematic approximation for the study of adsorbed thin films are described elsewhere [10,11]. For surfactant monolayers adsorbed at the air–solution interface, the main features of interest – in addition to film thickness and surface coverage – are the relative positions of the chains, head, and water, and the widths of their distributions normal to the interface. Such structural features can be obtained through analysis of complementary $R(Q)$ profiles, determined at different isotopic compositions using hydrogen/deuterium labelling of the surfactant. This is known as a partial structure factor (PSF) analysis, which is valid under the kinematic approximation. Depending on the labelling scheme, Eq. 5.1.4 may be expressed in terms of numerous partial structure factors that are descriptive of the various components in the interface [10,12]. Below is a brief description of such analysis where a simple binary system consisting of a surfactant solute, A, and a solvent, S, are considered. Then the scattering length density may be represented as

$$\rho(z) = N_S(z)b_S + N_A(z)b_A \qquad (5.1.6)$$

where $N_A(z)$ and $N_S(z)$ are the number densities of solute and solvent respectively and b_i are the scattering lengths. Combining Eq. 5.1.4 and 5.1.6 gives

$$R(Q_z) = \frac{16\pi^2}{Q_z^2}\left[b_A{}^2 h_{AA} + b_S{}^2 h_{SS} + 2b_A b_S h_{AS}\right] \qquad (5.1.7)$$

where the h_{ii} and h_{ij} are the PSFs.

h_{ii} are self-terms that contain information about distributions of the individual components, and are one-dimensional Fourier transforms of $N_i(z)$:

$$h_{ii}(Q_z) = |N_i(Q_z)|^2 \qquad (5.1.8)$$

h_{ij} are cross-terms that describe the relative positions of the different components. In the example given here, of a surfactant solute and solvent, assuming that the distributions of A and S at the interface are exactly even (symmetrical about the centre) and odd respectively [13], then the following relationship hold,

$$h_{AS} = \pm(h_{AA}h_{SS})^{1/2}\sin(Q_z\delta_{AS}) \qquad (5.1.9)$$

where δ is the separation between the centres of the surfactant and solvent distributions. The distributions may not be exactly even/odd, and deviations from this assumption may affect the accuracy with which δ_{AS} can be determined. Circumstances where this approximation fails has been discussed in full elsewhere [14], but this is not expected to arise for surfactants such as Aerosol-OT or its derivatives [15,16].

In principle, the $N_i(z)$ can be obtained by Fourier transformation of the PSFs, but in practice, an analytical function that best represents the form of $N_i(z)$ is assumed. The function is then Fourier transformed and fitted to the experimental data. For monolayer of soluble surfactants, it is shown that a Gaussian distribution is a good representation of the number density profile, $N_A(z)$, [17]:

$$N_A(z) = N_{A0}\exp\left(\frac{-4z^2}{\sigma_A^{\,2}}\right) \qquad (5.1.10)$$

where N_{A0} is the maximum number density and σ_A is the full width at the 1/e of the maximum number density. The total adsorbed amount in the monolayer, Γ_m, is related to N_{A0} through

$$\Gamma_m = \frac{1}{A_s} = \frac{\sigma_A N_{A0}\pi^{1/2}}{2} \qquad (5.1.11)$$

where A_s is the area per molecule.

For the interfacial solvent distribution, a convenient analytical form is the tanh function given by

$$N_S = N_{S0}\left[\frac{1}{2}+\frac{1}{2}\tanh\left(\frac{z}{\zeta}\right)\right] \qquad (5.1.12)$$

where N_{S0} is the number density of water in the bulk solution and ζ is the width parameter. The respective PSFs for distributions described by Eqs. 5.1.10 and 5.1.12 are then

$$Q_z^2 h_{AA} = \frac{\pi\sigma_A^2 N_{A0}^2 Q_z^2}{4}\exp\left(-\frac{Q_z^2\sigma_A^2}{8}\right) \qquad (5.1.13)$$

$$Q_z^2 h_{SS} = \frac{N_{S0}^2\zeta^2\pi^2 Q_z^2}{4}\operatorname{cosech}^2\left(\frac{\zeta\pi Q_z}{2}\right) \qquad (5.1.14)$$

The cross PSF, h_{AS}, can be obtained directly by combining the above equations for h_{AA} and h_{SS} into Eq. 5.1.9 and fitting the resulting function for δ_{AS}:

$$Q_z^2 h_{AS} = \frac{\sigma_A N_{S0} N_{A0}\pi^{3/2}\zeta Q_z^2}{4}\exp\left(-\frac{Q_z^2\sigma_A^2}{16}\right)\operatorname{cosech}\left(\frac{\zeta\pi Q_z}{2}\right)\sin\pi\delta_{AS} \qquad (5.1.15)$$

Structural parameters (with the exception of δ_{AS}) obtained from the kinematic approximation are dependent upon the assumed distribution shapes. For the solute, however, it can be shown that the surface coverage, Γ_m, is independent of any assumptions made about the $N_A(z)$ distribution [10]. For a monolayer with a Gaussian distribution at the surface of water that is contrast matched to air, NRW, the reflectivity is given by [18,19].

$$\frac{Q_z^2 R(Q_z)}{16\pi^2} \approx (\Gamma_m N_a b_A)^2 \exp(-Q_z^2\sigma_A^2) \qquad (5.1.16)$$

where N_a is the Avogadro constant.

As $Q_z \rightarrow 0$, the reflectivity is independent of the distribution width, σ_A, and a plot of $\ln Q_z^2 R(Q_z)$ vs. Q_z^2 extrapolated to $Q_z = 0$ yields a model independent value for Γ_m.

The kinematic approximation assumes all scattering is due to single events, i.e., effects of multiple scattering within the sample are ignored. Therefore this approximation is only valid when the scattering is weak, that is, the incident intensity, I_o is much greater than the scattered intensity, I_s. When applied to reflection, the approximation breaks down in the region $Q \rightarrow Q_c$ since $I_s \rightarrow I_o$, and the scattering is no longer "weak". Thus interpretation of reflectivity data using the kinematic theory is strictly only valid far from the region of total reflection. As a result, Eq. 5.1.4 is only approximate and fails at low Q. To utilise the entire range of reflectivity data available, and to account for the failure of the kinematic approximation as $Q_z \rightarrow Q_c$, each calculated $R(Q_z)$ needs to be corrected before being compared with the observed reflectivity [8,20].

The reflection experiment

NR measurements were performed on the CRISP reflectometer at ISIS, Rutherford Appleton Laboratories, Didcot, UK. Information about the instrument and data normalisation can be found in [2,21]. The experiment was conducted on chain deuterated sodium di-hexyl sulfosuccinate, D-di-C6SS, at selected concentrations above and below the CMC on null reflecting water (NRW, 8.0 mol % D_2O in H_2O). In addition, for the partial structure factor experiments, measurements were made at the CMC on three different subphase contrasts – NRW, D_2O, and 1:1 mixture of D_2O:H_2O. The specular neutron reflection was measured as a function of the momentum transfer $Q = (4\pi \sin\theta)/\lambda$ normal to the interface. The wavelength range was $0.5 \rightarrow 6.5$Å and the incident angle θ was fixed at 1.5°, giving an accessible Q range of $0.05 \rightarrow 0.65$Å^{-1}. The reflectometer was calibrated with pure (distilled) D_2O and a flat background was subtracted from all reflectivity profiles. This was determined as $\sim 2.0 \times 10^{-6}$ by extrapolation to high Q values. The relevant $R(Q)$ profiles for the partial structure factor analysis were corrected and analysed following the method of Crowley [8,20] as mentioned in the previous section.

5.1.2 Tensiometry

Background theory

Many techniques exist for determining surface and interfacial tension of liquids; details can be found in standard texts [e.g., 22]. Du Noüy ring and drop volume tensiometry are two widely used methods, which were employed here.

Du Noüy Ring – the method involves measuring the force required to detach a ring or loop of wire from the surface of a liquid. A schematic is shown in Figure 5.3. Once immersed in the liquid, the ring is slowly raised upward and simultaneously the force F acting downward is measured. A maximum, F_{max}, is reached as the ring is pulled trough the interface, then F immediately decreases as the system becomes unstable. F_{max} is related to the surface tension of the liquid, γ, via Eq. 5.1.17

$$\gamma = \frac{\beta F_{max}}{4\pi R} \qquad (5.1.17)$$

where R is the radius of the ring measured from the centre of the ring to the centre of the wire) and β is a correction factor. This correction factor, calculated by Harkins and Jordan [23], accounts for the dependence of surface tension on the dimensions of the ring. β is a function of the density difference between the phases and the dimensionless variables R^3/V and R/r where V is the volume of liquid supported by the ring at F, and r is the ring radius.

Drop volume – the technique involves determination of the maximum size of drops formed at the end of a well-defined capillary. In this work, the Lauda TVT1 drop volume tensiometer was used. It is fully automated and sophisticated dosing regimes can be selected so that dynamic surface tension may be followed. A full description of this instrument is given elsewhere [24,25]. Briefly, as shown in Figure 5.4, the motor lowers a barrier onto a syringe plunger and so a drop forms at the capillary tip. The drop detachment is monitored by a light sensor.

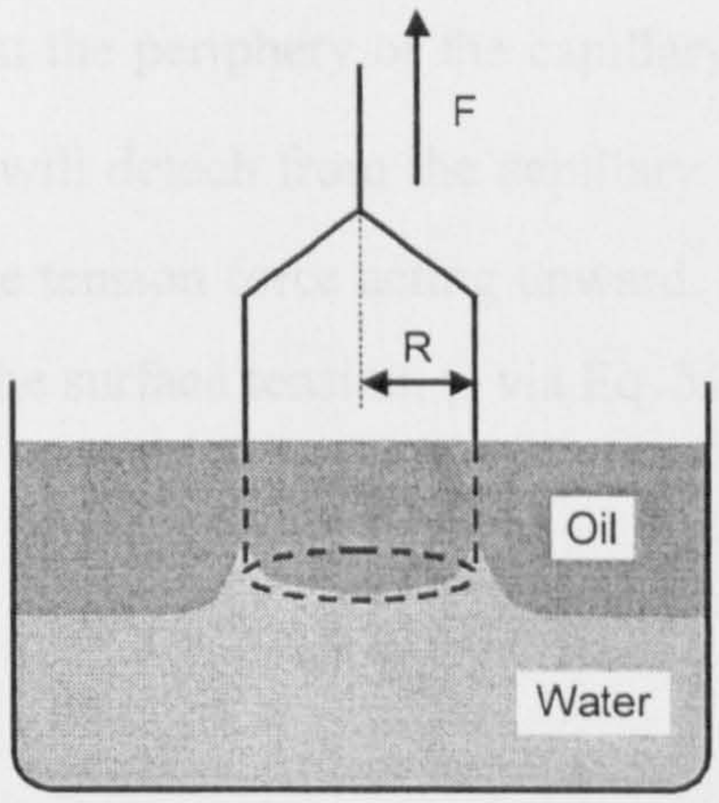

Figure 5.3 Schematic of the du Noüy ring set up.

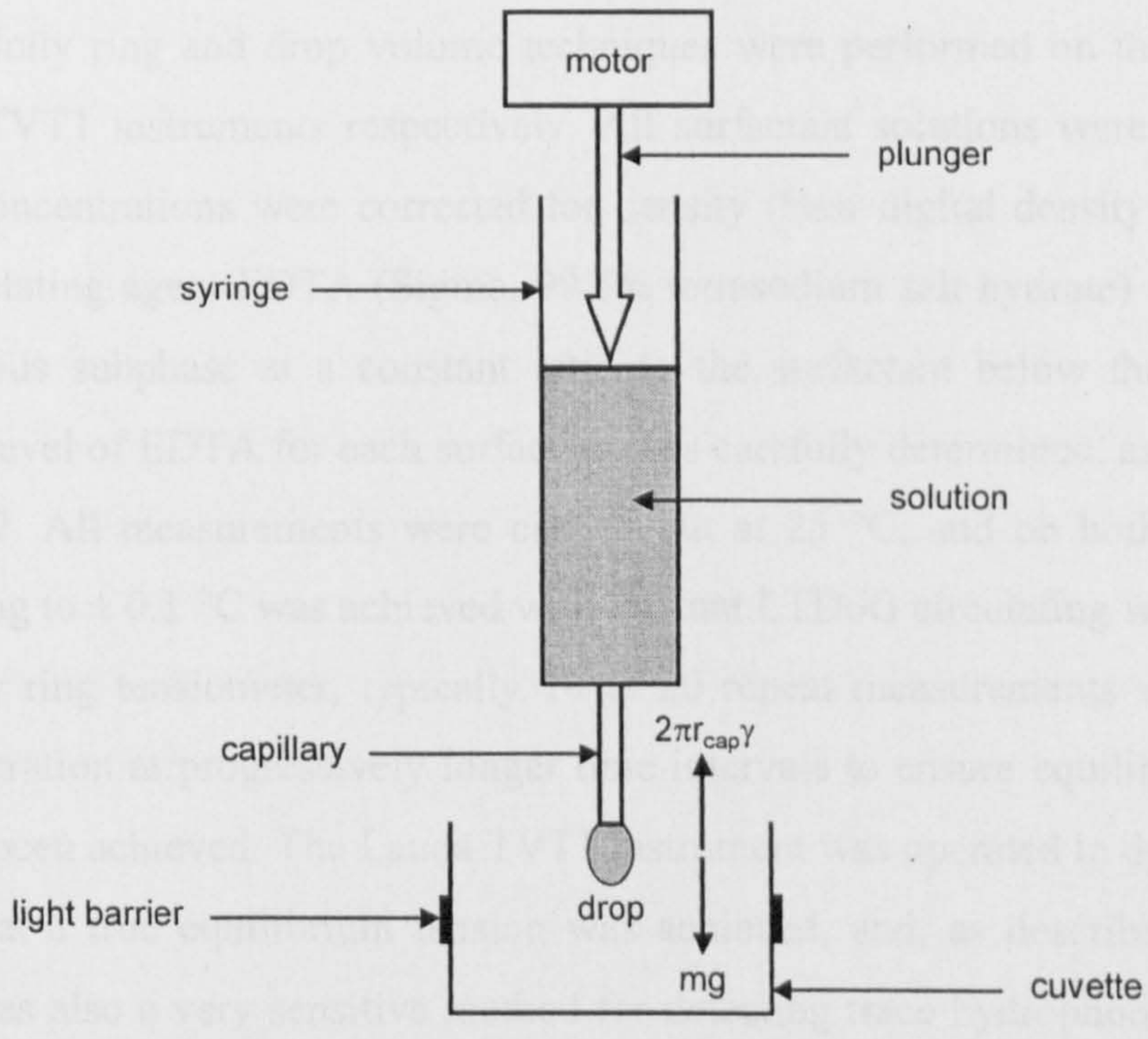

Figure 5.4 Schematic set up of the Lauda TVT1 drop volume instrument. Parameters are as described in the text.

For a drop of pure liquid at equilibrium, there is a force balance between the surface tension of the liquid acting at the periphery of the capillary ($2\pi r_{cap}\gamma$) and the force due to gravity (mg). This drop will detach from the capillary when the weight of the drop acting downward exceeds the tension force acting upward. Hence the maximum volume of the drop, V, is related to the surface tension, γ, via Eq. 5.1.18 [26]

$$\gamma = \frac{V\Delta\rho g}{2\pi r_{cap}} f \qquad (5.1.18)$$

where $\Delta\rho$ is the density difference between the two phases, g is the acceleration due to gravity, and r_{cap} is the capillary radius; f is a correction factor accounting for the point of drop detachment being not at the capillary tip but at its own neck [27].

The tensiometric experiments

Du Noüy ring and drop volume techniques were performed on the Krüss K10 and Lauda TVT1 instruments respectively. All surfactant solutions were prepared by mass, and concentrations were corrected for density (Paar digital density meter DMA 35). The chelating agent EDTA (Sigma, 99.5% tetrasodium salt hydrate) was included in the aqueous subphase at a constant ratio to the surfactant below the CMC. The appropriate level of EDTA for each surfactant was carefully determined, as described in Section 5.2.2. All measurements were carried out at 25 °C, and on both instruments thermostatting to ± 0.1 °C was achieved with a Grant LTD6G circulating water bath. On the du Noüy ring tensiometer, typically 10 to 20 repeat measurements were made at each concentration at progressively longer time intervals to ensure equilibrium surface tension had been achieved. The Lauda TVT1 instrument was operated in dynamic mode to ensure that a true equilibrium tension was achieved, and, as described in Section 5.2.2, this was also a very sensitive method for detecting trace hydrophobic impurities, that are likely to be present in the surfactant under study if the purification is not complete. Both instruments were calibrated using aqueous solutions of absolute ethanol. Agreement with literature values was typically ± 0.2 mN m^{-1} [28].

Cleaning of glassware

All sample glassware and tensiometer dishes were cleaned, soaked in Micro™ critical cleaning solution, rinsed repeatedly with distilled water, soaked in 50% nitric acid solution, rinsed well, and finally checked for cleanliness over a steam bath. For the drop volume tensiometer, syringes, plungers and capillaries were soaked in Micro™ solution and rinsed copiously with water before use. Before each measurement on the Krüss K10, the ring was cleaned in dilute HCl, rinsed and heated for a few seconds in the blue flame of a Bunsen burner. The cleanliness of the ring and sample dish, and for the Lauda TVT1 instrument, of the syringe, was checked by measuring the surface tension of water. This value was typically 72.6 ± 0.3 mN m^{-1} and 71.8 ± 0.2 mN m^{-1} on the du Noüy ring and drop volume tensiometer respectively.

5.1.3 Calculation of activity coefficients

When studying the surface tension-concentration behaviour of ionic surfactants, activity rather than concentration should be used. In very dilute solution, i.e., below 1 × 10^{-3} mol dm^{-3}, activity coefficients can safely be regarded as unity, so that activities may be replaced with concentrations. However, at higher concentrations, i.e., above 1 × 10^{-3} mol dm^{-3}, this assumption is no longer valid as Coulombic interactions between ions increase resulting in departure from ideal behaviour. Then recourse must be made to the Debye-Hückel theory, which relates activity coefficient to ionic strength. This is explained in detail in standard texts [29,30] and only relevant equations are given here. At very low electrolyte concentrations, the mean activity coefficient $\gamma_{\pm}$ can be calculated from the Debye-Hückel limiting law

$$\log \gamma_{\pm} = -A|z_+ z_-| I^{1/2} \qquad (5.1.19)$$

where z is the charge on the ion. I is the ionic strength and A is a constant respectively given by

$$I = \frac{1}{2}\sum_i m_i z_i^2 \qquad (5.1.20)$$

$$A = \frac{F^3}{4\pi N_a \ln 10}\left(\frac{\rho}{2(\varepsilon_o \varepsilon_r RT)^3}\right)^{1/2} \qquad (5.1.21)$$

where m is the molality, z is the charge valency, and ρ is the solvent density. Other symbols correspond to the following physical constants:

- Faraday constant, $F = 9.648 \times 10^4$ C mol^{-1}
- Avogadro constant, $N_a = 6.022 \times 10^{23}$ mol^{-1}
- gas constant, $R = 8.314$ J K^{-1} mol^{-1}
- vacuum permittivity, $\varepsilon_o = 8.854 \times 10^{-12}$ J^{-1} c^2 m^{-1},
- dielectric constant for water, $\varepsilon_r = 78.54$

The Debye-Hückel limiting law (Eq. 5.1.19) is valid for 1:1 electrolytes with concentrations below approximately 0.01 mol dm^{-3}. For other valence types, or higher concentration range, a more general expression must be used, known as the Debye-Hückel extended law

$$\log \gamma_{\pm} = -\frac{A|z_+ z_-| I^{1/2}}{1 + Ba I^{1/2}} \qquad (5.1.22)$$

where *a* is the mean effective ionic diameter which typically ranges from 3–9 Å [31] and B is a constant given by

$$B = \left(\frac{2F^2 \rho}{\varepsilon_0 \varepsilon_r RT}\right)^{1/2} \qquad (5.1.23)$$

Eq. 5.1.22 is valid for 1:1 electrolytes of concentrations up to 0.1 mol dm^{-3} [30].

In this work, Eqs. 5.1.19 and 5.1.22 were used to determine the activity coefficients of the surfactant solutions according to the concentration range involved. Activities, rather than concentrations, were used in the Gibbs adsorption equation to determine the surface excess. For all the surfactants studied, a value of 6 Å was assumed for the parameter *a*, which is approximately the diameter of a hydrated sodium ion [32]. For aqueous solutions at 298 K, A = 0.509 mol$^{-1/2}$ kg$^{1/2}$ and B = 3.282×10^9 m^{-1} mol$^{-1/2}$ kg$^{1/2}$.

5.2 ADSORPTION AT THE AIR-WATER INTERFACE: VALIDITY OF THE GIBBS EQUATION FOR IONIC SURFACTANTS

Neutron reflection (NR) and surface tension methods were compared for accessing the equilibrium adsorption isotherm of an ionic surfactant – di-hexyl sulfosuccinate (di-C6SS) – at the air-water interface. The experiments examined the validity of the Gibbs equation and the pre-factor 2, and assessed the effects of contaminants such as trace levels of polyvalent metal ions and hydrophobic impurities. The procedures for obtaining agreement between the neutronic and tensiometric isotherms are described.

5.2.1 The issue of the pre-factor *m* in the Gibbs equation for ionics

The exact form of the adsorption isotherm for 1:1 ionic surfactants is a fundamental issue in surfactant science, and is still a matter of debate [e.g., 33,34]. Proper knowledge of the surface coverage is important for explaining many surfactant related phenomena, such as interfacial molecular packing and the adsorption mechanism.

As described in Section 2.1.2, the adsorption isotherm can be obtained, indirectly, by analysing tensiometric data with the Gibbs equation. The general form is given by

$$\Gamma = -\frac{1}{m\mathrm{RT}}\frac{\mathrm{d}\gamma}{\mathrm{d}\ln a} \qquad (5.2.1)$$

where the terms have their usual meanings. The pre-factor m is theoretically dependent upon the surfactant type and structure, as well as the presence of extra electrolyte in the aqueous phase [35,36]. For various non-ionic and zwitterionic surfactants the expected value of 1 for the m-factor has been confirmed [8,37-39]. With a 1:1 ionic surfactant, in the absence of extra electrolyte, the thermodynamic treatment requires $m = 2$, implying an equimolar ratio of surfactant anion and counter cation in the interface. The motivation of this work was to test this thoroughly for the highly purified di-C6SS, and evaluate the criteria for "surface chemical purity".

In order to verify the Gibbs equation a complementary method for measuring Γ is needed. Early experiments employed radiotracer (RT) measurements using tritiated surfactants [40-43], and more recently neutron reflection (NR) [37-39,44-46] and surface second-harmonic generation (SHG) spectroscopy have been used [34]. In particular NR is a very accurate method since the surface excess around the CMC can be measured to about 5% [9]. As described in Section 5.1.1, using null reflecting water, it is possible to determine the absolute amount of surfactant ion in the monolayer [e.g., 37-39,44-46]. Fitting the measured reflectivity curves to a single uniform layer model gives values for the thickness τ, and scattering length density ρ, and surface coverage is then obtained through Eq. 5.1.3. It is worth noting that NR is a direct method, which essentially "counts" molecules in the film, whilst tensiometry is indirect, and interpretation of the γ–a curve always involves assumptions in terms of an adsorption equation.

Unlike NR, it is still unclear exactly what is being measured in tensiometric experiments. For certain systems, the neutronic and tensiometric isotherms can only be reconciled by invoking a net charge on the monolayer [e.g., 18,33]. This interpretation requires that there is a depletion layer, of unrealistically large dimensions (> 1000 Å), below the surface. Hence, there must be another reason for these differences in apparent coverages, and impurities are the prime suspects. In particular, surface-active impurities are expected to introduce discrepancies between any two independent methods.

For anionics the most important are polyvalent metal ions M^{n+}, and their effects have been described in studies of AOT [18], as well as in several other anionics [18,33,43,45,46]. It was shown that, when used at the correct level, the tetrasodium salt of ethylenediaminetetraacetic acid (EDTA) is an effective chelating agent, which effectively replaces M^{n+} with Na^+. Even at ppm levels any M^{n+} may give rise to a significant lowering of tension in the pre-CMC range [18,45]. In general, at trace levels of M^{n+}, there is no dramatic effect on the form of the γ–ln a curve, for example the manifestation of a minimum or shoulder around the CMC. Therefore, inorganic contaminants are more difficult to detect than organic impurities, which can be quite effectively removed by separation procedures based on foam fractionation [46-52].

In neutron reflection studies of Cs^+, Na^+ and H^+ perfluorooctanaote [32] and Na^+ AOT [18], it was found that the pre-factor 2 agreed with NR data, only in the presence of EDTA. Downer *et al.* performed detailed work with sodium perfluorononanoate ($C_8F_{17}COO^-\ Na^+$) and 9-H perfluorononanoate ($H\text{-}C_8F_{16}COO^-\ Na^+$) [45]. Background levels of Ca^{2+}, the principal contaminant, were determined by atomic absorption spectroscopy: the ratio surfactant:Ca^{2+} was found to be typically 10,000:1. Based on these results, careful studies of the effects of various M^{n+} ions on pre-CMC tensions were performed, so as to determine the optimum level of EDTA. Comparison of the tensiometric and neutronic Γ–c curves indicated $m \approx 1.7$. Next D_2O, which is normally "used as received" for the NR experiments, was assessed for Ca^{2+} content, showing that this must also be considered. For example, a surfactant at its CMC of 1 mmol dm^{-3}, made up in NRW, would result in a surfactant:Ca^{2+} ratio of typically 333:1. Once this effect had been taken into account, repeat NR experiments with higher EDTA ratios, were then consistent with $m = 2$.

In terms of cationics, Motschmann *et al.* have recently studied 1-dodecyl-4-dimethylaminopyridinium bromide by tensiometry and SHG [34], and the two methods were indicated $m = 1.28$ for this surfactant. An elaborate procedure was employed to calibrate the SHG signal, by studying the response for an insoluble monolayer of a related C20 chain compound, as a function of surface pressure. Recently, the interesting case of gemini surfactants of the type $[C_nH_{2n+1}\text{–}N\text{–}(CH_3)_2\text{–}(CH_2)_s\text{–}N\text{–}(CH_3)_2\text{–}C_nH_{2n+1}]$ Br_2 has been examined using neutrons [44]. These are 2:1 electrolytes for which the Gibbs factor is expected to be 3, and with an aromatic xylyl spacer group this was indeed confirmed. However, for the more common systems with aliphatic spacer groups $s = 3$, 4, 6, and 12, it was found that m tends to 2. The observations with cationics [34,44] can be rationalised by invoking formation of a (partial) surfactant-counterion complex at the interface. This suggests that chemical specificity may play a role, and cationics must be assessed on a case-by-case basis, which is a point also borne out here for anionics. Recently, a more limited study of Cn-TAB's, with $n = 12$, 14 and 16, was described [53], and the results for these systems at the CMC indicate an m-factor of 2.

The following section describes careful studies of the equilibrium adsorption behaviour of one custom synthesised and highly purified anionic, sodium di-hexyl sulfosuccinate (di-C6SS), which is a structural relative of Aerosol-OT (AOT, bis (2-ethylhexyl) sodium sulfosuccinate). For the NR experiment, the deuterated derivative (D-di-C6SS) was prepared, where the tails only were deuterated, and comparisons were made with recent studies on D-AOT [15,16,18]. Here the adsorption isotherm for the anionic H/D-di-C6SS is shown to be consistent with $m = 2$. However, it is demonstrated that to achieve this agreement extreme care must be taken to eliminate various sources of contamination.

5.2.2 Detection of surface-active impurities by tensiometry

For this study, DV tensiometry was used to measure the tensions of aqueous solutions of di-C6SS at three different stages of its purification. The corresponding γ–ln a plots (before and after various treatments) are shown in Figure 5.5. Polynomials were fitted to the pre-CMC curves, to generate local gradients, then the Gibbs equation was used with $m = 2$ to give the area per molecule at the CMC. Tensiometric results are given in Table 5.1. The CMC was determined to be (12.5 ± 0.3) mmol dm^{-3}, and the three samples gave identical values within experimental error. This result compares well with literature data [47]. All the γ–ln a curves show clean breaks at the CMC, with no minima or shoulders. However, both the limiting surface tensions γ_{cmc}, and the pre-CMC portions of the curves differ significantly, with a radical change in the slope resulting in large discrepancies between the effective areas per molecule A_{cmc}: as discussed below this depends crucially on the purification treatment. These molecular areas drop from (74 ± 3) $Å^2$ down to (58 ± 3) $Å^2$ for the "raw" and "pure" surfactant respectively. The difference is well outside experimental errors and points to the presence of impurities.

Williams *et al.* [47] studied di-alkyl sodium sulfosuccinates and described purification procedures to obtain a clean break at the CMC. The different re-crystallisation and foaming processes covered were effective at removing traces of residual alcohol and other hydrophobic impurities. For di-C6SS they determined the

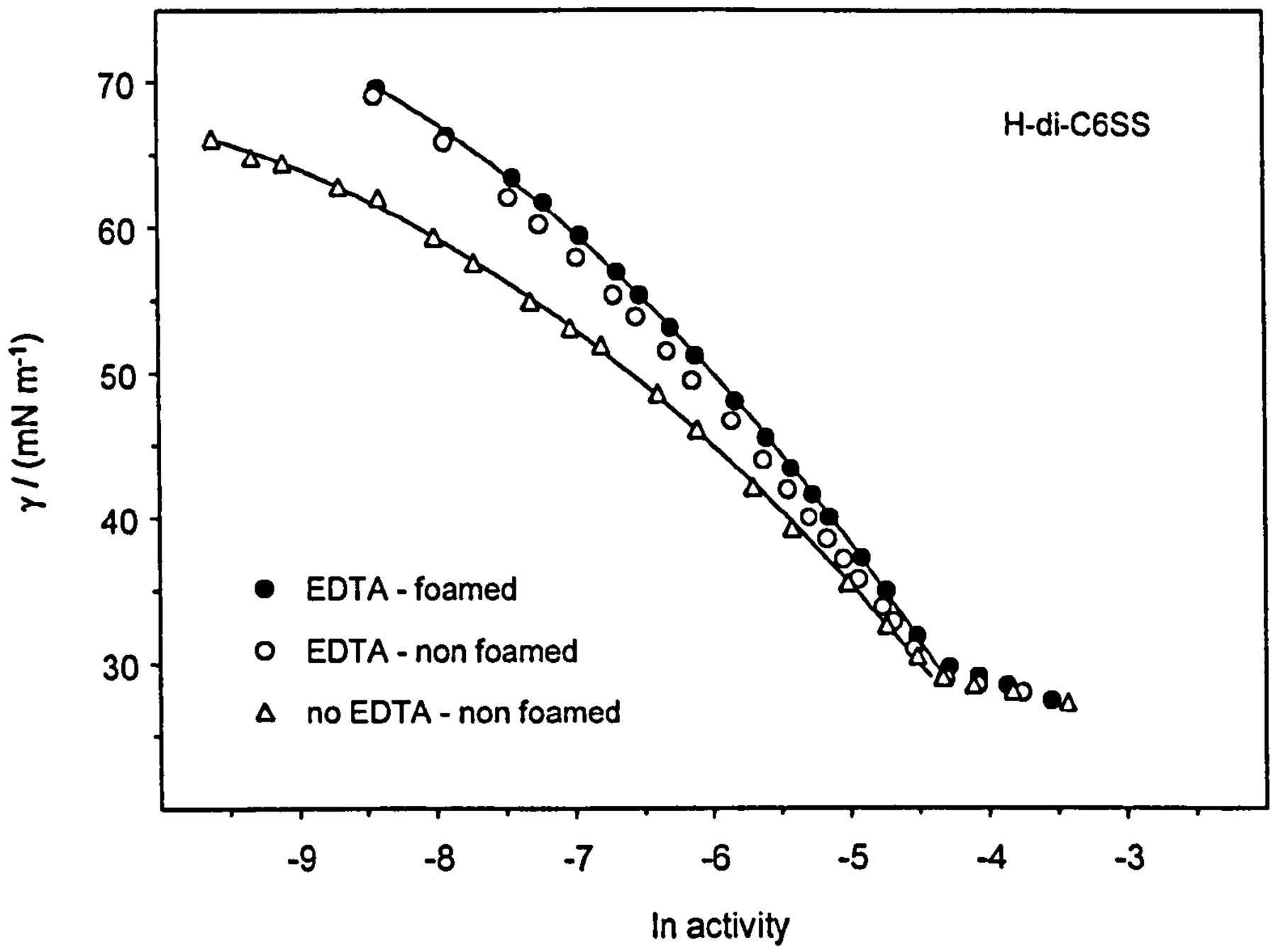

Figure 5.5 Surface tension behaviour of H-di-C6SS solutions at 25°C. The polynomial lines fitted to the pre-CMC data were used to calculate surface excesses.

Table 5.1 Parameters derived from drop volume tension measurements on H-di-C6SS at different stages of purification

H-di-C6SS	CMC / (mmol dm^{-3})	γ_{cmc} / (mN m^{-1})	A_{cmc} (± 3 / Å^2)
No EDTA – no foam fractionation	12.2	29.15	74
EDTA – no foam fractionation	12.5	29.06	62
EDTA – foam fractionation	12.7	30.09	58

limiting area per molecule to be 74 $Å^2$, which matches the value for the so-called non-purified di-C6SS (Table 5.1). Hence, there are still purity issues to resolve.

The first of these is the effect of trace polyvalent cationic species M^{n+}, which were previously detected in AOT [18] and in several other anionic surfactants [33,43,46], giving rise to a significant lowering of the tensions in the pre-CMC concentrations range. Second are other trace hydrophobic impurities, which produce a similar but less pronounced effect by introducing a slight time dependence of the surface tension. Both of these aspects are discussed below, together with the purification procedures involved.

Inorganic contaminants

Polyvalent cations will adsorb preferentially to the sodium ions, and this can lower the surface tension in the pre-CMC region, an effect that is clearly demonstrated in Figure 5.5. As low concentrations are reached, the tensions tend to a much lower value than the expected 72.5 mN m^{-1}, i.e., the surface tension for pure water, which is indicative of the presence of divalent species. If EDTA is added to the solution a different curve is obtained. The "best" level of EDTA was determined by measuring γ at fixed surfactant concentration, but varying the amount of EDTA in the range 10^{-9} to 10^{-2} mol dm^{-3}, as shown in Figure 5.6. These measurements were carried out at approximately 1/24, 1/12 and 1/6 × CMC. In all three cases, a plateau of constant γ was reached in between a range of EDTA between 5×10^{-5} to 1×10^{-4} mol dm^{-3}. This region is presumably where all divalent species are completely complexed by EDTA, and thus are effectively removed from the interface. Above a concentration of 1×10^{-4} mol dm^{-3}, a decrease in γ is observed, consistent with the onset of a "swamping electrolyte" condition.

Sodium salts used in the sulfonation step are an obvious source of ions such as Ba^{2+}, Ca^{2+} and Mg^{2+}. As noted before [45], the ppm levels present in these reagents would be sufficient to give rise to the effects seen here. If the surfactant itself is the source of contamination, to be effective over the whole isotherm, a constant surfactant to EDTA ratio must be used. By inspection of Figure 5.6, a ratio surfactant:EDTA of

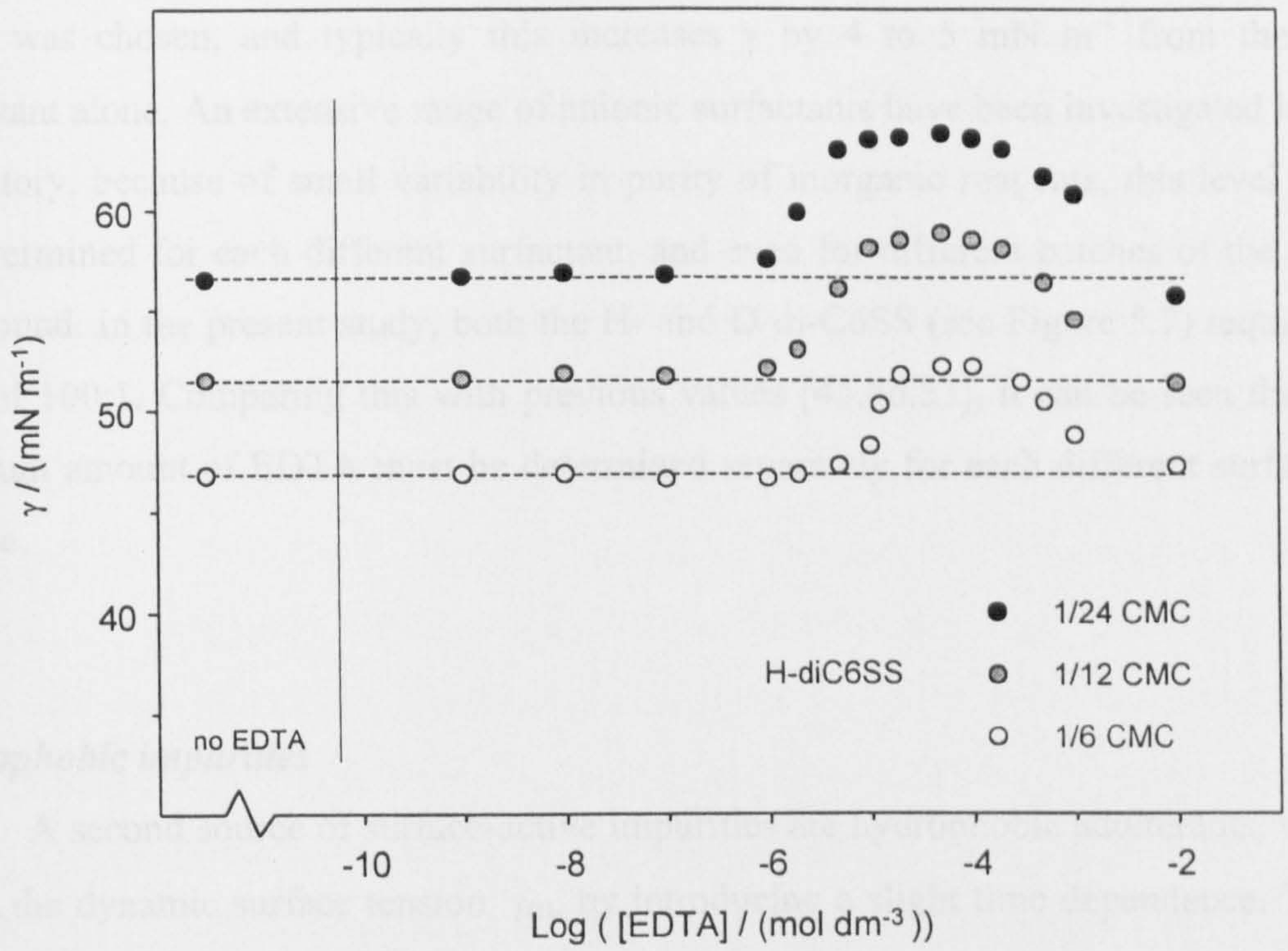

Figure 5.6 Effect of EDTA on surface tensions of H-di-C6SS solutions at various concentrations below the CMC.

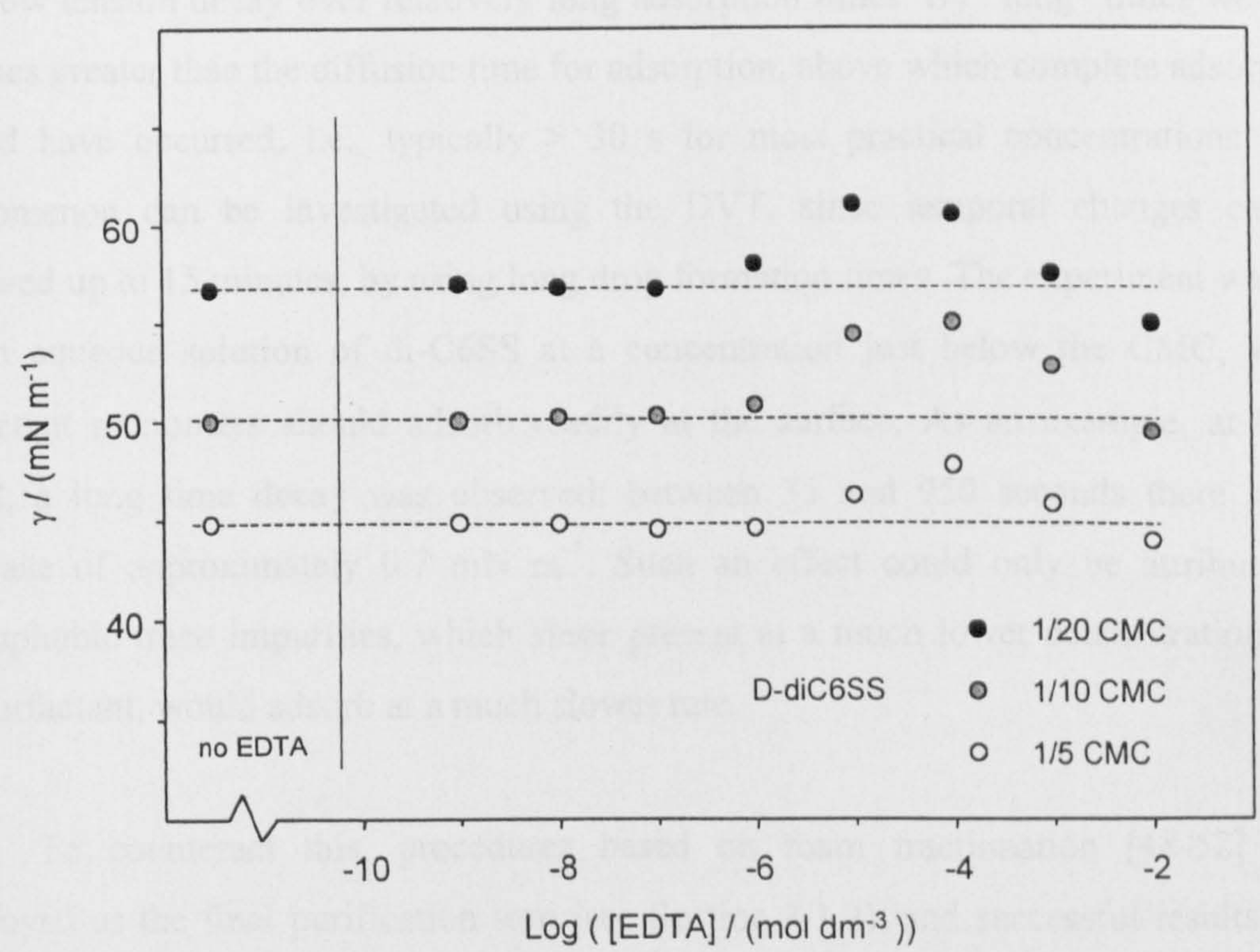

Figure 5.7 Effect of EDTA on surface tensions of D-di-C6SS solutions at various concentrations below the CMC.

100:1 was chosen, and typically this increases γ by 4 to 5 mN m^{-1} from the raw surfactant alone. An extensive range of anionic surfactants have been investigated in our laboratory, because of small variability in purity of inorganic reagents, this level must be determined for each different surfactant, and even for different batches of the same compound. In the present study, both the H- and D-di-C6SS (see Figure 5.7) required a ratio of 100:1. Comparing this with previous values [45,46,53], it can be seen that the optimum amount of EDTA must be determined separately for each different surfactant sample.

Hydrophobic impurities

A second source of surface-active impurities are hydrophobic adulterants, which affect the dynamic surface tension, $\gamma_{(t)}$, by introducing a slight time dependence. These may be alcohols, and also long-chain surfactant homologues. The criterion of a highly pure surfactant can also be considered in terms of a weak time dependence of γ. Mysels *et al.* [48-50] first recognised the impact of trace hydrophobic impurities, and discussed the slow tension decay over relatively long adsorption times. By "long" times we refer to times greater than the diffusion time for adsorption, above which complete adsorption should have occurred, i.e., typically > 30 s for most practical concentrations. This phenomenon can be investigated using the DVT, since temporal changes can be followed up to 15 minutes, by using long drop formation times. The experiment was run on an aqueous solution of di-C6SS at a concentration just below the CMC, where surfactant monomers should adsorb readily at the surface. As an example, at 0.5 × CMC, a long time decay was observed: between 35 and 950 seconds there was a decrease of approximately 0.7 mN m^{-1}. Such an effect could only be attributed to hydrophobic trace impurities, which since present at a much lower concentration than the surfactant, would adsorb at a much slower rate.

To counteract this, procedures based on foam fractionation [48-52] were employed as the final purification step (see Section 4.1.2), and successful results were obtained to eliminate temporal changes of the tension values over long adsorption times. Measurements of the dynamic surface tension $\gamma_{(t)}$ were used to monitor the purification. After 10 hours foaming, the decay had been reduced to approximately 0.2 mN m^{-1},

between 35 and 950 seconds. After 72 hours of foam fractionation the decay had completely disappeared, and a stable γ value was reached in less than 60 seconds, which remained constant up to 15 minutes. This is illustrated in Figure 5.8, where variations of the tension values of H-di-C6SS, at 0.5 × CMC, before and after foam fractionation, are shown for a drop formation time up to 950 seconds. Both the H- and D-di-C6SS were foam fractionated for three days and the γ–ln a curves were re-examined. As can be seen in Tables 5.1 and 5.2, the γ_{cmc} values before purification differ significantly, 29.1 and 28.6 ± 0.1 mN m^{-1} for the H- and D- surfactants respectively. This suggests they are contaminated to slightly different levels. However, after the foam fractionation was completed, the two values agreed within 0.1 mN m^{-1}, and both compounds gave essentially identical γ–ln a curves. As shown in Figure 5.5, the isotherms before and after foam fractionation (both with EDTA) are very similar. This can be explained by the way equilibrium surface tensions were determined using the dynamic mode on the DVT. For the non-foamed samples, relatively short drop formation times were used - typically up to 150 seconds - so that the effect of the hydrophobic impurities was not emphasised. Then the intercept of the plot $\gamma_{(t)}$–1/time$^{1/2}$ (i.e., γ at $t \rightarrow \infty$) was taken as the equilibrium surface tension. On the other hand, for the foamed samples much longer times were used over which a stable value was reached and determined to be the equilibrium surface tension. Thus, an even larger discrepancy might be obtained if longer times were used for the non-foamed samples.

Figure 5.9 shows adsorption isotherms of H-di-C6SS derived from surface tension measurements at different stages of the purification. The surface excess was calculated using the Gibbs equation, in terms of activity, and $m = 2$. Clearly, addition of EDTA has a marked effect on the adsorption, while foam fractionation leads to a much smaller change. The effective head group areas, A_{cmc}, before the foaming process, were determined to be 62 and 63 ± 3 $Å^2$ for the H- and D-di-C6SS respectively, as compared to 58 and 60 ± 3 $Å^2$ after complete purification (Tables 5.1 and 5.2). Considering the experimental error on the tensiometric measurements, this latter change is minor compared to the effect of EDTA, which decreased A_{cmc} by 12 ± 3 $Å^2$.

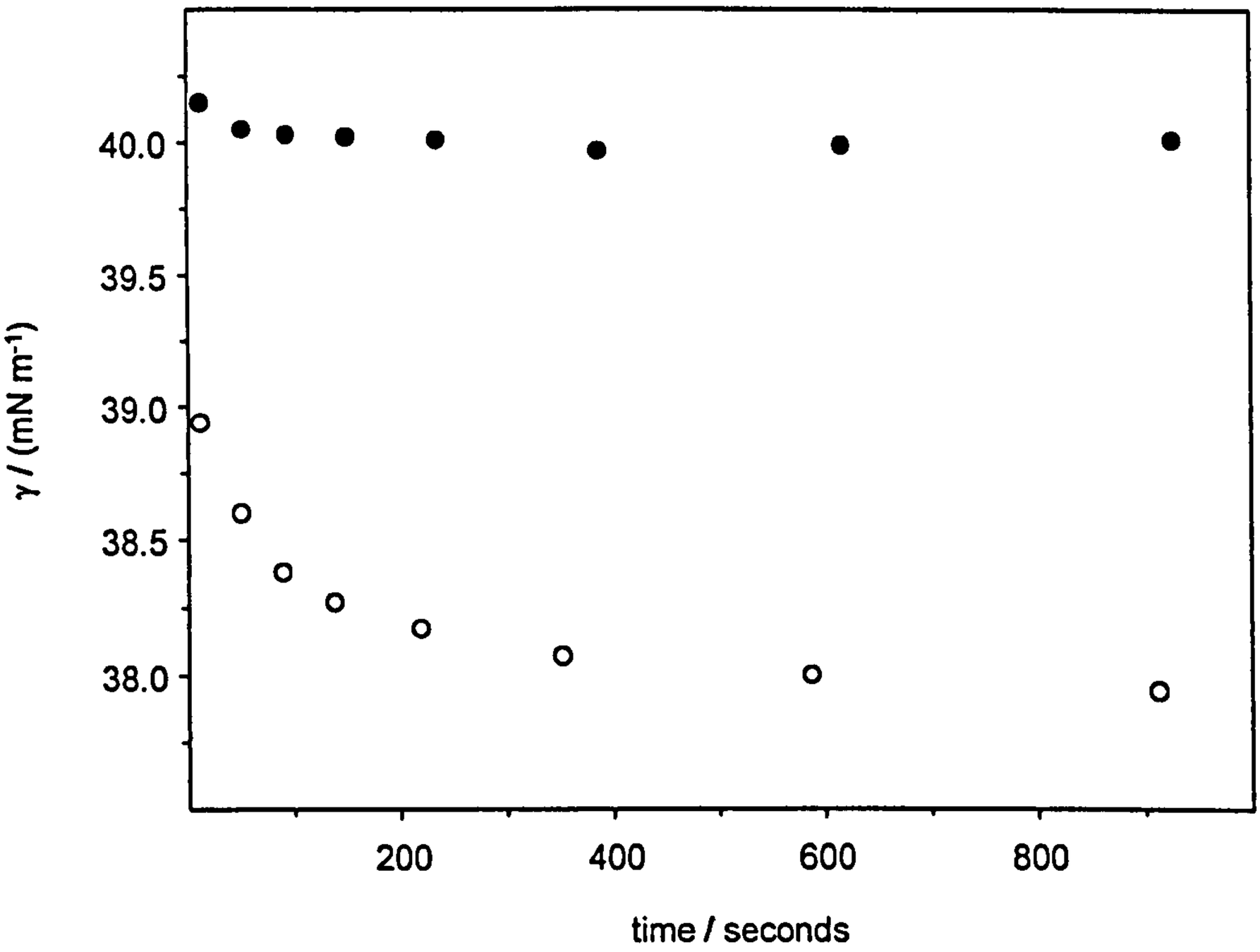

Figure 5.8 Temporal surface tension decay of H-di-C6SS solutions at 0.5 × CMC (6.1 mmol dm^{-3}). (○) unfoamed; (●) foam fractionated.

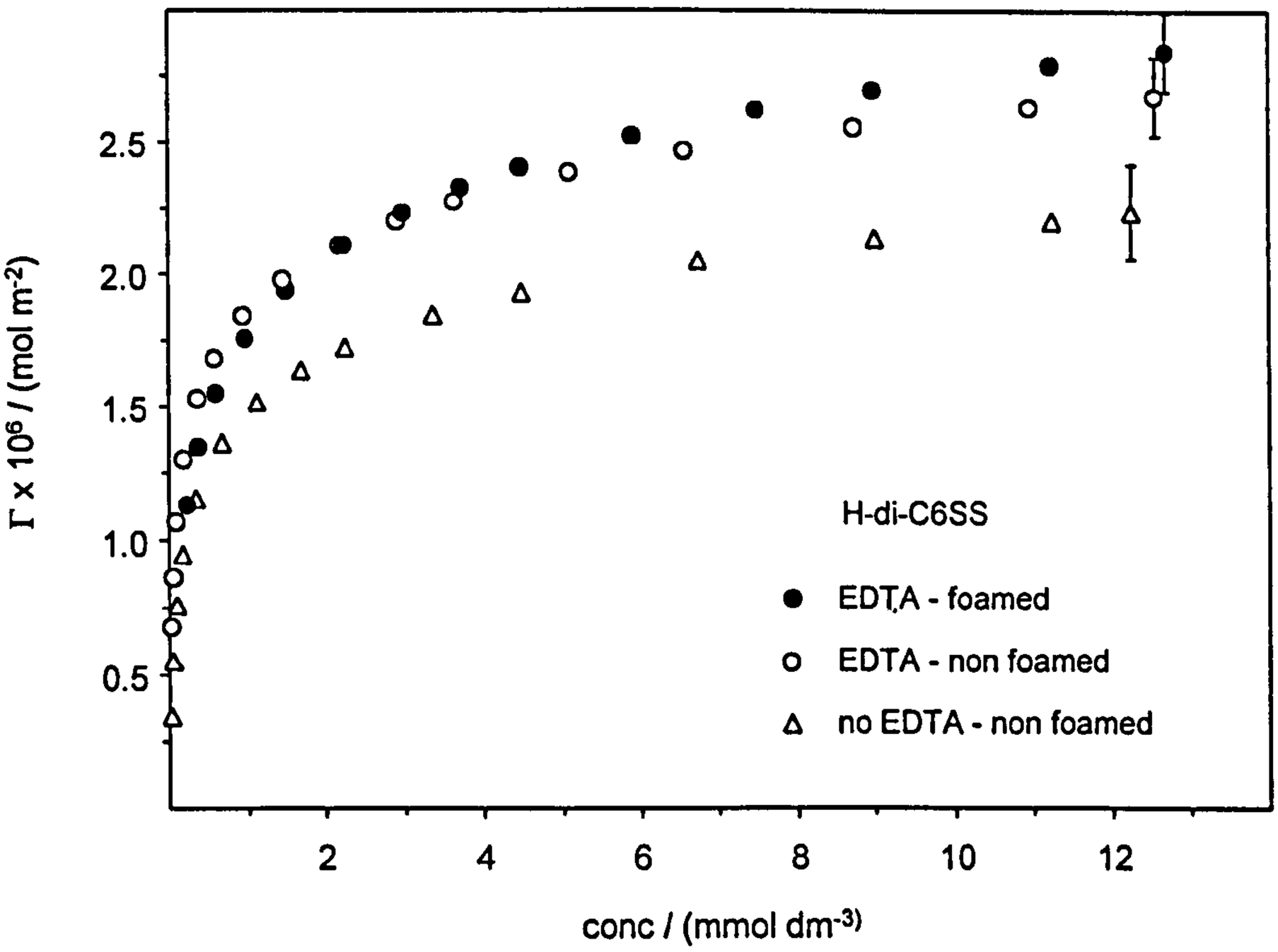

Figure 5.9 Adsorption isotherms derived from surface tension measurements of H-di-C6SS solutions under various conditions of purity.

Table 5.2 Parameters derived from tensiometry and neutron reflectivity measurements with D-di-C6SS in the presence of EDTA

D-di-C6SS	CMC / (mmol dm^{-3})	γ_{cmc} / (mN m^{-1})	A_{cmc} / $Å^2$
DVT – no foam fractionation	12.4	29.15	63 ± 3
DVT – foam fractionation	12.9	29.06	60 ± 3
NR – foam fractionation	-	-	59 ± 2

5.2.3 Surface coverage from neutron reflection

As mentioned in Section 5.1.1, surface coverages obtained from NR correspond to the absolute amount of surfactant ions in the monolayer, whereas the Gibbs surface excess corresponds to the sum over the surfactant ion and its counterion, and it includes any depletion of surfactant just below the surface. Thus the presence of surface-active impurities will introduce a discrepancy between the two techniques. Reflectivity measurements were carried out on the fully purified deuterated di-C6SS in order to assess the level of purity required to obtain complete agreement between neutron reflection and tensiometry, and to validate (or otherwise) the use of the Gibbs 2 pre-factor.

Measurements were made in the range CMC/40 to 2 × CMC, in the presence of EDTA. As shown in Figure 5.10, analyses of the reflectivity curves in terms of a single uniform layer (using Eq. 5.2.2), indicated a progressive thickening: at CMC/40 it was 11.4 ± 1.5 Å moving up to 17.8 ± 1.5 Å at the CMC. For the same concentrations, the molecular area decreased from 214 ± 8 to 59 ± 2 $Å^2$. At twice the CMC, the area per molecule remained essentially the same as at the CMC, as expected for a pure surfactant: this is a key indication of purity. If surface-active (hydrophobic) impurities were present they would adsorb strongly below the CMC, but above would be dissolved in micelles, thereby altering the surface composition and the apparent adsorbed amount.

The parameters (scattering length density, ρ, and film thickness, τ) obtained from the uniform single layer model fit and the derived surface coverages, Γ (calculated from Equation 5.1.3), are summarised in Table 5.3 below. As described in Section 5.1.1, an alternative way to obtain Γ values from NR data is to assume a Gaussian scattering length distribution normal to the surface, and use an approximate form for the reflectivity given by Equation 5.1.16. Hence, as shown in Figure 5.11 for selected concentrations of D-di-C6SS below the CMC, adsorption can be obtained from the intercept of a plot $\ln\left[R(Q)\cdot Q^2/16\pi^2\right]$ vs. Q^2 extrapolated to $Q = 0$. This yields a model independent value for Γ (values given in Table 5.3). In applying Eq. 5.1.16, the low Q region only was used, i.e., $Q < 0.09$ $Å^{-1}$, where the signals are strongest.

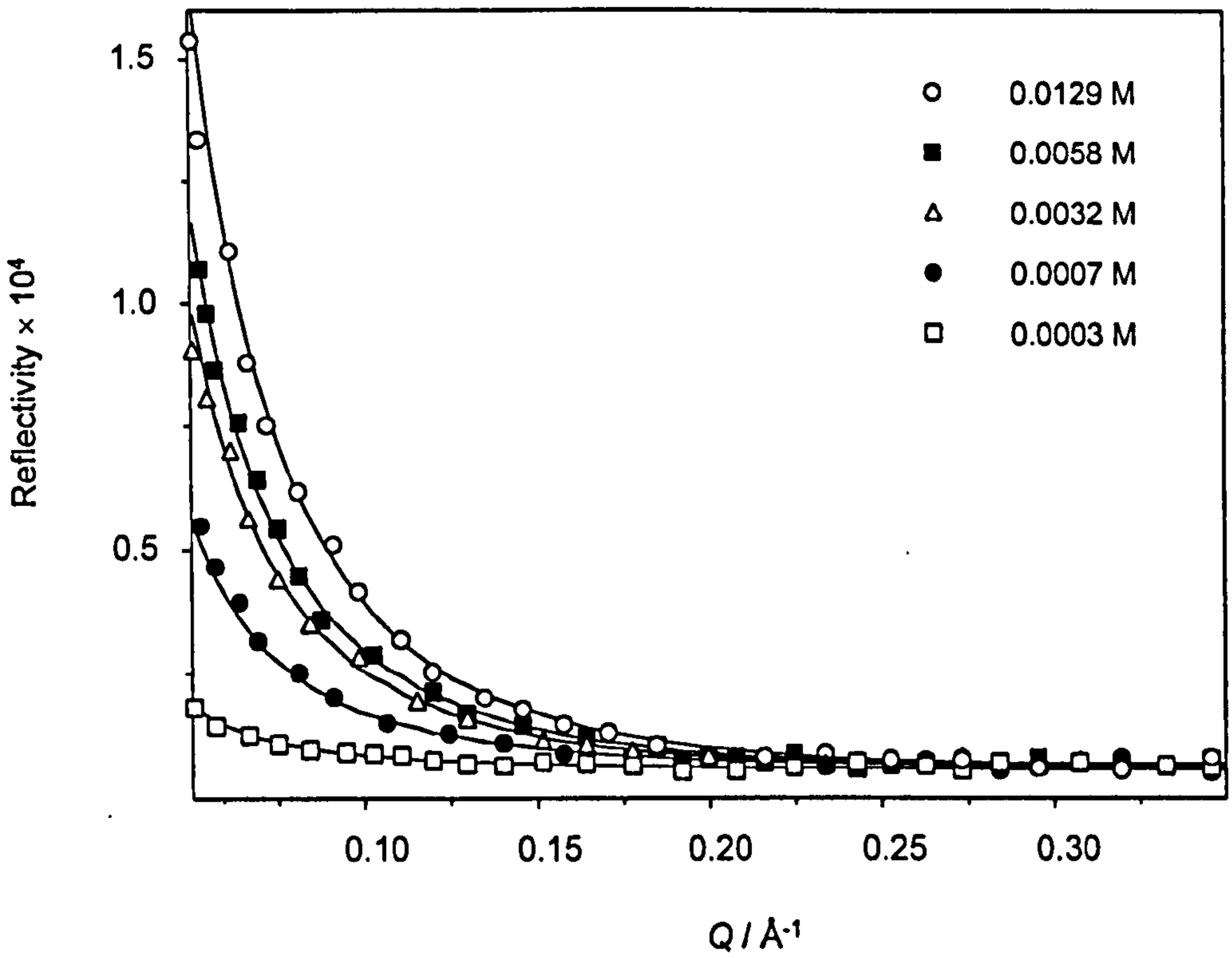

Figure 5.10 NR profiles for D-di-C6SS on NRW with EDTA at and below the CMC. The lines are fits to the uniform single layer model.

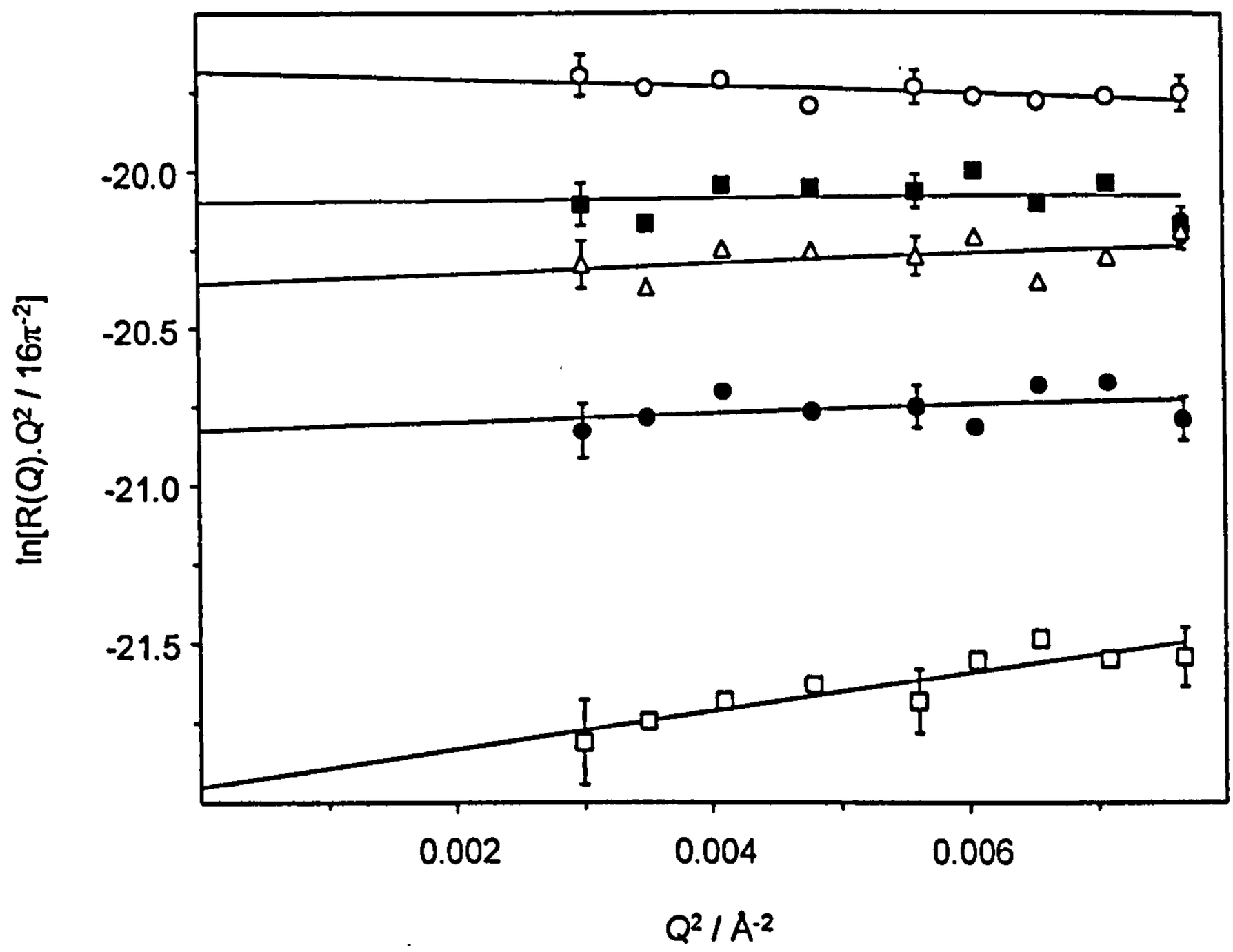

Figure 5.11 NR data for D-di-C6SS on NRW with EDTA, plotted in terms of Eq. 5.1.16. Surfactant concentrations are 0.0129 (○), 0.0058 (■), 0.0032 (△), 0.0007 (●), and 0.0003 (□) mol dm^{-3}. The lines are least squares fits. Characteristic error bars are shown.

Table 5.3 Fitted parameters and surface coverages obtained from analysis of NR data using the single layer model. Model independent coverages as obtained from Fig. 5.13 and Eq. 5.1.16 are given for comparison purposes

	Single uniform layer model				Model free coverage	
[D-di-C6SS] / mmol dm^{-3}	σ / Å	ρ / (10^{-6} $Å^{-2}$)	Γ / (10^{-6} mol m^{-2})	A_s / $Å^2$	Γ / (10^{-6} mol m^{-2})	A_s / $Å^2$
12.90	17.76	3.00	2.80	59.3	2.79	59.5
11.61	17.30	2.84	2.59	64.2	2.55	65.2
9.68	17.27	2.87	2.61	63.6	2.53	65.7
7.74	15.73	3.10	2.57	64.7	2.58	64.3
5.81	16.27	2.68	2.30	72.3	2.27	73.0
4.52	17.31	2.70	2.46	67.5	2.45	67.9
3.23	17.19	2.36	2.14	77.8	2.00	83.2
1.94	14.79	2.37	1.84	90.1	1.84	90.1
1.29	15.71	2.31	1.90	87.2	1.90	87.2
0.65	14.39	2.05	1.55	107.2	1.58	105.1
0.32	11.42	1.29	0.78	213.8	0.90	184.5

Figure 5.12 shows the surface excess for D-di-C6SS determined by NR (as given in Table 5.3) and tensiometry. Identical sets of foamed-cleaned samples were studied by both techniques and the Γ–c isotherms agree well. Recall, with NR the surface excess can be measured to an accuracy of about 5% [9]. So the coverages close to the CMC obtained for non-foamed samples by DVT also agree reasonably well with neutron data from foam fractionated systems, at least within experimental errors. A consequence of this agreement is that a NR isotherm, plotted as Γ–ln a, can be integrated to yield the γ–ln a curve via Eq. 5.2.2 [e.g., ref. 39],

$$\Delta\gamma = -m\mathrm{RT}\int_{\ln a_1}^{\ln a_2}\Gamma \, d\ln a \qquad (5.2.2)$$

The constant of integration is taken to be the surface tension of pure water. Figure 5.13 shows the comparison, and between 30 and 52 mN m^{-1} the agreement is excellent. At higher tensions the deviation is a reflection of the uncertainties in determining Γ at relatively low coverage. The level of agreement indicated on Figure 5.11 is similar to that found for single chain zwitterionic betaines [38,39].

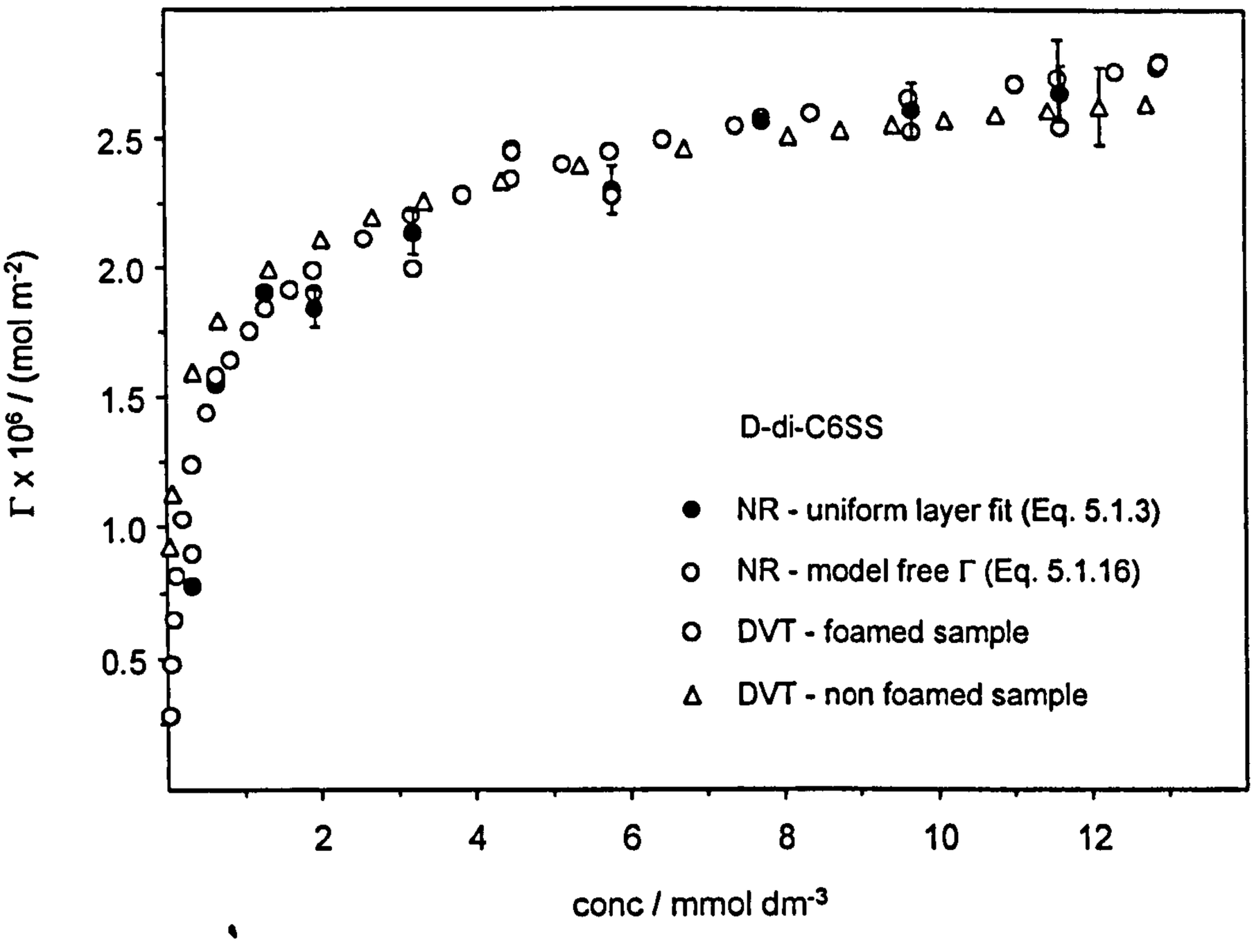

Figure 5.12 Adsorption isotherms obtained from neutronic and tensiometric measurements of D-di-C6SS solutions before and after foam fractionation.

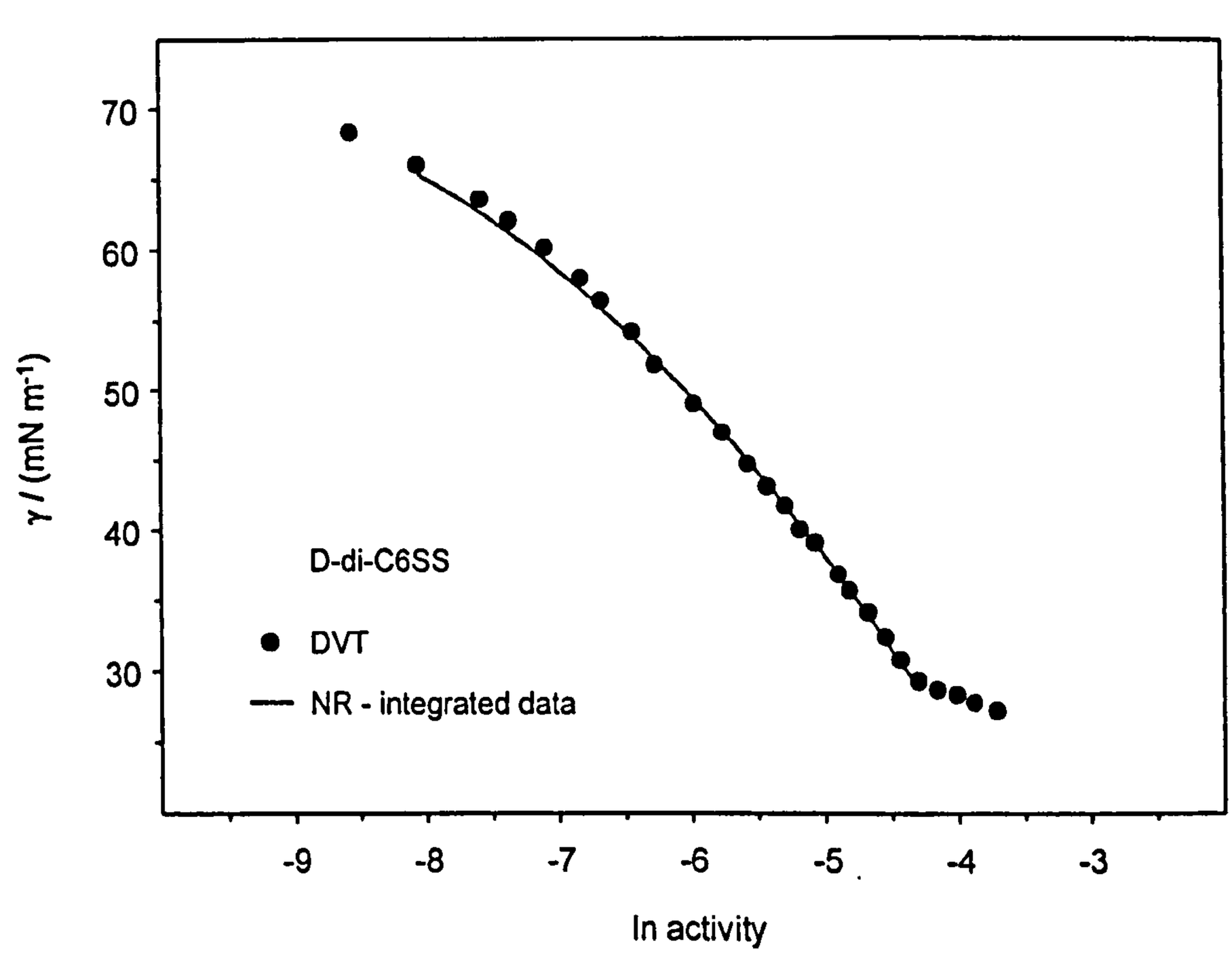

Figure 5.13 Comparison between measured surface tensions of D-di-C6SS solutions at 25 °C and the behaviour predicted by integrating neutron data (● in Figure 5.12).

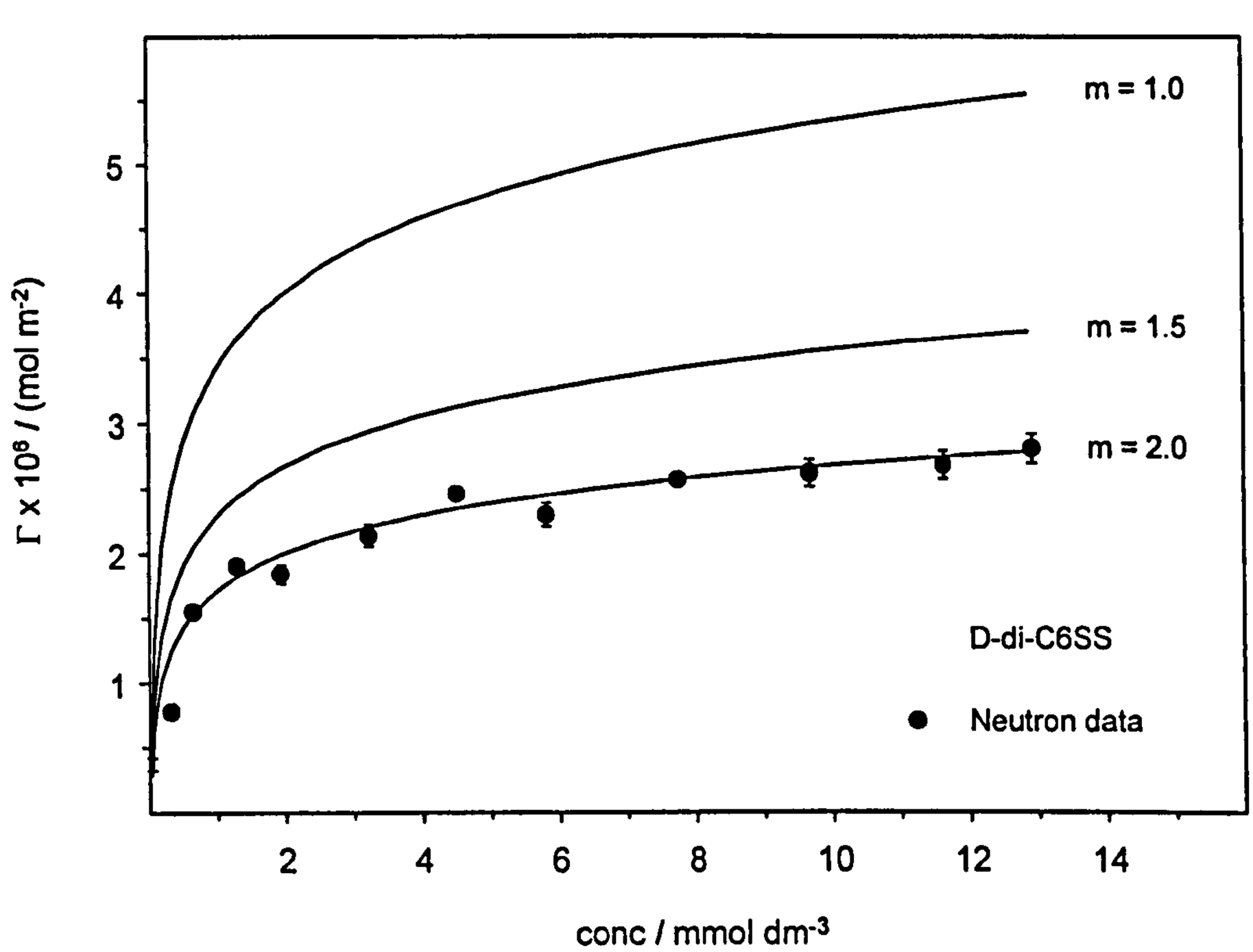

Figure 5.14 Comparison of neutronic and tensiometric adsorption isotherms of D-di-C6SS with different possible values of the Gibbs pre-factor *m*.

Figure 5.14 clearly demonstrates that the NR and tensiometric data are consistent with a pre-factor of between 2.0 and 1.95. A more accurate assessment of *m* is outside the resolution of the two different methods. Nevertheless, to obtain this agreement it is essential that the surfactant is "surface chemically pure", and extreme care must be taken to achieve this state. Therefore, for di-C6SS both the anions and cations adsorb similarly, and the assumption of 1:1 ion adsorption, which is implicit in the Gibbs factor of 2, has been confirmed for this compound. This result was tested by co-workers from the University of Bristol for three custom synthesised fluorocarbon anionics, which are closely related to di-C6SS, and three common cationic surfactants [53]. For the anionics, the same purification procedure as for di-C6SS was followed, and for the commercial *n*-alkyltrimethylammonium bromide (C*n*-TAB) cationic series several re-crystallisations were performed. Good agreements between NR and DVT data were obtained and it was confirmed that the Gibbs pre-factor of 2 also applies for all of these 1:1 ionic surfactants.

5.2.4 Conclusions

The studies of the proteated and deuterated forms of di-C6SS ionic surfactant by neutron reflectivity and tensiometry demonstrate the validity of the factor of 2 in the Gibbs equation. The effect of impurities has been addressed in detail. Most important is the issue of cation contamination, which is an inevitable and unavoidable consequence of the synthetic route. With sodium surfactants the M^{n+} ions can be effectively removed from the interface, and the Na^+ level replenished, by adding Na_4EDTA. The optimum amount of EDTA must be determined experimentally for each batch of surfactant so that there is a sufficient amount to chelate the unwanted metals, but its presence should not exert any other (noticeable) influence on the surface tension. Hydrophobic impurities seem to present less of a problem for the custom-made di-C6SS, and these can be separated with a rather time-consuming foam fractionation process.

5.3 EFFECT OF CHAIN STRUCTURE ON AGGREGATION AND INTERFACIAL PACKING

In the following section, the adsorption and aggregation properties of several Aerosol-OT related compounds in water are presented. Following the findings regarding the validity of the Gibbs equation with a pre-factor of 2 for ionic surfactants, tensiometry could be used with confidence to assess surface coverages and head group areas at the CMC for a wide range of different compounds. The purpose of this study is to identify any structure-performance relationship in the surfactant series, and in particular to find if, as generally thought, there is anything unique about Aerosol-OT structure.

In pursuit of this aim, three surfactant series, as shown in Figure 5.15 and 5.16, have been synthesised and relevant properties characterised. The first set, denoted "di-C*n*SS" with $n = 4, 5, 6, 7$ and 8, are linear chains sodium di-alkyl sulfosuccinates. These can be directly compared to the second series, "AOTs", that includes six branched chain sodium di-alkyl sulfosuccinates, including Aerosol-OT itself. These surfactants span extremes of branching, from 3,5,5-trimethyl-1-hexyl, through 2-ethyl-1-hexyl (AOT) to 1-ethyl-2-methyl-1-pentyl (see Figure 5.15), and therefore it is possible to delineate structure-performance relationships. For comparison purposes, the total carbon number per chain was maintained at 8, as for AOT, except for AOT④, which has C9 chains but can be related to AOT③ since it contains the same alkyl branches. Finally, the third group is phenyl-tipped sodium di-alkyl sulfosuccinates, "di-PhC*n*SS", with both linear and branched chains (see Figure 5.16), so that comparisons can be drawn to the first two sets.

After a brief introduction to the specificity of AOT, the effect of chain branching is discussed by studying the properties of the di-C*n*SS and AOTs series at the air–water (a–w) interface. Changes upon introduction of a phenyl group (di-PhC*n*SS series) are then described separately. By comparing all these structural variants, it is expected to pinpoint the effects of chain branching in AOT itself.

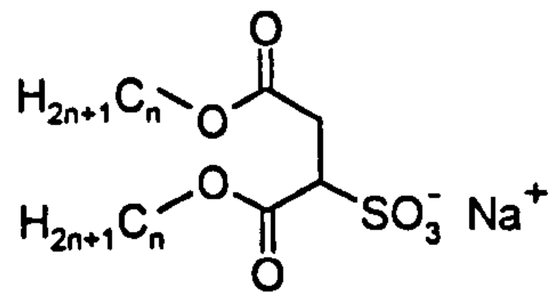

di-C*n*SS (*n* = 4 to 8)
Sodium bis(1-alkyl) sulfosuccinate

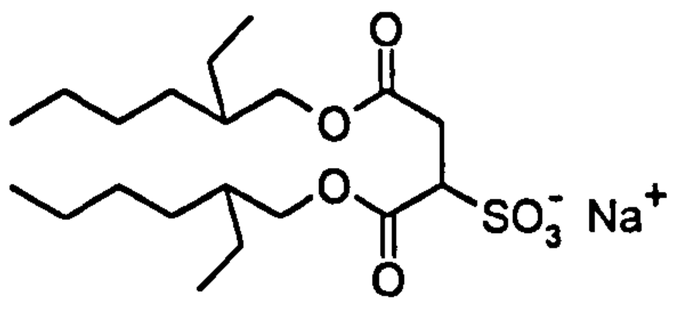

AOT① (Aerosol-OT)
Sodium bis(2-ethylhexyl)
sulfosuccinate

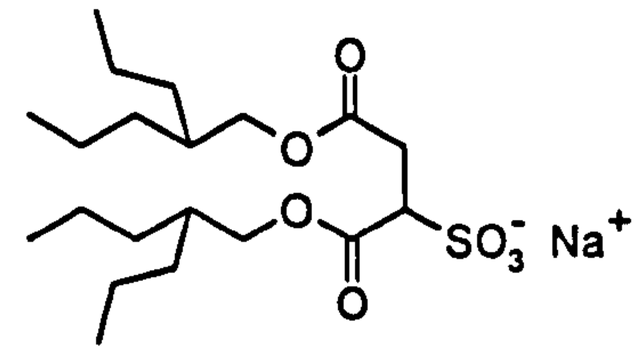

AOT②
Sodium bis(2-propyl-1-pentyl)
sulfosuccinate

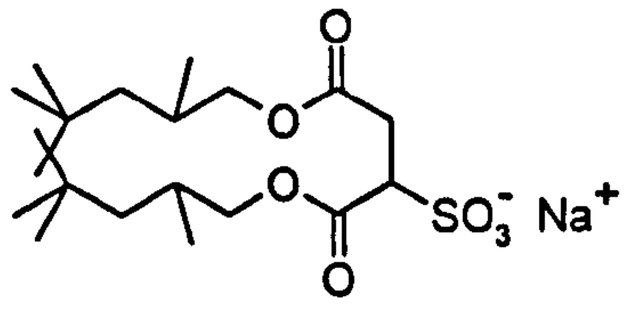

AOT③
Sodium bis(2,4,4-trimethyl-1-pentyl)
sulfosuccinate

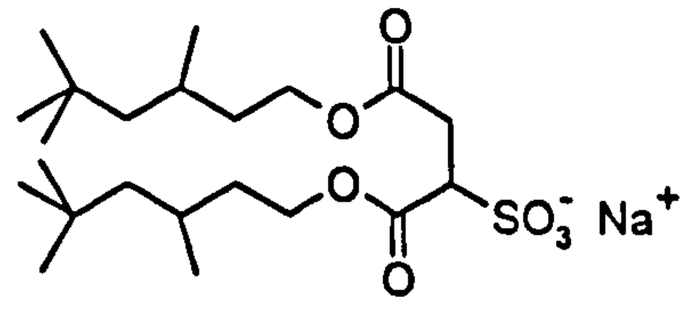

AOT④
Sodium bis(2,5,5-trimethyl-1-hexyl)
sulfosuccinate

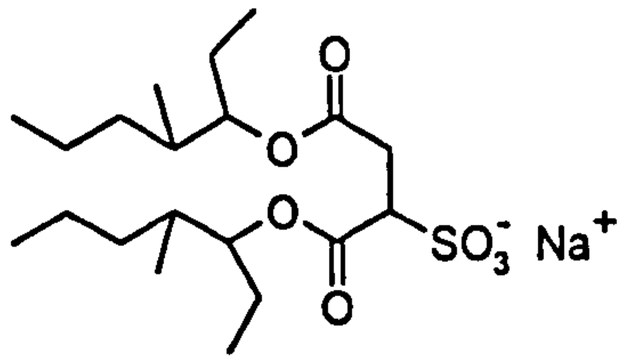

AOT⑤
Sodium bis(1-ethyl-2-methyl-1-pentyl)
sulfosuccinate

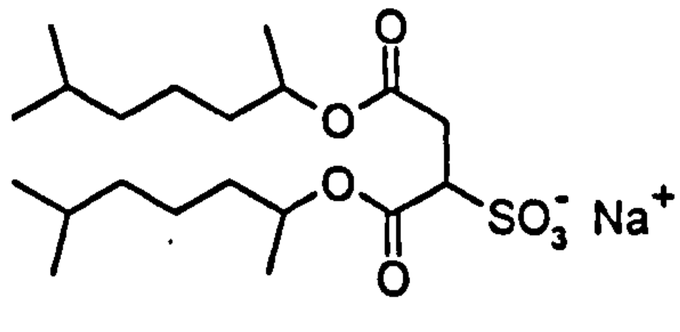

AOT⑥
Sodium bis(1,4-dimethyl-1-hexyl)
sulfosuccinate

Figure 5.15 Schematic molecular structures of di-C*n*SS and AOTs surfactants.

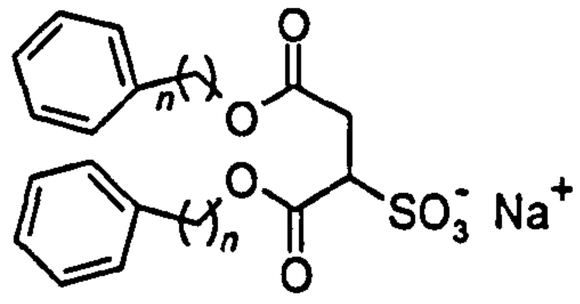

di-PhC*n*SS (*n* = 2 to 5)
Sodium bis(*n*-phenyl-alkyl)
sulfosuccinate

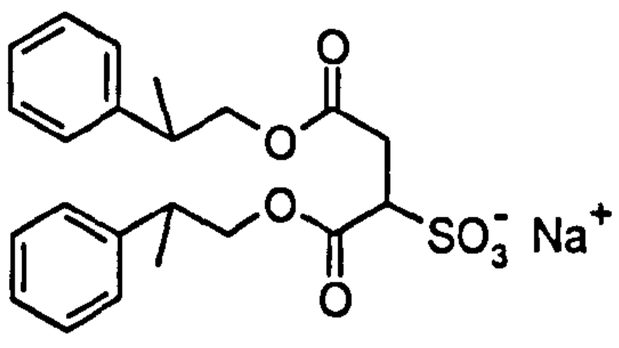

Br-di-PhC3SS
Sodium bis(2-phenyl-2-methyl)
sulfosuccinate

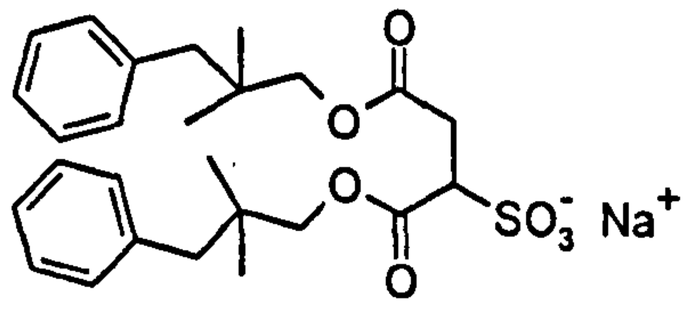

Br-di-PhC5SS
Sodium bis(3-phenyl-2,2-dimethyl)
sulfosuccinate

Figure 5.16 Schematic molecular structures of linear (di-PhC*n*SS) and branched (Br-di-PhC*n*SS) phenyl-tipped surfactants.

5.3.1 What is so special about Aerosol-OT?

The relationship between surfactant molecular structure and phase behaviour is a central question in colloid science, especially with regard to adsorption and aggregation. The critical micelle concentration CMC, surface excess Γ and limiting surface tension γ_{cmc} are characteristic of any given surfactant, and so these are useful quantities. For homologous surfactants an array of such values can be helpful in identifying structure-performance relationships. In particular, interfacial packing can be related to the length and nature of hydrophobic chains, as well as size, charge and polarity of hydrophilic head group. In terms of aggregation, Israelachvili and co-workers [54] suggested that molecular shape plays a major role via the surfactant critical packing parameter P_c, which is defined as the ratio of the volume of the surfactant hydrophobic part and the critical head group area times the chain length (see Chapter 2, Section 2.3.3). Thus the P_c value is generally used to predict interfacial curvature and microemulsion type (i.e., Winsor I, II or III).

For Aerosol-OT (AOT), however, P_c cannot account on its own for the very diverse phase behaviour encountered. As well as being one of the few surfactants that can form co-surfactant free microemulsions, AOT exhibits a remarkably rich aqueous phase behaviour, encompassing aqueous micellar, vesicular, lamellar, bi-continuous cubic and reverse hexagonal liquid crystalline phases. As such, AOT is a classical example for theoretical studies, and is also widely used industrially [55-62]. The literature on this compound is unsurprisingly vast and still growing: for example, in the 1990's alone over 1500 papers were published. However, despite this interest, no clear explanation has yet been given to account for the unusual efficiency of AOT, especially in microemulsions. In explaining any structure-property relationship to account for its rich phase behaviour and ability to form microemulsions, the inverted truncated cone-shaped, well-balanced structure of the molecule is often loosely mentioned. However, this does not explain the water-rich phase behaviour of AOT where positive and planar curvatures dominate. In particular, the function of the two ethyl side branches remains unclear.

Neutron reflection (NR) has been used to study AOT adsorption at the aqueous-air interface [15,16]. Li *et al.* employed a detailed isotopic labelling scheme to determine the layer structure, as well as the surface excess Γ [15,16]. Surprisingly, it was found that the layer thickness did not change with increasing Γ, and this is in contrast to all other surfactants that have been studied in this way. It was proposed the apparent constant thickness is due to concentration-induced conformational changes of the chains. In the present study NR has been used to study deuterated di-hexyl sulfosuccinate D-di-C6SS, which is essentially AOT without the ethyl branches, and so a direct comparison can be made with AOT. Therefore, any specific effects of ethyl branching can be identified. In addition, extensive surface tension measurements were carried out on the various series of sodium sulfosuccinates.

Several studies have been carried out at the a–w on various surfactant series using neutron reflection and/or tensiometry [63-65] and more recently ellipsometry [66], but chain branching effects have received little attention [67-69]. In this work further experiments have been carried out at the oil-water interface in microemulsions, and results are reported in Chapter 6. It is of particular interest to examine how both the a–w and o–w interfaces respond to these changes in surfactant molecular structure. Surprisingly, comparative studies of adsorption at these two different interfaces are few and far between [70].

5.3.2 Di-C6SS versus AOT: monolayer structures from neutron reflectivity

From NR data, as discussed in Section 5.2.3, adsorbed amounts were determined using single layer fits. Table 5.4 re-calls the derived parameters – i.e., layer thickness τ, scattering length density ρ, and head group area A_{cmc} – at the CMC only, for D-di-C6SS. In addition, values for fully deuterated AOT determined by Li *et al.* [15,16] are given for comparison purposes. Obviously, from comparison of the A_{cmc} values, the linear compound can pack in a more efficient manner, with an interfacial area approximately 20 $Å^2$ smaller than the value for the branched compound. This relates directly to the molecular geometry. The presence of alkyl side branches increases the hydrophobic volume, hence the larger A_{cmc} values for AOT.

Table 5.4 Structural parameters of D-di-C6SS and AOT on NRW determined from neutron reflection using a single uniform layer model

Surfactant	τ (± 1.5 / Å)	ρ / 10^{-6} Å^{-2}	A_{cmc} (± 2 / Å^2)
D-di-C6SS	17.8	3.00	59
D-AOT[a]	18.0	2.78	78

[a] Data for AOT as in references 15 and 16.

Table 5.5 Structural parameters of D-di-C6SS and AOT obtained from kinematic analyses using partial structure factors

Surfactant	σ_A (± 1 / Å)	ζ (± 1 / Å)	δ_{AS} (± 0.5 / Å)
D-di-C6SS	15	5.3	5.0
D-AOT[a]	13–15	4.0	4.5–6.0

[a] Data for AOT are for the chains and head group, respectively as in references 15 and 16.

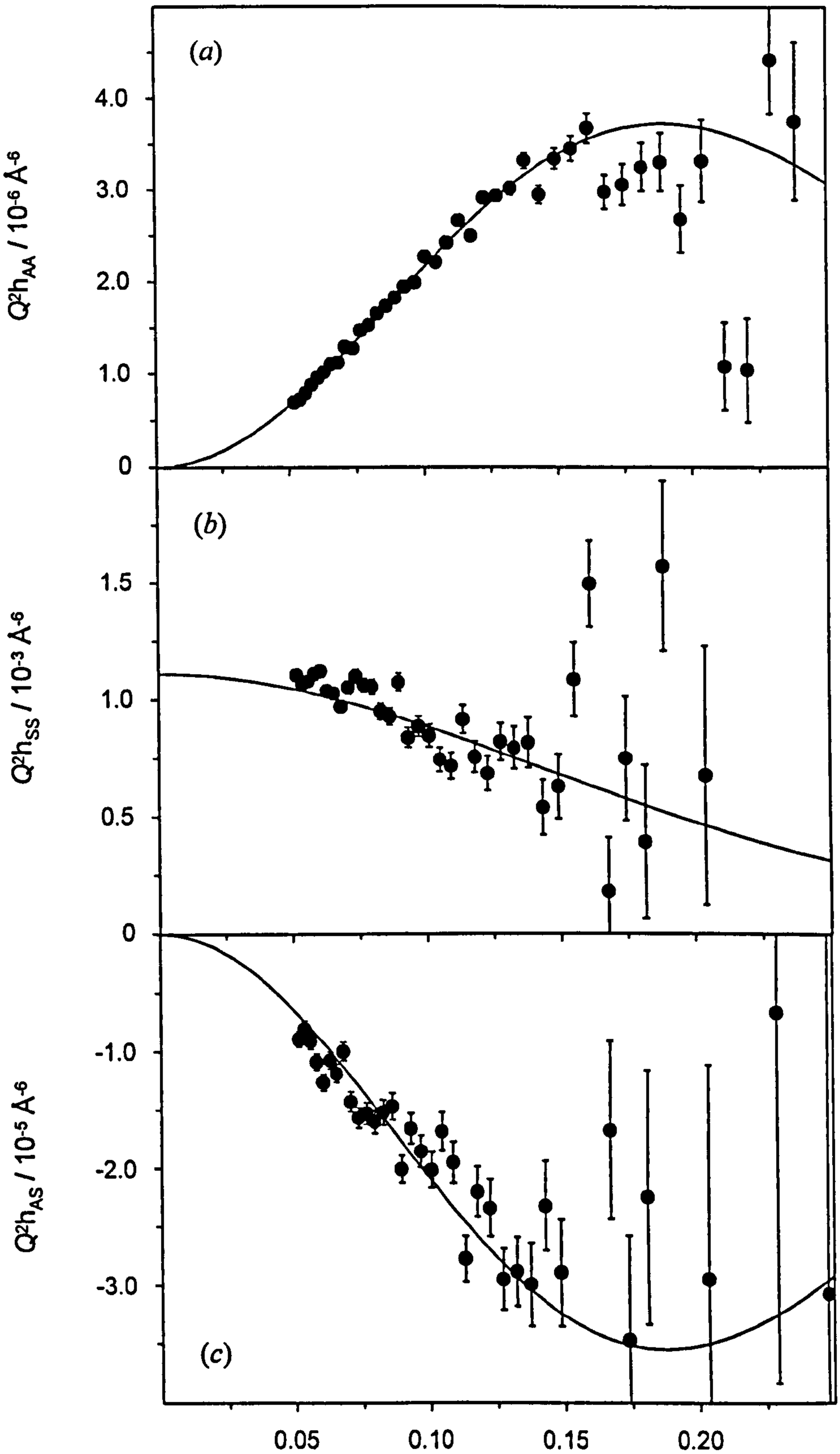

Figure 5.17 Partial structure factors for D-di-C6SS at the CMC: (*a*) surfactant as a whole, (*b*) water, (*c*) cross-term between the surfactant and water. The lines are best fits using the parameters of Table 5.5.

As seen in Table 5.4, at the respective CMC's both layers have similar thicknesses. However, the change in film thickness with concentration is different. For D-diC6SS, as reported previously in Table 5.3 (see p.157), the film was found to thicken progressively from 11.4 ± 1.5 Å at CMC/40 to 17.8 ± 1.5 Å at the CMC (1.29×10^{-2} mol dm^{-3}). For AOT itself [16], it remained constant at 18.0 ± 1.5 Å over the range CMC/300 up to the CMC (2.5×10^{-3} mol dm^{-3}).

Further structural features can be obtained through analysis of complementary R(Q) profiles, using the partial structure factor (PSF) analysis, which is valid under the kinematic approximation. Relevant details have been given in Section 5.1.1, and a full description can be found elsewhere [10,12]. The experiments were performed at the CMC with three different isotopic compositions of aqueous subphase (NRW, D_2O, and 1:1 mixture of D_2O:H_2O). For D-di-C6SS, with the isotopic labelling scheme used here, PSF experiments yield distributions for water and the surfactant as a whole, perpendicular to the interface. Experimentally determined PSFs, and fits using appropriate equations (see Section 5.1.1, Eqs. 5.1.13 to 5.1.15), are shown in Figure 5.17. The parameters derived from PSF analyses are listed in Table 5.5.

As mentioned earlier, it is of interest to compare the layer structures of D-di-C6SS and the ethyl-branched AOT. Relevant data from references 15 and 16 are therefore also included in Table 5.5. Recall that the single-slab analysis at the CMC (Table 5.4) indicated similar thicknesses, which may be expected since the long chain on both molecules is C6. Similar comparisons can also be drawn using Table 5.5. For the linear chain di-C6SS, the Gaussian width for the whole surfactant molecule, σ_A, was determined to be 15 ± 1 Å. Direct comparison with the work by Li *et al.* [16] on AOT is not straightforward, since the study includes two separate PSF analyses, with two or three specifically labelled fragments. However, comparisons can be made for the case of deuterated terminal butyl portions of the hexyl groups so that the remainder of the molecule is considered to be a modified head group. The Gaussian widths for chains, σ_C, and head, σ_H, were then determined to be 13 and 15 ± 1 Å respectively, with a separation δ_{CH} of 2 ± 1 Å. When taken together σ_C and σ_H for AOT do differ significantly from the total width σ_A for D-di-C6SS. However, to make clear comparisons two additional factors must be considered:

i) with AOT the value of δ_{CH}, the separation between the chains and head width distributions, was explained by invoking a tilt of the ethyl and butyl groups being away from the surface normal. Translating this to D-di-C6SS, hexyl chain tilting would reduce σ_A. However, this does not fit with the more efficient packing of D-di-C6SS over AOT, as judged by the relative molecular areas A_{cmc}.

ii) At its CMC the film roughness for AOT is believed to be 10–12 Å [16], and this contributes to the interfacial width. Since similar thicknesses were obtained (Table 5.4), the roughness of each layer must differ slightly, with the linear sulfosuccinate having a smoother layer.

Fits for the solvent self-term, h_{SS}, and the surfactant-solvent cross term, h_{AS} are shown in Figures 5.17(*b*) and (*c*): these yield a width for the water distribution ζ of 5.3 ± 1 Å, and a separation between surfactant and solvent distributions δ_{AS} = 5.0 ± 0.5 Å. The results can be compared to AOT (Table 5.5), which had a solvent width ζ 4 ± 1 Å, and separation δ_{AS} 4.5 and 6.0 ± 0.5 Å respectively. Considering the whole molecule these are essentially the same as for the linear analogue. Therefore, similarity in δ_{AS} values for the two structures, and the slightly lower ζ value, indicates that D-di-C6SS is more immersed in the water than the branched AOT, as one would expect considering its greater hydrophilicity (higher CMC).

Finally, the layer can also be described in terms of volume fraction profiles, which indicate composition perpendicular to the surface. Figure 5.18 shows these for D-di-C6SS and water. Estimates for molecular volumes of each fragment (Table 5.6) determined from bulk densities and partial specific volumes [66,71,72] were used in the calculations. Substantial penetration of the water into the surfactant film is evident, and so a degree of immersion for D-di-C6SS can be estimated [63]. If there were no overlap of the surfactant and water distributions, then the centre-to-centre separation would be half the sum of their widths. However, δ_{AS} is determined as 5 Å, so there must be an overlap of about 5 Å, considering this in terms of the surfactant distribution width gives a degree of immersion of approximately 34 %. This compares with between 24 and 31% for AOT (from values in references 15 and 16), and 39% calculated for a di-C5 fluorinated AOT analogue [73].

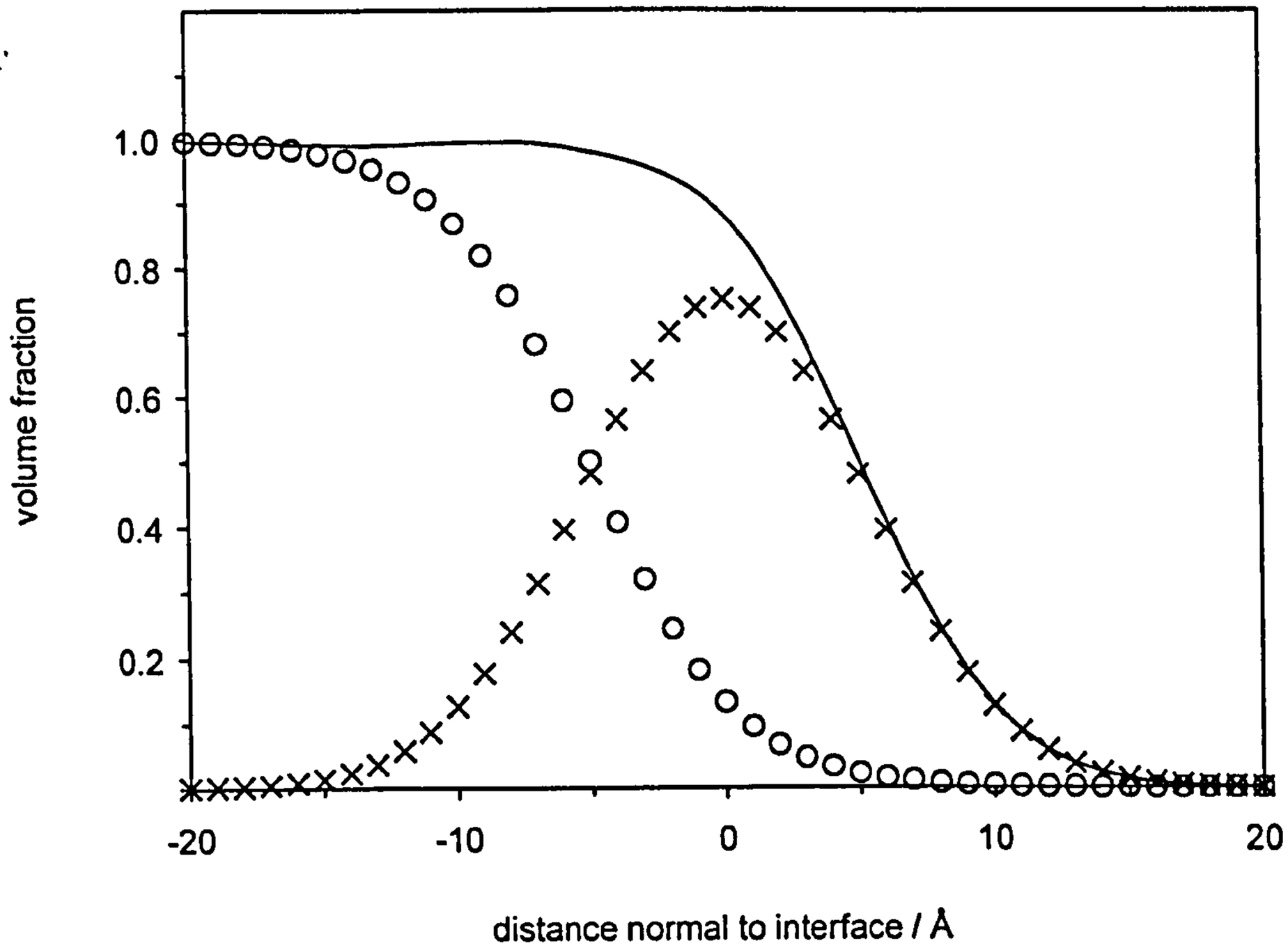

Figure 5.18 Volume fraction profiles for a D-di-C6SS film at the CMC, using values from Tables 5.5 and 5.6: surfactant distribution (×), solvent distribution (○), and total volume fraction (—).

Table 5.6 Molecular fragments of D-di-C6SS used to calculate volume fraction profiles in Figure 5.18[a]

Fragment type	Volume / Å^3
$OOCCH_2CHSO_3COO$	210
C_6D_{13}	190
H_2O	30

[a] Values taken from references 16 and 74.

The above section, together with results from Part 5.2 have *i*) established how to measure adsorptions of such anionic surfactants, and *ii*) compared the layer structure of AOT and di-C6SS. This has shown that the ethyl branching in AOT has an important effect on molecular packing (increase in A_{cmc} of around 20 Å^2), but perpendicular to the interface there is similar layer structure. With this in hand it is now possible to compare absolute adsorptions as a function of surfactant chain structure for all the surfactants shown in Figure 5.15.

5.3.3 Effect of chain branching from equilibrium surface tension

As discussed earlier, all measurements were carried out with EDTA to mask any effects of trace M^{n+} species. The surfactant:EDTA ratios were 150:1, 30:1, 100:1, 50:1, 500:1 for di-C4SS, di-C5SS, di-C6SS, di-C7SS, di-C8SS respectively, and 120:1, 55:1, 35:1, 45:1, 100:1 and 48:1 for AOT①, -②, -③, -④, -⑤, and -⑥ respectively. For the standard AOT① the CMC and γ_{cmc} results are in excellent agreement with various literature data for the normal commercial material [e.g., ref. 18], which are (2.5 ± 0.5) × 10^{-3} mol dm^{-3} and 30 ± 0.5 mN m^{-1} respectively. Since no relevant literature value could be found for other branched compounds, this agreement with AOT lends confidence to the results.

Micellisation properties

Equilibrium γ–ln a plots for the di-C*n*SS and AOT surfactants are shown, respectively, in Figures 5.19 and 5.20 (divided in parts (*a*) to (*c*) for clarity of the graphs). All curves display clean breaks at the CMC with no minima or shoulders, which would indicate surface-active impurities. The pre-CMC curves are well described by polynomials, which are also included on the plots. Tables 5.7 and 5.8 give values for the CMC's, limiting surface tensions γ_{cmc}, and head group areas A_{cmc} derived from these data. Figure 5.21 summarises the different adsorption isotherms derived using equation 5.2.1. Note that a reduced concentration axis conc/CMC has been used so that the different surfactants can be readily compared. To help identify effects of chain structure, the schematic molecular diagrams have also been included.

Table 5.7 CMCs and parameters derived from surface tension measurements for the linear sodium sulfosuccinates, di-C*n*SS

di-C*n*SS	CMC / (mmol dm^{-3})	γ_{cmc} / (mN m^{-1})	A_{cmc} (± 2 / Å^2)
C4	187 ± 3	32.8	71 (73)[a]
C5	50.9 ± 0.3	31.1	66 (68)
C6	12.5 ± 0.3	29.1	62 (63)
C7	3.55 ± 0.03	29.8	57 (58)
C8	0.911 ± 0.003	30.4	55 (55)

[a] Values of A_{cmc} in parentheses are derived using concentrations rather than activities.

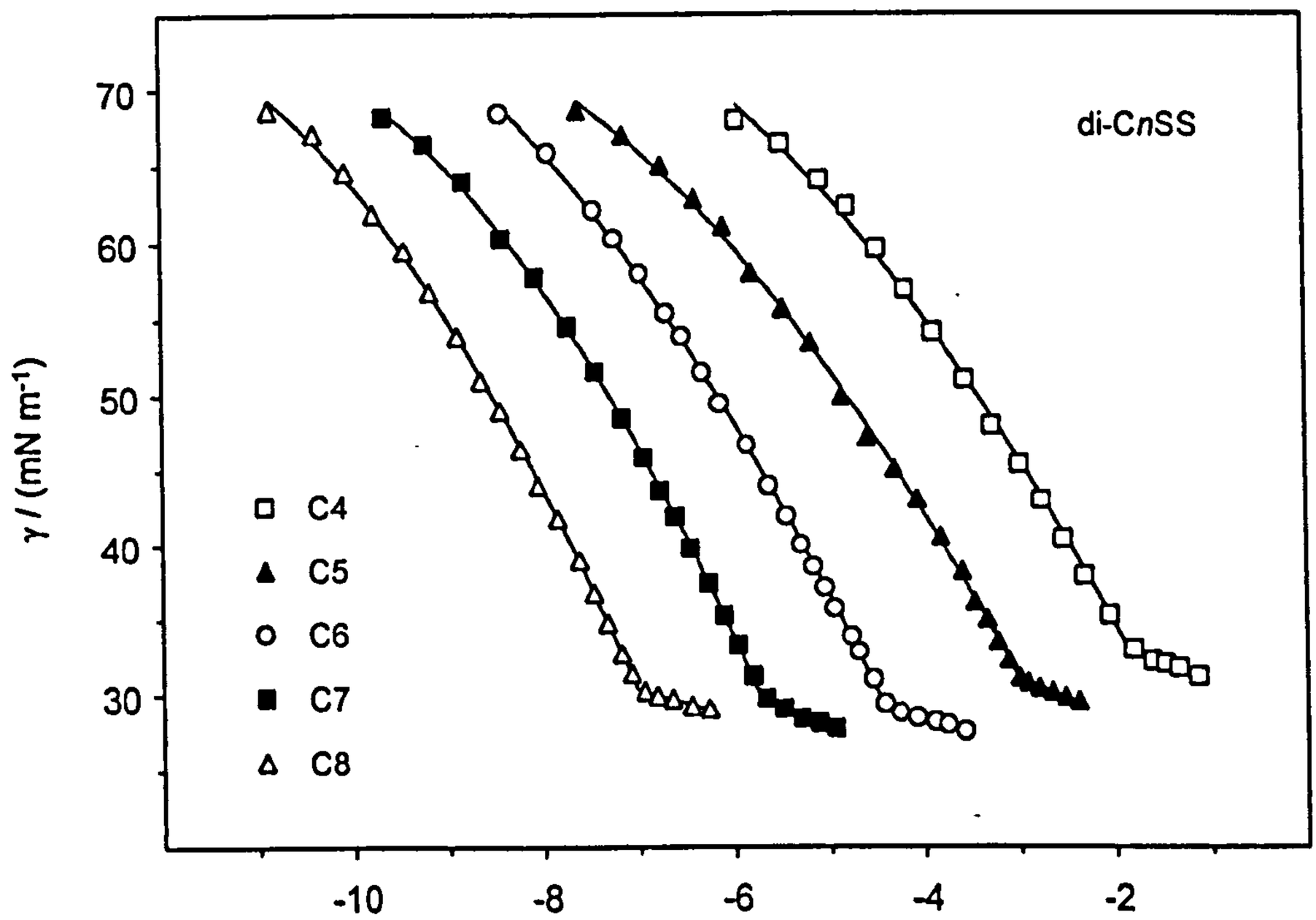

Figure 5.19 Equilibrium air–water interfacial tension γ_{eq} vs. ln activity for di-C*n*SS surfactants at 25 °C in water with EDTA. Polynomial lines fitted to pre-CMC data are shown. The parameters derived from these analyses are listed in Table 5.7.

Table 5.8 CMCs, parameters derived from surface tension measurements, and branching factor for the branched sodium sulfosuccinates, AOTs

AOT	CMC ($\pm$ 0.03 / mmol dm^{-3})	γ_{cmc} ($\pm$ 1 / mN m^{-1})	A_{cmc} ($\pm$ 2 / Å^2)	branching factor
①	2.56	30.8	75	1.67
②	3.18	29.7	77	2.40
③	4.36	27.3	73	1.60
④	1.10	28.1	70	1.33
⑤	7.15	30.3	80	2.80
⑥	2.83	29.1	70	1.33

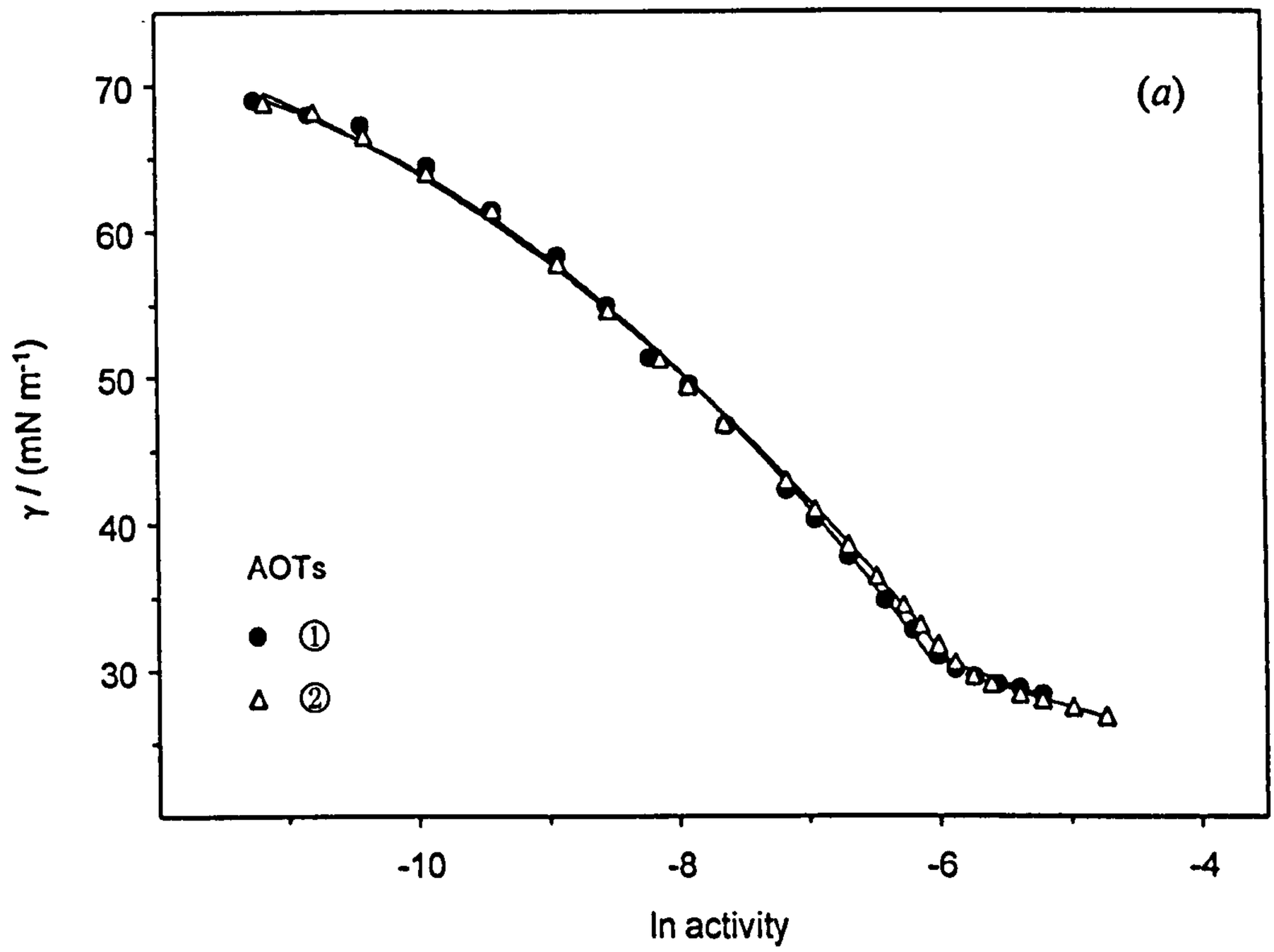

Figure 5.20 γ–ln a plots for (*a*) for AOT① and -② at 25 °C in water with EDTA. Polynomial lines fitted to pre-CMC data are shown. The parameters derived from these analyses are listed in Table 5.8.

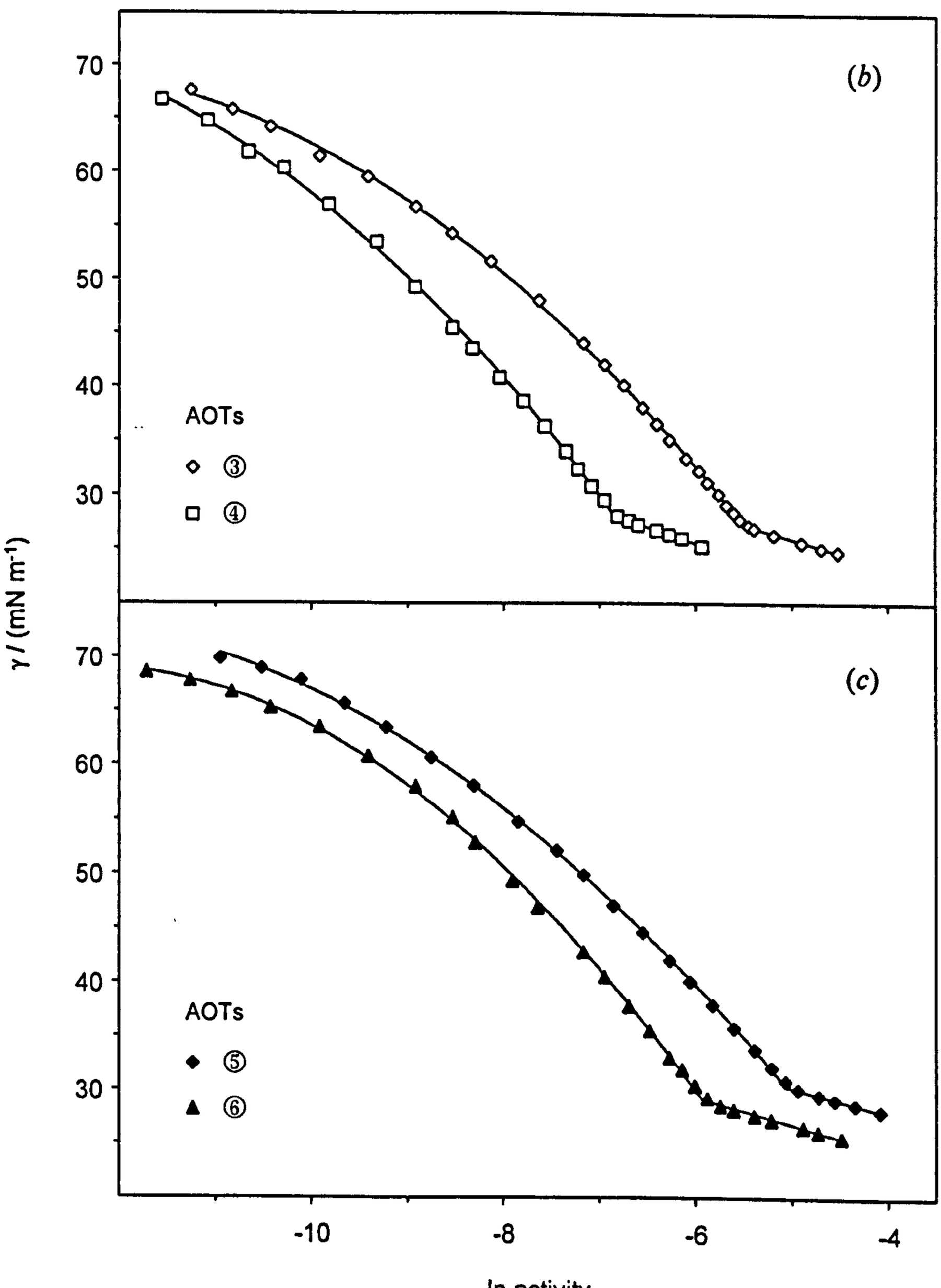

Figure 5.20 (suite) γ–ln a plots for (*b*) AOT③ and -④, and (c) AOT⑤ and -⑥ at 25 °C in water with EDTA. Polynomial lines fitted to pre-CMC data are shown. Tensiometric parameters are listed in Table 5.8.

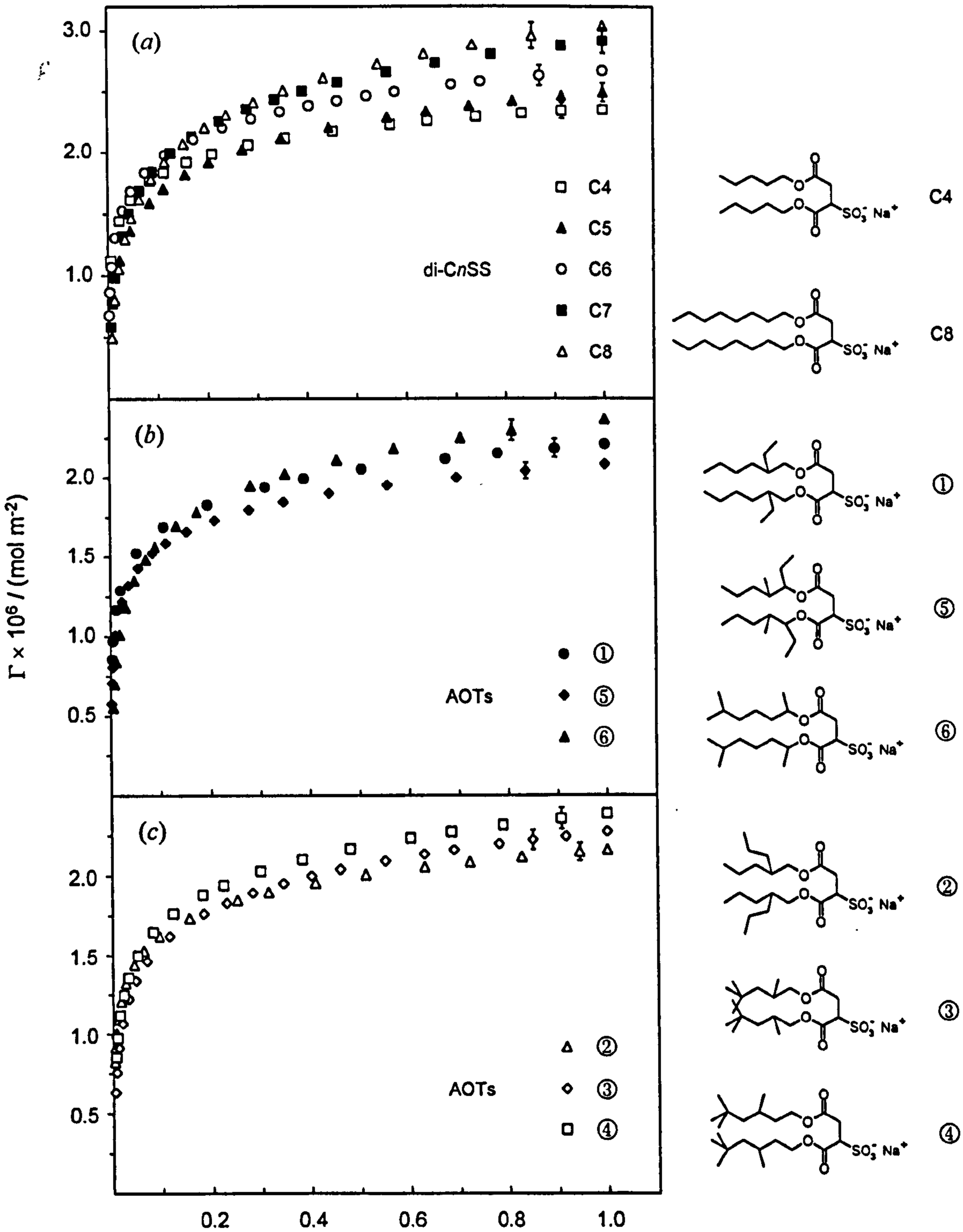

Figure 5.21 Γ vs. reduced concentration (conc/CMC) adsorption isotherms of di-C*n*SS and AOT surfactants derived from γ–ln a data. For each curve a characteristic error bar around the CMC is given.

As expected for the di-C*n*SS series, log(CMC) displays a linear dependence on carbon number, with a gradient of -0.29 (Figure 5.22). This compares favourably with values from Williams *et al.* [47] and with literature data on other anionic surfactants [74], and also for cationics [9,17,75,76]. Within the branched series, links between CMC and alkyl chain length are less obvious, since nearly all compounds have the same carbon number. However, the classic trend of a decreasing CMC with increasing *effective* chain length is observed, i.e., considering the carbon number of the longest linear portion only. Therefore, as shown on Figure 5.22, the branched sulfosuccinates can be considered as having either two linear chains five carbons long (AOT②, -③, and -⑤), or a length of C6 (AOT①, -④, and -⑥). Hence, AOT③ and -④ can be compared as direct linear analogues differing by one CH_2 group per chain. Although for only two data points (AOT③ and -④), the gradient of -0.30 for the dotted line in Figure 5.22 compares well with that for other di-C*n*SS's. The effect of each individual branch on CMC is difficult to identify, in all cases, addition of alkyl side groups to the linear tails decreases the CMC significantly; for example when comparing the AOTs to di-C5SS or di-C6SS. On the other hand, when set against linear C8 chains, di-C8SS, the branched C8 compounds give higher CMC's due to their shorter effective tails. The same general observations have been reported in references 67 and 68, where it was possible to investigate an even wider range of branched anionic surfactants.

Efficiency and Traube factors

Table 5.10 shows the relative surfactant efficiencies, $C_{\pi/2}$ / CMC, as defined in Section 2.1.3. As expected for the linear series, a significant increase in efficiency is observed upon increase of the chain length, and it also increases with decreasing CMC at a given temperature. The least hydrophobic surfactants have the poorest efficiency, e.g., di-C4SS, and the most hydrophobic have the greatest efficiency, e.g., di-C8SS. Adding alkyl side branches has a marked effect on surfactant efficiency. If one consider the linear part of the chain (i.e., a C6 chain) then the efficiency increases (now comparing $C_{\pi/2}$ values), but when set against the same total number of carbon atoms (i.e., C8), efficiency is decreased. Within the branched series, relative efficiencies are very similar, although an exception worth noting is the slightly higher value of AOT⑥. That can be accounted for the fact that AOT⑥, with only two methyls, has a very small branching extent and is thus structurally closer to the linear compounds.

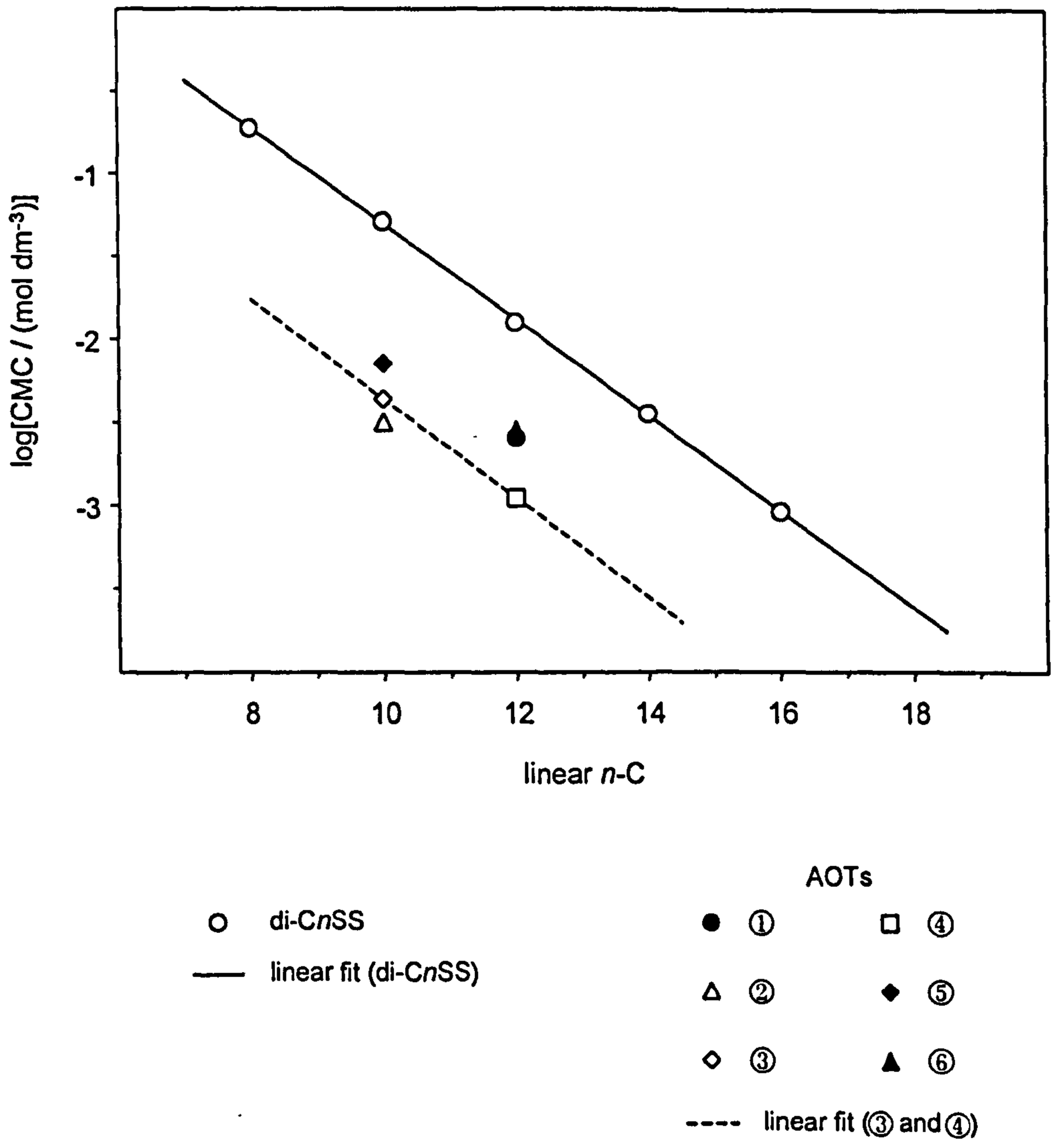

Figure 5.22 Variation of the CMC with the carbon number of the longest linear portion, for both linear and branched surfactants.

Table 5.9 Efficiency of di-C*n*SS's and AOTs. π_{cmc} is the limiting surface pressure ($\gamma_o - \gamma$). $C_{\pi/2}$ is the concentration of surfactant required to lower the surface tension by half the surface pressure at the CMC, $\gamma_{\pi/2}$

Surfactant	π_{cmc} / (mN m^{-1})	$\gamma_{\pi/2}$ / (mN m^{-1})	$C_{\pi/2}$ / (mmol dm^{-3})	$C_{\pi/2}$ / CMC
di-C4SS	39.7	52.7	24.8	0.13
di-C5SS	41.4	51.8	6.96	0.14
di-C6SS	43.4	50.8	1.94	0.16
di-C7SS	42.7	51.2	0.63	0.17
di-C8SS	42.1	51.5	0.18	0.19
AOT①	41.7	51.7	0.29	0.11
AOT②	42.8	51.1	0.31	0.10
AOT③	45.2	49.9	0.37	0.09
AOT④	44.4	50.3	0.12	0.11
AOT⑤	42.2	51.4	0.63	0.09
AOT⑥	43.4	50.8	0.33	0.12

Table 5.10 Traube factors for the di-C*n*SS surfactants. Concentrations are in mmol dm^{-3}

Surfactant	$\gamma = 40$ mN m^{-1}		$\gamma = 45$ mN m^{-1}		$\gamma = 50$ mN m^{-1}		$\gamma = 55$ mN m^{-1}		average	
	C_{40}	K_T	C_{45}	K_T	C_{50}	K_T	C_{55}	K_T	K_T	ΔG_{ads} [a]
di-C4SS	90.3		55.4		33.0		19.1			
		3.85		3.82		3.87		4.02	3.89	-3.37
di-C5SS	23.5		14.5		8.54		4.74			
		4.51		4.32		4.06		3.73	4.16	-3.53
di-C6SS	5.20		3.35		2.10		1.27			
		3.17		3.10		3.05		3.02	3.09	-2.79
di-C7SS	1.64		1.08		0.69		0.42			
		3.57		3.50		3.42		3.36	3.46	-3.08
di-C8SS	0.46		0.31		0.20		0.13			

[a] ΔG_{ads} is the free energy of adsorption per additional (incremental) CH_2 group per chain.

For a homologous series of surfactants, adsorption efficiency can be related to the length of the hydrophobic chain (see Section 2.1.3). According to Traube's rule, the concentration, C, required to lower the surface tension by a set amount, often decreases in a regular manner with increments to chain length, i.e., $C_n/C_{n+1} = K_T$. From the Traube factor K_T, it is possible to obtain an estimate for the standard free energy change of the individual ethylene group, $\Delta G_{ads}(CH_2)$. Table 5.9 shows the calculated Traube factors for the linear sulfosuccinate surfactants. For sequential members of the series, the average K_T is between 3 and 4, i.e., since the compounds are linear double chain surfactants, $K_T \approx 1.73 - 2$ per additional CH_2 group. Using these K_T data and Equation 2.1.20 gives $\Delta G_{ads}(CH_2)$ between -3.5 and -2.8 kJ mol^{-1} (see last column of Table 5.10). This value of free energy change per additional CH_2 group is similar to those obtained by Eastoe *et al.* for the linear di-chained glucamides [64] and dialkyl phosphatidyl cholines [65]. Homologous single-chain surfactants usually give $\Delta G_{ads}(CH_2) \approx -3$ kJ mol^{-1} [77].

Effectiveness of surfactants

Linear versus branched can also be compared in terms of effectiveness at reducing tension. Rosen [78] defined the effectiveness of a surfactant at the air-solution interface as "*the amount of reduction attained at the CMC, any reduction beyond the CMC being considered relatively insignificant*". So effectiveness can also be expressed in terms of a limiting surface tension (γ_{cmc}). With linear chains, the general trend is a decrease of γ_{cmc} with increasing carbon number, reflecting an increase in hydrophobicity [47,79]. The increase in effectiveness observed here (about 4 mN m^{-1}) is rather small compared to other homologous double chain surfactants, where typical changes are around 10 mN m^{-1} between the extremes of hydrophobicity [64,65]. A further increase in effectiveness can be achieved via chain branching, in particular, addition of methyl groups near the chain tips gives lower γ_{cmc} (i.e., AOT③ and -④, giving 27.3 and 28.1 mN m^{-1} respectively). This results from an increase in the CH_3:CH_2 ratio per head group, since CH_3 has a lower surface energy than CH_2 [79]. On the other hand, branching closer to the head group does not have much effect (see for instance AOT⑤). When compared to their linear equivalents, of the same effective chain length, the branched compounds are not especially efficient in terms of γ_{cmc}, and even within this group the normal AOT① does not stand out as being special.

Molecular packing at the air–water interface

One of the clearest ways of characterising an adsorbed layer is in terms of the surface excess and area per head group, since it gives indication about molecular packing efficiency. The tensiometric A_{cmc} for AOT① is 75 ± 2 Å, comparing very well with 78 ± 4 $Å^2$ obtained using NR by Li *et al.* [15,16]. This confirms, yet again, the reliability of tensiometry, provided the surfactant is of high purity.

Values and variations of head group areas for the di-C*n*SS series are presented in Table 5.7 and Figure 5.23(*a*) respectively. It is important to mention the case of di-C4SS and di-C5SS, which fit nicely with the general trend. Due to the high CMC's (50.9 and 187 mmol dm^{-3}, respectively), and therefore relatively large amounts of EDTA present, the Debye-Hückel limiting law was inappropriate (valid only for concentrations in the range 1 – 10 mmol dm^{-3}). As mentioned in Section 5.1.3, an extended law was employed instead, that allowed the calculation of activity coefficients for concentrations higher than 10 mmol dm^{-3}. This trend, of a decrease in molecular area with increased chain length has been found with various other surfactant systems [63-65]. This behaviour is thought to arise owing to a change in the hydration structure of the head group [80], as well as a decrease in the chain rigidity. These results are further validated by including the limiting head group area of insoluble di-C12SS, which has been determined Karaman *et al.* [81] using the Langmuir-Blodgett technique (45 $Å^2$). As shown on Figure 5.23(*a*) this result is in line with the trend for soluble di-C*n*SS compounds.

Clearly, addition of alkyl side branches promotes a significant increase in A_{cmc} (Tables 5.7 and 5.8), which is of the order of +10 to 20 $Å^2$ compared to di-C6SS. This noticeable decrease in interfacial packing reflects the presence of bulkier hydrophobic groups, but within the branched series Table 5.8 indicates only minor changes, with the maximum variation of order of the experimental uncertainty. However, it is worth noting the following observations:

i) the two extreme extents of branching (i.e., AOT⑤ and -⑥) correspond to maximum and minimum head group areas, of 80 and 70 ± 2 $Å^2$ respectively.

ii) A_{cmc} is dependent on the position and length of the branch on the linear chain.

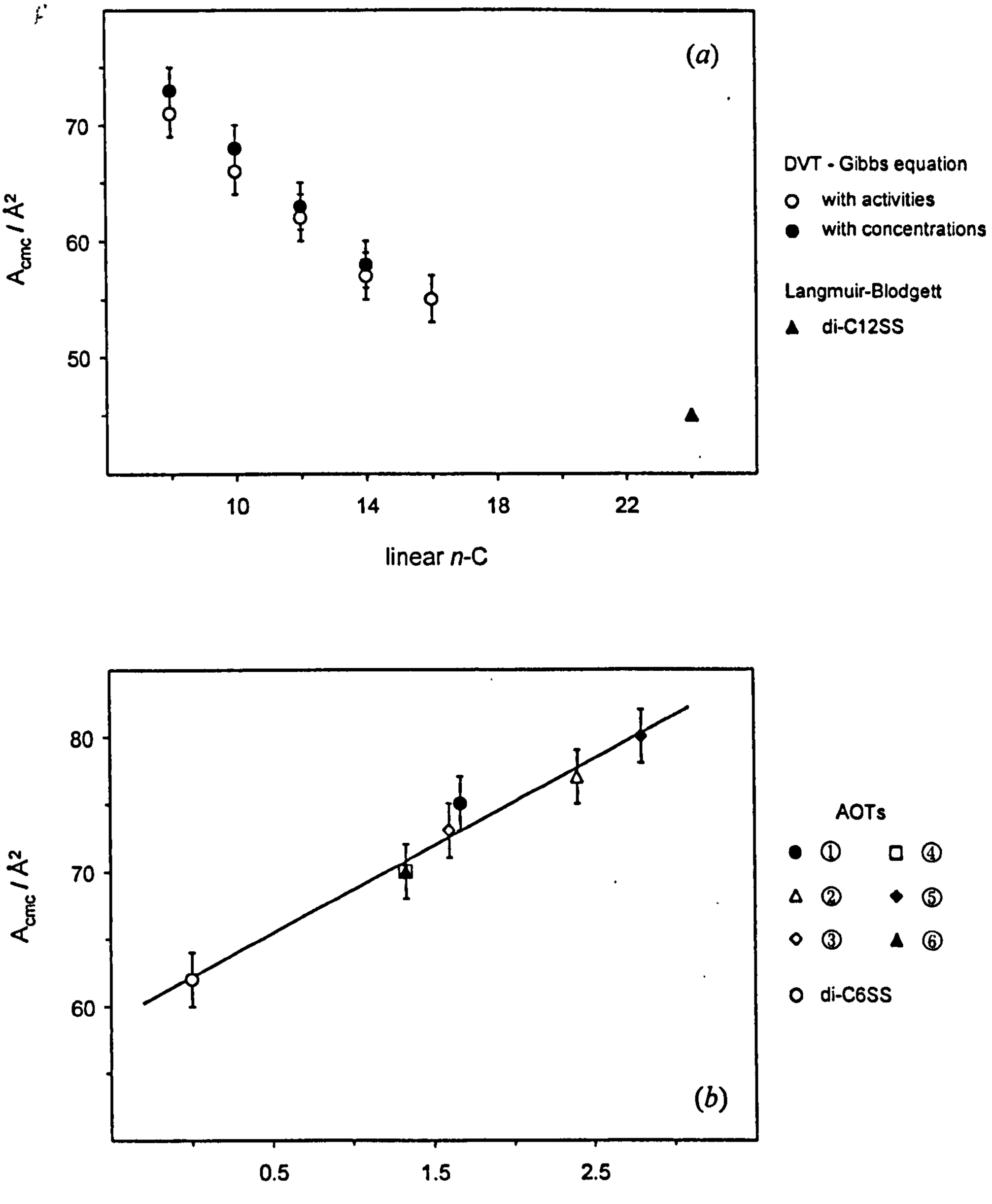

Figure 5.23 Variation of head group areas: (*a*) with carbon number for the linear chain di-C*n*SS series; (*b*) with branching factor (as defined in the text) for the AOTs series and di-C6SS. Head group area of di-C12SS (▲) determined by the Langmuir-Blodgett technique as reported in reference 81.

To illustrate this, an empirical "branching factor" was calculated and included in Table 5.8, and on Figure 5.23(*b*). This factor accounts for contributions from both the extent, and position, of a branch relative to the head group. Examples of branching factor calculations are shown below.

- AOT④: approaching the head group, 2 methyl- in position 2 and 1 methyl- in position 4 on a C6 linear chain, i.e., $[2\cdot(1\times 2)+(1\times 4)]/6=1.33$.
- AOT⑤: approaching the head group, 1 methyl- in position 4 and 1 ethyl- in position 5 on a C5 linear chain, i.e., $[(1\times 4)+(2\times 5)]/5=2.80$.

Thus, using such values Figure 5.23(*b*) clearly shows the dependence of the head group area on the structure of the hydrophobic group: increasing the branch length and/or branching closer to the head group increases the molecular area, as one would expect owing to geometrical constraints. Such trends, although not expressed in terms of a branching factor, have been reported for a series of linear and branched alkyl pyridinium halides [67]. Also included in Figure 5.23(*b*) is the linear di-C6SS, which has a branching factor of zero, and as shown this fits well within the general trend. Therefore, the results obtained from this comparative study are consistent with changes in hydrophobic chain structure. Note how normal AOT, hailed by some as a wonder surfactant, falls into line with its structural relatives.

5.3.4 Effect of phenyl-tipped chain structures

The aqueous properties of a third series of di-chain anionic surfactants (linear and branched dialkyl-*n*-phenyl sodium sulfosuccinates) were studied to investigate effects of terminal hydrophobic group chemistry. The chemical structures of the compounds are shown in Figure 5.16 (Section 5.3). Surface tension measurements and screening experiments for EDTA levels were carried out as before. γ–ln activity plots for the linear and branched compounds are shown in Figure 5.24(*a*) and (*b*) respectively, and apart from di-PhC3SS (discussed later), breaks at the CMC were clearly defined. Adsorption isotherms were derived using the Gibbs equation with a pre-factor of 2. Γ versus reduced concentration (concentration/CMC) plots are shown in Figure 5.25.

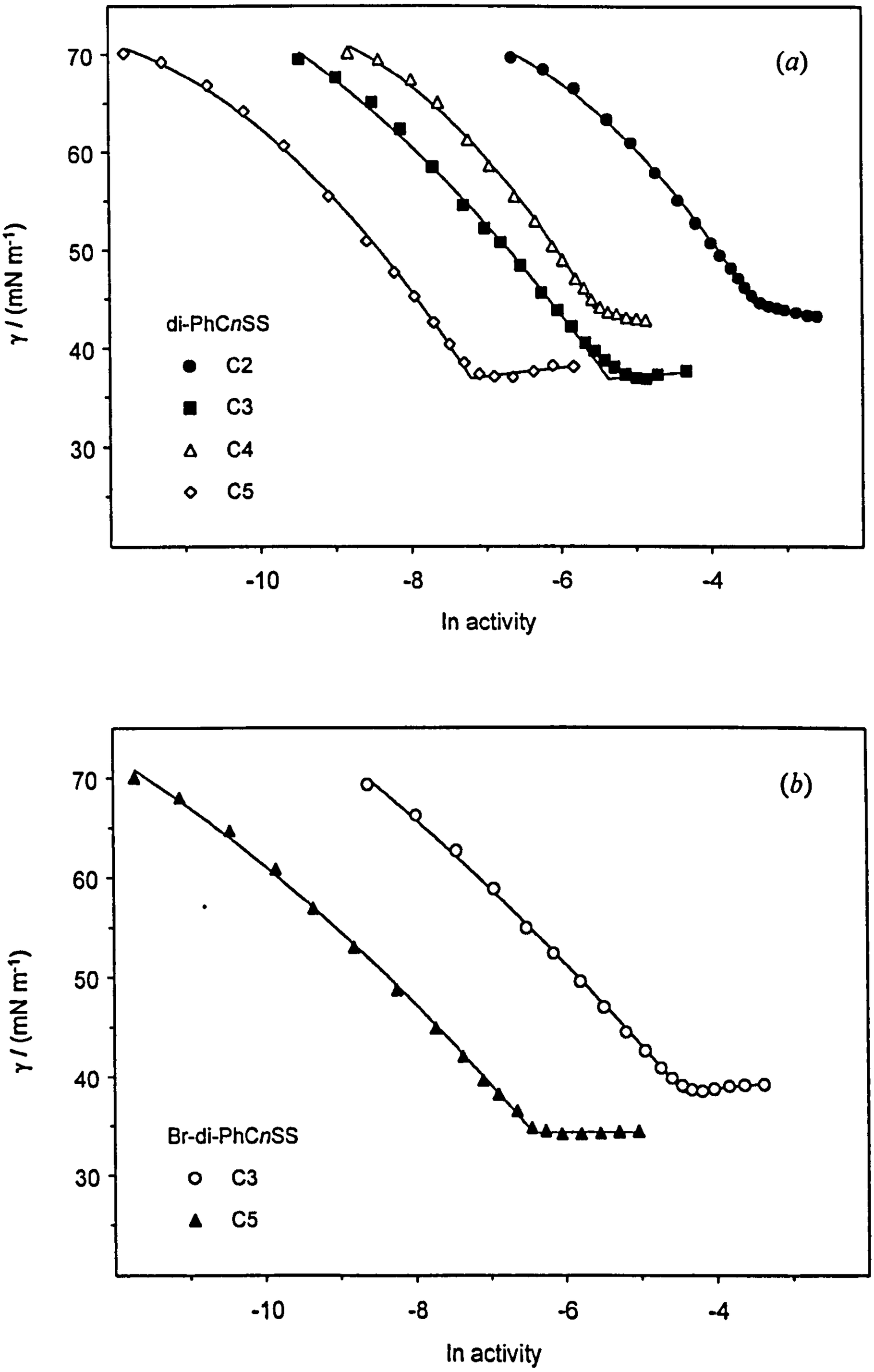

Figure 5.24 Equilibrium air–water interfacial tension γ_{eq} vs. ln activity for the phenyl-tipped sulfosuccinate surfactants at 25 °C in water with EDTA. (*a*) Linear series, di-PhC*n*SS, (*b*) branched series, Br-di-PhC*n*SS. Polynomial lines fitted to pre-CMC data are shown. The parameters derived from these analyses are listed in Table 5.11.

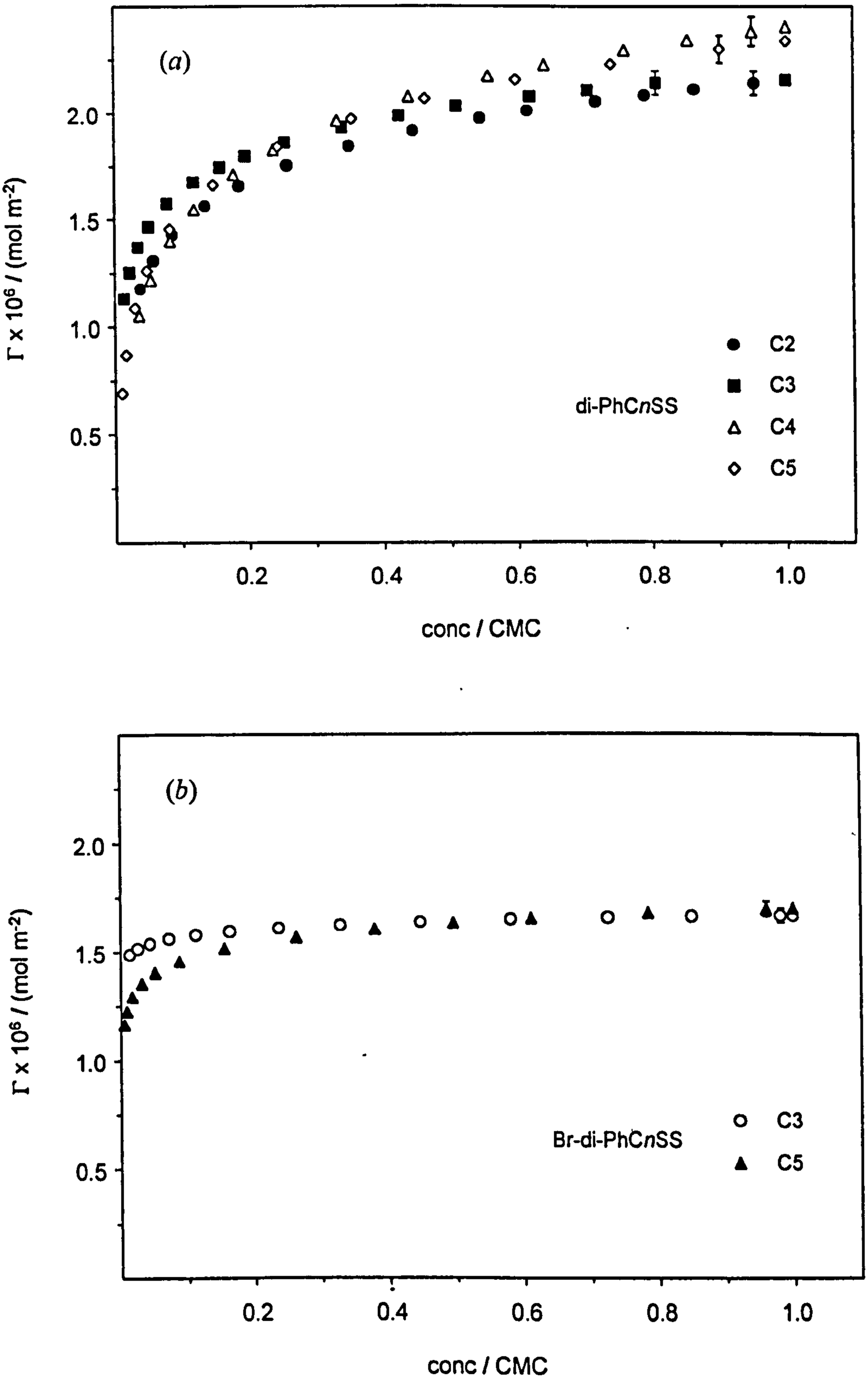

Figure 5.25 Γ vs. reduced concentration adsorption isotherms of phenyl-tipped sulfosuccinates derived from γ–ln a data. (*a*) Linear series, di-PhC*n*SS, (*b*) branched series, Br-di-PhC*n*SS.

For the linear C3 compound, a slight minimum in surface tension was observed around the CMC. This is suggestive of alcohol impurities, left over from the synthesis. As reported in Chapter 4, di-PhC3SS, di-PhC5SS, and the two branched phenyl sulfosuccinates are waxy compounds and could not be re-crystallised. Unless foam fractionation purification is carried out, any trace of organic contaminations (such as alcohols) not effectively removed during the distillation of the diester are likely to affect the tensiometric properties of the surfactant. Foam fractionation is an effective but time-consuming purification technique. Considering the minor effect on surface tension behaviour and poor efficiency of the phenyl sulfosuccinates in microemulsion systems (see Chapter 6), the compounds were not purified further.

CMCs and molecular packing

Replacement of the terminal methyl end group with a phenyl changes significantly the aqueous properties of the surfactant. Parameters derived from Figures 5.24 and 5.25 – i.e., CMCs, and effective head group areas, A_{cmc} – are given in Table 5.11. Figures 5.26 and 5.27 show the variation of CMCs and A_{cmc}, respectively, with the linear part of the chain length, *n*-C. Re-call that each phenyl group was accounted for by 3.5 normal -CH_2- groups (see Section 2.1.3).

For the linear compounds, although the number of compounds studied (C2 to C5) is limited, an even/odd effect is clearly observed. This effect has been reported for various homologous series of soluble amphiphiles both at the air–water [82-84] and liquid–liquid [85] interfaces. More recently, Lukenheimer *et al.* investigated this phenomenon in more detail by studying a–w adsorption of a series of non-ionics, *n*-alkyldimethylphosphine oxides, with a chain length varying from C6 to C14 [52]. CMCs and calculated adsorption parameters (standard free energy of adsorption and limiting surface area per molecule) revealed distinct effects of alternation with even/odd chain length. The reason for such behaviour is still not clearly understood, but one feasible explanation was given in terms of Gutmann's donor–acceptor approach [86]. It states that a donor–acceptor bond is always shortened, whereas that of the neighbouring bond is lengthened to a certain amount. This alternating shortening and lengthening of the bond lengths extends throughout the whole molecule, so that the chain terminal groups should be in a somewhat different molecular state depending on whether they belong to the odd or the even members.

Table 5.11 Parameters derived from surface tension measurements of the linear and branched phenyl-tipped sodium sulfosuccinates

Surfactant	EDTA ratio below CMC	CMC / (mmol dm^{-3})	γ_{cmc} ($\pm$ 1 / mN m^{-1})	A_{cmc} ($\pm$ 2 / Å^2)
di-PhC2SS	2000:1	34.6 ± 0.3	44.6	77
di-PhC3SS	300:1	5.04 ± 0.03	36.9	77
di-PhC4SS	300:1	4.21 ± 0.03	44.1	69
di-PhC5SS	1800:1	0.778 ± 0.003	37.0	71
Br-di-PhC3SS	95:1	13.8 ± 0.3	38.4	100
Br-di-PhC5SS	160:1	1.72 ± 0.03	34.3	98

Table 5.12 Efficiency of phenyl-tipped sodium sulfosuccinates. π_{cmc} is the limiting surface pressure ($\gamma_o - \gamma$). $C_{\pi/2}$ is the concentration of surfactant required to lower the surface tension by half the surface pressure at the CMC, $\gamma_{\pi/2}$

Surfactant	π_{cmc} / (mN m^{-1})	$\gamma_{\pi/2}$ / (mN m^{-1})	$C_{\pi/2}$ / (mmol dm^{-3})	$C_{\pi/2}$ / CMC
di-PhC2SS	27.9	58.6	8.32	0.24
di-PhC3SS	35.6	54.7	0.74	0.15
di-PhC4SS	28.4	58.3	1.06	0.25
di-PhC5SS	35.5	54.8	0.13	0.17
Br-di-PhC3SS	34.1	55.5	1.50	0.11
Br-di-PhC5SS	38.2	53.4	0.14	0.08

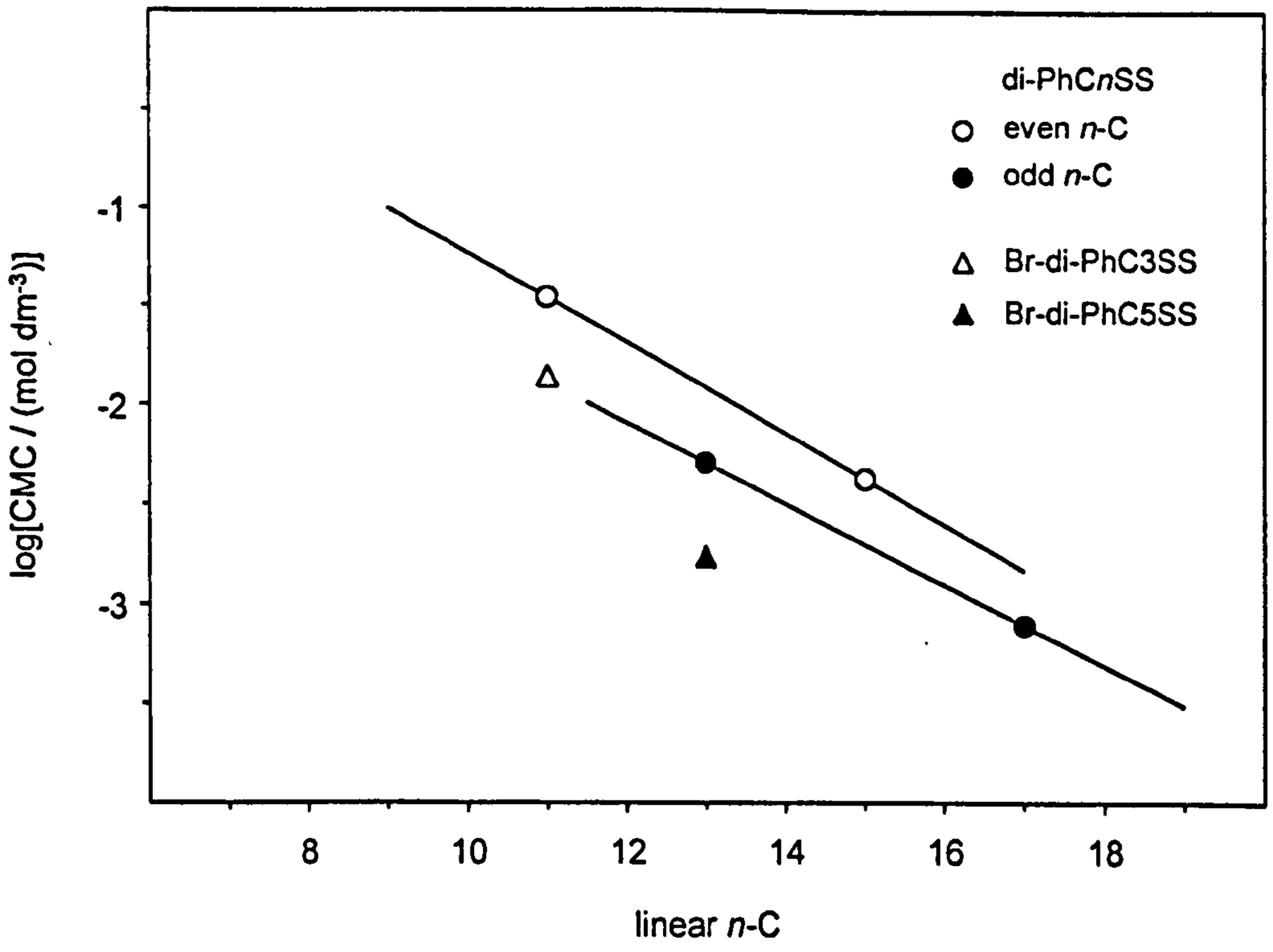

Figure 5.26 Variation of the CMC with the carbon number of the longest linear portion, for both linear and branched phenyl-tipped sulfosuccinate surfactants.

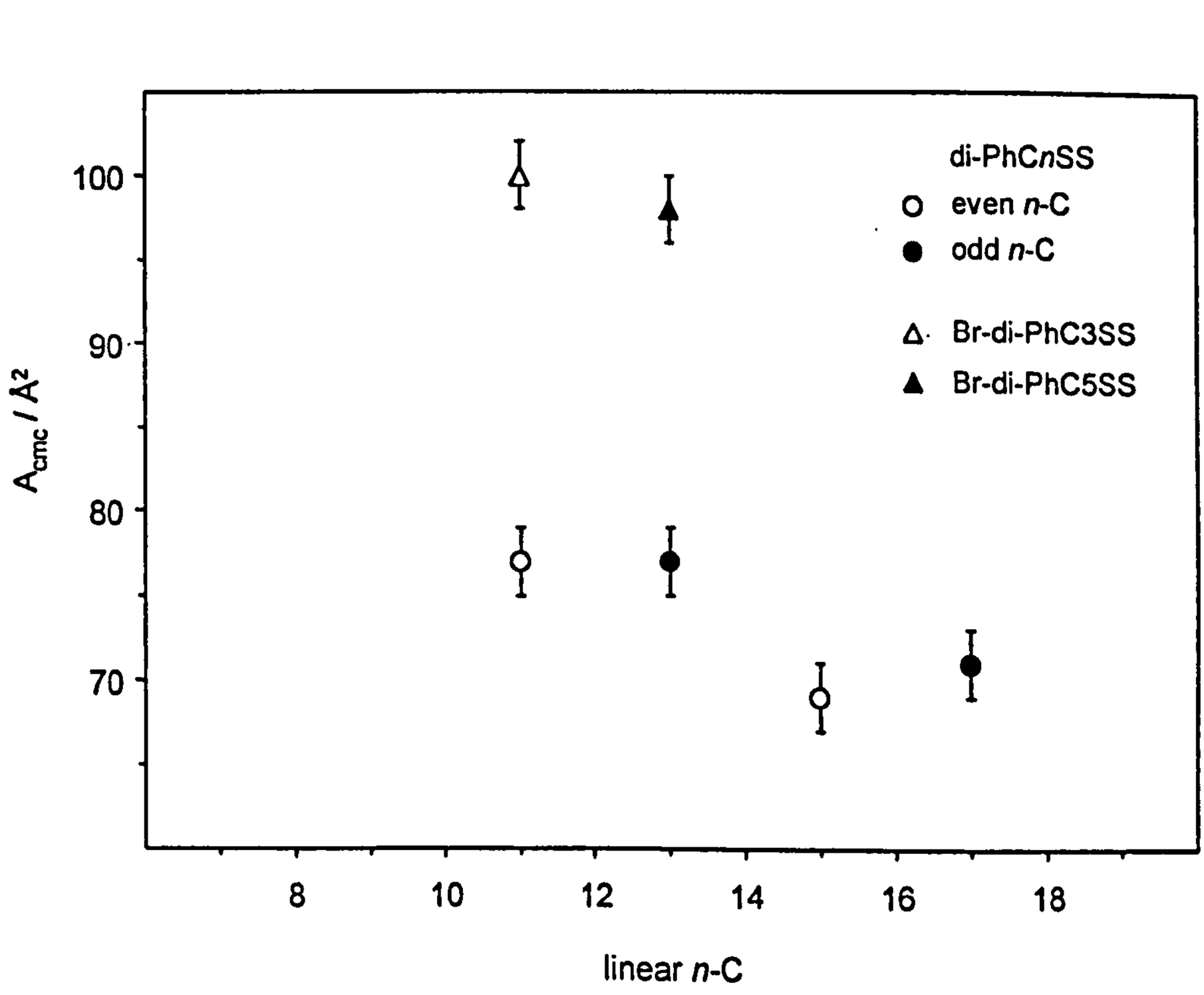

Figure 5.27 Variation of the head group area, A_{cmc}, with the carbon number of the longest linear portion, for di-PhC*n*SS surfactants.

Here with a rather bulky terminal group, this effect may be much more pronounced than for simple *n*-alkyl chain compounds such as the di-C*n*SS and AOTs series. The limited extent of chain length involved in the study of the di-*n*-alkyl sulfosuccinates may also explain why no even/odd effect could be observed. It has been reported that amphiphiles of relatively simple molecular structures, such as *n*-alkyldimethylphosphine oxides, *n*-alkanoic acids, and *n*-alkanols, exhibit only small differences between the even- and odd-membered characteristics [83].

Supporting this phenomenon are values of molecular head group areas obtained for the linear phenyl sulfosuccinates (Table 5.11). In contrast to their di-*n*-alkyl analogues, the decay in A_{cmc} is not observed upon addition of each methylene group, but rather on addition of every 2 groups, i.e., following the even/odd series. However, it should be re-called that a larger number of homologues should be investigated to confirm such a trend. A limitation is the difficulty to synthesise longer di-chain phenyl sulfosuccinates of high chemical surface purity. From a more general viewpoint, A_{cmc} values correlate with molecular geometric features, i.e., the presence of the phenyl group increases the molecular volume of the tail in comparison to a simple alkyl chain, thus giving rise to a less dense adsorbed monolayer (increased A_{cmc}).

Turning to adsorption properties of the two branched phenyl sulfosuccinates, results from tensiometry are unsurprising. When comparing compounds according to their effective chain length (linear *n*-C only), i.e., Br-di-PhC3SS/di-PhC2SS and Br-di-PhC5SS/di-PhC4SS, addition of alkyl side branches decreases the CMC (see Figure 5.26). When considering the total number of carbon atoms, i.e., Br-di-PhC3SS/ di-PhC3SS and Br-di-PhC5SS/di-PhC5SS, the branched compounds show higher CMC's due to more favourable hydrophobic interactions in the monomeric solution, i.e., larger "oil-like" surface area for the branched tails. With regard to molecular packing at the surface, once again, A_{cmc} values show that both branching and presence of a phenyl group give a "bulkier" hydrophobic group, and thus a less efficient molecular packing.

Efficiency and effectiveness

As before, the efficiency of the phenyl sulfosuccinates may be evaluated by calculating the concentration of surfactant required to lower the surface tension by half the surface pressure at the CMC, $C_{\pi/2}$. Table 5.12 summarises the data. Once again, within the linear series, efficiency increases with alkyl chain length and the even/odd alternation is also observed. When compared to their di-*n*-alkyl analogues (see Table 5.9), assuming a phenyl group is equivalent to about 3.5 -CH_2- groups, the trend of efficiency (as given by $C_{\pi/2}$) increasing with *n*-C is still valid.

A striking difference observed upon replacement of the methyl end group with a phenyl group is the change in limiting surface tensions, γ_{cmc}. The introduction of the relatively polarisable phenyl group, that contains a large area of delocalised electrons, increases γ_{cmc} to above 40 mN m^{-1} for the even-members of the linear series (see Table 5.11). Phenyl end groups thus decrease the surfactant effectiveness, of both the linear and branched series. Similar high γ_{cmc} values have been reported by Pitt *et al.* [79] who studied the effect of the chemistry of terminal groups in di-chain and tri-chain anionic series (sodium sulfosuccinates and sulfotricarballylates) on limiting surface tensions. Varying from fluoroalkyl ($CF_3.[CF_2]_n$– and $H.[CF_2.CF_2]_n$–) through alkyl (with methyl branches) to aryl groups gives a progressive decrease in effectiveness of the surfactant (i.e., increase in γ_{cmc} values). They also reported values for non-ionic sugar-based surfactants containing aryl-ended tails and *n*-alkyl tails (classed as two-tail bisgluconamides), of chemical structure $[CH_2.NH.CO.(CHOH)_4CH_2OH]_2 - C - R_2$ with R = phenyl.$(CH_2)_3$, and *n*-C_6H_{13}, respectively. The limiting values of 41 mN m^{-1} and 31 mN m^{-1}, respectively, commensurate with those obtained in the present study for the corresponding sufosuccinates, i.e., di-PhC3SS and di-C6SS (compare 37 mN m^{-1} and 29 mN m^{-1}).

An overall comparison of all the double-tailed sulfosuccinates studied in this work therefore gives the following trend, in terms of surfactant effectiveness and chemistry of the terminal group: CH_3CH_2- > -CH_2-CH_2- > phenyl-. This observation agrees with previous reported results [79].

5.4 LIQUID CRYSTALLINE MESOPHASES

To complete the physico-chemical characterisation, the concentrated surfactant region was studied through identification of liquid crystalline mesophases formed on dilution of the pure solid surfactant. Liquid crystal phases have been introduced in Section 2.4 and only a description of the experimental procedure is briefly given here. Rather than a complete construction of the phase map, i.e., varying temperature and surfactant concentration, the study was limited to "phase-cut" experiments at constant temperature, which allow the different liquid crystal structures to be identified. Observations can then be discussed in terms of surfactant structures.

5.4.1 Polarising light microscopy

A convenient way to examine liquid crystal phase behaviour of surfactants is to make use of their birefringence. A brief description of the principle of birefringence and response to polarised light follows, more details can be found elsewhere [87-89]. The refractive index of a substance is dependent on electron density, and optical anisotropy in the sample arises from anisotropic electron distribution in the material. Surfactants in liquid crystals have anisotropically orientated head groups, and hence liquid crystalline mesophases can have a direction-dependent refractive index, i.e., they are birefringent.

Figure 5.28 illustrates the effect of passing a plane-polarised light through such samples. Recall first that an unpolarised light beam entering a birefringent material may be considered to be resolved into two beams, oscillating in mutually perpendicular planes [87]. When the birefringent material is placed between crossed polars, its appearance in the field of view then depends on the orientation relative to the plane of polarised light. Referring to Figure 5.28 (*a*) and (*c*), since one of the two principal optical axes of the material is parallel to the light polarisation, polarised light leaves the sample as it entered along either of the vibration directions. Subsequently, the beam is blocked by the second polar (the analyser), set at 90° to the first one, and the material appears dark in the field of view.

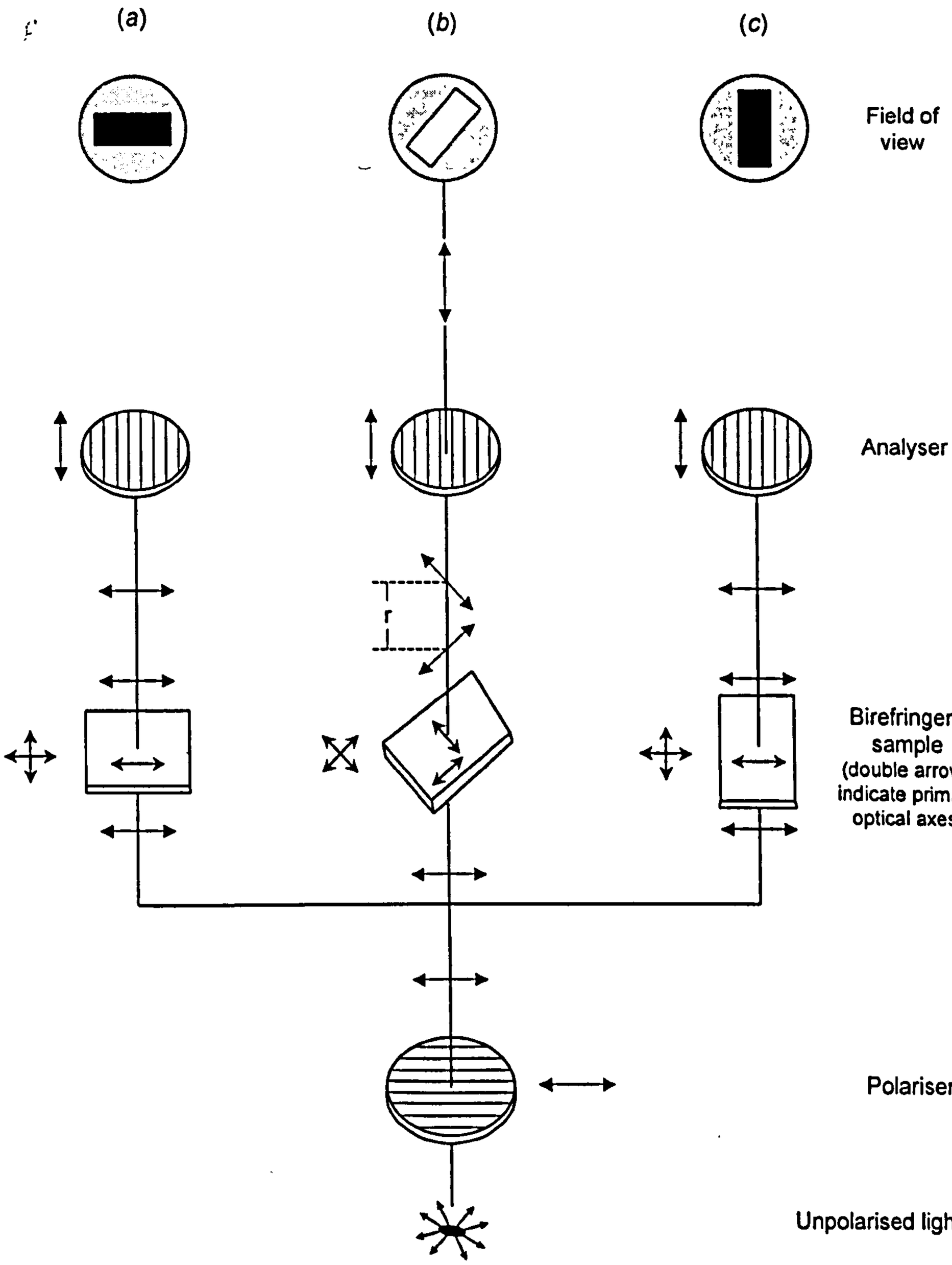

Figure 5.28 Appearances of a birefringent material between crossed polars (redrawn from [87]).

Now referring to Figure 5.28 (*b*), if the optical axes of the sample are out of alignment with the light, the beam is resolved into the two perpendicular components, refracted at boundaries of different refractive indices. Both are partially transmitted by the analyser and the sample therefore appears bright. As the refractive index is direction dependent, the two components travel at different speeds, causing a phase difference. This interference gives rise to different patterns characteristic of the mesophase present. The phase difference on emerging depends on the difference in refractive indices and the thickness of the sample. In the case of non-birefringent samples, there is no interaction and the beam passes through unchanged. The sample therefore appears dark when viewed through crossed polarisers.

For this work, a Nikon Optiphot-2 microscope fitted with polarising filters and a Linkam heating/cooling stage was used. Images were captured digitally on a PC via a video camera and colour video copy processor connected to the microscope.

The liquid crystal phase progression of each surfactant was investigated by the solvent penetration method (i.e., phase cut experiment). A small amount of surfactant was placed on a microscope slide, under a cover slip. The slide was mounted on the heating stage and the temperature was raised until the sample became fluid and entirely isotropic. After slowly cooling the sample (1.0 °C min^{-1}) to 25°C, a drop of water was added at the edge of the cover slip. As the water penetrated the surfactant, a concentration gradient was produced from water at one side to pure surfactant at the other, enabling the whole range of mesophases to be observed.

5.4.2 Influence of chain structure

With no added water, at 25 °C, all sodium sulfosuccinates exhibit the fan-like texture characteristic of hexagonal phases. The corresponding pictures for the three series are shown in Figures 5.29(*a*), 5.30(*a*), and 5.31(*a*). Phase-cut diagrams after water penetration for each of the surfactants are given in parts (*b*) and (*c*) of Figures 5.29 to 5.31. The liquid crystal region of Aerosol-OT phase diagram has been introduced in Chapter 2 (see Figure 2.8). The positions and appearance of the different

regions are well characterised, and hence this provides a reference for the structurally related succinates discussed here. The characteristic phase progression of AOT with decreasing surfactant concentration is detailed below.

- Reverse hexagonal (H_2): fan-like or mosaic texture, at the highest surfactant concentration.
- Cubic (V_2): non-birefringent
- Lamellar (L_α): parallel streak pattern, sometimes with Maltese-cross shaped spherulites
- Myelins: small dynamic regions of the lamellar phase, positioned where the lamellar phase gives way to an isotropic solution
- Micellar solution: non-birefringent, at the greatest water concentration.

For most compounds studied in this work, the phase progression noted above was observed, although myelins did not always show up. Given the very close molecular geometry of the surfactants and the similarities in their dilute aqueous properties, this is fairly unsurprising. A few exceptions are to be noted though. On increasing chain length within the di-C*n*SS series no cubic phase was visible for the C8 and longer chained surfactants, with the transition appearing to be directly from reverse hexagonal to lamellar. This idea of a limited phase behaviour as chain length increases is also observed in the phase progression of di-PhC5SS, where the occurrence of a very thin intermediate cubic phase can just be determined. With di-PhC5SS chains corresponding to approximately two C8.5, this means that the limit in chain length giving normal phase progression is about a C8 or C9. Supporting information comes from liquid crystal phase maps of related fluorocarbon sulfosuccinates [90]. Short chain compounds such as di-CF2 and di-HCF4 gave the same phase progression as di-C5SS and di-C6SS, whereas the longer chain compound di-HCF6 showed behaviour analogous to di-C8SS. One last phase progression "anomaly" to be reported is the phase map of AOT④ where no discernible change in liquid crystal phase was observed. This is rather surprising since its homologue AOT③, which is only shorter by one carbon atom per linear chain, does show the typical phase diagram. One explanation could be down to the total number of carbons per chain (i.e., including branches) being C9, and therefore corresponding to the same limiting chain length as observed for di-C8SS and di-Ph-C5SS.

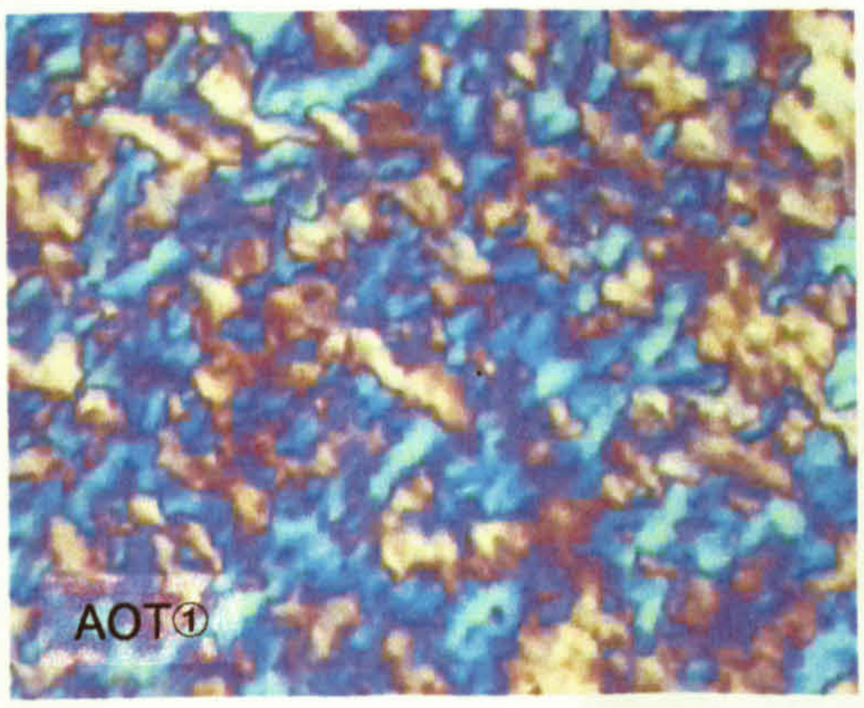

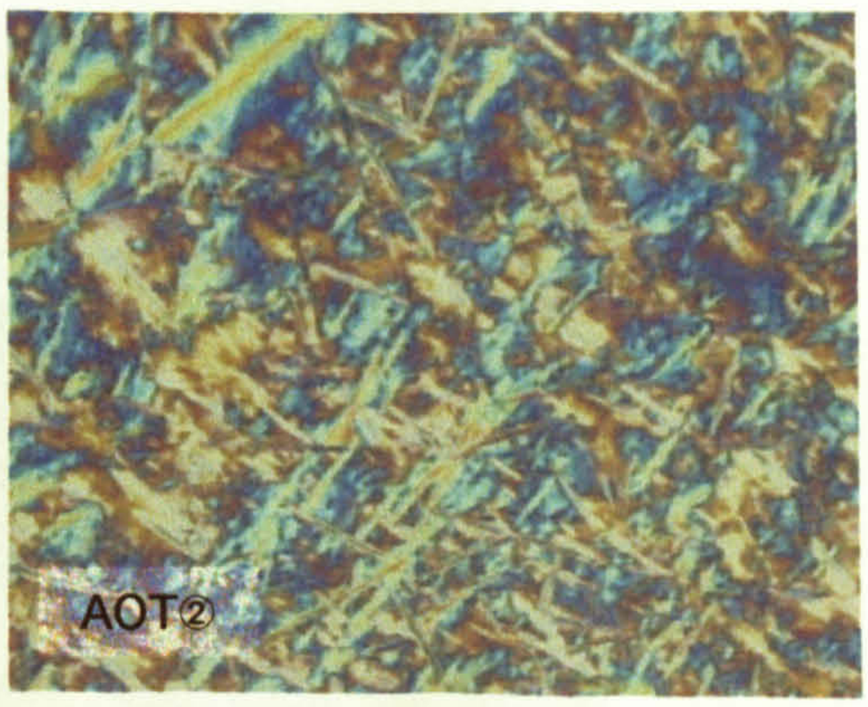

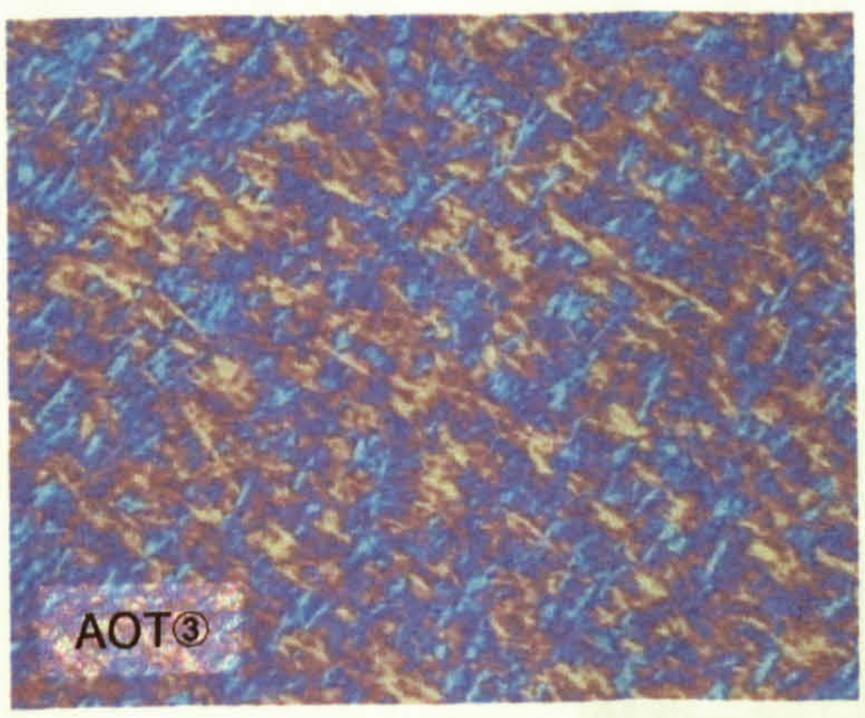

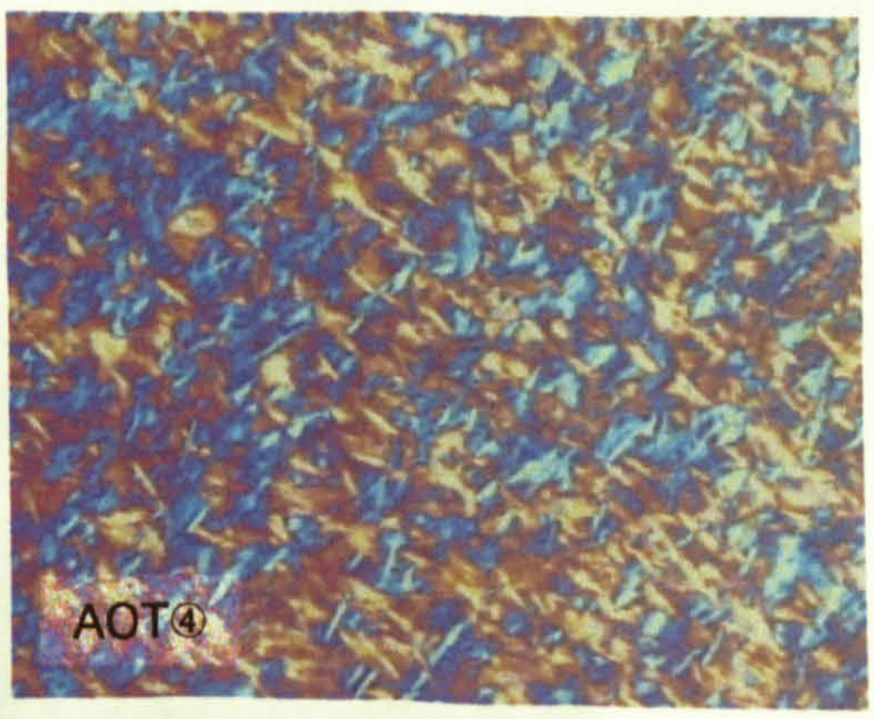

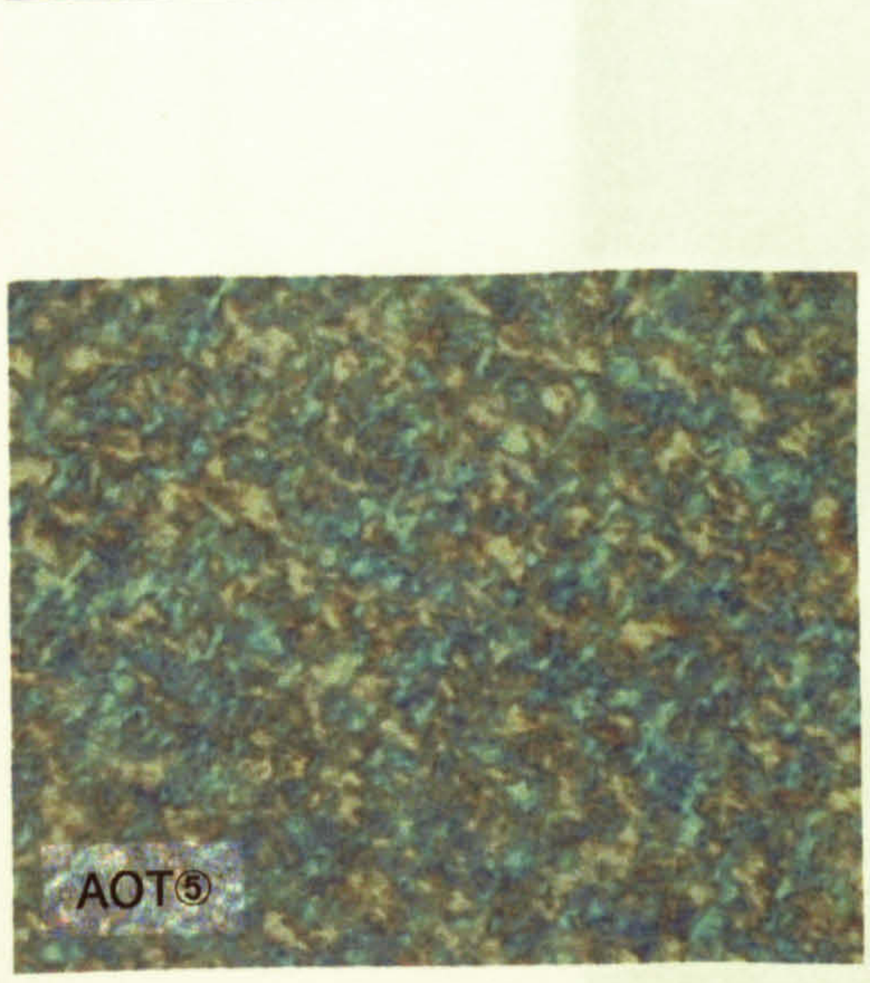

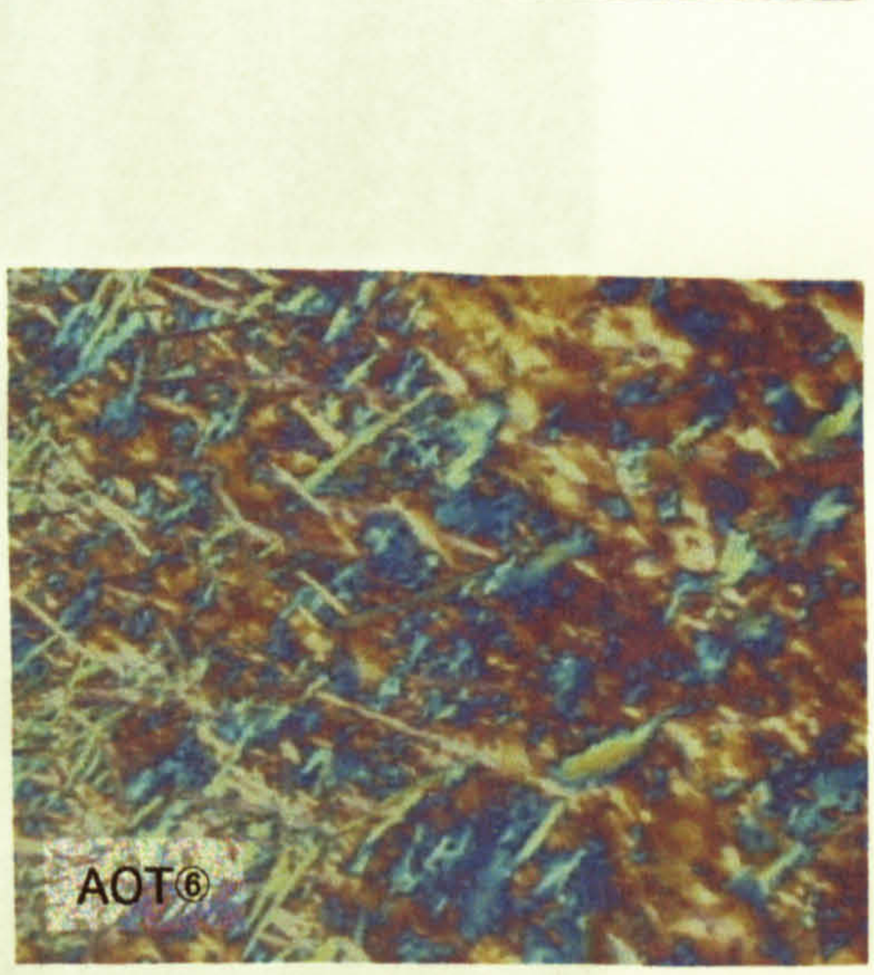

Figure 5.29(*a*) Polarising light microscope pictures of AOTs series: solid phase before water penetration (reverse hexagonal phase, H_2).

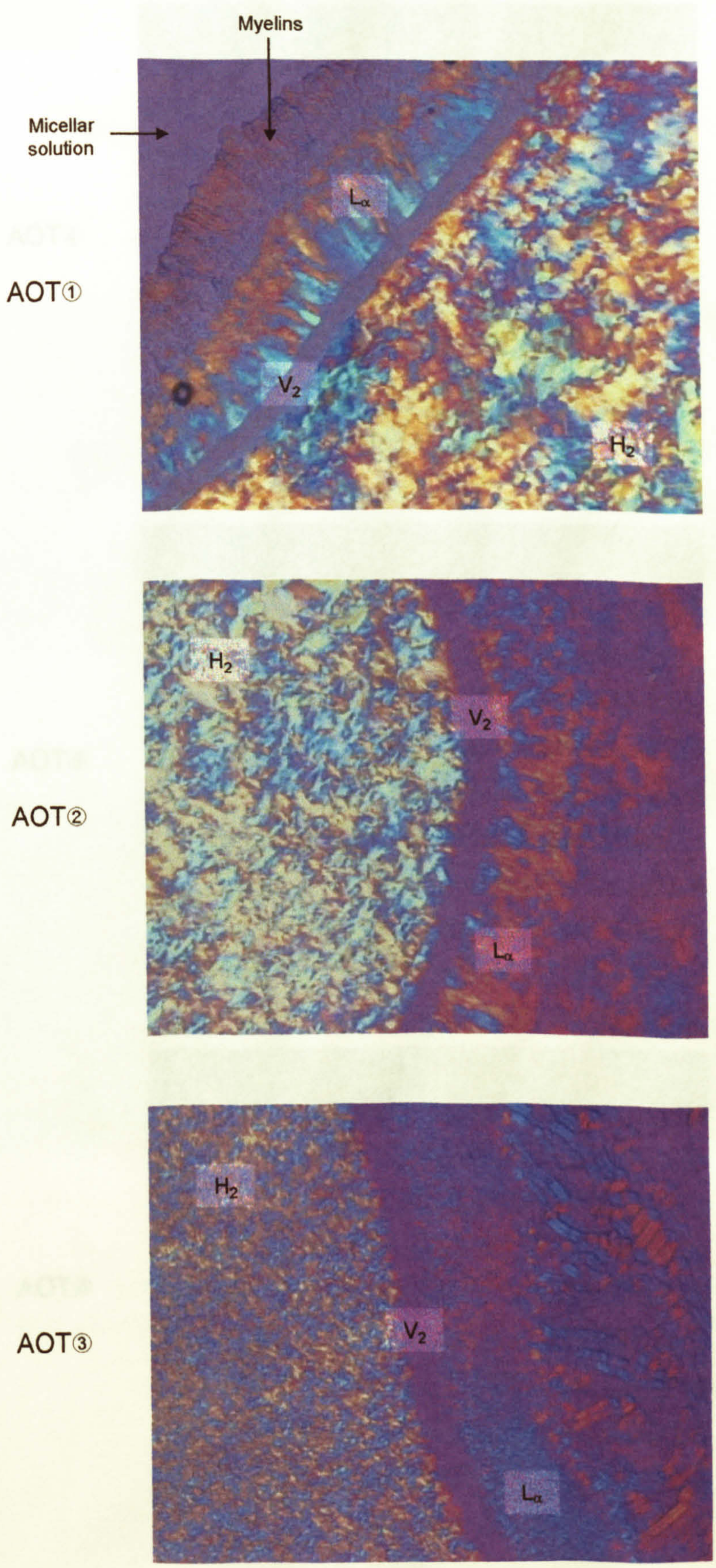

Figure 5.29(*b*) Liquid crystalline phases formed by AOT①, -②, and -③ after water penetration (see text for details of phase structures and symbols).

AOT④

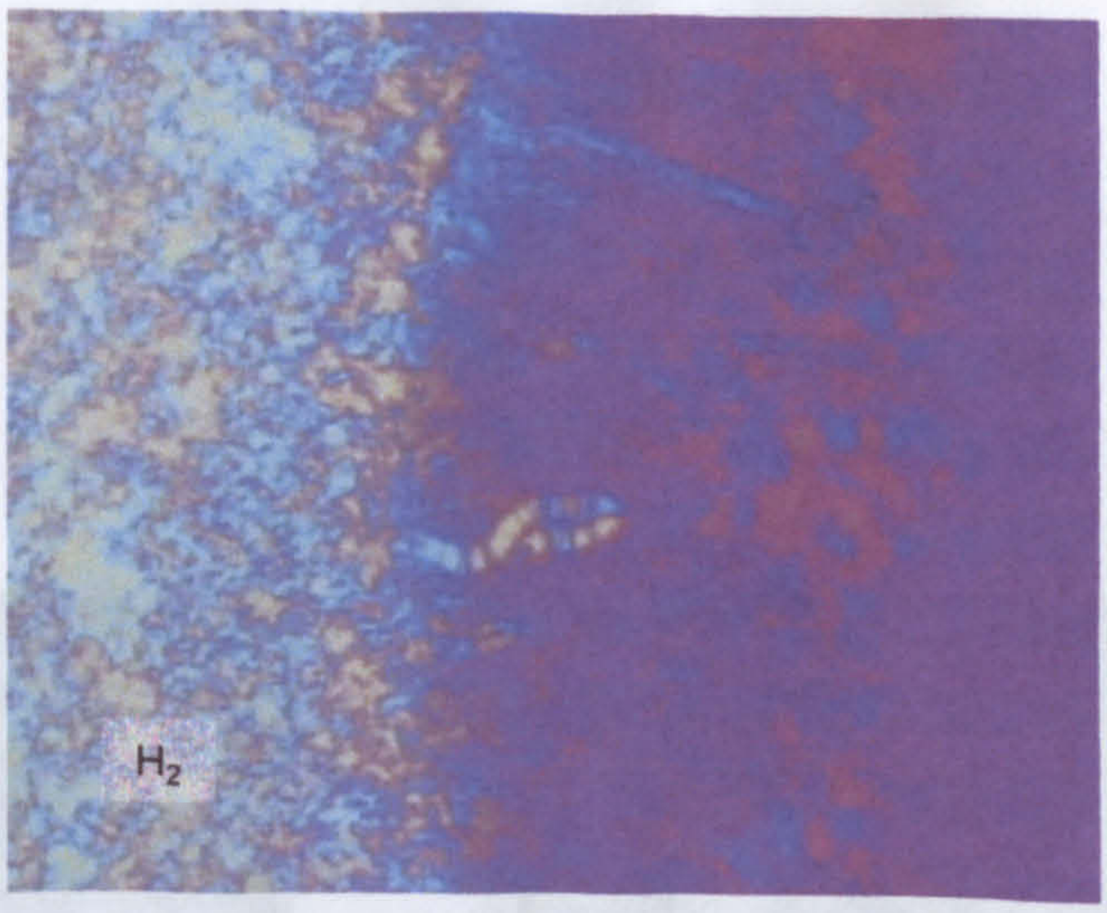

AOT⑤

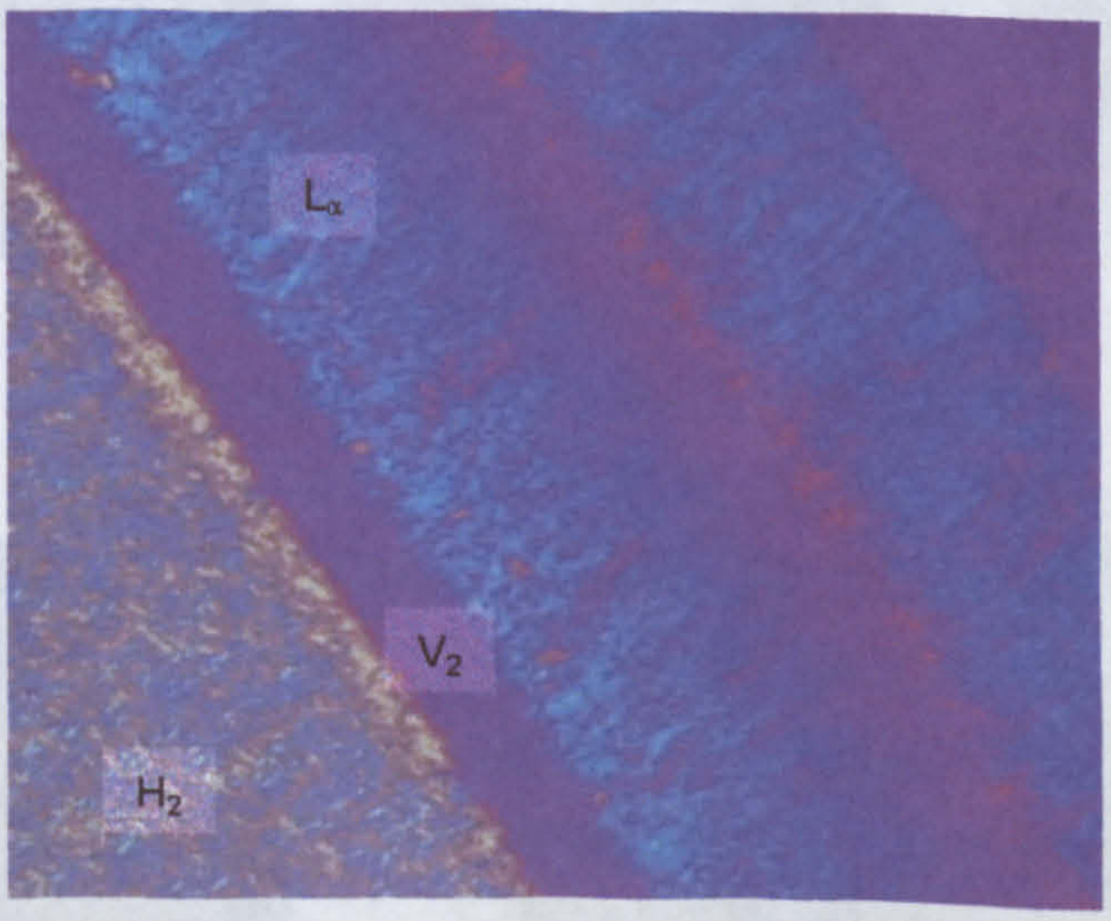

AOT⑥

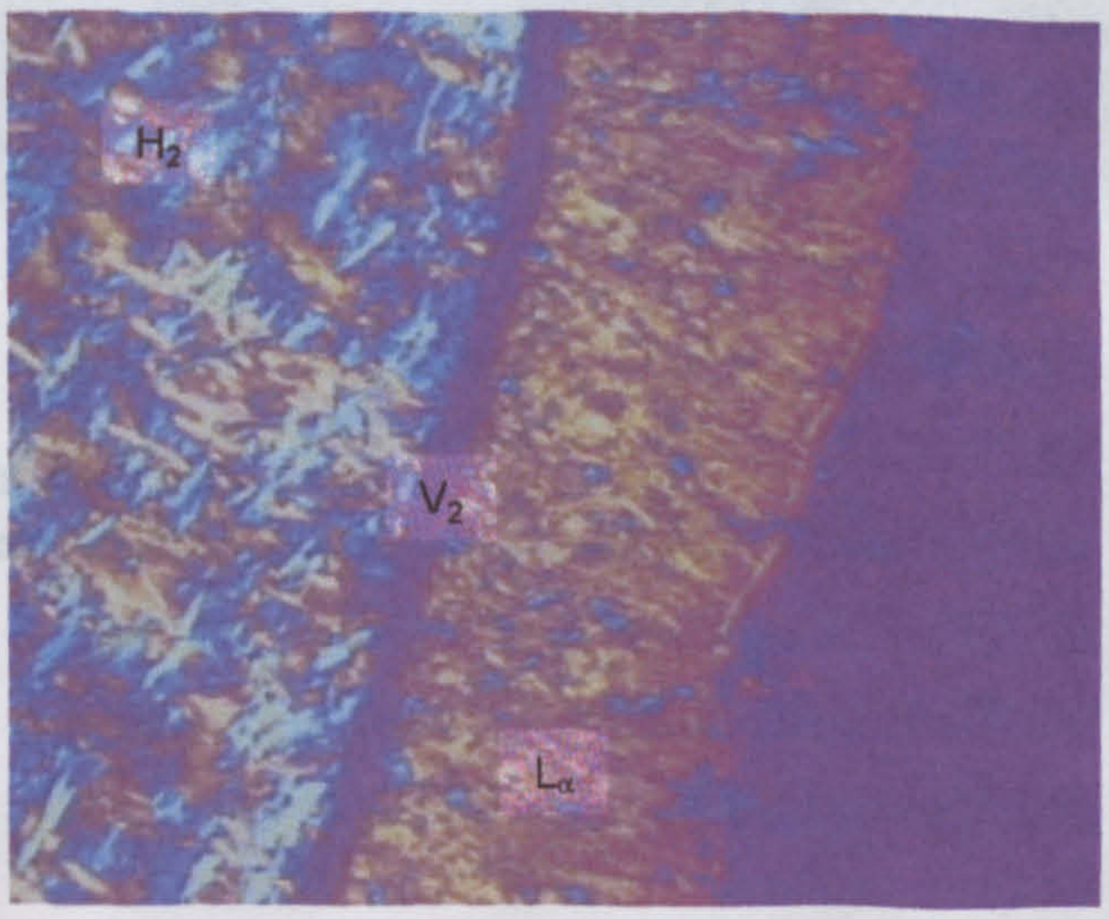

Figure 5.29(*c*) Liquid crystalline phases formed by AOT④, -⑤, -⑥ after water penetration.

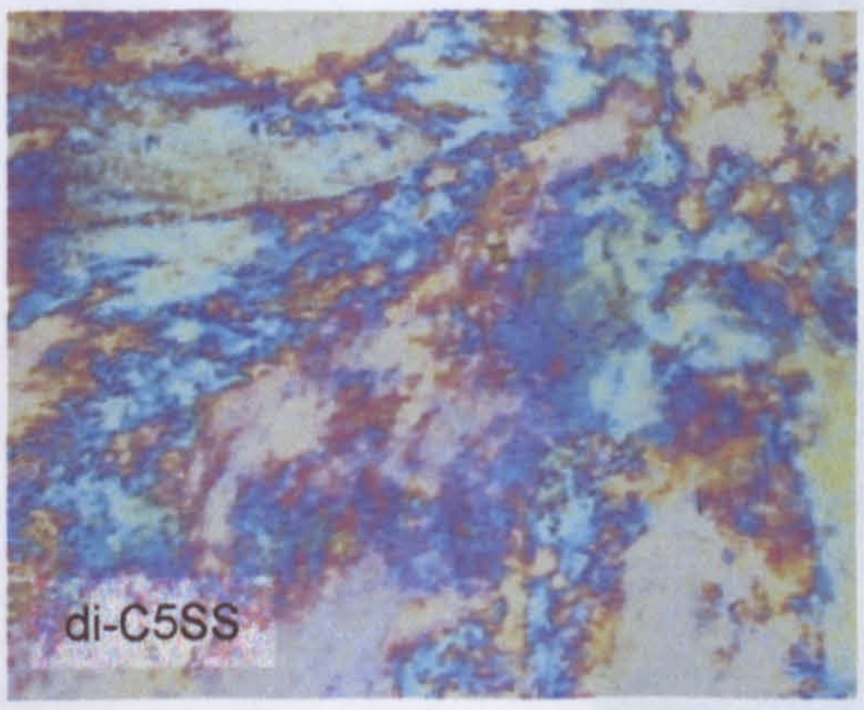

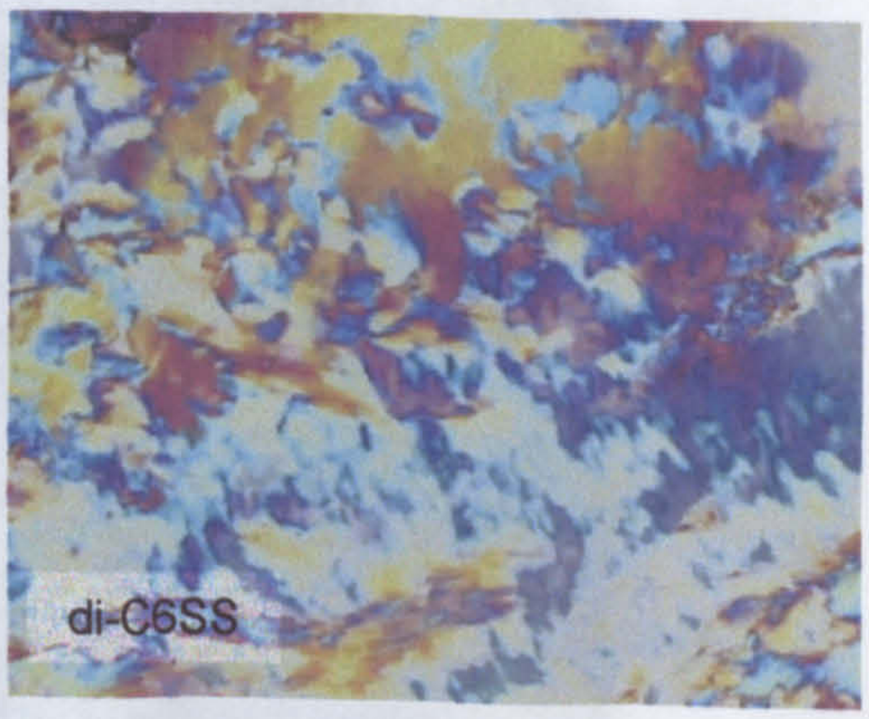

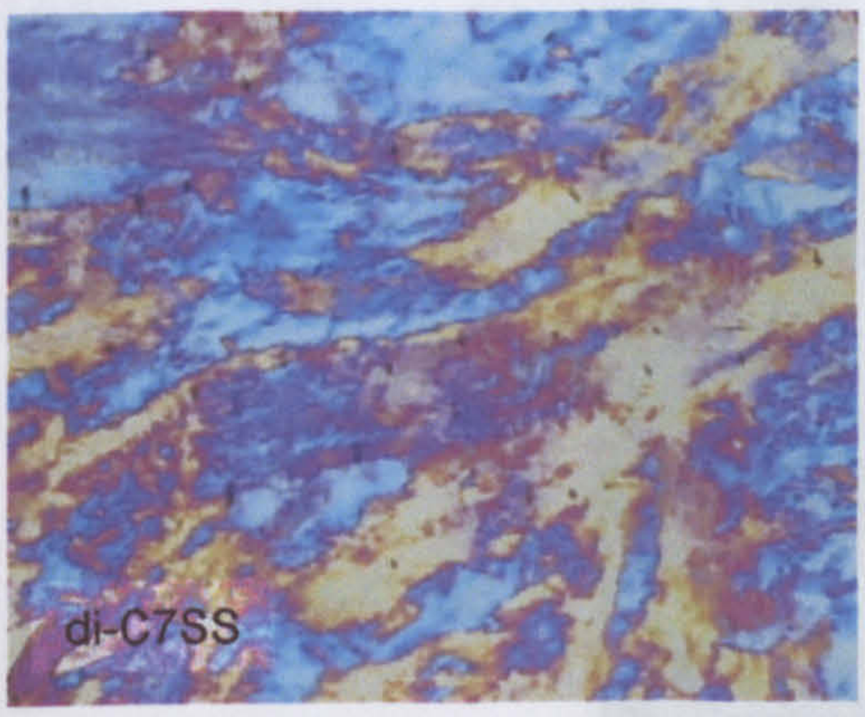

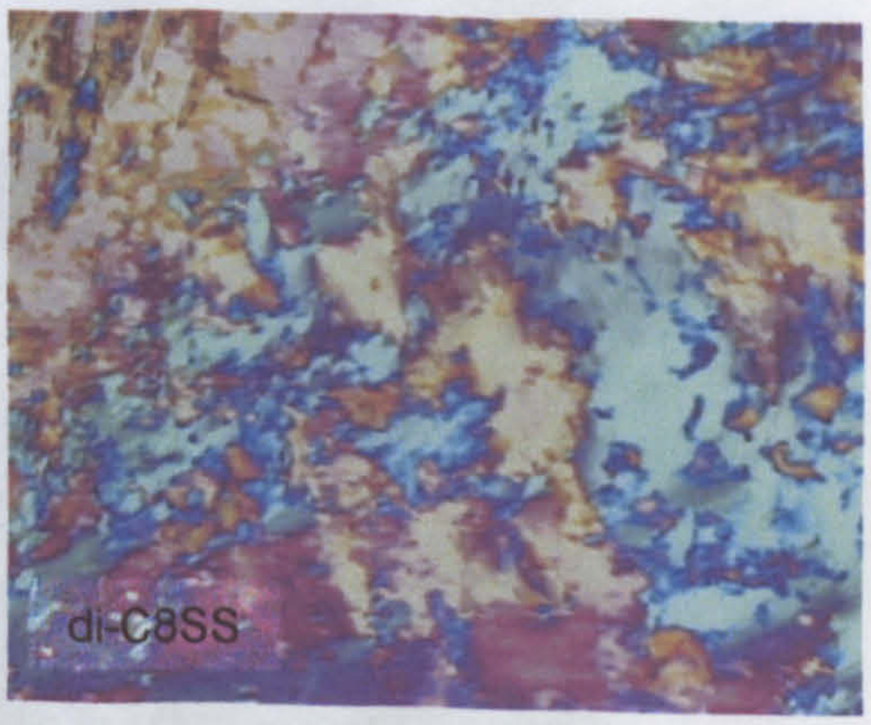

Figure 5.30(*a*) Polarising light microscope pictures of di-C*n*SS series: solid phase before water penetration (reverse hexagonal phase, H_2).

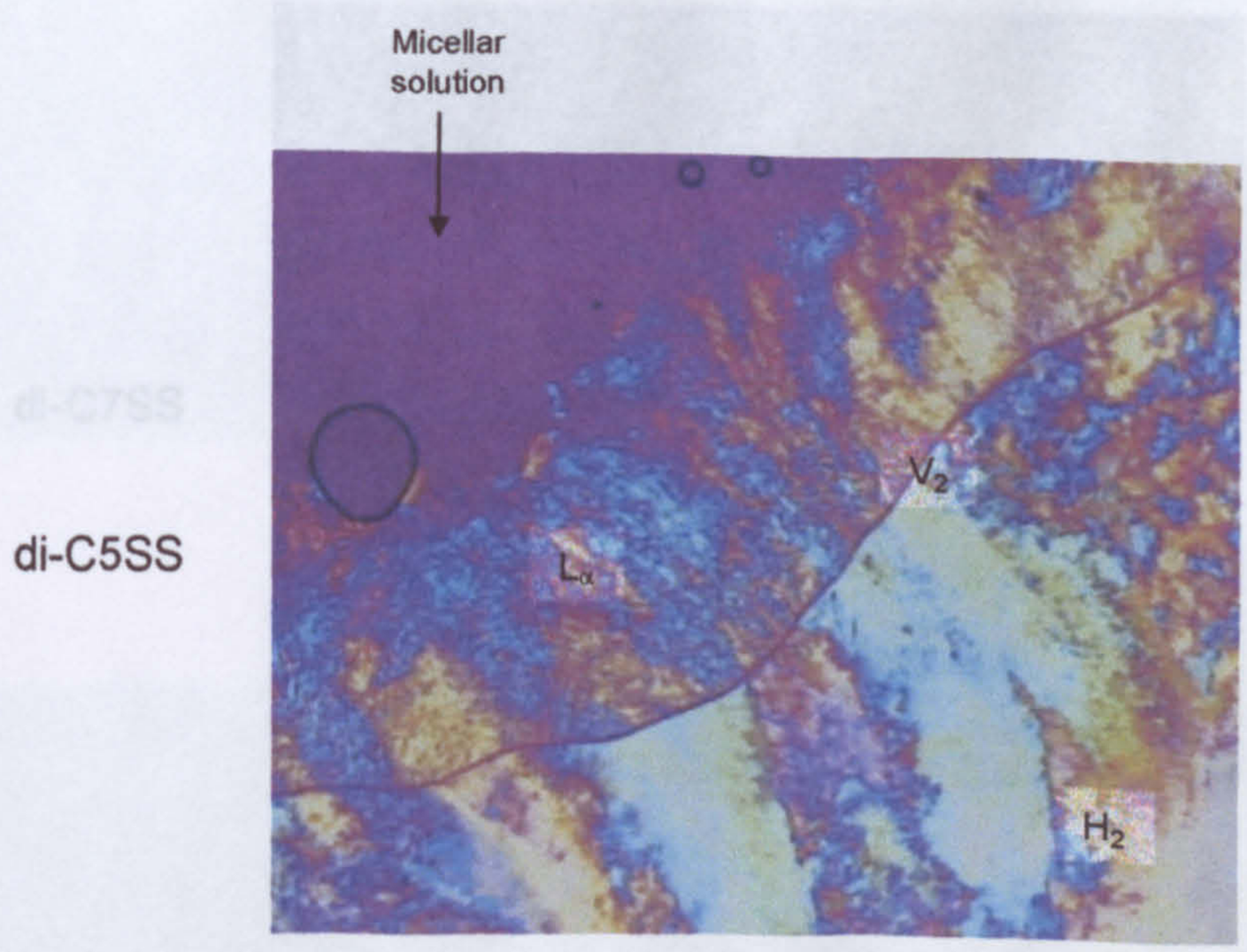

Figure 5.30(*b*) Liquid crystalline phases formed by di-C5SS and di-C6SS after water penetration.

di-C7SS

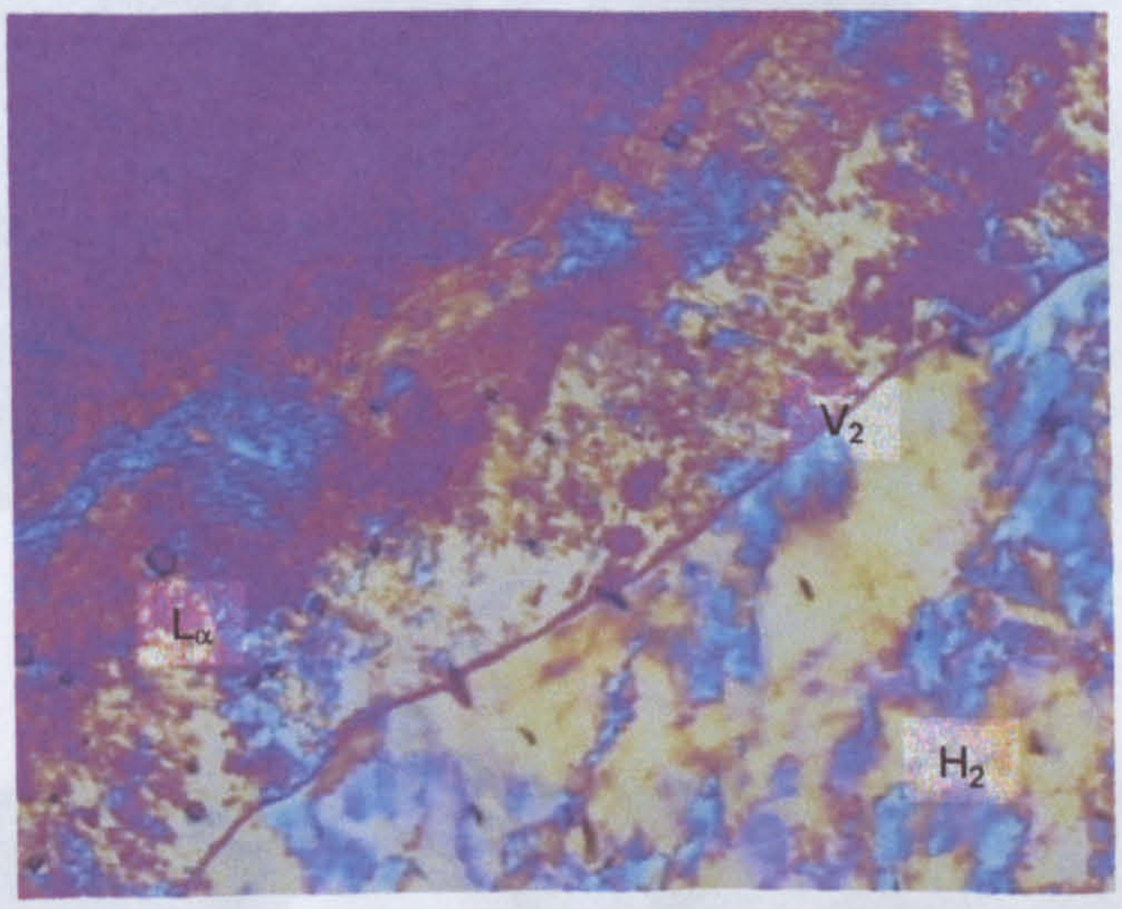

di-C8SS

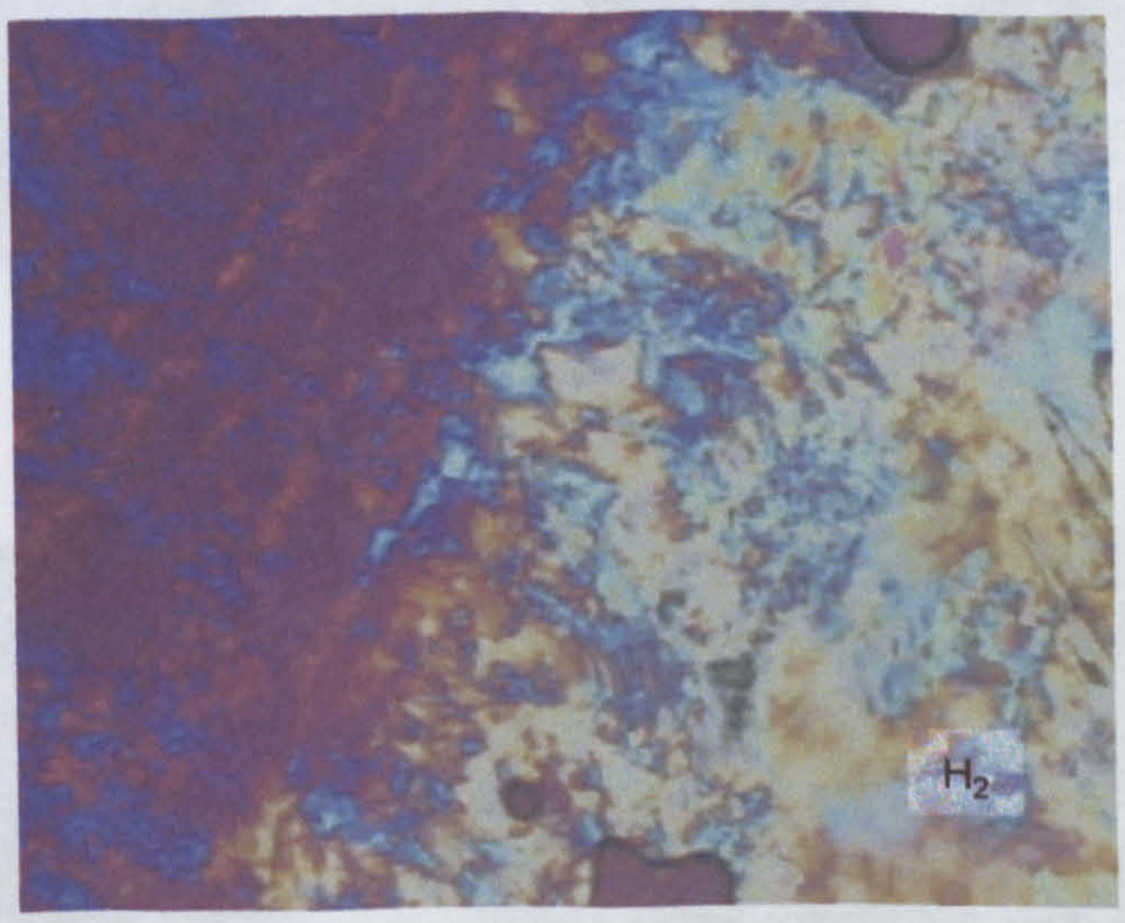

Figure 5.30(*c*) Liquid crystalline phases formed by di-C7SS and di-C8SS after water penetration.

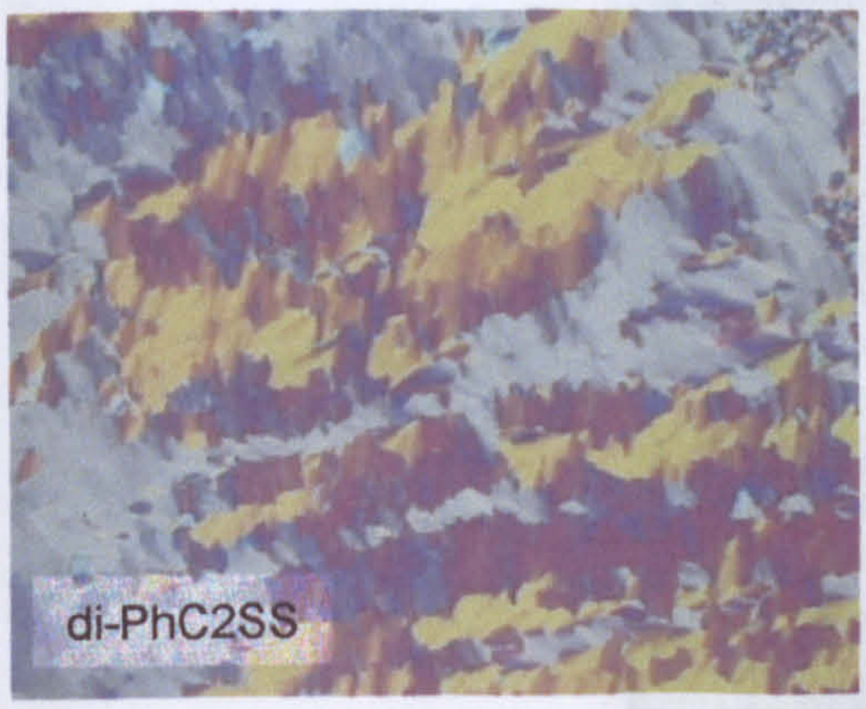

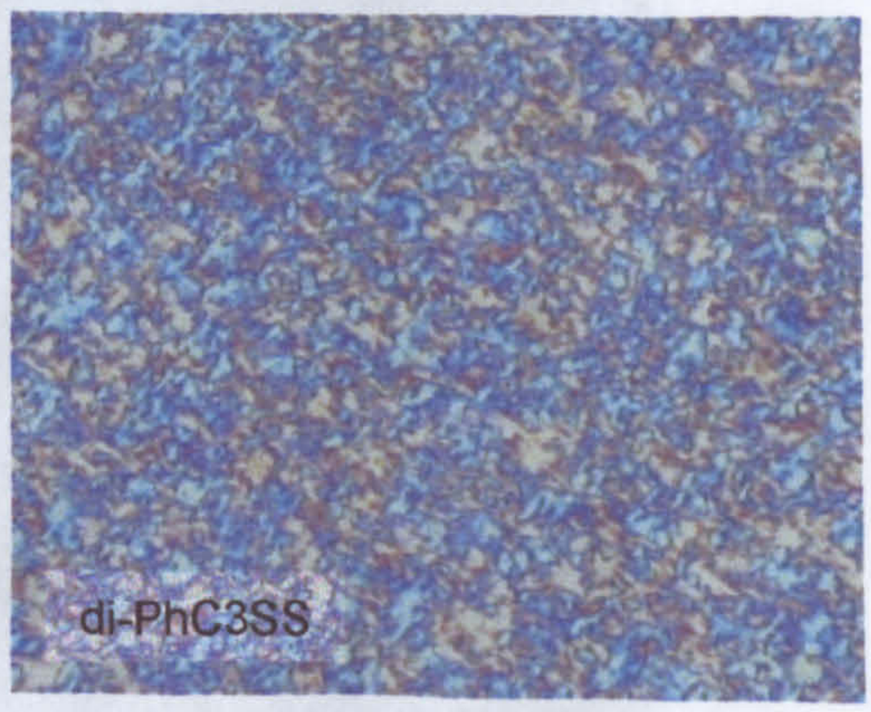

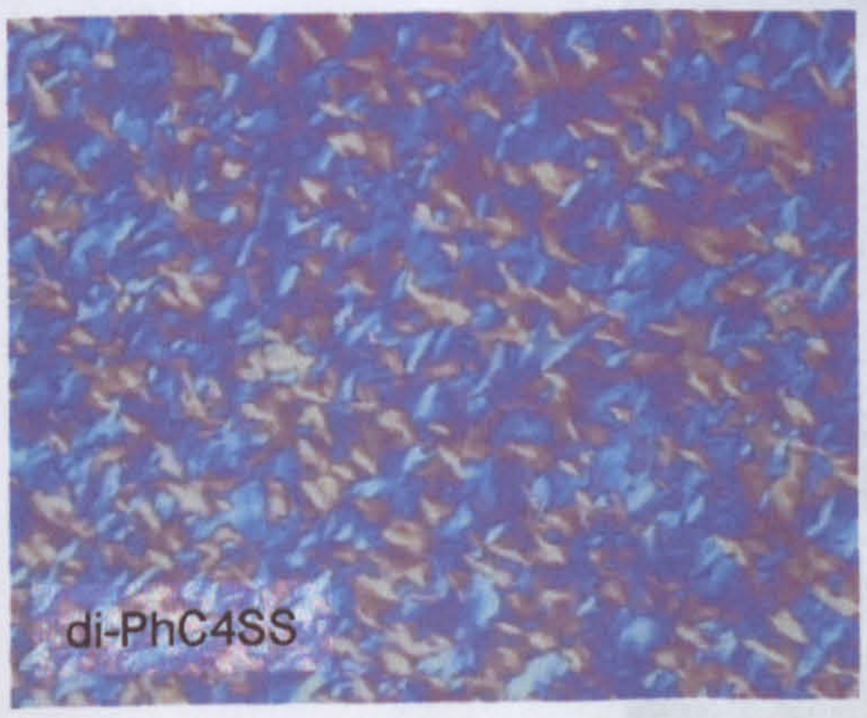

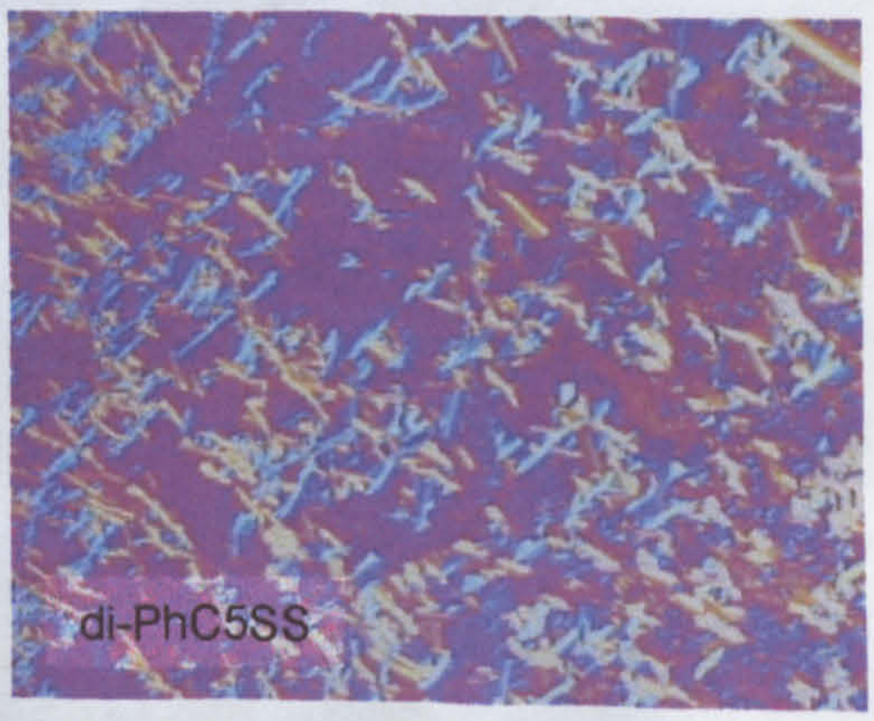

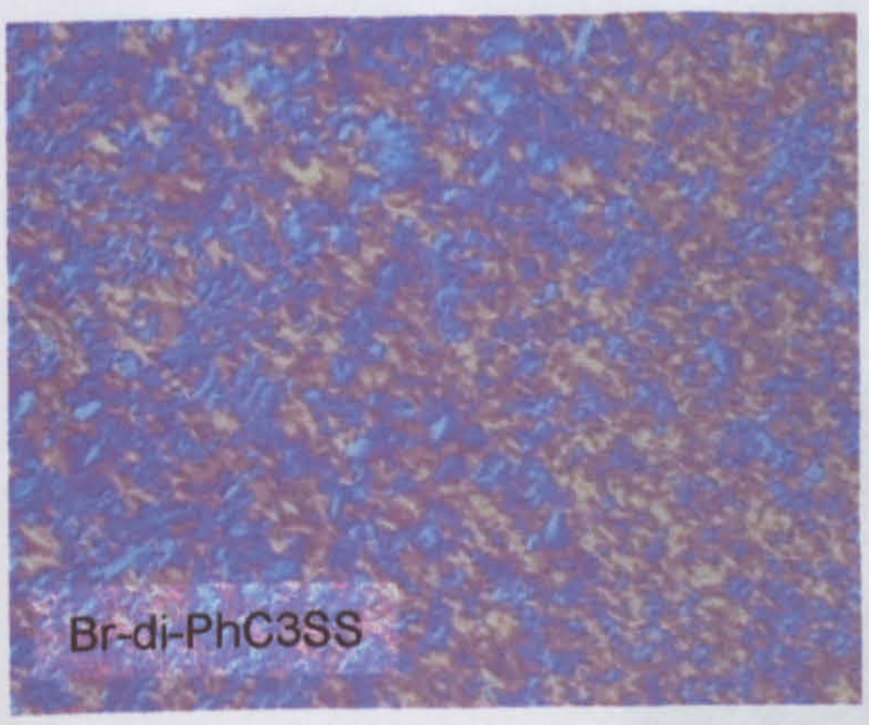

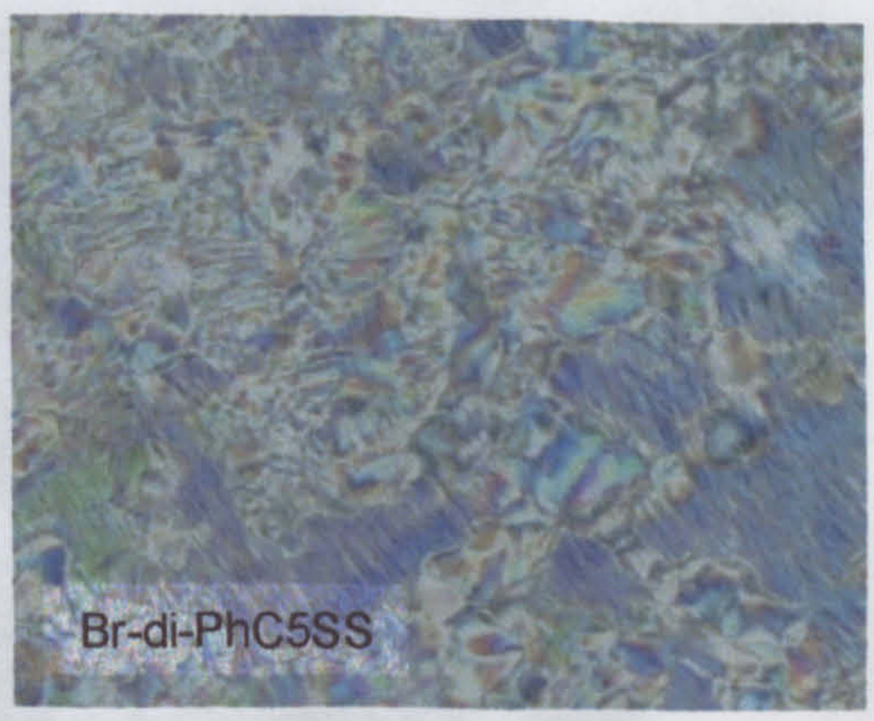

Figure 5.31(*a*) Polarising light microscope pictures of di-PhC*n*SS and Br-di-PhC*n*SS series: solid phase before water penetration (reverse hexagonal phase, H_2).

di-PhC2SS

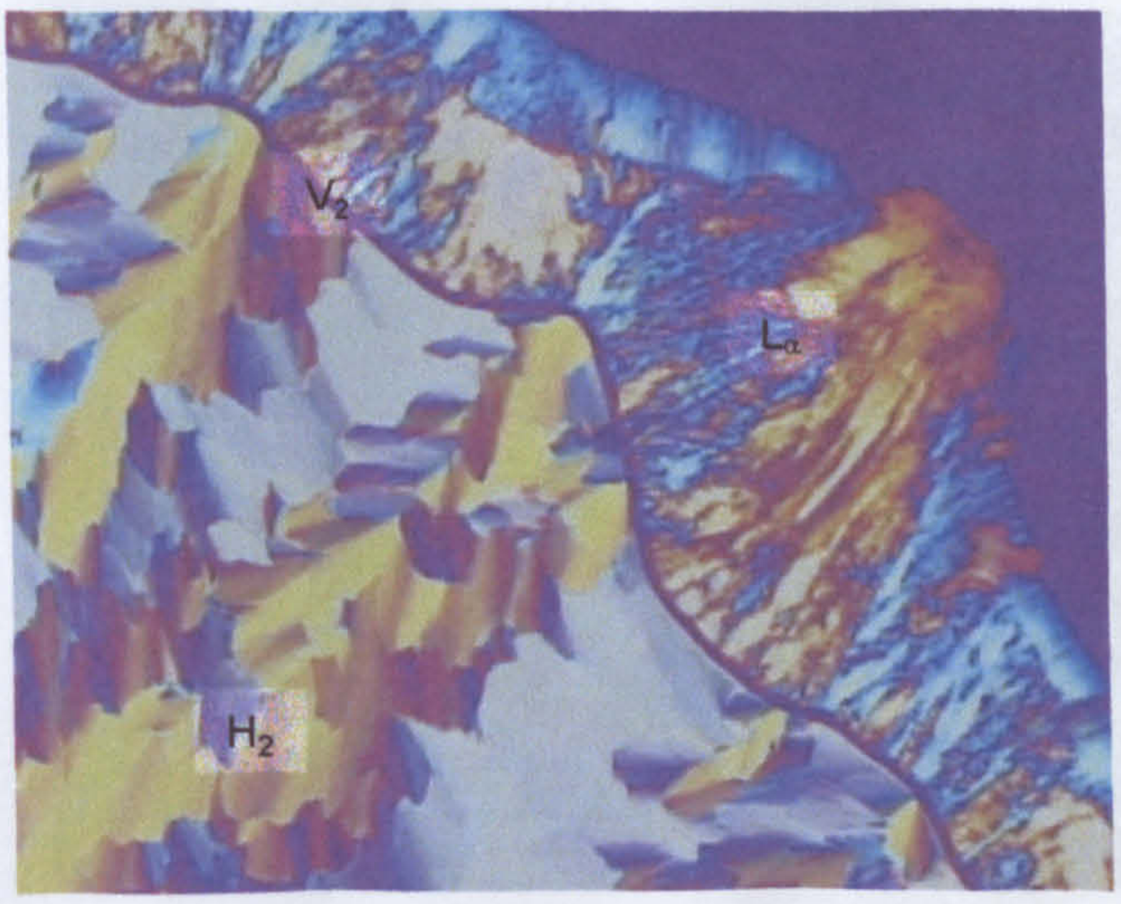

di-PhC3SS

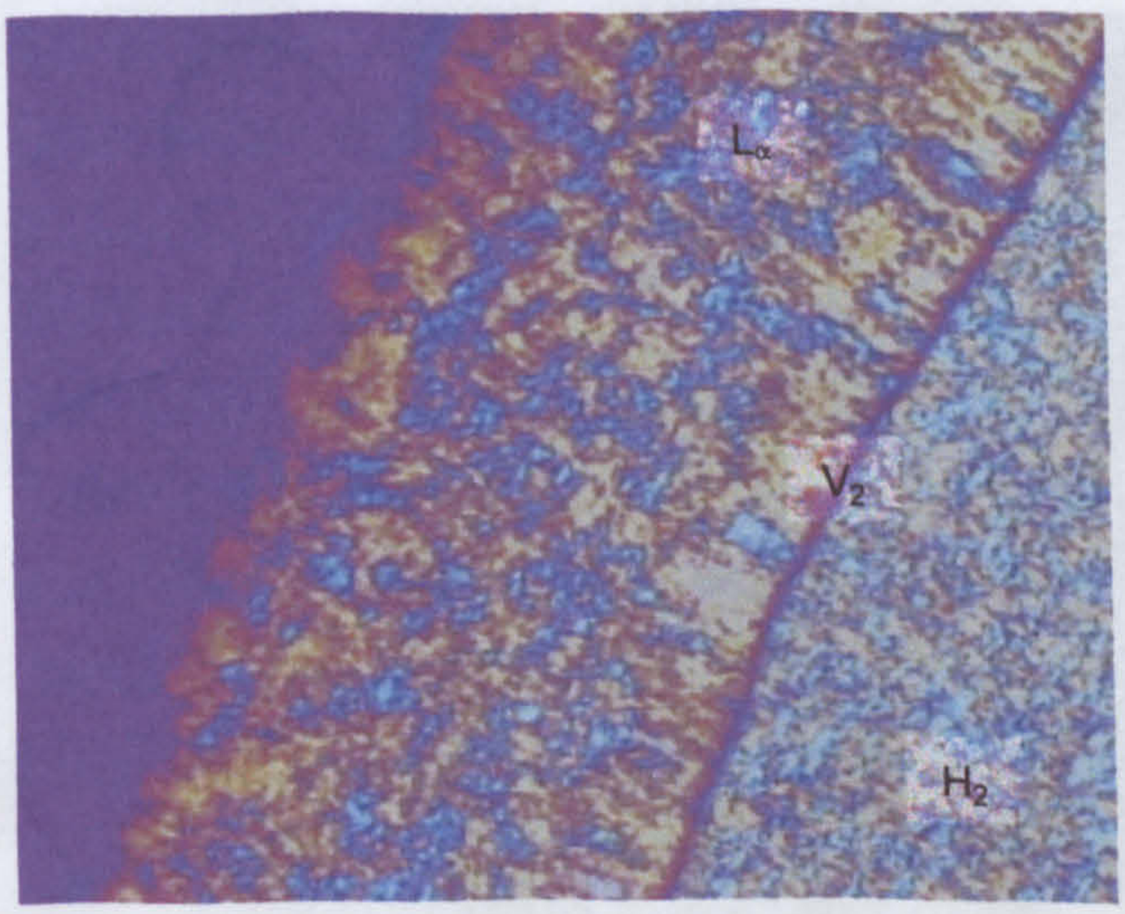

di-PhC4SS

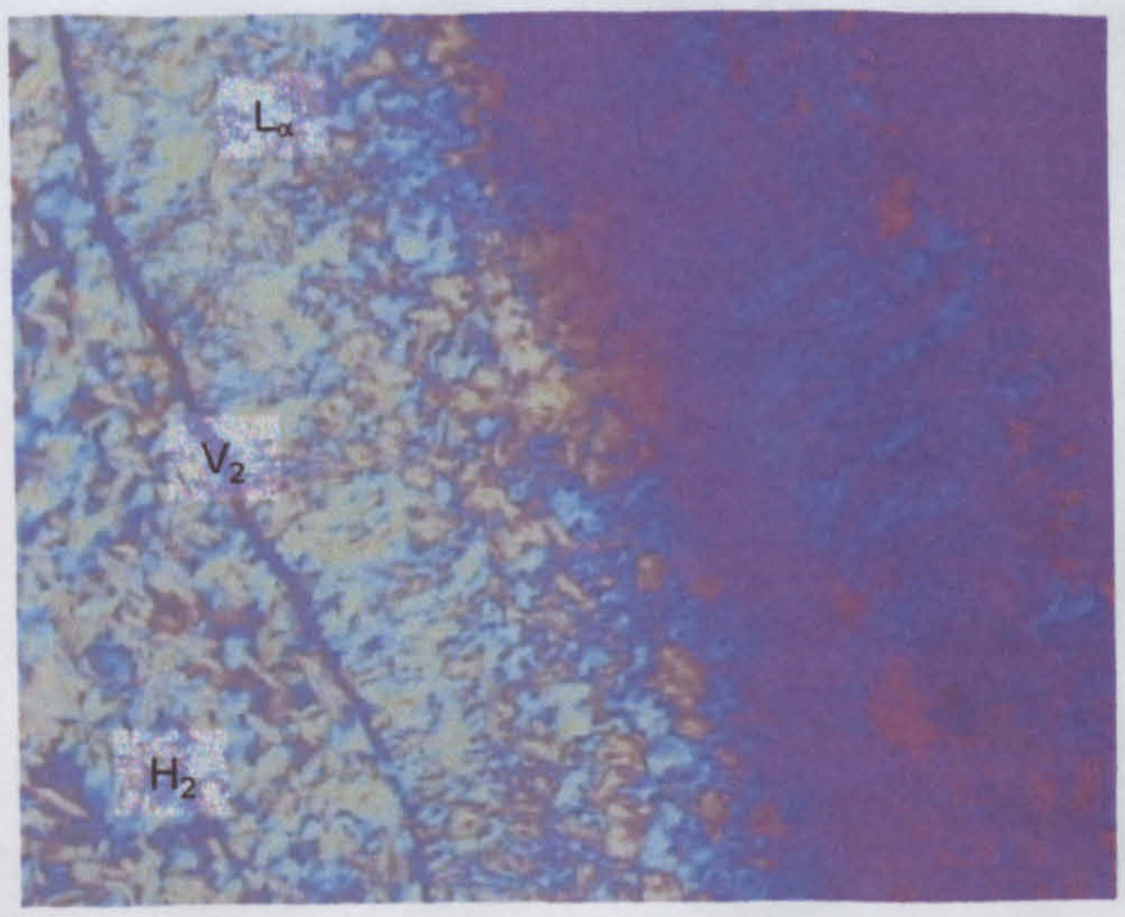

Figure 5.31(*b*) Liquid crystalline phases formed by di-PhC2SS, di-PhC3SS and di-PhC4SS after water penetration.

di-PhC5SS

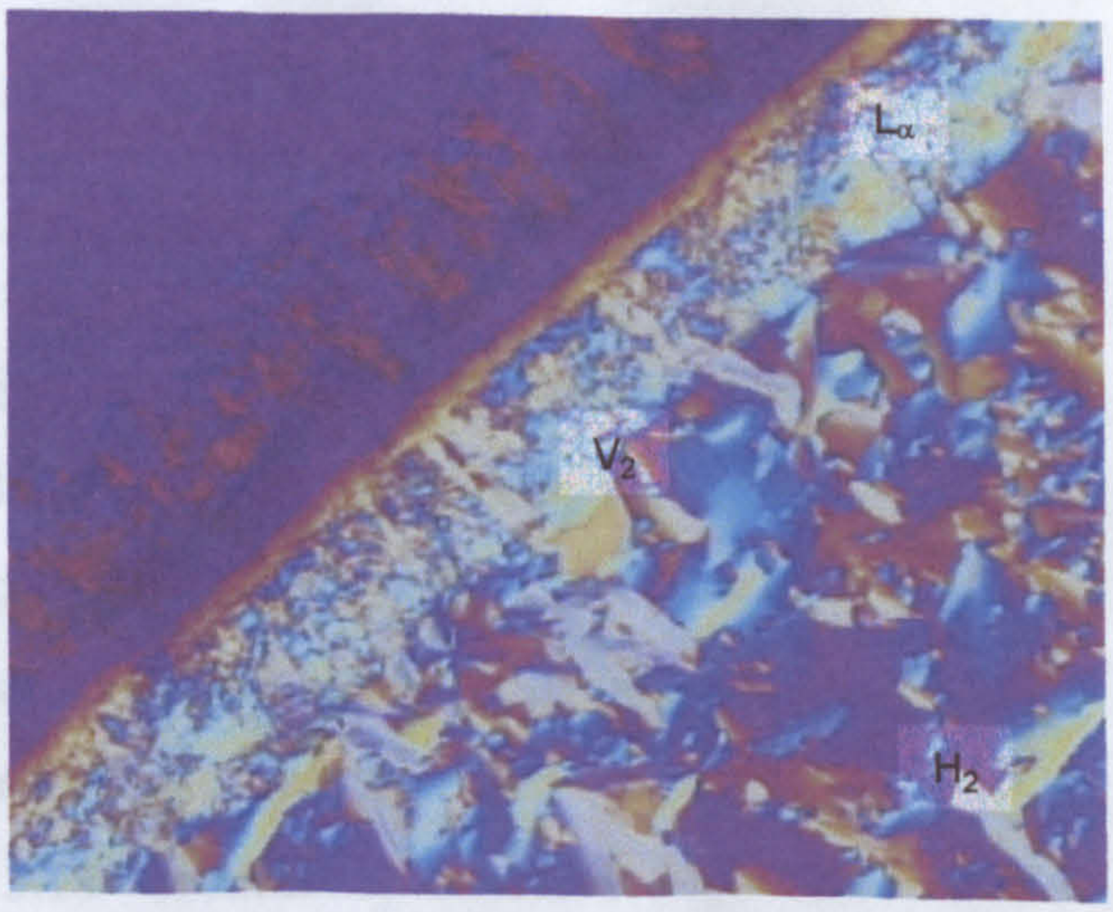

Br-di-PhC3SS

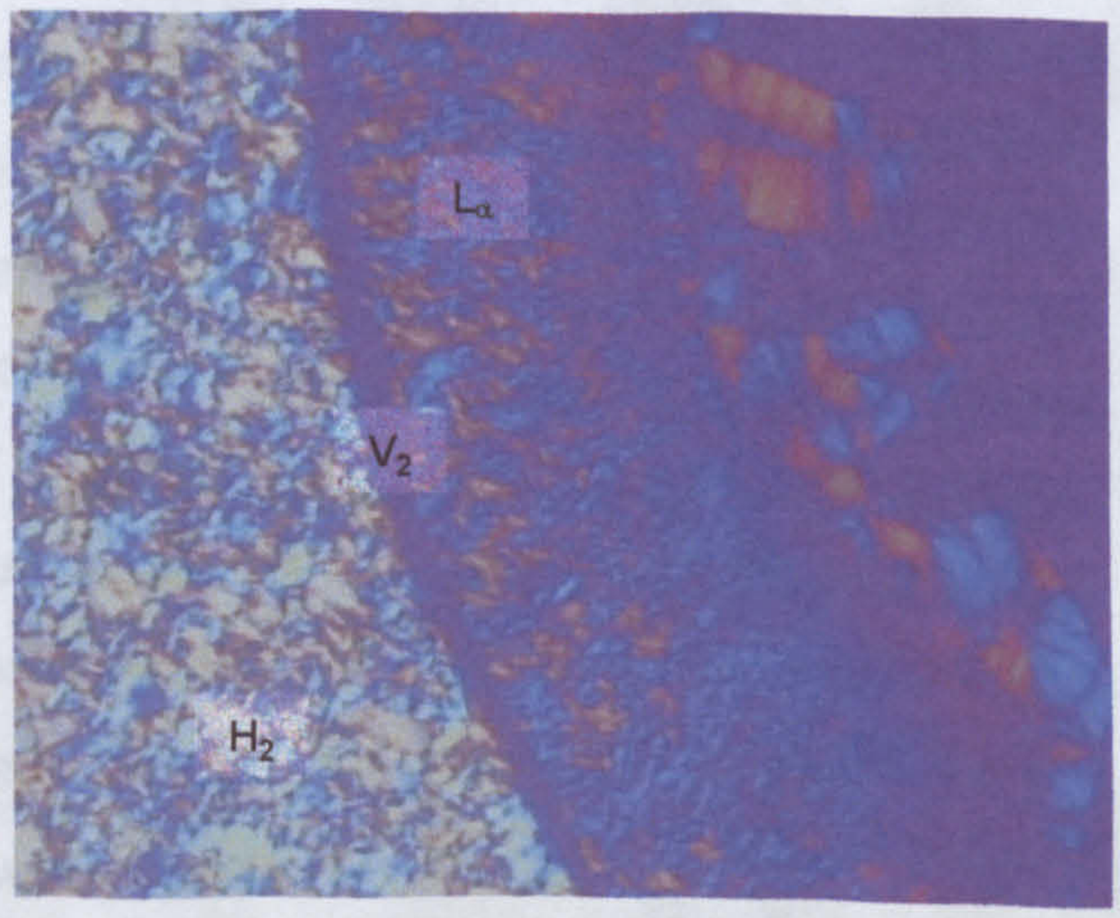

Br-di-PhC5SS

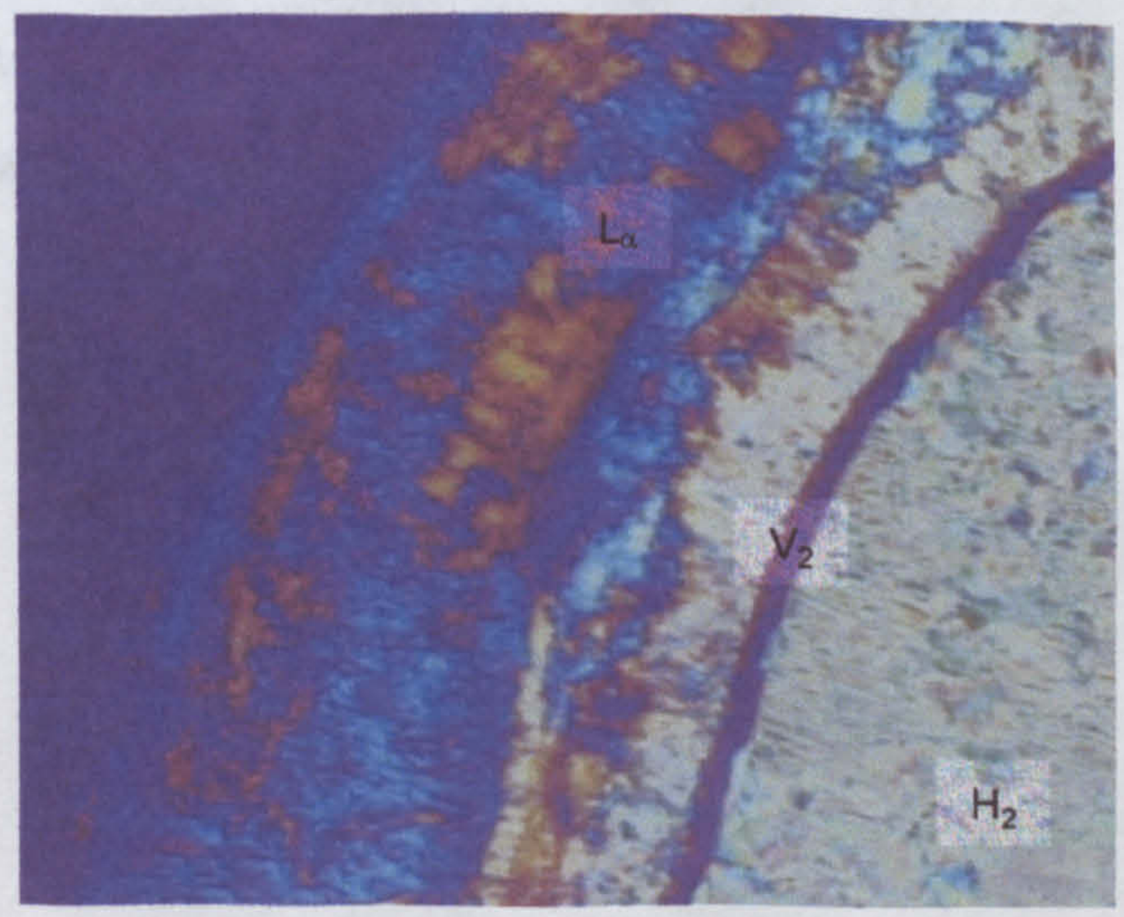

Figure 5.31(*c*) Liquid crystalline phases formed by di-PhC5SS, Br-di-PhC3SS and Br-di-PhC5SS after water penetration.

5.5 GENERAL CONCLUSIONS

In this chapter the aggregation and adsorption properties of three series of related hydrocarbon di-chain anionic surfactants have been compared, with the aim to identify the effect of branching and varying the terminal group in the linear chains. To the question "what is so special about Aerosol-OT?", one can clearly say so far that, with regard to its dilute aqueous phase behaviour, the answer is nothing! This statement can be justified by comparing the absolute adsorptions of AOT, and ten structurally related compounds (Figure 5.15). Examining molecular area demands in a monolayer at the CMC A_{cmc} in terms of a chain branching factor (Figure 5.23) shows that AOT behaves in a readily understandable fashion. The branched chain compounds demonstrate a significant increase in A_{cmc}, between 10 – 20 $Å^2$ over those found for equivalent carbon number straight chain systems. Furthermore, slight variations in A_{cmc} were detected reflecting changes in packing owing to differing extents of chain branching. However, AOT is no special case, and it fits into the general pattern of behaviour for all the sulfosuccinates studied here. Surfactant effectiveness was also found to follow the molecular structure of the compounds, and a clear example is the high limiting surface tensions obtained for the phenyl-tipped series.

In this part of the work, to examine the air–water interface, no special effects due to the 2-ethyl-1-hexyl chains were observed. The next phase is to investigate adsorption at oil–water interfaces with microemulsions, in an attempt to reveal why Aerosol-OT is so effective as a stabiliser.

5.6 REFERENCES

1. Born, M.; Wolf, E., *'Principles of Optics'*, 6th edition, Pergamon Press, 1980, Oxford.
2. Eastoe, J. '*Small-Angle Neutron Scattering*' in '*New Physico-Chemical Techniques for the Characterisation of Complex Food Systems*', (ed. Dickinson, E.), p268-294, Blackie, 1995, Glasgow.
3. Abelès, F. *Ann. Phys. (Paris)* **1948**, *3*, 504.
4. Heavens, O. J. *'Optical Properties of Thin Solid Films'*, Butterworths Scientific Publications, 1955, London.
5. Nevot, L.; Croce, P. *Rev. Phys. Appl.* **1980**, *15*, 761.
6. Sinha, S. K.; Sirota, E. B.; Garoff, S.; Stanley, H. B. *Phys. Rev. B* **1988**, *38*, 2297.
7. Thomas, R. K.; Penfold, J. *J. Phys. Condens. Matter* **1990**, *2*, 1369.
8. Lu, J. R.; Simister, E. A.; Lee, E. M.; Thomas, R. K.; Rennie, A. R.; Penfold, J. *Langmuir* **1992**, *8*, 1837.
9. Simister, E. A.; Thomas, R. K.; Penfold, J.; Aveyard, R.; Binks, B. P.; Cooper, P.; Fletcher, P. D. I.; Lu, J. R.; Sokolowski, A. *J. Phys. Chem.* **1992**, *96*, 1383.
10. Crowley, T.; Lee, E. M.; Simister, E. A.; Thomas, R. K. *Physica B* **1991**, *173*, 143.
11. Lu, J. R.; Simister, E. A.; Thomas, R. K.; Penfold, J. *J. Phys. Chem.* **1993**, *97*, 6024.
12. Simister, E. A.; Lee, E. M.; Thomas, R. K.; Penfold, J. *J. Phys. Chem.* **1992**, *96*, 1373.
13. Cooke, D. J.; Lu, J. R.; Lee, E. M.; Thomas, R. K.; Pitt, A. R.; Simister, E. A.; Penfold, J. *J. Phys. Chem.* **1996**, *100*, 10298.
14. Simister, E. A.; Lee, E. M.; Thomas, R. K.; Penfold, J. *Macromol. Rep.* **1992**, *A29*, 155.
15. Li, Z. X.; Lu, J. R.; Thomas, R. K.; Penfold, J. *Prog. Colloid Polym. Sci.* **1995**, *98*, 243.
16. Li, Z. X.; Lu, J. R.; Thomas, R. K.; Penfold, J. *J. Phys. Chem. B* **1997**, *101*, 1615.
17. Lu, J. R.; Li, Z. X.; Smallwood, J. A.; Thomas, R. K.; Penfold, J. *J. Phys. Chem.* **1995**, *99*, 8233.
18. Li, Z. X.; Lu, J. R.; Thomas, R. K. *Langmuir* **1997**, *13*, 3681.
19. Li, Z. X.; Lu, J. R.; Thomas, R. K.; Rennie, A. R.; Penfold, J. *J. Chem. Soc. Faraday Trans.* **1996**, *92*, 565.
20. Crowley T.L. *Physica A* **1993**, *195*, 354.
21. Penfold, J.; Richardson, R. M.; Zarbakhsh, A.; Webster, J. R. P.; Bucknall, D. G.; Rennie, A. R.; Jones, R. A. L.; Cosgrove, T.; Thomas, R. K.; Higgins, J. S.; Fletcher, P. D. I.; Dickinson, E.; Roser, S. J.; McLure, I. A.; Hillman, A. R.; Richards, R. W.; Staples, E. J.; Burgess, A. N.; Simister, E. A.; White, J. W. *J. Chem. Soc. Faraday Trans.* **1997**, *93*, 3899.
22. Adamson, A. W. *'Physical Chemistry of Surfaces'*, 4th edition, John Wiley & Sons, 1982, New York, p 4-48.
23. Harkins, W. D.; Jordan, H. F. *J. Am. Chem. Soc.* **1930**, *52*, 1751.
24. Miller, R.; Joos, P.; Fainerman, V. B. *Adv. Colloid Interface Sci.* **1994**, *49*, 249.
25. Fainerman, V. B., Miller, R.; Joos, P. *Colloid Polym. Sci.* **1994**, *272*, 731.
26. Rusanov, A. I.; Prokhorov, V. A. *'Interfacial Tensiometry'*, (Eds. Möbius, D.; Miller, R.), Elsevier, 1996, Amsterdam.

27. Miller, R.; Schano, K-H.; Hofmann, A. *Colloids Surf. A* **1994**, *92*, 33.
28. Bircumshaw, L. L. *J. Chem. Soc.* **1922**, *121*, 887.
29. Atkins, P. W. *'Physical Chemistry'*, 6th edition, Oxford University Press, 1998, Oxford.
30. Robbins, J. *'Ions in Solution'* Oxford University Press, 1972, Oxford.
31. Levine, I. N. *'Physical Chemistry'*, 4th edition, McGraw-Hill Book Co., 1995, Singapore.
32. Moore, W. J. *'Physical Chemistry'*, 5th edition, Longman, 1972, London.
33. An, S. W.; Lu, J. R.; Thomas, R. K.; Penfold, J. *Langmuir* **1996**, *12*, 2446.
34. Bae, S.; Haage, K.; Wantke, K.; Motschmann, H. *J. Phys. Chem. B* **1999**, *103*, 1045.
35. Hall, D. G. *Colloids Surf. A* **1994**, *90*, 285.
36. Hall, D. G.; Pethica, B. A.; Shinoda, K. *Bull. Chem. Soc. Jpn.* **1975**, *48*, 324.
37. Thomas, R. K.; Lu, J. R.; Lee, E. M.; Penfold, J.; Flitsch, S. L. *Langmuir* **1993**, *9*, 1352.
38. Hines, J. D.; Garrett, P. R.; Rennie, G. K.; Thomas, R. K.; Penfold, J. *J. Phys. Chem. B* **1997**, *101*, 7121.
39. Hines, J. D.; Garrett, P. R.; Rennie, G. K., Thomas, R. K., Penfold, J. *J. Phys. Chem. B* **1997**, *101*, 9215.
40. Tajima, K.; Muramatsu, M.; Sasaki, T. *Bull. Chem. Soc. Jpn.* **1970**, *43*, 1991.
41. Tajima, K. *Bull. Chem. Soc. Jpn.* **1970**, *43*, 3063.
42. Tajima, K. *Bull. Chem. Soc. Jpn.* **1971**, *44*, 1767.
43. Cross, A. W.; Jayson, G. G. *J. Colloid Interface Sci.* **1994**, *162*, 45.
44. Li, Z. X.; Dong, C. C.; Thomas, R. K. *Langmuir* **1999**, *15*, 4392.
45. Downer, A. D.; Eastoe, J.; Pitt, A. R.; Penfold, J.; Heenan, R. K. *Colloids Surf. A* **1999**, *156*, 33.
46. Downer, A.; Eastoe, J.; Pitt, A. R.; Simister, E. A.; Penfold, J. *Langmuir* **1999**, *15*, 7591.
47. Williams, E. F.; Woodberry, N. T.; Dixon, J. K. J. *Colloid Interface Sci.* **1957**, *12*, 452.
48. Elworthy, P. H.; Mysels, K. J. *J. Colloid Interface Sci.* **1966**, *21*, 331.
49. Mysels, K. J. *Langmuir* **1986**, *2*, 423.
50. Mysels, K. J.; Florence, A. *J. Colloid Interface Sci.* **1973**, *43*, 577.
51. Lukenheimer, K. *J. Colloid Interface Sci.* **1989**, *131*, 580.
52. Lukenheimer, K.; Haage, K.; Hirte, R. *Langmuir* **1999**, *15*, 1052.
53. Eastoe, J.; Nave, S.; Downer, A.; Paul, A.; Rankin, A.; Tribe, K.; Penfold, J. *Langmuir* **2000**, *16*, 4511.
54. Israelachvili, J. N.; Mitchell, D. J.; Ninham, B. W. *J. Chem. Soc., Faraday Trans. 2* **1976**, *72*, 1525.
55. Robinson, B. H.; Toprakcioglu, C.; Dore, J. C.; Chieux, P. *J. Chem. Soc., Faraday Trans. 1* **1984**, *80*, 13; Toprakcioglu, C.; Dore, J. C.; Robinson, B. H.; Howe, A. M.; Chieux, P. *J. Chem. Soc., Faraday Trans. 1* **1984**, *80*, 413.
56. Kotlarchyk, M.; Chen, S-H.; Huang, J. S.; Kim, M. W. *Phys. Rev. A* **1984**, *29*, 2054.
57. Aveyard, R.; Binks, B. P.; Clark, S.; Mead, J. *J. Chem. Soc., Faraday Trans. 1* **1986**, *82*, 125.
58. Eastoe, J.; Young, W. K.; Robinson, B. H.; Steytler, D. C. *J. Chem. Soc. Faraday Trans.* **1990**, *86*, 2883.
59. Eastoe, J.; Robinson, B. H.; Steytler, D. C.; Thorn-Leeson, D. *Adv. Coll. Int. Sci.* **1991**, *36*, 1.
60. Hirai, M.; Hirai, R. K.; Sanada, M; Iwase, H.; Mitsuya, S. *J. Phys. Chem. B* **1999**, *103*, 9658.

61. Moulik, S. P.; De, G. C.; Panda, A. K.; Bhowmik, B. B.; Das, A. R. *Langmuir* **1999**, *15*, 8361.
62. Rees, G. D.; Evans-Gowing, R.; Hammond, S. J.; Robinson, B. H. *Langmuir* **1999**, *15*, 1993.
63. Lu, J. R.; Li, Z. X.; Su, T. J.; Thomas, R. K.; Penfold, J. *Langmuir* **1993**, *9*, 2408.
64. Eastoe, J.; Rogueda, P.; Howe, A. M.; Pitt, A. R.; Heenan, R. K. *Langmuir* **1996**, *12*, 2701.
65. Eastoe, J.; Dalton, J. S.; Heenan, R. K. *Langmuir* **1998**, *14*, 5719.
66. Bell, G. R.; Manning-Benson, S.; Bain, C. D. *J. Phys. Chem. B* **1998**, *102*, 218.
67. Nusselder, J. J. H.; Engberts, J. B. F. N. *J. Org. Chem.* **1991**, *56*, 5522.
68. Varadaraj, R.; Bock, J.; Valint, P.; Zushma, S.; Thomas, R. *J. Phys. Chem.* **1991**, *95*, 1671.
69. Gol'Din, G. S.; Averbakh, K. O.; Shpagina, T. A. *Colloid J. USSR* **1991**, 53, 528.
70. Wormuth, K. R.; Zushma, S. *Langmuir* **1991**, *7*, 2048.
71. Tanford, C. *J. Phys. Chem.* **1972**, *76*, 3020.
72. Lu, J. R.; Hromadova, M.; Thomas, R. K.; Penfold, J. *Langmuir* **1993**, *9*, 2417.
73. Downer, A; Eastoe, J; Pitt, A. R.; Simister, E. A.; Penfold, J. *Langmuir* **1999**, *15*, 7591.
74. Gu, T.; Sjöblom, J. *Colloids Surf. A* **1992**, *64*, 39.
75. Lee, E. M.; Thomas, R. K.; Penfold, J.; Ward, R. C. *J. Phys. Chem.* **1989**, *93*, 381.
76. Lyttle, D. J.; Lu, J. R.; Su, T. J.; Thomas, R. K.; Penfold, J. *Langmuir* **1995**, *11*, 1001.
77. Clint, J. in '*Surfactant Aggregation*', Blackie Academic, 1992, Glasgow, p115.
78. Rosen, M. J. in '*Surfactants and Interfacial Phenomena*', 2nd edition, John Wiley & Sons, 1989, New York, p64-168.
79. Pitt, A. R.; Morley, S. D.; Burbidge, N. J.; Quickenden, E. L. *Colloids Surf. A* **1996**, *114*, 321.
80. Lunkenheimer, K.; Haage, K.; Miller, R. *Colloids Surf.* **1987**, *22*, 215.
81. Karaman, M. E.; Ninham, B. W.; Pashley, R. M. *J. Phys. Chem.* **1994**, *98*, 11512.
82. Lukenheimer, K.; Miller, R. *J. Colloid Interface Sci.* **1987**, *120*, 176.
83. Lukenheimer, K.; Burczyk, B.; Piasecki, A.; Hirte, R. *Langmuir* **1991**, *7*, 1765.
84. Lukenheimer, K.; Czichocki, G.; Hirte, R.; Barsyk, W. *Colloids Surf. A* **1995**, *101*, 187.
85. Goebel, A.; Lukenheimer, K. *Langmuir* **1997**, *13*, 369.
86. Gutmann, V. '*The Donor–Acceptor Approach to Molecular Interactions*', Plenum Press, 1978, London.
87. Barron, A. L. E. in '*Using the Microscope*', 3rd edition, Chapman & Hall, 1965, London, p130.
88. Information on Liquid Crystals can be found at http://plc.cwru.edu/.
89. Chandrasekhar, S. '*Liquid Crystals*' Cambridge University Press, 1992, New York.
90. Paul, A. Ph.D. Thesis, Bristol, 2001.

CHAPTER 6

MICROEMULSION PHASE BEHAVIOUR OF DI-CHAIN SODIUM SULFOSUCCINATES

Following the results obtained at the air–water interface and correlations found between molecular structures and adsorption behaviour, this chapter examines the effect of chain structure on packing in curved films at oil-water interfaces. The same Aerosol-OT-related compounds (i.e., di-C*n*SS, AOTs and di-PhC*n*SS series) were investigated in terms of microemulsion formation and stability. Particular emphasis is given to the branched sulfosuccinates with the aim to identify why Aerosol-OT is such an efficient water-in-oil (w/o) microemulsifier, and to clarify the function of the alkyl side branches. More generally, studying each of the three amphiphilic series should give information about interactions between molecular structure and surfactant efficiency, as well as interfacial film properties.

Microemulsion formation and stability were investigated by establishing binary phase stability diagrams at constant surfactant composition and pressure. When required, the surfactant aqueous phase solubility was measured as a function of temperature, and this was correlated to the microemulsion phase behaviour. Small-Angle Neutron Scattering (SANS) was then used to characterise the microemulsion aggregates and adsorbed films. Water droplet radii and interfacial molecular areas were determined from model fitting, and related to chain architecture. Finally, SANS and interfacial tension measurements were combined to calculate mean film bending rigidities.

6.1 INTRODUCTION

To what extent does surfactant molecular structure affect the microscopic properties of an interfacial film? It has been long established that hydrophilic-hydrophobic balance plays a crucial role in formation and stability of colloidal dispersions and self-assembly structures. Furthermore, there is a close link between surfactant structure and interfacial film curvature, which is an important characteristic of microemulsions. Aerosol-OT is widely used in microemulsion studies due to its exceptional efficiency. However, the specific reason why this particular di-chain compound is such a good microemulsifier remains unclear, and surely the perceived "cone-like molecular structure" is not the whole story. To reveal any unique structural features of AOT itself, three series of sodium sulfosuccinates have been synthesised and their properties characterised at both air-water and oil-water interfaces. As discussed in Chapter 5, in relation to aqueous systems, undoubtedly, chain shape and structure affect packing as well as surfactant efficiency in terms of surface tension lowering. In particular, alkyl chain branching promotes a significant increase in the head group area reflecting the change in molecular shape. However, within this group AOT itself did not exhibit any unusual behaviour. To complete this investigation of surfactant structure-performance relationships it is interesting to examine the oil-water interface, and it should be possible to delineate if molecular shape is the unique answer as to why AOT is such a useful and versatile surfactant, especially for microemulsions.

The compounds of interest have been identified in the previous chapter (see Figs. 5.15 and 5.16). Small-angle neutron scattering (SANS) was used to characterise the structure of the aggregates and films, close to the Winsor II boundary. SANS is an ideal method for resolving microemulsion structure: it can provide quantitative information on interfacial packing in terms of a mean area per molecule, and interfacial curvature via the preferred droplet size and shape. In particular, since different domains can be contrasted by selective deuteration, a self-consistent picture of the internal droplet and film structure can be obtained by simultaneous analysis of a core-shell-drop (CSD) contrast series [1,2]. Therefore, when applied to the different AOT homologues, keeping the oil chain length constant, the specific effects of chain branching should be identified.

There is a vast literature devoted to studying AOT w/o microemulsions, using many different structural and physical techniques, and over a wide range of experimental conditions (e.g., temperature and pressure [3]). In particular, Kotlarchyk *et al.* [4,5] have carried out detailed SANS experiments to determine the size and shape of reverse micelles. These studies have shown if the system is far from phase boundaries, then the aggregates may be considered as weakly interacting discrete polydisperse spherical water droplets, coated by a curved surfactant monolayer. Varying parameters such as temperature or oil chain length does not have any significant effect on the nature or size of these aggregates. However, changing the surfactant counterions (say from Na^+ to M^{2+} ions) alters the phase diagram, due to a reduction in the aqueous solubility of the M^{2+}AOT surfactants, and in some cases this can also induce structural changes to cylindrical aggregates in microemulsions [6]. Surprisingly little is known about the response of phase behaviour and structure to slight variations in the chain architecture. Atkinson *et al.* [7] have described systems formed by a branched di-chain and a linear tri-chain AOT analogue, the first of which is also included in the present study and is referred to as AOT④. It was found that both molecules show similar phase stability behaviour and aggregate structure as AOT, and they are capable of solubilising large amounts of water. However, since this AOT④ is a branched C9 compound, whilst AOT is C8, it is not possible to identify any specific contribution of the ethyl side branch in AOT from that study alone.

6.2 PHASE BEHAVIOUR

A convenient way to convey w/o phase stability is at fixed surfactant concentration, thereby removing a degree of freedom. For each surfactant, binary phase diagrams expressed as w vs. temperature (where w = [water]/[surfactant]) were determined in order to locate the phase boundaries.

6.2.1 Experimental

Microemulsion phase equilibria were determined by visual inspection of samples made-up in clean, stoppered 5 ml volumetric flasks, thermostatted by a heater-cooler-circulator water bath accurate to ± 1 °C. Samples were made-up with D_2O (Fluorochem,

99.9% D atom) and the appropriate proteated alkane solvent (Aldrich or Sigma, HPLC grade). In all cases, the surfactant concentration was kept constant at 0.10 mol dm^{-3}. For the di-C*n*SS series, 1-hexanol (Aldrich) was used as a co-surfactant and the microemulsion oil phase was a 9:1 v/v hexane/hexanol mixture. For the AOTs and phenyl sulfosuccinates series, the oil phase was heptane and toluene respectively. Supporting data – for the AOTs phase behaviour only – were obtained by determining the surfactant aqueous solubility. Aqueous samples of 0.05 – 0.10 wt% surfactant were studied over the temperature range 3 – 85 °C by visual inspection of the transition from biphasic to monophasic (translucent) systems.

6.2.2 Effect of chain branching

Unlike AOT, none of the linear sodium sulfosuccinates di-C*n*SS (n = 4 to 8) formed a microemulsion phase alone and a co-surfactant (medium chain alcohol) was necessary. The phase stability diagram for di-C6SS in water/hexane-hexanol system is shown in Figure 6.1 (*a*). Considering the 30 °C isotherm as a function of w, four distinct regions appear. First a relatively large amount of water is solubilised and a single w/o microemulsion phase (L_2) is observed up to $w \approx 64$, which is the maximum water uptake under these conditions. Below $w \approx 64$ the systems were transparent and of low viscosity. This transition corresponds to a water solubilisation boundary (Winsor II system), where all surfactant is assumed to be present in the w/o portion, and the film is at a natural curvature radius (minimum in film bending energy) defined by w_{max}. A further increase in water content (from $w \approx 77$) promotes the formation of a second single phase, which differs from the first L_2-phase, since the samples are bluish-white and more viscous. This region just above the Winsor II phase is believed to be bicontinuous. Finally at around $w \approx 90$ a critical-type separation is observed: the lower phase is viscous and obviously surfactant-rich whereas the upper phase is oil-like and essentially surfactant-free. As for AOT, this upper transition reflects an increase in aqueous solubility with temperature.

Similar phase stability diagrams were found for other linear chain compounds, but the phase boundaries shift towards higher temperatures for longer chains, and lower temperatures for shorter chains. For di-C4SS and di-C5SS a limited phase diagram was

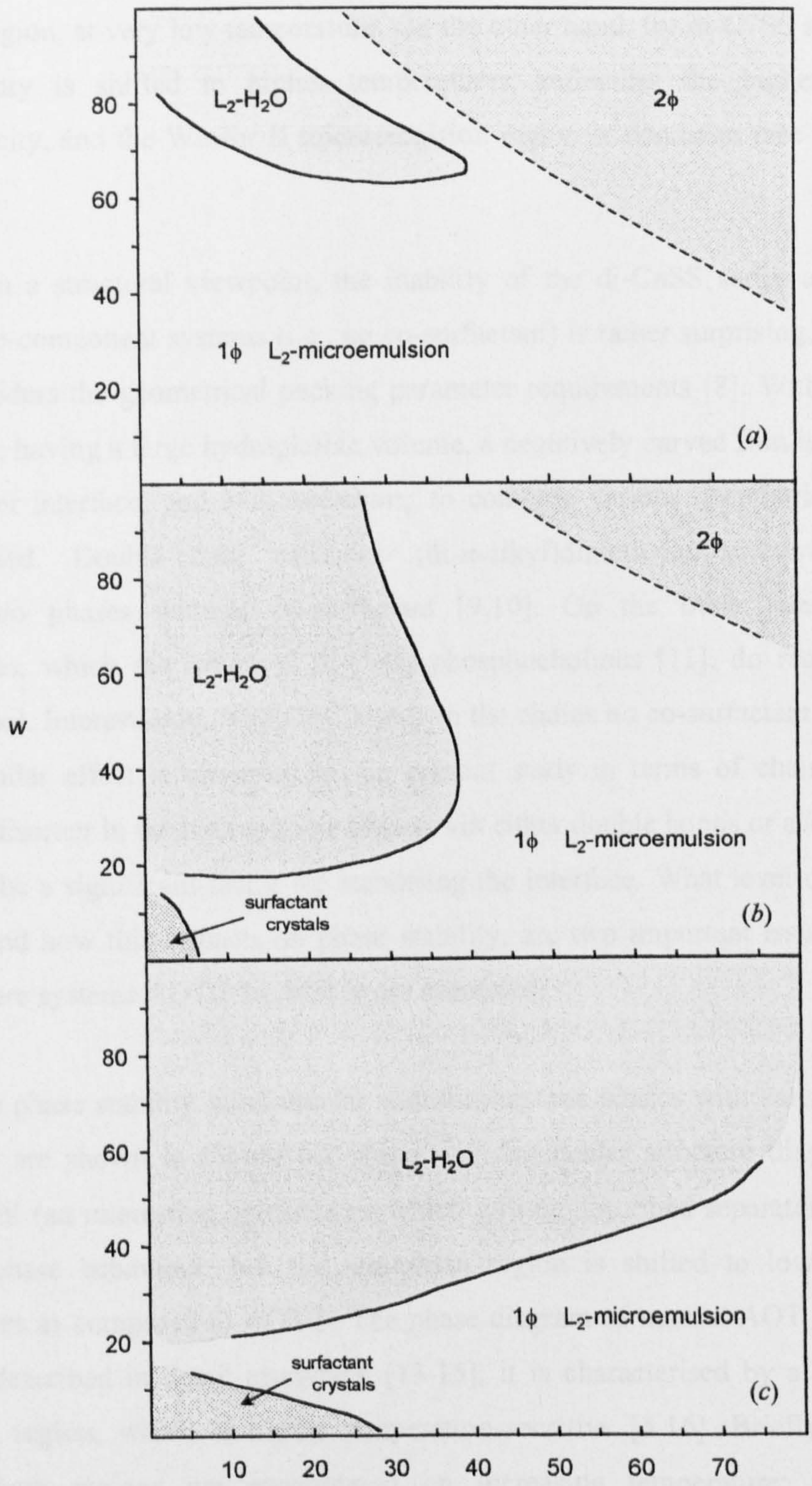

Figure 6.1 w/o microemulsion phase stability diagrams for (*a*) di-C6SS, (*b*) di-C7SS, and (*c*) di-C8SS in water/hexane:hexanol = 9:1 systems. [Surfactant] = 0.10 mol dm^{-3}, (—) is for the Winsor II (solubilisation) boundary, and (---) is for the high-temperature stability boundary (or haze boundary).

found, showing only the transition from an L_2-microemulsion to the two-phase separated region, at very low temperature. On the other hand, for di-C7SS and di-C8SS this boundary is shifted to higher temperatures, reflecting the higher surfactant hydrophobicity, and the Winsor II microemulsion region is dominant (see Figures. 6.1 (*b*) and (*c*)).

From a structural viewpoint, the inability of the di-C*n*SS series at stabilising simple three-component systems (i.e., no co-surfactant) is rather surprising, particularly if one considers the geometrical packing parameter requirements [8]. With double-tail compounds, having a large hydrophobic volume, a negatively curved film is expected at the oil-water interface, and it is interesting to compare various chemistries that have been studied. Double-chain cationics (di-*n*-alkyl)dimethylammonium bromides, stabilise w/o phases without co-surfactant [9,10]. On the other hand, synthetic zwitterionics, which are saturated di-chain phosphocholines [11], do require a short chain alcohol. Interestingly, with C=C bonds in the chains no co-surfactant is necessary [12]; a similar effect is observed in the present study in terms of chain branching. Structural disorder in the hydrophobic chains, via either double bonds or alkyl branches, appears to be a significant factor for stabilising the interface. What level of disorder is required, and how this impacts on phase stability, are two important issues addressed below, where systems AOT① to AOT⑥ are discussed.

The phase stability windows for water-in-heptane phases with various branched surfactants are shown in Figure 6.2 along with molecular structure diagrams. Apart from AOT⑥ (an interesting special case which will be described separately), there is a common phase behaviour, but the one-phase region is shifted to lower or higher temperatures as compared to AOT①. The phase diagram of normal AOT (i.e., AOT①) has been described in detail elsewhere [13-15], it is characterised by a large funnel-shaped L_2 region, which is highly temperature-sensitive [5,16]. Briefly considering AOT①, three regions are encountered on increasing temperature: a Winsor II microemulsion (L_2-H_2O), a single phase L_2-microemulsion, and a critical-type bi-phasic system. The first transition represents the solubilisation limit (or Winsor II boundary), whilst the second transition is a high-temperature haze boundary, above which the surfactant partitions into water.

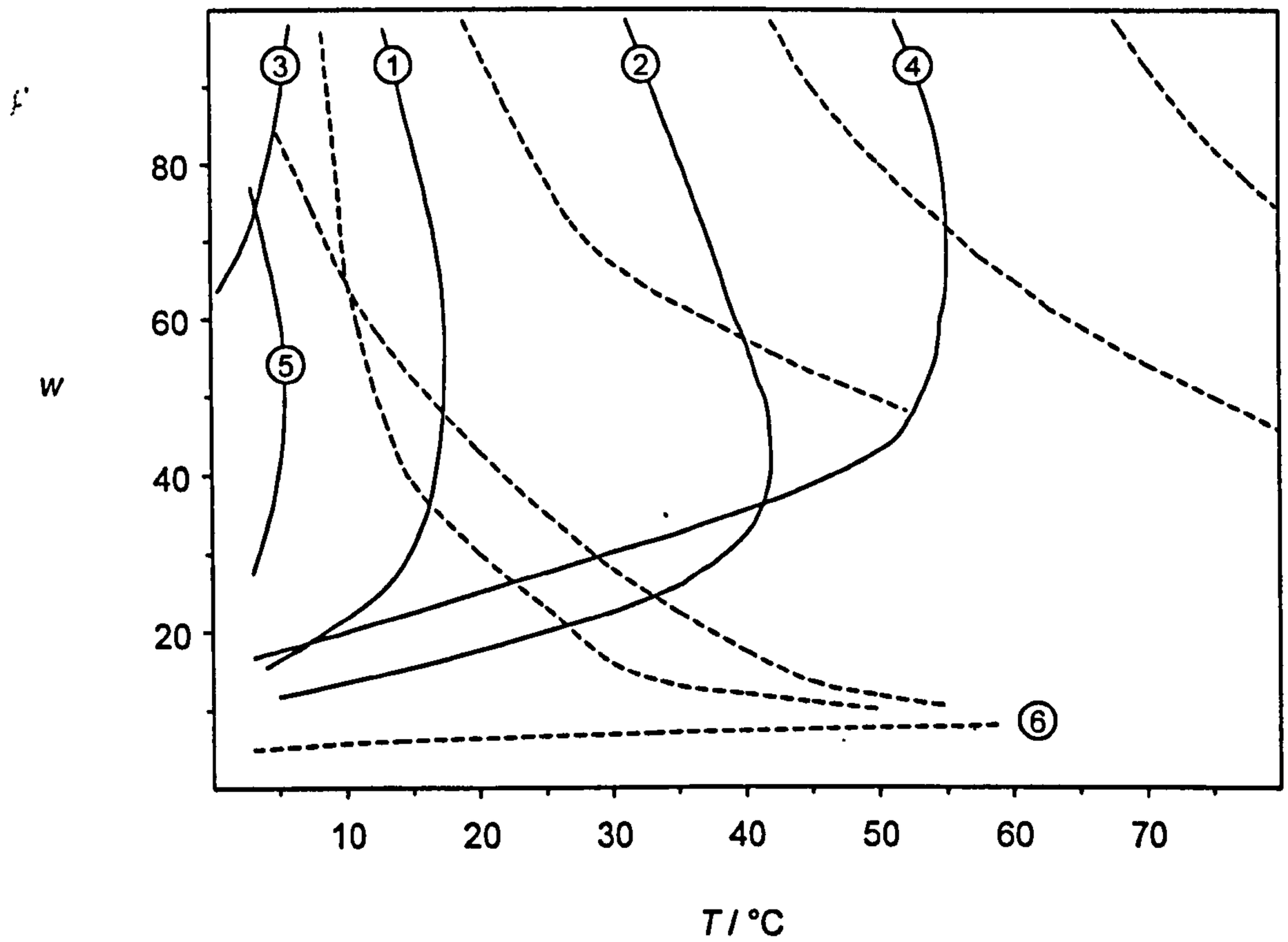

Figure 6.2 w/o microemulsion phase stability diagrams and schematic molecular structures for the AOTs series in water/heptane systems. [Surfactant] = 0.10 mol dm^{-3}, (—) is for the Winsor II (solubilisation) boundary, and (---) is for the high-temperature stability boundary (or haze boundary).

It is clear that these branched compounds are, in general, just as efficient as normal AOT, but temperature is the limiting factor. However, AOT⑥ is notable for its different behaviour, there is a limited L_2-microemulsion phase up to $w \approx 5 - 7$, above which a critical-type two-phase system exists, and there is a low temperature sensitivity. Such a poor efficiency surely cannot be the result of contaminants since, as described in Chapter 4, great care has been taken. In particular, electrolyte impurities (mainly excess sodium salts from the sulfonation) were thoroughly removed, and such contaminants are known to dramatically alter the microemulsion phase behaviour [17]. Considering the tail structure of this compound – 1,4-dimethyl-1-hexyl – it is believed that there is insufficient branching, so that the compound resembles a linear sulfosuccinate like di-C6SS. Tensiometric data obtained at the air-water interface (see Section 5.3.3) give support to this idea. These results show AOT⑥ has the highest molecular packing efficiency (i.e., lowest head group area) amongst the AOTs series. Therefore, it would seem that chain disorder in AOT⑥ is insufficient to stabilise a negatively curved interface. On the other hand, addition of a co-surfactant with AOT⑥ resulted in an enhanced L_2 phase, as was observed for the di-C*n*SS surfactants. Such a large difference between the phase-stability of AOT⑥ and the other branched compounds appears to be directly correlated with chemical structure, clearly showing the impact of chain branching. However, can chain structures also account for the sequence of phase stability for AOT's ① – ⑤, as shown on Figure 6.2?

Studies at the air-water interface have shown packing efficiency correlates with chain structure in terms of an empirical branching factor (Section 5.3.3); this accounts for the position and extent of branching within a hydrophobic group. However, for oil-water systems the situation appears to be more complicated, since the sequence in phase-stability does not match exactly the order in branching factor. Considering the significant effect of temperature the aqueous phase solubility of each AOTs was investigated. Figure 6.3 shows the results: at fixed surfactant wt% a transition between a biphasic and monophasic system defines the temperature where surfactant becomes totally miscible with water. Comparison with Figure 6.2 shows that this boundary dictates the transition from a single microemulsion phase to a two-phase separation in the oil-water system. For example, the solubility of AOT④ in water is low, and consequently the microemulsion phase region is shifted to high temperature.

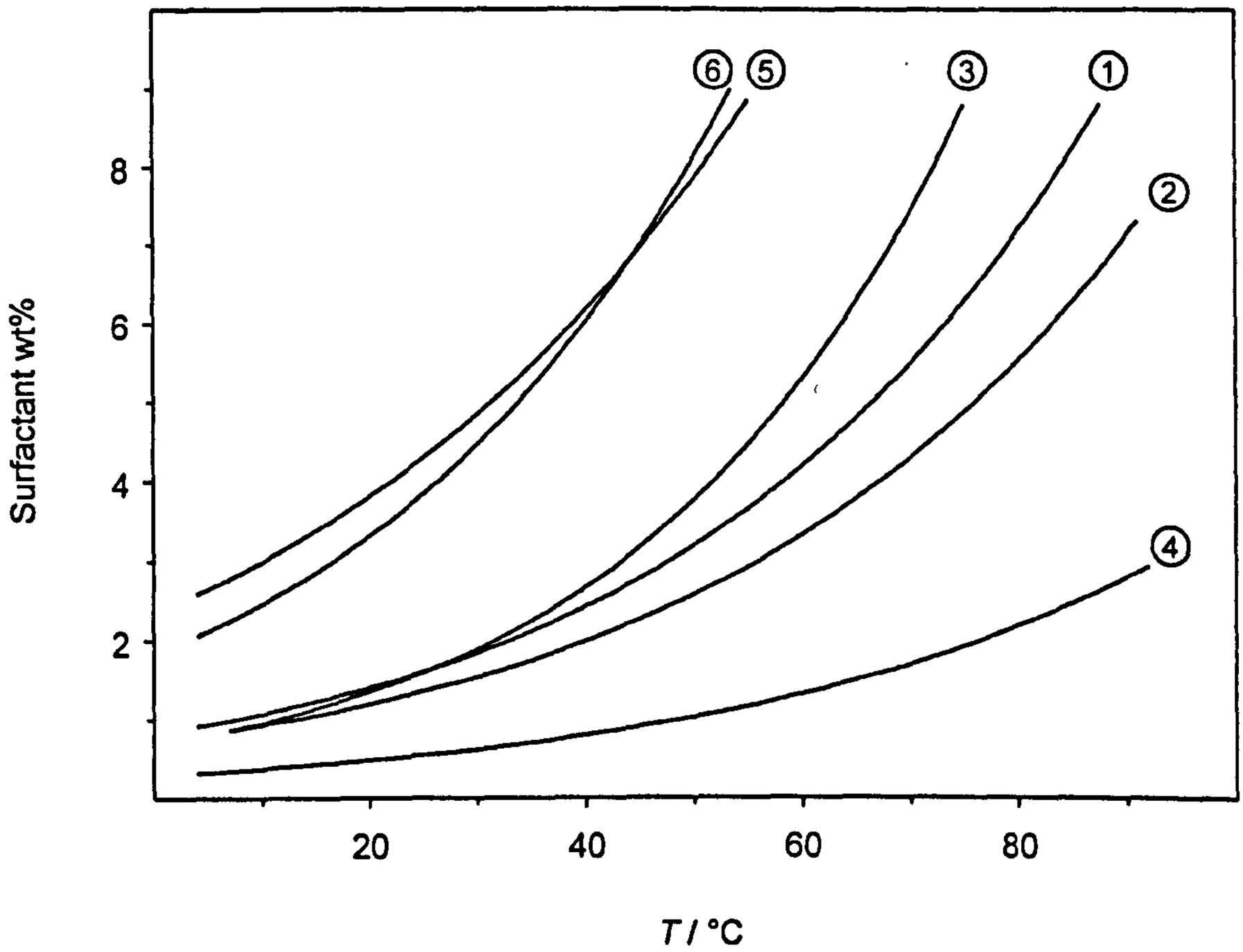

Figure 6.3 Solubility of the AOTs series in water as a function of temperature. The boundary line indicates the temperature above which the surfactant completely dissolves in water (biphasic to monophasic transition).

Next consider AOT④ and ⑤, which have two extreme branching factors, 1.33 and 2.80 respectively. As reported in Chapter 5 they had the lowest and highest values respectively for (1) head group areas A_{cmc}, 70 and 80 ± 2 Å^2, and (2) CMC's, 1.10×10^{-3} and 7.15×10^{-3} mol dm^{-3}. These results clearly illustrate differences in hydrophobicity: as a result of increased branching, the packing efficiency is reduced giving higher A_{cmc}, and at the same time there is a higher CMC. Now, considering Figures 6.2 and 6.3 together shows that these two compounds behave accordingly in the microemulsion and aqueous binary systems, in that they sit at extremes on the temperature scale. For AOT① with a branching factor of 1.67, A_{cmc} and CMC of 75 Å^2 and 2.56×10^{-3} mol dm^{-3} respectively, it is reasonable for its microemulsion phase to be located in between AOT④ and ⑤. However, with AOT② and ③ the correlation fails, so it seems a simplistic branching factor alone cannot account for such subtle variations in chemical structure.

Considering microemulsion stability, normal AOT is thus not a unique "wonder surfactant", however it seems to possess the most suitable structure in terms of temperature-solubility behaviour. Changing the oil gives different stability ranges, as reported for AOT④ by Atkinson *et al.* [7], where this compound is optimised in decane, giving a funnel-shaped microemulsion region centered at ~ 28 °C.

6.2.3 Effect of phenyl-tipped chain structures

Water-in-oil phase stability diagrams of di-phenyl sodium sulfosuccinates were studied using *n*-heptane and toluene (see Figure 6.4), and compared to normal AOT. Main features are:

i) None of the compounds formed a single microemulsion phase in the water/heptane system, whereas AOT did, suggesting oil/chain interactions are significant. Toluene was then used, successfully, for this study.

ii) No single microemulsion region was observed for the linear chain compounds with $n = 2$ and 3. This was put down to the hydrophobic moiety being too short, and a relatively high Krafft temperature (> 35 °C). For longer linear chain amphiphiles, unlike the di-C*n*SS series, no co-surfactant was required. This might reflect the slight chain disorder introduced by the phenyl end groups.

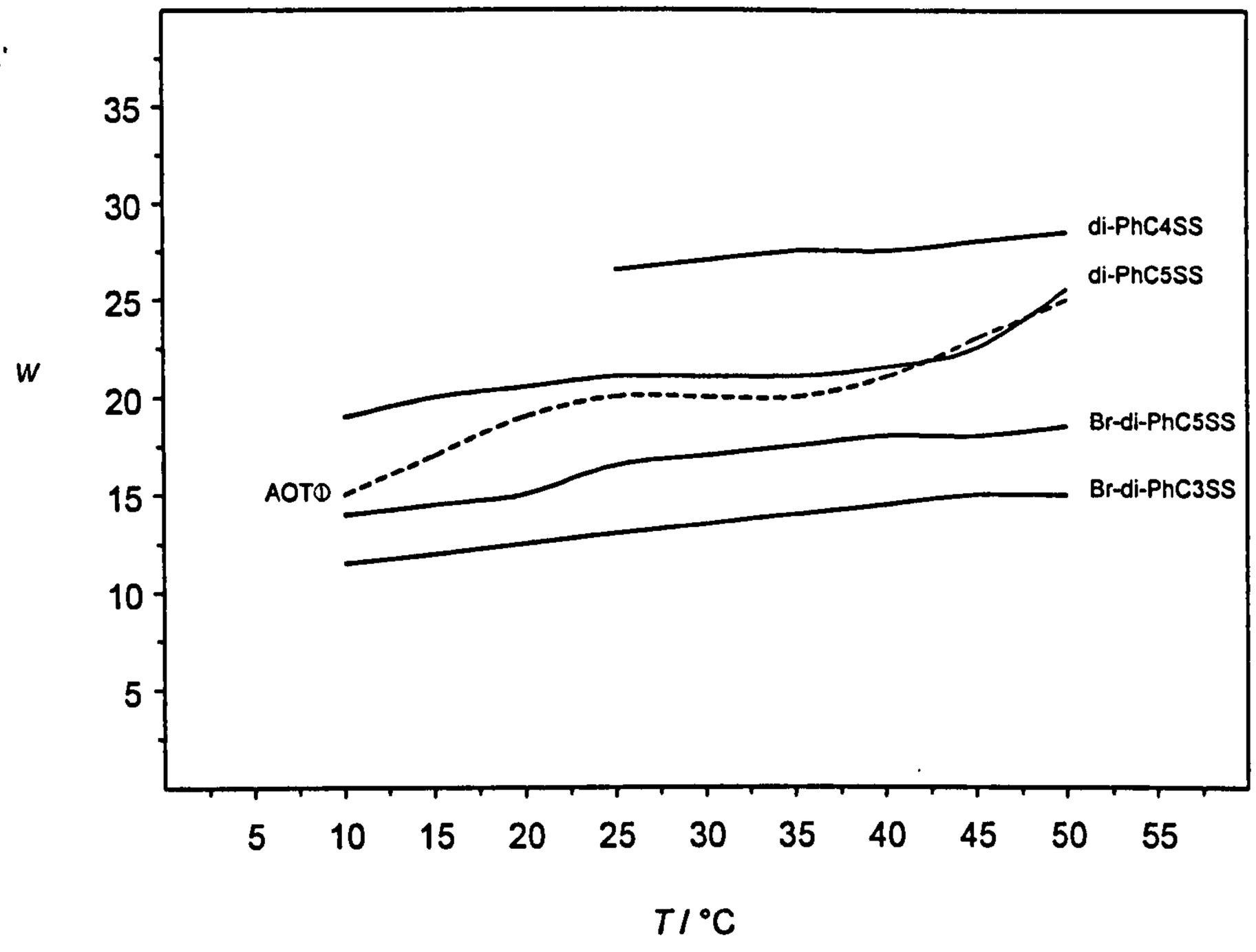

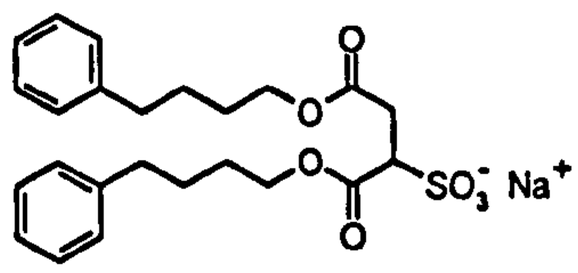

di-PhC4SS

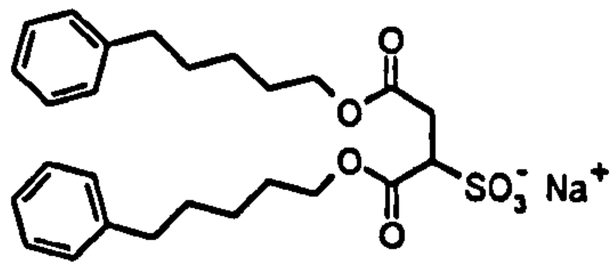

di-PhC5SS

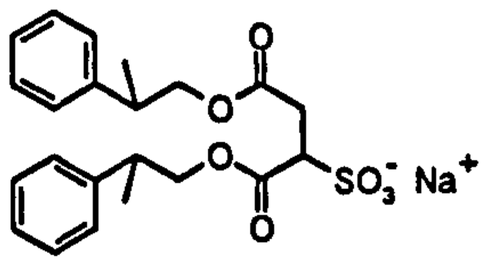

Br-di-PhC3SS

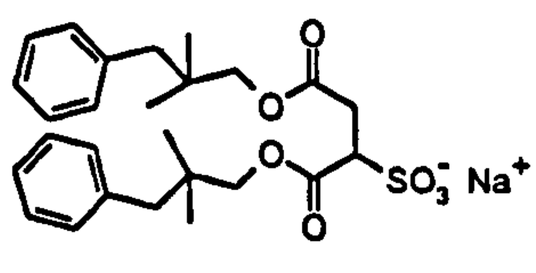

Br-di-PhC5SS

Figure 6.4 w/o microemulsion phase stability diagrams and schematic molecular structures for the di-phenyl sulfosuccinate series in water/toluene systems. Phase diagram for AOTⓉ (---) in toluene is given for comparison purpose. In all cases, lines are for the Winsor II (solubilisation) boundary. [Surfactant] = 0.10 mol dm^{-3}.

iii) Linear and branched phenyl sulfosuccinates show very limited phase stability in the temperature window studied (5–50 °C). In this range, only the solubilisation (Winsor II) boundary is observed – i.e., separating a single L_2-microemulsion phase from a two-phase (L_2-microemulsion + excess water) as temperature is increased. Unlike AOTs in water/heptane microemulsions, branched compounds, in particular, are characterised by a very low water solubilisation capacity ($w_{max} < 25$). AOT① itself shows a poor efficiency, reflecting unfavourable oil/chain interactions. Upper phase boundaries could only be observed for the branched compounds at very high temperatures – approx. > 70 °C (using an air-gun) – reflecting a possible "AOT-like" phase behaviour. However, experiments were limited by such extreme temperatures and evaporation of toluene.

6.3 MICROEMULSION FILM STRUCTURE FROM SANS

This section describes the phase structure of w/o microemulsions obtained by Small-Angle Neutron Scattering (SANS). Particular emphasis was given to the branched sulfosuccinate (AOTs) series, as a large range of w values was accessible. On the other hand, due to the limited phase stability of di-C*n*SS and di-PhC*n*SS surfactants, di-C6SS, di-PhC4SS, di-PhC5SS, and Br-di-PhC5SS only were investigated.

6.3.1 Experimental and fitting procedures

Details of SANS theory, data analysis, and instrumentation (LOQ and D22) have been given in Chapter 3. Hence, this section deals only with experimental and fitting aspects. Microemulsion samples were prepared by mass in 1 or 5 ml flasks and pre-equilibrated at the appropriate temperature for about 24 hours prior to the SANS measurements. Experiments were carried out on the D22 diffractometer at ILL (Grenoble, France), using a neutron wavelength of $\lambda = 10$ Å, and on the time-of-flight LOQ instrument at ISIS, U.K., where incident wavelengths are $2.2 \leq \lambda \leq 10$ Å [18]. Q ranges were 0.0035 – 0.359 $Å^{-1}$ on D22 and 0.009 – 0.249 $Å^{-1}$ at LOQ. Absolute intensities for I(Q) (cm^{-1}) were determined to within 5% by measuring the incoherent scattering from 1 mm of H_2O at ILL, while at ISIS a partially deuterated polymer

standard was used [19]. Accepted procedures for data treatment and background substraction were employed [18].

The least-squares *FISH* program was used to model and fit I(Q) data [9,20]. In this work, a core-shell Schultz polydisperse sphere model, with a hard-sphere structure factor $S_{hs}(Q)$ was used. For some AOTs microemulsion samples close to the high-temperature stability (haze) boundary, it was necessary to include an attractive Ornstein-Zernicke (O-Z) structure factor S(Q,ξ). This S(Q) effectively takes into account additional scattering at low Q, so that the O-Z function describes a decaying particle distribution with ξ a correlation length (see Chapter 3 Section 3.4.5 for mathematical definition of these S(Q) functions). With these models, different complementary contrasts may be fitted individually or simultaneously. For each surfactant, at a common w value, a contrast series was fitted simultaneously: core contrast D_2O/H-surf/H-alkane (D/H/H), shell contrast D_2O/H-surf/D-alkane (D/H/D) and drop contrast H_2O/H-surf/D-alkane (H/H/D).

In the *FISH* program, parameters may be fixed, tied together, or constrained as the fits proceeds. Since the sample composition and scattering length densities are known, the adjustable parameters required are the most probable core radius and polydispersity width, R_c^{av} and σ/R_c^{av}, as well as the apparent film thickness, t_s, and if used ξ and S(0), the structure factor at $Q = 0$. Hence this represents three (or five with S(Q)) free parameters fitted to three data sets simultaneously. In addition to the CSD simultaneous analysis, the individual core SANS data sets for a variation of w values were analysed on their own using the core-shell Schultz polydisperse sphere model. The water concentration defines ϕ_c, the core volume fraction; adding in the surfactant gives an overall value ϕ_d for the droplets. For each component the scattering length density (Table 6.1) ρ, was calculated from equation 6.3.1,

$$\rho = \sum_i b_i / V_m \qquad (6.3.1)$$

where b_i are the nuclear scattering lengths as given in the literature [18] and V_m is the molecular volume, which can be obtained from mass density. For the surfactants, a mass density of 1 g cm^{-3} was assumed. The constraints were $\phi_{hs}=\phi_d$ and $R_c^{av} = R_{drop}^{av}$,

together with the known ρ values for solvents. For any given set of parameters the core volume fraction ϕ_c defines the absolute scattering intensity, and ± 10% of the known value was allowed in the modelling.

Table 6.1 Mass densities, molecular volumes V_m, and scattering length densities ρ of surfactants and solvents at temperatures used in this work

	Temperature / °C	Density / (g cm^{-3})	($V_m \times 10^{21}$) / cm^{-3}	($\rho \times 10^{-10}$) / cm^{-2}
h-AOT①	22	1.0	1.429	0.542
h-AOT②	45	1.0	1.429	0.542
h-AOT③	9	1.0	1.429	0.542
h-AOT④	50	1.0	1.339	0.486
h-AOT⑤	9	1.0	1.429	0.542
h-di-C6SS	25	1.0	1.648	0.681
h-di-PhC4SS	25	1.0	1.305	1.233
h-di-PhC5SS	25	1.0	1.230	1.142
h-Br-di-PhC5SS	25	1.0	1.230	1.142
H_2O	9	1.000	33.43	-0.561
	22, 25	0.997	33.33	-0.560
	45	0.991	33.13	-0.556
	50	0.989	33.06	-0.555
D_2O	9	1.106	33.26	6.367
	22, 25	1.104	33.20	6.356
	45	1.098	33.02	6.321
	50	1.096	32.96	6.309
h-heptane	9	0.694	4.171	-0.556
	22, 25	0.684	4.111	-0.548
	45	0.663	3.985	-0.531
	50	0.656	3.943	-0.526
d-heptane	9	0.804	4.163	6.380
	22, 25	0.794	4.111	6.301
	45	0.773	4.003	6.134
	50	0.767	3.972	6.087
h-hexane	25	0.659	4.605	-0.576
d-hexane	25	0.767	4.607	6.140
h-hexanol	25	0.814	4.798	-0.321
h-toluene	25	0.862	5.634	0.935
d-toluene	25	0.943	5.668	5.662

6.3.2 Effect of chain branching

To determine the size and structure of the microemulsion aggregates SANS experiments were performed with each compound and a series of w values. As described above, the linear series involves the study of quaternary water-surfactant-alkane-alcohol systems so that direct comparison with the tertiary AOTs-based systems cannot be made. Therefore, this section focuses largely on the SANS data obtained for the branched sulfosuccinates in ternary systems, while di-C6SS data are only briefly presented, in view of the comparison with the glutaconate di-C6GLU system discussed in Chapter 7. For the branched compounds, experimental temperatures were carefully chosen so as to be at equivalent points with respect to phase boundaries (i.e., the same reduced temperature). The experiments were performed close to the solubilisation (Winsor II) boundary where droplets interact weakly. For normal AOT, aggregates are then well described as polydisperse spheres, with a hard-sphere structure factor to account for spatial correlations [14]. However, it should be noted that the situation differs slightly for AOT③ and ⑤, which were both studied at 9 °C (see Fig. 6.2 for position of isotherm within phase-stability diagrams).

CSD model and droplet structure

Example SANS data for the core, shell, and drop contrasts are shown on Figure 6.5 for (*a*) AOT① at w = 30, 22 °C, and (*b*) AOT④ at w = 30, 50 °C, along with the fitted I(Q) functions. At high Q these three contrasts can be clearly distinguished on a log-log plot, and in particular the shell contrast gives a good indication of polydispersity. Using the simultaneous CSD analysis, with only three free parameters (R_c^{av}, σ / R_c^{av}, and t_s) describing three data sets, the fits show this is a robust and reasonable model. Similar simultaneous analyses were performed on the other AOTs at w = 30 and the resulting shell contrasts and fits are shown in Figure 6.6. Fitted parameters are summarised in Table 6.2 along with the branching factor values. Considering the water core data, it is clear that the two most highly branched compounds, AOT② and ⑤, have a much lower water solubilisation capacity with a decrease in droplet size of ~ 3 – 6 Å (i.e., outside the uncertainties). This is indicative of more negative interfacial curvature due to the greater chain volume of AOT② and ⑤.

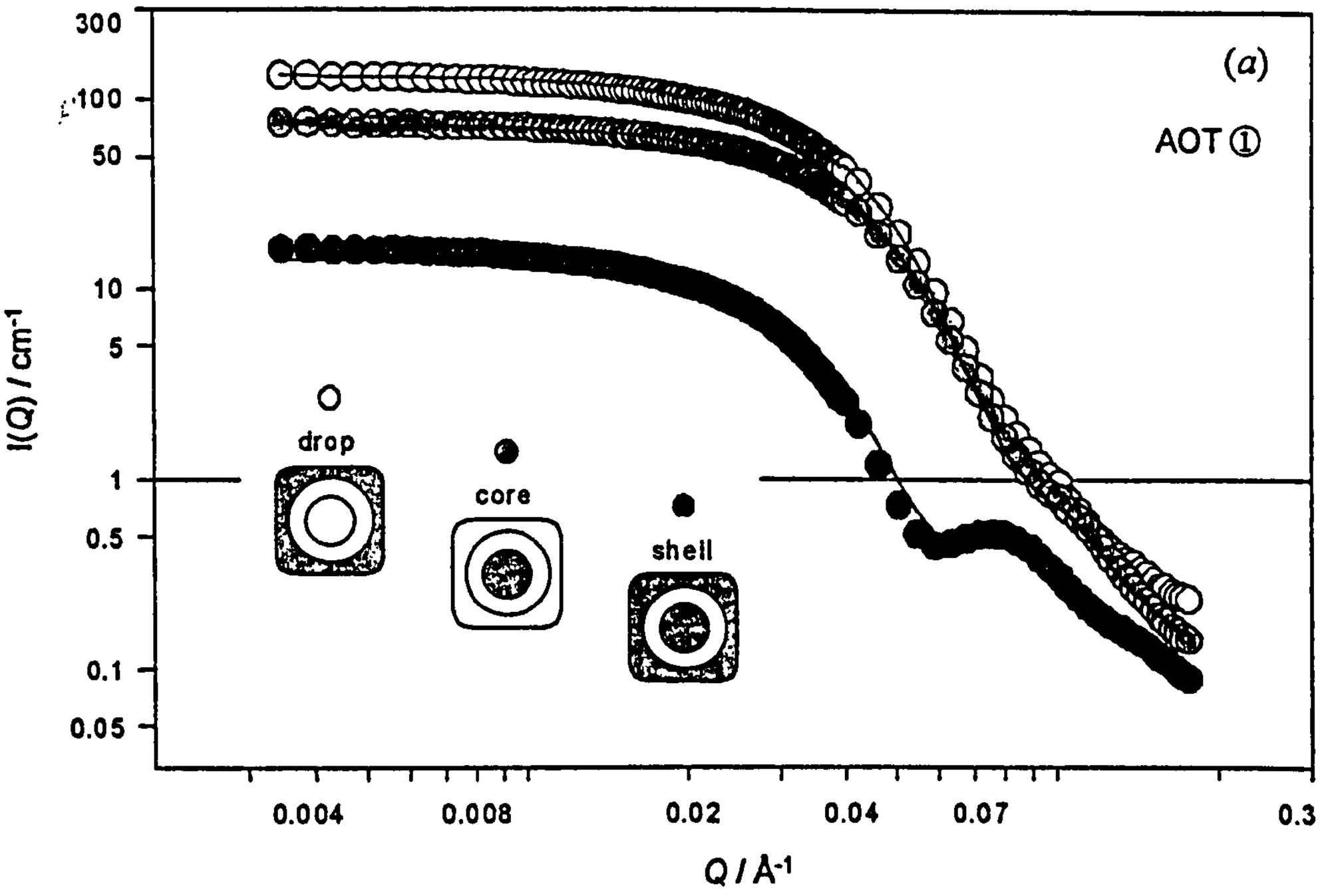

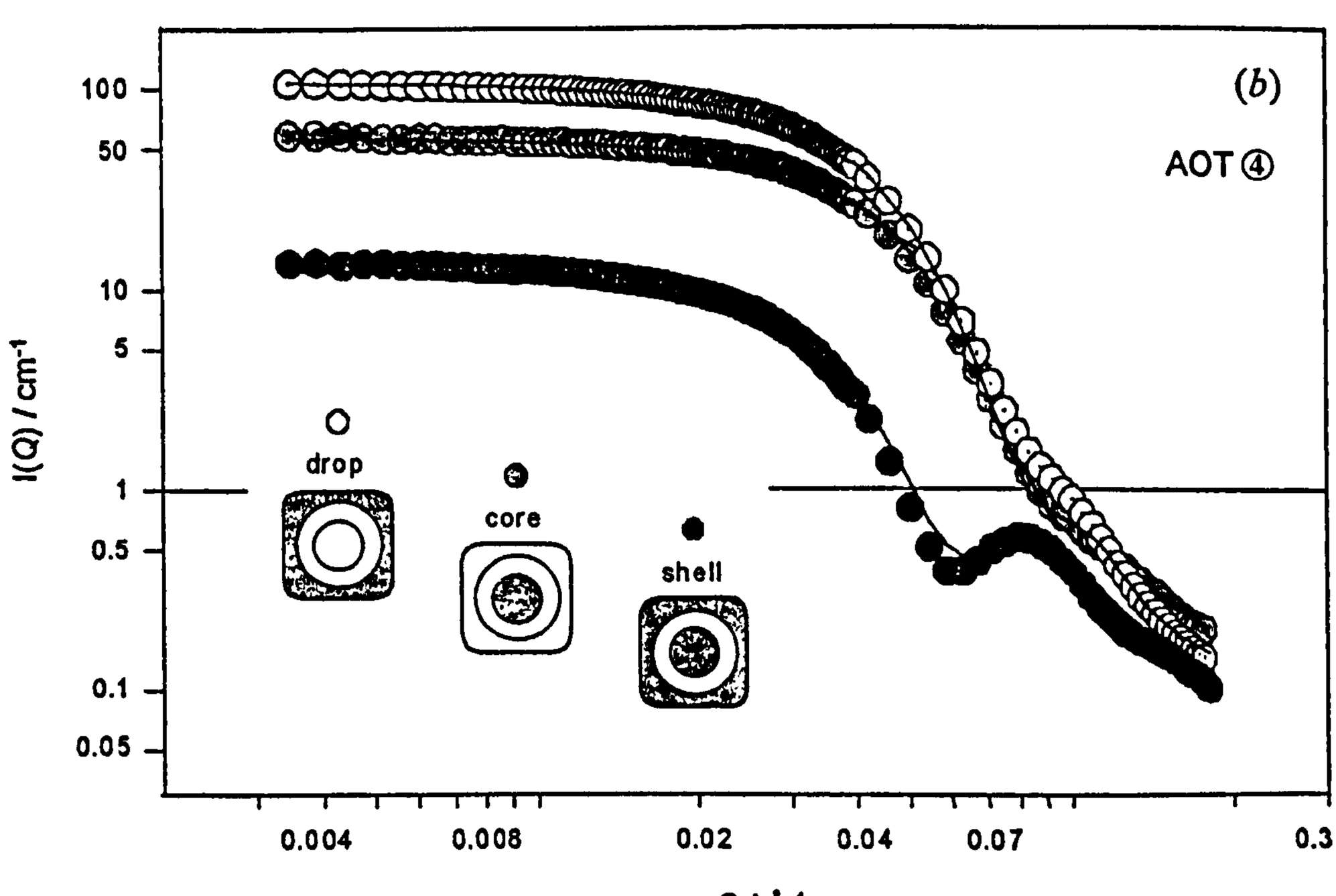

Figure 6.5 SANS data from D22 for (*a*) AOT① at 22 °C, and (*b*) AOT④ at 50 °C microemulsions. $w = 30$, $\phi_c = 0.027$. The simultaneous fit to the Schultz core-shell model and error bars on the data are shown.

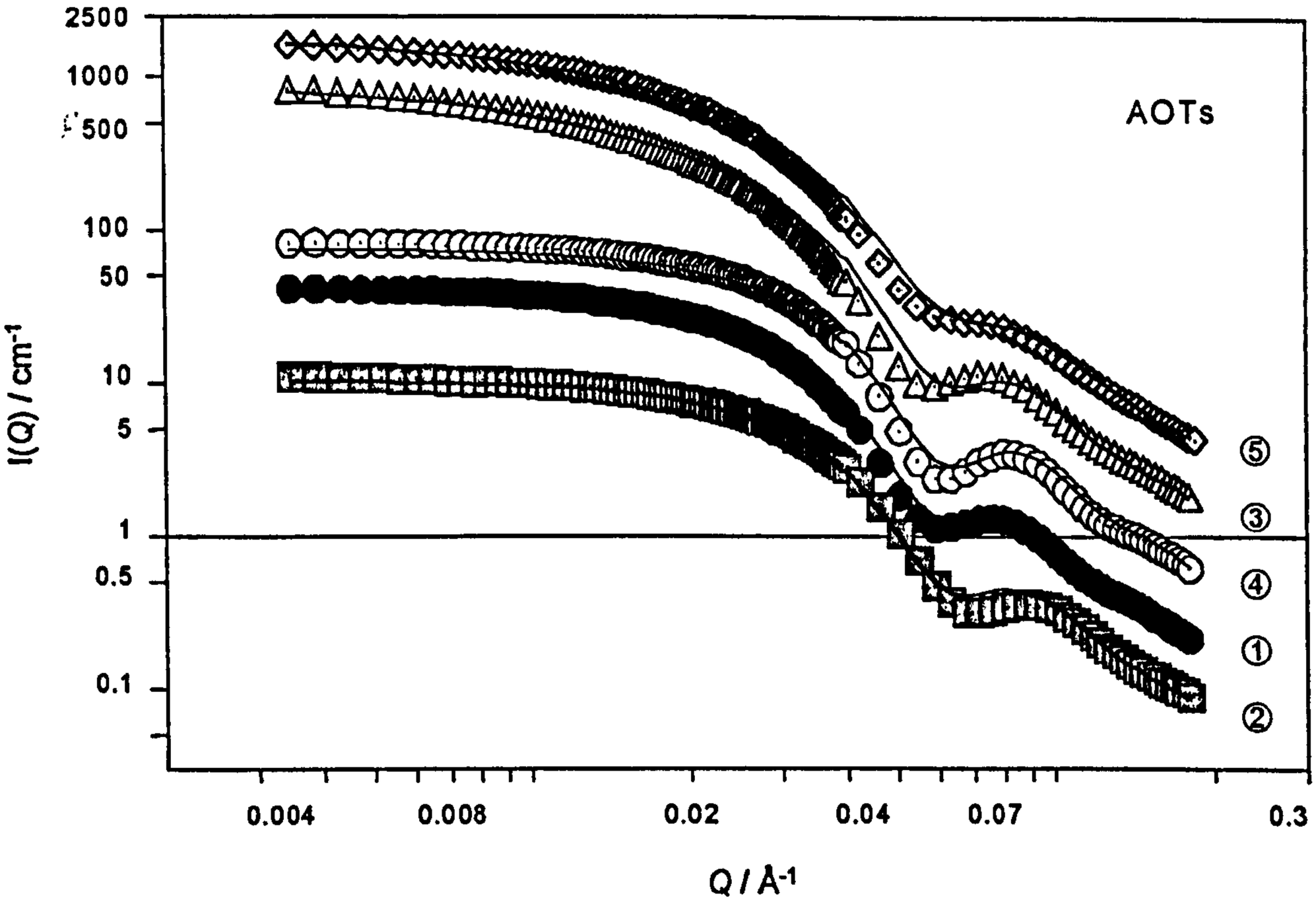

Figure 6.6 Shell contrast data from D22 for the AOTs series and fits to the Schultz core-shell model. [surfactant] = 0.5 mol dm^{-3}. Data/fits for each surfactant have been multiplied as follows: AOT① × 2.5, -③ × 20, -④ × 6, -⑤ × 50.

Table 6.2 Values obtained from the simultaneous analysis of core-shell-drop SANS data from AOTs w/o microemulsions at $w = 30$, $\phi_c = 0.03$, and $\phi_d = 0.05$[a]

AOT	T / °C	Branching factor	Water core		Surfactant film
			R_c^{av} / Å	σ/R_c^{av}	t_s / Å
⑤	9	2.80	40.5	0.28	8.4
②	45	2.40	41.3	0.23	8.7
①	22	1.67	46.1	0.22	9.1
③	9	1.60	43.4	0.24	8.6
④	50	1.33	45.0	0.19	9.4

[a] Parameters: R_c^{av}, average radius of water core; t_s, apparent shell thickness; σ / R_c^{av}, width of the Schultz distribution function. Uncertainties: R_c^{av} and t_s, ± 1 Å; σ / R_c^{av}, ± 0.01. The branching factor is defined in Chapter 5 (Section 5.3.3).

It is worth noting in Figure 6.6 that AOT⑤ presents a less pronounced "bump" at high Q, which indicates a larger polydispersity, as was obtained from the fit (Table 6.2). This is rather surprising since polydispersity generally arises owing to thermal fluctuations, and for normal AOT Kotlarchyk *et al*. found high values but only above 30 °C [4,21]. However they did not investigate in the very low temperature range. Also evident from Figure 6.6 is the enhanced scattering at low Q for AOT③ and ⑤, indicating strong droplet-droplet attractions ($S(Q)>1$ at $Q = 0$). Although not obvious from Figure 6.2, attractive interactions correspond to the system being close to a critical-type transition. As a result, the $I(Q)$ profiles for both compounds were analysed using an Ornstein-Zernicke $S(Q)$ [22].

Results from simultaneous fits also show that for any surfactant there is no significant oil penetration into the chains and a sharp-step model describes the interfacial structure well [9,12,20]. Fitted values for the thickness of the surfactant layer t_s are given in Table 6.2 and for AOT① it is 9.1 ± 1 Å, which agrees reasonably well with various literature SANS data [4,12,23]. Although the AOTs have very similar values for t_s (within error), it is worth noting that AOT① and ④, with the two longest tails (effectively C6 chains as compared to C5 for AOT②, ③ and ⑤), give the two highest film thicknesses. This shows that even such subtle structural changes can be identified by SANS, and for systems of this kind the technique has "molecular resolution".

w variation and molecular areas

Figure 6.7 shows the $I(Q)$ profiles and fitted functions for various w values with AOT② in core contrast only. Note that due to the large number of data points obtained on the D22 instrument a 12.5% rebinning was applied for clarity of presentation. The fitted parameters are the core radius R_c^{av} and Schultz scale factor only.

For AOT microemulsions, Kotlarchyk *et al*. have shown that the polydispersity was a function of temperature but not of w [21], so this was fixed, using the value obtained from the CSD and/or shell fitted $I(Q)$ profiles. The scattering from these systems, as well as all other AOTs, shows a similar trend to that observed for normal AOT microemulsions. The relatively flat region at small angles ($Q < 0.02$ Å^{-1}) indicates spherical non-interacting particles (with the exception of AOT③ and ⑤ as mentioned previously). At higher Q the scattering scales as approximately Q^{-4}, characteristic of

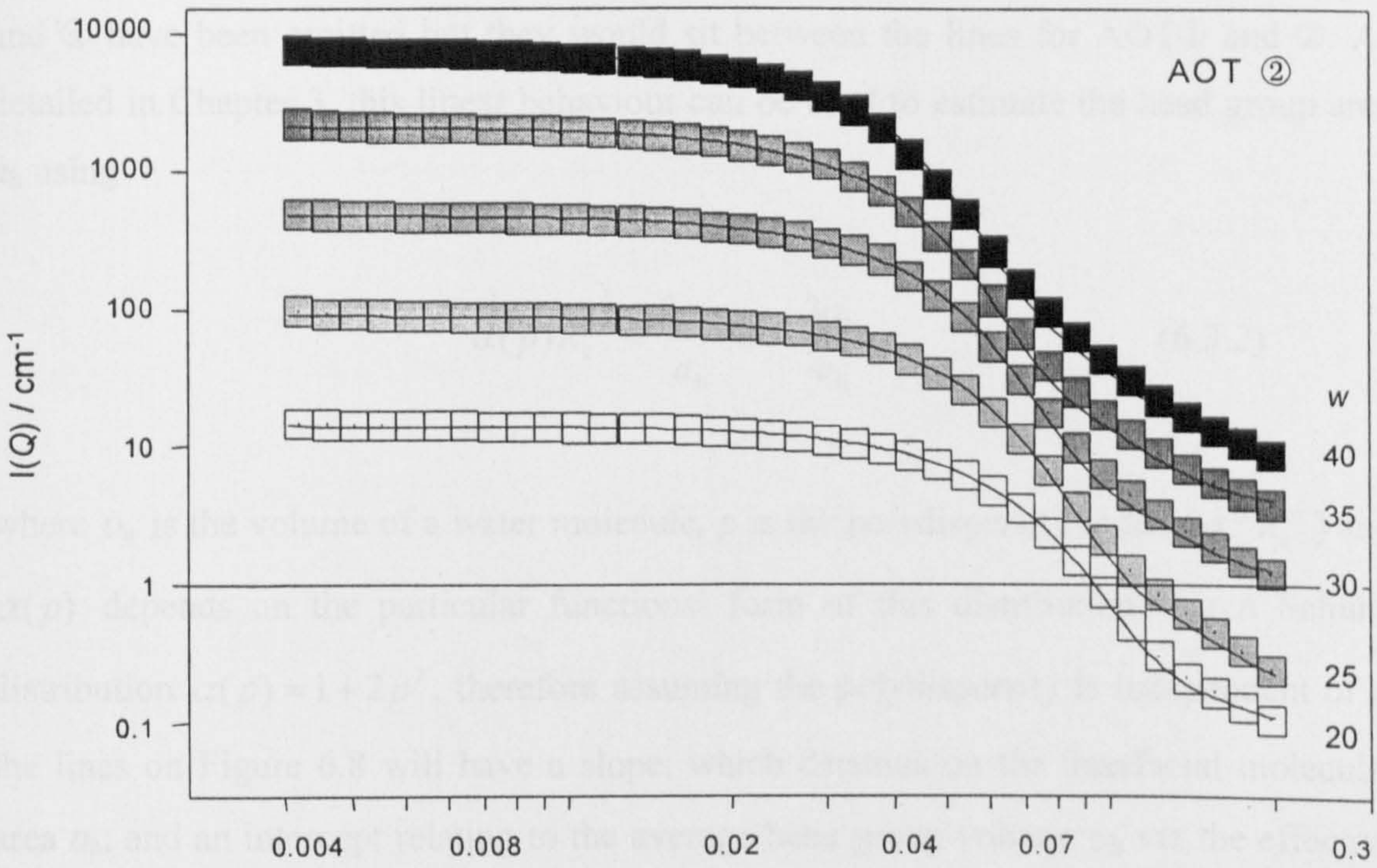

Figure 6.7 Core contrast data from D22 and fits (—) to a Schultz polydisperse sphere model for Winsor II microemulsion of AOT②. The oil is *n*-heptane, [AOT②] = 0.5 mol dm^{-3}, and $T = 9$ °C. Data/fits for each w values have been multiplied as follows: $w = 40 \times 50, 35 \times 20, 30 \times 8, 25 \times 3$.

sharp, smooth oil-water interface. Fitted values are summarised in Table 6.3 and as observed from the simultaneous analysis, AOT② and ⑤ with the two bulkier hydrophobic groups of the series have smaller droplet radii.

For each compound, a linear R_c vs. w relationship was obtained, which is shown on Figure 6.8 for AOT①, ② and ⑤. For clarity purposes, data and linear fits for AOT③ and ④ have been omitted but they would sit between the lines for AOT① and ②. As detailed in Chapter 3, this linear behaviour can be used to estimate the head group area a_h using

$$\alpha(p)R_c^{av} = \frac{3\upsilon_w}{a_h}w + \frac{3\upsilon_h}{a_h} \qquad (6.3.2)$$

where υ_w is the volume of a water molecule, p is the polydispersity index (σ / R_c^{av}) and $\alpha(p)$ depends on the particular functional form of this distribution. For a Schultz distribution $\alpha(p) = 1 + 2p^2$, therefore assuming the polydispersity is independent of w the lines on Figure 6.8 will have a slope, which depends on the interfacial molecular area a_h, and an intercept relating to the average head group volume υ_h via the effective surfactant head group radius r_h

$$r_h = \left(\frac{3\upsilon_h}{4\pi}\right)^{1/3} \qquad (6.3.3)$$

The head group area can also be derived from core contrast data at high Q using the Porod equation, which for sharp interfaces is

$$\left\{I(Q).Q^4\right\} = 2\pi\Delta\rho^2\Sigma \qquad (6.3.4)$$

where $\Delta\rho = (\rho_{D_2O} - \rho_{oil})$ the contrast step and Σ is the total area per unit volume [24]. Assuming that all N surfactant molecules per unit volume are adsorbed, then $a_h(\text{Porod}) \approx \Sigma / N$. Examples of Porod plots are given in Figure 6.9 for (*a*) AOT③, and (*b*) AOT④, and results derived from Eq. 6.3.2 and 6.3.4 are given in Table 6.4.

Table 6.3 Fitted mean water core radii from core SANS D22 and LOQ data for the AOTs series

AOT	Mean water core radius $R_c^{av} \pm 1$ Å						
	$w = 10$	$w = 15$	$w = 20$	$w = 25$	$w = 30$	$w = 35$	$w = 40$
①	21.6	27.7	32.9	38.9	45.8	51.4	58.2
②	20.4	26.2	31.1	37.3	43.0	49.2	54.5
③	20.3	25.8	30.9	37.2	43.1	49.1	55.8
④	21.2	27.6	33.6	-	45.4	51.7	58.5
⑤	-	-	28.9	34.8	39.9	44.7	-

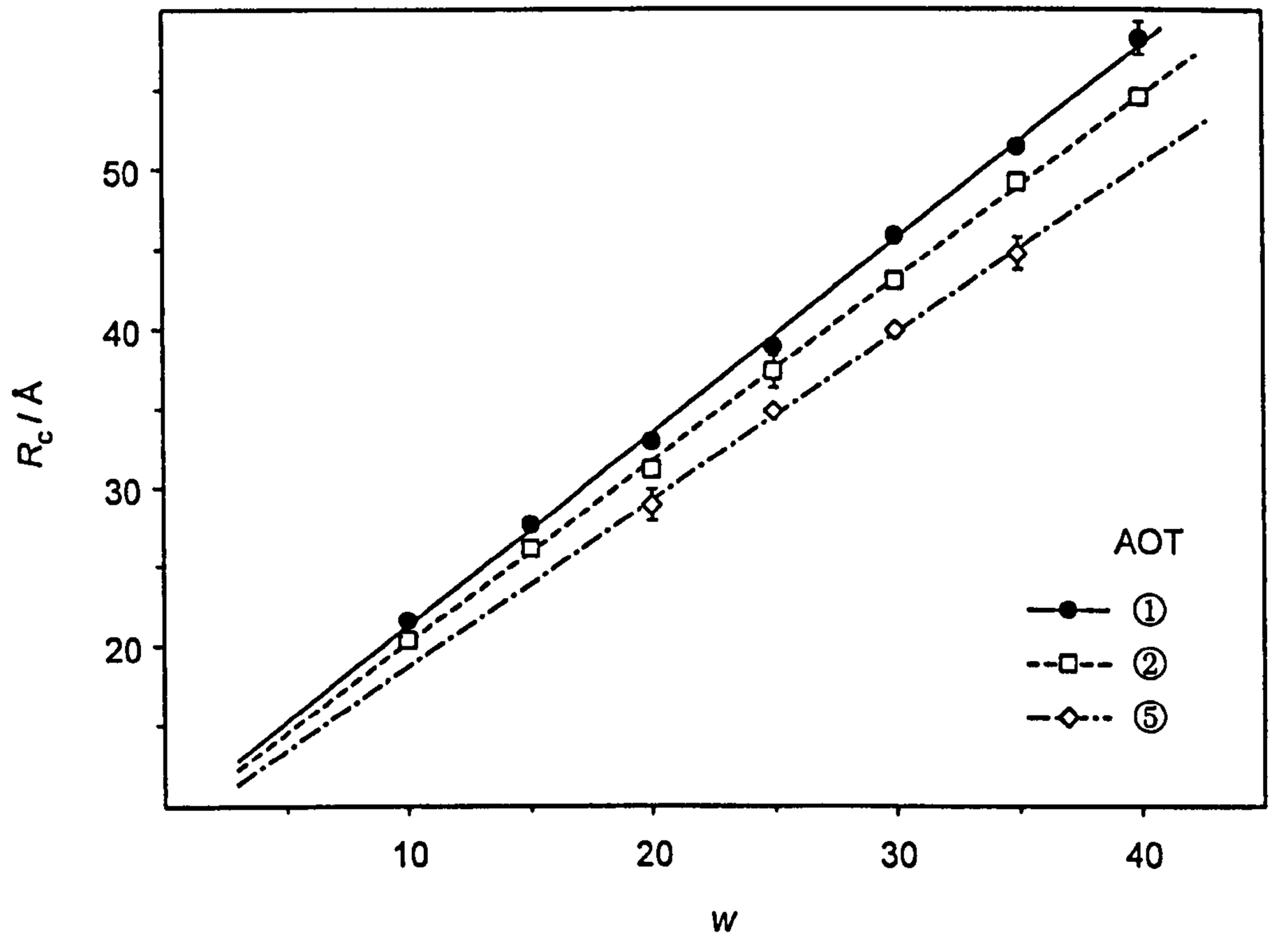

Figure 6.8 Water droplet radius R_c versus w for AOT①, -②, and -⑤ w/o microemulsions. R_c values are from SANS analysis of core contrasts as given in Table 6.3. Note that the supporting data for w = 10 and 15 are from LOQ. Example error bars are shown.

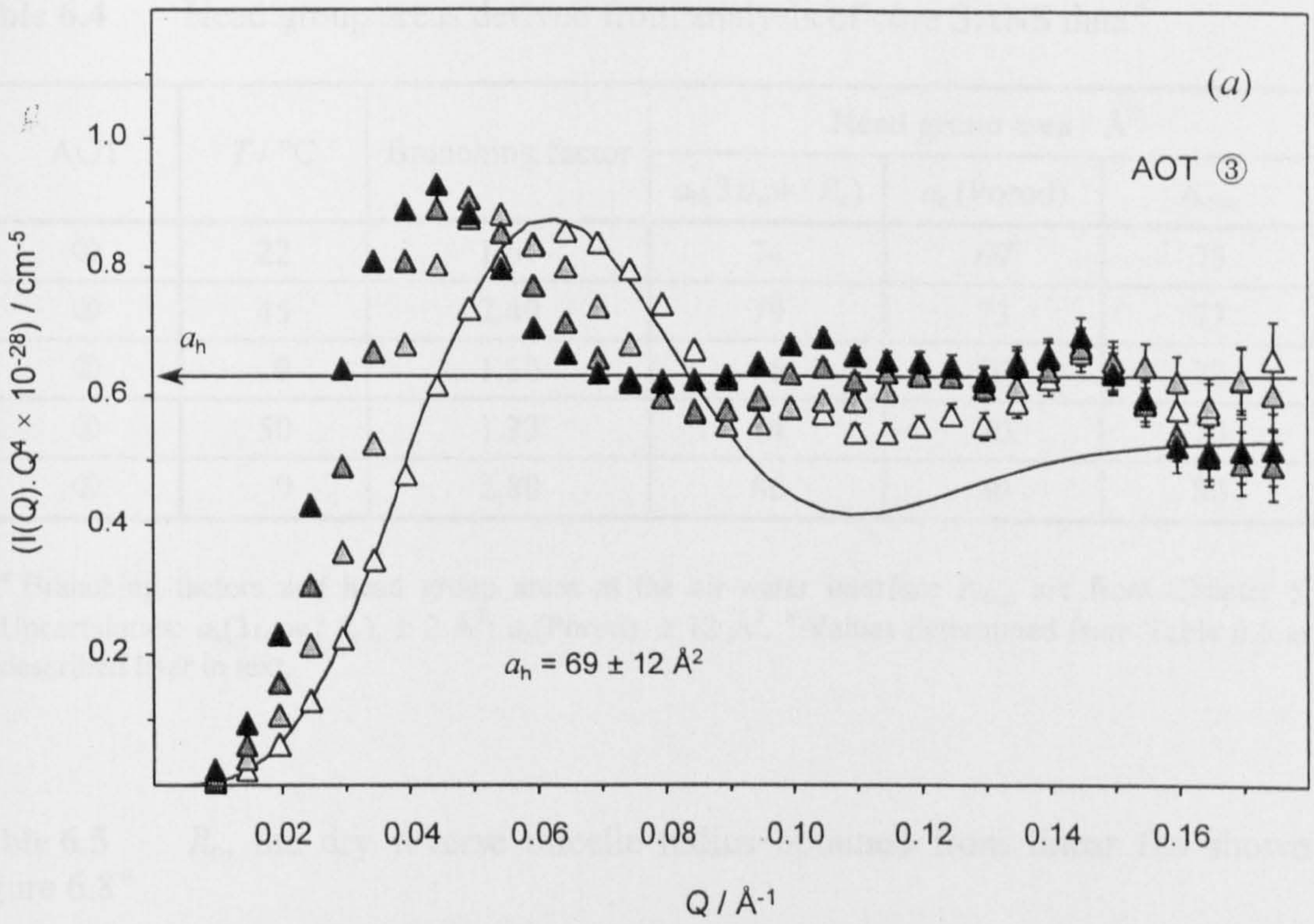

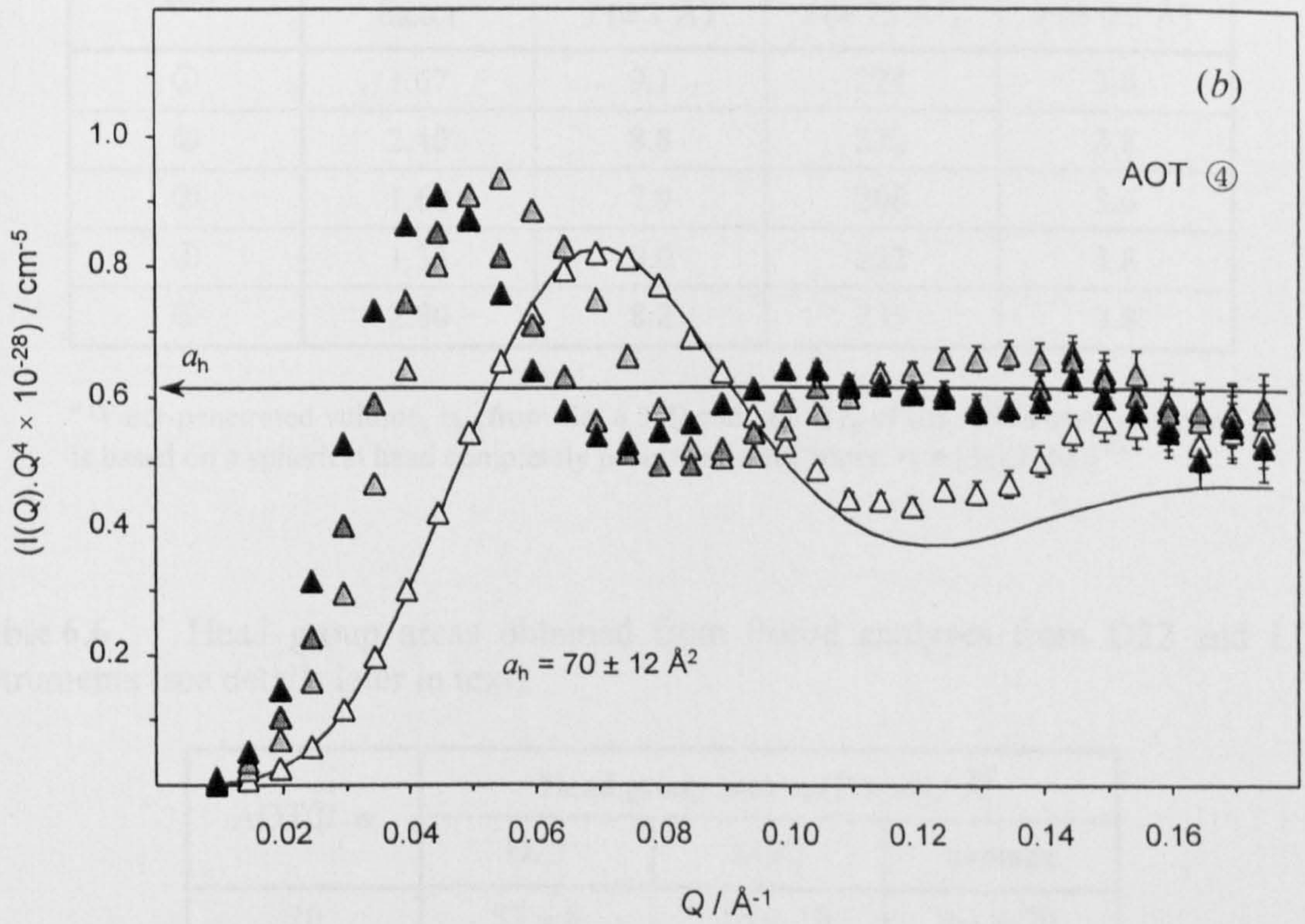

Figure 6.9 Porod plots of D22 data from (*a*) AOT③ and (*b*) AOT④ Winsor II microemulsions. The *w* variation is 25 (Δ), 30 (Δ), 35 (▲), 40 (▲). For $w = 25$ the model fit is also shown.

Table 6.4 Head group areas derived from analysis of core SANS data[a]

AOT	T / °C	Branching factor	Head group area / Å^2		
			$a_h(3\upsilon_w w / R_c)$	a_h (Porod)	A_{cmc}
①	22	1.67	74	69[b]	75
②	45	2.40	79	73	77
③	9	1.60	76	69	73
④	50	1.33	74	70	70
⑤	9	2.80	86	80	80

[a] Branching factors and head group areas at the air-water interface A_{cmc} are from Chapter 5. Uncertainties: $a_h(3\upsilon_w w / R_c)$, ± 2 Å^2; a_h(Porod), ± 12 Å^2. [b] Values determined from Table 6.6 as described later in text.

Table 6.5 R_0, the dry reverse micelle radius obtained from linear fits shown in Figure 6.8[a]

AOT	Branching factor	R_o / (± 1 Å)	υ_h / (± 25 Å^3)	r_h / (± 0.5 Å)
①	1.67	9.1	224	3.8
②	2.40	8.8	232	3.8
③	1.60	7.9	200	3.6
④	1.33	9.0	222	3.8
⑤	2.80	8.2	235	3.8

[a] Water-penetrated volume, υ_h (from Eq. 6.3.2) and radius r_h of the AOTs head group. r_h is based on a spherical head completely penetrated with water. $r_h = [3\upsilon_h / (4\pi)]^{1/3}$.

Table 6.6 Head group areas obtained from Porod analyses from D22 and LOQ instruments (see details later in text)

AOT① w	Head group area a_h (Porod) / Å^2		
	D22	LOQ	average
20	57 ± 8	69 ± 19	63 ± 20
25	62 ± 9	74 ± 12	68 ± 14
30	68 ± 10	76 ± 8	72 ± 13
35	70 ± 10	74 ± 8	72 ± 13
40	70 ± 10	72 ± 6	71 ± 12

Agreement between a_h values derived from the two equations is reasonable given the assumptions involved, monodisperse spheres for Eq. 6.3.2 and sharp-step interfaces for Eq. 6.3.4. For AOT①, values from the *w* variation and Porod plots are 74 ± 2 Å^2 and 69 ± 12 Å^2 respectively. Particular attention has been given to the determination of the latter value, and its associated uncertainty and will be discussed below. These results compare favourably with reported data for normal AOT [4,21,25].

SANS measurements have been performed on AOT④ by Atkinson *et al.* [7] using a different oil phase and experimental temperature (water-in-decane microemulsions at 25 °C), and much larger droplet sizes (~ 10 to 15 Å) were obtained. As observed with normal AOT [25], water core radii should show no significant dependence on the alkane chain length. However, the position within the phase-stability diagram can explain such differences: for AOT, Kotlarchyk *et al.* [21] reported an increase in radius, only close to the critical point. In the work of Atkinson *et al.* samples were located in the upper part of the funnel-shaped single phase, where the L_2-microemulsion phase is quite narrow. In this case interactions are likely to be present, as revealed by the bluish-white appearance of samples in this region. The experiments performed here were in the proximity of the Winsor II boundary, therefore it is not possible to compare directly the radii from the two studies.

Another explanation for the differences is plausible. With ionic surfactants, a small decrease in droplet size could be due to the presence of small quantities of electrolyte carried forward from the sulfonation: decreasing electrostatic repulsion between head groups would favour more negative curvature and enhanced interfacial packing. However, the compound used in the present study was of high purity (see Chapters 4 and 5), so the microemulsion stability is consistent with the solubility of the surfactant in water (see previous section), as well as the phase behaviour described by Atkinson *et al.* Inorganic contaminants cannot therefore explain such a large difference in radii between the two studies.

Keeping in mind the different chain structures involved (Fig. 6.2), useful information on the film packing can be derived from the SANS data (Tab. 6.4 and 6.5):

i) Head group areas (Table 6.4) correlate well with the extent of branching in the chain, i.e., AOT② and ⑤ with the two highest branching factors pack less efficiently and so can solubilise less water as mentioned previously.

ii) The molecular packing in the curved oil-water film is very close to that found at the air-water surface (see values for A_{cmc}), indicating that the microemulsion interface can be described as a liquid-like condensed surfactant film. Similar observations have been reported for the double-chain cationic didodecylammonium bromide, with head group areas of 60 – 68 $Å^2$ at the air-water interface [26] and 56 – 61 $Å^2$ in microemulsion systems [9].

iii) From linear fits in Figure 6.8, values of head group area a_h and intercept R_o can give estimates for the volume of the water-penetrated portion of a single surfactant head group υ_h (Eq. 6.3.2), and the radius of the surfactant polar head group r_h (Eq. 6.3.3). Values are summarised in Table 6.5, and υ_h and r_h for AOT① compare favourably with those estimated by other workers [21,23,27]. Furthermore, adding the intercept R_o, which corresponds to the radius of the polar core (i.e., head group and any bound water) to the fitted tail length t_s (Table 6.2), gives a consistent value for the reverse micelle radius. For the branched sulfosuccinates, data from Tables 6.2 and 6.5 give ~ 16.5 – 18.5 Å ($R_o + t_s$), which compares favourably with that estimated for normal AOT [23,28].

However, considering the assumptions, the model-dependence and the derived uncertainties it is dangerous to read too much into these results. Still, looking back at the extremes in tail structure and widths of hydrocarbon backbones involved, which must be less than 5 Å in each tail, the variation in head group areas obtained from SANS appear to be reasonable.

As mentioned earlier, relatively large uncertainties are associated with head group areas determined using the Porod equation. These can be readily explained by comparing data from the two different SANS instruments (D22 and LOQ). The $\{I(Q).(Q)^4\}$ vs. Q representation is very sensitive to small changes in Q, and so the large discrepancy observed in the maximum values of $I(Q).(Q)^4$ would be only minor on a log–log format. Variations over this Q range are believed to arise from the different methods of data normalisation, with respect to the wavelength dependence of transmission.

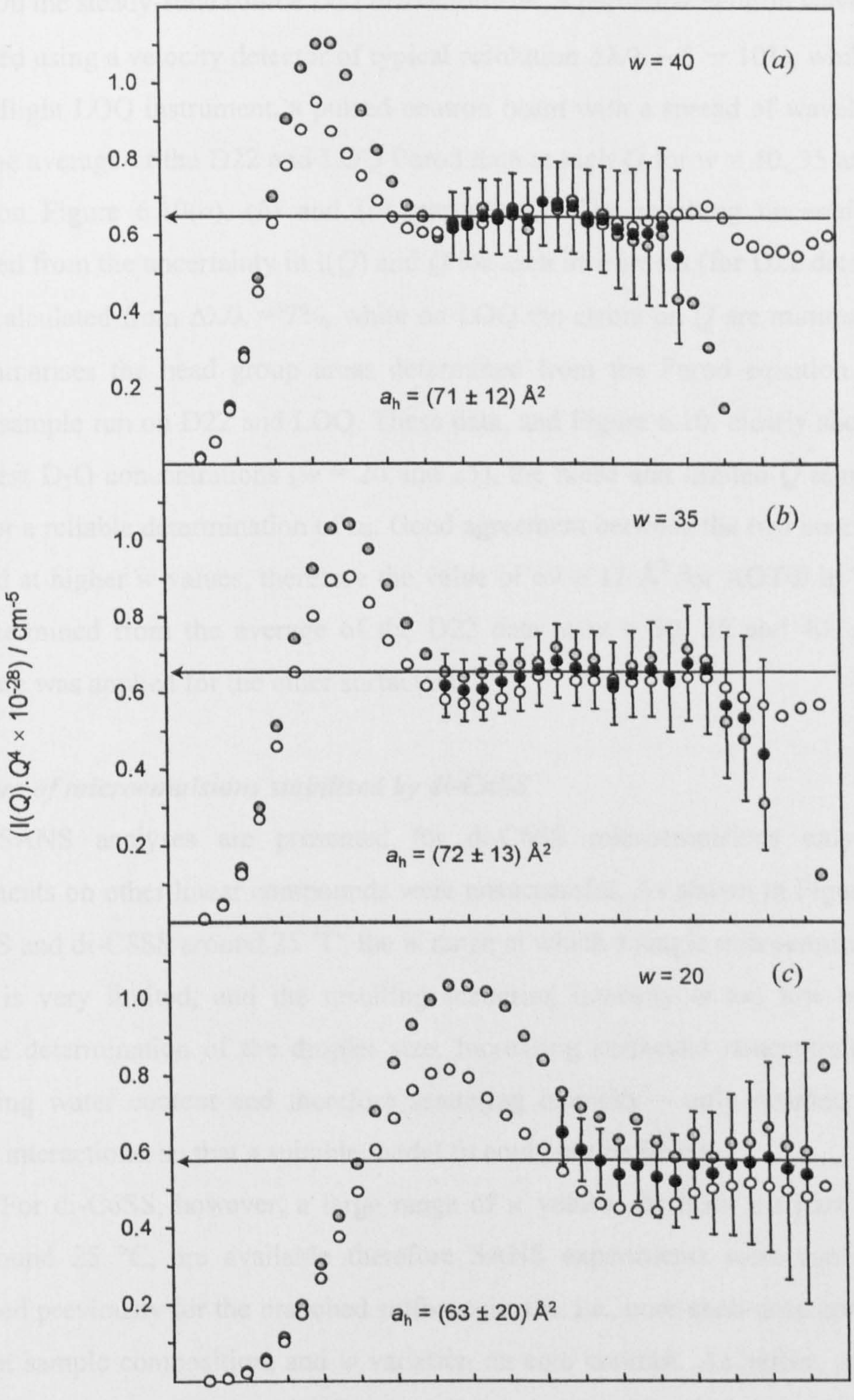

Figure 6.10 SANS data from D22 and LOQ on core contrasts of AOT① for (*a*) w = 40, (*b*) w = 35, and (*c*) w = 20. Markers: (○) LOQ, (○) D22, (●) average data from the two instruments. Error bars are shown for the averaged data only.

On the steady-state source D22 diffractometer, a particular neutron wavelength λ is selected using a velocity detector of typical resolution $\Delta\lambda/\lambda \sim 5 \rightarrow 10\%$, whilst on the time-of-flight LOQ instrument, a pulsed-neutron beam with a spread of wavelengths is used. The average of the D22 and LOQ Porod data at high Q for $w = 40$, 35 and 20 are shown on Figure 6.10(*a*), (*b*) and (*c*) respectively. The resulting uncertainties are calculated from the uncertainty in I(Q) and Q for each instrument (for D22 data error on Q was calculated from $\Delta\lambda/\lambda = 7\%$, while on LOQ the errors on Q are minimal). Table 6.6 summarises the head group areas determined from the Porod equation for each AOT① sample run on D22 and LOQ. These data, and Figure 6.10, clearly show that at the lowest D_2O concentrations ($w = 20$ and 25), the noise and limited Q range do not allow for a reliable determination of a_h. Good agreement between the two instruments is obtained at higher w values, therefore the value of 69 ± 12 Å^2 for AOT① in Table 6.4 was determined from the average of the D22 data at $w = 30$, 35 and 40. A similar procedure was applied for the other surfactants.

Structure of microemulsions stabilised by di-CnSS

SANS analyses are presented for di-C6SS microemulsions only as trial experiments on other linear compounds were unsuccessful. As shown in Figure 6.1, for di-C7SS and di-C8SS around 25 °C, the w range at which a single microemulsion phase occurs is very limited, and the resulting scattering intensity is too low to give an accurate determination of the droplet size. Increasing surfactant concentration – i.e., increasing water content and therefore scattering intensity – only resulted in strong droplet interactions, so that a suitable model fit could not be found.

For di-C6SS, however, a large range of w values, far from the haze boundary and around 25 °C, are available therefore SANS experiments were carried out as described previously for the branched sulfosuccinates, i.e., core-shell-drop contrasts at a constant sample composition, and w variation on core contrast. As before, systems are well described as polydisperse spheres with a hard-sphere structure factor. CSD and single core data are shown in Figures 6.11 and 6.12 respectively, with model fits. Simultaneous fitting analyses allowed the determination, for $w = 30$, of the water core radius, polydispersity, and surfactant film thickness, which were, respectively, $R_c^{av} = 30.8 \pm 1$ Å, $\sigma / R_c^{av} = 0.26 \pm 0.01$, and $t_s = 8.8 \pm 1$ Å.

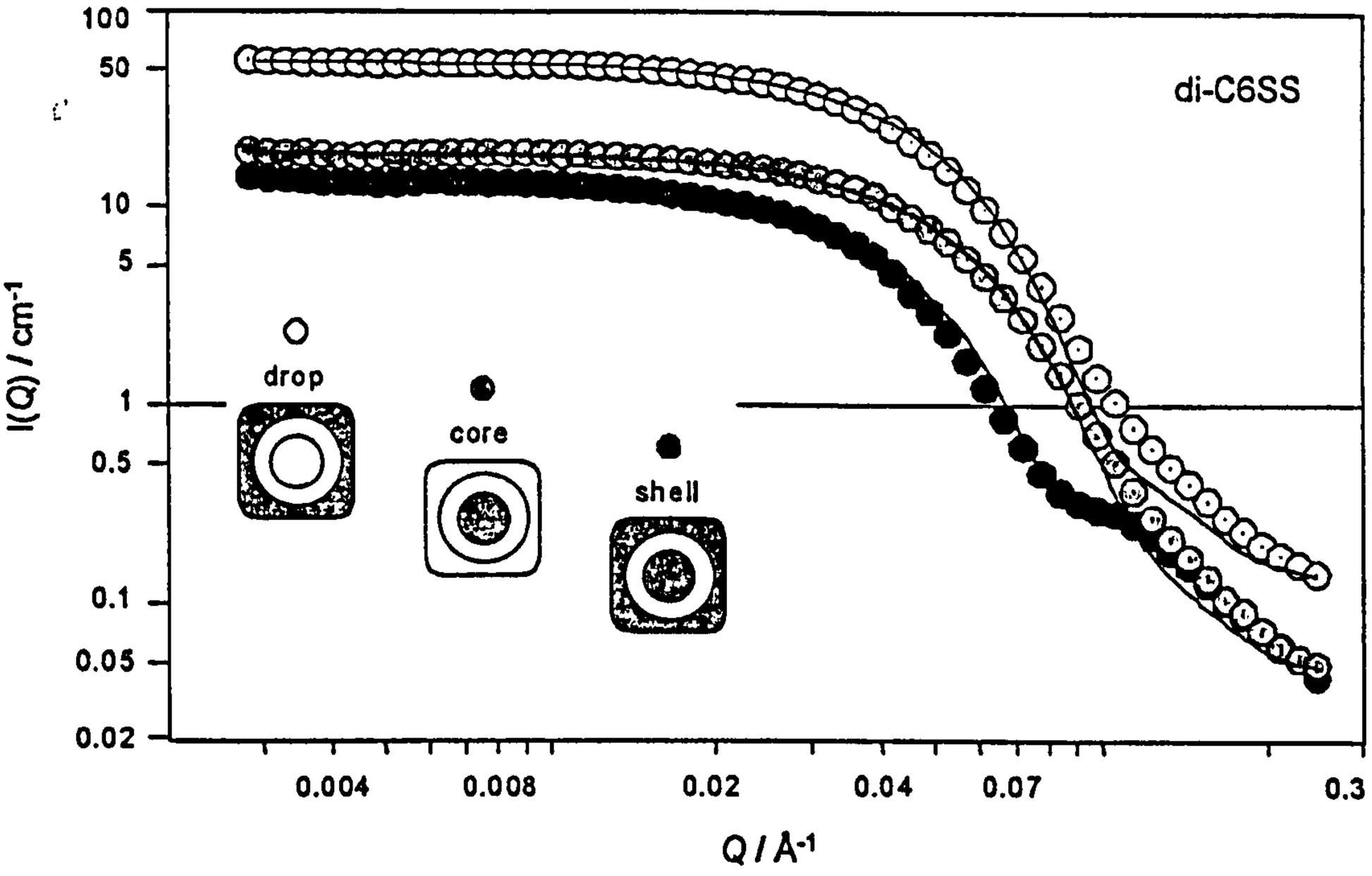

Figure 6.11 SANS data from D22 for di-C6SS microemulsions at $w = 30$, $\phi_c = 0.03$, and $T = 25$ °C. [di-C6SS] = 0.05 mol dm^{-3}. The simultaneous fit (—) to the Schultz core-shell model and error bars on the data are shown.

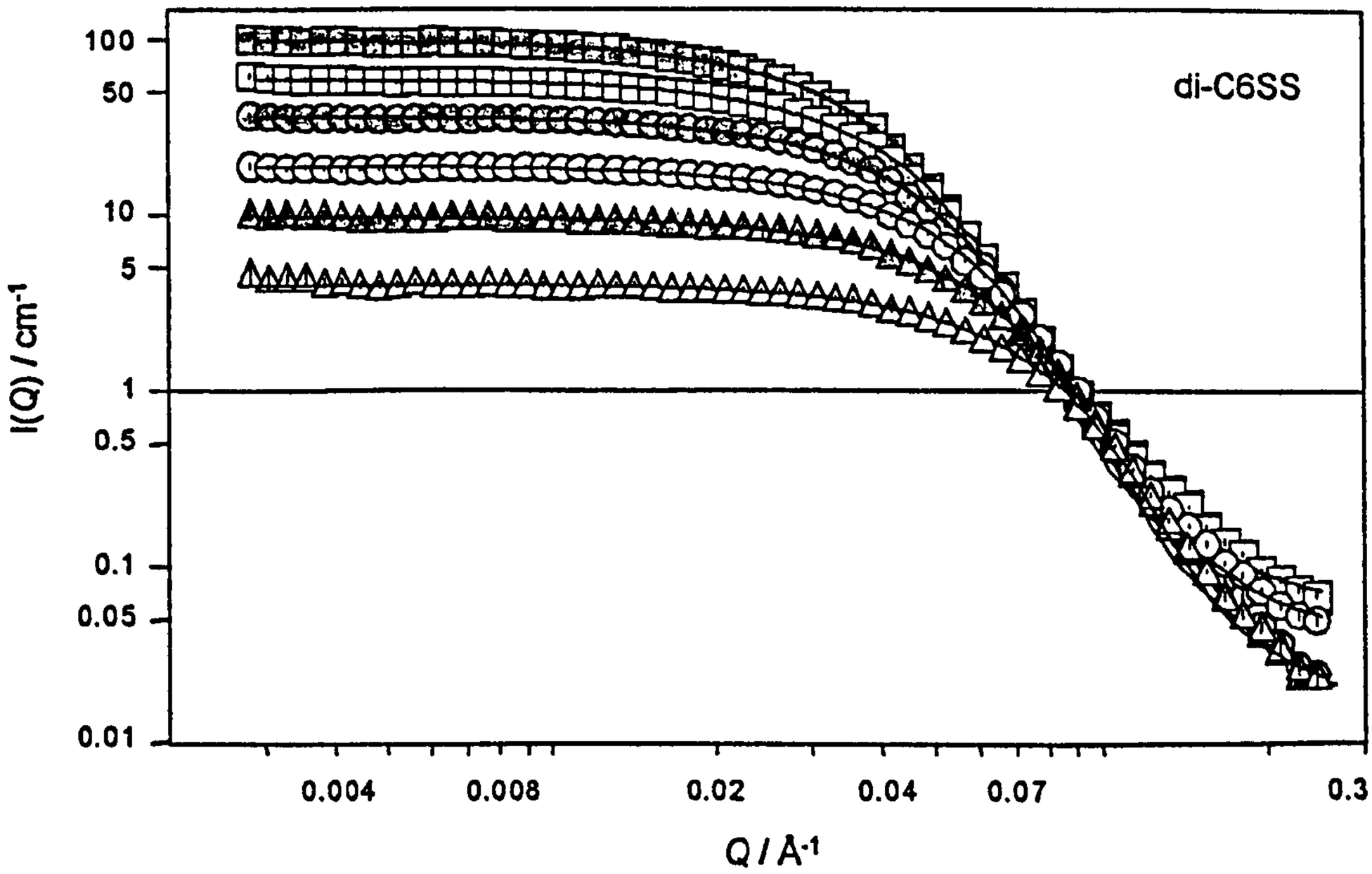

Figure 6.12 SANS core contrast data from D22 and fits (—) to a Schultz polydisperse sphere model for Winsor II microemulsions of di-C6SS. [surf] = 0.05 mol dm^{-3}, $T = 25$ °C. $w = 20$ (△), 25 (▲), 30 (○), 35 (●), 40 (□), 45 (■).

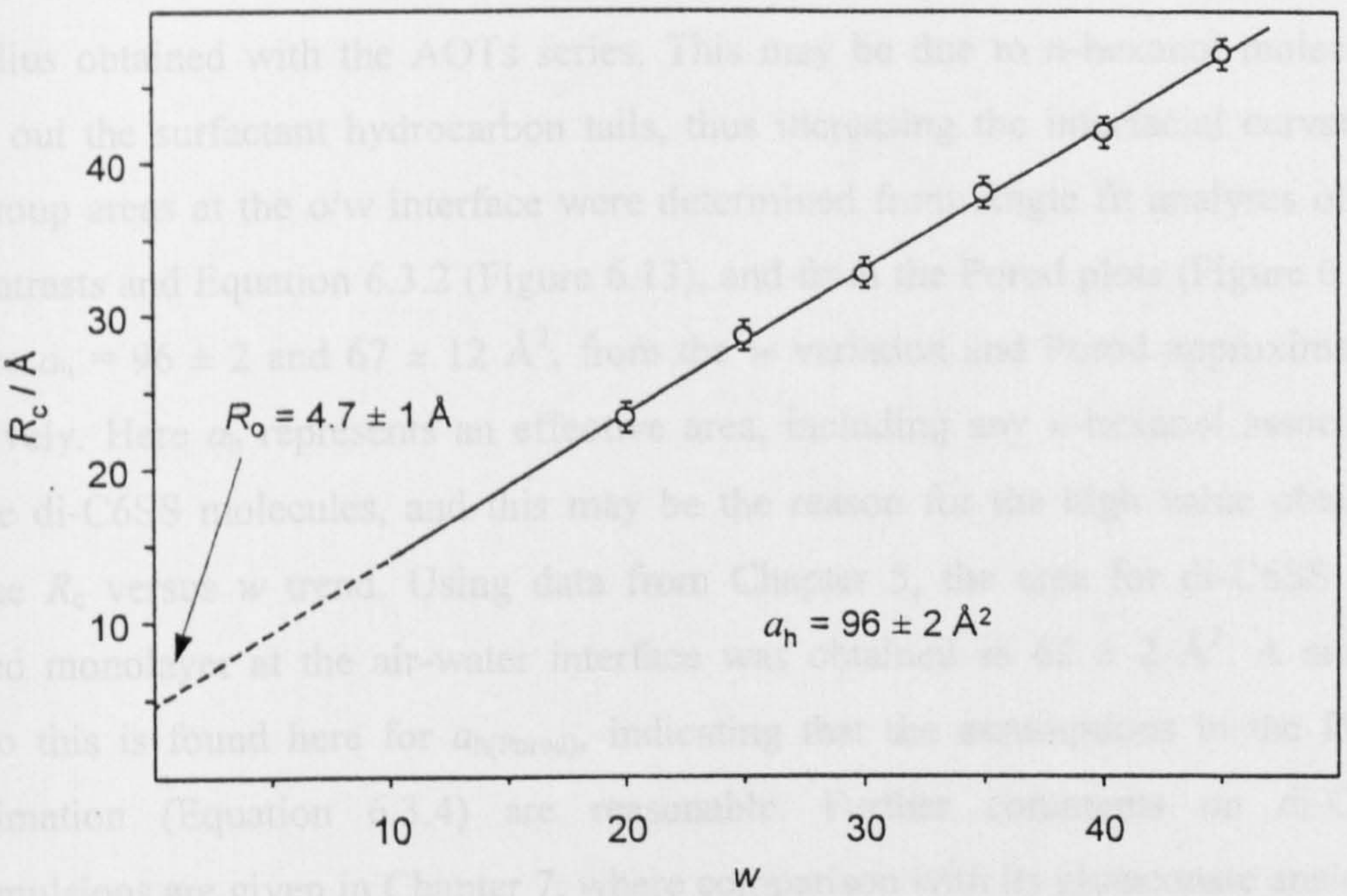

Figure 6.13 Water droplet radius R_c versus w for di-C6SS w/o microemulsions. R_c values are from SANS analysis of core contrasts (Figure 6.12).

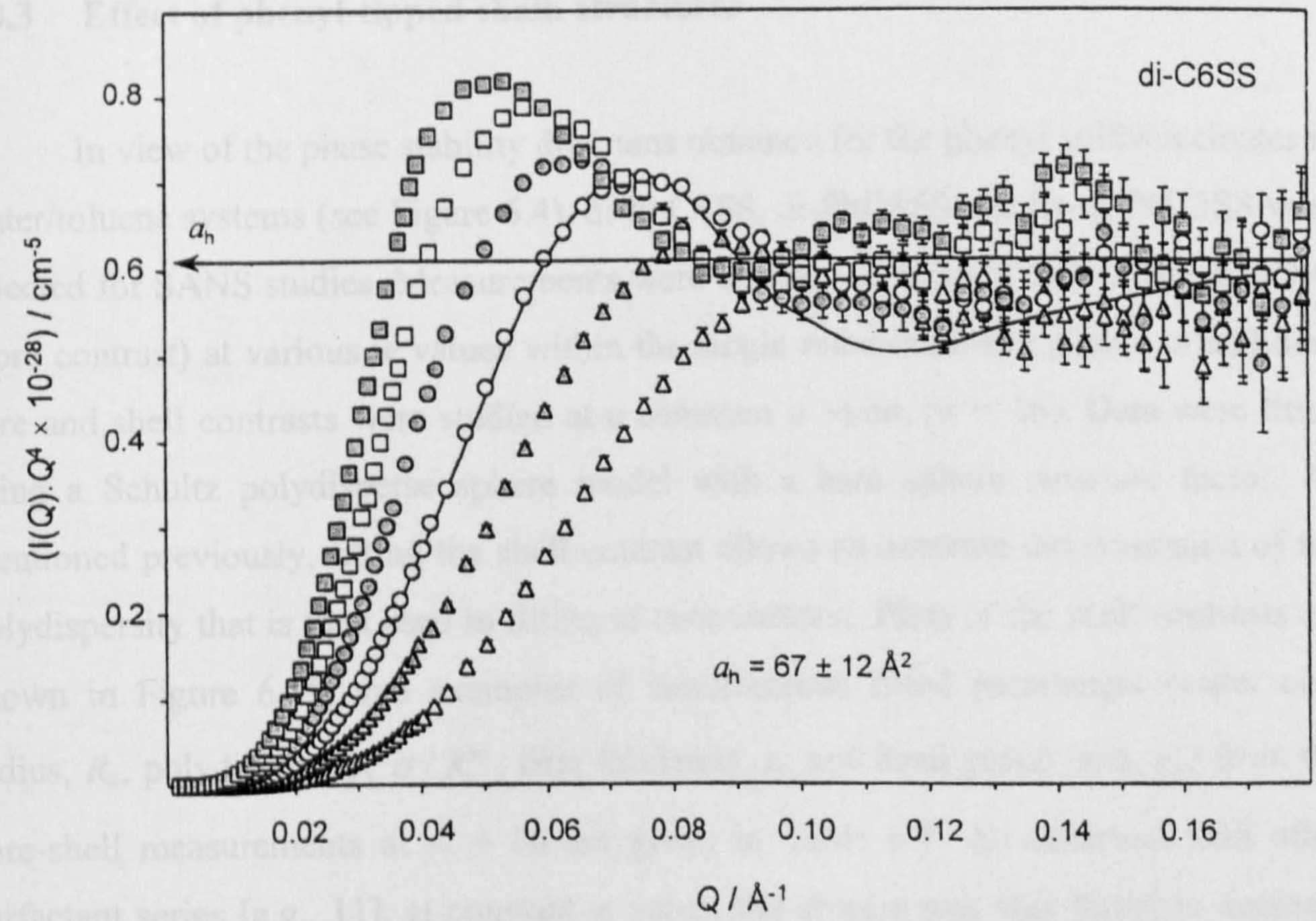

Figure 6.14 Porod plot of D22 data from Winsor II di-C6SS microemulsions. [surf] = 0.05 mol dm^{-3}, T = 25°C. w = 20 (△), 25 (▲), 30 (○), 35 (●), 40 (□), 45 (■). For w = 30 the model fit (—) and example error bars at high Q are shown. A level of scattering, representing an average area per head group, a_h, is also shown.

Looking back to Table 7.2 shows that R_c^{av} is much smaller (about 10 – 15 Å) than any core radius obtained with the AOTs series. This may be due to *n*-hexanol molecules spacing out the surfactant hydrocarbon tails, thus increasing the interfacial curvature. Head group areas at the o/w interface were determined from single fit analyses of the core contrasts and Equation 6.3.2 (Figure 6.13), and from the Porod plots (Figure 6.14). They are a_h = 96 ± 2 and 67 ± 12 Å^2, from the *w* variation and Porod approximation respectively. Here a_h represents an effective area, including any *n*-hexanol associated with the di-C6SS molecules, and this may be the reason for the high value obtained from the R_c versus *w* trend. Using data from Chapter 5, the area for di-C6SS in a saturated monolayer at the air-water interface was obtained as 62 ± 2 Å^2. A similar value to this is found here for $a_{h(Porod)}$, indicating that the assumptions in the Porod approximation (Equation 6.3.4) are reasonable. Further comments on di-C6SS microemulsions are given in Chapter 7, where comparison with its glutaconate analogue di-C6GLU can be made.

6.3.3 Effect of phenyl-tipped chain structures

In view of the phase stability diagrams obtained for the phenyl sulfosuccinates in water/toluene systems (see Figure 6.4), di-PhC4SS, di-PhC5SS and Br-di-PhC5SS were selected for SANS studies. Measurements were carried out at 25 °C in toluene and D_2O (core contrast) at various *w* values within the single microemulsion phase. In addition, core and shell contrasts were studied at a common *w* value (w = 16). Data were fitted using a Schultz polydisperse sphere model with a hard sphere structure factor. As mentioned previously, fitting the shell contrast allows an accurate determination of the polydispersity that is then used in fitting of core contrast. Plots of the shell contrasts are shown in Figure 6.15, and examples of simultaneous fitted parameters (water core radius, R_c, polydispersity, σ / R_c^{av}, film thickness, t_s, and head group area, a_h) from the core-shell measurements at w = 16 are given in Table 6.7. As observed with other surfactant series [e.g., 11], at constant *w* value, the droplet size was found to decrease slightly as the chain length *n* was increased, while the polydispersity remained approximately the same.

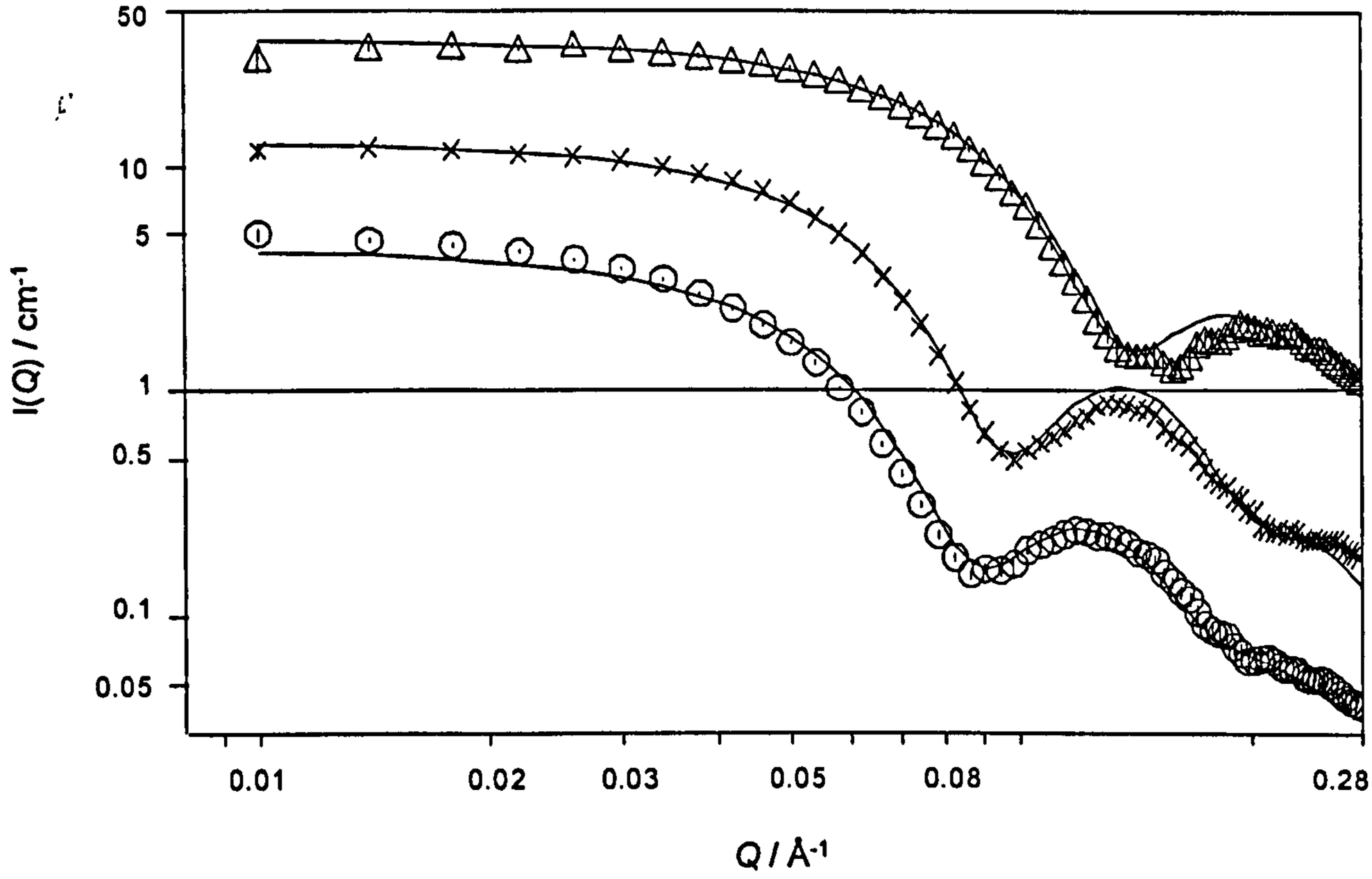

Figure 6.15 Shell contrast data from LOQ and fits (—) to the Schultz core-shell model for di-PhC*n*SS microemulsions in toluene. $w = 16$, [surf] = 0.10 mol dm^{-3}, $T = 25$ °C. Data/fits have been multiplied as follows: di-PhC4SS (○), di-PhC5SS × 3.5 (×), Br-di-PhC5SS × 20 (△).

Table 6.7 Parameters derived from simultaneous analyses of core-shell contrasts at a common w value

Surfactant	$w \pm 1$	$\sigma/R_c^{av} \pm 0.01$	$R_c \pm 1$ / Å	$t_s \pm 1$ / Å	$a_h \pm 2$ [a] / Å^2
di-PhC4SS	16	0.20	29.5	8.2	51
di-PhC5SS	16	0.18	28.8	9.0	55
Br-di-PhC5SS	16	0.19	24.7	6.0	74

[a] Head group areas a_h are calculated using Equation 6.3.2.

It is interesting to compare di-PhC5SS and Br-di-PhC5SS since the compounds have identical molecular weight (same number of C atoms), and only differ by the structure of their hydrophobic tails. The branched compound solubilises slightly less water (even less than di-PhC4SS), although its effective tail is shorter. This indicates that a certain length is required to give a well balanced molecule, with respect to its hydrophobic and hydrophilic moieties. At the same time, at constant chain length – i.e., comparing di-PhC2SS/Br-di-PhC3SS and di-PhC3SS/Br-di-PhC5SS – it is clear that adding methyl branch increases the efficiency of the surfactant to solubilise water, as well as reducing considerably the Krafft temperature. Recall the inability of di-PhC2SS and di-PhC3SS at forming single microemulsion phase, whereas Br-di-PhC3SS and Br-di-PhC5SS (their equivalent in terms of effective chain length) do. From simultaneous core-shell fits, film thicknesses correspond well with the change in effective chain length.

Example core contrast data for di-PhC4SS in D_2O/toluene and derived Porod plots are shown in Figures 6.16 and 6.17 respectively. Although not shown, similar plots were obtained for di-PhC5SS, Br-di-PhC5SS and AOT①. As before, average head group areas were obtained from R_c vs. w variations and Porod approximations. Data are summarised in Table 6.8 along with values obtained for AOT① in a similar D_2O/toluene systems. One limitation associated with these systems is the small w range available (see Figure 6.4, generally $w < 25$), so that scattering intensities are weak, and the fitting is less accurate (with the exception of di-PhC4SS). As expected, the average core radius was found to increase as a function of w, and linear R_c vs. w trends were obtained (Figure 6.18). As given in Table 6.8, values of a_h calculated using Equations 6.3.2 and 6.3.4 agree reasonably well, and, as for the AOTs series, the branching effect is clearly seen with an increase in a_h of about 15 – 20 Å^2 (see di-PhC5SS vs. Br-di-PhC5SS). Less efficient packing is observed compared with AOT①, indicating solvent interactions. Considering the low w range accessible and the derived uncertainties associated to model fits, further detailed analyses of film structure are not really possible (e.g., υ_h, r_h, R_o,). Still, the variation in head group areas obtained for these phenyl systems seems reasonable and corresponds to changes in surfactant molecular structure.

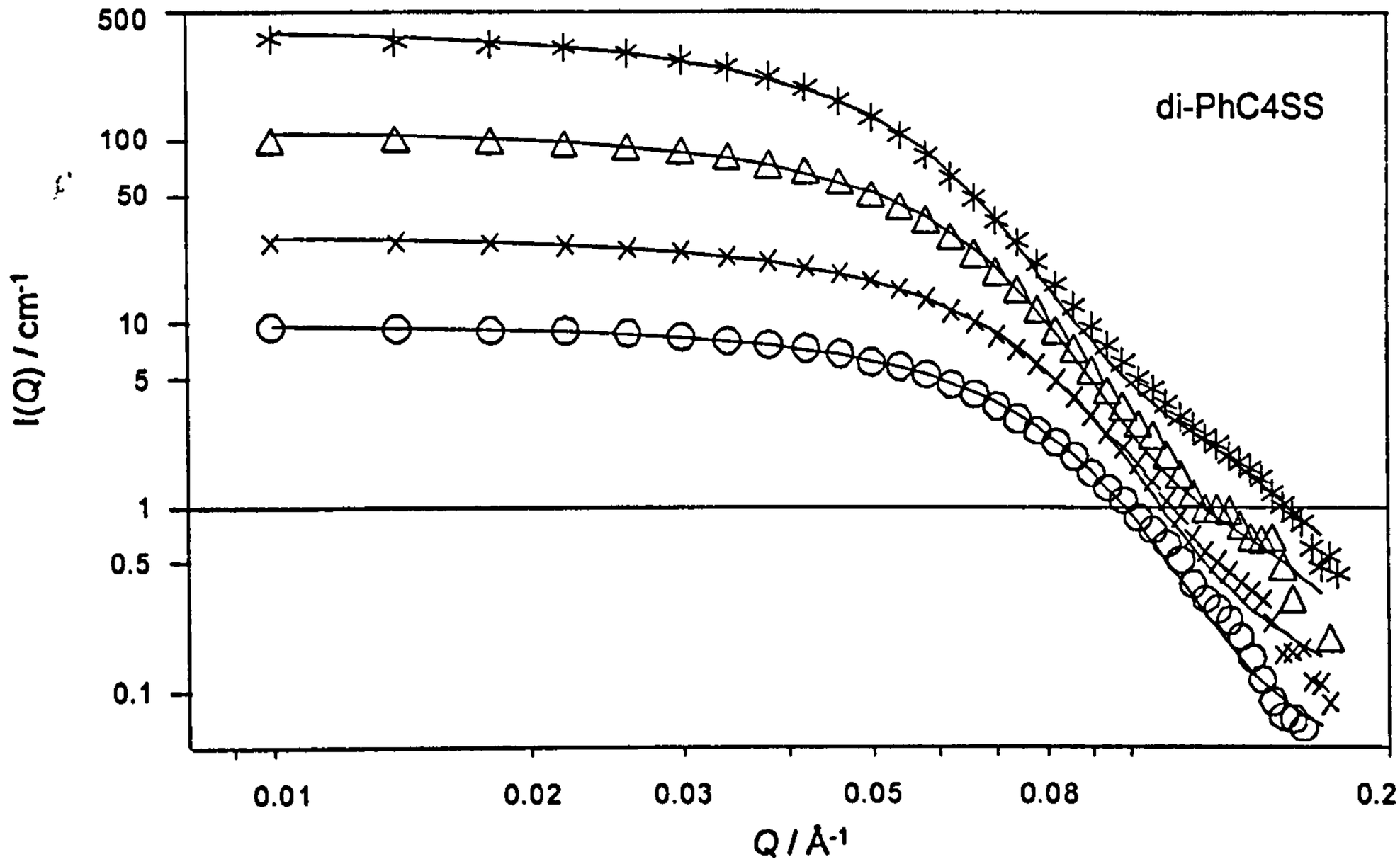

Figure 6.16 Core contrast data from LOQ and fits (—) to a Schultz polydisperse sphere model for Winsor II microemulsions of di-PhC4SS in toluene. [surf] = 0.10 mol dm^{-3}, T = 25 °C. Data/fits have been multiplied as follows: w = 16 (○), 18 × 2 (×), 22 × 4 (△), 26 × 8 (∗).

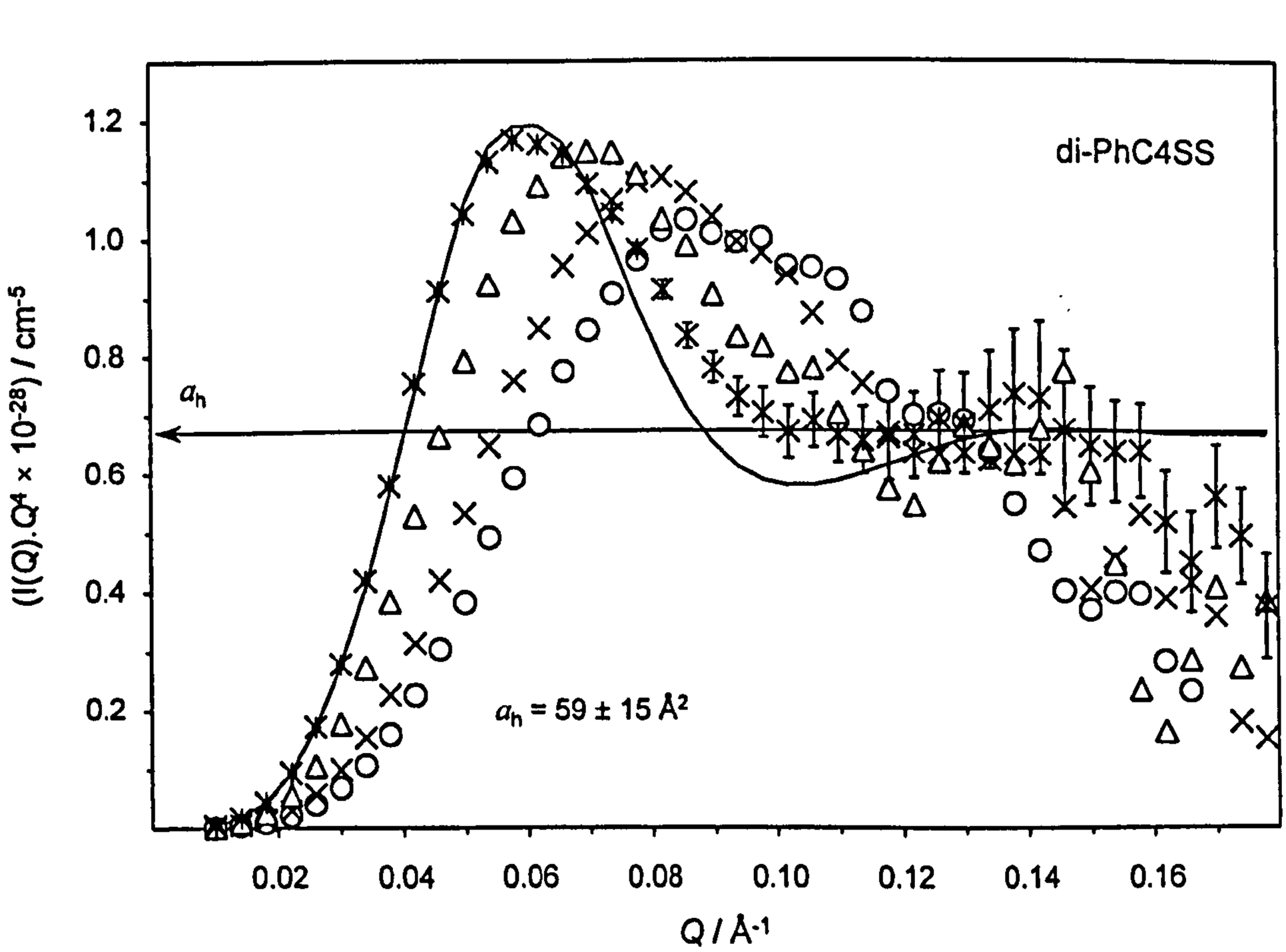

Figure 6.17 Porod plot of LOQ data from Winsor II di-PhC4SS microemulsions. [surf] = 0.10 mol dm^{-3}, T = 25°C. w = 16 (○), 18 (×), 22 (△), 26 (∗). For w = 26 the model fit (—) and error bars are shown. A level of scattering, representing an average area per head group, a_h, is also shown.

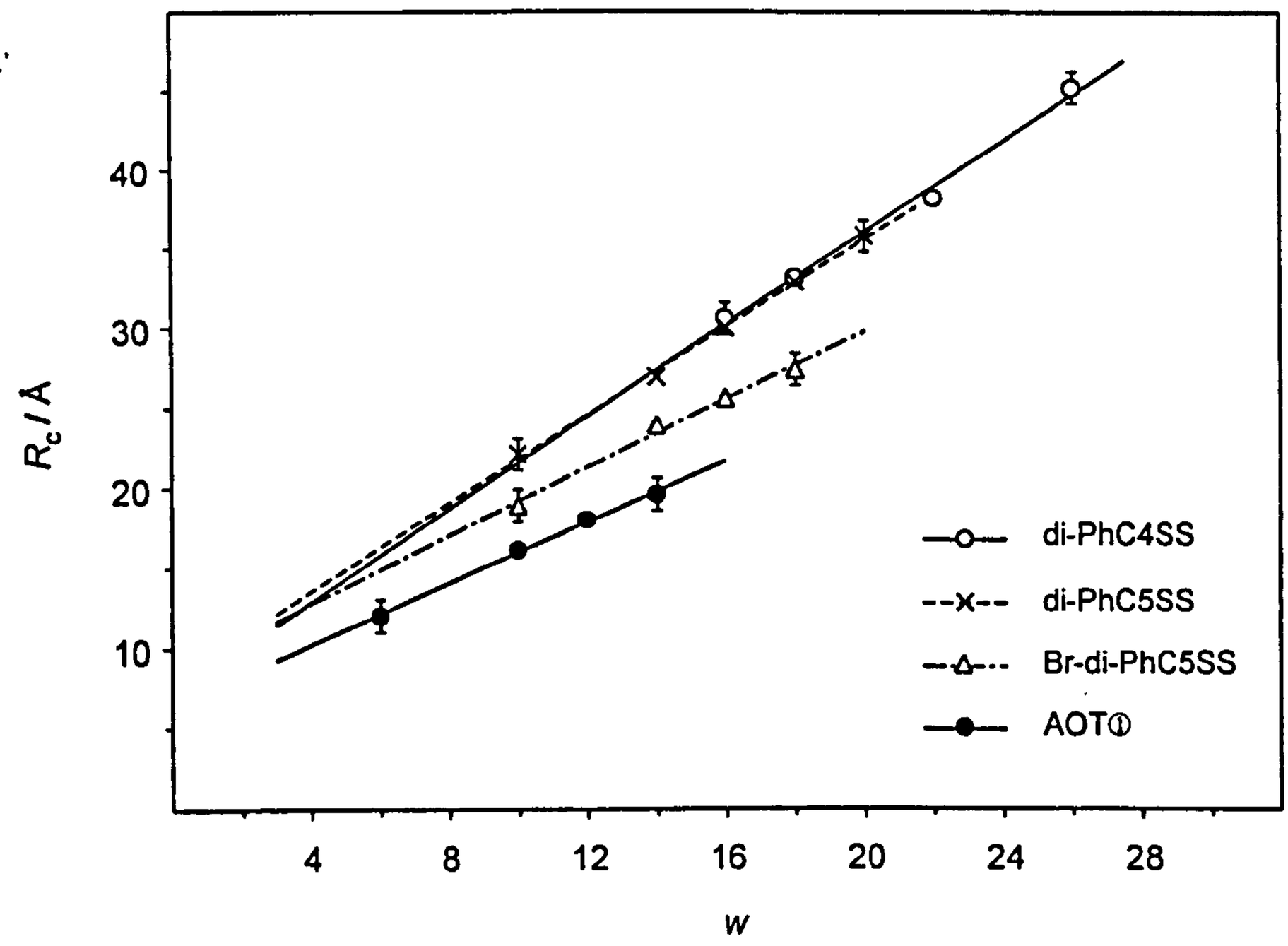

Figure 6.18 Water droplet radius R_c versus w for di-PhC4SS (○), di-PhC5SS (×) and Br-di-PhC5SS (△) w/o microemulsions. R_c values are from SANS analysis of core contrasts.

Table 6.8 Head group areas derived from analysis of core SANS data[a]

Surfactant	Head group area / Å^2		
	$a_h(3\upsilon_w w / R_c)$	a_h (Porod)	A_{cmc}
di-PhC4SS	63	59	69
di-PhC5SS	66	58	71
Br-di-PhC5SS	85	72	98
AOT①	94	88	75

[a] Head group areas at the air-water interface A_{cmc} are from Chapter 5. Uncertainties: $a_h(3\upsilon_w w / R_c)$, ± 3 Å^2; a_h(Porod), ± 15 Å^2; A_{cmc} ± 2 Å^2.

6.4 INTERFACIAL TENSIONS AND FILM RIGIDITIES

Interfacial tensions, $\gamma_{o/w}$, in brine-AOTs-heptane systems were measured using a spinning-drop tensiometer to find out if there is any link to the phase diagram and progressions with molecular structure. In addition, $\gamma_{o/w}$ between water-in-oil microemulsion and excess water phase in the Winsor II samples formed with selected AOTs surfactants were measured to calculate the mean bending film rigidities, by combination with SANS data.

6.4.1 Experimental: spinning-drop tensiometry (SDT)

Spinning-drop tensiometry may be used to measure very low interfacial tensions (< ~ 1.5 mN m^{-1}) between two liquids, for example those found in microemulsion systems (γ may be as low as 10^{-4} mN m^{-1}). A schematic of the spinning-drop tensiometer is shown in Figure 6.19. A drop of the least dense phase is injected into a capillary containing the second (more dense) phase, and as the capillary is spun at higher angular velocities ω, the drop lengthens. If interfacial tensions were absent, the rotating droplet would elongate indefinitely until it became infinitesimally narrow. However, with surfactants, droplet elongation is retarded when centrifugal forces are balanced by opposing interfacial tension forces. The droplet is then in an equilibrium position on the axis of rotation.

The equation relating the diameter of the drop to the interfacial tension for high angular velocities forming a cylindrical drop was suggested by Vonnegut [29]:

$$\gamma = \frac{1}{4}\Delta\rho\omega^2 r^3 \qquad (6.4.1)$$

where γ is the interfacial tension in mN m^{-1}; $\Delta\rho$ is the density difference between the two phases in kg m^{-3}, r is the radius of the drop in metres, and ω is the angular velocity in radians s^{-1}. In Equation 6.4.1 the effect of gravity is ignored, and it is assumed that the length of the droplet is much larger than its radius, which occurs at sufficiently high frequency of revolution.

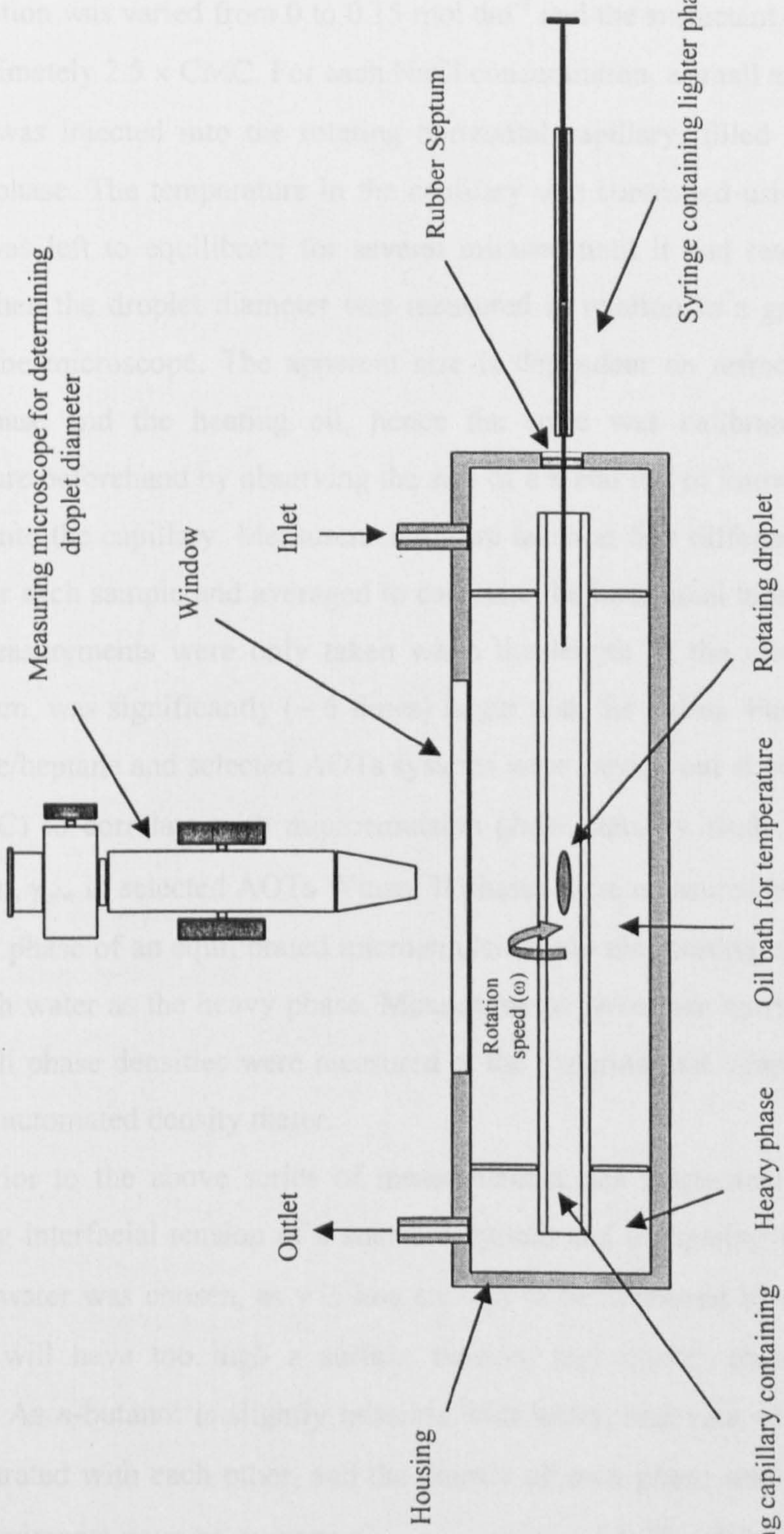

Figure 6.19 Schematic of Spinning-Drop Tensiometer.

The Krüss SITE 04 spinning-drop tensiometer was used to measure $\gamma_{o/w}$. Heptane–water interfacial tensions of AOTs/NaCl systems were measured at 25 ± 0.2 °C following the method described by Aveyard *et al.* [30]. The background electrolyte concentration was varied from 0 to 0.15 mol dm^{-3} and the surfactant concentration fixed at approximately 2.5 × CMC. For each NaCl concentration, a small amount of *n*-heptane (1-2 μl) was injected into the rotating horizontal capillary, filled with the surfactant aqueous phase. The temperature in the capillary was controlled using an oil bath. The droplet was left to equilibrate for several minutes until it had reached its maximum radius. Then the droplet diameter was measured in relation to a graduated scale seen through the microscope. The apparent size is dependent on refractive indices of the heavy phase and the heating oil, hence the scale was calibrated at the working temperature beforehand by observing the size of a metal rod of known diameter (1 mm) inserted into the capillary. Measurements were taken at five different rotating capillary speeds for each sample and averaged to calculate the interfacial tension using Equation 6.4.1. Measurements were only taken when the length of the elongated droplets, at equilibrium, was significantly (~ 6 times) larger than the radius. Further measurements with brine/heptane and selected AOTs systems were carried out at high temperature (45 and 50 °C) to correlate with microemulsion phase stability study. In addition to the NaCl scan, $\gamma_{o/w}$ in selected AOTs Winsor II phases were measured by injecting ~1 μl of the upper phase of an equilibrated microemulsion into the rotating capillary, which was filled with water as the heavy phase. Measurements were then carried out as described above. All phase densities were measured at the experimental temperature with a Paar DMA 35 automated density meter.

Prior to the above series of measurements, the instrument was calibrated by measuring interfacial tension of a standard system and comparing with literature data. Butanol–water was chosen, as γ is low enough to be measured by SDT. Longer chain alcohols will have too high a surface tension, and shorter chain alcohols will be miscible. As *n*-butanol is slightly miscible with water, and vice versa, the two liquids were saturated with each other, and the density of each phase was measured at 25 °C. SDT experiments gave an average $\gamma_{butanol/water}$ value of 1.72 ± 0.05 mN m^{-1}. This value compares well with that determined by Donahue *et al.* [31] using the pendent drop method (1.8 mN m^{-1}), and by Villers *et al.* [32] using the Wilhelmy plate method (1.67 mN m^{-1}).

6.4.2 Interfacial tensions: effect of chain structure

The *n*-heptane–water interfacial tensions for the AOTs series as a function of [NaCl] are shown in Figure 6.20. Results for AOT① are similar to those obtained in *n*-heptane by Aveyard *et al.* [30,33], with a minimum $\gamma_{o/w}$ value of ~ 4×10^{-4} mN m^{-1}, at approximately 0.047 mol dm^{-3} electrolyte concentration. Apart from AOT⑥, all other systems exhibit a tension minimum at a certain salt concentration, and the behaviour is entirely consistent with the progression Winsor I → III → II as [NaCl] increases. In terms of the minimum $\gamma_{o/w}$ value, differences are minor, but the trend of decreasing $\gamma_{o/w}$ with increasing effective chain length is observed. AOT④ with C6 linear chains exhibits the lowest $\gamma_{o/w}$ value (~ 2×10^{-4} mN m^{-1}), while AOT②, -③, and -⑤ with C5 linear chains give slightly higher values (~ 6×10^{-4}, 8×10^{-4}, and 1×10^{-3} mN m^{-1} respectively). A similar trend, but with larger changes in tension, has been reported by Sottmann and Strey for the non-ionics C_iE_j [34] with temperature scans. In this series, changing the surfactant size from C_6E_2 to $C_{12}E_5$ in a balanced fashion (increasing both i and j simultaneously) decreased significantly the minimum interfacial tension, from 0.3 to 0.006 mN m^{-1}. Here, the major difference between these anionics is the amount of electrolyte required to produce Winsor inversion:

- For AOT① to ⑤, the critical NaCl concentration correlates with the overall surfactant aqueous solubility (see Figure 6.3), i.e., just as in the microemulsion phase behaviour (Figure 6.2). At low salt concentration, the surfactant resides in the aqueous phase, so that compounds of lower solubility (e.g., AOT④ and ②) will transfer to the oil phase at lower electrolyte concentration. This trend underlines once more the important effect of surfactant aqueous phase solubility.
- For AOT⑥, the absence of ultra-low tensions confirms its poor microemulsifying performance (see phase stability diagram, Figure 6.2), and supports the idea of a minimum branching requirement to form co-surfactant free microemulsions.

To further explore the link between phase stability, aqueous solubility and interfacial tensions, [NaCl] scan experiments were repeated for AOT①, -②, and -④ at high temperatures. These compounds stabilise L_2-microemulsion around 25, 45 and 50 °C respectively, so that measurements with varying [NaCl] in the range 0 – 0.15 mol dm^{-3} were carried out at three temperatures. Results are shown in Figure 6.21.

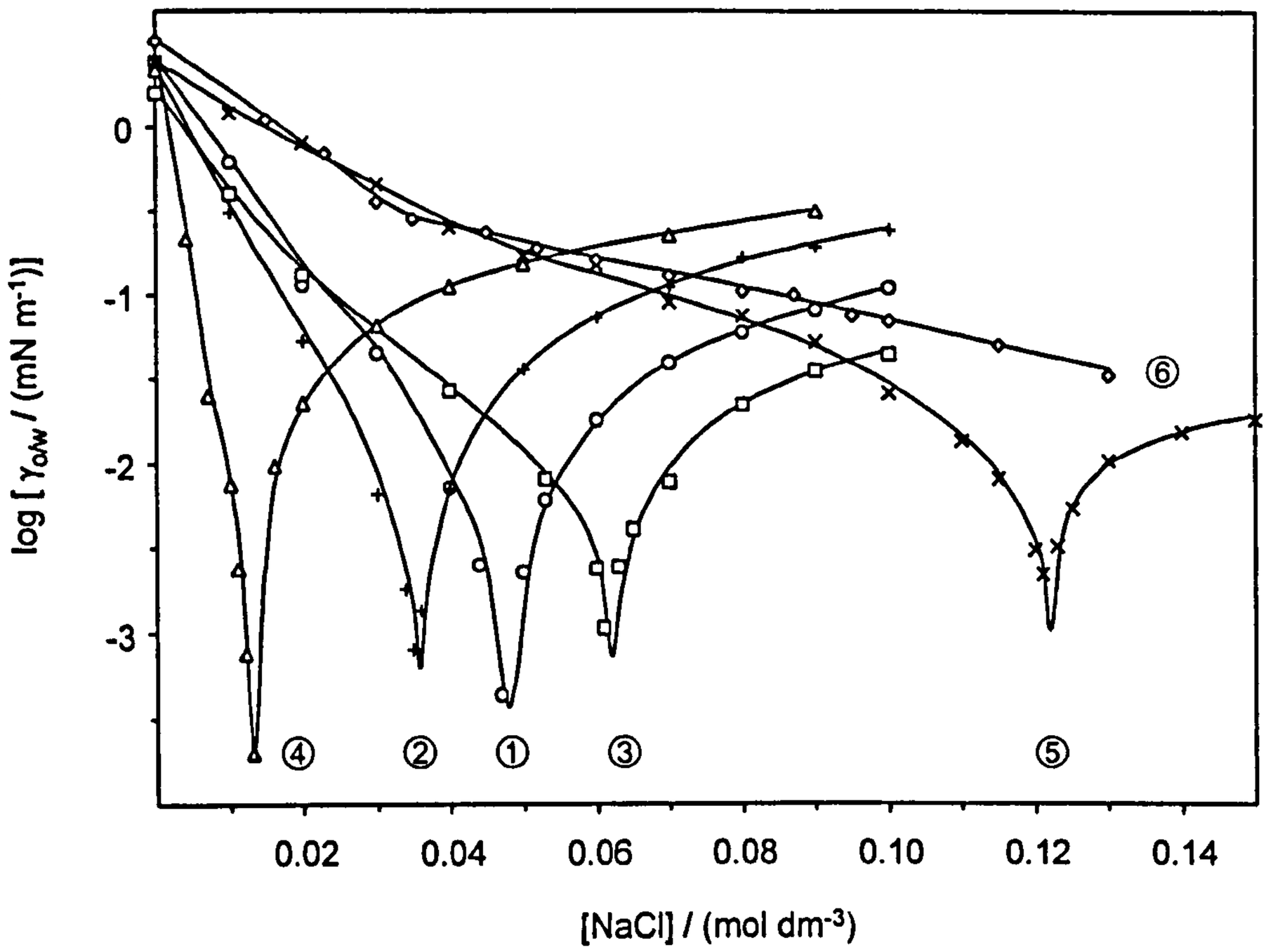

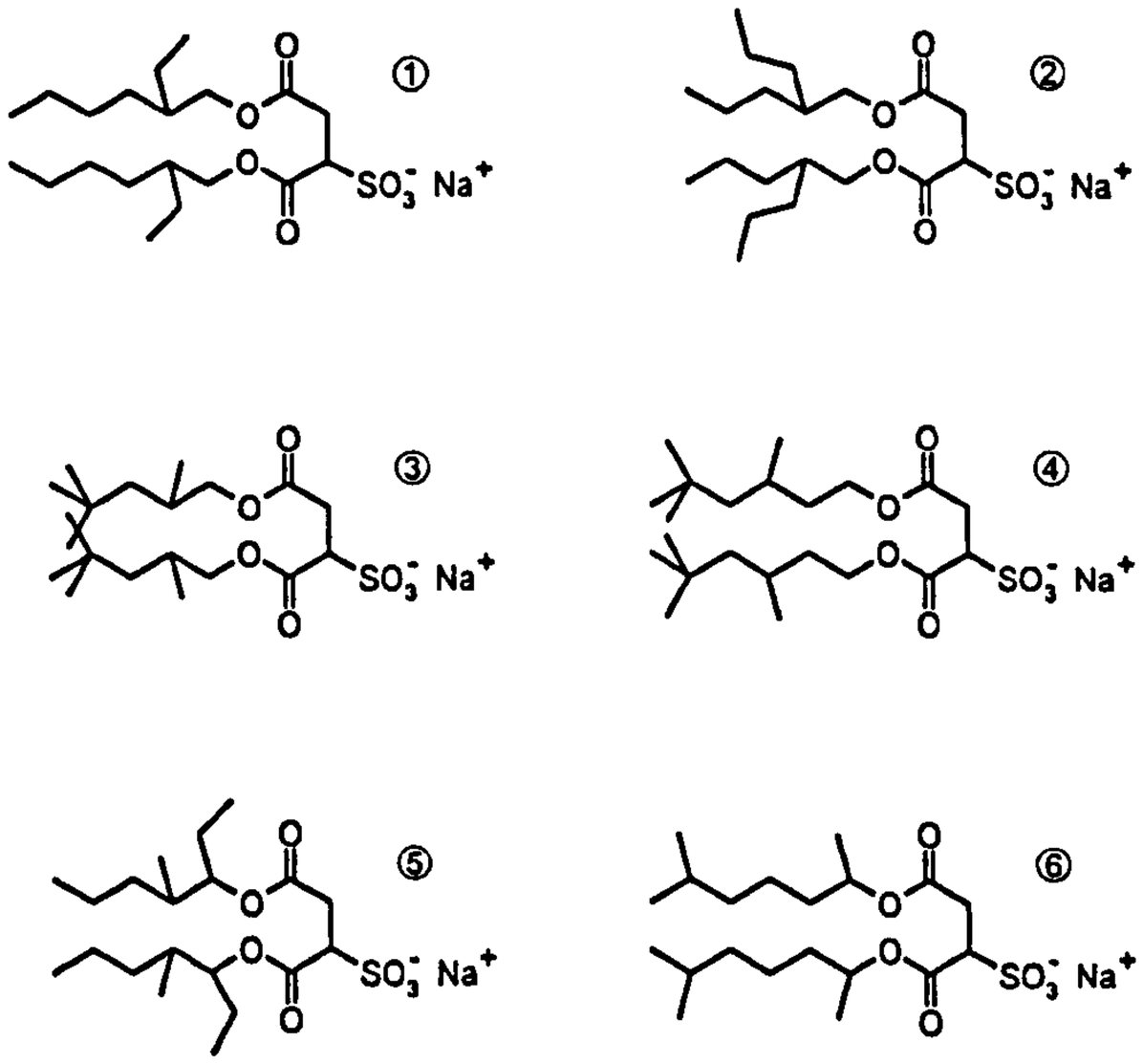

Figure 6.20 *n*-Heptane–water interfacial tensions for AOTs surfactants as a function of NaCl concentration at 25 ± 0.2 °C. In all cases the surfactant concentration is above the CMC, so aggregates are present in the heptane or the aqueous phase. Lines are guide to the eye.

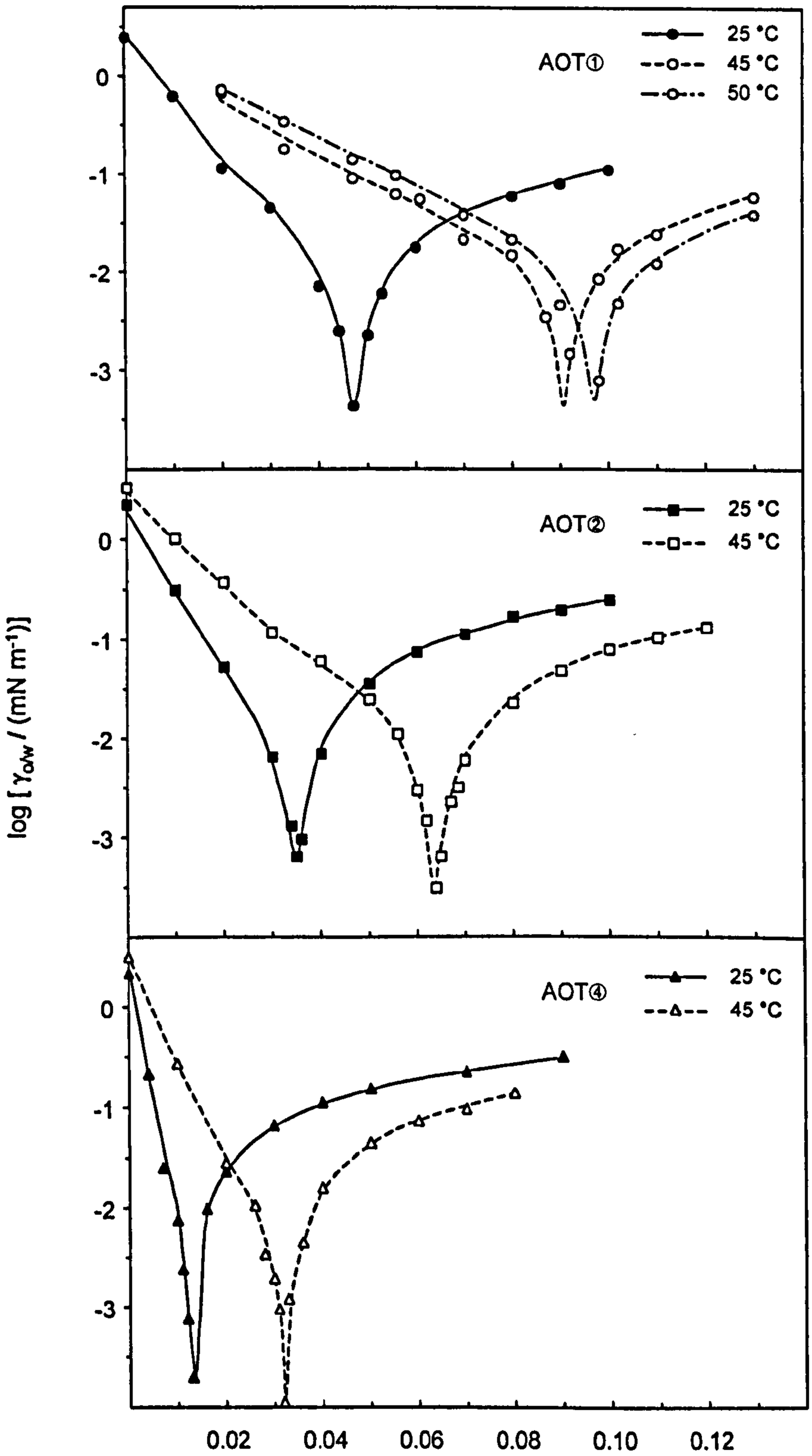

Figure 6.21 Effect of temperature on variation of w/o interfacial tensions with NaCl concentration for selected AOTs surfactants. Surfactant concentrations are above the CMC. Lines are guide to the eye.

Clearly, temperature strongly affects the position of the minimum of the interfacial tension curves. As expected, since the surfactant resides principally in the aqueous phase at low salt concentration, and aqueous solubility is favoured by high temperature, increasing temperature shifts the minimum to higher salt concentrations. The magnitude of this shift will then be different for the three surfactants as it is dependent on the shape of the solubility curve (see Figure 6.3). For example, the shift in AOT④ system at 25 and 50 °C is small compared to AOT① because the increase in surfactant aqueous solubility is much smaller over this temperature range. On the other hand, unlike non-ionics [34], temperature does not affect the minimum $\gamma_{o/w}$ value.

6.4.3 Surfactant film rigidities

The interfacial tensions $\gamma_{o/w}$ between the microemulsion stabilised by selected AOTs and excess aqueous phases were measured for samples at maximum water solubilisation (w_{max}). Experiments were carried out at 15 °C for AOT①, and 25 °C for AOT②, and -④ as described in Section 6.4.1 on samples at w = 25, 20, and 24 respectively. Microemulsions were left to equilibrate at 25 °C for at least 48 hours, and the upper L_2-microemulsion phase was used for SDT experiments. Identical pre-equilibrated samples were analysed by SANS at the appropriate temperature to obtain the maximum droplet radius, R_{max}^{av}, and polydispersity, σ/R_{max}^{av}. As described in Section 3.3.2, by combining SDT and SANS data, surfactant film rigidities expressed as $(2K+\overline{K})/k_BT$ may be calculated via

$$2K+\overline{K}=\frac{k_BT}{8\pi(\sigma/R_{max}^{av})^2}-\frac{k_BT}{4\pi}f(\phi) \qquad (6.4.2)$$

and

$$2K+\overline{K}=\gamma_{o/w}(R_{max}^{av})^2-\frac{k_BT}{4\pi}f(\phi) \qquad (6.4.3)$$

SDT and SANS data are summarised in Table 6.9, and these were used to calculate $(2K+\overline{K})$.

Table 6.9 Film rigidity results for AOTs stabilised Winsor II w/o microemulsions with *n*-heptane[a]

AOT	w_{max}	ϕ_{water}	R_{max}^{av} / Å	σ/R_{max}^{av}	$\gamma_{o/w}$ / (mN m^{-1})	$(2K+\overline{K})/(k_BT)$	
						Eq.6.4.2	Eq.6.4.3
①	25	0.0453	40.6	0.23	0.062	1.08	0.58
②	20	0.0363	31.5	0.21	0.100	1.25	0.58
④	24	0.0435	36.5	0.20	0.240	1.32	1.11

[a] Experimental temperatures are 15 °C for AOT①, and 25 °C for AOT② and -④. Uncertainties: w_{max}, ± 1; R_{max}^{av} ± 1 Å; σ/R_{max}^{av} ± 0.1; $\gamma_{o/w}$ ± 0.05 mN m^{-1}; $(2K+\overline{K})/k_BT$ ± 0.15.

Comparison of the last two columns of Table 6.9 clearly indicates that values of film rigidity calculated via Eq. 6.4.2 are all higher than those obtained using Eq. 6.4.3. It is unlikely this discrepancy is due to errors in $\gamma_{o/w}$ as the same value was obtained on each repeat measurement. Previous work [10,11,35] has shown overall that values of $2K+\overline{K}$ calculated from interfacial tension measurements (Eq. 6.4.3) and droplet polydispersity (Eq. 6.4.2) agree well. It should be noted, though, that discrepancies of about the same order of magnitude as those observed here have been reported by other workers [36,37] for DDAB systems. They were explained by the possible formation of vesicles and bilayers at the macroscopic interface between the microemulsion and excess water phase, so that Eq. 6.4.3 was not applicable (valid for monolayers only). However, this cannot be applied here on AOT-like compounds, and the exact reason for the discrepancy is unclear. Nevertheless, both methods result in an increase in bending energy with chain length. This trend has been reported for various series of surfactants in WII w/o microemulsions [e.g., 10,11], and it was found that $2K+\overline{K}$ scales with the surfactant chain length C_{surf} so that $2K+\overline{K} \sim C_{surf}^{2.4}$. In the present study, however, the number of suitable compounds is too small to draw accurate conclusions. The determination of film rigidities of linear chain sulfosuccinates (di-C*n*SS) could not be made as SANS data were unsuitable, and measurements of interfacial tensions failed due to the slight miscibility of the co-surfactant (*n*-hexanol) in the aqueous phase.

6.5 GENERAL CONCLUSIONS

In order to reveal any specificity in the chemical structure of Aerosol-OT, aqueous and microemulsion phase behaviour of a range of linear, branched, and phenyl-tipped AOT-analogues has been studied. Small-Angle Neutron Scattering was used to quantify adsorption and molecular packing at curved interfaces, and results were compared with data obtained at the planar interface (Chapter 5). Considering results from both aqueous and microemulsion systems, the following points can be made:

(1) The structure of the hydrocarbon backbone clearly dictates interfacial packing, and for the AOTs series the surfactant packing-structure relationship is well described by an empirical branching factor. It is interesting to compare packing at the two different interfaces, air-water and oil-water, and as shown by the results in Table 6.4, there are no striking differences. This suggests that, in terms of the surfactant film alone, the two interfaces are very similar.

(2) Formation of simple ternary microemulsion systems requires a certain amount of disorder in the hydrophobic moiety, as shown by comparing the behaviour of linear versus branched compounds, and considering the effect of substituting methyl with phenyl at the tail end group.

(3) Within the branched series, this film curvature scales with surfactant hydrophobic size (at least considering extremes in chain branching), so that water solubilisation correlates with chain structure.

From a more general viewpoint, the versatility of normal AOT is not unique, and its acclaimed "cone-like molecular structure" does not explain its efficiency as a microemulsifier. With respect to tail structure, AOT fits into the general pattern of behaviour of the other branched compounds. They are all characterised by a high water solubilisation capacity, with formation of a liquid-like condensed interfacial film. The major difference comes from aqueous solubility with respect to temperature, which affects the location of the L_2 phase, but not efficiency in microemulsions. Observation of the Winsor phase progression upon addition of electrolyte confirms the important effect of temperature on the phase behaviour of such compounds.

6.6 REFERENCES

1. Eastoe, J.; Dong, J.; Hetherington, K. J.; Steytler, D. C.; Heenan, R., K. *J. Chem. Soc., Faraday Trans.* **1996**, *92*, 65.
2. Eastoe, J.; Hetherington, K. J.; Sharpe, D.; Dong, J.; Heenan, R. K.; Steytler, D. C. *Langmuir* **1996**, *12*, 3876.
3. Eastoe, J.; Robinson, B. H.; Steytler, D. C. *J. Chem. Soc., Faraday Trans.* **1990**, *86*, 511.
4. Kotlarchyk, M.; Chen, S.-H.; Huang, J. S.; Kim, M. W. *Phys. Rev. A*. **1984**, *29*, 2054.
5. Chen, S. H.; Chang, S.-L.; Strey, R. *J. Chem. Phys.* **1990**, *93*, 1907.
6. Eastoe, J.; Fragneto, G.; Robinson, B. H.; Towey, T. F.; Heenan, R. K.; Leng, F. J. *J. Chem. Soc., Faraday Trans.* **1992**, *88*, 461.
7. Atkinson, P. J.; Robinson, B. H.; Howe, A. M.; Pitt, A. R. *Colloids Surf. A* **1995**, *94*, 231.
8. Mitchell, D. J.; Ninham, B. W. *J. Chem. Soc., Faraday Trans. 2* **1981**, *77*, 601.
9. Eastoe, J.; Hetherington, K. J.; Dalton, J. S.; Sharpe, D.; Lu, J. R.; Heenan, R. K. *J. Colloid Interface Sci.* **1997**, *190*, 449.
10. Eastoe, J.; Sharpe, D.; Heenan, R. K.; Egelhaaf, S. U. *J. Phys. Chem. B*, **1997**, *101*, 945.
11. Eastoe, J.; Sharpe, D. *Langmuir* **1997**, *13*, 3289.
12. Eastoe, J.; Hetherington, K. J.; Sharpe, D.; Dong, J.; Heenan, R. K.; Steytler, D. C. *Colloids Surf. A* **1997**, *128*, 209.
13. Kunieda, H.; Shinoda, K. *J. Colloid Interface Sci.* **1979**, *70*, 577.
14. Robinson, B. H.; Toprakcioglu, C.; Dore, J. C.; Chieux, P. *J. Chem. Soc., Faraday Trans. 1* **1984**, *80*, 13.
15. Eastoe, J.; Robinson, B. H.; Steytler, D. C.; Thorn-Leeson, D. *J. Colloid Interface Sci.* **1991**, *36*, 1.
16. Kunieda, H.; Shinoda, K. *J. Colloid Interface Sci.* **1980**, *75*, 601.
17. Hou, M. J.; Kim, M.; Shah, D. O. *J. Colloid Interface Sci.* **1988**, *123*, 398.
18. Information of SANS data processing can be found at http://isise.rl.ac.uk/LargeScale/LOQ/loq.htm and http://www.ill.fr
19. Wignall, G. D.; Bates, F. S. *J. Appl. Crystallogr.* **1987**, *20*, 28.
20. Bumajdad, A.; Eastoe, J.; Heenan, R. K.; Lu, J. R.; Steytler, D. C.; Egelhaaf, S. U. *J. Chem. Soc., Faraday Trans.* **1998**, *94*, 2143.
21. Kotlarchyk, M.; Chen, S.-H.; Huang, J. S. *J. Phys. Chem.* **1982**, *86*, 3273.
22. Ornstein, L. S.; Zernicke, F. *Proct. Sect. Sci. K. Med. Akad. Wet.* **1914**, *17*, 793.
23. Kotlarchyk, M.; Huang, J. S.; Chen, S.-H. *J. Phys. Chem.* **1985**, *89*, 4382.
24. Porod, G. *Kolloid Z* **1951**, *124*, 82.
25. Eastoe, J.; Young, W. K.; Robinson, B. H.; Steytler, D. C. *J. Chem. Soc., Faraday Trans.* **1990**, *86*, 2883.
26. Evans, D. F.; Wennerström, H. '*The Colloidal Domain*'; VCH: New York, 1994.
27. Cabos, C.; Delord, P. *J. App. Crystallogr.* **1979**, *12*, 502.
28. Hirai, M.; Kawai-Hirai, R.; Sanada, M.; Iwase, H.; Mitsuya, S. *J. Phys. Chem. B*, **1999**, *103*, 9658.
29. Vonnegut, B. *Rev. Sci. Instr.* **1941**, *13*, 6.

30. Aveyard, R; Binks, B. P.; Clark, S.; Mead, J. *J. Chem. Soc. Faraday Trans. 1* **1986**, *82*, 125.
31. Donahue, J.; Bartell, F. E. *J. Phys. Chem.* **1952**, *56*,480.
32. Villers, D.; Platten, J. K. *J. Phys. Chem.* **1988**, *92*, 4023.
33. Aveyard, R; Binks, B. P.; Mead, J. *J. Chem. Soc. Faraday Trans. 1* **1986**, *82*, 1755.
34. Sottmann, T.; Strey, R. *Ber. Bunsenges. Phys. Chem.* **1996**, *100*, 237.
35. Gradzielski, M.; Meunier, J.; Binks, B. P. *Phys. Rev. E* **1996**, *54*, 3900.
36. Hetherington, K. J. Ph.D. Thesis, Bristol, 1998.
37. Bumajdad, A. Ph.D. Thesis, Bristol, 2000.

CHAPTER 7

SOLUTION PROPERTIES OF DI-CHAIN SODIUM SULFOGLUTACONATES

In order to give a more complete study of surfactant structure–performance relationships, it is of interest to investigate the effect of head group chemistry. This chapter describes adsorption and aggregation behaviour of two novel double-chain anionic sulfoglutaconate surfactants. These are similar to the succinates, such as normal AOT, but with a modified hydrophilic moiety (bearing one extra -CH_2- spacer). The objective is to identify effects of head group structure on surfactant performance. As such, considering the surfactant series investigated in the two preceding chapters, and in view of their well-characterised solution properties, the di-hexyl- and bis(2-ethylhexyl)-hydrophobic groups were chosen (i.e., the compounds called di-C6SS- and AOT respectively) to form di-C6GLU and AOTGLU. As before, the planar air-solution surface was characterised by tensiometry, while small-angle neutron scattering and spinning drop tensiometry are used to study oil-water interfaces. Binary (dilute regime and lyotropic mesophases) and ternary phase diagrams (water-in-oil microemulsions) are also described. All results are discussed with particular reference to the regular succinate systems.

In terms of molecular packing both systems are found to be very similar, showing the minor role of the head group compared to the tail. From phase behaviour studies, unsurprisingly, the linear di-C6GLU based system still requires a co-surfactant to stabilise w/o microemulsions. More interestingly though, AOTGLU proved to be even more efficient than normal AOT in terms of microemulsion stability, despite exhibiting a similar oil-water interfacial tension behaviour.

7.1 INTRODUCTION

Changes in the molecular structure of surfactants have important consequences for physico-chemical solution properties, and hence on potential applications. As shown in Chapters 5 and 6 at constant head group structure, surface activity, aggregation properties, and microemulsion formation and stability are dramatically affected by even small structural variations of the hydrophobic group. Trends in interfacial tensions and molecular packing were found to correlate with the extent of chain branching (at constant total carbon number). With the sulfosuccinates, the aqueous solubility with respect to temperature plays an equally important role: by affecting oil-water tension, it determines the location of the single-phase microemulsion region. This latter observation shows that the exceptional behaviour of Aerosol-OT cannot be explained just in terms of a suitable "cone-like" geometry, but must rely on a more subtle and complex balance between its hydrophobic and hydrophilic moieties. To further explore this idea, it is therefore important to investigate the effect of head group structure. To this aim, the glutaconate analogues of Aerosol-OT (or AOT①) and di-C6SS, AOTGLU and di-C6GLU respectively, have been synthesised and their solution properties characterised at both the air-water and oil-water interface. The chemical structures of the glutaconate and succinate surfactants are shown in Figure 7.1.

In the study of double-chain amphiphiles, there is a vast literature devoted to the influence of chain structure on adsorption and micellar properties [e.g., refs 1-5]. Small changes in the chemical architecture of the hydrophilic part, though, have not been so systematically studied. This is partly due to a lack of suitable compounds. Most reported studies deal with single-chain surfactants, and in particular the effect of incorporating or increasing the ethylene oxide (EO) units. With non-ionics, the size of the EO head group has a large influence in determining the interfacial molecular area; increasing the EO content increases the CMC and decreases the surface excess in a regular fashion [6,7]. With ionics, the effect of incorporation of ethoxy groups between the hydrocarbon chain and the hydrophilic group has also been studied [7 and references therein]. It was found that in both cationic and anionic systems, a decrease in the CMC and increase in the limiting surface tension is observed upon ethoxylation.

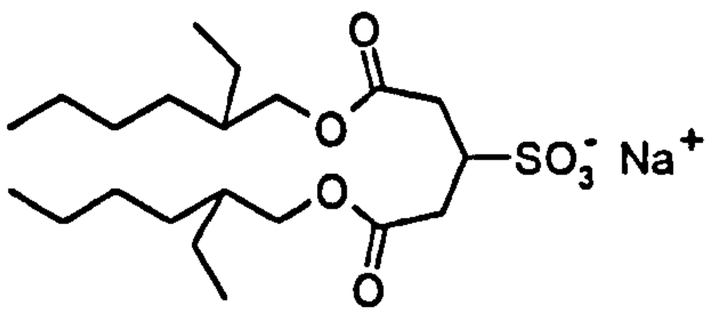

AOTGLU
Sodium bis(2-ethylhexyl)
sulfoglutaconate

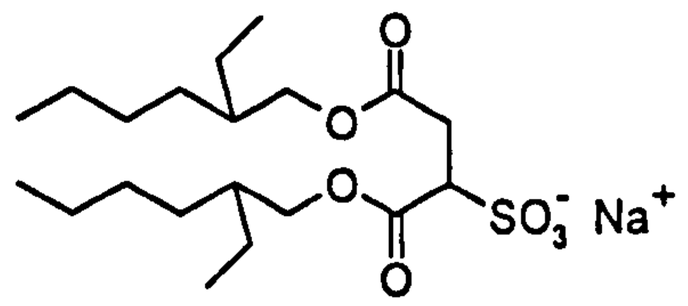

AOT① (Aerosol-OT)
Sodium bis(2-ethylhexyl)
sulfosuccinate

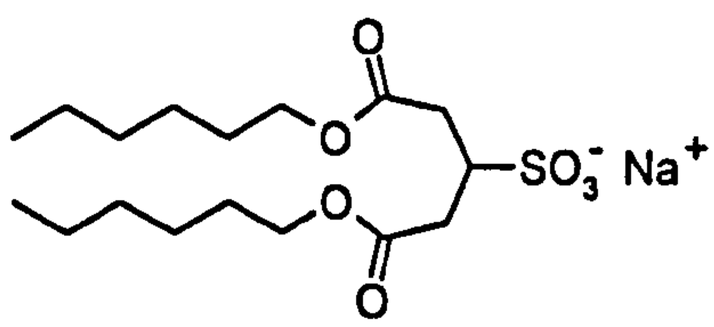

di-C6GLU
Sodium bis(1-hexyl)
sulfoglutaconate

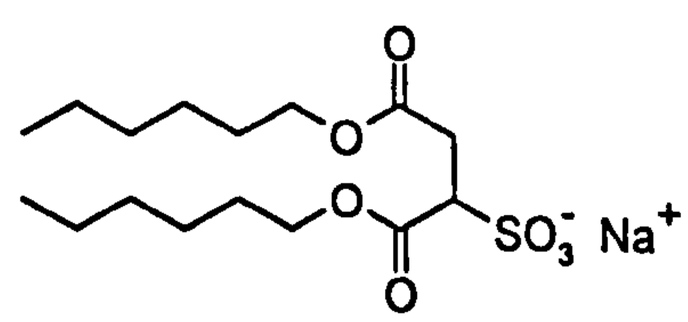

di-C6SS
Sodium bis(1-hexyl)
sulfosuccinate

Figure 7.1 Schematic molecular structures of surfactants examined in this Chapter. Structures of the linear and branched sulfosuccinates are also shown for comparison purposes.

More recently, Okano *et al.* [8] have studied structural variations into cationic surfactants of the form $C_{16}H_{33}N^{+}(CH_3)_2$–$(CH_2)_n$–$C_6H_5$ Cl^{-}. As expected, varying n from 0 to 3 decreases the CMC from 1.26×10^{-3} down to 0.10×10^{-3} mol dm^{-3}. More interestingly though, when plotting the data for n = 1-3, log(CMC) displays a linear dependence on carbon number with a gradient of -0.3, i.e., similar to the decay observed upon addition of -CH_2- groups in a typical hydrocarbon chain. At the same time, an increase of the interfacial head group area of approximately 15 $Å^2$ is reported as a result of an increase in the surfactant head group volume. Variation in the hydrophilicity of the head group does not always follow this simple pattern: in studying a series of new cationic surfactants with sulfonium head groups, zu Putlitz *et al.* [9] observed a significant increase in CMC upon replacement of a 2-hydroxylethyl group with a diethyl or dimethyl groups. This unexpected behaviour was explained by secondary interactions stabilising the structure, such as methyl-methyl or ethyl-ethyl interactions arising from proximity of these short alkyl groups.

In terms of AOT-based compounds and head group structure, only a few studies have been reported in contrast to the vast literature available on the aqueous and microemulsion phase behaviour of Aerosol-OT. With the exception of several studies on sodium bis(2-ethylhexyl) phosphate (NaDEHP) and the effect of head group polarity [10-12], most research has focused on the effect of counterion type [13-19]. More relevant to the present study is the recent work completed by Adrian Downer from Bristol University on solution properties of various fluorinated di-chain anionic surfactants [20]. In particular it is interesting to emphasize the results obtained from tensiometry and neutron reflectivity experiments on two linear sodium sulfoglutaconates (DHCF4GLU and DCF4GLU) at the air-water interface and the comparison with their sulfosuccinate analogues (DHCF4 and DCF4). The four chemical structures are shown in Figure 7.2. Briefly, the presence of the -CH_2- spacer group decreases the CMC and increases slightly the efficiency of the surfactant, while no significant change in interfacial molecular packing was observed. Comparison with the above surfactants will be drawn throughout the present study, and research will be taken one step further by evaluating the oil-water curved interface.

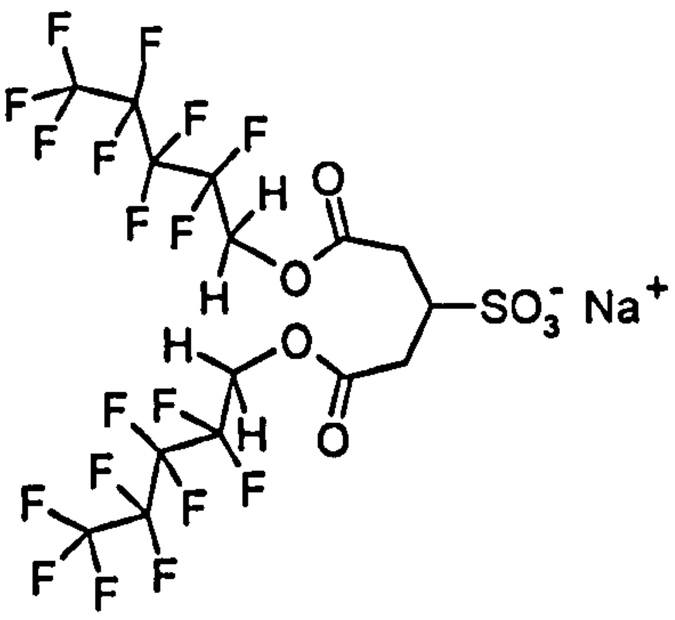

DCF4GLU
sodium 1H,1H-bis(perfluoropentyl)
-2-sulfoglutaconate

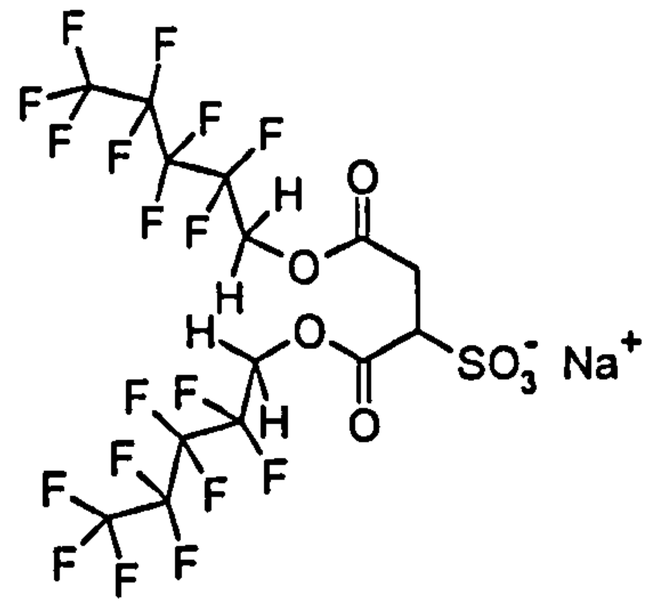

DCF4
sodium 1H,1H-bis(perfluoropentyl)
-2-sulfosuccinate

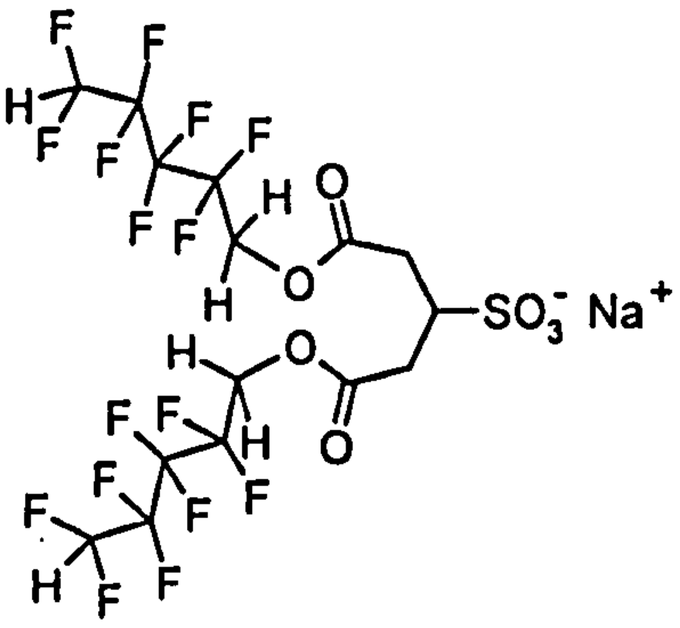

DHCF4GLU
sodium 1H,1H,5H-bis(octafluoropentyl)
-2-sulfoglutaconate

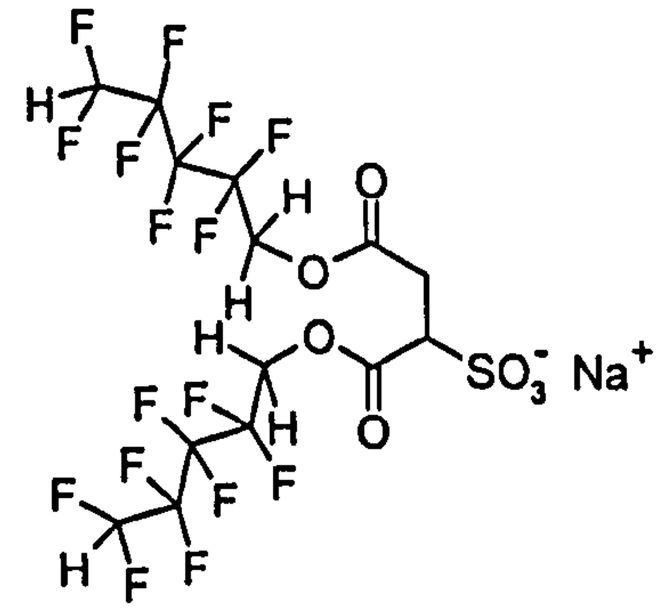

DHCF4
sodium 1H,1H,5H-bis(octafluoropentyl)
-2-sulfosuccinate

Figure 7.2 Schematic molecular structures of the fluorinated glutaconate and succinate surfactants. (Redrawn from [20])

7.2 EXPERIMENTAL

The techniques for studying interfacial tensions and water-in-oil microemulsions have been described previously in Chapters 5 and 6. Hence only a brief description is necessary here.

7.2.1 Chemicals

The procedures for preparation and purification of glutaconate surfactants have been described in Chapter 4. Elemental analysis and ^{1}H NMR (JEOL Lambda 300) gave results consistent with the expected chemical structures (see Section 4.2). Following the detailed study on di-C6SS, and the small improvements offered by the time-consuming foam fractionation process, this last purification procedure was not employed. Experiments with the succinate series show that this final step is not necessary for reliable comparisons to be drawn from tensiometric data, and leaving it out does not affect the microemulsion phase boundaries. Deuterated solvents *n*-heptane-d_{16}, *n*-hexane-d_{14} (Aldrich, >99% D-atom) and D_2O (Fluorochem, 99.9% D-atom) were used as received. Proteated alkane solvents were obtained from either Aldrich or Sigma (HPLC grade); H_2O was of ultrahigh purity (RO100HP Purite Water system or Millipore Milli-Q Plus system). Note that for measurements of oil-water interfacial tensions, *n*-heptane-h_{16} was passed through chromatographic silica (Silica gel-60, Merck) and distilled before use to remove traces of polar impurities. The electrolyte was sodium chloride (GPR, 99.5%, BDH). All glassware was washed in Micro critical cleaning solution, rinsed repeatedly with water, soaked in 50% nitric acid solution, rinsed well, and finally checked for cleanliness over a steam bath.

7.2.2 Interfacial tensions

Air–water equilibrium surface tensions were measured with a drop-volume (DV) tensiometer (Lauda TVT1), operating in dynamic mode. Samples were made up by mass and concentrations were corrected for density (Paar digital density meter DMA 35). EDTA (99.5% tetrasodium salt hydrate, Sigma) was used in all surfactant solutions at the appropriate ratio to sequester any polyvalent cations that are known to

contaminate such anionic surfactants [21]. This procedure is described fully in Section 7.3.1. All measurements were carried out at a constant temperature of 25.0 ± 0.1 °C using a circulating thermostatted bath (Grant LTD 6G).

n-Heptane–water interfacial tensions of AOTGLU/NaCl systems were measured at 25.0 ± 0.2 °C using a Krüss SITE 04 spinning drop tensiometer following the method described by Aveyard *et al.* [22]. Details of the technique and calibration of the tensiometer have been given in Section 6.4.1. The background electrolyte concentration was varied from 0 to 0.1 mol dm^{-3} and AOTGLU concentration fixed at 45 mmol dm^{-3} (i.e., approximately 2.5 × CMC). For each NaCl concentration, a small amount of *n*-heptane (1-2 μl) was injected into the surfactant aqueous phase, and the droplet diameter was measured for five different rotating capillary speeds (see Figure 6.19). The interfacial tension was taken as the average of the five repeat measurements using equation 6.4.1. In addition to the NaCl scan, $\gamma_{o/w}$ in an AOTGLU Winsor II phase was measured by injecting ~1 μl of the upper phase of an equilibrated microemulsion into the rotating capillary, which was filled with water as the heavy phase. The temperature was fixed at 15.0 ± 0.2 °C to ensure the sample – of composition $w = [H_20]/[AOTGLU] = 50$ – was located in the WII region. The apparent droplet size is dependent on refractive indices of the heavy phase and the heating oil, hence the scale was calibrated at this temperature beforehand (see Section 6.4.1). All phase densities were measured at the experimental temperature with a Paar DMA 35 automated density meter.

7.2.3 Water-in-oil microemulsions

Phase stability diagrams

Microemulsion phase equilibria were determined by visual inspection of samples made-up in clean, stoppered 5 ml volumetric flasks, thermostatted by a heater-cooler-circulator water bath accurate to ± 0.1 °C. The composition parameter, *w*, is given by [water]/[surfactant] and for the phase diagrams, the surfactant concentration was kept constant at 0.10 mol dm^{-3}. For di-C6GLU, *n*-hexanol (Aldrich) was used as a co-surfactant and the microemulsion oil phase was a 9:1 v/v hexane/hexanol mixture.

The aqueous solubility of AOTGLU was determined by visual inspection of the phase boundary between biphasic and monophasic (translucent) phases. Aqueous samples of 0.05 to 10 wt% surfactant were studied over the temperature range 3–85 °C.

SANS analysis

SANS experiments were carried out on D22 at ILL (France), using a neutron wavelength of λ = 10 Å, and some supporting data were taken on LOQ at ISIS (UK), where incident wavelengths are $2.2 \leq \lambda \leq 10$ Å [23]. The momentum transfer Q is $(4\pi/\lambda)$ $\sin(\theta/2)$ with θ the scattering angle. The Q ranges were 0.0035 – 0.359 $Å^{-1}$ on D22 and 0.009 – 0.249 $Å^{-1}$ at LOQ. Absolute intensities for I(Q) (cm^{-1}) were determined to within 5% by measuring the incoherent scattering from 1 mm of H_2O at ILL, while at ISIS a partially deuterated polymer standard was used [24]. Accepted procedures for data treatment were employed [23]. Samples were pre-equilibrated for about 48 hours prior to the SANS measurements, which were made at 25.0 ± 0.2 °C. In the region of Q overlap the agreement in absolute values of I(Q) between different instruments and samples was typically ± 5%.

As described in Chapter 6 for the sulfosuccinates systems, the microemulsion droplets were treated as spherical core-shell particles with a Schultz distribution in core radius. A polydisperse hard-sphere model [25] was used to include a structure factor $S_{hs}(Q)$ that accounts for the finite droplet volume fraction, and for some samples of di-C6GLU microemulsions which were close to the high-temperature stability (haze) boundary, it was necessary to include an attractive Ornstein-Zernicke (O-Z) structure factor S(Q,ξ). Neutron scattering theory is detailed in Chapter 3 and relevant comments for the SANS analysis have already been given in Section 6.3.1. The least-squares *FISH* program was used to analyse the SANS data [4,26]. For each surfactant, identical contrasts to those studied in Chapter 6 were used, and the adjustable parameters required in the fitting analysis were, as before, the most probable core radius and polydispersity width, R_c^{av} and σ/R_c^{av}, the apparent film thickness, t_s, and if used ξ and S(0), the structure factor at Q = 0. Table 7.1 gives the scattering length density, ρ, for each component calculated from mass densities and molecular volumes (see Chapter 6, Equation 6.3.1).

Table 7.1 Mass densities at 25°C, molecular volumes V_m, and scattering length densities ρ

	Density / (g cm^{-3})	($V_m \times 10^{21}$) / cm^{-3}	($\rho \times 10^{-10}$) / cm^{-2}
h-AOTGLU	1.0	1.383	0.513
h-di-C6GLU	1.0	1.587	0.642
H_2O	0.997	33.33	-0.560
D_2O	1.104	33.20	6.356
h-heptane	0.684	4.111	-0.548
d-heptane	0.794	4.111	6.301
h-hexane	0.659	4.605	-0.576
d-hexane	0.767	4.607	6.140
h-hexanol	0.814	4.798	-0.321

7.3 AQUEOUS SYSTEMS

In the following discussion, most data for di-C6SS and AOTGLU surfactants are presented with the data obtained in Chapters 5 and 6 for their sulfosuccinate analogues. For comparison purposes, some tables and figures summarise the results for both sets of compounds.

7.3.1 Surface tension

Air–water equilibrium surface tension measurements were used to check surface chemical purity of the surfactants and to determine adsorption isotherms. As detailed in Chapter 5, anionic surfactants can be affected by inorganic contaminants. An obvious source of impurities are sodium salts used in the sulfonation step that introduce polyvalent cations (mainly Mg^{2+}, Ca^{2+} and Ba^{2+}). Even at trace levels, such contaminants can lower significantly the tensions in the pre-CMC region by adsorbing preferentially to the sodium ions, so it is necessary to introduce an appropriate amount of the chelating agent EDTA. This effect is shown in Figures 7.3 and 7.4 for AOTGLU and di-C6GLU respectively. In both cases, two sets of measurements – at two different surfactant concentrations – were performed to determine the "best level" of EDTA. These concentrations were 1/5, 2/3, and 1/10, 1/3 × CMC for AOTGLU and di-C6GLU, and the EDTA concentration was varied in the range 10^{-9} to 10^{-2} mol dm^{-3}. Note that a rough determination of the CMC was carried out beforehand giving 1.8×10^{-3} and 11.6×10^{-3} mol dm^{-3} for the branched and linear glutaconate respectively. In both cases, a plateau of constant γ was reached between a range of EDTA from 5×10^{-5} and 1×10^{-4} mol dm^{-3}, and ratios surfactant:EDTA of 80:1 and 130:1 were chosen for AOTGLU and di-C6GLU respectively.

Figures 7.5 and 7.6 show the γ–ln activity curves for two glutaconates in the presence of EDTA, and also shown are data for the succinates AOT① and di-C6SS as reported in Chapter 5. The activity coefficients were obtained from the Debye-Hückel limiting law (see Section 5.2). The plots show clean breaks at the CMC with no indications of minima or shoulders, which may arise if impurities are present. Polynomials fitted to the pre-CMC data were used to generate surface excesses Γ using the Gibbs equation for 1:1 dissociating compounds (see Eq. 2.1.15). Figures 7.7 and 7.8 illustrate the different adsorption isotherms.

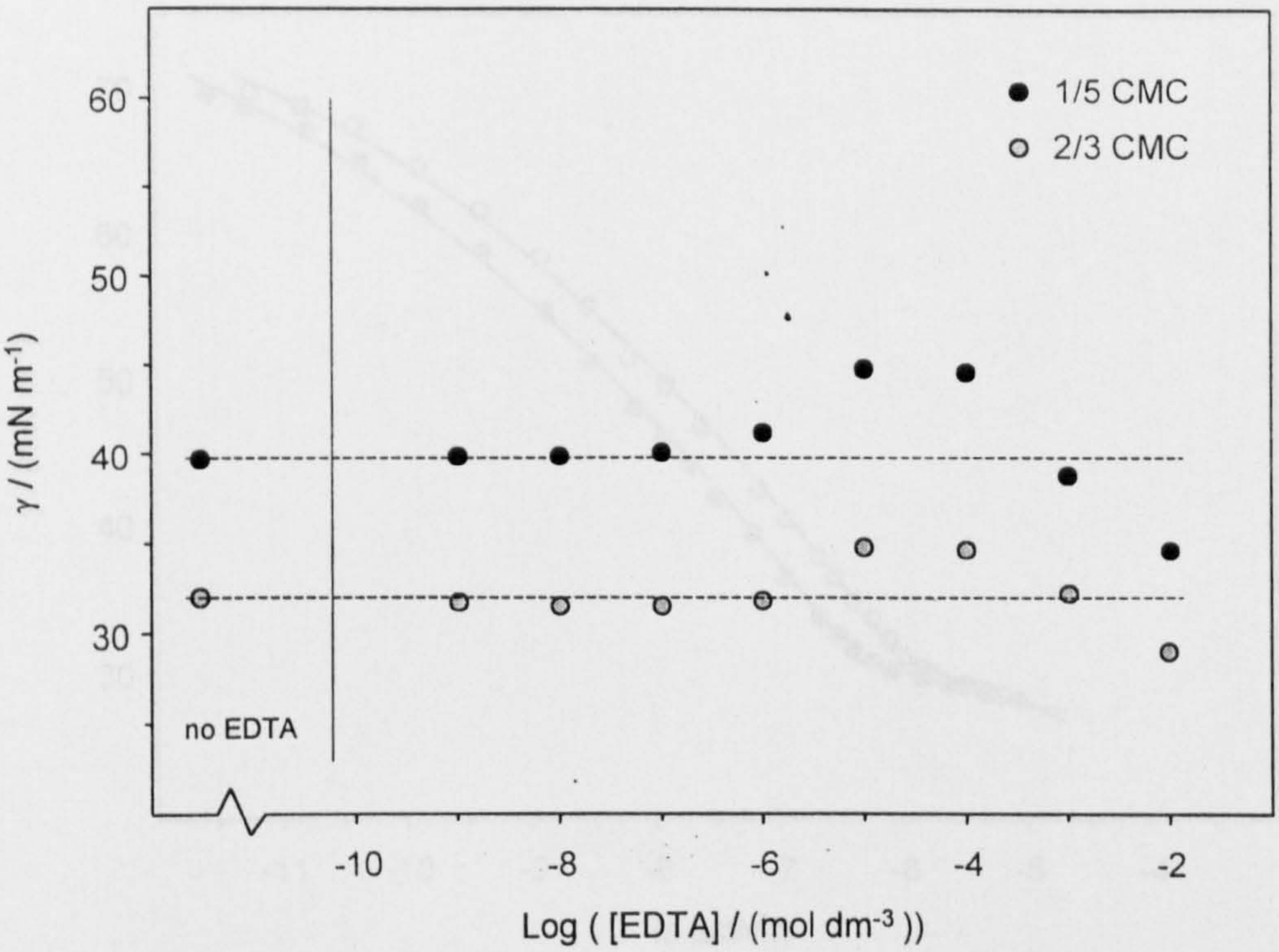

Figure 7.3 Effect of EDTA on surface tensions of AOTGLU solutions for concentrations below the CMC. The lines are guides to the eye.

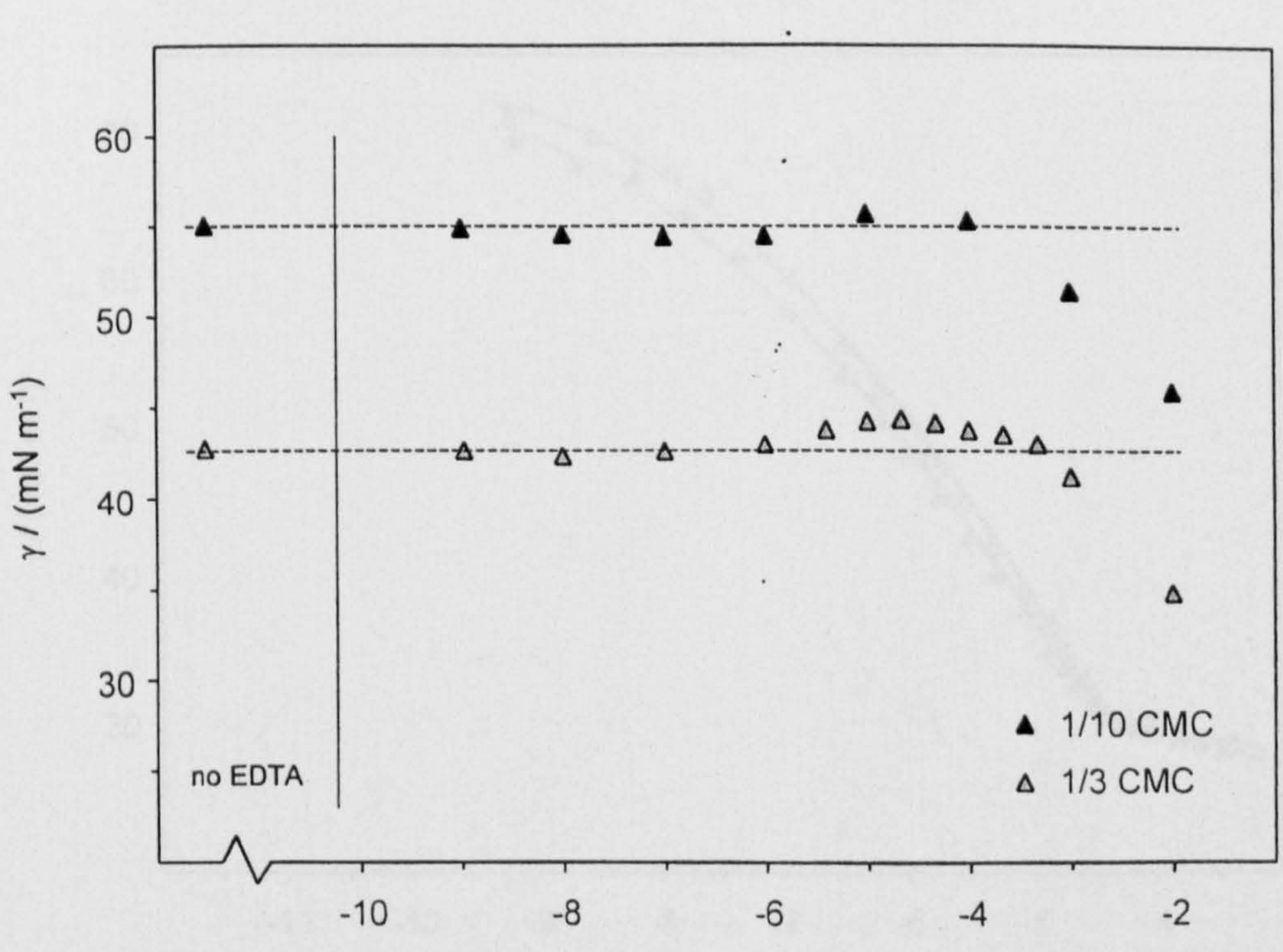

Figure 7.4 Effect of EDTA on surface tensions of di-C6GLU solutions for concentrations below the CMC. The lines are guides to the eye.

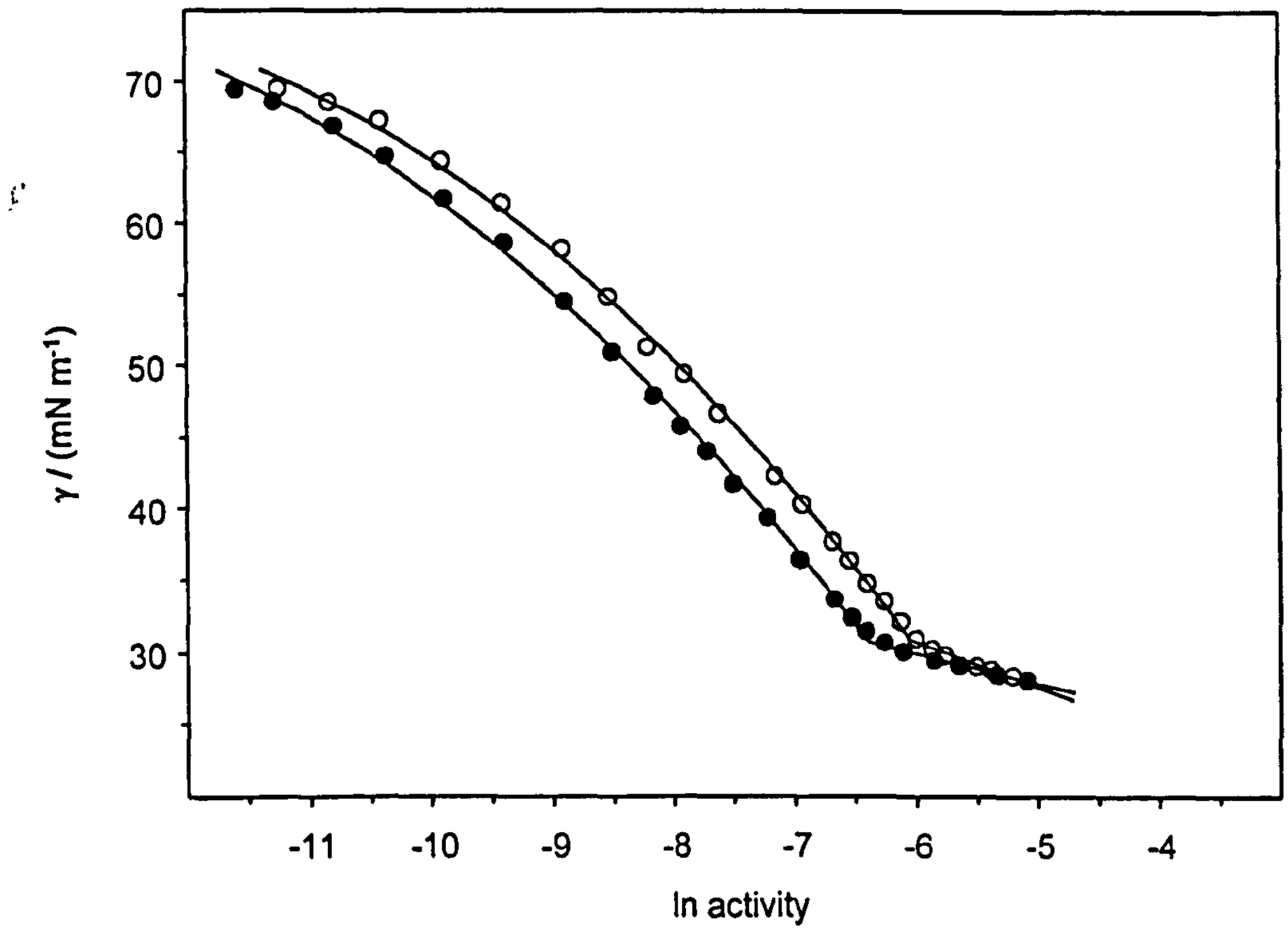

Figure 7.5 γ–ln *a* plots for AOTGLU (●) and AOT① (○) at 25°C with EDTA present in the subphase at a ratio [80:1] and [120:1] respectively.

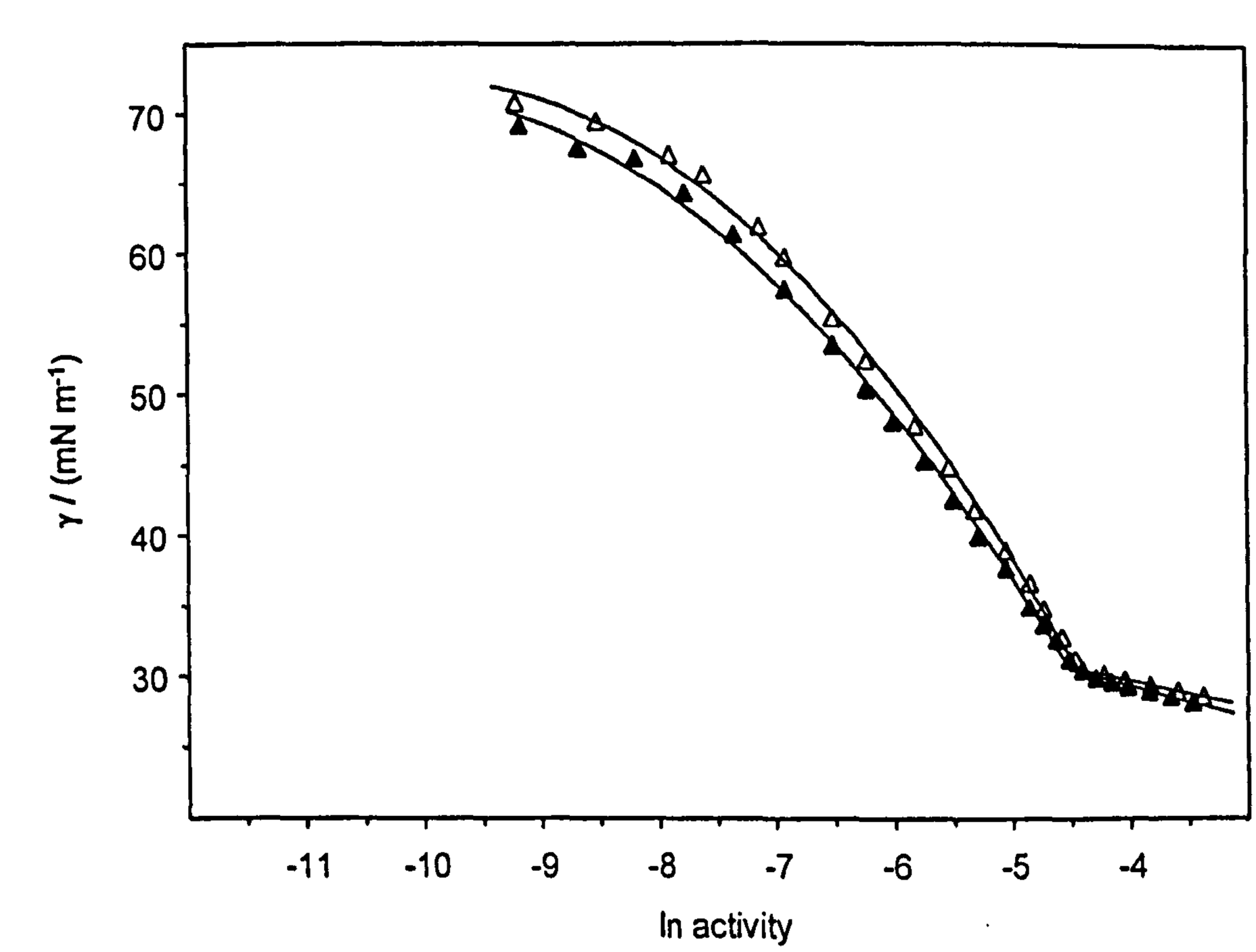

Figure 7.6 γ–ln *a* for di-C6GLU (▲) and di-C6SS (△) at 25°C with EDTA present in the subphase at a ratio [130:1] and [100:1] respectively.

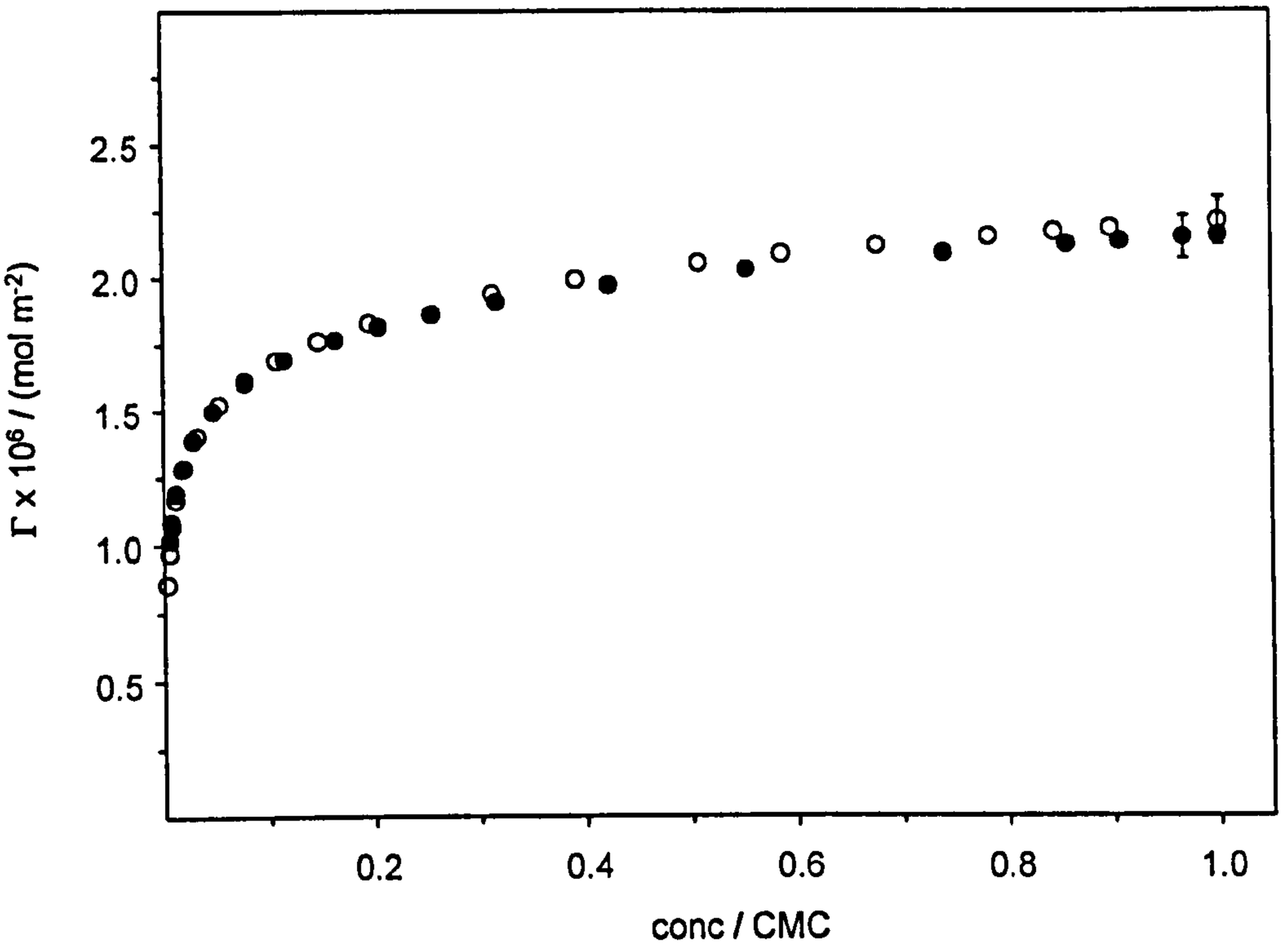

Figure 7.7 Surface excess vs reduced concentration (conc/CMC) adsorption isotherms for AOTGLU (●) and AOT① (○) derived from γ-ln *a* data (Fig. 7.5). For each curve a characteristic error bar around the CMC is given.

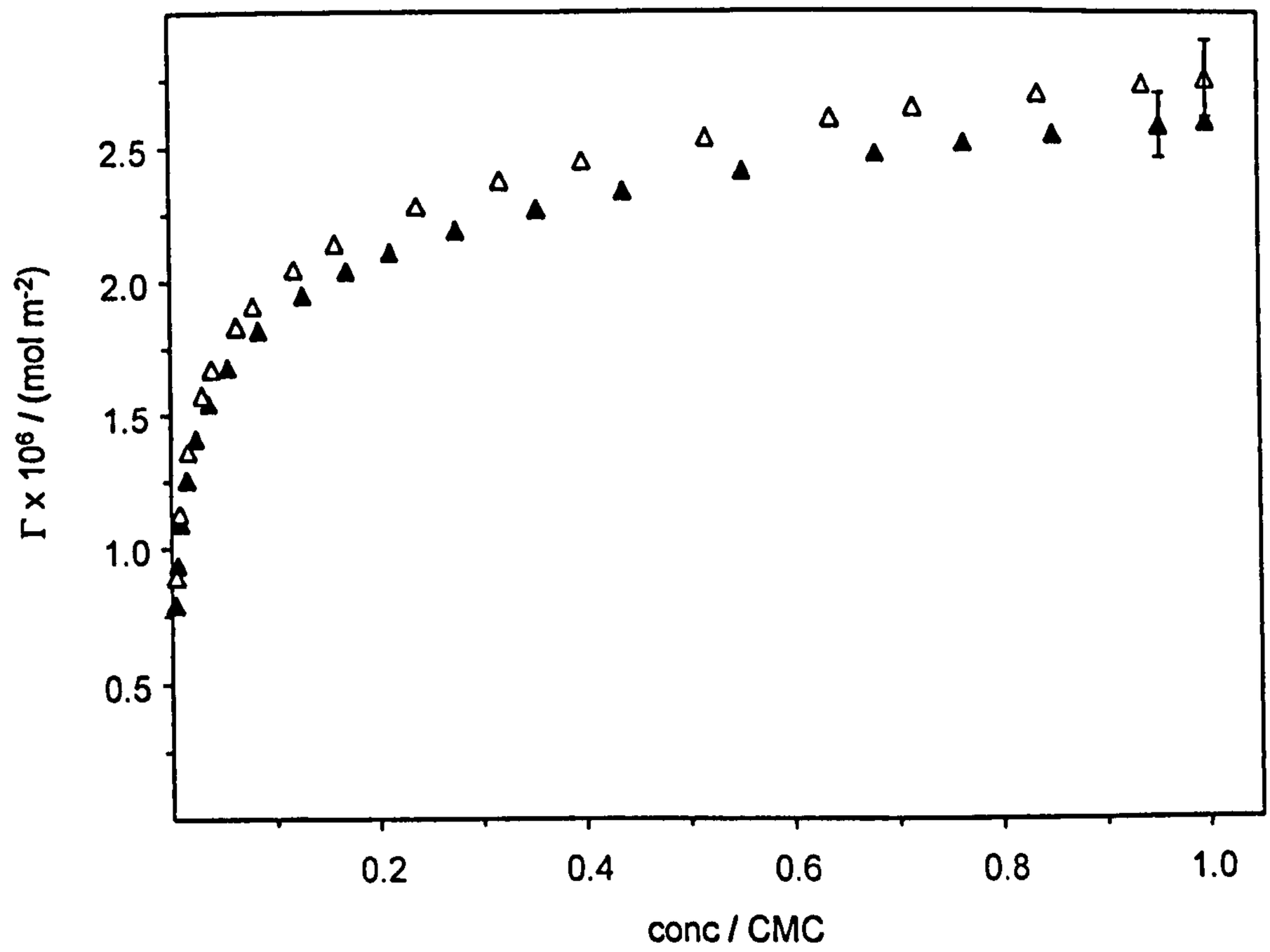

Figure 7.8 Surface excess vs reduced concentration (conc/CMC) adsorption isotherms for di-C6GLU (▲) and di-C6SS (△) derived from γ-ln *a* data (Fig. 7.6).

Table 7.2 Parameters derived from surface tension measurements of glutaconate and succinate surfactants in solutions. For all measurements T = 25°C. The ratios surfactant:EDTA are determined as described in the text

Surfactant	EDTA ratio below CMC	CMC / (mmol dm^{-3})	$\gamma_{cmc} \pm 0.5$ / (mN m^{-1})	$\Gamma_{cmc} \times 10^{-6}$ / (mol m^{-2})	$A_{cmc} \pm 2$ / $Å^2$
AOTGLU	80:1	1.78	30.8	2.16	77
AOT①	120:1	2.56	30.8	2.21	75
di-C6GLU	130:1	11.7	30.5	2.59	64
di-C6SS	100:1	12.5	30.1	2.67	62

Table 7.3 Comparison of efficiency of glutaconate and succinate surfactants. π_{cmc} is the limiting surface pressure ($\gamma_o - \gamma$). $C_{\pi/2}$ is the concentration of surfactant required to lower the surface tension by half the surface pressure at the CMC, $\gamma_{\pi/2}$

Surfactant	π_{cmc} / (mN m^{-1})	$\gamma_{\pi/2}$ / (mN m^{-1})	$C_{\pi/2}$ / (mmol dm^{-3})	$C_{\pi/2}$ / CMC
AOTGLU	41.7	51.7	0.19	0.11
AOT①	41.7	51.7	0.29	0.11
diC6GLU	42.0	51.5	1.81	0.16
diC6SS	43.4	50.8	1.94	0.16

Note that reduced concentration axis, conc/CMC, was used so that each set of surfactants can be readily compared. Table 7.2 gives values for the CMC's, limiting surface tensions γ_{cmc}, surface excess Γ_{cmc} and A_{cmc} at the CMC obtained from these plots. There appear to be no reports of aqueous solution properties of the glutaconates in the literature. Comparisons between both sets of CMC data are in agreement with an increase in hydrophobicity on addition of an extra $-CH_2-$ in the glutaconate head group. However, this methylene effect is by no means comparable to the effect of adding a $-CH_2-$ group in the alkyl chain (e.g., see data for di-C*n*SS series in Section 5.3.3). A similar trend was reported for the fluorinated sulfoglutaconates and sulfosuccinates (Figure 7.2) [20]. γ_{cmc} values are very similar, and so are the relative surfactant efficiencies, $C_{\pi/2}$/CMC, given in Table 7.3 (as defined in Section 2.1.3). This is in contrast with the marked increase in surfactant efficiency on increasing chain length: going from a C4 to a C8 in the di-C*n*SS series increases the relative efficiency from 0.13 to 0.19. This clearly illustrates the minor influence of head groups compared to chains in affecting adsorption. With regard to molecular packing, the glutaconates occupy a slightly larger area at the CMC as one would expect considering the larger head group, however, the difference is marginal considering the uncertainties involved. It should also be noted that glutaconate molecules are symmetric with respect to the sulfonate group and this may effect their orientation at the interface. Surface coverages of the fluorinated glutaconates and succinates were determined by neutron reflectivity [20] and this gave similar A_{cmc} values for both types of compound.

7.3.2 Aqueous solubility

It was observed in Section 6.2.3 that the aqueous solubility of branched sulfosuccinates is greatly affected by temperature. Although not directly related to the CMC trend, this reflects small changes in the hydrophobic/hydrophilic balance of the surfactant and shows the high sensitivity to small changes in chain architecture. The aqueous solubility of AOTGLU as a function of temperature is shown on Figure 7.9(*a*), and compared to AOT①.

Clearly, the glutaconate surfactant is more hydrophobic. Interestingly, comparing this with Figure 7.9(*b*) (AOTs aqueous solubility) indicates similar locations for the solubilisation boundaries of AOTGLU and AOT② – the latter has chain structure (2-propyl-1-pentyl). Since this transition dictates the high-temperature (haze) boundary

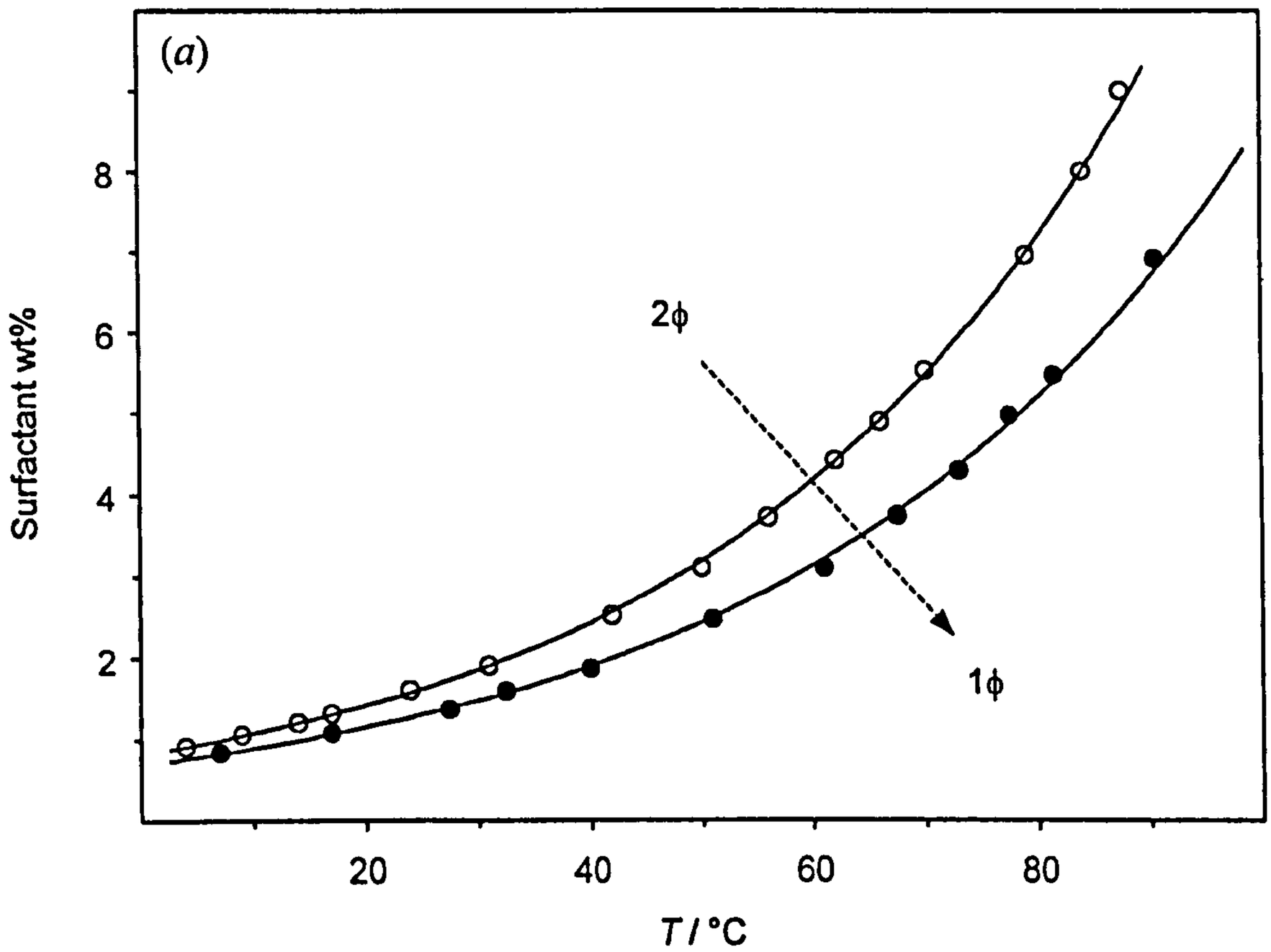

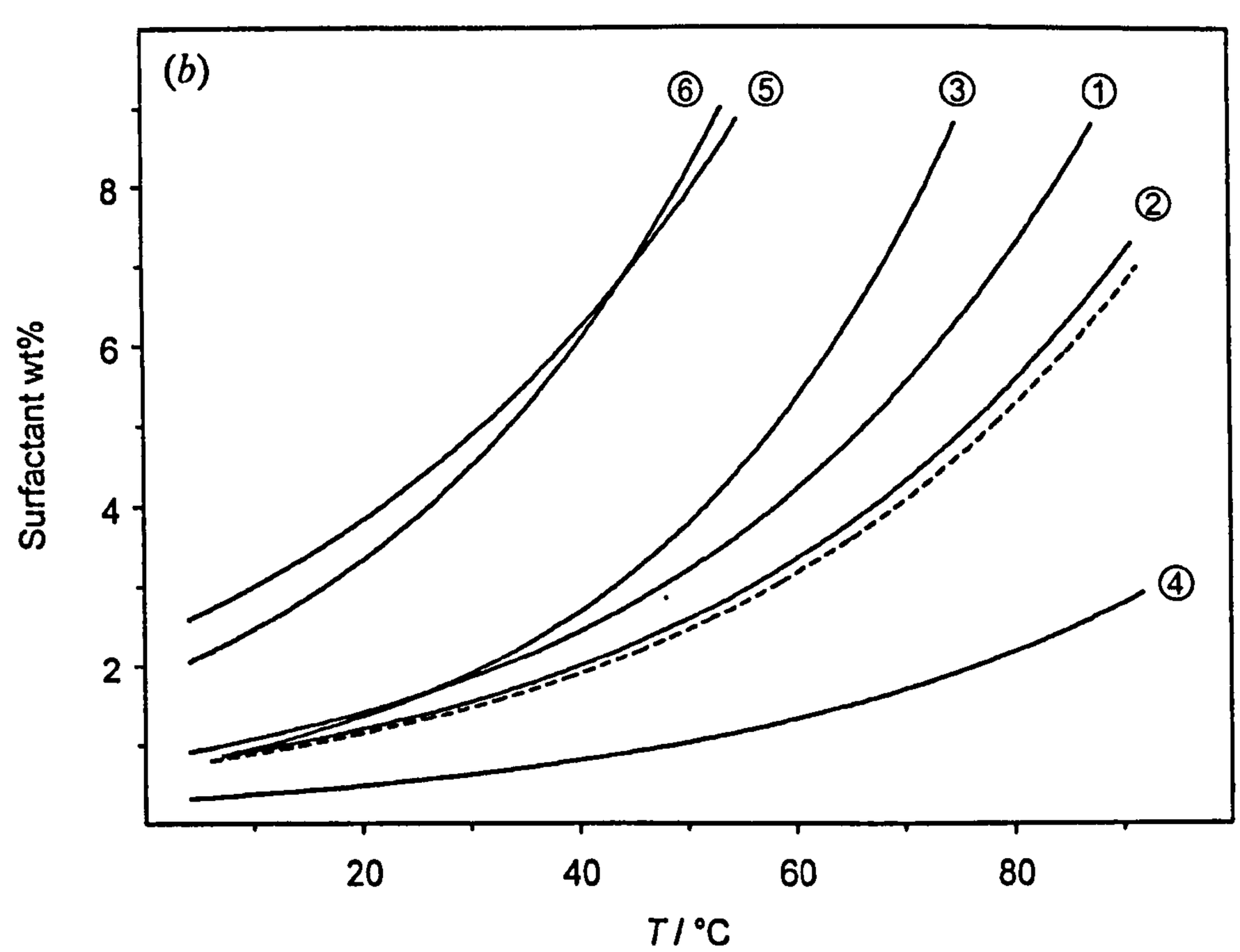

Figure 7.9 (*a*) Solubility of AOTGLU (●) and AOT① (○) in water as a function of temperature. Boundary lines indicate the temperature above which the surfactant completely dissolves in water (biphasic to monophasic transition). (*b*) Aqueous solubility of AOTGLU (---) compared to the AOTs series (—).

of w/o microemulsions, it is of interest to see how this will translate to ternary systems; this is described in Section 7.4.1. This solubility experiment was not carried out on the linear glutaconate owing to high solubility. Just like its succinate analogue, no Krafft point could be measured within the temperature range available (T_K may be close to 0 °C).

7.3.3 Liquid crystalline mesophases

Using the phase cut technique, described in Section 5.4.1, the various lyotropic phases formed by AOTGLU and di-C6GLU on dilution with water were observed using a polarising light microscope.

Figure 7.10 shows (*a*) the reverse hexagonal phase (H_2) formed by pure AOTGLU (no water), and (*b*) the phase sequence observed after water penetration. Just like all other branched sulfosuccinates (see Section 5.4.2), the same phase progression pattern was observed irrespective of chain or head structure, i.e., on increasing surfactant concentration: reverse hexagonal (H_2), cubic, lamellar (L_α) and micellar (L_1) phases. The melting temperature of AOTGLU was reported as 170 ± 5 °C (180 ± 5 °C for normal AOT). Figure 7.10 (*a*) and (*b*) are the corresponding pictures for the linear di-C6GLU. From (*b*), it is obvious that the gradient-diluted system differs from normal AOT, AOTGLU, or even di-C6SS. The melting temperature of di-C6GLU was found to be significantly lower than di-C6SS at 130 ± 5 °C (200 ± 5 °C for di-C6SS), and after cooling and water penetration, the typical phase progression (L_α, V_2, and H_2) was not observed. Instead, only dilution of the reverse hexagonal phase was seen. This behaviour coincides with phase cut diagrams of linear sodium sulfosuccinates. As chain length increases, existence of three distinct liquid crystal mesophases becomes less obvious, and disappears for ~ C8 to C9 chain surfactants (Section 5.4.2). This increase in surfactant hydrophobicity also coincides with the loss of phase sequence for di-C6GLU compared to di-C6SS. However, reasons for such behaviour are unclear. As described previously, glutaconate/succinate pairs show similar packing in dilute aqueous systems, and so was expected in the concentrated regime (i.e., as AOTGLU and AOT do). A more detailed study of this part of phase diagram (by varying surfactant content and temperature) might explain the different behaviour of di-C6SS and di-C6GLU. However, such experiments are rather time-consuming and could not be performed.

(*a*)

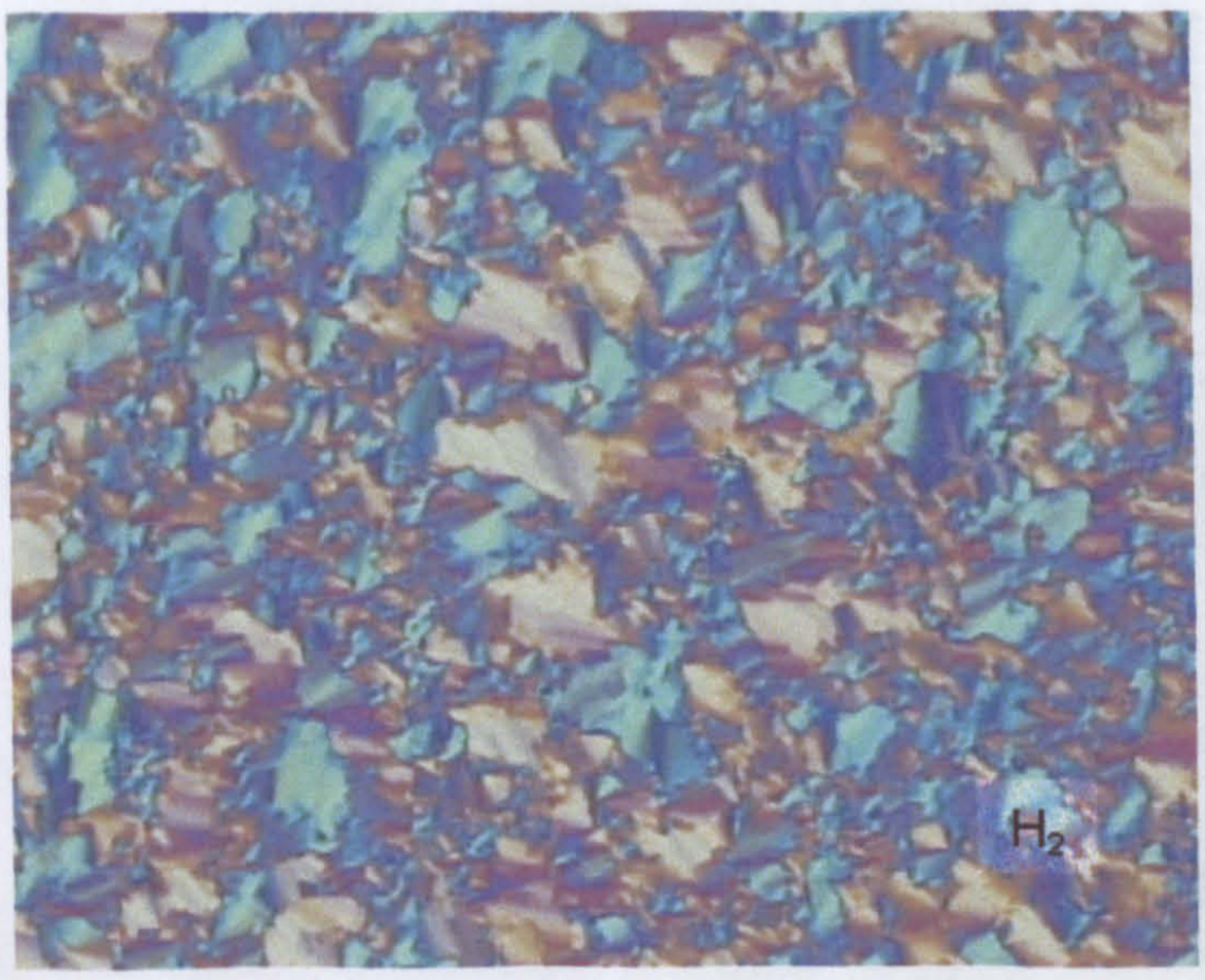

(*b*)

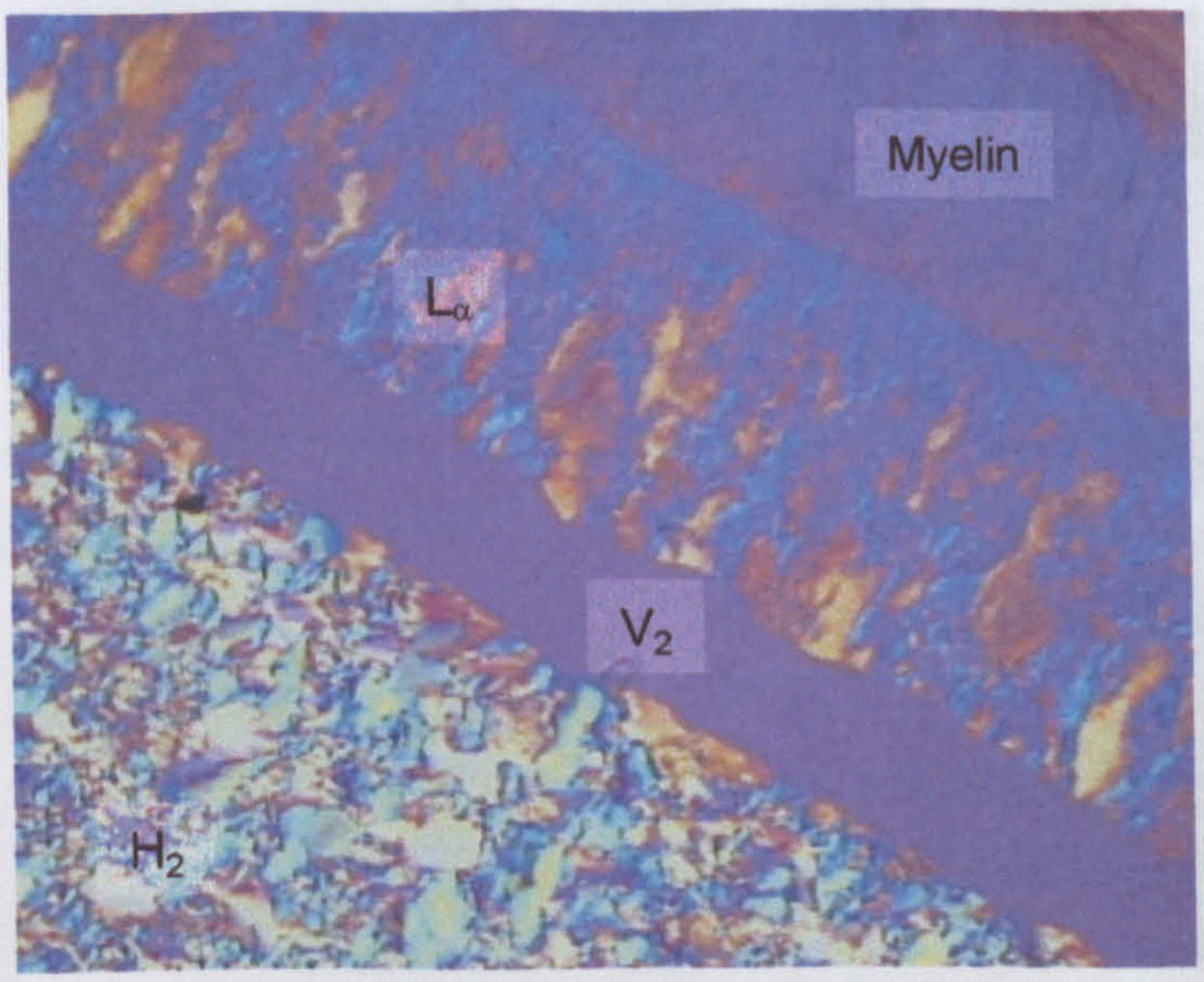

Figure 7.10 Liquid crystalline phases formed by AOTGLU. (*a*) no water. (*b*) phase cut diagram after water penetration (see text for details of symbols).

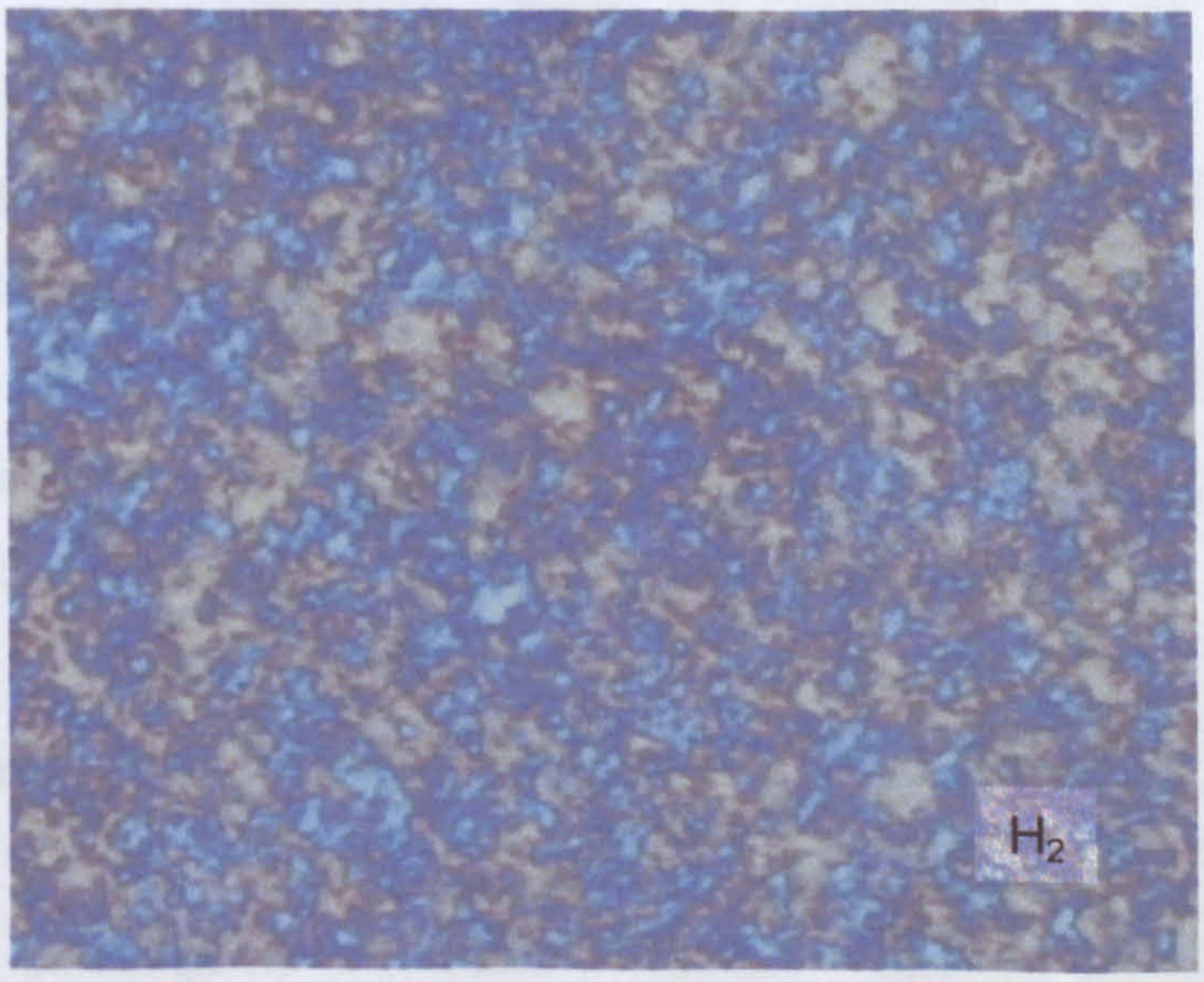

(*a*)

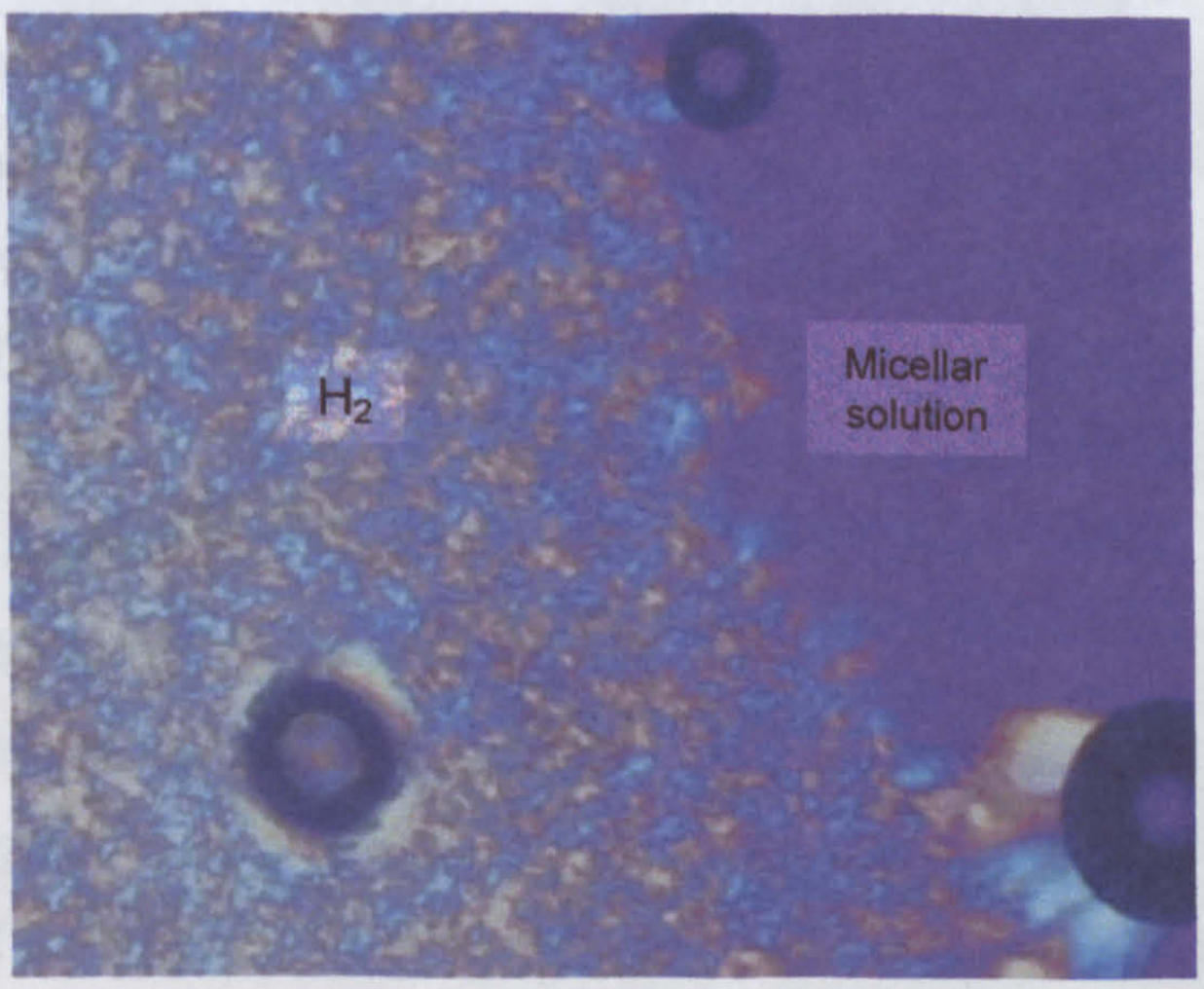

(*b*)

Figure 7.11 Liquid crystalline phases formed by di-C6GLU. (*a*) no water. (*b*) phase cut diagram after water penetration.

7.4 MICROEMULSION SYSTEMS

Water-in-oil microemulsions formed with AOTGLU and di-C6GLU were characterised using phase stability studies at fixed surfactant concentration, and small-angle neutron scattering. The objective was to identify the extent of the single phase L_2 region as well as characterise the microemulsion droplets and interfacial film. In addition, interfacial tensions were measured for AOTGLU systems in an attempt to quantify the surfactant film rigidity.

7.4.1 Water-in-oil phase stability diagrams

As already observed for the linear di-chain sulfosuccinates, attempts to form simple ternary microemulsions stabilised by di-C6GLU alone failed, so as before *n*-hexanol was used as a co-surfactant with *n*-hexane. Therefore, direct comparisons between microemulsion structures stabilised by linear and branched surfactants could not be made, however, reference will be made to the succinate systems. In all cases, phase equilibria were determined as a function of temperature and water content. Figures 7.12 and 7.13 display phase stability diagrams for AOTGLU in water/heptane and di-C6GLU in water/hexane-hexanol systems respectively (note the corresponding succinate systems are also included for comparison purposes). For each surfactant, phase diagrams are expressed as w vs. temperature, where w = [water]/[surfactant], and the Winsor II (or solubilisation) and high-temperature stability (or haze) boundaries – noted T_s and T_u respectively – were determined.

Figure 7.12 shows that the AOT-like phase behaviour [27-29] is conserved with AOTGLU. Interestingly, the glutaconate is even more efficient at solubilising water for the same temperature range. The shift of the upper boundary, T_u, towards higher temperatures was expected since it reflects the overall aqueous surfactant solubility: it corresponds to a critical-type biphasic system where surfactant becomes totally soluble in the aqueous phase. The lower solubilisation boundary, T_s, is characteristic of surfactant efficiency: it corresponds to the maximum water uptake at a specific temperature (w_{max}) with all surfactant present in the w/o portion. The film is also at a natural curvature radius (minimum in the film bending energy). In the temperature range 5–20 °C, it is clear that AOTGLU solubilises larger amounts of water than its

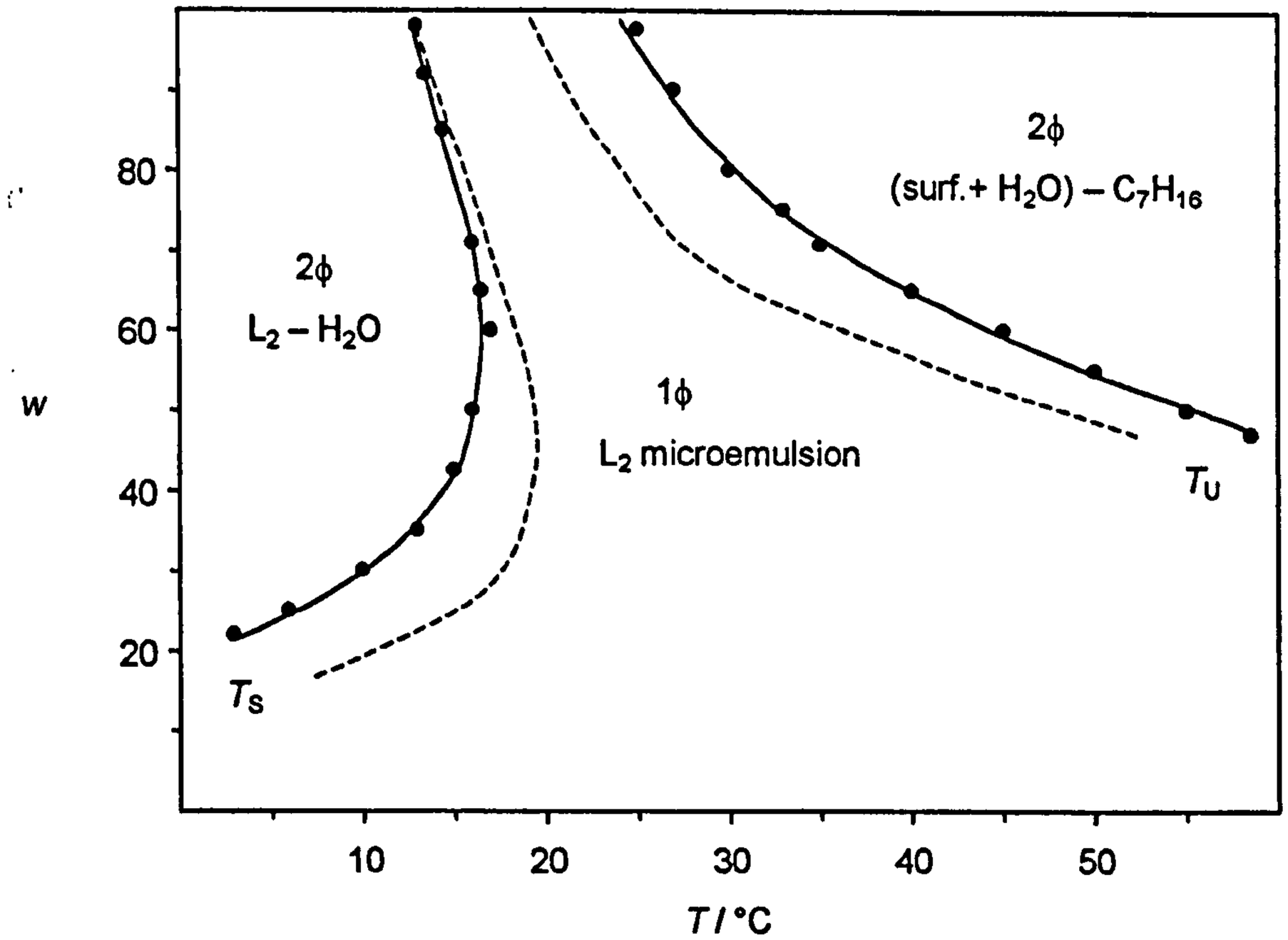

Figure 7.12 w/o microemulsion phase diagrams for AOTGLU (-●-) and AOT① (---) in water/heptane systems. In both cases [surf] = 0.1 mol dm^{-3}, T_S is for Winsor II (or solubilisation) boundary, and T_U is for high-temperature stability boundary (or haze boundary).

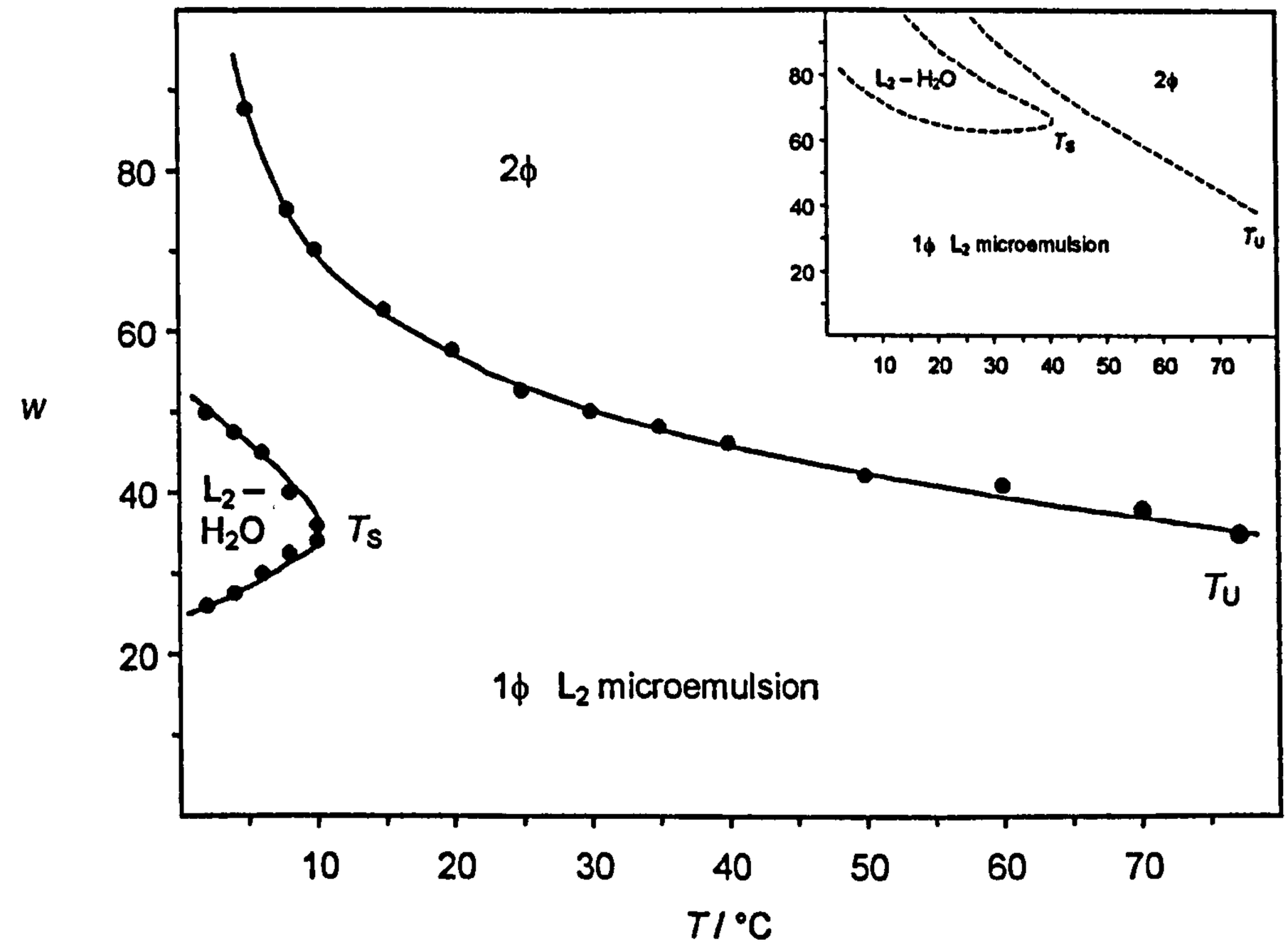

Figure 7.13 w/o microemulsion phase diagram for di-C6GLU (-●-) in water/hexane:hexanol (9:1) system. [surf] = 0.1 mol dm^{-3}. The inset shows behaviour for di-C6SS (---) under similar experimental conditions.

cousin normal AOT. As was reported earlier, AOTGLU and AOT② display similar aqueous solubility with increasing temperature. However, this does not translate to three-component microemulsions: with AOT② the L_2-region is centred around a higher temperature than for AOTGLU. This shows that although temperature is a limiting factor, other determinant parameters characterise the solubilisation boundary. There the interfacial packing of the surfactant molecules play an important role and characterisation of the film structure and microemulsion droplets near the WII boundary by SANS, should give useful information. Recently, Eastoe *et al.* have studied water-in-CO_2 (w/c) microemulsions stabilised by a range of di-chain fluorinated anionic surfactants [30]. In a search to improve surfactant efficiency in these pressurised systems – i.e., at constant temperature and water content a surfactant that would reduce the critical pressure P_c, above which single phase w/c microemulsion forms – DHCF4 and DHCF4GLU (see Figure 7.2) were investigated. Comparison of the behaviour of the two compounds shows that the glutaconate reduces P_c by about 10-15 bars so the minor change in the head group gave a slight improvement in phase stability, just like seen here for normal w/o microemulsions stabilised by AOTGLU.

The phase stability diagram for di-C6GLU in water/hexane-hexanol is shown in Figure 7.13. The phase sequences are similar to the succinate system (shown inset) with occurrence of a relatively large single phase L_2-domain separating a restricted WII (L_2+H_2O) region from a critical-type biphasic phase. Surprisingly, T_s and T_u are located at significantly lower temperatures and w values than in the succinate system, indicative of di-C6GLU being less hydrophobic and less efficient than its succinate analogue. The WII region is limited to both a small temperature (3–10 °C) and w (25–50) range. This is in contrast with the microemulsion phase behaviour of AOTGLU or DHCF4GLU in w/c systems. The reason for the unusual trend in the phase behaviour of di-C6GLU and di-C6SS is unclear. In dilute aqueous systems, as for the branched surfactants, tensiometric data indicated very similar CMCs and molecular packing. Microemulsion phases were thus expected to be rather similar in terms of temperature windows of the phase boundaries. Due to the high hydrophilic character of both surfactants, overall aqueous solubilities could not be measured, and unlike AOTGLU and AOT systems, the relative hydrophobicity of the two di-hexyl amphiphiles could not be assessed. Thus, it is difficult to predict the relative position of the T_u boundaries in Figure 7.13. In addition, the presence of a co-surfactant does not allow for a strict comparison between the linear and branched sets of amphiphiles.

7.4.2 Microemulsion droplet and film structure from SANS

CSD model and droplet structure

As mentioned previously, simultaneous analysis of core-shell-drop contrasts gives reliable information about the size and structure of microemulsion aggregates. To allow direct comparison with the succinate systems, experimental conditions identical to those described in Chapter 6 for di-C6SS and AOT① were used, i.e., systems close to the solubilisation (Winsor II) boundary where droplets interact weakly. SANS data for the core, shell, and drop contrasts of AOTGLU and di-C6GLU (w = 30, 25 °C) along with the fitted I(Q) functions are shown in Figures 7.14 and 7.15 respectively. Both systems are well described by a polydisperse sphere model with a hard-sphere structure factor. However, for di-C6GLU I(Q) profiles (for w = 30 and above) were analysed using an Ornstein-Zernicke S(Q) to account for attractive droplet interactions. Fitted parameters are summarised in Table 7.4 along with values for the succinate systems.

Generally, w/o films stabilised by glutaconates are very similar to the succinate systems. All compounds have C6 effective chain lengths, hence the identical fitted surfactant film thicknesses, t_s, around 9 ± 1 Å. As already observed in Chapter 6 for di-C6SS, microemulsions stabilised by di-C6GLU have high polydispersity due to the presence of the co-surfactant. This is clearly illustrated by the shell contrast at high Q and σ / R_c^{av} values. Figure 7.16 regroups all the core, shell and drop contrasts and allows comparison between each set of surfactants. Clearly, major differences are seen on change in chain, rather than in head group, structures. Comparing succinates and glutaconates (i.e., white against grey markers) shows almost identical plots, whereas branched and linear compounds (i.e., circles against triangles) shows differences at high Q (> 0.03 Å^{-1}). These differences arise from changes in radii and polydispersity.

From water core data, both glutaconates have a slightly lower water solubilisation capacity than the succinates with a decrease in droplet size of about 3 Å. This corresponds to a more negative interfacial curvature. Considering each set of compounds, since the hydrophobic moiety remains unchanged, the molecular packing is not influenced by chain length or side branch factors, but only by the head group volume. At identical sample composition, if droplets of similar aggregation number were assumed to form, a slight increase in head group volume should produce larger droplets, with a less negatively curved interfacial film. Therefore, with glutaconates

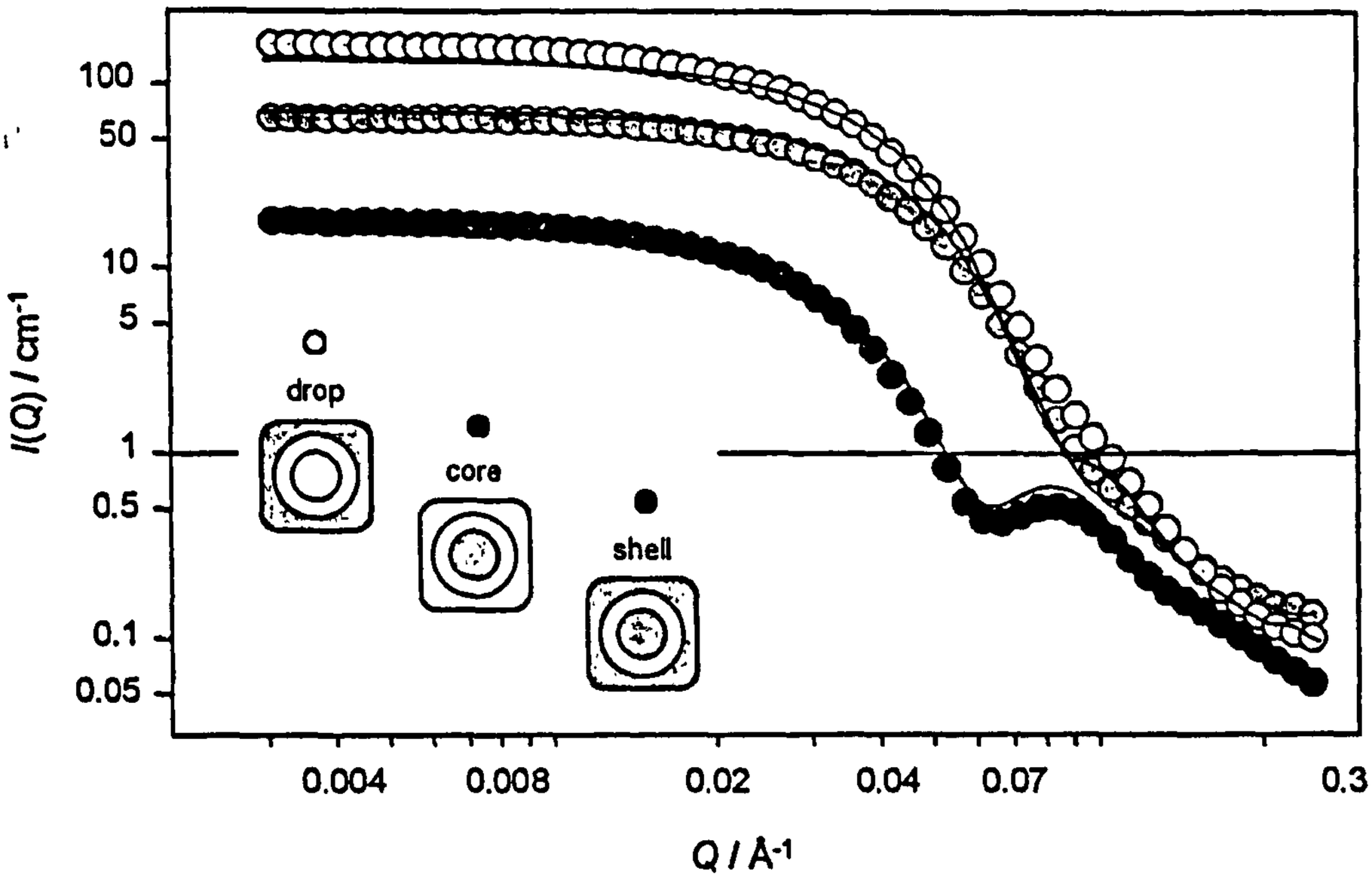

Figure 7.14 SANS data from D22 for AOTGLU microemulsions at $w = 30$, $\phi_c = 0.03$, and $T = 25°C$. [surf] = 0.05 mol dm^{-3}. The simultaneous fit (—) to the Schultz core-shell model and error bars on the data are shown.

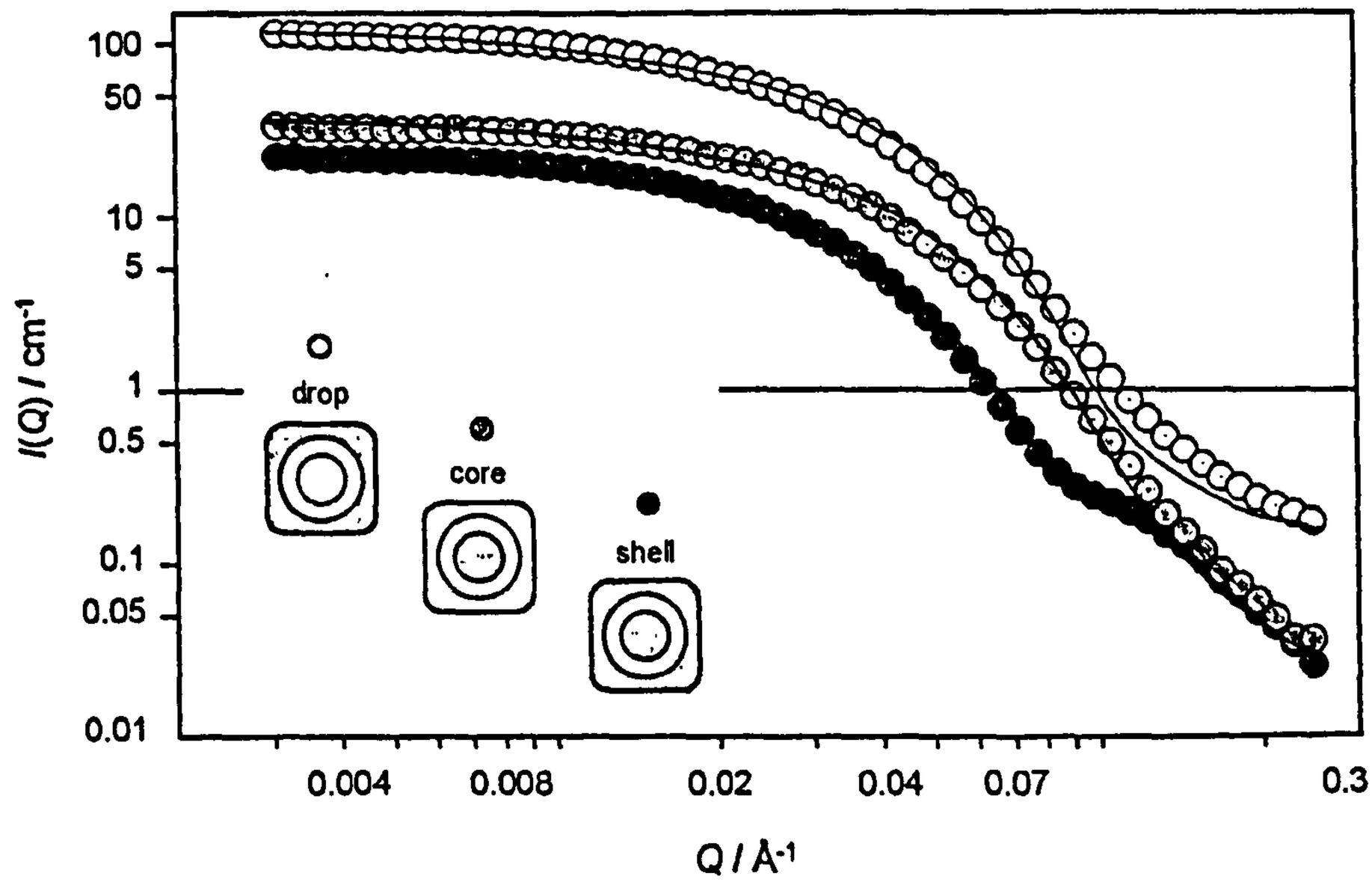

Figure 7.15 SANS data from D22 for di-C6GLU microemulsions at $w = 30$, $\phi_c = 0.03$, and $T = 25°C$. [surf] = 0.05 mol dm^{-3}. The simultaneous fit (—) to the Schultz core-shell model and error bars on the data are shown.

Table 7.4 Values obtained from simultaneous analyses of core-shell-drop SANS data from the glutaconate and succinate w/o microemulsions at $w = 30$, $\phi_c = 0.03$, $\phi_d = 0.05$[a]

Surfactant	T / °C	Water core		Surfactant film
		R_c^{av} / Å	σ / R_c^{av}	t_s / Å
AOTGLU	25	42.5	0.21	9.1
AOT①	22	46.1	0.22	9.1
di-C6GLU	25	28.1	0.32	8.8
di-C6SS	25	30.8	0.26	8.8

[a] Parameters: R_c^{av}, average radius of water core; t_s, apparent shell thickness; σ / R_c^{av}, width of the Schultz distribution function. Uncertainties: R_c^{av} and t_s, ± 1 Å; σ / R_c^{av}, ± 0.01.

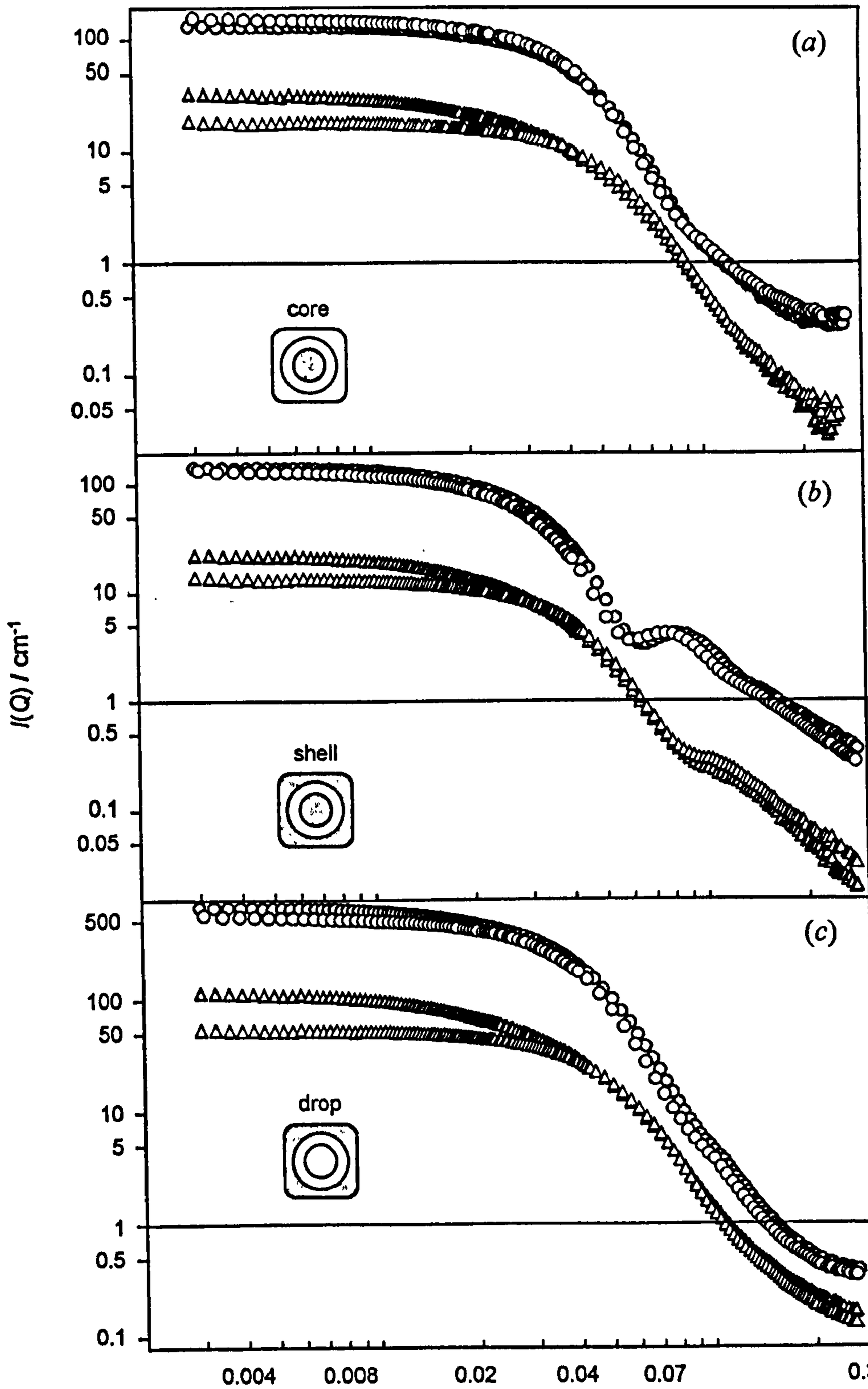

Figure 7.16 SANS D22 data from Winsor II glutaconate and sulfosuccinate microemulsions. For all systems, $w = 30$, $\phi_c = 0.03$, [surf] = 0.05 mol dm^{-3}, $T = 25$°C. AOTGLU (○), AOT① (○), di-C6GLU (△), di-C6SS (△). Note: for clarity of presentation, each AOTGLU and AOT① data set is multiplied by an arbitrary constant: in (*a*) × 2, in (*b*) × 8, and in (*c*) × 4.

producing the smaller water droplets, their aggregation number must be slightly smaller. Another possible factor influencing the decrease in R_c^{av} may be a decrease in head group repulsions. Due to the extra -CH_2- group, glutaconates are symmetrical around the sulfonate function and may pack more efficiently, whereas succinates are more likely to have their SO_3^- groups closer one another, and repulsion between charges may space them out. In any case, radii differ by only a few angstroms (but outside uncertainties), showing the minor effect of head groups with respect to chains (see Section 6.4).

w Variation and molecular areas

Figures 7.17 and 7.18 shows the I(Q) profiles and the fitted functions for various w values with AOTGLU and di-C6GLU in core contrast. Fitted parameters are the core radius R_c^{av} and Schultz scale factor. The classic effect of increasing microemulsion droplet radius with increase water content is observed and a linear relationship R_c vs. w is obtained as shown in Figures 7.19 and 7.20. Fitted radius values are given in Table 7.5. As given in Chapter 6, the head group area a_h was then estimated using

$$\alpha(p)R_c^{av} = \frac{3\upsilon_w}{a_h}w + \frac{3\upsilon_h}{a_h} \qquad (7.4.1)$$

Assuming the polydispersity is independent of w, a_h was obtained from the slope, and the intercept gave the average head group volume υ_h via the surfactant head group radius r_h

$$r_h = \left(\frac{3\upsilon_h}{4\pi}\right)^{1/3} \qquad (7.4.2)$$

Data derived from Eq. 7.4.1 and 7.4.2 are given in Table 7.6. Also included are the head group areas derived from core contrast data at high Q using the Porod approximation (see Eq. 6.3.4 given in Section 6.3.2). Porod plots of D22 data from AOTGLU and di-C6GLU microemulsions are given in Figures 7.21 and 7.22 respectively.

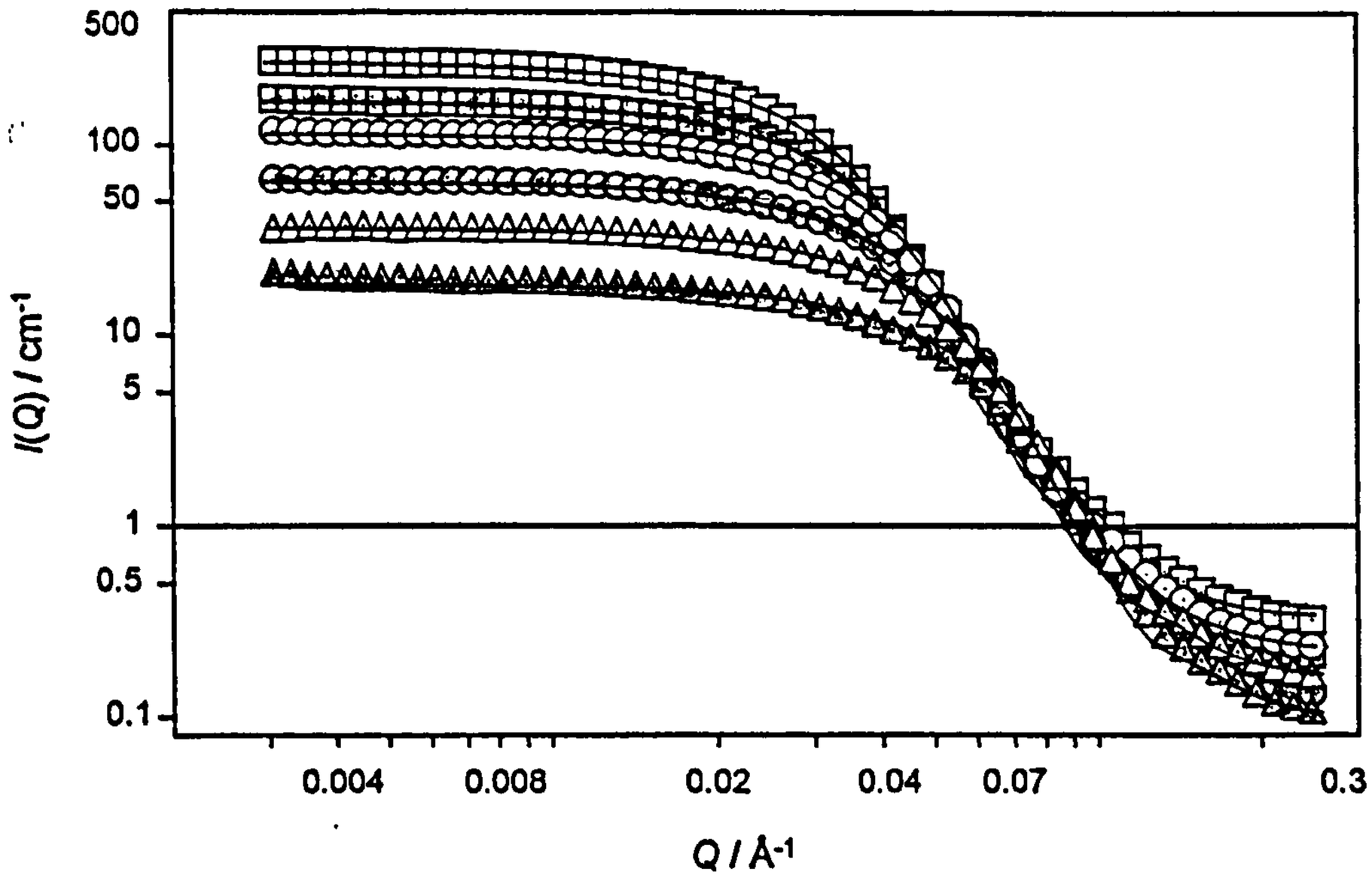

Figure 7.17 SANS core contrast data from D22 and fits (—) to a Shultz polydisperse sphere model for Winsor II microemulsions of AOTGLU. [surf] = 0.05 mol dm^{-3}, T = 25°C. w = 20 (▲), 25 (△), 30 (◉), 35 (○), 40 (■), 45 (□).

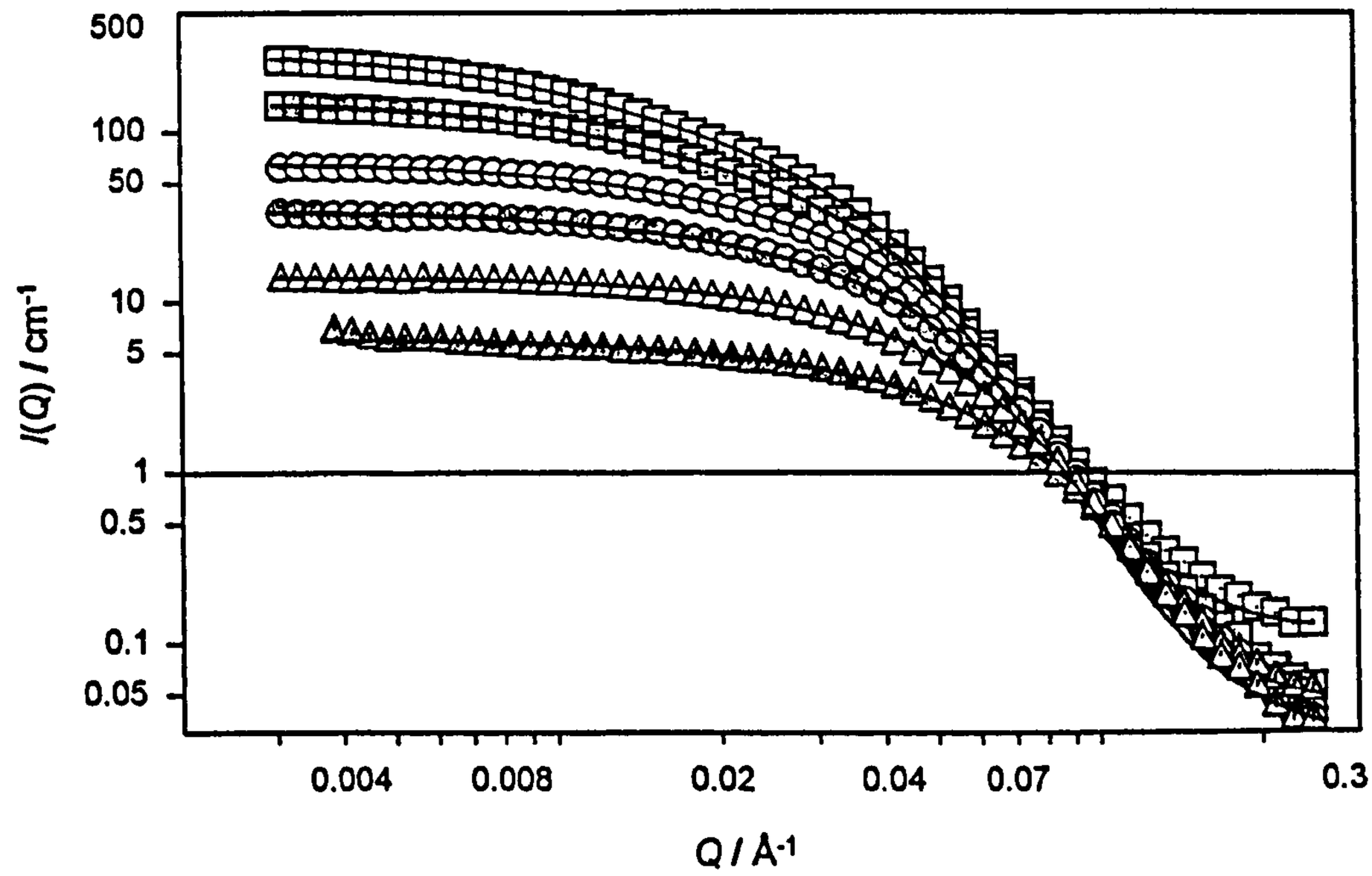

Figure 7.18 SANS core contrast data from D22 and fits (—) to a Shultz polydisperse sphere model for Winsor II microemulsions of di-C6GLU. [surf] = 0.05 mol dm^{-3}, T = 25°C. w = 20 (▲), 25 (△), 30 (◉), 35 (○), 40 (■), 45 (□).

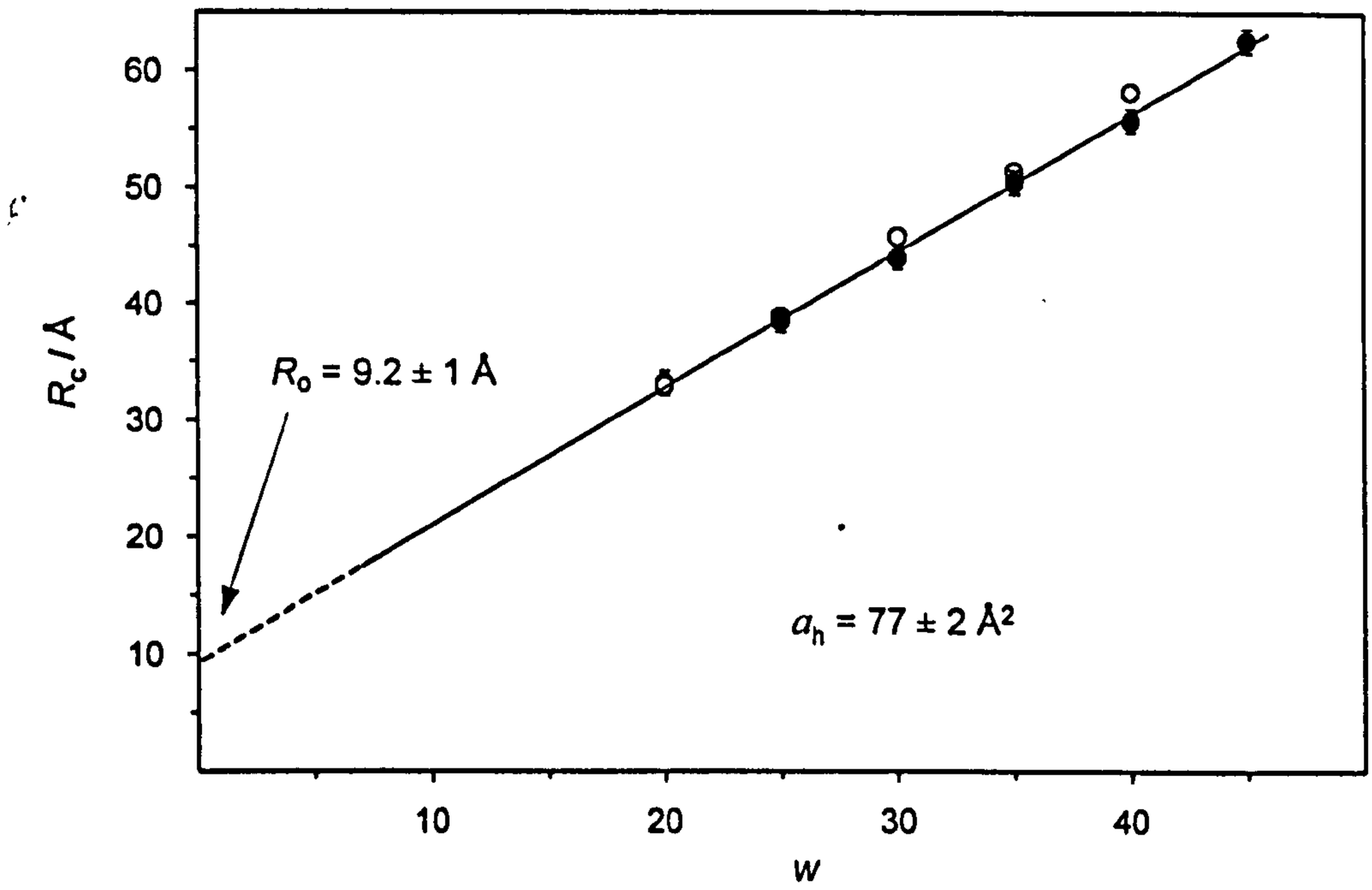

Figure 7.19 Water droplet radius R_c versus w for AOTGLU (-●-) w/o microemulsions. R_c values are from SANS analysis of core contrasts as given in Table 7.5. Example error bars are shown and data for AOT① microemulsions (○) are also shown (see Chapter 6) for comparison purposes.

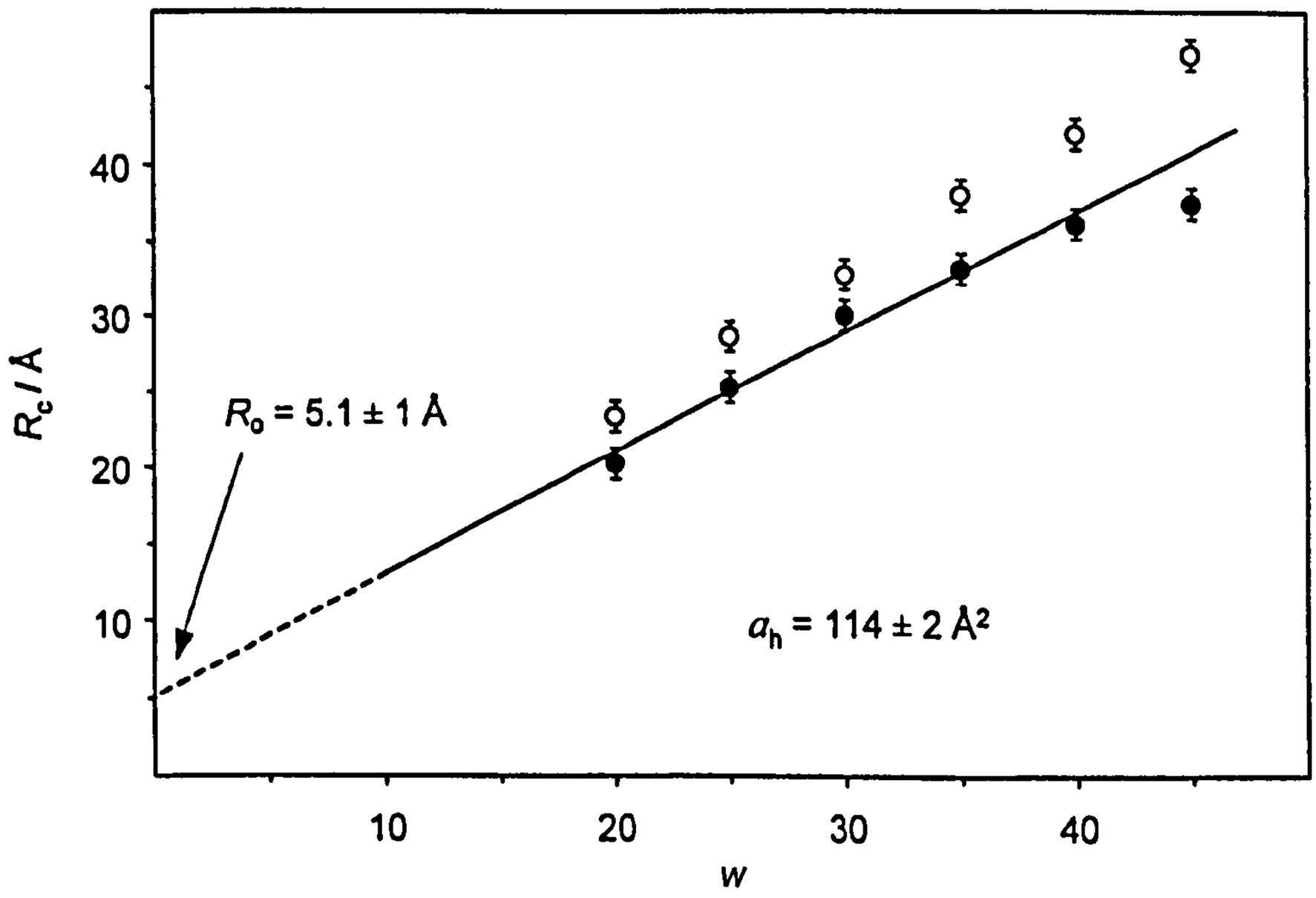

Figure 7.20 Water droplet radius R_c versus w for di-C6GLU (-●-) w/o microemulsions. R_c values are from SANS analysis of core contrasts as given in Table 7.5. Data for di-C6SS microemulsions (○) are also shown (see Chapter 6) for comparison purposes.

Table 7.5 Fitted mean water core radii from core SANS D22 data for the glutaconate and succinate w/o microemulsions

Surfactant	Mean water core radius $R_c^{av} \pm 1$ Å					
	$w = 20$	$w = 25$	$w = 30$	$w = 35$	$w = 40$	$w = 45$
AOTGLU	33.1	38.5	44.0	50.5	55.8	62.6
AOT①	32.9	38.9	45.8	51.4	58.2	-
di-C6GLU	20.2	25.2	30.0	33.1	36.1	37.5
di-C6SS	23.3	28.6	32.7	38.0	42.0	47.2

Table 7.6 Head group areas derived from analyses of core SANS data, and R_o the dry reverse micelle radius obtained from linear fits shown in Figs. 7.19 and 7.20[a]

Surfactant	T / °C	Head group area / Å^2		$R_o \pm 1$ Å	$\upsilon_h \pm 25$ Å^3	$r_h \pm 0.5$ Å
		$a_h(3\upsilon_w w/R_c)$	a_h(Porod)			
AOTGLU	25	77	76	9.2	236	3.8
AOT①	22	74	69	9.1	224	3.8
di-C6GLU	25	114	71	5.1	194	3.6
di-C6SS	25	96	67	4.7	150	3.3

[a] υ_h, water-penetrated volume (from Eq. 7.4.2) and r_h, radius of the surfactant head group (see detail in text). Uncertainties: $a_h(3\upsilon_w w/R_c)$, ± 2 Å^2; a_h(Porod), ± 12 Å^2.

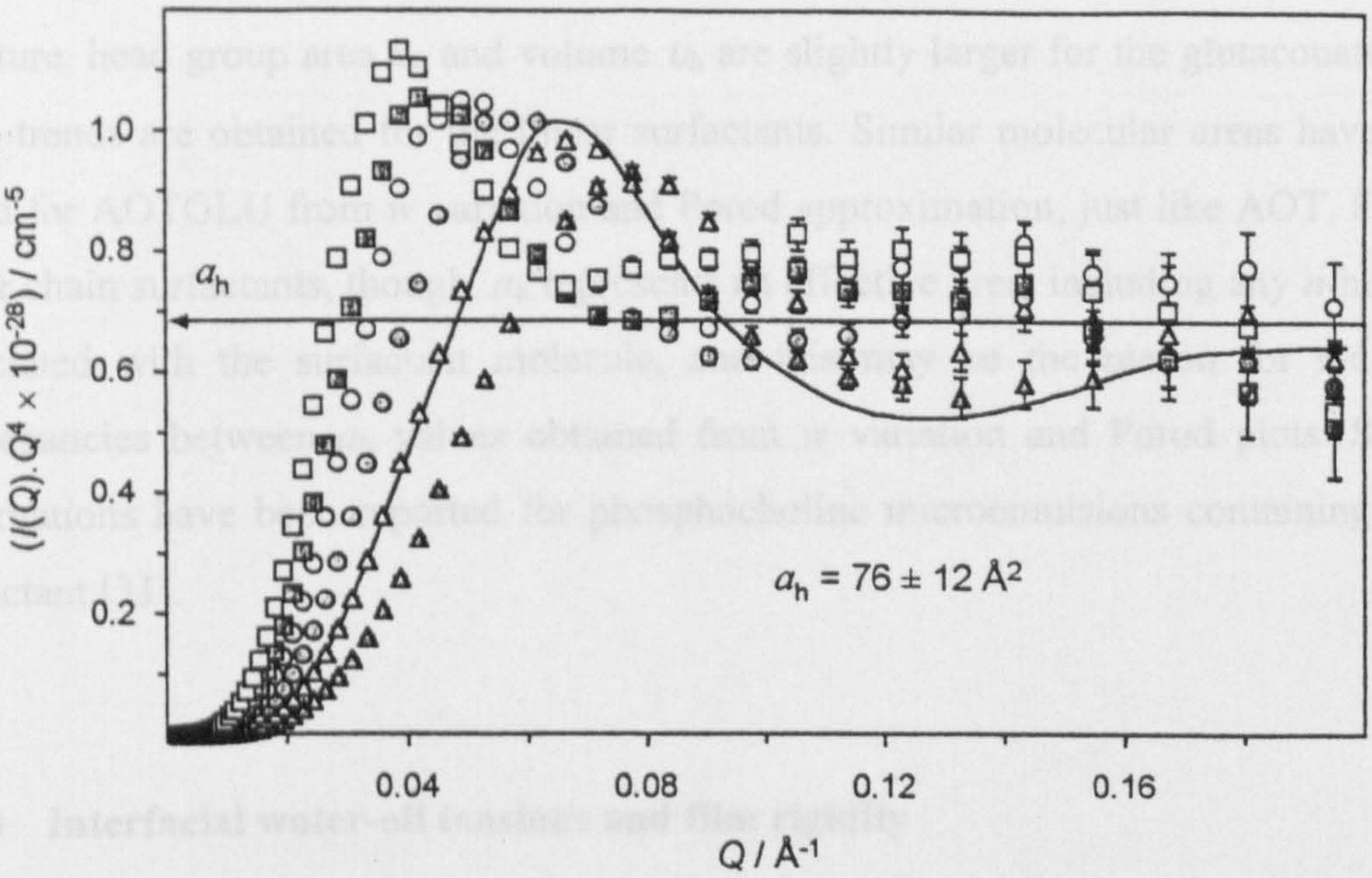

Figure 7.21 Porod plot of D22 data from Winsor II AOTGLU microemulsions. [surf] = 0.05 mol dm^{-3}, T = 25°C. w = 20 (▲), 25 (△), 30 (●), 35 (○), 40 (▣), 45 (□). For w = 25 the model fit (—) and example error bars at high Q are shown. A level of scattering, representing an average area per head group, a_h, is also shown.

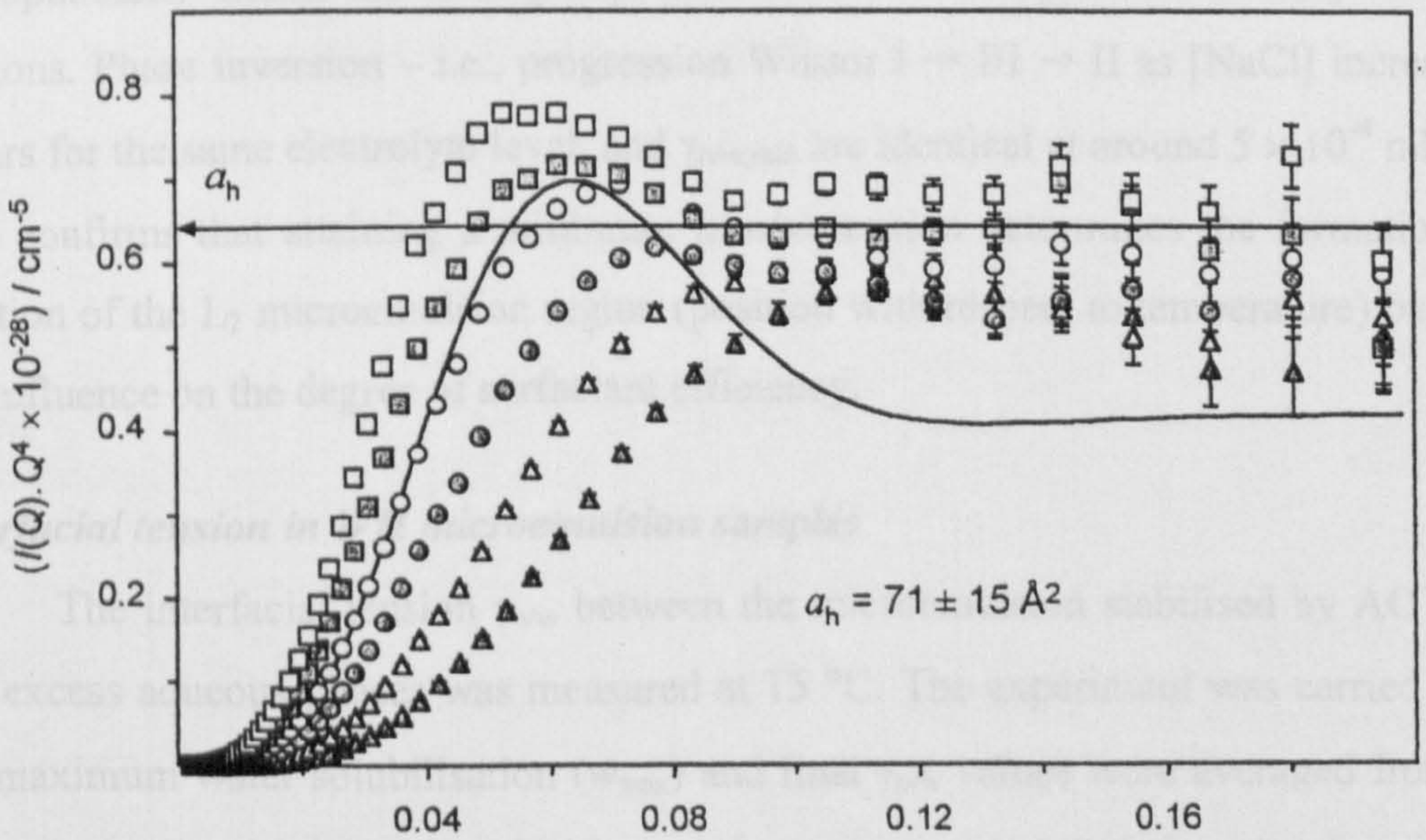

Figure 7.22 Porod plot of D22 data from Winsor II di-C6GLU microemulsions. [surf] = 0.05 mol dm^{-3}, T = 25°C. w = 20 (▲), 25 (△), 30 (●), 35 (○), 40 (▣), 45 (□). For w = 35 the model fit (—) and example error bars at high Q are shown. A level of scattering, representing an average area per head group, a_h, is also shown.

Again, AOTGLU shows similar behaviour to AOT. As expected from molecular structure, head group area a_h and volume υ_h are slightly larger for the glutaconate. The same trends are obtained for the linear surfactants. Similar molecular areas have been found for AOTGLU from w variation and Porod approximation, just like AOT. For the linear chain surfactants, though, a_h represents an effective area, including any *n*-hexanol associated with the surfactant molecule, and this may be the reason for the large discrepancies between a_h values obtained from w variation and Porod plots. Similar observations have been reported for phosphocholine microemulsions containing a co-surfactant [31].

7.4.3 Interfacial water-oil tensions and film rigidity

n-Heptane–water interfacial tensions

The *n*-heptane–water interfacial tensions for AOTGLU as a function of [NaCl] are shown in Figure 7.23 along with data for AOT. Results from both systems are identical showing that o/w tensions are not affected by the slight increase in hydrophobicity within the head group. This behaviour compares favourably with a/w tensions. Phase inversion – i.e., progression Winsor I → III → II as [NaCl] increases – occurs for the same electrolyte level, and $\gamma_{o/w,min}$ are identical at around 5×10^{-4} mN m^{-1}. This confirms that attaining a minimum in o/w tension determines the formation and position of the L_2 microemulsion region (position with respect to temperature) but does not influence on the degree of surfactant efficiency.

Interfacial tension in WII microemulsion samples

The interfacial tension $\gamma_{o/w}$ between the microemulsion stabilised by AOTGLU and excess aqueous phases was measured at 15 °C. The experiment was carried out at the maximum water solubilisation (w_{max}) and final $\gamma_{o/w}$ values were averaged from two sets – i.e., two microemulsion droplets – of measurements (carried out as described in Section 7.2.2). An identical pre-equilibrated sample was analysed by SANS to obtain the maximum droplet radius, R_{max}^{av}, and polydispersity, σ/R_{max}^{av}, at 15 °C. Data for AOTGLU and AOT (as in Chapter 6) are summarised in Table 7.7, and were used to calculate film rigidities using Equations 6.4.2 and 6.4.3 (see Section 6.4.2).

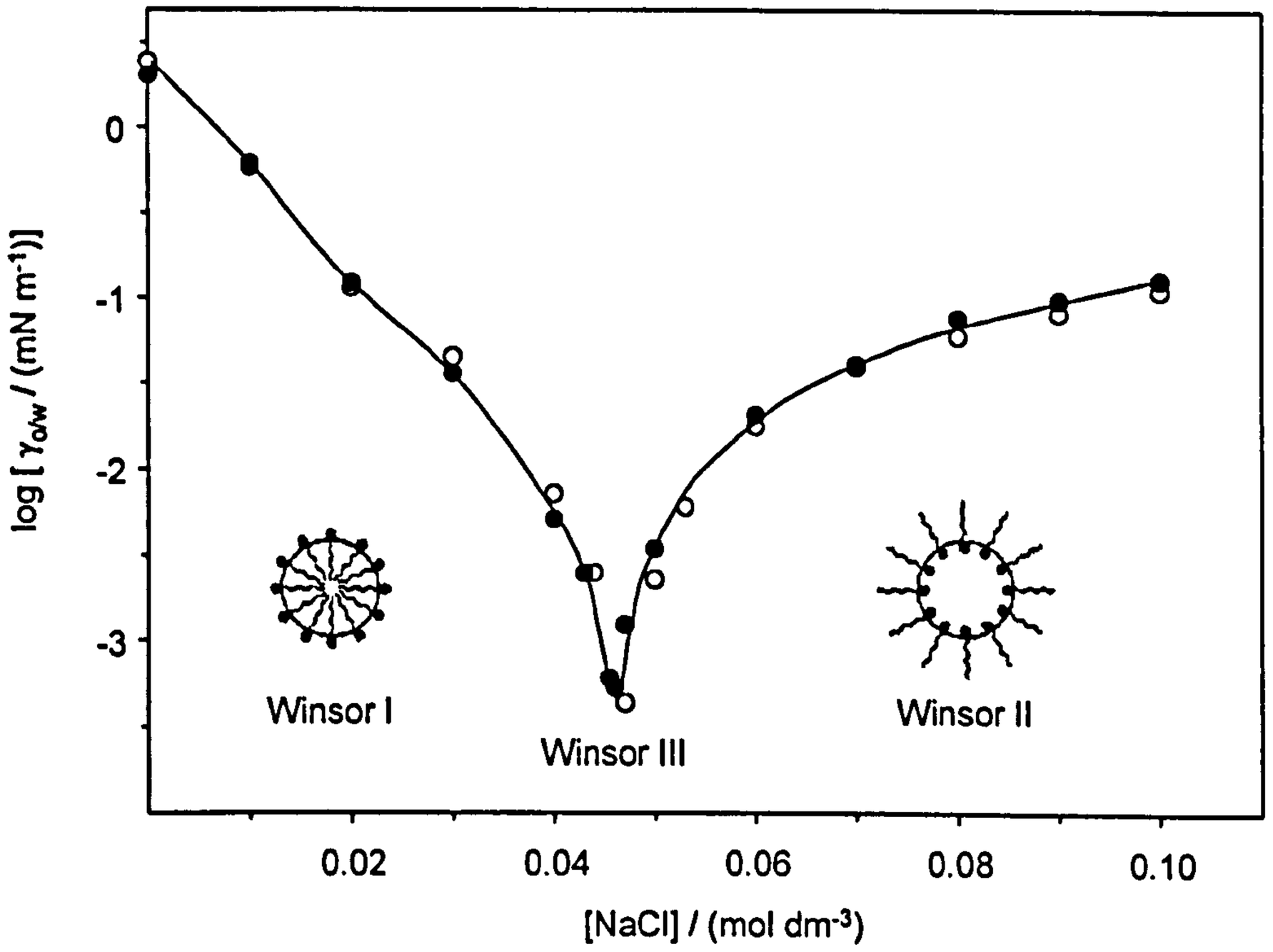

Figure 7.23 *n*-Heptane–water interfacial tensions for AOTGLU (●) and AOT① (○) surfactants as a function of NaCl concentration. Temperature = 25.0 ± 0.2 °C. In all cases the surfactant concentration is above the CMC, so aggregates are present in the heptane or the aqueous phase. The line is a guide to the eye.

Table 7.7 Film rigidity results for AOTGLU and AOT stabilised Winsor II w/o microemulsions with *n*-heptane at 15 °C [a]

Surfactant	w_{max}	ϕ_{water}	R^{av}_{max} / Å	σ/R^{av}_{max}	$\gamma_{o/w}$ / (mN m^{-1})	$(2K+\bar{K})/(k_BT)$	
						Eq.6.4.2	Eq.6.4.3
AOTGLU	42	0.0762	56.4	0.22	0.057	1.11	0.74
AOT	25	0.0453	40.6	0.23	0.062	1.08	0.58

[a] Uncertainties: w_{max}, ± 1; R^{av}_{max} ± 1 Å; σ/R^{av}_{max} ± 0.1; $\gamma_{o/w}$ ± 0.05 mN m^{-1}; $(2K+\bar{K})/k_BT$ ± 0.15.

As observed in Chapter 6 the two approaches used to calculate $(2K + \overline{K})/k_B T$ result in different rigidities. Nevertheless, as expected, both surfactant films show similar properties in terms of bending rigidity, and considering the uncertainties involved no clear effect can be detected owing to modification of the surfactant head group.

Interfacial tensions and film rigidity of microemulsions stabilised by di-C6GLU were not investigated. Due to the presence of *n*-hexanol as a co-surfactant, experiments are more complex, and considering the above data obtained for the branched compounds, no further information are expected to be found.

7.5 GENERAL CONCLUSIONS

The effect of varying head group chemistry in two model Aerosol-OT derivated surfactants – the glutaconates AOTGLU and di-C6GLU – was investigated in terms of aqueous behaviour and microemulsion formation. A common observation is the similarities in the physico-chemical properties of the glutaconate and succinate surfactants. Addition of one methylene to the head group has much less effect than in the alkyl chain. Looking back to results from Chapters 5 and 6 shows that chain structure has a more important effect both in terms of overall aqueous solubility with temperature and molecular packing. A slight improvement in terms of surfactant efficiency in microemulsion was observed with AOTGLU, and this was related to a small decrease of the surfactant overall aqueous solubility. In terms of molecular packing and microemulsion film properties, although differences are in most cases within experimental uncertainties, results follow the small change in molecular geometry, and this underlines that relation between molecular architecture and surfactant efficiency is very subtle.

7.6 REFERENCES

1. Schurtenberger, P.; Peng, Q.; Leser, M. E.; Luisi, P.-L. *J. Colloid Interface Sci.* **1993**, *156*, 43.
2. Svitova, T. F.; Smirnova, Y. P.; Pisarev, S. A.; Berezina, N. A. *Colloids Surf. A* **1995**, *98*, 107.
3. Eastoe, J.; Rogueda, P.; Howe, A. M.; Pitt, A. R.; Heenan, R. K. *Langmuir*, **1996**, *12*, 2701.
4. Eastoe, J.; Hetherington, K. J.; Dalton, J. S.; Sharpe, D.; Lu, J. R.; Heenan, R. K. *J. Colloid Interface Sci.* **1997**, *190*, 449.
5. Eastoe, J.; Hetherington, K. J.; Sharpe, D.; Steytler, D. C.; Egelhaaf, S.; Heenan, R. K. *Langmuir* **1997**, *13*, 2490.
6. Lange, H.; Jeschke, P. '*Surface monolayers*' in '*Nonionic Surfactants*', (ed. Schick, M.J.), Surfactant Science Series vol. 23, p1-44, Marcel Dekker Inc., 1987, New York.
7. Aratano, M.; Ikeda, N. '*Adsorption of Surfactants at a Gas-Liquid Interface*' in '*Structure-Performance relationships in Surfactants*', (eds. Esumi, K.; Ueno, M.), Surfactant Science Series vol 70, p112-118, Marcel Dekker Inc., 1997, New York.
8. Okano, L. T.; Quina, F. H.; El Seoud, O. A. *Langmuir*, **2000**, *16*, 3119.
9. zu Putlitz, B.; Hentze, H.-P.; Landfester, K.; Antonietti, M. *Langmuir*, **2000**, *16*, 3214.
10. Steytler, D. C.; Sargeant, D. L.; Welsh, G. E.; Robinson, B. H.; Heenan, R. K. *Langmuir*, **1996**, *12*, 5312.
11. Li, Q.; Weng, S.; Wu, J.; Zhou, N. *J. Phys. Chem. B* **1998**, *102*, 3168.
12. Kurumada, K.-I.; Nagamine, S.; Tanigaki, M. *Colloids Surf. A* **1999**, *148*, 305.
13. Khan, A.; Fontell, K.; Lindman, B. *J. Colloid Interface Sci.* **1984**, *101*, 193.
14. Eastoe, J.; Chatfield, S.; Heenan, R. K. *Langmuir* **1994**, *10*, 1650.
15. Eastoe, J.; Fragneto, G.; Robinson, B. H.; Towey, T. F.; Heenan, R. K.; Leng, F. J. *J. Chem. Soc. Faraday Trans.* **1992**, *88*, 461.
16. Capuzzi, G.; Pini, F.; Gambi, C. M. C.; Monduzzi, M.; Baglioni, P.; Teixeira, J. *Langmuir* **1997**, *13*, 6927.
17. Sheu, E. Y.; Lo Nostro, P.; Capuzzi, G.; Baglioni, P. *Langmuir* **1999**, *15*, 6671.
18. Novaki, L. P.; Pires, P. A. R.; El Seoud, O. A. *Colloid Polym. Sci.* **2000**, *278*, 143.
19. Pitzalis, P.; Angelico, R.; Soderman, O.; Monduzzi, M. *Langmuir* **2000**, *16*, 442.
20. Downer, A. Ph.D. Thesis, Bristol, 2000.
21. Eastoe, J.; Nave, S.; Downer, A.; Paul, A.; Rankin, A.; Tribe, K.; Penfold, J. *Langmuir* **2000**, *16*, 4511.
22. Aveyard, R; Binks, B. P.; Clark, S.; Mead, J. *J. Chem. Soc. Faraday Trans. 1* **1986**, *82*, 125.
23. Information of SANS data processing can be found at http://isise.rl.ac.uk/LargeScale/LOQ/loq.htm and http://www.ill.fr.
24. Wignall, G. D.; Bates, F. S. *J. Appl. Crystallogr.* **1987**, *20*, 28.
25. Kotlarchyk, M.; Chen, S.-H.; Huang, J. S.; Kim, M. W. *Phys. Rev. A.* **1984**, *29*, 2054.
26. Bumajdad, A.; Eastoe, J.; Heenan, R. K.; Lu, J. R.; Steytler, D. C.; Egelhaaf, S. U. *J. Chem. Soc., Faraday Trans.* **1998**, *94*, 2143.
27. Kunieda, H.; Shinoda, K. *J. Colloid Interface Sci.* **1979**, *70*, 577.

28. Robinson, B. H.; Toprakcioglu, C.; Dore, J. C.; Chieux, P. *J. Chem. Soc., Faraday Trans. 1* **1984**, *80*, 13.

29. Eastoe, J.; Robinson, B. H.; Steytler, D. C.; Thorn-Leeson, D. *J. Colloid Interface Sci.* **1991**, *36*, 1.

30. Eastoe, J.; Downer, D.; Paul, A.; Steytler, D. C.; Rumsey, E.; Penfold, J; Heenan, R. K. *Phys. Chem. Chem. Phys.* **2000**, *2*, 5235.

31. Eastoe, J.; Sharpe, D. *Langmuir* **1997**, *13*, 3289.

PROJECT CONCLUSIONS

Sulfosuccinate and sulfoglutaconate surfactants have been synthesised and characterised with respect to their adsorption and aggregation properties in aqueous and microemulsion systems. In particular, the effect of chain structure on these properties was investigated by varying chain length and extent of branching, and by substituting terminal methyl for phenyl groups.

The first important issue to be addressed was the level of surfactant chemical purity required for reliable studies. For these anionics, it was found essential to develop a rigorous cleaning procedure to remove all traces or organic contaminants and, more importantly, excess salts as these may alter dramatically phase boundaries in water-in-oil systems. Combining neutron reflection and tensiometry at the air-water interface provided a powerful means of assessing surfactant purity, and established how to determine reliable adsorption isotherms of such anionics from surface tension measurements.

With regard to aqueous systems and interfacial adsorption, the surfactant surface activity increases with chain length and denser adsorption layers form. Branching the hydrophobic moiety decreases the surfactant packing efficiency with an increase in molecular area of 10 – 20 $Å^2$, and, at constant head group structure, this may be predicted from simple geometry requirements. The presence of phenyl groups terminating the alkyl chains reduced even further the packing efficiency (~ 15 – 20 $Å^2$), and increased the limiting surface tension by approximately 10 – 15 mN m^{-1}. Introducing a CH_2 group in the head group resulted in minor changes relative to the effect of alkyl chains. The reduction in CMC is less than would be expected for an extra CH_2 group introduced in the tail, indicating that the hydrophobicity of the CH_2 unit is dependent upon its environment. Similarly, comparison with data for the di-C*n*SS and AOTs series indicated that interfacial packing and limiting surface tension values are mainly determined by the tail rather the head group structure.

In oil-water systems, it has been shown that alkyl side branches and/or phenyl-tipped groups are important in microemulsion formation. They increase the value of P_c, the critical packing parameter, and allow a more negatively curved interfacial film.

For the AOTs series, it was found that the single microemulsion phase domain was dictated by the surfactant aqueous solubility, so that temperature plays a crucial role. Provided the extent of branching was high enough to allow simple ternary microemulsion formation, all AOTs displayed similar efficiency as microemulsifiers, and no special effects due to the 2-ethylhexyl chains of Aerosol-OT were observed. Fitting SANS data at various *w* compositions within the single microemulsion phase domain showed that spherical water droplets stabilised by a surfactant monolayer are present. For linear chain surfactant series (di-C*n*SS and di-PhC*n*SS), a decrease in the maximum amount of solubilised water, w_{max}, was observed as the chain length increased, which is consistent with an increased affinity for the oil phase. For the branched sulfosuccinates only very small variations in film structure (film thickness, molecular areas) were found, and these could be related to surfactant chain architecture.

With regard to film rigidities, values of the bending parameters $(2K + \overline{K})$ for the interfacial films could only be determined for a limited number of surfactants. Since experiments were conducted on some isomeric branched compounds only, and resulting data were very similar, no special correlation with molecular structure could be established. Experiments on the di-C*n*SS series would have given interesting results on the dependence of the bending film rigidity on chain length. However, time limitations prevented spinning-drop experiments on these quaternary microemulsion systems.

This research work therefore highlights the importance of surfactant chain-tip chemistry. Small variations in the molecular structure have significant effects on the physico-chemical properties of air-water and oil-water interfaces, and most importantly on the surfactant ability to stabilise microemulsions.